Reduced order modelling for parametrized time-domain vibro-acoustic problems. Application to the design of structures subjected to underwater explosions

Ladya Khoun

École Doctorale de Sciences Mathématiques de Paris Centre

THÈSE DE DOCTORAT

Discipline : Mathématiques Appliquées

Présentée par **Ladya KHOUN**

Réduction de modèles pour les problèmes vibro-acoustique transitoires paramétriques - Application aux problèmes de pré-dimensionnement de structures immergées aux ondes de choc d'explosion.

Soutenue le 22 janvier 2021 devant le jury composé de :

Président :	**Céline GRANDMONT**	Directrice de recherche CNRS, Inria de Paris
Rapporteur :	**Anthony NOUY**	Professeur, École Centrale Nantes
	Simona PEROTTO	Professeur associé, Politecnico di Milano
Examinateur :	**Yvon MADAY**	Professeur, Sorbonne Université (directeur)
	Nora AÏSSIOUENE	Ingénieur de recherche, Sorbonne Université
	Mickaël ABBAS	Ingénieur - chercheur, EDF R&D
	Cédric LEBLOND	Ingénieur de recherche, Naval Group
	Olga MULA	Maître de conférence, Université Paris Dauphine
Invité :	**Jean-François SIGRIST**	HDR, Expert naval

Remerciements

La réussite de cette thèse a été possible grâce à la contribution de nombreuses personnes à qui je voudrais témoigner toute ma reconnaissance.

Tout d'abord, je souhaite remercier mon directeur de thèse Yvon MADAY, pour sa confiance, sa patience et surtout ses conseils tout au long de ces trois ans. Je remercie également mon encadrant universitaire Nora AÏSSIOUENE, pour sa grande disponibilité, ses remarques et ses suggestions judicieuses dans mon travail.

Coté encadrant industriel, je suis très reconnaissant envers Cédric LEBLOND pour sa disponibilité, ses conseils, son explication constamment sur les applications industrielles de mes travaux de recherche et surtout sa grande qualité humaine qui m'ont permis de rester motivé et serein même dans les moments difficiles. Je remercie aussi Mickaël ABBAS pour sa grande disponibilité et son efficacité qui m'ont permis d'avancer très vite les travaux d'implémentation dans *code_aster*. Un grand merci également à Yannick TAMPANGO pour les discussions fructueux sur mon travail.

Je remercie Anthony NOUY et Simona PEROTTO d'avoir accepté la charge de rapporteur et pour leurs lecteurs attentives, la qualité de leurs remarques. J'adresse mes plus sincère remerciements à Céline GRANDMONT, Olga MULA et Jean-François SIGRIST qui m'ont fait l'honneur de faire parti de mon jury.

Je suis aussi très reconnaissant envers mes deux maîtres du stage de fin d'étude, Guillaume DROUET et Ayaovi Dzifa KUDAWOO, pour la formation de programmation dans *code_aster* qui m'a été précieuse dans cette thèse. En suite, je tiens à remercier Damien MAVALEIX-MARCHESSOUX, Romain FARGERE, Bruno LEBLE et Quentin RAKOTOMALALA pour les échanges enrichissants. Un grand merci également à Stéphane PRIGENT pour son aide informatique et à tous les membres du département CESMAN qui m'ont accueilli chaleureusement.

Je remercie aussi Chetra MANG, Sodarith SENG, Ratanak DIN, Mohethrith EANG, Buthan IEA d'avoir m'hébergé à Paris pour chaque réunion d'avancement. Je n'oublie pas tous les membres d'Association des Polytechniciens Khmers (AXK) que je souhaite remercier pour les bon moments amicaux. Grâce à leur présence, je ne me sens jamais seul tout au long de mes études en France et dans cette aventure doctorale.

Mes plus profonds remerciements vont à mes parents, Khoeun TUN et Chantha YOU, qui m'ont offert, en toute circonstance, toutes les chances pour réaliser mes rêves. Je suis très reconnaissant pour les efforts qu'ils ont consacrés pour que je puisse poursuivre mes études supérieurs dans les meilleurs conditions. Je dois un grand merci également à Claudie et Daniel DUSART qui me considèrent comme leur propre fils. J'apprécie profondément leurs encouragements et surtout leurs précieuses conseils pour la vie. Grâce à eux, je me sens vraiment que j'ai aussi une famille en France. Un grand remercie également à mes grand-parents, mes oncles, mes tantes, mon frère, mes cousins et mes amis qui ont été des soutiens permanents tout au long de mes études. Une spéciale remerciement va à ma copine Kim Ay CHHUN pour les encouragements dans les moments difficiles.

Finalement, je profite de cette occasion pour exprimer ma plus profonde gratitude à toutes les personnes qui m'ont éduqué.

Résumé

Dans cette thèse, nous développons une technique de réduction de modèles pour les problèmes vibro-acoustiques transitoires paramétriques dans un code de calcul par éléments finis industriel, *code_ aster*, dans le but de traiter des problèmes de complexité industrielle. En particulier, l'approche est illustrée ici pour le problème du dimensionnement des structures immergées assujetties à une explosion sous-marine. Trois formulations du couplage vibro-acoustique sont considérées dans ce travail : formulation en déplacement structure - pression fluide $(\mathbf{u}_s, p)$, formulation en déplacement structure - potentiel de vitesse fluide $(\mathbf{u}_s, \phi)$ et formulation en déplacement structure - potentiel de déplacement fluide - pression fluide $(\mathbf{u}_s, p, \varphi)$. Pour commencer, nous implémentons dans *code_ aster* deux nouvelles formulations, les formulations en $(\mathbf{u}_s, p)$ et en $(\mathbf{u}_s, \phi)$ ainsi que les chargements provenant d'une onde de choc. Ensuite, différentes techniques de stabilisation de modèles d'ordre réduit basé sur la projection de Petrov-Galerkin sont proposées. Selon les techniques de stabilisation proposées, nous ajoutons quelques modifications dans l'algorithme glouton et POD-Glouton classiques dans la construction de la base réduite. Nous traitons aussi le cas où la dépendance en paramètre n'est pas affine. Dans ce cas, nous proposons d'utiliser la Méthode d'Interpolation Empirique (EIM) de manière purement algébrique et en boite noire pour retrouver une approximation sous la forme affine en paramètre. Ce point est nécessaire dans la construction d'un procédure hors-ligne/en-ligne efficace pour assurer la performance des modèles d'ordre réduits dans la phase en ligne. Le cas où la géométrie de la structure est considérée comme un paramètre du problème est aussi abordé dans cette thèse. Dans ce cas, nous choisissons la méthode basée sur le déplacement d'un maillage au sens d'un solide déformable (SEMMT) pour paramétrer la variabilité de la forme de la structure. Quelques études numériques et les applications industrielles sont aussi présentées pour illustrer l'efficacité des techniques de réduction de modèles proposées.

Mots clés : Méthode des éléments finis, Couplage vibro-acoustique, Interaction de la structure immergée et l'onde de choc acoustique, Explosion sous-marine, Réduction de modèles, Méthode d'Interpolation Empirique (EIM), Technique de déplacement du maillage au sens d'un solide déformable (SEMMT), Algorithme POD-Glouton.

Abstract

In this thesis, we developed a reduced order modelling framework for parametrized time-domain vibro-acoustic finite element model into an open-source industrial software, *code_ aster*, with the aim of tackling large scale industrial problems. In particular, it is illustrated here for the design of submerged structures subjected to underwater explosion. Three formulations of vibro-acoustic coupling are considered in this work: formulation in structure displacement - fluid pressure - fluid displacement potential $(\mathbf{u}_s, p, \varphi)$, in structure displacement - fluid pressure $(\mathbf{u}_s, p)$ and in structure displacement - fluid velocity potential $(\mathbf{u}_s, \phi)$. First, we implement within *code_ aster* two new formulations, in $(\mathbf{u}_s, p)$ and in $(\mathbf{u}_s, \phi)$, and the excitation induced by the primary acoustic shock wave. Next, different stabilization techniques for Petrov-Galerkin projection based model order reduction are proposed for each formulation. According to the stabilization techniques in hand, we propose to make some modifications in the classical Greedy and POD-Greedy algorithm for the construction of the reduced basis. We deal both in the case of affine and non-affine parametrized problems. In the case of non-affine parametrized problem, we propose to exploit the Empirical Interpolation Method (EIM) in a purely algebraic and black box way for recovering an approximation with an affine parameter dependence. This is one of the main ingredients for the construction of an efficient offline/online decomposition procedure to ensure the performance of the reduced order models at the online stage. We also consider the case where the geometry of the structure domain represents the parameter of the problem, for which we chose to employ the Solid Extension Mesh Moving Technique (SEMMT) for parametrizing the varying shape domain (mesh). Some numerical studies and some industrial applications are also performed in order to illustrate the efficiency of the proposed reduced order modelling framework.

Keywords: Finite element method, Vibro-acoustic coupling, Interaction of submerged structure and acoustic shock wave, Underwater explosion, Model order reduction, Empirical Interpolation Method (EIM), Solid Extension Mesh Moving Technique (SEMMT), POD-Greedy Algorithm.

Contents

Introduction

Vibro-acoustic phenomena, which is one of the fluid-structure interaction problem, are interested in noise and vibration of structure systems in presence of a compressible fluid. Many industrial problems are involved by this phenomena, for instance the noise reduction in auto motive industry, the acoustic discretion and target identification in naval industry, the design of structures for seismic loading in nuclear engineering, ...

In this thesis, we are mainly interested in a particular case of naval industry where vibro-acoustic coupling is introduced by the interaction of the submerged structure and the primary acoustic shock wave generated by an underwater explosion [40]. The prediction of the behaviour of the submerged structures under these kind of excitations is of paramount importance in the design of the hulls and appendices of submarine and in the safety justification of equipments inside the submarine. In both cases, the design of structures requires the prediction of some physical quantities over a range of values of the model parameter. In the design of the hull and the appendix of submarine, the main parameter can be for instance the mechanical properties, the geometry of the structure and the characteristics of the underwater explosion. In the safety justification of the equipments inside of the submarine, the main parameters can be the size and the material constitutive of the equipment and the characteristic of the underwater explosion.

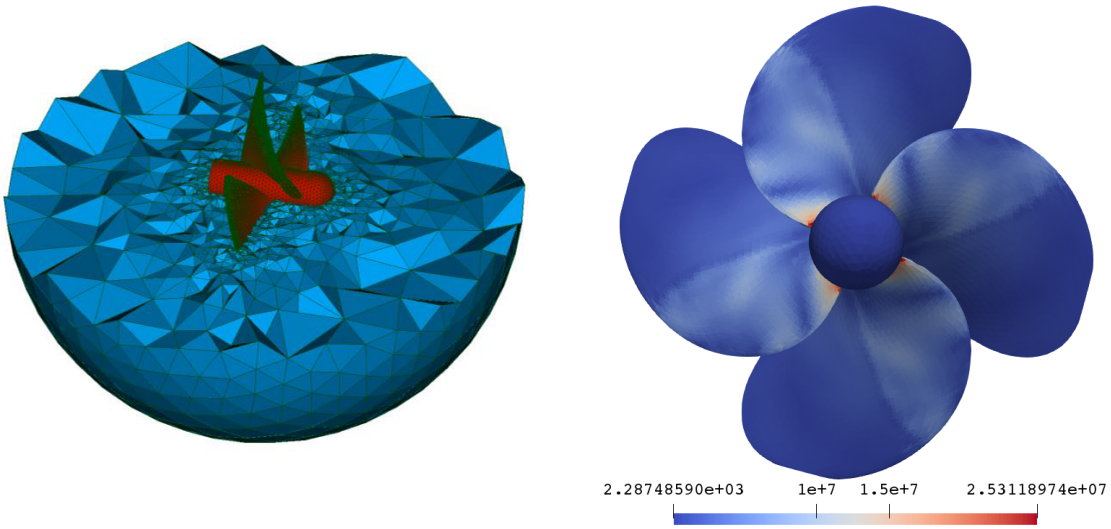

Figure 1: First example of industrial problem involved by vibro-acoustic phenomena: Computation of Von-Mises stresses in an elastic propeller under a primary shock wave of underwater explosion using a finite element model.

Some analytical and semi-analytical approaches have been proposed in [28, 82] to allow this parametric analysis. However, the proposed methods are restricted to a very simple geometry of the structure. Numerical modelling of vibro-acoustic problem is still required in order to tackle the case where the structure under consideration has a complex geometry.

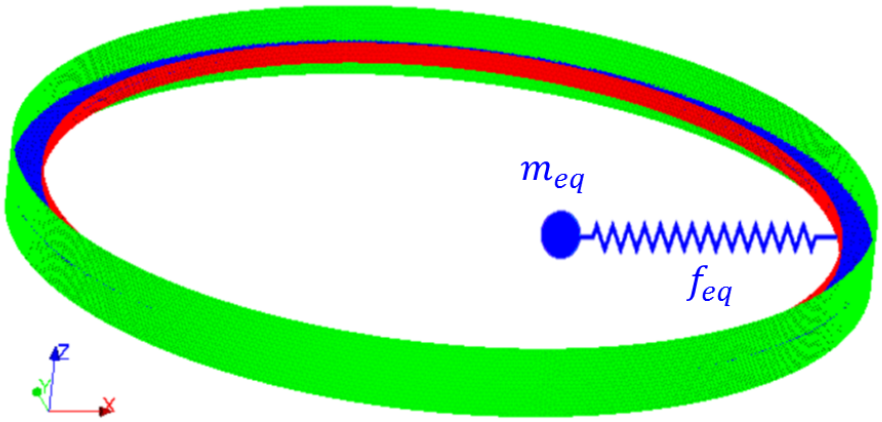

Figure 2: Second example of industrial problem involved by vibro-acoustic phenomena: Analysis of the behaviour of an equipment (modelled by a spring-mass system) inside a submarine subjected to the primary shock wave of underwater explosion with a finite element model.

In the field of numerical vibro-acoustics, one of the most commonly used numerical methods is the finite element method [51, 127]. Finite element modelling of vibro-acoustic problem is nowadays available in many industrial software. The open-source software *code_aster* [52], which is developed since the last three decades by EDF R&D, provides also this possibility.

For industrial problems, the number of degrees of freedom in the finite element models is usually huge which makes the use of these high-fidelity models unaffordable in the situation where the physical quantities of interest must be evaluated for a huge number of parameters values, as required in our problems stated above. To overcome this bottleneck, we can turn to model order reduction techniques which aim at reducing the computational complexity and the costs associated with the high-fidelity models, also called the full order model (FOM), without losing significantly the accuracy. The main idea of reduced order modelling techniques consists in replacing the full order model (FOM) by a reduced order model (ROM), featuring a much lower dimension, but still able to express accurately the physical quantities of interest of the problem under consideration.

Originally introduced in the 1970's for non-linear structural analysis in [3, 102] and analysed in [18, 110], the reduced basis method (RBM) emerged as one of the most successful reduced order modelling technique for parametrized Partial Differential Equations (PDEs). The reduced basis method has been applied in the different types of time-independent PDEs for instance in harmonic Maxwell's equations in [38], in elasticity problem [73, 123], in steady Navier-Stokes equation in [91]. For parametrized frequency domain vibro-acoustic problems, a reduced order modelling based on the reduced basis method has also been recently analysed in [83].

Objectives of thesis

In the previous context of collaboration of Naval Group and EDF R&D, the greedy algorithm for the construction of the reduced basis proposed in [83] has been implemented in the source of *code_aster*. Even though the reduced order modelling of parametrized frequency vibro-acoustic problem can be already sufficient in some applications in naval engineering, for instance in acoustic discretion under hydrodynamic loading in [85], other applications such as the design of submerged structures to transient loads induced for instance by underwater explosion, require the extension to the case of time-domain problem.

The main objective of this thesis is to propose and implement a parametrized stable reduced order model for time-domain vibro-acoustic problem in the open-source software *code_aster*. Afterwards, the application of the proposed reduced order modelling techniques into the interaction of submerged structure and underwater explosion's primary shock wave problem is our main targets.

Thesis contributions

For vibro-acoustic problems, there are various formulations depending on the choice of the variables to describe the state of the fluid and the structure. Since the formulation based on structure displacement - fluid pressure - fluid displacement potential $(\mathbf{u}_s, p, \varphi)$, which is the only formulation already implemented in *code_aster*, is not the best formulation for our problem of interest, the first work of the thesis is to implement two new formulations. The first one is the formulation based on structure displacement - fluid pressure $(\mathbf{u}_s, p)$ and the second one is the formulation based on structure displacement - fluid velocity potential $(\mathbf{u}_s, \phi)$. The loading induced by the primary shock wave of an underwater explosion is also implemented and validated during the thesis.

For time-dependent problem, one of the main challenges in model order reduction is to preserve the stability of the original full order model. The second contribution of this thesis is to propose a stabilization technique in reduced order modelling of these three finite element formulations. The stabilization technique for the formulation in $(\mathbf{u}_s, p)$ and in $(\mathbf{u}_s, \phi)$ has already been proposed in the literature [121]. For the formulation in $(\mathbf{u}_s, p, \varphi)$, a stabilization technique is proposed in this thesis. To start, we are interested in the reduced basis constructed by a greedy algorithm applied in the corresponding frequency domain, as proposed in [83]. According to the stabilization techniques in hand, some modifications in the classical greedy algorithm are then introduced. Numerical results on the study of the stability and the accuracy of the proposed reduced order models are then given.

As we observed numerically that the reduced basis based on the frequency domain solution is not accurate enough for the high frequency excitation, which is the case of our problem of interest, we propose to use alternative method for constructing an accurate reduced basis. Based on the idea of POD-Greedy Algorithm [64, 65, 107], we propose an algorithm to built a stable parametrized reduced order model for each formulation. We divide the reduced order modelling framework into two cases. First, we assume an affine parameter dependence on the

operators and the right-hand side of the finite element model. It occurs when the properties of constitutive material of the structure, such as the Young's modulus or the density, play the role of the parameter in our problem. Then, we consider the cases for which this assumption is no longer valid. For examples, these cases occur when we consider the geometry of the structure domain as the parameter of the problem. To recover the efficiency of the reduced order model, which is mainly based on the affine dependence in parameter assumption, we proposed to exploit the Empirical Interpolation Method (EIM) [17] purely in an algebraical and black box way. For the shape parametrization, we proposed to employ the mesh motions technique [115, 117]. In both cases of affine and non-affine parametrized problems, some numerical results and industrial applications are also given in order to illustrate the efficiency of the proposed reduced order modelling technique.

Organization of manuscript

This manuscript is divided into two parts.

In the first part, we give an introduction to the finite element modelling of the problem of interest. This part is divided into two chapters :

- Chapter 1 describes the finite element models of time-domain vibro-acoustic problem. Three formulations are considered : formulation in $(\mathbf{u}_s, p)$, formulation in $(\mathbf{u}_s, \phi)$ and formulation in $(\mathbf{u}_s, p, \varphi)$. These three formulations are presented in terms of strong formulation (*i.e* in form of a PDE) as well as in terms of finite element models. The main advantages and drawbacks of each formulation are also pointed out.

- In Chapter 2, we focus on the finite element modelling of the interaction of submerged structure and underwater explosion's primary acoustic shock wave problem. This chapter starts with a short introduction on the underwater explosion phenomena. Next, an overview on different formulations of the corresponding finite element model of the considered fluid-structure interaction problems is given. To validate the implementation of the loading induced by the shock wave and the formulation in $(\mathbf{u}_s, p)$ and in $(\mathbf{u}_s, \phi)$ in *code_ aster*, two study cases are presented. The first one is a 2D configuration academical problem for which a semi-analytical solution is available. The second validation case is an extension of the first study case into a 3D configuration.

In the second part, the reduced order modelling techniques are considered. This part is divided into three chapters :

- Chapter 3 gives an introduction to the reduced order modelling technique of time-domain vibro-acoustic problem. The focus in this chapter is mainly put on the stability-preserving model order reduction. Different stabilization techniques are presented for each formulation given in Chapter 1-2. We are also interested in the accuracy of reduced order models based on the reduced basis of the frequency domain. Two numerical studies are given in order to verify the stability and investigate the accuracy of the proposed reduced order models.

- Chapter 4 aims at extending the approach proposed in Chapter 3 into the case of a parametrized time-domain vibro-acoustic problem. Since we observed numerically in Chapter 3 that the reduced basis based on the frequency is not accurate enough, we propose to use an alternative way to construct the reduced basis based on the well known POD-Greedy Algorithm [64, 65, 107]. Numerical experiments on the efficiency and the application of the proposed reduced order modelling framework in the industrial problems are then investigated.

- Chapter 5 is devoted to extend the reduced order modelling framework proposed in Chapter 4 into the case where the affine parameter dependence assumption is not valid. We are also interested in the case where the geometry of the domain represents the parameter of the problem. For the construction of the parametrized mesh, the mesh motions technique [115, 117] is used. By exploiting the Empirical Interpolation Method (EIM) [17] purely in an algebraical way to obtain an approximation in form of affine parameter dependence, a framework of reduced order model is then proposed and investigated numerically. Numerical results in the industrial problems are also presented to show the efficiency of the proposed reduced order modelling framework.

Finally, conclusions arising from this work and suggestions for future works are offered in the last part of the manuscript. It is then followed by some appendices.

List of Figures

List of Algorithms

List of Tables

Part I

Finite element modelling

Chapter 1

Finite element modelling of vibro-acoustic problem

Various industrial problems, ranging from civil to naval engineering, from power nuclear to aerospace industries, are concerned by Fluid-Structure Interaction (FSI). In the most general cases, Fluid-Structure Interaction has to be taken into account in the model when a structure is in contact with a fluid. Vibro-acoustic problem is one of the fluid-structure interaction problem which is involved in noise and vibration of structure systems in presence of a compressible fluid. In the field of vibro-acoustic simulation, one of the most commonly used numerical methods is the finite element method [51, 127]. The purpose of this chapter is to give an overview on the finite element modelling of transient vibro-acoustic problems. In the first section, the modelling assumptions of vibro-acoustic coupling are presented. Depending on the choice of the variables to describe the state of the fluid, different formulations of vibro-acoustic coupling can be found in the literature (for instance, see [53, 54, 97, 113]). In this chapter, we are only interested in three different formulations: formulation in displacement structure-pressure $(\mathbf{u}_s, p)$, formulation in displacement structure-fluid velocity potential $(\mathbf{u}_s, \phi)$ and formulation in displacement structure-pressure-fluid displacement potential $(\mathbf{u}_s, p, \varphi)$. A short presentation of these three formulations is given in Section 1.2. Formulation in $(\mathbf{u}_s, p, \varphi)$ is actually the only formulation implemented in the official version of *code_ aster*. The formulation in $(\mathbf{u}_s, p)$ and in $(\mathbf{u}_s, \phi)$ are implemented in *code_ aster* [52] during the thesis.

1.1 Modelling of vibro-acoustic coupling

Vibro-acoustic systems, which are also called *structural acoustic systems* or *fluid-structure interaction for compressible fluid*, concern noise and vibration of structure systems coupled with acoustic fluids. Vibro-acoustic problem can be distinguished in two main categories:

- *interior problem* where the fluid is contained in a structure as illustrated in Figure 1.1a,
- *exterior problem* where the structure is totally submerged in an unbounded fluid domain as illustrated in Figure 1.1b.

In this section, we recall the basic equations governing the structure and the fluid of vibro-acoustic problem. Let us denote by Ω_s and Ω_f the volume occupied by the structure and the

fluid, respectively. We assume here that Ω_s and Ω_f are two regular open sets of $\mathbb{R}^d$ (with $d = 2$ or 3) and we denote by Γ the interface between the structure and the fluid (see Figure 1.1). It is considered here that the coupled system is in the context of small perturbation around its steady state, in which the fluid and the structure are at rest, and that the effects of gravity are neglected. In the following subsections, we give a review of the equations which describe the motion of structure, the motion of fluid and the coupling condition respectively in Section 1.1.1, 1.1.2 and 1.1.3.

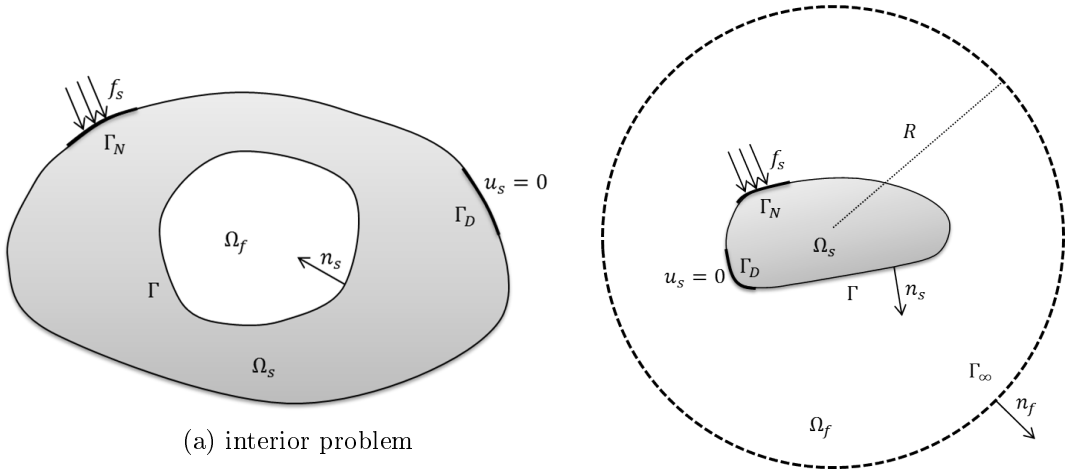

(a) interior problem

(b) exterior problem

Figure 1.1: Geometrical representation of a vibro-acoustic coupling

1.1.1 Structural equations

Under the assumption of small perturbation, the dynamic motion of the structure is classically described by [86, 113]:

$$\begin{cases} \rho_s \ddot{\mathbf{u}}_s - \text{div } \underline{\underline{\sigma_s}}(\mathbf{u}_s) = \mathbf{0} & \text{in } \Omega_s \\ \underline{\underline{\sigma_s}}(\mathbf{u}_s) \cdot \mathbf{n}_s = \mathbf{f}_s & \text{on } \Gamma_N \\ \mathbf{u}_s = \mathbf{0} & \text{on } \Gamma_D \end{cases} \tag{1.1}$$

where ρ_s is the density of the structure, $\underline{\underline{\sigma_s}}$ is Cauchy stress tensor, $\mathbf{n}_s$ is outward unit normal vector of the domain Ω_s and $\mathbf{u}_s$ is the displacement field of structure. The first equation of the system (1.1) is known as the momentum balance equation in the structure in absence of the external volume force. The second and the third equations are respectively the Neumann and Dirichlet boundary conditions.

The relation between the Cauchy stress tensor $\underline{\underline{\sigma_s}}$ and the displacement field $\mathbf{u}_s$ is modelled by the constitutive equation. First, let us recall the notion of the strain tensor which is is given by:

$$\underline{\underline{e_s}}(\mathbf{u}_s) := \frac{1}{2}[\nabla \mathbf{u}_s + \nabla \mathbf{u}_s^T + \nabla \mathbf{u}_s^T \cdot \nabla \mathbf{u}_s] \tag{1.2}$$

Under the small perturbation assumption, the second order contribution of displacement can be discarded in the displacement-strain relation (1.2), so that we have:

$$\underline{\underline{e_s}}(\mathbf{u}_s) \approx \underline{\underline{\epsilon_s}}(\mathbf{u}_s) := \frac{1}{2}[\nabla \mathbf{u}_s + \nabla \mathbf{u}_s^T] \tag{1.3}$$

where $\underline{\underline{\epsilon_s}}$ is called linearised strain tensor.

In the following, we recall the constitutive equation of a linear elastic isotropic material. In the case that the structure is supposed to be constituted by a linear elastic material, we have the relation between the Cauchy stress tensor $\underline{\underline{\sigma_s}}$ and the linearised strain tensor $\underline{\underline{\epsilon_s}}$:

$$\underline{\underline{\sigma_s}}(\mathbf{u}_s) = \underline{\underline{\underline{\mathcal{C}}}} : \underline{\underline{\epsilon_s}}(\mathbf{u}_s) \tag{1.4}$$

where $\underline{\underline{\underline{\mathcal{C}}}}$ is a symmetric tensor of order 4 which depends on the properties of the material. In addition, if the structure constitutive material is supposed to be homogeneous and isotropic which means that the material properties are constant through out the volume occupied by the structure and they do not depend on any particular direction of observation, the constitutive equation is described by the Hooke law which can be formulated in various equivalent ways, all using two material parameters. A formulation of the Hooke law can be expressed as follow:

$$\underline{\underline{\sigma_s}}(\mathbf{u}_s) = \lambda \ \mathrm{div}(\mathbf{u}_s)\underline{\underline{1}} + 2\mu\underline{\underline{\epsilon_s}}(\mathbf{u}_s) \tag{1.5}$$

where λ and μ are the Lamé coefficients and $\underline{\underline{1}}$ denotes the identity tensor. The material properties of an isotropic linear elastic can also be characterized by the Young's modulus E and the Poisson's ratio ν. The Young's modulus measures the stiffness of the material. The value of Poisson's ratio varies between -1 and 0.5. It quantifies the Poisson effect: when stretched in a given direction, the material tends to contract (when $\nu > 0$) or expand (when $\nu < 0$) in other directions. Most materials have Poisson's ratio ranging between 0 (for material which tends to be insensitive to the Poisson effect) and 0.5 (in which case the material tends to be incompressible). The relation between E and ν with the Lamé coefficients λ and μ writes:

$$E = \frac{\mu(3\lambda + 2\mu)}{\lambda + \mu}, \quad \nu = \frac{\lambda}{2(\lambda + \mu)} \tag{1.6}$$

and inversely

$$\lambda = E\frac{\nu}{(1+\nu)(1-2\nu)}, \quad \mu = E\frac{1}{2(1+\nu)} \tag{1.7}$$

For the case where the structure material has more complex constitutive law, such as anisotropic elasticity, we refer to [19, 86, 89].

1.1.2 Fluid equations

We recall that the coupled system is supposed to be in the context of small perturbation around its steady state where the fluid and the structure are both at rest. Moreover, we neglect the effects of gravity. At the first order, the momentum conservation equation and the mass conservation equation are given respectively by [97, 113]:

$$\rho_0 \ddot{\mathbf{u}}_f - \mathrm{div}\ \underline{\underline{\sigma_f}} = \mathbf{0}, \text{ in } \Omega_f \tag{1.8}$$

$$\dot{\rho}_f + \rho_0 \mathrm{div}\ \dot{\mathbf{u}}_f = 0, \text{ in } \Omega_f \tag{1.9}$$

where ρ_0 is the fluid density at the steady state, $\underline{\underline{\sigma_f}}$ is Cauchy stress tensor in the fluid, ρ_f is the fluid density and $\mathbf{u}_f$ is the displacement field of fluid.

Since the fluid is supposed to have a linear acoustic behaviour, we have the following relation between the stress tensor $\underline{\underline{\sigma_f}}$ and the pressure p:

$$\underline{\underline{\sigma_f}} = -p\underline{\underline{1}} \tag{1.10}$$

and the relation between the density ρ_f and the pressure p:

$$p = c_0^2 \rho_f \tag{1.11}$$

where c_0 is the speed of sound in the fluid.

The state of the fluid can be described by various variables. In the following, we give a review of the fluid equations in terms of pressure p, velocity potential ϕ and displacement potential φ.

Fluid equations in terms of pressure

The state of the fluid is usually described by the pressure. Taking the divergence of the momentum conservation equation (1.8) and using the relation (1.10) gives:

$$\rho_0 \text{div } \ddot{\mathbf{u}}_f + \Delta p = 0, \text{ in } \Omega_f \tag{1.12}$$

while a time derivation of the mass conversation equation (1.9) combining with the relation (1.11) provides:

$$\frac{1}{c_0^2}\ddot{p} + \rho_0 \text{div} \ddot{\mathbf{u}}_f = 0, \text{ in } \Omega_f \tag{1.13}$$

Injecting the relation $\rho_0 \text{div} \ddot{\mathbf{u}}_f = -\ddot{p}/c_0^2$, given from Equation (1.13), into Equation (1.12) yields the wave equation formulated in terms of pressure:

$$\frac{1}{c_0^2}\ddot{p} - \Delta p = 0, \text{ in } \Omega_f \tag{1.14}$$

Fluid equations in terms of velocity potential

The state of the fluid can also be described by the velocity potential ϕ which is defined by:

$$\dot{\mathbf{u}}_f = \boldsymbol{\nabla}\phi \tag{1.15}$$

Using the relations (1.10)-(1.15) in the momentum conservation equation (1.8) provides:

$$\boldsymbol{\nabla}(p + \rho_0 \dot{\phi}) = \mathbf{0}, \text{ in } \Omega_f \tag{1.16}$$

which implies the relation between the pressure and the velocity potential:

$$p = -\rho_0 \dot{\phi} \tag{1.17}$$

Using the relations (1.11)-(1.17) and the definition of velocity potential ϕ in the relation (1.15) in the mass conservation equation (1.9) yields the wave equation for ϕ:

$$\frac{1}{c_0^2}\ddot{\phi} - \Delta\phi = 0, \text{ in } \Omega_f \tag{1.18}$$

Fluid equations in terms of displacement potential and pressure

Let us describe here the state of the fluid by two variables: the pressure p and the displacement potential φ which is defined by:

$$\mathbf{u}_f = \boldsymbol{\nabla}\varphi \tag{1.19}$$

Using the relations (1.10)-(1.19) in the momentum conservation equation (1.8) provides:

$$\boldsymbol{\nabla}(p + \rho_0\ddot{\varphi}) = \mathbf{0}, \text{ in } \Omega_f \tag{1.20}$$

which gives the first the relation of the pressure and the velocity potential:

$$\frac{1}{\rho_0 c_0^2}p + \frac{1}{c_0^2}\ddot{\varphi} = 0, \text{ in } \Omega_f \tag{1.21}$$

Taking a time derivation of the mass conservation equation (1.9) and using the relations (1.11)-(1.19) gives another relation of the pressure and the velocity potential:

$$\frac{1}{c_0^2}\ddot{p} + \rho_0\Delta\ddot{\varphi} = 0, \text{ in } \Omega_f \tag{1.22}$$

1.1.3 Interface fluid-structure equations

On the fluid-structure interface Γ, we have the continuity of normal stress and the normal displacement which are given respectively by equations (1.23) and (1.24):

$$\underline{\underline{\sigma_s}}(\mathbf{u}_s)\cdot\mathbf{n}_s = -p\mathbf{n}_s \tag{1.23}$$

$$\mathbf{u}_s\cdot\mathbf{n}_s = \mathbf{u}_f\cdot\mathbf{n}_s \tag{1.24}$$

Since the fluid and the structure are supposed to be at rest initially, the continuity of normal displacement is equivalent to the continuity of normal velocity or to the continuity of normal accelerations which are given respectively by Equations (1.25) and (1.26):

$$\dot{\mathbf{u}}_s\cdot\mathbf{n}_s = \dot{\mathbf{u}}_f\cdot\mathbf{n}_s \tag{1.25}$$

$$\ddot{\mathbf{u}}_s\cdot\mathbf{n}_s = \ddot{\mathbf{u}}_f\cdot\mathbf{n}_s \tag{1.26}$$

Interface fluid-structure equations in terms of $\mathbf{u}_s$ and p

The continuity of normal stress described by Equation (1.23) is already expressed in terms of $\mathbf{u}_s$ and p. Let us now express the continuity of normal acceleration in terms of $\mathbf{u}_s$ and p. By

using the relation (1.10) in the momentum conservation equation (1.8), we have the relation between the displacement field $\mathbf{u}_f$ and the pressure p:

$$\ddot{\mathbf{u}}_f = -\frac{1}{\rho_0}\boldsymbol{\nabla} p \tag{1.27}$$

which implies that the continuity of normal acceleration described by Equation (1.26) is equivalent to:

$$\ddot{\mathbf{u}}_s \cdot \mathbf{n}_s = -\frac{1}{\rho_0}\boldsymbol{\nabla} p \cdot \mathbf{n}_s \tag{1.28}$$

Interface fluid-structure equations in terms of $\mathbf{u}_s$ and ϕ

Let us now express the fluid-structure interface equations in terms of $\mathbf{u}_s$ and ϕ. By using the relation (1.17) in (1.23) and the definition of the velocity potential (1.15) in (1.25), the interface fluid-structure equations are equivalent to:

$$\underline{\underline{\sigma_s}}(\mathbf{u}_s) \cdot \mathbf{n}_s = \rho_0 \dot{\phi} \mathbf{n}_s \tag{1.29}$$

$$\dot{\mathbf{u}}_s \cdot \mathbf{n}_s = \boldsymbol{\nabla}\phi \cdot \mathbf{n}_s \tag{1.30}$$

Interface fluid-structure equations in terms of $\mathbf{u}_s$ and φ

Let us now express the interface fluid-structure equations in terms of $\mathbf{u}_s$ and φ. By using the relation (1.21) in (1.23) and the definition of the displacement potential (1.19) in (1.26), the interface fluid-structure equations are equivalent to:

$$\underline{\underline{\sigma_s}}(\mathbf{u}_s) \cdot \mathbf{n}_s = \rho_0 \ddot{\varphi} \mathbf{n}_s \tag{1.31}$$

$$\ddot{\mathbf{u}}_s \cdot \mathbf{n}_s = \boldsymbol{\nabla}\ddot{\varphi} \cdot \mathbf{n}_s \tag{1.32}$$

1.1.4 Modelling of radiation condition for exterior problem

For exterior problem, the propagation wave in the fluid must comply with the radiation condition, also known as the Sommerfeld condition which stipulates that waves are not reflected at infinity. The radiation condition is formulated as follows:

$$\lim_{r\to\infty} r^{(d-1)/2}\left(\boldsymbol{\nabla} p \cdot \mathbf{n}_f + \frac{\dot{p}}{c_0}\right) = 0 \tag{1.33}$$

The Sommerfeld condition is stated as an asymptotic condition so that its numerical implementation with finite element-based techniques is not straightforward. To alleviate this, one can use an approximation of this radiated condition which allows for a finite element representation. In the following, we present an approximation of Sommerfeld condition proposed by the BGT method in [22] (which is named after its authors: A. Bayliss, M. Gunzburger, E. Turkel). A truncated fluid domain at finite distance is required in order to use the BGT method, as illustrated in Figure 1.1. The geometry of the enclosing volume can be varied depending on

the problem to be tackled. A specific boundary condition is then imposed on the boundary of the truncated domain. The zero-order radiation condition (BGT-0) is defined by:

$$\boldsymbol{\nabla} p \cdot \mathbf{n}_f + \frac{\rho_0}{Z_C} \dot{p} = 0 \tag{1.34}$$

where $Z_C = \rho_0 c_0$. Note that the zero-order BGT condition (1.34) is equivalent to the exact condition of radiation for plane wave propagation. The first-order radiation condition (BGT-1) is defined by:

$$\boldsymbol{\nabla} p \cdot \mathbf{n}_f + \rho_0 \left(\frac{1}{Z_C} \dot{p} + \frac{1}{Z_R} p \right) = 0 \tag{1.35}$$

where $Z_C = \rho_0 c_0$. To approximate the behaviour of a wave asymptotically by a cylindrical (spherical) wave travelling to infinity, it is usual to truncate fluid domain as a cylinder or half-cylinder (sphere or half sphere) with radius R and the value of the constant Z_R is given by $Z_R = 2\rho_0 R$ ($Z_R = \rho_0 R$). Note that the first-order BGT condition (1.35) is equivalent to the exact condition of radiation for spherical wave propagation.

For high-order BGT method, we refer to [22, 67, 94, 113]. For other modelling of radiation condition techniques, we refer to [23] for the Perfectly Matched Layer, to [78] for the Dirichlet to Neumann map and to [9, 10, 11, 29] for the Infinite Element.

1.2 Finite element models of time-domain vibro-acoustic problem

In the previous section, we see that we can use various variables to describe the state of the fluid in the coupled system. The different choices of the variable to describe the state of the fluid give different coupling formulations. In this chapter, we consider only three coupling formulations in which the state of the structure is always described by the displacement $\mathbf{u}_s$. The first one is the formulation in $(\mathbf{u}_s, p)$, where the state of the fluid is described by the pressure p. The second formulation is the formulation in $(\mathbf{u}_s, \phi)$, where the state of the fluid is described by velocity potential ϕ. The last formulation is the formulation in $(\mathbf{u}_s, p, \varphi)$ where the state of the fluid is described by two variables: the pressure p and the displacement potential φ.

1.2.1 Formulation in $(\mathbf{u}_s, p)$

The most natural vibro-acoustic coupling is in $(\mathbf{u}_s, p)$ couple since these two variables represent two physical quantities of the problem. The strong formulation in $(\mathbf{u}_s, p)$ couple of an interior

problem is given by:

$$\begin{cases} \rho_s \ddot{\mathbf{u}}_s - \text{div } \underline{\underline{\sigma_s}}(\mathbf{u}_s) = \mathbf{0} & \text{in } \Omega_s \\ \underline{\underline{\sigma_s}}(\mathbf{u}_s) = \underline{\underline{\underline{\mathcal{C}}}} : \underline{\underline{\epsilon_s}}(\mathbf{u}_s) & \text{in } \Omega_s \\ \underline{\underline{\sigma_s}}(\mathbf{u}_s) \cdot \mathbf{n}_s = \mathbf{f}_s & \text{on } \Gamma_N \\ \mathbf{u}_s = \mathbf{0} & \text{on } \Gamma_D \\ \underline{\underline{\sigma_s}}(\mathbf{u}_s) \cdot \mathbf{n}_s = -p\mathbf{n}_s & \text{on } \Gamma \\ \ddot{\mathbf{u}}_s \cdot \mathbf{n}_s = -\dfrac{1}{\rho_0} \boldsymbol{\nabla} p \cdot \mathbf{n}_s & \text{on } \Gamma \\ \dfrac{1}{c_0^2}\ddot{p} - \Delta p = 0 & \text{in } \Omega_f \end{cases} \tag{1.36}$$

We denote by $H^1_{\Gamma_D}(\Omega_s)^d := \{\mathbf{v} \in H^1(\Omega_s)^d, \mathbf{v} = 0 \text{ on } \Gamma_D\}$, T the final time of interest and we assume that $\mathbf{f}_s \in L^2(]0,T[; L^2(\Gamma_N)^d)$. The corresponding weak formulation of the problem (1.36) reads: Find $\mathbf{u}_s \in C([0,T]; H^1_{\Gamma_D}(\Omega_s)^d) \cap C^1([0,T]; L^2(\Omega_s)^d)$ and $p \in C([0,T]; H^1(\Omega_f)) \cap C^1([0,T]; L^2(\Omega_f))$ such that for all $(\delta\mathbf{u}_s, \delta p) \in H^1_{\Gamma_D}(\Omega_s)^d \times H^1(\Omega_f)$, we have:

$$\begin{aligned} &\frac{d^2}{dt^2} \int_{\Omega_s} \rho_s \mathbf{u}_s(t,\mathbf{x}) \cdot \delta\mathbf{u}_s(\mathbf{x}) d\mathbf{x} + \int_{\Omega_s} \underline{\underline{\epsilon_s}}(\delta\mathbf{u}_s(\mathbf{x})) : \underline{\underline{\underline{\mathcal{C}}}} : \underline{\underline{\epsilon_s}}(\mathbf{u}_s(t,\mathbf{x})) d\mathbf{x} \\ &\qquad + \int_{\Gamma} p(t,\mathbf{x})[\delta\mathbf{u}_s(\mathbf{x}) \cdot \mathbf{n}_s(\mathbf{x})] d\mathbf{x} = \int_{\Gamma_N} \mathbf{f}_s(t,\mathbf{x}) \cdot \delta\mathbf{u}_s(\mathbf{x}) d\mathbf{x} \\ &\frac{d^2}{dt^2} \int_{\Omega_f} \frac{1}{c_0^2} p(t,\mathbf{x}) \delta p(\mathbf{x}) d\mathbf{x} + \int_{\Omega_f} \nabla p(t,\mathbf{x}) \cdot \nabla \delta p(\mathbf{x}) d\mathbf{x} \\ &\qquad - \frac{d^2}{dt^2} \int_{\Gamma} \rho_0 [\mathbf{u}_s(t,\mathbf{x}) \cdot \mathbf{n}_s(\mathbf{x})] \delta p(\mathbf{x}) d\mathbf{x} = 0 \end{aligned} \tag{1.37}$$

The dynamic of the coupled problem spatially discretized using finite element method are then described by the set of ordinary differential equations:

$$\underbrace{\begin{bmatrix} \mathbf{M}_s & \mathbf{0} \\ -\rho_0 \mathbf{K}_c^T & \mathbf{M}_f \end{bmatrix}}_{\mathbf{M}_{up}} \begin{bmatrix} \ddot{\mathbf{U}}_s \\ \ddot{\mathbf{P}} \end{bmatrix} + \underbrace{\begin{bmatrix} \mathbf{K}_s & \mathbf{K}_c \\ \mathbf{0} & \mathbf{K}_f \end{bmatrix}}_{\mathbf{K}_{up}} \begin{bmatrix} \mathbf{U}_s \\ \mathbf{P} \end{bmatrix} = \begin{bmatrix} \mathbf{F}_s \\ \mathbf{0} \end{bmatrix} \tag{1.38}$$

where the vector $\mathbf{U}_s$ and $\mathbf{P}$ contains respectively the nodal value of structural displacement and fluid pressure. The sub matrices $\mathbf{M}_s$, $\mathbf{M}_f$, $\mathbf{K}_s$, $\mathbf{K}_f$, $\mathbf{K}_c$ and the right-hand side $\mathbf{F}$ are defined by:

$$\begin{aligned} (\mathbf{M}_s)_{ij} &= \int_{\Omega_s} \rho_s \mathbf{N}_i^s \cdot \mathbf{N}_j^s \ , \ (\mathbf{K}_s)_{ij} = \int_{\Omega_s} \underline{\underline{\epsilon_s}}(\mathbf{N}_j^s) : \underline{\underline{\underline{\mathcal{C}}}} : \underline{\underline{\epsilon_s}}(\mathbf{N}_i^s) \\ (\mathbf{M}_f)_{ij} &= \int_{\Omega_f} \frac{1}{c_0^2} N_i^f N_j^f \ , \ (\mathbf{K}_f)_{ij} = \int_{\Omega_f} \boldsymbol{\nabla} N_i^f \cdot \boldsymbol{\nabla} N_j^f \\ (\mathbf{K}_c)_{ij} &= \int_{\Gamma} N_j^f \ (\mathbf{N}_i^s \cdot \mathbf{n}_s) \ \ , \ \mathbf{F}_i = \int_{\Gamma_N} \mathbf{f}_s \cdot \mathbf{N}_i^s \end{aligned} \tag{1.39}$$

where $(\mathbf{N}_i^s)_{i=1,\cdots,n_s}$ and $(N_i^f)_{i=1,\cdots,n_f}$ are the finite element basis functions in the structural part and in the fluid part, respectively. The matrices $\mathbf{M}_s$, $\mathbf{M}_f$ are known as the mass matrices

of the structural part and the fluid part, respectively. The matrices $\mathbf{M}_s$, $\mathbf{M}_f$ are symmetric positive definite. The matrices $\mathbf{K}_s$, $\mathbf{K}_f$ are known as the stiffness matrices of the structural part and the fluid part, respectively. The matrices $\mathbf{K}_s$, $\mathbf{K}_f$ are symmetric positive semi-definite. The matrix $\mathbf{K}_c$ represents the vibro-acoustic coupling matrix.

In the case of exterior problem where the radiated condition is approximated by BGT-1 method, which imposes the boundary condition (1.35) on the truncated boundary Γ_∞, the dynamic of the coupled problem spatially discretized using finite element method are then described by the set of ordinary differential equations:

$$\underbrace{\begin{bmatrix} \mathbf{M}_s & \mathbf{0} \\ -\rho_0 \mathbf{K}_c^T & \mathbf{M}_f \end{bmatrix}}_{\mathbf{M}_{up}} \begin{bmatrix} \ddot{\mathbf{U}}_s \\ \ddot{\mathbf{P}} \end{bmatrix} + \underbrace{\begin{bmatrix} \mathbf{0} & \mathbf{0} \\ \mathbf{0} & \frac{\rho_0}{Z_C}\mathbf{Q} \end{bmatrix}}_{\mathbf{C}_{up}^{ext}} \begin{bmatrix} \dot{\mathbf{U}}_s \\ \dot{\mathbf{P}} \end{bmatrix} + \underbrace{\begin{bmatrix} \mathbf{K}_s & \mathbf{K}_c \\ \mathbf{0} & \mathbf{K}_f + \frac{\rho_0}{Z_R}\mathbf{Q} \end{bmatrix}}_{\mathbf{K}_{up}^{ext}} \begin{bmatrix} \mathbf{U}_s \\ \mathbf{P} \end{bmatrix} = \begin{bmatrix} \mathbf{F}_s \\ \mathbf{0} \end{bmatrix} \tag{1.40}$$

where the matrix $\mathbf{Q}$ is a positive semi-definite matrix, defined by:

$$\mathbf{Q}_{ij} = \int_{\Gamma_\infty} N_i^f N_j^f \tag{1.41}$$

Even though the matrices $\mathbf{M}_s$, $\mathbf{M}_f$, $\mathbf{K}_s$ and $\mathbf{K}_f$ are symmetric, the mass matrix $\mathbf{M}_{up}$ and the stiffness matrices $\mathbf{K}_{up}$, $\mathbf{K}_{up}^{ext}$ of the coupled system **are not symmetric** which is a **major disadvantage of this coupled formulation.**

1.2.2 Formulation in $(\mathbf{u}_s, \phi)$

In order to obtain a symmetric formulation, Everstine proposes in [53] an alternative by using the fluid velocity potential, defined by the relation (1.15), instead of the pressure to describe the state of the fluid part of the system. The strong formulation in $(\mathbf{u}_s, \phi)$ of an interior problem is given by:

$$\begin{cases} \rho_s \ddot{\mathbf{u}}_s - \text{div } \underline{\underline{\sigma_s}}(\mathbf{u}_s) = \mathbf{0} & \text{in } \Omega_s \\ \underline{\underline{\sigma_s}}(\mathbf{u}_s) = \underline{\underline{\underline{\underline{\mathcal{C}}}}} : \underline{\underline{\epsilon_s}}(\mathbf{u}_s) & \text{in } \Omega_s \\ \underline{\underline{\sigma_s}}(\mathbf{u}_s) \cdot \mathbf{n}_s = \mathbf{f}_s & \text{on } \Gamma_N \\ \mathbf{u}_s = \mathbf{0} & \text{on } \Gamma_D \\ \underline{\underline{\sigma_s}}(\mathbf{u}_s) \cdot \mathbf{n}_s = \rho_0 \dot{\phi} \mathbf{n}_s & \text{on } \Gamma \\ \dot{\mathbf{u}}_s \cdot \mathbf{n}_s = \boldsymbol{\nabla}\phi \cdot \mathbf{n}_s & \text{on } \Gamma \\ \dfrac{1}{c_0^2}\ddot{\phi} - \Delta\phi = 0 & \text{in } \Omega_f \end{cases} \tag{1.42}$$

We denote by $H^1_{\Gamma_D}(\Omega_s)^d := \{\mathbf{v} \in H^1(\Omega_s)^d, \mathbf{v} = 0 \text{ on } \Gamma_D\}$, T the final time of interest and we assume that $\mathbf{f}_s \in L^2(]0,T[; L^2(\Gamma_N)^d)$. The corresponding weak formulation of the problem (1.42) reads: Find $\mathbf{u}_s \in C([0,T]; H^1_{\Gamma_D}(\Omega_s)^d) \cap C^1([0,T]; L^2(\Omega_s)^d)$ and $\phi \in C([0,T]; H^1(\Omega_f)) \cap$

$C^1([0,T];L^2(\Omega_f))$ such that for all $(\delta\mathbf{u}_s, \delta\phi) \in H^1_{\Gamma_D}(\Omega_s)^d \times H^1(\Omega_f)$, we have:

$$\begin{aligned}
&\frac{d^2}{dt^2}\int_{\Omega_s}\rho_s\mathbf{u}_s(t,\mathbf{x})\cdot\delta\mathbf{u}_s(\mathbf{x})d\mathbf{x} + \int_{\Omega_s}\underline{\underline{\epsilon_s}}(\delta\mathbf{u}_s(\mathbf{x})) : \underline{\underline{\underline{\mathcal{C}}}} : \underline{\underline{\epsilon_s}}(\mathbf{u}_s(t,\mathbf{x}))d\mathbf{x} \\
&\qquad - \frac{d}{dt}\int_{\Gamma}\rho_0\phi(t,\mathbf{x})[\delta\mathbf{u}_s(\mathbf{x})\cdot\mathbf{n}_s(\mathbf{x})]d\mathbf{x} = \int_{\Gamma_N}\mathbf{f}_s(t,\mathbf{x})\cdot\delta\mathbf{u}_s(\mathbf{x})d\mathbf{x} \\
&-\frac{d^2}{dt^2}\int_{\Omega_f}\frac{\rho_0}{c_0^2}\phi(t,\mathbf{x})\delta\phi(\mathbf{x})d\mathbf{x} - \rho_0\int_{\Omega_f}\nabla\phi(t,\mathbf{x})\cdot\nabla\delta\phi(\mathbf{x})d\mathbf{x} \\
&\qquad - \frac{d}{dt}\int_{\Gamma}\rho_0[\mathbf{u}_s(t,\mathbf{x})\cdot\mathbf{n}_s(\mathbf{x})]\delta\phi(\mathbf{x})d\mathbf{x} = 0
\end{aligned} \tag{1.43}$$

The dynamic of the coupled problem spatially discretized using finite element method are then described by the set of ordinary differential equations:

$$\underbrace{\begin{bmatrix}\mathbf{M}_s & \mathbf{0}\\ \mathbf{0} & -\rho_0\mathbf{M}_f\end{bmatrix}}_{\mathbf{M}_{u\phi}}\begin{bmatrix}\ddot{\mathbf{U}}_s\\ \ddot{\mathbf{\Phi}}\end{bmatrix} + \underbrace{\begin{bmatrix}\mathbf{0} & -\rho_0\mathbf{K}_c\\ -\rho_0\mathbf{K}_c^T & \mathbf{0}\end{bmatrix}}_{\mathbf{C}_{u\phi}}\begin{bmatrix}\dot{\mathbf{U}}_s\\ \dot{\mathbf{\Phi}}\end{bmatrix} + \underbrace{\begin{bmatrix}\mathbf{K}_s & \mathbf{0}\\ \mathbf{0} & -\rho_0\mathbf{K}_f\end{bmatrix}}_{\mathbf{K}_{u\phi}}\begin{bmatrix}\mathbf{U}_s\\ \mathbf{\Phi}\end{bmatrix} = \begin{bmatrix}\mathbf{F}_s\\ \mathbf{0}\end{bmatrix} \tag{1.44}$$

where the vectors $\mathbf{U}_s$, $\mathbf{\Phi}$ contain respectively the nodal value of structural displacement and fluid velocity potential with the matrices $\mathbf{M}_s$, $\mathbf{M}_f$, $\mathbf{K}_s$, $\mathbf{K}_f$, $\mathbf{K}_c$ and the right-hand side $\mathbf{F}_s$ are defined in (1.39).

In the case of exterior problem where the radiated condition is approximated by the BGT-1 method, it leads to impose the following boundary condition on the truncated boundary Γ_∞:

$$\boldsymbol{\nabla}\phi\cdot\mathbf{n}_f + \rho_0\left(\frac{1}{Z_C}\dot{\phi} + \frac{1}{Z_R}\phi\right) = 0 \tag{1.45}$$

The dynamic of the coupled problem spatially discretized using finite element method are then described by the set of ordinary differential equations:

$$\begin{aligned}
&\underbrace{\begin{bmatrix}\mathbf{M}_s & \mathbf{0}\\ \mathbf{0} & -\rho_0\mathbf{M}_f\end{bmatrix}}_{\mathbf{M}_{u\phi}}\begin{bmatrix}\ddot{\mathbf{U}}_s\\ \ddot{\mathbf{\Phi}}\end{bmatrix} + \underbrace{\begin{bmatrix}\mathbf{0} & -\rho_0\mathbf{K}_c\\ -\rho_0\mathbf{K}_c^T & -\frac{\rho_0^2}{Z_C}\mathbf{Q}\end{bmatrix}}_{\mathbf{C}^{ext}_{u\phi}}\begin{bmatrix}\dot{\mathbf{U}}_s\\ \dot{\mathbf{\Phi}}\end{bmatrix} \\
&\qquad + \underbrace{\begin{bmatrix}\mathbf{K}_s & \mathbf{0}\\ \mathbf{0} & -\rho_0\left(\mathbf{K}_f + \frac{\rho_0}{Z_R}\mathbf{Q}\right)\end{bmatrix}}_{\mathbf{K}^{ext}_{u\phi}}\begin{bmatrix}\mathbf{U}_s\\ \mathbf{\Phi}\end{bmatrix} = \begin{bmatrix}\mathbf{F}_s\\ \mathbf{0}\end{bmatrix}
\end{aligned} \tag{1.46}$$

where the matrix $\mathbf{Q}$ is defined in (1.41).

Clearly, the coupled formulations (1.44) and (1.46) are both symmetric. Note that the value of the pressure can be obtained by computing the time derivative of velocity potential with the relation (1.17). Note that the common used time-integration schemes (such as Newmark scheme, Wilson scheme, ...) also explicitly compute the time derivative of the primal variables. In these cases, we could obtain the value of the pressure from the velocity potential through the

relationship (1.17) without additional computation cost. Even though this coupled formulation is symmetric, its **major disadvantage** is that the coupling matrix $\mathbf{K}_c$ **is a sub-matrix of the coupled damping matrix** $\mathbf{C}_{u\phi}$ so that in the modal analysis, one always needs to solve a quadratic eigenvalue problem (QEP).

1.2.3 Formulation in $(\mathbf{u}_s, p, \varphi)$

To obtain a symmetric formulation without having the coupling matrix as a sub-matrix of the coupled damping matrix, we can turn to the formulation in $(\mathbf{u}_s, p, \varphi)$. In this formulation, we use two variables to describe the state of the fluid: *the pressure* and *the displacement potential* which is defined in (1.19). The strong formulation in $(\mathbf{u}_s, p, \varphi)$ of an interior problem is given by:

$$\begin{cases} \rho_s \ddot{\mathbf{u}}_s - \text{div } \underline{\underline{\sigma_s}}(\mathbf{u}_s) = \mathbf{0} & \text{in } \Omega_s \\ \underline{\underline{\sigma_s}}(\mathbf{u}_s) = \underline{\underline{\underline{\underline{\mathcal{C}}}}} : \underline{\underline{\epsilon_s}}(\mathbf{u}_s) & \text{in } \Omega_s \\ \underline{\underline{\sigma_s}}(\mathbf{u}_s) \cdot \mathbf{n}_s = \mathbf{f}_s & \text{on } \Gamma_N \\ \mathbf{u}_s = \mathbf{0} & \text{on } \Gamma_D \\ \underline{\underline{\sigma_s}}(\mathbf{u}_s) \cdot \mathbf{n}_s = \rho_0 \ddot{\varphi} \mathbf{n}_s & \text{on } \Gamma \\ \ddot{\mathbf{u}}_s \cdot \mathbf{n}_s = \boldsymbol{\nabla} \ddot{\varphi} \cdot \mathbf{n}_s & \text{on } \Gamma \\ \dfrac{1}{\rho_0 c_0^2} p + \dfrac{1}{c_0^2} \ddot{\varphi} = 0 & \text{in } \Omega_f \\ \dfrac{1}{c_0^2} \ddot{p} + \rho_0 \Delta \ddot{\varphi} = 0 & \text{in } \Omega_f \end{cases} \tag{1.47}$$

We denote by $H^1_{\Gamma_D}(\Omega_s)^d := \{\mathbf{v} \in H^1(\Omega_s)^d, \mathbf{v} = 0 \text{ on } \Gamma_D\}$, T the final time of interest and we assume that $\mathbf{f}_s \in L^2(]0,T[; L^2(\Gamma_N)^d)$. The corresponding weak formulation of the problem (1.47) reads: Find $\mathbf{u}_s \in C([0,T]; H^1_{\Gamma_D}(\Omega_s)^d) \cap C^1([0,T]; L^2(\Omega_s)^d)$, $p \in C^1([0,T]; L^2(\Omega_f))$ and $\varphi \in C^1([0,T]; H^1(\Omega_f))$ such that for all $(\delta\mathbf{u}_s, \delta p, \delta\varphi) \in H^1_{\Gamma_D}(\Omega_s)^d \times L^2(\Omega_f) \times H^1(\Omega_f)$, we have:

$$\begin{aligned} \frac{d^2}{dt^2} \int_{\Omega_s} \rho_s \mathbf{u}_s(t,\mathbf{x}) \cdot \delta\mathbf{u}_s(\mathbf{x}) d\mathbf{x} + \int_{\Omega_s} \underline{\underline{\epsilon_s}}(\delta\mathbf{u}_s(\mathbf{x})) : \underline{\underline{\underline{\underline{\mathcal{C}}}}} : \underline{\underline{\epsilon_s}}(\mathbf{u}_s(t,\mathbf{x})) d\mathbf{x} \\ - \frac{d^2}{dt^2} \int_\Gamma \rho_0 \varphi(t,\mathbf{x}) [\delta\mathbf{u}_s(\mathbf{x}) \cdot \mathbf{n}_s(\mathbf{x})] d\mathbf{x} \\ = \int_{\Gamma_N} \mathbf{f}_s(t,\mathbf{x}) \cdot \delta\mathbf{u}_s(\mathbf{x}) d\mathbf{x} \\ \frac{1}{\rho_0 c_0^2} \int_{\Omega_f} p(t,\mathbf{x}) \delta p(\mathbf{x}) d\mathbf{x} + \frac{d^2}{dt^2} \int_{\Omega_f} \frac{1}{c_0^2} \varphi(t,\mathbf{x}) \delta p(\mathbf{x}) d\mathbf{x} = 0 \\ - \frac{d^2}{dt^2} \int_{\Omega_f} \rho_0 \nabla\varphi(t,\mathbf{x}) \cdot \nabla\delta\varphi(\mathbf{x}) d\mathbf{x} + \frac{d^2}{dt^2} \int_{\Omega_f} \frac{1}{c_0^2} p(t,\mathbf{x}) \delta\varphi(\mathbf{x}) d\mathbf{x} \\ - \frac{d^2}{dt^2} \int_\Gamma \rho_0 [\mathbf{u}_s(t,\mathbf{x}) \cdot \mathbf{n}_s(\mathbf{x})] \delta\varphi(\mathbf{x}) d\mathbf{x} = 0 \end{aligned} \tag{1.48}$$

The dynamic of the coupled problem spatially discretized using finite element method are

then described by the set of ordinary differential equations:

$$\underbrace{\begin{bmatrix} \mathbf{M}_s & \mathbf{0} & -\rho_0\mathbf{K}_c \\ \mathbf{0} & \mathbf{0} & \mathbf{M}_f \\ -\rho_0\mathbf{K}_c^T & \mathbf{M}_f & -\rho_0\mathbf{K}_f \end{bmatrix}}_{\mathbf{M}_{up\varphi}} \begin{bmatrix} \ddot{\mathbf{U}}_s \\ \ddot{\mathbf{P}} \\ \ddot{\boldsymbol{\varphi}} \end{bmatrix} + \underbrace{\begin{bmatrix} \mathbf{K}_s & \mathbf{0} & \mathbf{0} \\ \mathbf{0} & \frac{1}{\rho_0}\mathbf{M}_f & \mathbf{0} \\ \mathbf{0} & \mathbf{0} & \mathbf{0} \end{bmatrix}}_{\mathbf{K}_{up\varphi}} \begin{bmatrix} \mathbf{U}_s \\ \mathbf{P} \\ \boldsymbol{\varphi} \end{bmatrix} = \begin{bmatrix} \mathbf{F}_s \\ \mathbf{0} \\ \mathbf{0} \end{bmatrix} \tag{1.49}$$

where the vectors $\mathbf{U}_s$, $\mathbf{P}$ and $\boldsymbol{\varphi}$ contain respectively the nodal value of structural displacement, fluid pressure and fluid velocity potential with the matrices $\mathbf{M}_s$, $\mathbf{M}_f$, $\mathbf{K}_s$, $\mathbf{K}_f$, $\mathbf{K}_c$ and the right-hand side $\mathbf{F}_s$ are defined in (1.39).

Using the relation (1.21) in the approximated radiated condition of the BGT-1 condition (1.35), we obtain an equivalent boundary condition on Γ_∞:

$$\boldsymbol{\nabla}\ddot{\varphi}\cdot\mathbf{n}_f + \rho_0\left(\frac{1}{Z_C}\dddot{\varphi} + \frac{1}{Z_R}\ddot{\varphi}\right) = 0 \tag{1.50}$$

The use of the boundary condition (1.50) implies that the dynamic of the coupled problem spatially discretized using finite element method for exterior problem are described by the set of ordinary differential equations:

$$\underbrace{\begin{bmatrix} \mathbf{0} & \mathbf{0} & \mathbf{0} \\ \mathbf{0} & \mathbf{0} & \mathbf{0} \\ \mathbf{0} & \mathbf{0} & -\frac{\rho_0^2}{Z_C}\mathbf{Q} \end{bmatrix}}_{\mathbf{I}^{ext}_{up\varphi}} \begin{bmatrix} \dddot{\mathbf{U}}_s \\ \dddot{\mathbf{P}} \\ \dddot{\boldsymbol{\varphi}} \end{bmatrix} + \underbrace{\begin{bmatrix} \mathbf{M}_s & \mathbf{0} & -\rho_0\mathbf{K}_c \\ \mathbf{0} & \mathbf{0} & \mathbf{M}_f \\ -\rho_0\mathbf{K}_c^T & \mathbf{M}_f & -\rho_0\mathbf{K}_f - \frac{\rho_0^2}{Z_R}\mathbf{Q} \end{bmatrix}}_{\mathbf{M}^{ext}_{up\varphi}} \begin{bmatrix} \ddot{\mathbf{U}}_s \\ \ddot{\mathbf{P}} \\ \ddot{\boldsymbol{\varphi}} \end{bmatrix}$$

$$+ \underbrace{\begin{bmatrix} \mathbf{K}_s & \mathbf{0} & \mathbf{0} \\ \mathbf{0} & \frac{1}{\rho_0}\mathbf{M}_f & \mathbf{0} \\ \mathbf{0} & \mathbf{0} & \mathbf{0} \end{bmatrix}}_{\mathbf{K}_{up\varphi}} \begin{bmatrix} \mathbf{U}_s \\ \mathbf{P} \\ \boldsymbol{\varphi} \end{bmatrix} = \begin{bmatrix} \mathbf{F}_s \\ \mathbf{0} \\ \mathbf{0} \end{bmatrix} \tag{1.51}$$

where the matrix $\mathbf{Q}$ is defined in (1.41).

Clearly, the coupled formulations (1.49) and (1.51) are both symmetric. However, in case of exterior problem using the boundary condition of BGT-1 method, the coupled formulation (1.51) is of order 3. To obtain a system of order 2 in this formulation, we remark that the relation (1.21) implies that:

$$\begin{bmatrix} \mathbf{0} & \mathbf{0} & \mathbf{0} \\ \mathbf{0} & \mathbf{0} & \mathbf{0} \\ \mathbf{0} & \mathbf{0} & -\frac{\rho_0^2}{Z_C}\mathbf{Q} \end{bmatrix} \begin{bmatrix} \dddot{\mathbf{U}}_s \\ \dddot{\mathbf{P}} \\ \dddot{\boldsymbol{\varphi}} \end{bmatrix} = \begin{bmatrix} \mathbf{0} & \mathbf{0} & \mathbf{0} \\ \mathbf{0} & \mathbf{0} & \mathbf{0} \\ \mathbf{0} & \frac{\rho_0}{Z_C}\mathbf{Q} & \mathbf{0} \end{bmatrix} \begin{bmatrix} \dot{\mathbf{U}}_s \\ \dot{\mathbf{P}} \\ \dot{\boldsymbol{\varphi}} \end{bmatrix} \tag{1.52}$$

so that the system (1.51) is equivalent to:

$$\underbrace{\begin{bmatrix} \mathbf{M}_s & \mathbf{0} & -\rho_0\mathbf{K}_c \\ \mathbf{0} & \mathbf{0} & \mathbf{M}_f \\ -\rho_0\mathbf{K}_c^T & \mathbf{M}_f & -\rho_0\mathbf{K}_f - \frac{\rho_0^2}{Z_R}\mathbf{Q} \end{bmatrix}}_{\mathbf{M}_{up\varphi}^{ext}} \begin{bmatrix} \ddot{\mathbf{U}}_s \\ \ddot{\mathbf{P}} \\ \ddot{\boldsymbol{\varphi}} \end{bmatrix} + \underbrace{\begin{bmatrix} \mathbf{0} & \mathbf{0} & \mathbf{0} \\ \mathbf{0} & \mathbf{0} & \mathbf{0} \\ \mathbf{0} & \frac{\rho_0}{Z_C}\mathbf{Q} & \mathbf{0} \end{bmatrix}}_{\mathbf{C}_{up\varphi}^{ext}} \begin{bmatrix} \dot{\mathbf{U}}_s \\ \dot{\mathbf{P}} \\ \dot{\boldsymbol{\varphi}} \end{bmatrix}$$

$$+ \underbrace{\begin{bmatrix} \mathbf{K}_s & \mathbf{0} & \mathbf{0} \\ \mathbf{0} & \frac{1}{\rho_0}\mathbf{M}_f & \mathbf{0} \\ \mathbf{0} & \mathbf{0} & \mathbf{0} \end{bmatrix}}_{\mathbf{K}_{up\varphi}} \begin{bmatrix} \mathbf{U}_s \\ \mathbf{P} \\ \boldsymbol{\varphi} \end{bmatrix} = \begin{bmatrix} \mathbf{F}_s \\ \mathbf{0} \\ \mathbf{0} \end{bmatrix} \tag{1.53}$$

Since the formulation in $(\mathbf{u}_s, p, \varphi)$ uses two variables to describe the state of the fluid, the number of degrees of freedom in this formulation **is larger than** the one in the formulation in $(\mathbf{u}_s, p)$ and in $(\mathbf{u}_s, \phi)$ for the same mesh and the more we have the number of nodes in the fluid part, the more it becomes significant. Furthermore, note that the damping matrix $\mathbf{C}_{up\varphi}^{ext}$ of the formulation (1.53) is not symmetric. Therefore, this formulation is clearly not the best formulation to employ for the simulation of a transient exterior problem compared to the formulation in $(\mathbf{u}_s, p)$ and in $(\mathbf{u}_s, \phi)$. However, since the coupled mass matrix $\mathbf{M}_{up\varphi}$ and the coupled stiffness matrix $\mathbf{M}_{up\varphi}$ are both symmetric and the coupling matrix $\mathbf{K}_c$ is not a sub-matrix of the coupled damping matrix as the formulation in $(\mathbf{u}_s, \phi)$, the formulation in $(\mathbf{u}_s, p, \varphi)$ is **more suitable for the modal analysis** of a interior problem than the formulation in $(\mathbf{u}_s, p)$ and in $(\mathbf{u}_s, \phi)$.

1.3 Conclusions

In this chapter, a short review on the modelling of vibro-acoustic coupling is presented. Depending on the choice of the variables representing the state of fluid, several formulations can be found in literature. Three formulations of the transient vibro-acoustic problem have been given in terms of strong formulation in PDE as well as in terms of finite element models. In order to approximate the radiation condition for exterior problems, we propose to use the BGT-1 method which requires a truncated fluid domain and use a specific boundary condition. For the formulation in $(\mathbf{u}_s, p)$, the system of second-order ordinary differential equations of finite element model is always non-symmetric. While modelling the radiation condition by BGT-1 method, the formulation in $(\mathbf{u}_s, \phi)$ is still symmetric. For the formulation in $(\mathbf{u}_s, p, \varphi)$, the approximated radiation condition of BGT-1 method implies that the finite element model can be described by a symmetric system of third-order ordinary differential equations or by a non-symmetric second order system.

Even though the three formulations presented in this chapter are equivalent, each formulation has its advantages and drawbacks. The main drawback of the formulation in $(\mathbf{u}_s, p)$ is that it results in non-symmetric system. Contrary to the formulation in $(\mathbf{u}_s, p)$, the symmetric property represents a major advantage of the formulation in $(\mathbf{u}_s, \phi)$ while the presence of the vibro-acoustic coupling matrix in the global damping matrix is the major drawback of this formulation, especially for modal analysis. The symmetry of the global mass and stiffness matrix of coupled system and the absence of the vibro-acoustic coupling matrix in the global

damping matrix are the major advantages of the formulation in $(\mathbf{u}_s, p, \varphi)$ for modal analysis of an interior problem. On the contrary, its main drawback is that using two variables to describe the state fluid leads to a larger number of degrees of freedom compared to the formulation in $(\mathbf{u}_s, p)$ and $(\mathbf{u}_s, \phi)$.

In addition to the advantages and drawbacks mentioned here, we will see in the next chapter that the choice of the variables representing the state of fluid has a non-negligible impact in finite element modelling of submerged structure and shock wave problem (see Remark 2.4.1) as well as in reduced order modelling in Chapter 3.

Chapter 2

Finite element modelling of interaction of submerged structure and shock wave problem

The survivability of naval ships and submarines is of paramount importance to those who design, build and sail them. Underwater explosions, produced by the detonation of a submerged high explosive device, clearly represents a serious threat to that survivability. Hence, underwater explosion is a major phenomena to be taken into account in the design of submerged structures.

Under the hypothesis that the explosion is far enough from the submerged structure of interest, the loading produced by the explosion can be modelled without taking into account the presence of the structure. Conventionally, the underwater explosion can be viewed as the generation of acoustic shock waves which propagate at the sound speed in the fluid, and the fluid flows caused by the dynamic interaction of the detonation product gases and the surrounding water. As a consequence, the study of the behaviour of a submerged structure submitted to an underwater explosion can be split in two main parts. The first part consists of the interaction of submerged structure and acoustic shock waves problem. The second part is the case of loading induced by the fluid flows created by gases bubbles.

In this thesis, we are only interested in the interaction of submerged structure and shock waves problem under the hypothesis that the explosion is far enough from the submerged structure and the free surface of the fluid. The goal of this chapter is to give a presentation of the finite element modelling of interaction of submerged structure and shock wave problems. This chapter is organized as follows. We begin by a short presentation of underwater explosion phenomena in the first section. The modelling of primary acoustic shock wave of an underwater explosion is then given in Section 2.2. In Section 2.3, the modelling assumptions of interaction of submerged structure and shock wave is presented. As in the classical vibro-acoustic coupling, different choices of the variables for describing the state in the fluid yield different coupling formulations of finite element model. In this chapter, we are interested in four formulations: formulation in displacement structure-scattered velocity potential $(\mathbf{u}_s, \phi^{sca})$, in displacement structure-radiated velocity potential $(\mathbf{u}_s, \phi^{rad})$, in displacement structure-radiated pressure $(\mathbf{u}_s, p^{rad})$ and in displacement structure-radiated pressure-radiated displacement potential $(\mathbf{u}_s, p^{rad}, \varphi^{rad})$. The presentation of these four formulations is given in the Section 2.4.

The loadings of shock wave have been implemented in *code_aster* during the thesis. In Section 2.5, we propose a numerical validation of our implementation with two test cases. The first validation case is an academic case in a 2D configuration where a semi-analytical solution is available. The second validation case is an extension of the 2D configuration used in first validation case, into a 3D configuration.

2.1 Underwater explosion

From the point of view of damage to submerged structures, the underwater explosion can be modelled by the generation of acoustic waves together with the fluid flows produced by the dynamic interaction between the explosion gas bubbles and the surrounding water. The shock wave propagation phase occurs in millisecond-order timescales, while the bubble expansion and contraction phase occurs in second-order timescales. Such a large difference (about a three order of magnitude) in the time scales between these two phenomena does pose challenges for the computational methods which intend to include both phases. The sequence of physical effects of an underwater explosion is usually illustrated by the classical figure 2.1 of Snay (1956) [114].

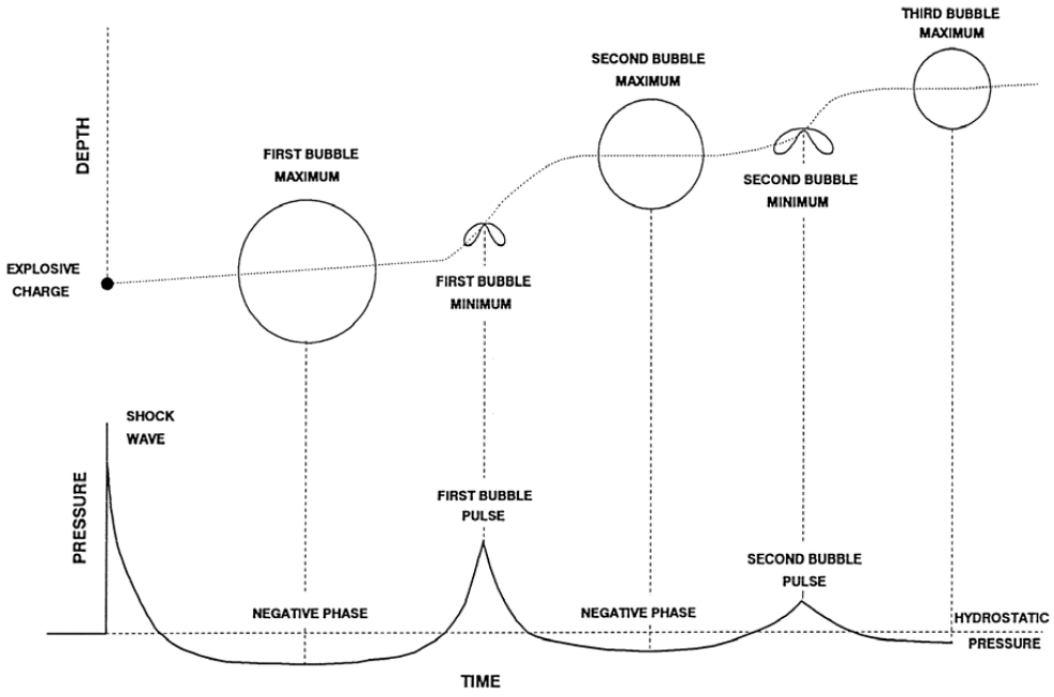

Figure 2.1: The sequence of physic effects of an underwater explosion, sourced from [42]

2.1.1 Primary acoustic shock wave

The primary acoustic shock wave, generated when the detonation wave within the explosive reaches the water-explosive interface, travels out though the water at a very high speed as a spherical wave. The very high pressures associated with the shock wave can cause considerable damage on any submerged structure which is not strong enough to resist this loading. About

50 % of the initial chemical energy of the explosive is transmitted to the fluid in this initial shock wave. At first, the speed of the shock wave is approximately about ≈ 5000 m/s. The speed of the shock wave decreases rapidly and stabilizes at the speed of the sound in the fluid at $c_0 \approx 1500$ m/s (as shown in Figure 2.2) after a very short distance of about 20 times the charge radius.

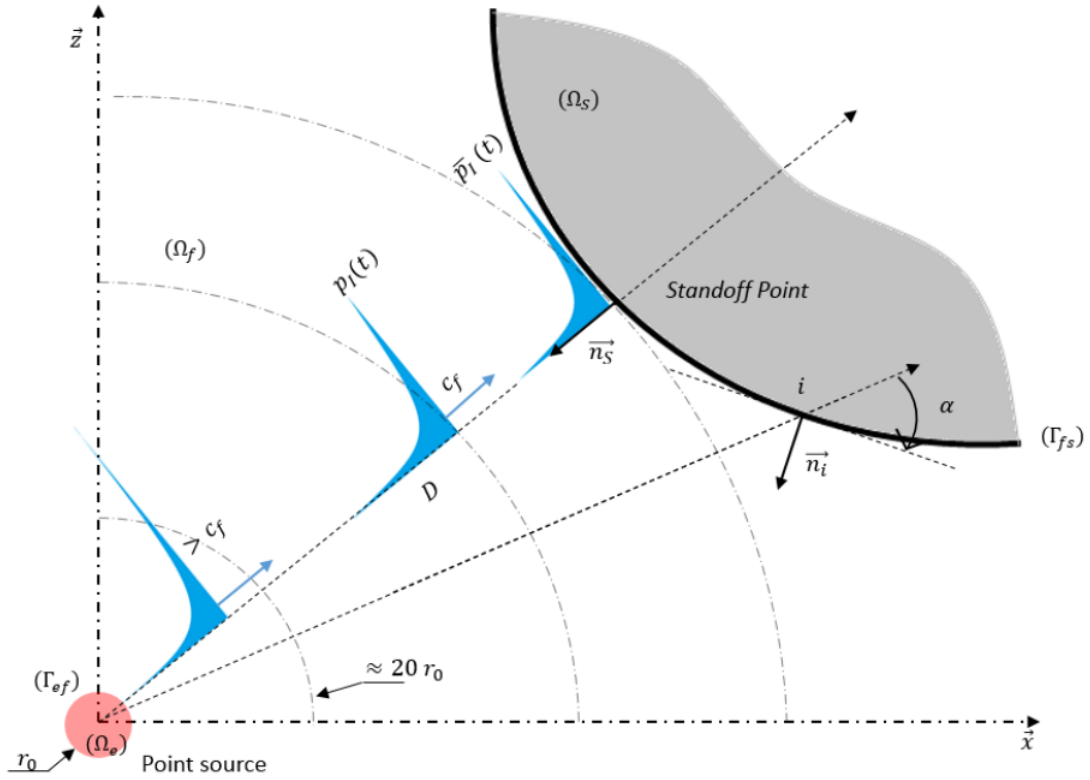

Figure 2.2: Geometric representation of the propagation of underwater explosion's shock waves, source from [28].

As schematically illustrated in Figure 2.1, at a target point in the fluid located at a distance greater than 20 times the charge radius, the pressure increases quasi-instantly to a peak value P_m and then decreases rapidly which can be expressed at a first approximation by:

$$p(t) = P_m e^{-t/T_c} \tag{2.1}$$

where $t = 0$ is the arrival time of the shock wave at the target point, T_c denotes the constant that describes the exponential decay. The variation of constant P_m and T_c depends on the kind of the explosive material and the distance D from the charge. In case of the explosive material is Trinitrotoluene (TNT), it has been shown in [108] that the variation is well described by the relations:

$$P_m = 52.16 \cdot 10^6 \left(\frac{W^{1/3}}{D} \right)^{1.13} \tag{2.2}$$

$$T_c = 96.5 \cdot 10^{-6} \left(W^{1/3}\right) \left(\frac{W^{1/3}}{D}\right)^{-0.22} \tag{2.3}$$

where P_m is in Pascal, T_c is in second, W is the mass of TNT in kilogramme and the distance D is in meters.

When the shock wave arrives at a target point in the fluid, the fluid particle at that point is subjected simultaneously to a flow with the velocity $v_f(t)$ at direction of wave propagation. In case of plane waves, the relation between the pressure $p(t)$ and the velocity $v_f(t)$ is given by:

$$v_f(t) = \frac{p(t)}{\rho_0 c_0} \tag{2.4}$$

where ρ_0 is the fluid density and c_0 is the sound speed in the fluid. The relation (2.4) is validated only for plane waves, so it can be used only if the submerged structure is sufficiently far from the explosion. Taking the spherical nature of the shock waves into account, the relation between the pressure $p(t)$ and the velocity $v_f(t)$ is given by:

$$v_f(t) = \frac{p(t)}{\rho_0 c_0} + \frac{1}{\rho_0 D} \int_0^t p(\tau) d\tau \tag{2.5}$$

The representation of the primary shock wave of an underwater explosion using the relations (2.1) and (2.5) can be applied for any size of explosion, from a few grams to a nuclear weapon, detonated at any depth in the water. It is however accurate only for $0 < t < T_c$. The formulas of pressure and velocity profiles of an underwater shock wave, which can be validated until $7T_c$, will be given in Section 2.2.

2.1.2 Dynamic behaviour of bubble

The subsequence development of the bubble and its interaction with the surrounding water create other phenomena which can also inflict considerable damage on the submerged structure, particularly if the bubble is formed nearby. After emission of the primary shock wave, the pressure in the gas bubbles is significantly reduced. It is however still significantly higher than external hydrostatic pressure. This causes the bubble to expand rapidly. The pressure in the bubble decreases as the bubble volume increases. Because of the inertia of the outward flowing fluid, the expansion persists beyond the point at which the pressure in the gas bubble and the hydrostatic pressure in the surrounding fluid are balanced. According to Cole [40], the maximum radius of the bubble of the first phase of expansion depends on the mass of explosive material and the depth of the explosion. When the explosive material is Trinitrotoluene (TNT), it is given experimentally by the following relation [40]:

$$R_{max} = J \left(\frac{W}{H + 10}\right)^{1/3} \tag{2.6}$$

where the radius R_{max} and the depth of explosion H are in meter and W is the mass of TNT in kilogramme. According to Swift (1947) [116], the value of constant J is approximately ≈ 3.36 m$^{4/3}$kg$^{-1/3}$. According to Swisdak (1978) [118], the value of constant J is approximately ≈ 3.50 m$^{4/3}$kg$^{-1/3}$.

When the expansion is finally stops, the pressure in the bubble is less than the hydrostatic pressure which causes the bubble to begin contracting. The duration T, since the beginning of explosion until the bubble reaches its minimum radius, depends also on the mass of explosive material and on the depth of the explosion. In case of the explosive material is TNT (Trinitrotoluene), it can be approximated experimentally by the following relation [40]:

$$T = K\frac{W^{1/3}}{(H+10)^{5/6}} \tag{2.7}$$

where the constant K is approximately ≈ 2.11 $\mathrm{sm}^{5/6}\mathrm{kg}^{-1/3}$ according to [118] and [116]. As in the expansion phase, the internal pressure of the bubble is much higher than the surrounding hydrostatic pressure when the bubble reaches its minimum radius. A new acoustic shock wave is then generated and a new cycle of expansion and contraction is then set to begin. The peak value of pressure of the new shock wave is about between 10 % to 15 % of the primary shock wave. However, this new shock wave can also inflict damage, with the same order as the primary shock wave, to any submerged structure because the decreasing is slower than the primary shock wave. Since a new shock wave is generated and travels out through the surrounding fluid at each phase of expansion, the bubble loses progressively its energy. The amplitude of pulsation decreases at each iteration. The sequence of expansion-contraction can repeat a numerous times. As an example, it has been observed experimentally 12 sequences of expansion-contraction in [75].

2.2 Modelling of primary acoustic shock wave of an underwater explosion

The pressure profiles of shock waves characterised by a simple exponential decay by the relation (2.1) is a good approximation only for $t \leq T_c$. In fact, the decay of pressure is not as fast as in the relation (2.1) for $t > T_c$. Now, let us put the focus on the modelling of primary acoustic shock of underwater explosion which can be validated for times much longer than the expression given in Section 2.1.1. According to the dimensionless analysis in [55, 106], the pressure profile of an underwater explosion shock wave at the distance r from the charge is given by the following relation:

$$P(t) = P_c\left[\frac{a_c}{r}\right]^{1+A}\mathcal{F}\left(\left[\frac{a_c}{r}\right]^{B}\frac{v_c}{a_c}t\right) \tag{2.8}$$

where a_c is the charge radius and the constant P_c, v_c, A and B depend on the kind of explosive materials. For the case of TNT (Trinitrotoluene) explosive material, these constants are given by:

$$P_c = 1.67 \text{ GPa}, v_c = 1010 \text{ m/s}, A = 0.18, B = 0.185 \tag{2.9}$$

according to [106], and

$$P_c = 1.42 \text{ GPa}, v_c = 992 \text{ m/s}, A = 0.13, B = 0.18 \tag{2.10}$$

according to [40] and the function $\mathcal{F}$ is a double exponential decay:

$$\mathcal{F}(t) = 0.8251e^{-1.338t} + 0.1749e^{-0.1805t}, \ t \leq 7 \tag{2.11}$$

For a given mass of explosive material M_{exp}, the charge radius a_c can be approximately by $a_c \approx \left(\frac{M_{exp}}{4\pi\rho_{exp}}\right)^{1/3}$ where ρ_{exp} is is mass density of the explosive material. For the case of TNT, the mass density is approximately given by $\rho_{tnt} \approx 1.52 \cdot 10^3$ kg/m^3.

At a distance greater than 20 times the charge radius, the shock wave propagates with the speed of sound in the fluid c_0. So, for $r > R_l$ we have:

$$p(t,r) = P_c \left[\frac{a_c}{r}\right]^{1+A} \mathcal{F}\left(\left[\frac{a_c}{r}\right]^B \frac{\tau}{T_c}\right) H(\tau), \quad \tau = t - (r - R_l)/c_0 \tag{2.12}$$

where H is Heaviside function and we denote by $R_l = 20a_c$ with a_c is the charge radius and $T_c = a_c/v_c$. We remark in the relation (2.8) that the pressure profile of primary shock wave decreases as a function of the distance r, faster than the classical spherical acoustic wave in which we have the decreasing as a function in $1/r$ (as illustrated in Figure 2.3).

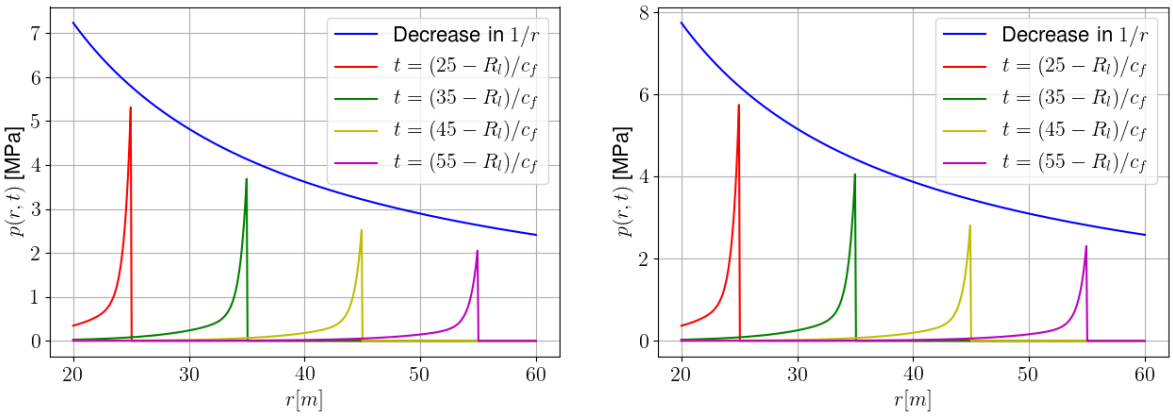

Figure 2.3: The pressure profiles of shock wave according to the relation (2.12) for the explosion of $W = 50$ kg in TNT. *Left*: case using the data of Cole [40]. *Right*: case using the data of Price [106]. The blue curve represent the decreasing in $1/r$ using the peak value at times $t = (20 - R_l)/c_0$

The expression of the fluid particle's velocity corresponding to the shock wave are usually required in the study of interaction of submerged structure and shock wave. To compute the corresponding fluid velocity, it is usual to introduce the velocity potential ϕ which is defined by:

$$p(t,r) = -\rho_0 \frac{\partial \phi}{\partial t}(t,r) \tag{2.13}$$

where ρ_0 is the fluid density. Using the initial condition $\phi(r, [r - R_l]/c_0) = 0$, the velocity potential ϕ can be explicitly expressed as

$$\phi(t,r) = -\frac{P_c}{\rho_0}\left[\frac{a_c}{r}\right]^{1+A} \int_0^\tau \mathcal{F}\left(\left[\frac{a_c}{r}\right]^B \frac{\zeta}{T_c}\right) d\zeta, \ \tau = t - (r - R_l)/c_0 \tag{2.14}$$

Since the shock wave is a spherical wave, then only radial component of velocity $v_r = \partial\phi(t,r)/\partial r$ is non-zero. Deriving the velocity potential ϕ according to r gives an expression of the radial component of velocity:

$$v_r(t,r) = \frac{p(t,r)}{\rho_0 c_0} + \frac{P_c T_c}{\rho_0 r}\left[\frac{a_c}{r}\right]^{1+A-B}(1+A-B)\mathcal{G}\left(\left[\frac{a_c}{r}\right]^{B}\frac{\tau}{T_c}\right)H(\tau) + \frac{p(t,r)}{\rho_0}\frac{\tau}{r}B \qquad (2.15)$$

where the function $\mathcal{G}$ defined by $\mathcal{G}(t) := \int_0^t \mathcal{F}(\zeta)d\zeta$. For the case of TNT (Trinitrotoluene) explosive material, the function is explicitly defined by $\mathcal{G}(t) = 1.5856 - 0.6167e^{-1.338t} - 0.9690e^{-0.1805t}$. We remark that the relation (2.4) can be found from the relation (2.15) by taking $A = -1$ and $B = 0$ in the case of plane waves. Figure 2.4 illustrates an example of the fluid particle's velocity profiles of shock wave according to the relation (2.15) for the explosion of $W = 50$ kg in TNT.

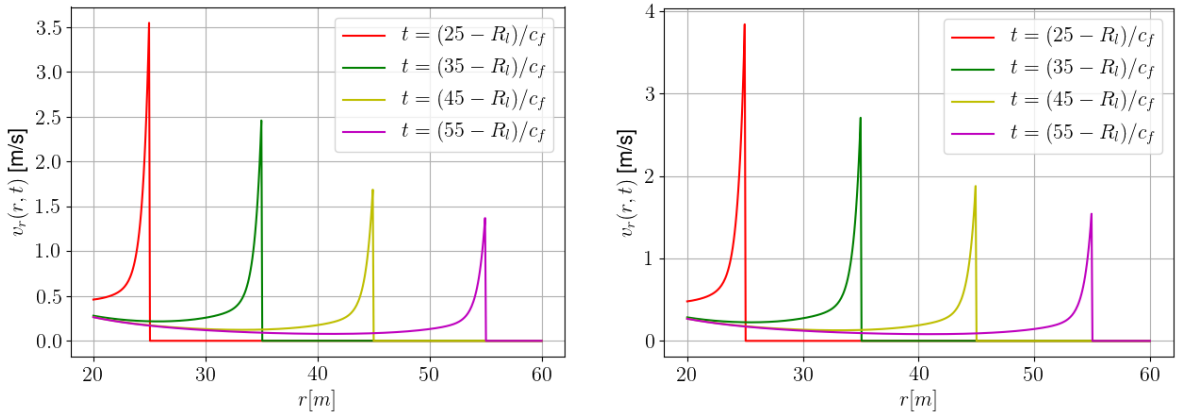

Figure 2.4: The fluid particle's velocity profiles of shock wave according to the relation (2.15) for the explosion of $W = 50$ kg in TNT. *Left*: case using the data of Cole [40]. *Right*: case using the data of Price [106]

2.3 Modelling of interaction of submerged structure and shock wave problem

In the previous section, the modelling of primary shock wave of underwater explosion is presented. The aim of this section is to present the modelling of the interaction of submerged structure and shock wave problems.

The problem of interest is formulated as follows. We consider a linear elastic structure $\Omega_s \subset \mathbb{R}^d$ (with $d = 2$ or 3) submerged in an infinite acoustic fluid domain. Both structure and fluid are supposed to be at rest initially. We denote by Γ the interface between the structure and the fluid. The submerged structure is supposed to be subjected to a shock wave with the known profile of incident pressure p^{inc} and velocity $\mathbf{v}^{inc}$. A geometrical representation of the problem is illustrated in Figure 2.5.

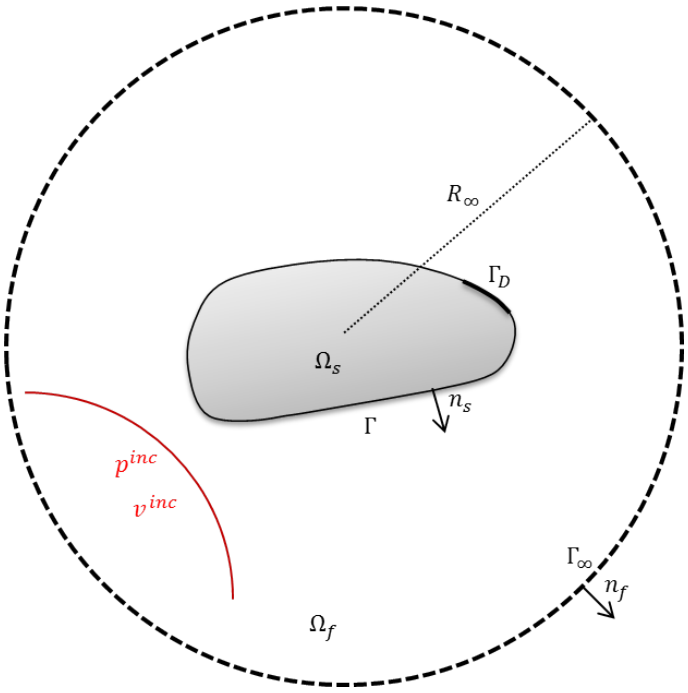

Figure 2.5: Geometrical representation: a submerged structure subjected to a shock wave with the known profile of incident pressure p^{inc} and velocity $\mathbf{v}^{inc}$.

Under the assumption of small perturbations, the dynamic motion of the structure is classically described by:

$$\begin{cases} \rho_s \ddot{\mathbf{u}}_s - \text{div } \underline{\underline{\sigma_s}}(\mathbf{u}_s) = \mathbf{0} & \text{in } \Omega_s \\ \mathbf{u}_s = \mathbf{0} & \text{on } \Gamma_D \\ \underline{\underline{\sigma_s}}(\mathbf{u}_s) \cdot \mathbf{n}_s = -p^{tot}\mathbf{n}_s & \text{on } \Gamma \end{cases} \tag{2.16}$$

with $\mathbf{u}_s$ is the displacement of structure, $\mathbf{n}_s$ is outward unit normal of the structure, ρ_s is structure density, $\underline{\underline{\sigma_s}}$ is Cauchy stress tensor and p^{tot} is the total pressure in the fluid. The total pressure in the fluid is decomposed by three components: $p^{tot} = p^{inc} + p^{ref} + p^{rad}$. The first component p^{inc} is the *incident* pressure which is a given of the problem. The second component $p^{ref}$is the *reflected* pressure which is the diffraction of the incident pressure by the rigid submerged structure assumed rigid and motionless. The last component p^{rad} is the *radiated* pressure which is induced by the motion of the structure. The reflected and the radiated pressure are governed by the equations:

$$\begin{cases} \dfrac{1}{c_0^2}\ddot{p} - \Delta p = 0 & \text{in } \Omega_f \\ \boldsymbol{\nabla} p \cdot \mathbf{n}_f + \rho_0 (\dfrac{1}{Z_C}\dot{p} + \dfrac{1}{Z_R} p) = 0 & \text{on } \Gamma_\infty \end{cases} \tag{2.17}$$

with c_0 is the speed of sound in the fluid, ρ_0 is the density of the fluid and $\mathbf{n}_f$ is outward unit normal of the fluid. The first equation is the well known wave equation. The second equation is the BGT condition [22] of order 1 applied on the boundary Γ_∞ of the truncated fluid domain (as presented in Section 1.1.4). On the interface Γ between the structure and the fluid, the

boundary condition of the reflected and the radiated pressure are expressed as following:

$$\begin{cases} \boldsymbol{\nabla} p^{ref} \cdot \mathbf{n}_s = -\boldsymbol{\nabla} p^{inc} \cdot \mathbf{n}_s & \text{on } \Gamma \\ \boldsymbol{\nabla} p^{rad} \cdot \mathbf{n}_s = -\rho_0 \ddot{\mathbf{u}}_s \cdot \mathbf{n}_s & \text{on } \Gamma \end{cases} \tag{2.18}$$

The first equation consists of imposing that the resultant of normal reflected and incident acceleration is zero. The second equation means that the radiated acceleration and structure acceleration have the same normal component on the interface. The system equations (2.18) is equivalent to the continuity of normal acceleration on the fluid-structure interface.

It is also possible to describe the state of the fluid by the velocity potential which is defined by:

$$\mathbf{v}_f = \boldsymbol{\nabla}\phi, \; p = -\rho_0 \dot{\phi} \tag{2.19}$$

where $\mathbf{v}_f$ is the velocity of fluid particle. The total velocity potential can also be decomposed by three components: $\phi^{tot} = \phi^{inc} + \phi^{ref} + \phi^{rad}$. The reflected and the radiated velocity potential are also governed by the wave equation and the BGT boundary condition [22] of order 1 given by Equation (2.17). On the interface Γ between the structure and the fluid, the boundary condition of the reflected and the radiated velocity potential are given by:

$$\begin{cases} \boldsymbol{\nabla} \phi^{ref} \cdot \mathbf{n}_s = -\mathbf{v}^{inc} \cdot \mathbf{n}_s & \text{on } \Gamma \\ \boldsymbol{\nabla} \phi^{rad} \cdot \mathbf{n}_s = \dot{\mathbf{u}}_s \cdot \mathbf{n}_s & \text{on } \Gamma \end{cases} \tag{2.20}$$

where the first equation consists of imposing that the resultant of normal reflected and incident velocity is zeros and the second equation means that the radiated velocity and structure velocity have the same normal component on the interface. The system equations (2.20) is equivalent to the continuity of normal velocity on the fluid-structure interface.

2.4 Finite element models of interaction of submerged structure and shock wave problems

Depending on the choice of the variables to describe the state of the fluid and the structure, various formulations can be found in the literature for modelling the coupled problem of interest. In the following, we present the formulations in displacement structure - scattered velocity potential $(\mathbf{u}_s, \phi^{sca})$, in displacement structure - radiated velocity potential $(\mathbf{u}_s, \phi^{rad})$, in displacement structure - radiated velocity potential $(\mathbf{u}_s, p^{rad})$ and in displacement structure - radiated pressure - radiated displacement potential $(\mathbf{u}_s, p^{rad}, \varphi^{rad})$.

Remark 2.4.1 We recall that in the case of the shock wave induced by an underwater explosion, the incident pressure defined by Equation (2.12) is a discontinuous function both in time and in space, more precisely $p^{inc} \in L^2(]0, \infty[; L^2(\Gamma))$. For this reason, the first equation of the system equations (2.18) which aim at imposing that the resultant of normal reflected and incident acceleration is zero, is only defined in sense of distribution. This singularity makes impossible the use of the formulation in displacement structure - scattered pressure $(\mathbf{u}_s, p^{sca})$ or in displacement structure - scattered pressure - scattered displacement potential $(\mathbf{u}_s, p^{sca}, \varphi^{sca})$ in finite element modelling.

2.4.1 Formulation in $(\mathbf{u}_s, \phi^{sca})$

Let us define the scattered pressure by $p^{sca} := p^{ref} + p^{rad}$ and the scattered velocity potential $\phi^{sca} := \phi^{ref} + \phi^{rad}$ as the potential corresponding to the the scattered pressure. The strong formulation of the problem formulated with $(\mathbf{u}_s, \phi^{sca})$ is given by:

$$\begin{cases} \rho_s \ddot{\mathbf{u}}_s - \text{div } \underline{\underline{\sigma_s}}(\mathbf{u}_s) = \mathbf{0} & \text{in } \Omega_s \\ \underline{\underline{\sigma_s}}(\mathbf{u}_s) = \underline{\underline{\underline{\mathcal{C}}}} : \underline{\underline{\epsilon_s}}(\mathbf{u}_s) & \text{in } \Omega_s \\ \mathbf{u}_s = \mathbf{0} & \text{on } \Gamma_D \\ \underline{\underline{\sigma_s}}(\mathbf{u}_s) \cdot \mathbf{n}_s = \rho_0 \dot{\phi}^{sca} \mathbf{n}_s - p^{inc} \mathbf{n}_s & \text{on } \Gamma \\ \boldsymbol{\nabla} \phi^{sca} \cdot \mathbf{n}_s = \dot{\mathbf{u}}_s \cdot \mathbf{n}_s - \mathbf{v}^{inc} \cdot \mathbf{n}_s & \text{on } \Gamma \\ \frac{1}{c_0^2} \ddot{\phi}^{sca} - \Delta \phi^{sca} = 0 & \text{in } \Omega_f \\ \boldsymbol{\nabla} \phi^{sca} \cdot \mathbf{n}_f = -\rho_0 (\frac{1}{Z_C} \dot{\phi}^{sca} + \frac{1}{Z_R} \phi^{sca}) & \text{on } \Gamma_\infty \end{cases} \tag{2.21}$$

We denote by $H^1_{\Gamma_D}(\Omega_s)^d := \{\mathbf{v} \in H^1(\Omega_s)^d, \mathbf{v} = 0 \text{ on } \Gamma_D\}$, T the final time of interest and we assume that $\mathbf{v}^{inc} \in L^2(]0,T[; L^2(\Gamma)^d)$ and $p^{inc} \in L^2(]0,T[; L^2(\Gamma))$. The corresponding weak formulation of the problem (2.21) reads: Find $\mathbf{u}_s \in C([0,T]; H^1_{\Gamma_D}(\Omega_s)^d) \cap C^1([0,T]; L^2(\Omega_s)^d)$ and $\phi^{sca} \in C([0,T]; H^1(\Omega_f)) \cap C^1([0,T]; L^2(\Omega_f))$ such that for all $(\delta\mathbf{u}_s, \delta\phi^{sca}) \in H^1_{\Gamma_D}(\Omega_s)^d \times H^1(\Omega_f)$, we have:

$$\begin{aligned} &\frac{d^2}{dt^2} \int_{\Omega_s} \rho_s \mathbf{u}_s(t,\mathbf{x}) \cdot \delta\mathbf{u}_s(\mathbf{x}) d\mathbf{x} + \int_{\Omega_s} \underline{\underline{\epsilon_s}}(\delta\mathbf{u}_s(\mathbf{x})) : \underline{\underline{\underline{\mathcal{C}}}} : \underline{\underline{\epsilon_s}}(\mathbf{u}_s(t,\mathbf{x})) d\mathbf{x} \\ &\quad - \frac{d}{dt} \int_\Gamma \rho_0 \phi^{sca}(t,\mathbf{x}) [\delta\mathbf{u}_s(\mathbf{x}) \cdot \mathbf{n}_s(\mathbf{x})] d\mathbf{x} = -\int_\Gamma p^{inc}(t,\mathbf{x}) \left[\delta\mathbf{u}_s(\mathbf{x}) \cdot \mathbf{n}_s(\mathbf{x})\right] d\mathbf{x} \\ &-\frac{d^2}{dt^2} \int_{\Omega_f} \frac{\rho_0}{c_0^2} \phi^{sca}(t,\mathbf{x}) \delta\phi^{sca}(\mathbf{x}) d\mathbf{x} - \rho_0 \int_{\Omega_f} \nabla\phi^{sca}(t,\mathbf{x}) \cdot \nabla\delta\phi^{sca}(\mathbf{x}) d\mathbf{x} \\ &\quad - \frac{d}{dt} \int_{\Gamma_\infty} \frac{\rho_0^2}{Z_C} \phi^{sca}(t,\mathbf{x}) \delta\phi^{sca}(\mathbf{x}) d\mathbf{x} - \int_{\Gamma_\infty} \frac{\rho_0^2}{Z_R} \phi^{sca}(t,\mathbf{x}) \delta\phi^{sca}(\mathbf{x}) d\mathbf{x} \\ &\quad - \frac{d}{dt} \int_\Gamma \rho_0 [\mathbf{u}_s(t,\mathbf{x}) \cdot \mathbf{n}_s(\mathbf{x})] \delta\phi^{sca}(\mathbf{x}) d\mathbf{x} = -\int_\Gamma \left[\mathbf{v}^{inc}(t,\mathbf{x}) \cdot \mathbf{n}_s(\mathbf{x})\right] \delta\phi^{sca}(\mathbf{x}) d\mathbf{x} \end{aligned} \tag{2.22}$$

The dynamic of the coupled problem spatially discretized using finite element method and the BGT-1 boundary condition [22] (see Section 1.1.4) for modelling the Sommerfeld condition are then described by the set of ordinary differential equations:

$$\mathbf{M}_{u\phi} \ddot{\mathbf{X}}^{sca}_{u\phi} + \mathbf{C}^{ext}_{u\phi} \dot{\mathbf{X}}^{sca}_{u\phi} + \mathbf{K}^{ext}_{u\phi} \mathbf{X}^{sca}_{u\phi} = \mathbf{F}^{sca}_{u\phi} \tag{2.23}$$

with

$$\mathbf{F}^{sca}_{u\phi} = \begin{bmatrix} \mathbf{F}^{sca}_s \\ \mathbf{F}^{sca}_\phi \end{bmatrix}, \mathbf{X}^{sca}_{u\phi} = \begin{bmatrix} \mathbf{U}_s \\ \mathbf{\Phi}^{sca} \end{bmatrix} \tag{2.24}$$

where the vector $\mathbf{U}_s$ contains the nodal displacement of the structure and $\mathbf{\Phi}^{sca}$ contains the nodal value of scattered velocity potential of the fluid. The matrices $\mathbf{M}_{u\phi}$, $\mathbf{C}^{ext}_{u\phi}$ and $\mathbf{K}^{ext}_{u\phi}$ are defined in Equation (1.46) of Section 1.2.2. The right-hand side is given by $\mathbf{F}^{sca}_{s,j} :=$

$-\int_\Gamma p^{inc}(\mathbf{N}_j^s \cdot \mathbf{n}_s)$, $\mathbf{F}_{\phi,j}^{sca} := -\int_\Gamma \rho_0(\mathbf{v}^{inc} \cdot \mathbf{n}_s)N_j^f$ where $\mathbf{N}^s$ and N^f are respectively the finite element basis of the structural and the fluid part.

2.4.2 Formulation in $(\mathbf{u}_s, \phi^{rad})$

By pre-computing the reflected pressure which depends only on the geometry of the structure and using the radiated velocity potential to describe the state of the fluid in the coupled system, the strong formulation in $(\mathbf{u}_s, \phi^{rad})$ is given by:

$$\begin{cases} \rho_s \ddot{\mathbf{u}}_s - \text{div } \underline{\underline{\sigma_s}}(\mathbf{u}_s) = \mathbf{0} & \text{in } \Omega_s \\ \underline{\underline{\sigma_s}}(\mathbf{u}_s) = \underline{\underline{\underline{\mathcal{C}}}} : \underline{\underline{\epsilon_s}}(\mathbf{u}_s) & \text{in } \Omega_s \\ \mathbf{u}_s = \mathbf{0} & \text{on } \Gamma_D \\ \underline{\underline{\sigma_s}}(\mathbf{u}_s) \cdot \mathbf{n}_s = -p^{inc}\mathbf{n}_s - p^{ref}\mathbf{n}_s + \rho_0 \dot{\phi}^{rad} & \text{on } \Gamma \\ \boldsymbol{\nabla}\phi^{rad} \cdot \mathbf{n}_s = \dot{\mathbf{u}}_s \cdot \mathbf{n}_s & \text{on } \Gamma \\ \frac{1}{c_0^2}\ddot{\phi}^{rad} - \Delta\phi^{rad} = 0 & \text{in } \Omega_f \\ \boldsymbol{\nabla}\phi^{rad} \cdot \mathbf{n}_f = -\rho_0(\frac{1}{Z_C}\dot{\phi}^{rad} + \frac{1}{Z_R}\phi^{rad}) & \text{on } \Gamma_\infty \end{cases} \tag{2.25}$$

We denote by $H^1_{\Gamma_D}(\Omega_s)^d := \{\mathbf{v} \in H^1(\Omega_s)^d, \mathbf{v} = 0 \text{ on } \Gamma_D\}$, T the final time of interest and we assume that $\mathbf{v}^{inc} \in L^2(]0,T[; L^2(\Gamma)^d)$ and $p^{inc}, p^{ref} \in L^2(]0,T[; L^2(\Gamma))$. The corresponding weak formulation of the problem (2.25) reads: Find $\mathbf{u}_s \in C([0,T]; H^1_{\Gamma_D}(\Omega_s)^d) \cap C^1([0,T]; L^2(\Omega_s)^d)$ and $\phi^{rad} \in C([0,T]; H^1(\Omega_f)) \cap C^1([0,T]; L^2(\Omega_f))$ such that $\forall(\delta\mathbf{u}_s, \delta\phi^{rad}) \in H^1_{\Gamma_D}(\Omega_s)^d \times H^1(\Omega_f)$, we have:

$$\begin{aligned} &\frac{d^2}{dt^2}\int_{\Omega_s} \rho_s \mathbf{u}_s(t,\mathbf{x}) \cdot \delta\mathbf{u}_s(\mathbf{x}) d\mathbf{x} + \int_{\Omega_s} \underline{\underline{\epsilon_s}}(\delta\mathbf{u}_s(\mathbf{x})) : \underline{\underline{\underline{\mathcal{C}}}} : \underline{\underline{\epsilon_s}}(\mathbf{u}_s(t,\mathbf{x})) d\mathbf{x} \\ &\qquad - \frac{d}{dt}\int_\Gamma \rho_0 \phi^{rad}(t,\mathbf{x})[\delta\mathbf{u}_s(\mathbf{x}) \cdot \mathbf{n}_s(\mathbf{x})] d\mathbf{x} \\ &\qquad = -\int_\Gamma (p^{inc} + p^{ref})(t,\mathbf{x})\,[\delta\mathbf{u}_s(\mathbf{x}) \cdot \mathbf{n}_s(\mathbf{x})]\, d\mathbf{x} \\ &-\frac{d^2}{dt^2}\int_{\Omega_f} \frac{\rho_0}{c_0^2}\phi^{rad}(t,\mathbf{x})\delta\phi^{rad}(\mathbf{x}) d\mathbf{x} - \rho_0 \int_{\Omega_f} \nabla\phi^{rad}(t,\mathbf{x}) \cdot \nabla\delta\phi^{rad}(\mathbf{x}) d\mathbf{x} \\ &\qquad - \frac{d}{dt}\int_{\Gamma_\infty} \frac{\rho_0^2}{Z_C}\phi^{rad}(t,\mathbf{x})\delta\phi^{rad}(\mathbf{x}) d\mathbf{x} - \int_{\Gamma_\infty} \frac{\rho_0^2}{Z_R}\phi^{rad}(t,\mathbf{x})\delta\phi^{rad}(\mathbf{x}) d\mathbf{x} \\ &\qquad - \frac{d}{dt}\int_\Gamma \rho_0[\mathbf{u}_s(t,\mathbf{x}) \cdot \mathbf{n}_s(\mathbf{x})]\delta\phi^{rad}(\mathbf{x}) d\mathbf{x} = 0 \end{aligned} \tag{2.26}$$

The use of the $(\mathbf{u}_s, \phi^{rad})$ formulation yields, after a space-discretization by the finite element method, the following linear system of order 2:

$$\mathbf{M}_{u\phi}\ddot{\mathbf{X}}_{u\phi}^{rad} + \mathbf{C}_{u\phi}^{ext}\dot{\mathbf{X}}_{u\phi}^{rad} + \mathbf{K}_{u\phi}^{ext}\mathbf{X}_{u\phi}^{rad} = \mathbf{F}_{u\phi}^{rad} \tag{2.27}$$

with

$$\mathbf{F}_{u\phi}^{rad} = \begin{bmatrix} \mathbf{F}_s^{rad} \\ \mathbf{0} \end{bmatrix}, \mathbf{X}_{u\phi}^{rad} = \begin{bmatrix} \mathbf{U}_s \\ \mathbf{\Phi}^{rad} \end{bmatrix} \tag{2.28}$$

where the vector $\mathbf{U}_s$ contains the nodal displacement of the structure and $\mathbf{\Phi}^{rad}$ contains the nodal value of radiated velocity potential of the fluid.

We remark that in the $(\mathbf{u}_s, \phi^{rad})$ formulation, we have the same coupling mass, damping and stiffness matrices as the $(\mathbf{u}_s, \phi^{sca})$ formulation (see Equation (1.46) of Section 1.2.2 for their definition). The only different appears on the right-hand side which is given by $\mathbf{F}_{s,j}^{rad} := -\int_\Gamma (p^{inc} + p^{ref})(\mathbf{N}_j^s \cdot \mathbf{n}_s)$, where $\mathbf{N}^s$ is the finite element basis of the structural part, for the new coupled formulation.

2.4.3 Formulation in $(\mathbf{u}_s, p^{rad})$

By pre-computing the reflected pressure which depends only on the geometry of the structure and using the radiated pressure to describe the state of the fluid in the coupled system, the strong formulation in $(\mathbf{u}_s, p^{rad})$ is given by:

$$\begin{cases} \rho_s \ddot{\mathbf{u}}_s - \text{div } \underline{\underline{\sigma_s}}(\mathbf{u}_s) = 0 & \text{in } \Omega_s \\ \underline{\underline{\sigma_s}}(\mathbf{u}_s) = \underline{\underline{\underline{\underline{\mathcal{C}}}}} : \underline{\underline{\epsilon_s}}(\mathbf{u}_s) & \text{in } \Omega_s \\ \mathbf{u}_s = \mathbf{0} & \text{on } \Gamma_D \\ \underline{\underline{\sigma_s}}(\mathbf{u}_s) \cdot \mathbf{n}_s = -p^{inc}\mathbf{n}_s - p^{ref}\mathbf{n}_s - p^{rad}\mathbf{n}_s & \text{on } \Gamma \\ \boldsymbol{\nabla} p^{rad} \cdot \mathbf{n}_s = -\rho_0 \ddot{\mathbf{u}}_s \cdot \mathbf{n}_s & \text{on } \Gamma \\ \frac{1}{c_0^2}\ddot{p}^{rad} - \Delta p^{rad} = 0 & \text{in } \Omega_f \\ \boldsymbol{\nabla} p^{rad} \cdot \mathbf{n}_f = -\rho_0 (\frac{1}{Z_C}\dot{p}^{rad} + \frac{1}{Z_R} p^{rad}) & \text{on } \Gamma_\infty \end{cases} \tag{2.29}$$

We denote by $H^1_{\Gamma_D}(\Omega_s)^d := \{\mathbf{v} \in H^1(\Omega_s)^d, \mathbf{v} = 0 \text{ on } \Gamma_D\}$, T the final time of interest and we assume that $\mathbf{v}^{inc} \in L^2(]0,T[; L^2(\Gamma)^d)$ and $p^{inc}, p^{ref} \in L^2(]0,T[; L^2(\Gamma))$. The corresponding weak formulation of the problem (2.29) reads: Find $\mathbf{u}_s \in C([0,T]; H^1_{\Gamma_D}(\Omega_s)^d) \cap C^1([0,T]; L^2(\Omega_s)^d)$ and $p^{rad} \in C([0,T]; H^1(\Omega_f)) \cap C^1([0,T]; L^2(\Omega_f))$ such that $\forall (\delta\mathbf{u}_s, \delta p^{rad}) \in$

$H^1_{\Gamma_D}(\Omega_s)^d \times H^1(\Omega_f)$, we have:

$$\begin{aligned}
\frac{d^2}{dt^2}\int_{\Omega_s} \rho_s \mathbf{u}_s(t,\mathbf{x})\cdot\delta\mathbf{u}_s(\mathbf{x})d\mathbf{x} &+ \int_{\Omega_s} \underline{\underline{\epsilon_s}}(\delta\mathbf{u}_s(\mathbf{x})) : \underline{\underline{\underline{\underline{\mathcal{C}}}}} : \underline{\underline{\epsilon_s}}(\mathbf{u}_s(t,\mathbf{x}))d\mathbf{x} \\
&+ \int_\Gamma p^{rad}(t,\mathbf{x})[\delta\mathbf{u}_s(\mathbf{x})\cdot\mathbf{n}_s(\mathbf{x})]d\mathbf{x} \\
&= -\int_\Gamma (p^{inc}+p^{ref})(t,\mathbf{x})\,[\delta\mathbf{u}_s(\mathbf{x})\cdot\mathbf{n}_s(\mathbf{x})]\,d\mathbf{x} \\
\frac{d^2}{dt^2}\int_{\Omega_f} \frac{1}{c_0^2} p^{rad}(t,\mathbf{x})\delta p^{rad}(\mathbf{x})d\mathbf{x} &+ \int_{\Omega_f} \nabla p^{rad}(t,\mathbf{x})\cdot\nabla\delta p^{rad}(\mathbf{x})d\mathbf{x} \\
&+ \frac{d}{dt}\int_{\Gamma_\infty} \frac{\rho_0}{Z_C} p^{rad}(t,\mathbf{x})\delta p^{rad}(\mathbf{x})d\mathbf{x} \\
&+ \int_{\Gamma_\infty} \frac{\rho_0}{Z_R} p^{rad}(t,\mathbf{x})\delta p^{rad}(\mathbf{x})d\mathbf{x} \\
&- \frac{d^2}{dt^2}\int_\Gamma \rho_0[\mathbf{u}_s(t,\mathbf{x})\cdot\mathbf{n}_s(\mathbf{x})]\delta p^{rad}(\mathbf{x})d\mathbf{x} \\
&= 0
\end{aligned} \tag{2.30}$$

The use of the $(\mathbf{u}_s, p^{rad})$ formulation yields, after a space-discretization by the finite element method, the following linear system of order 2:

$$\mathbf{M}_{up}\ddot{\mathbf{X}}^{rad}_{up} + \mathbf{C}^{ext}_{up}\dot{\mathbf{X}}^{rad}_{up} + \mathbf{K}^{ext}_{up}\mathbf{X}^{rad}_{up} = \mathbf{F}^{rad}_{up} \tag{2.31}$$

with

$$\mathbf{F}^{rad}_{up} = \begin{bmatrix} \mathbf{F}^{rad}_s \\ \mathbf{0} \end{bmatrix}, \mathbf{X}^{rad}_{u\phi} = \begin{bmatrix} \mathbf{U}_s \\ \mathbf{P}^{rad} \end{bmatrix} \tag{2.32}$$

where the vector $\mathbf{U}_s$ contains the nodal displacement of the structure and $\mathbf{P}^{rad}$ contains the nodal value of radiated pressure in the fluid. The matrices $\mathbf{M}_{up}$, $\mathbf{C}^{ext}_{up}$ and $\mathbf{K}^{ext}_{up}$ are defined in Equation (1.40) of Section 1.2.1.

We remark that in the $(\mathbf{u}_s, p^{rad})$ coupled formulation, we have the same right-hand side vector as $(\mathbf{u}_s, \phi^{rad})$ coupled formulation and we recall that a major drawback of the $(\mathbf{u}_s, p^{rad})$ formulation is that the coupling mass matrix $\mathbf{M}_{up}$ and coupling stiffness matrix $\mathbf{K}^{ext}_{up}$ are non-symmetric.

2.4.4 Formulation in $(\mathbf{u}_s, p^{rad}, \varphi^{rad})$

By pre-computing the reflected pressure which depends only on the geometry of the structure and using two variables - the radiated pressure and the radiated displacement potential - to describe the state of the fluid in the coupled system, the strong formulation in $(\mathbf{u}_s, p^{rad}, \varphi^{rad})$

coupled is given by:

$$\begin{cases} \rho_s \ddot{\mathbf{u}}_s - \text{div } \underline{\underline{\sigma_s}}(\mathbf{u}_s) = 0 & \text{in } \Omega_s \\ \underline{\underline{\sigma_s}}(\mathbf{u}_s) = \underline{\underline{\underline{\underline{\mathcal{C}}}}} : \underline{\underline{\epsilon_s}}(\mathbf{u}_s) & \text{in } \Omega_s \\ \mathbf{u}_s = \mathbf{0} & \text{on } \Gamma_D \\ \underline{\underline{\sigma_s}}(\mathbf{u}_s) \cdot \mathbf{n}_s = -p^{inc}\mathbf{n}_s - p^{ref}\mathbf{n}_s + \rho_0 \ddot{\varphi} \mathbf{n}_s & \text{on } \Gamma \\ \boldsymbol{\nabla}\varphi^{rad} \cdot \mathbf{n}_s = \ddot{\mathbf{u}}_s \cdot \mathbf{n}_s & \text{on } \Gamma \\ \dfrac{1}{\rho_0 c_0^2} p^{rad} + \dfrac{1}{c_0^2}\ddot{\varphi}^{rad} = 0 & \text{in } \Omega_f \\ \dfrac{1}{c_0^2}\ddot{p}^{rad} + \rho_0 \Delta \ddot{\varphi}^{rad} = 0 & \text{in } \Omega_f \\ \boldsymbol{\nabla}\ddot{\varphi}^{rad} \cdot \mathbf{n}_f = -\rho_0 \left(\dfrac{1}{Z_C}\dddot{\varphi}^{rad} + \dfrac{1}{Z_R}\ddot{\varphi}^{rad} \right) & \text{on } \Gamma_\infty \end{cases} \tag{2.33}$$

We denote by $H^1_{\Gamma_D}(\Omega_s)^d := \{\mathbf{v} \in H^1(\Omega_s)^d, \mathbf{v} = 0 \text{ on } \Gamma_D\}$, T the final time of interest and we assume that $\mathbf{v}^{inc} \in L^2(]0,T[; L^2(\Gamma)^d)$ and $p^{inc}, p^{ref} \in L^2(]0,T[; L^2(\Gamma))$. The corresponding weak formulation of the problem (2.33) reads: Find $\mathbf{u}_s \in C([0,T]; H^1_{\Gamma_D}(\Omega_s)^d) \cap C^1([0,T]; L^2(\Omega_s)^d)$, $p^{rad} \in C^1([0,T]; L^2(\Omega_f))$ and $\varphi^{rad} \in C^1([0,T]; H^1(\Omega_f)) \cap C^2([0,T]; L^2(\Omega_f))$ such that for all $(\delta\mathbf{u}_s, \delta p^{rad}, \delta\varphi^{rad}) \in H^1_{\Gamma_D}(\Omega_s)^d \times L^2(\Omega_f) \times H^1(\Omega_f)$, we have:

$$\begin{aligned} \frac{d^2}{dt^2}\int_{\Omega_s} \rho_s \mathbf{u}_s(t,\mathbf{x}) \cdot \delta\mathbf{u}_s(\mathbf{x}) d\mathbf{x} + \int_{\Omega_s} \underline{\underline{\epsilon_s}}(\delta\mathbf{u}_s(\mathbf{x})) : \underline{\underline{\underline{\underline{\mathcal{C}}}}} : \underline{\underline{\epsilon_s}}(\mathbf{u}_s(t,\mathbf{x})) d\mathbf{x} \\ - \frac{d^2}{dt^2}\int_\Gamma \rho_0 \varphi^{rad}(t,\mathbf{x})[\delta\mathbf{u}_s(\mathbf{x}) \cdot \mathbf{n}_s(\mathbf{x})] d\mathbf{x} \\ = -\int_\Gamma (p^{inc} + p^{ref})(t,\mathbf{x}) \left[\delta\mathbf{u}_s(\mathbf{x}) \cdot \mathbf{n}_s(\mathbf{x})\right] d\mathbf{x} \\ \frac{1}{\rho_0 c_0^2}\int_{\Omega_f} p^{rad}(t,\mathbf{x}) \delta p^{rad}(\mathbf{x}) d\mathbf{x} + \frac{d^2}{dt^2}\int_{\Omega_f} \frac{1}{c_0^2}\varphi^{rad}(t,\mathbf{x})\delta p^{rad}(\mathbf{x}) d\mathbf{x} = 0 \\ -\frac{d^2}{dt^2}\int_{\Omega_f} \rho_0 \nabla\varphi^{rad}(t,\mathbf{x}) \cdot \nabla\delta\varphi^{rad}(\mathbf{x}) d\mathbf{x} + \frac{d^2}{dt^2}\int_{\Omega_f} \frac{1}{c_0^2} p^{rad}(t,\mathbf{x})\delta\varphi^{rad}(\mathbf{x}) d\mathbf{x} \\ - \frac{d^3}{dt^3}\int_{\Gamma_\infty} \frac{\rho_0^2}{Z_C}\varphi^{rad}(t,\mathbf{x})\delta\varphi^{rad}(\mathbf{x}) d\mathbf{x} \\ - \int_{\Gamma_\infty} \frac{\rho_0^2}{Z_R}\varphi^{rad}(t,\mathbf{x})\delta\varphi^{rad}(\mathbf{x}) d\mathbf{x} \\ - \frac{d^2}{dt^2}\int_\Gamma \rho_0 [\mathbf{u}_s(t,\mathbf{x}) \cdot \mathbf{n}_s(\mathbf{x})]\delta\varphi^{rad}(\mathbf{x}) d\mathbf{x} \\ = 0 \end{aligned} \tag{2.34}$$

The use of the $(\mathbf{u}_s, p^{rad}, \varphi^{rad})$ formulation yields, after a space-discretization by the finite element method, the following linear system of order 3:

$$\mathbf{I}^{ext}_{up\varphi} \dddot{\mathbf{X}}^{rad}_{up\varphi} + \mathbf{M}^{ext}_{up\varphi} \ddot{\mathbf{X}}^{rad}_{up\varphi} + \mathbf{K}_{up\varphi} \mathbf{X}^{rad}_{up\varphi} = \mathbf{F}^{rad}_{up\varphi} \tag{2.35}$$

with

$$\mathbf{F}^{rad}_{up\varphi} = \begin{bmatrix} \mathbf{F}^{rad}_{s} \\ \mathbf{0} \\ \mathbf{0} \end{bmatrix}, \mathbf{X}^{rad}_{up\varphi} = \begin{bmatrix} \mathbf{U}_s \\ \mathbf{P}^{rad} \\ \boldsymbol{\varphi}^{rad} \end{bmatrix} \tag{2.36}$$

where the vector $\mathbf{U}_s$ contains the nodal displacement of the structure, $\mathbf{P}^{rad}$ contains the nodal value of radiated pressure and $\boldsymbol{\varphi}^{rad}$ contains the nodal value of radiated displacement potential in the fluid. The matrices $\mathbf{I}^{ext}_{up\varphi}$, $\mathbf{M}^{ext}_{up\varphi}$ and $\mathbf{K}_{up\varphi}$ are defined in Equation (1.51) of Section 1.2.3. The right-hand side is defined by $\mathbf{F}^{rad}_{s,j} := -\int_\Gamma (p^{inc}+p^{ref})(\mathbf{N}^s_j \cdot \mathbf{n}_s)$ where $\mathbf{N}^s$ is the finite element basis of the structural part.

The finite element model (2.35) is a third order symmetric system. However, as mentioned in Section 1.2.3 of Chapter 2, we can obtain in this formulation an equivalent non-symmetric second order system:

$$\mathbf{M}^{ext}_{up\varphi}\ddot{\mathbf{X}}^{rad}_{up\varphi} + \mathbf{C}^{ext}_{up\varphi}\dot{\mathbf{X}}^{rad}_{up\varphi} + \mathbf{K}_{up\varphi}\mathbf{X}^{rad}_{up\varphi} = \mathbf{F}^{rad}_{up\varphi} \tag{2.37}$$

where the matrix $\mathbf{C}^{ext}_{up\varphi}$ is defined in Equation (1.53) of Section 1.2.3.

2.4.5 Pre-computing of reflected pressure

In order to use the formulation in $(\mathbf{u}_s, \phi^{rad})$, in $(\mathbf{u}_s, p^{rad})$ or in $(\mathbf{u}_s, p^{rad}, \varphi^{rad})$, it is necessary to pre-compute the reflected pressure. With the discontinuity of the incident shock wave of pressure, it is impossible to use the formulation in the reflected pressure because of the infinite pressure gradient at the shock front which implies that the acoustic loads associated become indeterminate. A practical solution in this case may model the shock front such that the pressure rise occurs over a period of time, designated the "rise time", to overcome the discontinuity at the shock front. This however may result in response with a poor accuracy in high frequencies, as if a filter was used. Even with the discontinuity at the shock front, it is however possible to use the formulation in the reflected velocity potential and compute the reflected pressure by the post-processing with Equation (2.19). The strong formulation of the reflected velocity potential is given by:

$$\begin{cases} \dfrac{1}{c_0^2}\ddot{\phi}^{ref} - \Delta\phi^{ref} = 0 & \text{in } \Omega_f \\ \boldsymbol{\nabla}\phi^{ref} \cdot \mathbf{n}_s = -\mathbf{v}^{inc} \cdot \mathbf{n}_s & \text{on } \Gamma \\ \boldsymbol{\nabla}\phi^{ref} \cdot \mathbf{n}_f = -\rho_0 \left(\dfrac{1}{Z_C}\dot{\phi}^{ref} + \dfrac{1}{Z_R}\phi^{ref} \right) & \text{on } \Gamma_\infty \end{cases} \tag{2.38}$$

We assume that $\mathbf{v}^{inc}$ is in $L^2(]0,T[; L^2(\Gamma)^d)$. The corresponding weak formulation of the problem (2.38) reads: Find $\phi^{ref} \in C([0,T]; H^1(\Omega_f)) \cap C^1([0,T]; L^2(\Omega_f))$ such that for all

$\delta\phi^{ref} \in H^1(\Omega_f)$, we have:

$$\begin{aligned} -\frac{d^2}{dt^2}\int_{\Omega_f}\frac{\rho_0}{c_0^2}\phi^{ref}(t,\mathbf{x})\delta\phi^{ref}(\mathbf{x})d\mathbf{x} - \rho_0\int_{\Omega_f}\nabla\phi^{ref}(t,\mathbf{x})\cdot\nabla\delta\phi^{ref}(\mathbf{x})d\mathbf{x} \\ - \frac{d}{dt}\int_{\Gamma_\infty}\frac{\rho_0^2}{Z_C}\phi^{ref}(t,\mathbf{x})\delta\phi^{ref}(\mathbf{x})d\mathbf{x} - \int_{\Gamma_\infty}\frac{\rho_0^2}{Z_R}\phi^{ref}(t,\mathbf{x})\delta\phi^{ref}(\mathbf{x})d\mathbf{x} \\ = -\int_{\Gamma}\left[\mathbf{v}^{inc}(t,\mathbf{x})\cdot\mathbf{n}_s(\mathbf{x})\right]\delta\phi^{ref}(\mathbf{x})d\mathbf{x} \end{aligned} \tag{2.39}$$

which yields, after a space-discretization by the finite element method, the following linear system of order 2:

$$-\rho_0\mathbf{M}_f\ddot{\mathbf{\Phi}}^{ref} - \frac{\rho_0^2}{Z_C}\mathbf{Q}\dot{\mathbf{\Phi}}^{ref} - \rho_0\left(\mathbf{K}_f + \frac{\rho_0}{Z_R}\mathbf{Q}\right)\mathbf{\Phi}^{ref} = \mathbf{F}^{ref} \tag{2.40}$$

where the vector $\mathbf{\Phi}^{ref}$ contains the nodal value of the reflected velocity potential and the right-hand side vector is given by: $\mathbf{F}_j^{ref} := -\int_\Gamma \rho_0(\mathbf{v}_f^{inc}\cdot\mathbf{n}_s)N_j$ with N is the shape function of the finite element method. Note that the usual time-integration schemes (such as Newmark scheme, Wilson scheme, ...) also explicitly compute the time derivative of the primal variables. In these cases, we could obtain the reflected pressure from the reflected velocity potential through the relationship (2.19) without additional computation cost.

2.5 Numerical validation of finite element models

In this section, we propose to validate the numerical model presented in the previous section. Two test cases are exposed. The first study case is a 2D academic case for which a semi-analytical solution is available. The second study case is an extension of the previous 2D-configuration study case into 3D-configuration. In both cases, the four finite element models presented in the previous section are investigated.

2.5.1 Test case 1: an elastic ring subjected to an acoustic shock wave

For the first study case, we are interested by an elastic ring submitted to an acoustic shock wave of underwater explosion. A graphical representation of the first study case is presented in Figure 2.6.

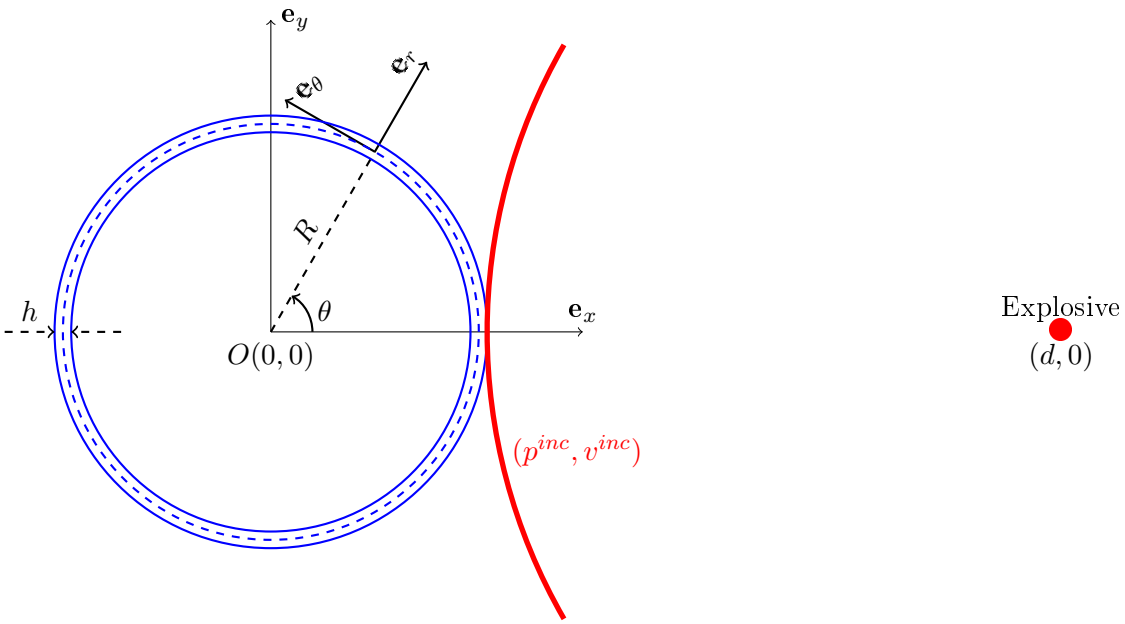

Figure 2.6: Graphical representation of the first study case

We suppose that the thickness h of the ring is very small compared to its radius R. Under this hypothesis, we can use the Love-Kirchoff model to describe the dynamical behaviour of the structure. Using the Love-Kirchoff model for structural part combined with Fourier series tool, the analytical solution of the problem in Laplace domain can be expressed explicitly in form of Fourier series. Thus, in order to obtain a semi-analytical solution, it is sufficient to truncate Fourier series representing the analytical solution in Laplace domain and employ a numerical inverse Laplace transform to return to time-domain. The presentation in details of the construction of the semi-analytical solution of the problem are given in Appendix B.

For numerical application, we suppose that the submerged structure - shock wave interaction problem consists of an elastic ring of radius $R = 1$ m with a thickness $h = 0.01$ m submerged in a fluid. It is excited by the primary acoustic shock wave which comes from an underwater explosion of 1 000 kg TNT at a distance $d = 100$ m from the centre of the ring. At $t = 0$, we suppose that the front of shock wave arrives at the stand-off point (the nearest point of the structure to explosion). The physical properties of the structure and the fluid in the problem are given in Table 2.1. The profile of the incident pressure and of the incident velocity are respectively given by the relations (2.12) and (2.15). For numerical application, we use the value of the constants P_c, v_c, A and B provided by Cole [40] as given in relation (2.10).

Structure	Fluid
Young's modulus $E = 200$ GPa	Speed of sound $c_0 = 1500$ m/s
Poisson's ratio $\nu = 0.28$	Density $\rho_0 = 1000$ kg/m^3
Density $\rho_s = 7800$ kg/m^3	

Table 2.1: Physical properties of the structure and the fluid in the problem

Finite element modelling

In order to approximate the radiation condition, a truncated fluid domain in form of a circle of radius $R_{bgt} = 3$ m is employed. On the boundary of the truncated fluid domain, the BGT-1 condition (1.35) is applied in order to approximate the outgoing sound wave by a cylindrical wave for which we use the value of impedance $Z_R = 2\rho_0 R_{bgt}, Z_C = \rho_0 c_0$. Both the elastic ring and the fluid are modelled using **quadratic triangular elements**. The finite element model is obtained by using a mesh in which the largest element size in the fluid part is 0.06 m and there are at least 4 elements in the thickness of the ring. The using mesh is illustrated in Figure 2.7.

In the finite element model, we have 172 473 degrees of freedom, 91 028 of which correspond to the structural part and 81 445 of which correspond to the acoustic fluid part for the formulation in $(\mathbf{u}_s, \phi^{sca})$, in $(\mathbf{u}_s, \phi^{rad})$ and in $(\mathbf{u}_s, p^{rad})$. For the formulation in $(\mathbf{u}_s, p^{rad}, \varphi^{rad})$, we have 253 918 degrees of freedom, 91 028 of which correspond to the structural part and 162 890 of which correspond to the acoustic fluid part. Furthermore, the non-symmetric finite element model (2.37) will be used in this study. For time-discretization of finite element model, Newmark scheme with a small numerical dissipation ($\gamma = 1/2 - \alpha$, $\beta = \frac{1}{4}(1-\alpha)^2$ where $\alpha = -0.2$) is employed by using the time step of size $\Delta t = 6.7 \cdot 10^{-6}$ s which means that the shock wave needs 100 time steps in order to travel the distance R.

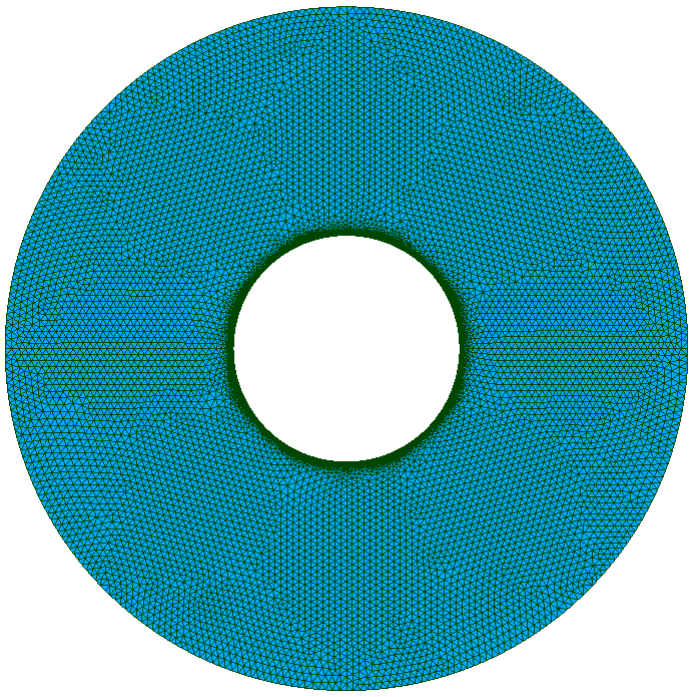

Figure 2.7: Mesh used in finite element modelling in the first study case

Analysis of numerical results

For numerical analysis, let us begin with the formulation in $(\mathbf{u}_s, \phi^{sca})$. The numerical and semi-analytical solution of radial and ortho-radial displacement are respectively illustrated in Figure 2.8a and 2.8b. In Figure 2.8a and 2.8b, the semi-analytical solutions are displayed by the full lines while the numerical solutions are displayed by dashed lines. Because of the geometrical symmetry in the problem, the ortho-radial displacement for $\theta = 0$ and $\theta = \pi$ is zero as shown in Figure 2.8b. We can see clearly that the numerical solution is in accordance with the semi-analytical solution. For the scattered pressure, Figure 2.9 plots the numerical and semi-analytical solution in the same graphic and Figure 2.10 plots the numerical and semi-analytical solution in two difference graphics. The results show that the scattered pressure obtained by the finite element model is also in accordance with the semi-analytical solutions. We remark that there are some unwanted oscillations in the semi-analytical solutions of the scattered pressure which are essentially due to the Gibb phenomena and numerical instabilities in inverse Laplace transform algorithm. In the numerical solutions, we have also some unwanted oscillations. However, it is less significant than those in semi-analytical solutions since numerical dissipations are implicitly introduced in the time-discretization scheme. For the case where Newmark scheme without numerical dissipation ($\beta = 1/4, \gamma = 1/2$) whose results are not displayed here, we observed large unwanted oscillations in the numerical solutions of finite element model which is essentially due to the discontinuity in time of the loading.

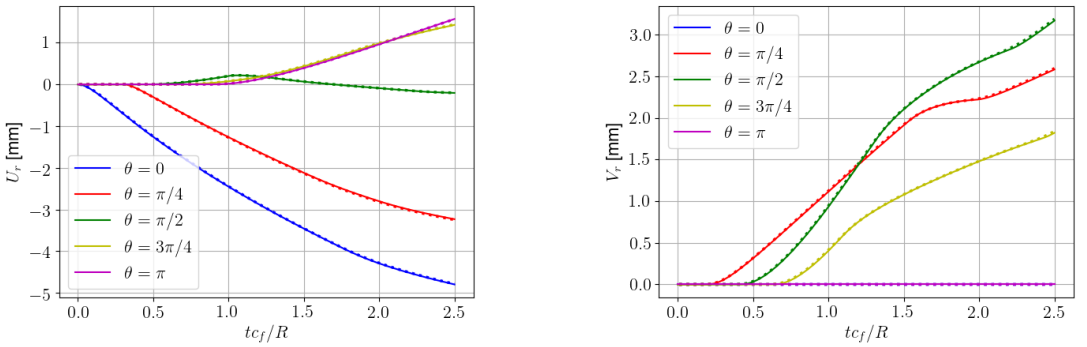

(a) Radial displacements U_r (b) Ortho-radial displacements V_r

Figure 2.8: Numerical solutions of finite element model in $(\mathbf{u}_s, \phi^{sca})$ (dashed lines) and semi-analytical solutions (full lines)

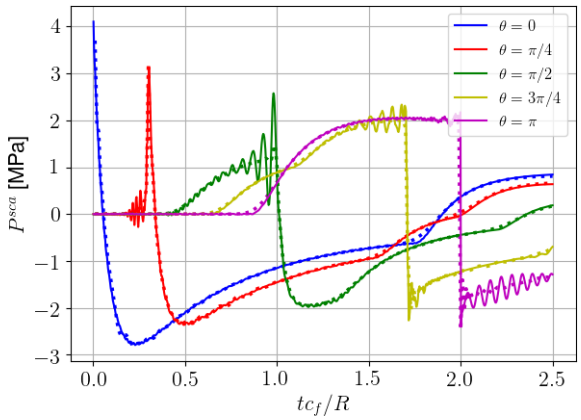

Figure 2.9: Numerical solutions of finite element model in $(\mathbf{u}_s, \phi^{sca})$ (dashed lines) and semi-analytical solutions (full lines) of the scattered pressure at fluid-structure interface

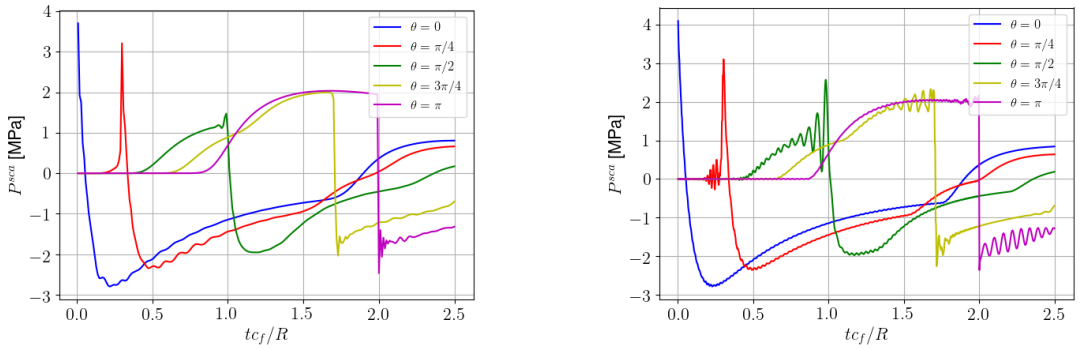

(a) Numerical solutions (b) Semi-analytical solutions

Figure 2.10: Numerical solutions of finite element model in $(\mathbf{u}_s, \phi^{sca})$ (left) and semi-analytical solutions (right) of the scattered pressure at fluid-structure interface

Let us now examine the formulations in $(\mathbf{u}_s, \phi^{rad})$, in $(\mathbf{u}_s, p^{rad})$ and in $(\mathbf{u}_s, p^{rad}, \varphi^{rad})$. We remind that the pre-computing of reflected pressure p^{ref} are required in order to use the formulation in $(\mathbf{u}_s, \phi^{rad})$ and $(\mathbf{u}_s, p^{rad})$. The same mesh of fluid part of the previous coupled model in $(\mathbf{u}_s, \phi^{sca})$ is used for the finite element modelling with the formulation in ϕ^{ref} (2.40). The reflected pressures are then obtained by the relation (2.19). Figure 2.11 shows the numerical and the semi-analytical solution of reflected pressure in the same graphic. Numerical solutions of finite element model are displayed in dashed lines while semi-analytical solutions are displayed in full lines. The numerical results show that the reflected pressures of finite element model in ϕ^{ref} are in agreement with the semi-analytical solutions. Figure 2.12 plots the numerical and semi-analytical solutions of the reflected pressure in two different graphics. As in the previous case, there are also unwanted oscillations in the semi-analytical solution. It is however less significant than in case of scattered pressure. Contrary to the case of scattered pressure where the semi-analytical solutions always have larger unwanted oscillations than those of numerical solutions, we observe that the numerical solutions of the reflected pressure cause larger unwanted oscillations than the semi-analytical solution for the case $\theta = 0$ and $\theta = \pi$.

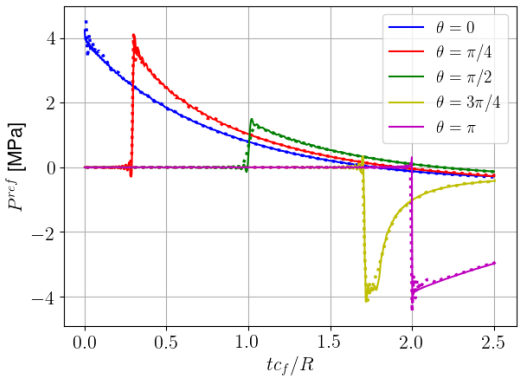

Figure 2.11: Numerical solutions of finite element model (dashed lines) and semi-analytical solutions (full lines) of the reflected pressure at fluid-structure interface

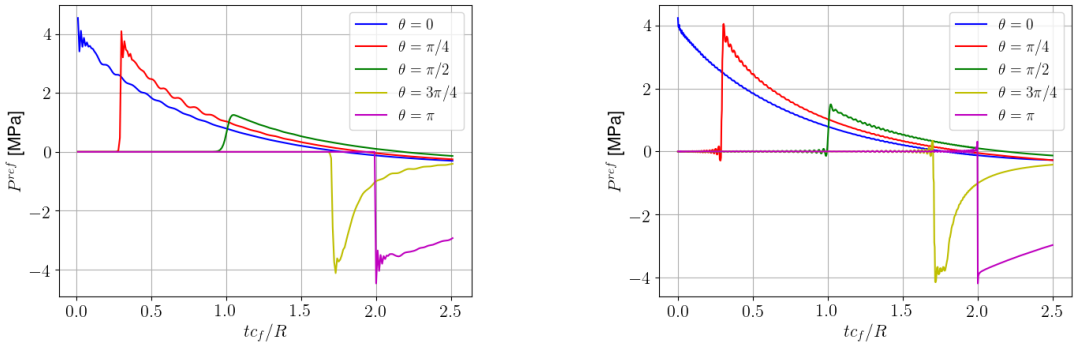

(a) Numerical solutions

(b) Semi-analytical solutions

Figure 2.12: Numerical solutions of finite element model (left) and semi-analytical solutions (right) of the reflected pressure at fluid-structure interface

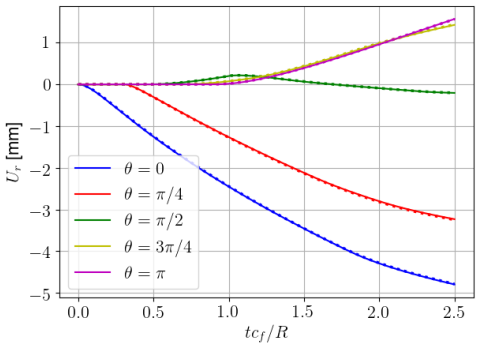

(a) Radial displacements U_r

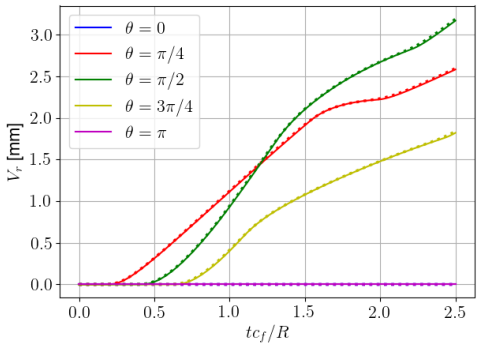

(b) Ortho-radial displacements V_r

Figure 2.13: Numerical solutions of finite element model in $(\mathbf{u}_s, \phi^{rad})$ (dashed lines) and semi-analytical solutions (full lines)

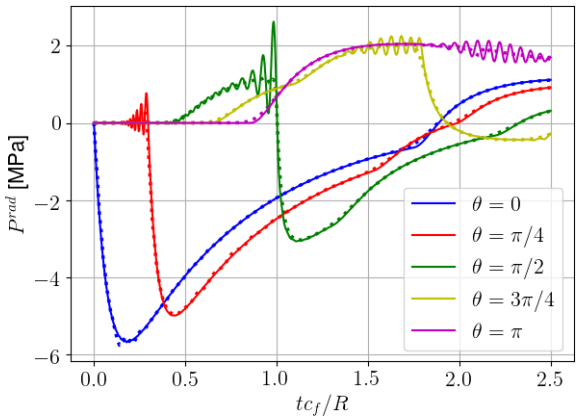

Figure 2.14: Numerical solutions of finite element model in $(\mathbf{u}_s, \phi^{rad})$ (dashed lines) and semi-analytical solutions (full lines) of the radiated pressure at fluid-structure interface

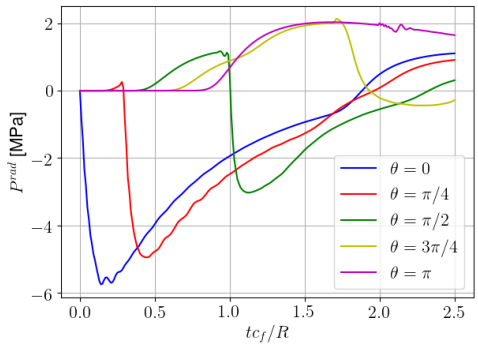

(a) Numerical solutions

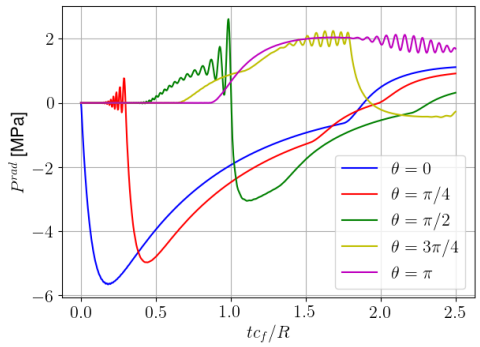

(b) Semi-analytical solutions

Figure 2.15: Numerical solutions of finite element model in $(\mathbf{u}_s, \phi^{rad})$ (left) and semi-analytical solutions (right) of the radiated pressure at fluid-structure interface

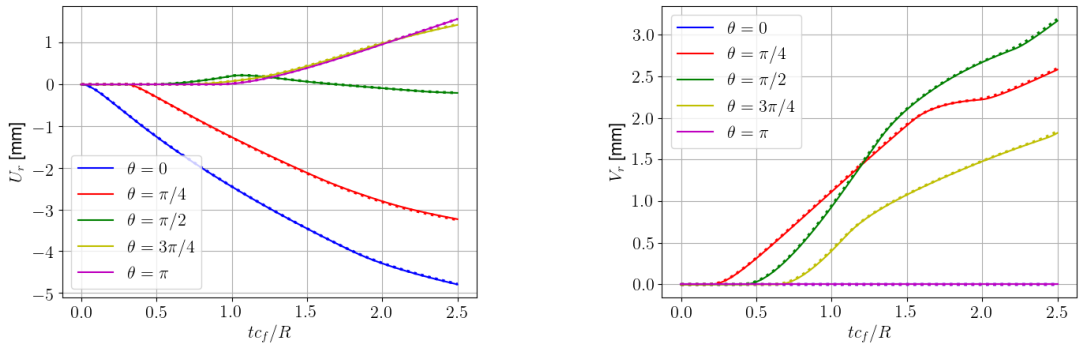

(a) Radial displacements U_r (b) Ortho-radial displacements V_r

Figure 2.16: Numerical solutions of finite element model in $(\mathbf{u}_s, p^{rad})$ (dashed lines) and semi-analytical solutions (full lines)

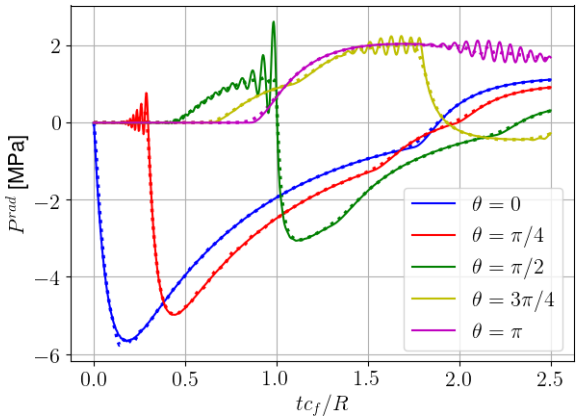

Figure 2.17: Numerical solutions of finite element model in $(\mathbf{u}_s, p^{rad})$ (dashed lines) and semi-analytical solutions (full lines) of the radiated pressure at fluid-structure interface

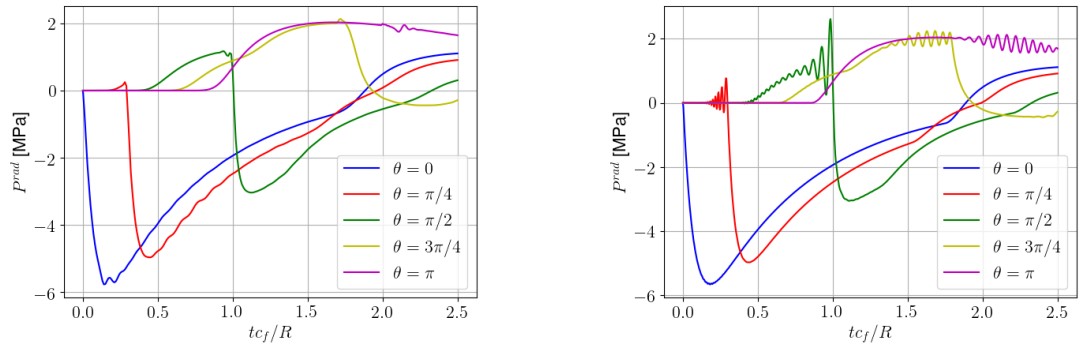

(a) Numerical solutions (b) Semi-analytical solutions

Figure 2.18: Numerical solutions of finite element model in $(\mathbf{u}_s, p^{rad})$ (left) and semi-analytical solutions (right) of the radiated pressure at fluid-structure interface

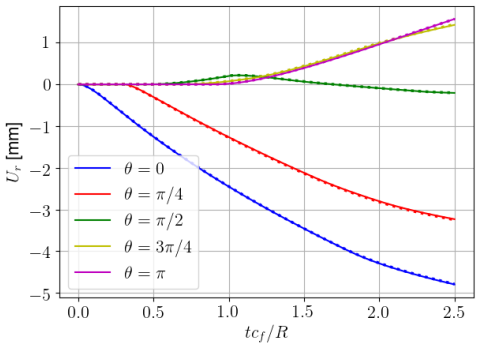

(a) Radial displacements U_r

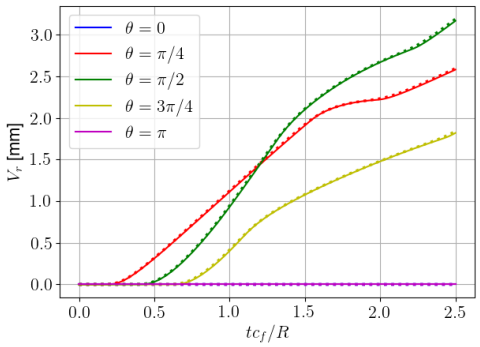

(b) Ortho-radial displacements V_r

Figure 2.19: Numerical solutions of finite element model in $(\mathbf{u}_s, p^{rad}, \varphi^{rad})$ (dashed lines) and semi-analytical solutions (full lines)

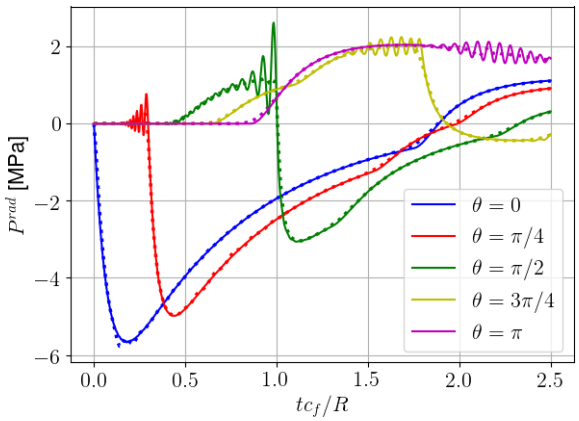

Figure 2.20: Numerical solutions of finite element model in $(\mathbf{u}_s, p^{rad}, \varphi^{rad})$ (dashed lines) and semi-analytical solutions (full lines) of the radiated pressure at fluid-structure interface

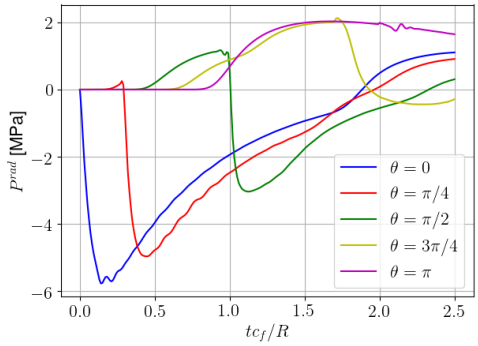

(a) Numerical solutions

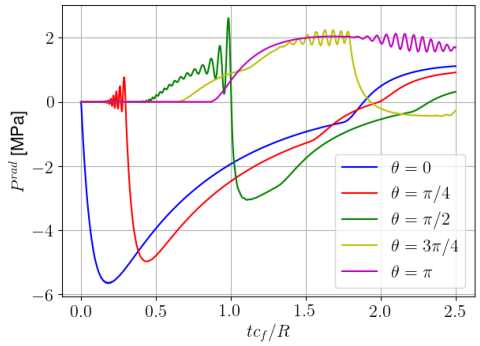

(b) Semi-analytical solutions

Figure 2.21: Numerical solutions of finite element model in $(\mathbf{u}_s, p^{rad}, \varphi^{rad})$ (left) and semi-analytical solutions (right) of the radiated pressure at fluid-structure interface

For the formulations in $(\mathbf{u}_s, \phi^{rad})$, $(\mathbf{u}_s, p^{rad})$ and $(\mathbf{u}_s, p^{rad}, \varphi^{rad})$, the results are respectively displayed in Figure 2.13, 2.16 and 2.19 for the radial and ortho-radial displacement. The radiated pressure are reported by Figure 2.14-2.15 for the formulation in $(\mathbf{u}_s, \phi^{rad})$, by Figure 2.17-2.18 for the formulation in $(\mathbf{u}_s, p^{rad})$ and by Figure 2.20-2.21 for the formulation in $(\mathbf{u}_s, p^{rad}, \varphi^{rad})$. We observe that these three formulations provide the same results which confirm numerically the equivalence as mentioned in Chapter 1. In comparison to the semi-analytical solution, the numerical results of these three formulations reveal the same observation as the formulation in $(\mathbf{u}_s, \phi^{sca})$.

As a conclusion, this study case allows us to validate our implementation of the loading induced by the shock wave and the new formulations $(\mathbf{u}_s, p)$ and $(\mathbf{u}_s, \phi)$ in a 2D configuration. Numerical results confirm that the three formulations presented in Chapter 1 are equivalent. Because of the discontinuity of the excitation provided by the shock wave, we note that a small numerical dissipation is required in Newmark scheme in order to filter the unwanted oscillation of high frequency.

Remark 2.5.1 It should be note that these parasite oscillations are induced by the dispersive nature of the Newmark scheme without dissipation ($\gamma = 1/2, \beta = 1/4$), which is consistent at order 2. When the dissipation is introduced, Newmark scheme becomes only consistent at order 1, and then numerically smooths the discontinuities: the dispersive nature, which is an order 3 phenomenon arising around discontinuities, is therefore no longer observed.

2.5.2 Test case 2: a section of cylindrical hull submitted to an acoustic shock wave

As the second study case, we consider an elastic structure with a form of a section of cylindrical hull submitted to an excitation induced by an underwater explosion in the same manner as in the first study case. Here, the domain occupied by the structure is $\Omega_s := \{(x, y, z) \in \mathbb{R}^3, R - e/2 < x^2 + y^2 < R + e/2, -h/2 < z < h/2\}$ where R, e and h denote respectively the radius, the thickness and the length of the cylindrical hull.

In order to render negligible the 3D-effect in z-direction, we impose a homogeneous Dirichlet boundary condition of the displacement in z-direction on the boundary $z = h/2$ and $z = -h/2$ of the structure Ω_s. We also assume that the thickness of the cylindrical hull is relatively small compared to its radius and that the radius of the hull is relatively small compared to distance of the explosion to the center of the hull. Under these assumptions, the semi-analytical solution of the first study case can be employed as the reference solution in our 3D-configuration problem.

For the numerical illustration, we use $R = 1$ m, $e = 0.01$ m and $h = 0.2$ m. The loading under consideration is excited by the primary acoustic shock wave, which comes from an underwater explosion of 1 000 kg TNT detonated at $(d, 0, 0)$, where $d = 100$ m. At $t = 0$, we suppose that the front of the shock wave arrives at the stand-off point (the nearest point of the structure to explosion). The physical properties of the structure and the fluid in the problem are given in Table 2.1. The profile of the incident pressure and of the incident velocity

are respectively given by the relations (2.12) and (2.15). In this study, we use the value of the constants P_c, v_c, A and B provided by Cole [40] as given in relation (2.10).

Finite element modelling

In order to approximate the radiation condition, a truncated fluid domain in form of a circle of cylindrical of radius $R_{bgt} = 3$ m and with the same length as the structure, is employed. On the boundary of the truncated fluid domain, the BGT-1 condition (1.35) is applied in order to approximate the outgoing sound wave by a cylindrical wave for which we use the value of impedance $Z_R = 2\rho_0 R_{bgt}, Z_C = \rho_0 c_0$. The structure part is modelled using the **quadratic triangular shell elements** [21]. The fluid part is modelled using **quadratic tetrahedron elements**. The using mesh is illustrated in Figure 2.7.

In the resulting finite element model, we have 230 067 degrees of freedom, 111 987 of which correspond to the structural part and 118 080 of which correspond to the acoustic fluid part for the formulation in $(\mathbf{u}_s, \phi^{sca})$, in $(\mathbf{u}_s, \phi^{rad})$ and in $(\mathbf{u}_s, p^{rad})$. For the formulation in $(\mathbf{u}_s, p^{rad}, \varphi^{rad})$, we have 348 147 degrees of freedom, 111 987 of which correspond to the structural part and 236 160 of which correspond to the acoustic fluid part and the non-symmetric finite element model (2.37) will be used in this study. For time-discretization of finite element model, Newmark scheme with a small numerical dissipation ($\gamma = 1/2 - \alpha$, $\beta = \frac{1}{4}(1-\alpha)^2$ where $\alpha = -0.2$) is employed by using the time step of size $\Delta t = 6.7 \cdot 10^{-6}$ s which means that the shock wave needs 100 time steps in order to travel the distance R.

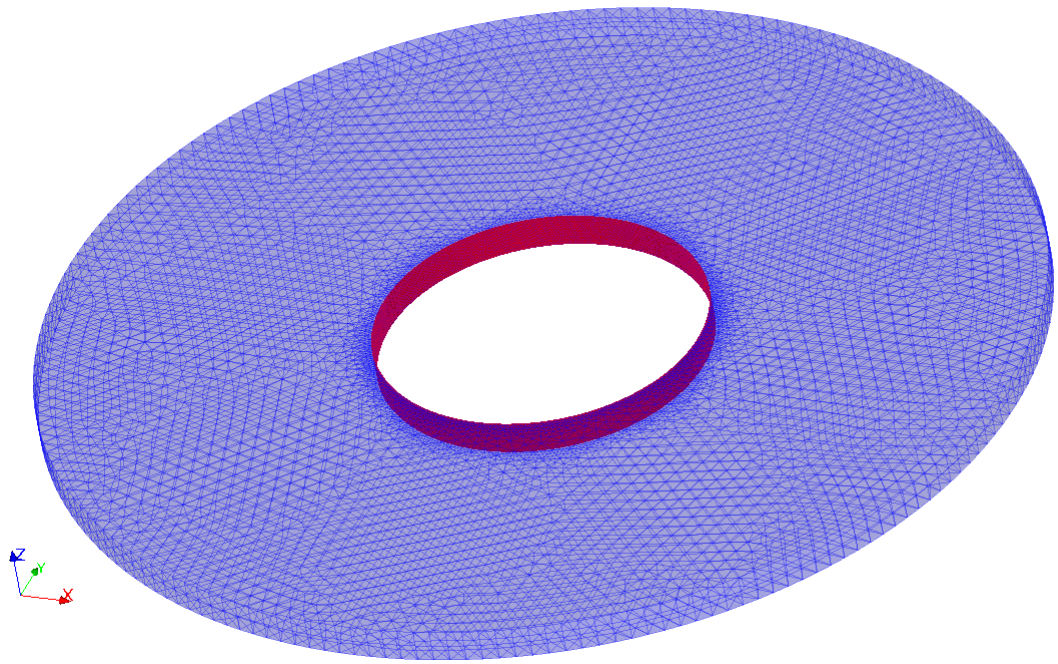

Figure 2.22: Mesh used in finite element modelling in the second validation case

Analysis of numerical results

For numerical analysis, let us begin with the formulation in $(\mathbf{u}_s, \phi^{sca})$. The numerical and reference solutions of radial and ortho-radial displacement at $z = 0$, are respectively illustrated in Figure 2.23a and 2.23b. In Figure 2.23a and 2.23b, the reference solutions are displayed by full lines while the numerical solutions are displayed by dashed lines. Because of the symmetric in the problem, the ortho-radial displacement for $\theta = 0$ and $\theta = \pi$ is zero as shown in Figure 2.23b. We can see clearly that the numerical solution is in accordance with the reference solution. For the scattered pressure, Figure 2.24 plots the numerical and reference solutions in the same graphic and Figure 2.25 plots the numerical and reference solution in two differences graphics. The results show that the scattered pressure obtained by the finite element model is also in accordance with the reference solution. We remark that there are some unwanted oscillations in the reference solutions of the scattered pressure which are essentially due to the Gibb phenomena and the numerical instabilities in inverse Laplace transform algorithm. In the numerical solutions, we have also some unwanted oscillations. However, it is less significant than the reference solutions since numerical dissipations are introduced in time-discretization scheme.

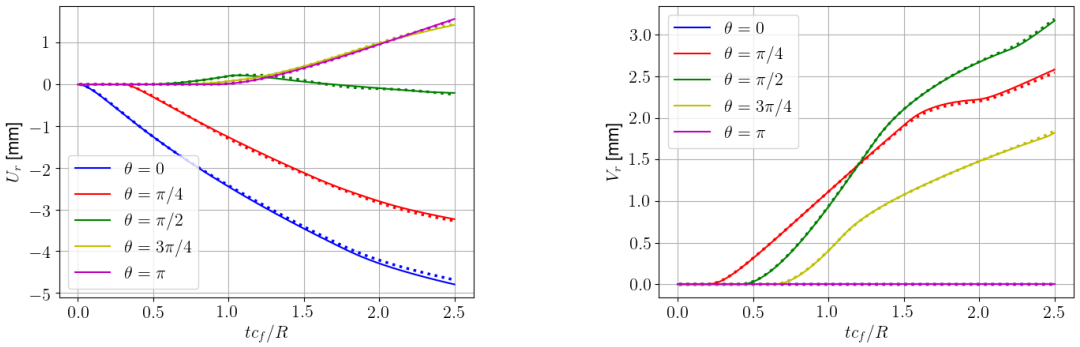

(a) Radial displacements U_r (b) Ortho-radial displacements V_r

Figure 2.23: Numerical solutions of finite element model in $(\mathbf{u}_s, \phi^{sca})$ (dashed lines) and reference solutions (full lines)

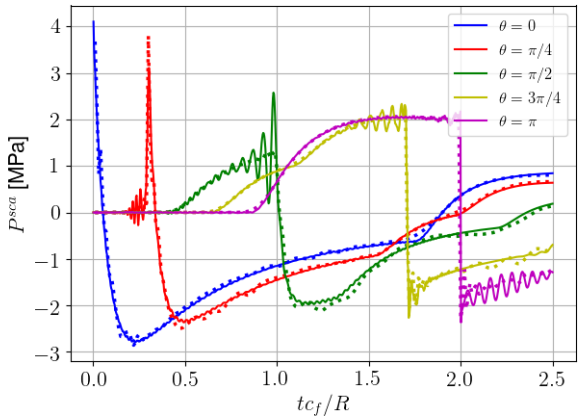

Figure 2.24: Numerical solutions of finite element model in $(\mathbf{u}_s, \phi^{sca})$ (dashed lines) and reference solutions (full lines) of the scattered pressure at fluid-structure interface

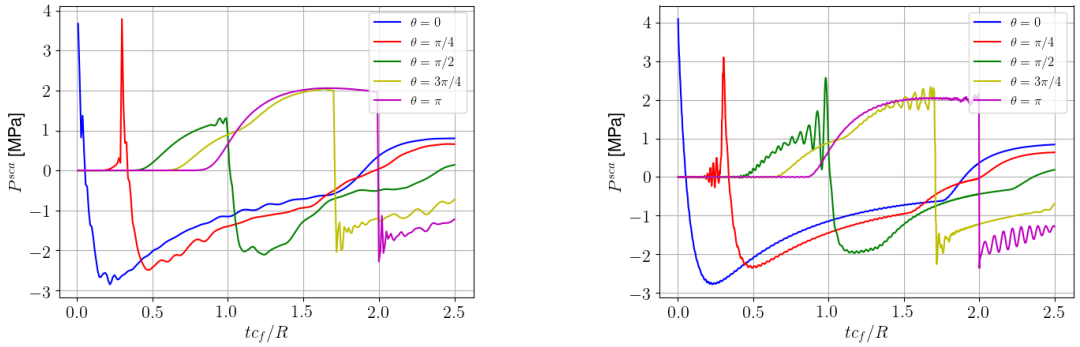

(a) Numerical solution (b) Reference solutions

Figure 2.25: Numerical solutions of finite element model in $(\mathbf{u}_s, \phi^{sca})$ (left) and reference solutions (right) of the scattered pressure at fluid-structure interface

Let us now interest in the formulations in $(\mathbf{u}_s, \phi^{rad})$, $(\mathbf{u}_s, p^{rad})$ and $(\mathbf{u}_s, p^{rad}, \varphi^{rad})$. We remind that the pre-computing of reflected pressure p^{ref} are required in order to use the formulation in $(\mathbf{u}_s, \phi^{rad})$ and $(\mathbf{u}_s, p^{rad})$. The same mesh of fluid part of the previous model in $(\mathbf{u}_s, \phi^{sca})$ are used for the finite element modelling in formulation in ϕ^{ref} (2.40). The reflected pressures are then obtained by the relation (2.19). Figure 2.26 shows the numerical and reference solutions of reflected pressure in the same graphic. Numerical solutions of finite element model are displayed in dashed lines while reference solution are displayed in full lines. The numerical results show that the reflected pressures of finite element model in ϕ^{ref} are in agreement with the reference solutions. Figure 2.27 plots the numerical and reference solutions of the reflected pressure in two different graphics. As in the previous case, there are also parasites oscillations in the reference solutions. It is however less significant than in case of scattered pressure. Contrary to the case of scattered pressure where the reference solutions always have parasites oscillations more significant than the numerical solutions, we observe that the numerical solutions of the reflected pressure cause parasites oscillations larger than the reference solutions for the case $\theta = 0$ and $\theta = \pi$.

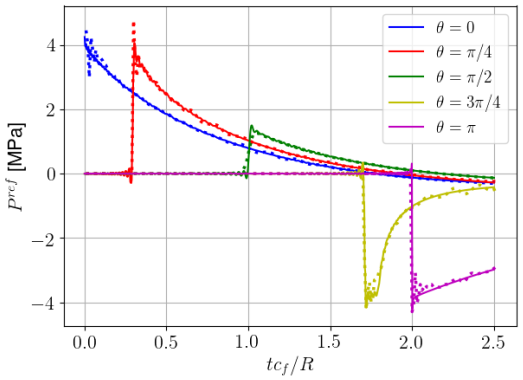

Figure 2.26: Numerical solutions of finite element model (dashed lines) and reference solutions (full lines) of the reflected pressure at fluid-structure interface

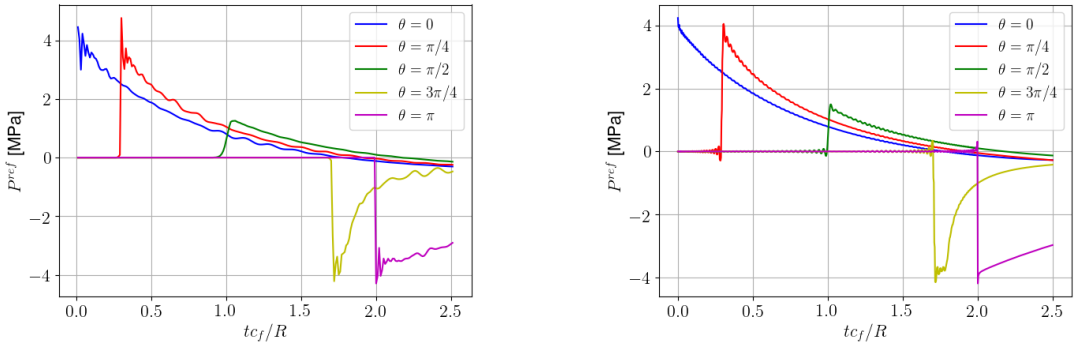

(a) Numerical solutions

(b) Reference solutions

Figure 2.27: Numerical solutions of finite element model (left) and reference solutions (right) of the reflected pressure at fluid-structure interface

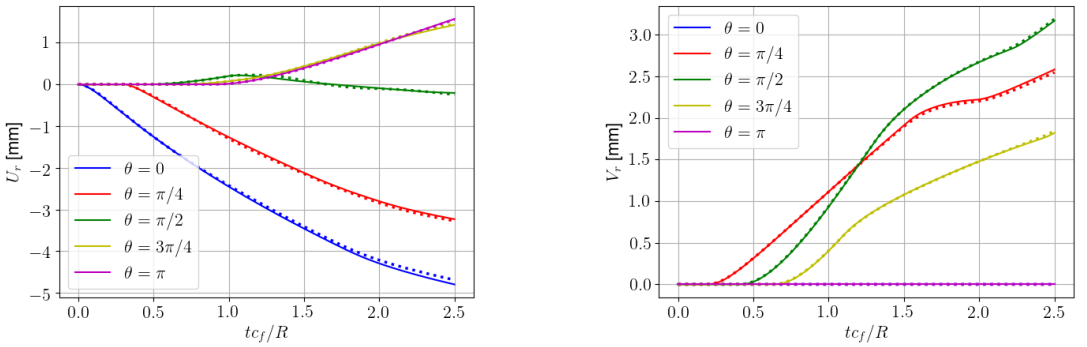

(a) Radial displacements U_r (b) Ortho-radial displacements V_r

Figure 2.28: Numerical solutions of finite element model in $(\mathbf{u}_s, \phi^{rad})$ (dashed lines) and semi-analytical solutions (full lines)

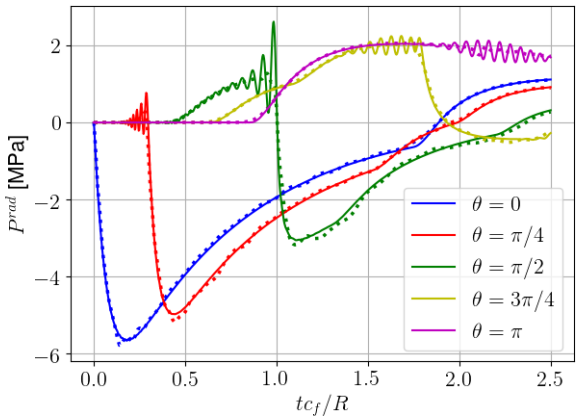

Figure 2.29: Numerical solutions of finite element model in $(\mathbf{u}_s, \phi^{rad})$ (dashed lines) and semi-analytical solutions (in full lines) of the radiated pressure at fluid-structure interface

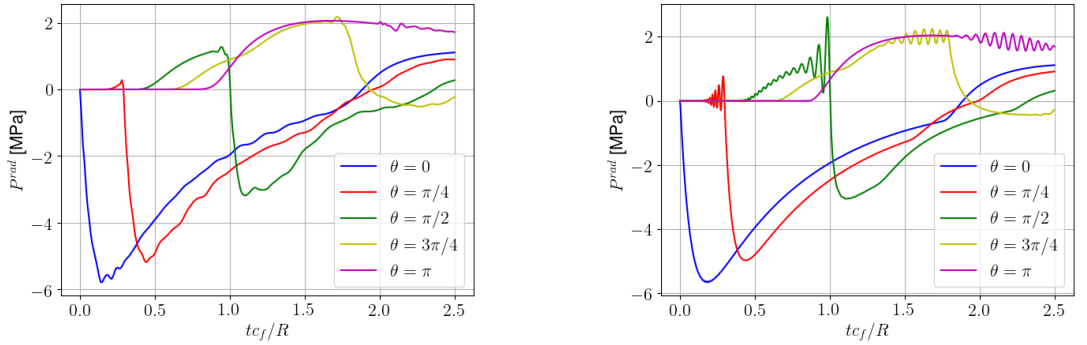

(a) Numerical solutions (b) Semi-analytical solutions

Figure 2.30: Numerical solutions of finite element model in $(\mathbf{u}_s, \phi^{rad})$ (left) and semi-analytical solutions (right) of the radiated pressure at fluid-structure interface

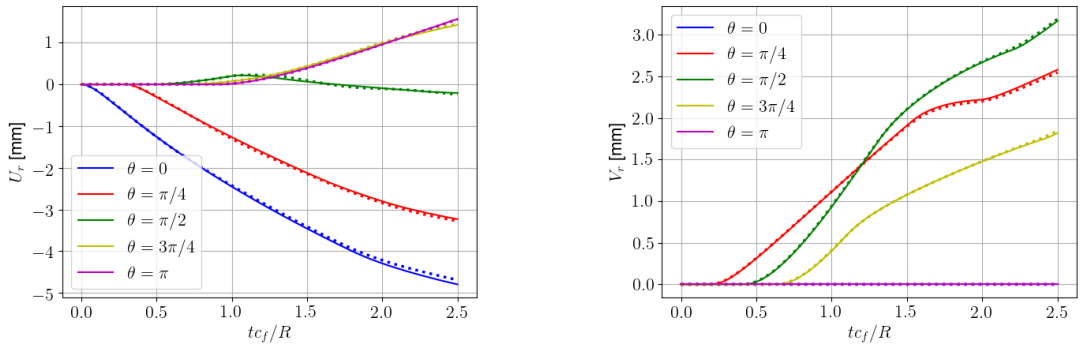

(a) Radial displacements U_r (b) Ortho-radial displacements V_r

Figure 2.31: Numerical solutions of finite element model in $(\mathbf{u}_s, p^{rad})$ (dashed lines) and semi-analytical solutions (full lines)

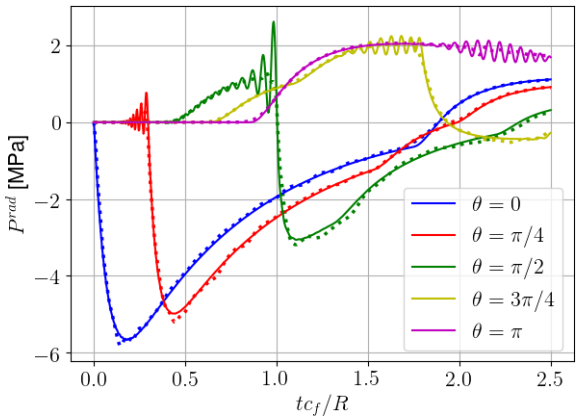

Figure 2.32: Numerical solutions of finite element model in $(\mathbf{u}_s, p^{rad})$ (dashed lines) and semi-analytical solutions (full lines) of the radiated pressure at fluid-structure interface

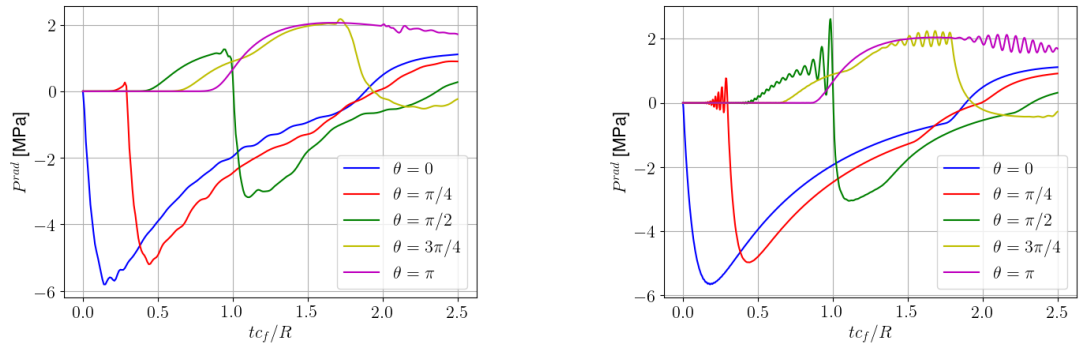

(a) Numerical solutions (b) Semi-analytical solutions

Figure 2.33: Numerical solutions of finite element model in $(\mathbf{u}_s, p^{rad})$ (left) and semi-analytical solutions (right) of the radiated pressure at fluid-structure interface

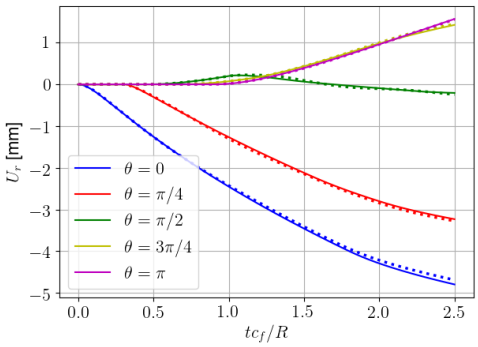

(a) Radial displacements U_r

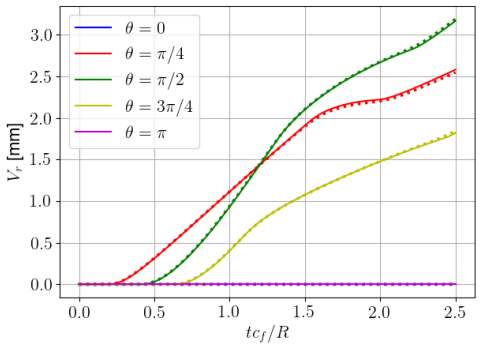

(b) Ortho-radial displacements V_r

Figure 2.34: Numerical solutions of finite element model in $(\mathbf{u}_s, p^{rad}, \varphi^{rad})$ (dashed lines) and semi-analytical solutions (full lines)

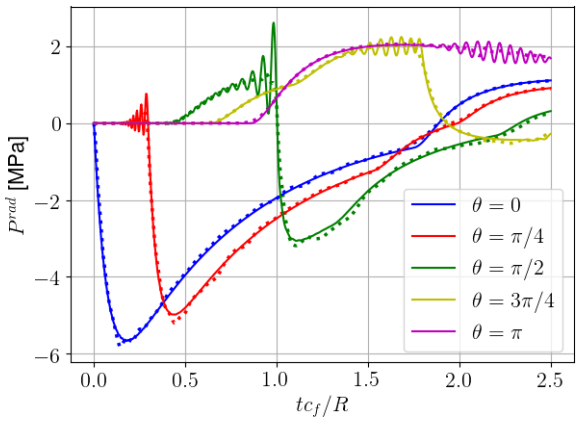

Figure 2.35: Numerical solutions of finite element model in $(\mathbf{u}_s, p^{rad}, \varphi^{rad})$ (dashed lines) and semi-analytical solutions (full lines) of the radiated pressure at fluid-structure interface

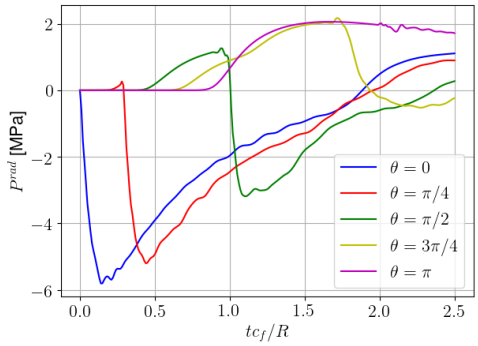

(a) Numerical solutions

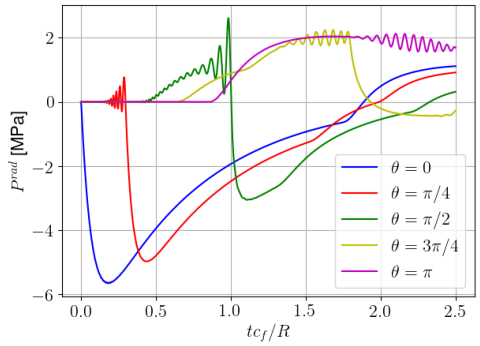

(b) Semi-analytical solutions

Figure 2.36: Numerical solutions of finite element model in $(\mathbf{u}_s, p^{rad}, \varphi^{rad})$ (left) and semi-analytical solutions (right) of the radiated pressure at fluid-structure interface

For the formulation in $(\mathbf{u}_s, \phi^{rad})$, in $(\mathbf{u}_s, p^{rad})$ and in $(\mathbf{u}_s, p^{rad}, \varphi^{rad})$, the results are respectively displayed in Figure 2.28, 2.31 and 2.34 for the radial and ortho-radial displacement. The radiated pressure are reported by Figure 2.29-2.30 for the formulation in $(\mathbf{u}_s, \phi^{rad})$, by Figure 2.32-2.33 for the formulation in $(\mathbf{u}_s, p^{rad})$ and by Figure 2.35-2.36 for the formulation in $(\mathbf{u}_s, p^{rad}, \varphi^{rad})$. We observe that these three formulations provide the same results which confirm numerically their equivalent as mentioned in Chapter 1. In comparison to the semi-analytical solution, the numerical results of these three formulation reveals the same observation as the formulation in $(\mathbf{u}_s, \phi^{sca})$.

As a conclusion, this study case allows us to validate our implementation of the loading induced by the shock wave and the new formulations $(\mathbf{u}_s, p)$ and $(\mathbf{u}_s, \phi)$ in a 3D configuration. Numerical results confirm that the three formulations presented in Chapter 1 are equivalent. Because of the discontinuity of the excitation provided by the shock wave, we also note in this study case that a small numerical dissipation is required in Newmark scheme in order to filter the unwanted oscillations of high frequency.

2.6 Conclusions

A short presentation of the underwater explosion phenomena and finite element modelling of interaction of submerged structure and shock wave problem are given in this chapter. Four formulations: *in displacement structure - scattered velocity potential* $(\boldsymbol{u}_s, \phi^{sca})$*, in displacement structure - radiated velocity potential* $(\boldsymbol{u}_s, \phi^{rad})$*, in displacement structure - radiated pressure* $(\boldsymbol{u}_s, p^{rad})$ *and in displacement structure - radiated pressure - radiated displacement potential* $(\boldsymbol{u}_s, p^{rad}, \varphi^{rad})$, of the fluid-structure interaction problem of interest have been presented in terms of strong formulation (PDE) as well as in terms of finite element models. Contrary to the formulation in $(\mathbf{u}_s, \phi^{sca})$, which requires only the knowledge on the shock wave (*i.e* incident pressure and velocity), other three formulations require a pre-computation of the reflected pressure.

In order to validate the implementation of the loading induced by the acoustic shock wave and the two new formulations in *code_aster*, numerical results on two test cases are presented in the last section of the chapter. Numerical results confirm that the three formulations presented in Chapter 1 are equivalent. It also indicates that a small numerical dissipation is required in Newmark family scheme in order to filter the high frequency oscillation due to the shock wave discontinuity.

Part II

Reduced order modelling

Chapter 3

Reduced order modelling of transient vibro-acoustic problem

In the previous chapters, finite element models of transient vibro-acoustic problem expressed in various formulations have been presented. In order to obtain an accurate solution from the finite element model, it is known that we have to ensure that the size of mesh is small enough for the highest frequency of interest. Because of the three-dimensional nature of acoustics, the number of elements increases dramatically as the size of the problem increases. In addition, since we use the approximation condition of radiation condition by BGT method [22, 67] for exterior problem, we need to truncate fluid domain at a distance sufficiently far enough from the propagation source. In practice, these requirements lead to having a large computational domain together with a very large number of elements to apply the finite element method of the full model. As expected, in the industrial context, it is not applicable to use the full model for many parameters. Therefore, we need to develop judicious numerical methods to solve this problem for many parameters reasonably fast.

In order to overcome the issue of computational costs, we can turn to the reduced order modelling techniques. The reduced basis method, which was originally introduced in the 1970's for non-linear structural analysis in [3, 102] and analysed in [18, 110], have been investigated as model order reduction technique in different parametrized stationary problems; such as in harmonic Maxwell's equations in [38], in elasticity problem [73, 123], in steady Navier-Stokes equation in [91]. For parametrized frequency domain vibro-acoustic problem, a reduced order modelling based on the reduced basis method has been analysed in [83]. The construction of the reduced order model in the work [83] is based on a Petrov-Galerkin projection on a suitable trial subspace and a suitable test subspace. An appropriate trial subspace can be built by an iterative Greedy Algorithm using the norm of residual as error indicator. Galerkin and Minimum Residual projections are then considered to determine the test subspace and construct the parametric reduced order model. Numerical results of industrial complexity show that the proposed reduced order model provides a very good approximation of the full model with the CPU time gain of several orders of magnitude depending on the desired accuracy.

Unfortunately, it has been shown in [27, 121] that the technique proposed in [83] can not be directly applied in time domain problem. For transient problem, it is necessary to ensure that the reduced order model preserves the stability properties of the full model. In the most general cases of time-dependent problem, the reduced order model based on a Petrov-Galerkin

projection does not preserve the stability of the full model. Several techniques of stabilization have been proposed in literature (for instance, see [96, 7, 25, 76, 119]). Balanced Truncation method proposed in [96] can ensure the stability of the Galerkin-reduced order model. Unfortunately, the computation of the reduced basis involves the Lyapunov equations which require a complexity of $\approx O(n^3)$, where n is the size of the full model, for the resolution. This complexity makes the application of this technique out of reach in the industrial problem. A general purpose optimization approaches to obtain a stable Petrov-Galerkin projection reduced order model are presented in [7] and [25]. For a given couple $(\mathbf{W}, \mathbf{V})$, the proposed approach aims to replace the left basis $\mathbf{W}$ by a new one $\tilde{\mathbf{W}}$ for which Petrov-Galerkin reduced order model based on the couple $(\tilde{\mathbf{W}}, \mathbf{V})$ is stable. The key idea is to solve a constrained optimization problem where the constraint is to enforce stability of reduced order model and the objective function to minimize is the difference between the resulting left basis and the original left basis in order to ensure that the loss accuracy in the stabilization process is as small as possible. The method proposed in [7] does not guarantee the existence of the solution of constrained optimization problem. The method proposed in [25] can guarantee the existence of the solution of constrained optimization problem. However the proposed algorithms are not guaranteed to terminate with a finite number of iterations. In 2014, a new approach for stabilizing unstable reduced order model through an a posteriori post-processing applied to algebraic reduced order model system is developed in [76]. The idea is to modify the unstable eigenvalues of the reduced order model system by moving these eigenvalues into the stable half of the complex plane. This approach can ensure that the modified reduced order model is stable however the accuracy of the stabilized reduced order model is not guaranteed.

Specifically for the case of time-domain vibro-acoustic finite element model, a stable reduced order modelling has been recently proposed in [121] for the formulation in $(\mathbf{u}_s, p)$ and in $(\mathbf{u}_s, \phi)$ for the case of an interior problem. For $(\mathbf{u}_s, \phi)$ based formulation, the idea is to modify the original formulation by changing the sign of the set of equations governing the acoustic part before employing Galerkin projection. For the case of $(\mathbf{u}_s, \phi)$ based formulation, the stability of Galerkin-reduced order model is achieved by choosing a particular form of the reduced basis in order to preserve the structure of the original full model. The proposed techniques are then extended to the case of exterior problem, where the radiation condition is modelled by the Infinite Element method [10], in [122].

The first objective of this chapter is to present the stabilization reduced order modelling technique proposed in [121] for the time domain vibro-acoustic finite element model in $(\mathbf{u}_s, p)$ and $(\mathbf{u}_s, \phi)$ couple and exploit the ideas to give a stabilization reduced order modelling technique for the finite element model in $(\mathbf{u}_s, p, \varphi)$ couple. The second objective of this chapter is to study the accuracy of the reduced order model based on the reduced basis built by a Greedy Algorithm applying on the corresponding frequency domain proposed in [83]. This chapter is organized as follows. In the first section, we recall the notion of stability and we verify that the finite element model in $(\mathbf{u}_s, p)$, $(\mathbf{u}_s, \phi)$ and in $(\mathbf{u}_s, p, \varphi)$ are all stable. In the second section, the stable reduced order models based on Petrov-Galerkin projection for the three formulations are given in Subsection 3.2.3, 3.2.4 and 3.2.5. The third section focuses on the construction of the reduced basis. Depending on the stabilization technique of each formulation, we propose to make some modifications in the classical Greedy Algorithm. Numericals validations of the stability and numerical study on the accuracy of reduced order model are given in Section 3.4. Finally, conclusions are offered in Section 3.5.

3.1 Full model and stability

In this chapter, the term of full model refers to the finite element model. We consider here the full model which is described by a set of ordinary differential equations:

$$\begin{cases} \mathbf{M}\ddot{\mathbf{X}}(t) + \mathbf{C}\dot{\mathbf{X}}(t) + \mathbf{K}\mathbf{X}(t) = f(t)\mathbf{F} \\ \mathbf{X}(t=0) = \mathbf{X}_0 \\ \dot{\mathbf{X}}(t=0) = \dot{\mathbf{X}}_0 \end{cases} \tag{3.1}$$

where $\mathbf{M}$, $\mathbf{C}$ and $\mathbf{K} \in \mathbb{C}^{n\times n}$ are respectively the given mass, damping and stiffness matrix of the problem, f is a time-dependent function and $\mathbf{F}$ is a vector of $\mathbb{C}^n$. Before talking about the reduced order modelling, let us recall briefly the notion of stability of the dynamical system (3.1).

Throughout this chapter, the stability means that the state of the system (3.1) is bounded (*i.e* $\exists\, C > 0$ such that $||\mathbf{X}(t)|| \leq C$, $\forall t \geq 0$) in the case of absence of the external force, for any initial condition. In general, it is difficult to directly study the stability of a second-order system. It is usual to work with an equivalent linear descriptor system since the criteria of the stability are well established for this kind of system. A linear descriptor system is governed by the set of equations:

$$\mathbf{E}\dot{\mathbf{Y}}(t) = \mathbf{A}\mathbf{Y}(t) + \mathbf{B}(t) \tag{3.2}$$

where $\mathbf{E}, \mathbf{A}$ are two matrices in $\mathbb{C}^{2n\times 2n}$, $\mathbf{B}$ is a time-dependent vector in $\mathbb{C}^{2n}$ and $\mathbf{Y} = \begin{bmatrix}\mathbf{X}(t) & \dot{\mathbf{X}}(t)\end{bmatrix}^T$. The definition of stability of a linear descriptor system (3.2) is given by the following definition [50].

Definition 3.1.1 *The linear descriptor system (3.2) is called* ***stable*** *if and only if all of eigenvalues of the following generalized eigenvalue problem:*

$$\boldsymbol{A}\boldsymbol{y} = \lambda \boldsymbol{E}\boldsymbol{y} \tag{3.3}$$

have a negative real part.

It is important to note that the second-order system (3.1) can be written as a linear descriptor system (3.2) with

$$\mathbf{E} = \begin{bmatrix}\mathbf{Q} & \mathbf{0} \\ \mathbf{0} & \mathbf{M}\end{bmatrix}, \mathbf{A} = \begin{bmatrix}\mathbf{0} & \mathbf{Q} \\ -\mathbf{K} & -\mathbf{C}\end{bmatrix} \text{ and } \mathbf{B}(t) = f(t)\begin{bmatrix}\mathbf{0} \\ \mathbf{F}\end{bmatrix} \tag{3.4}$$

where $\mathbf{Q}$ is an invertible matrix. Hence, we can use the following definition for the stability of a second order system (3.1).

Definition 3.1.2 *The dynamical system (3.1) is called* ***stable*** *if and only if all root of the polynomial* $P(s) := det(s^2\boldsymbol{M} + s\boldsymbol{C} + \boldsymbol{K})$ *have a negative real part.*

The roots of the polynomial $P(s)$ are also known as the **poles** of the system (3.1). The definition 3.1.2 is equivalent to stating that all the poles of the system must be in the closed left-half complex plane. In what follows, we give an overview on the mathematical conditions under

which the system (3.1) and (3.2) are stable. First, let us recall the notion of (semi)-definite positive of a matrix $\mathbb{C}^{n\times n}$.

Definition 3.1.3 *A matrix $\boldsymbol{A} \in \mathbb{C}^{n\times n}$ is called:*

- ***positive definite*** *if and only if we have $\Re(\boldsymbol{x}^H \boldsymbol{A}\boldsymbol{x}) > 0, \forall \boldsymbol{x} \in \mathbb{C}^n, \boldsymbol{x} \neq \boldsymbol{0}$*
- ***semi-positive definite*** *if and only if we have $\Re(\boldsymbol{x}^H \boldsymbol{A}\boldsymbol{x}) \geq 0, \forall \boldsymbol{x} \in \mathbb{C}^n$*

The following lemma gives a mathematical condition under which the linear descriptor system (3.2) is stable.

Lemma 3.1.1 *[121] The linear descriptor system (3.2) is stable if the matrix $\boldsymbol{E}$ is positive definite and hermitian and the matrix $-\boldsymbol{A}$ is positive semi-definite.*

Proof: Let $\lambda \in \mathbb{C}$ and $\mathbf{v} \in \mathbb{C}^n$ be the eigenvalue and the corresponding eigenvector of the generalized eigenvalue problem (3.3), by definition we have:

$$\begin{aligned} \mathbf{A}\mathbf{v} &= \lambda \mathbf{E}\mathbf{v} \\ \Rightarrow \mathbf{v}^H \mathbf{A}\mathbf{v} &= \lambda \mathbf{v}^H \mathbf{E}\mathbf{v} \end{aligned}$$

Since the matrix $\mathbf{E}$ is positive definite and hermitian, we have $\mathbf{v}^H\mathbf{E}\mathbf{v} \in \mathbb{R}$ and $\mathbf{v}^H\mathbf{E}\mathbf{v} > 0$. With the properties of positive semi-definiteness of the matrix $-\mathbf{A}$, we have then $\Re(\lambda) = \frac{\Re(\mathbf{v}^H\mathbf{A}\mathbf{v})}{\mathbf{v}^H\mathbf{E}\mathbf{v}} \leq 0$

□

The following lemma gives a mathematical condition under which the second-order system (3.1) is stable.

Lemma 3.1.2 *[121] The system (3.1) is stable if the mass and stiffness matrices $\boldsymbol{M}, \boldsymbol{K}$ are positive definite and hermitian and the damping matrix $\boldsymbol{C}$ is semi-positive definite.*

Proof: Since the stiffness matrix $\mathbf{K}$ is invertible, the second-order system (3.1) can be written as a linear descriptor (3.2) with

$$\mathbf{E} = \begin{bmatrix} \mathbf{K} & \mathbf{0} \\ \mathbf{0} & \mathbf{M} \end{bmatrix}, \mathbf{A} = \begin{bmatrix} \mathbf{0} & \mathbf{K} \\ -\mathbf{K} & -\mathbf{C} \end{bmatrix} \text{ and } \mathbf{B} = f(t) \begin{bmatrix} \mathbf{0} \\ \mathbf{F} \end{bmatrix}$$

Since the matrices $\mathbf{K}$ and $\mathbf{M}$ are positives definite and hermitian, the matrix $\mathbf{E}$ is also positive definite and hermitian. For any $\mathbf{x} = \begin{bmatrix} \mathbf{x}_1 & \mathbf{x}_2 \end{bmatrix}^T \in \mathbb{C}^{2n}$, we have

$$\Re(\mathbf{x}^H\mathbf{A}\mathbf{x}) = \Re(\begin{bmatrix} \mathbf{x}_1^H & \mathbf{x}_2^H \end{bmatrix} \begin{bmatrix} \mathbf{0} & \mathbf{K} \\ -\mathbf{K} & -\mathbf{C} \end{bmatrix} \begin{bmatrix} \mathbf{x}_1 \\ \mathbf{x}_2 \end{bmatrix}) = -\Re(\mathbf{x}_2^H\mathbf{C}\mathbf{x}_2) \leq 0$$

Thus, the matrix $-\mathbf{A}$ is positive semi-definite. Since the matrix $-\mathbf{A}$ is positive semi-definite and the matrix $\mathbf{E}$ is positive definite and hermitian, we can conclude that the second-order system (3.1) is stable according to Lemma 3.1.1

□

An extension of Lemma 3.1.2 for the case of the stiffness matrix is only positive semi-definite is given by the following lemma.

Lemma 3.1.3 *The system (3.1) is stable if the mass $\boldsymbol{M}$ is positive definite and hermitian, the stiffness $\boldsymbol{K}$ is positive semi-definite and hermitian, and the damping matrix $\boldsymbol{C}$ is positive semi-definite.*

Proof: Let λ is a root of the polynomial $P(s) = \det(s^2\mathbf{M} + s\mathbf{C} + \mathbf{K})$. By definition, there is a vector $\mathbf{x} \neq 0$ such that:

$$\begin{aligned} (s^2\mathbf{M} + s\mathbf{C} + \mathbf{K})\mathbf{x} &= 0 \\ \Rightarrow s^2(\mathbf{x}^H\mathbf{M}\mathbf{x}) + s(\mathbf{x}^H\mathbf{C}\mathbf{x}) + \mathbf{x}^H\mathbf{K}\mathbf{x} &= 0 \end{aligned}$$

The hypothesis of the lemma implies that $\mathbf{x}^H\mathbf{M}\mathbf{x} \in \mathbb{R}$, $\mathbf{x}^H\mathbf{M}\mathbf{x} > 0$, $\mathbf{x}^H\mathbf{K}\mathbf{x} \in \mathbb{R}$, $\mathbf{x}^H\mathbf{K}\mathbf{x} \geq 0$ and $\Re(\mathbf{x}^H\mathbf{C}\mathbf{x}) \geq 0$. Let us denote by $s_1 = a_1 + jb_1$ and $s_2 = a_2 + jb_2$ the solution of algebraic equation $s^2(\mathbf{x}^H\mathbf{M}\mathbf{x}) + s(\mathbf{x}^H\mathbf{C}\mathbf{x}) + \mathbf{x}^H\mathbf{K}\mathbf{x} = 0$. Then, we have $s_1 + s_2 = -\frac{\mathbf{x}^H\mathbf{C}\mathbf{x}}{\mathbf{x}^H\mathbf{M}\mathbf{x}}$ and $s_1 s_2 = \frac{\mathbf{x}^H\mathbf{K}\mathbf{x}}{\mathbf{x}^H\mathbf{C}\mathbf{x}}$ which implies:

$$\begin{cases} a_1 + a_2 = -\dfrac{\Re(\mathbf{x}^H\mathbf{C}\mathbf{x})}{\mathbf{x}^H\mathbf{M}\mathbf{x}} \leq 0 \\ a_1 a_2 - b_1 b_2 = \dfrac{\mathbf{x}^H\mathbf{K}\mathbf{x}}{\mathbf{x}^H\mathbf{M}\mathbf{x}} \geq 0 \\ a_1 b_2 + a_2 b_1 = 0 \end{cases}$$

- Case 1 : If $a_1 = 0$ ($a_2 = 0$), the inequality $a_1 + a_2 \leq 0$ implies that $a_2 \leq 0$ ($a_1 \leq 0$). Then, we have in this case $\Re(s_1) \leq 0, \Re(s_2) \leq 0$.

- Case 2 : If $a_1 \neq 0, a_2 \neq 0$. Suppose that a_1 and a_2 do not have the same sign. Then, we have $a_1 a_2 < 0$ and $a_2/a_1 < 0$. From the equation $a_1 b_2 + a_2 b_1 = 0$, we have $b_1 b_2 = -(a_2/a_1) > 0$. Since $a_1 a_2 < 0$ and $b_1 b_2 > 0$, we have a contradiction in the inequality $a_1 a_2 - b_1 b_2 \geq 0$. It means that a_1 and a_2 must have the same sign in which case the inequality $a_1 + a_2 \leq 0$ implies that $\Re(s_1) \leq 0, \Re(s_2) \leq 0$.

□

In the case of the second-order system (3.1) resulting from the finite element discretization of structural dynamic or acoustic problem, the mass matrix $\mathbf{M}$ is symmetric and positive definite and the stiffness matrix $\mathbf{K}$ is symmetric and positive semi-definite. Hence, we can directly conclude that the system is stable according to Lemma 3.1.3 in the condition that if we have a damping effect, it is represented by a positive semi-definite matrix. For finite element models of vibro-acoustic coupling presented in the previous chapter, the sufficient conditions of stability in Lemma 3.1.3 is not verified.

In what follows, we propose to verify the stability of the second order systems resulting from a finite element discretization of transient vibro-acoustic problem.

3.1.1 Stability of full model in $(\mathbf{u}_s, \phi)$

Let us begin with the formulation in $(\mathbf{u}_s, \phi)$ couple. In order to generalize our demonstration, we consider that the structural and fluid damping effects are also taken into account in the model. For the case of an interior problem, the full model of the formulation in $(\mathbf{u}_s, \phi)$ is given by:

$$\begin{bmatrix} \mathbf{M}_s & \mathbf{0} \\ \mathbf{0} & -\rho_0 \mathbf{M}_f \end{bmatrix} \begin{bmatrix} \ddot{\mathbf{U}}_s \\ \ddot{\mathbf{\Phi}} \end{bmatrix} + \begin{bmatrix} \mathbf{C}_s & -\rho_0 \mathbf{K}_c \\ -\rho_0 \mathbf{K}_c^T & -\rho_0 \mathbf{C}_f \end{bmatrix} \begin{bmatrix} \dot{\mathbf{U}}_s \\ \dot{\mathbf{\Phi}} \end{bmatrix} + \begin{bmatrix} \mathbf{K}_s & \mathbf{0} \\ \mathbf{0} & -\rho_0 \mathbf{K}_f \end{bmatrix} \begin{bmatrix} \mathbf{U}_s \\ \mathbf{\Phi} \end{bmatrix} = \begin{bmatrix} \mathbf{F}_s \\ \mathbf{F}_\phi \end{bmatrix} \tag{3.5}$$

where the matrices $\mathbf{C}_s$ and $\mathbf{C}_f$ represent respectively the structural and the fluid damping matrix. We restrict ourselves to the case where these two damping matrices are positive semi-definite. The stability of the system (3.5) is achieved as a particular case (where all matrices have real coefficients) of the following lemma.

Lemma 3.1.4 *If the mass matrices $\boldsymbol{M}_s$, $\boldsymbol{M}_f$ are hermitian and positive definite, the stiffness matrices $\boldsymbol{K}_s$ et $\boldsymbol{K}_f$ are hermitian and positive semi-definite and the damping matrices $\boldsymbol{C}_s$ and $\boldsymbol{C}_f$ are positive semi-definite, the dynamical system*

$$\underbrace{\begin{bmatrix} \boldsymbol{M}_s & \boldsymbol{0} \\ \boldsymbol{0} & -\rho_0 \boldsymbol{M}_f \end{bmatrix}}_{\boldsymbol{M}_{u\phi}} \begin{bmatrix} \ddot{\boldsymbol{U}}_s \\ \ddot{\mathbf{\Phi}} \end{bmatrix} + \underbrace{\begin{bmatrix} \boldsymbol{C}_s & -\rho_0 \boldsymbol{K}_c \\ -\rho_0 \boldsymbol{K}_c^H & -\rho_0 \boldsymbol{C}_f \end{bmatrix}}_{\boldsymbol{C}_{u\phi}} \begin{bmatrix} \dot{\boldsymbol{U}}_s \\ \dot{\mathbf{\Phi}} \end{bmatrix} + \underbrace{\begin{bmatrix} \boldsymbol{K}_s & \boldsymbol{0} \\ \boldsymbol{0} & -\rho_0 \boldsymbol{K}_f \end{bmatrix}}_{\boldsymbol{K}_{u\phi}} \begin{bmatrix} \boldsymbol{U}_s \\ \mathbf{\Phi} \end{bmatrix} = \begin{bmatrix} \boldsymbol{F}_s \\ \boldsymbol{F}_\phi \end{bmatrix} \tag{3.6}$$

is stable.

Proof: By changing the sign of the set of equations governing the degree of freedom of ϕ, it is obvious that the system (3.6) has the same properties of stability with the following system:

$$\underbrace{\begin{bmatrix} \mathbf{M}_s & \mathbf{0} \\ \mathbf{0} & \rho_0 \mathbf{M}_f \end{bmatrix}}_{\mathbf{M}_{mu\phi}} \begin{bmatrix} \ddot{\mathbf{U}}_s \\ \ddot{\mathbf{\Phi}} \end{bmatrix} + \underbrace{\begin{bmatrix} \mathbf{C}_s & -\rho_0 \mathbf{K}_c \\ \rho_0 \mathbf{K}_c^H & \rho_0 \mathbf{C}_f \end{bmatrix}}_{\mathbf{C}_{mu\phi}} \begin{bmatrix} \dot{\mathbf{U}}_s \\ \dot{\mathbf{\Phi}} \end{bmatrix} + \underbrace{\begin{bmatrix} \mathbf{K}_s & \mathbf{0} \\ \mathbf{0} & \rho_0 \mathbf{K}_f \end{bmatrix}}_{\mathbf{K}_{mu\phi}} \begin{bmatrix} \mathbf{U}_s \\ \mathbf{\Phi} \end{bmatrix} = \begin{bmatrix} \mathbf{F}_s \\ -\mathbf{F}_\phi \end{bmatrix} \tag{3.7}$$

We can now use Lemma 3.1.3 to conclude the stability of the system (3.7). It is obvious that the new coupling mass (stiffness) matrix $\mathbf{M}_{mu\phi}$ (resp. $\mathbf{K}_{mu\phi}$) is hermitian and positive (semi-) definite thanks to the properties of the sub matrix $\mathbf{M}_s$ and $\mathbf{M}_f$ (resp. $\mathbf{K}_s$ and $\mathbf{K}_f$). It remains now to show that the coupling damping matrix $\mathbf{C}_{mu\phi}$ is positive semi-definite. For all $\mathbf{x} = \begin{bmatrix} \mathbf{x}_1, \mathbf{x}_2 \end{bmatrix}^T$, we have:

$$\begin{aligned}\Re(\mathbf{x}^H\mathbf{C}_{mu\phi}\mathbf{x}) &= \Re(\begin{bmatrix}\mathbf{x}_1^H, \mathbf{x}_2^H\end{bmatrix}\begin{bmatrix}\mathbf{C}_s & -\rho_0\mathbf{K}_c\\ \rho_0\mathbf{K}_c^H & \rho_0\mathbf{C}_f\end{bmatrix}\begin{bmatrix}\mathbf{x}_1\\ \mathbf{x}_2\end{bmatrix})\\ &= \Re(\mathbf{x}_1^H\mathbf{C}_s\mathbf{x}_1 + \rho_0\mathbf{x}_2^H\mathbf{C}_f\mathbf{x}_2 - \rho_0\mathbf{x}_1^H\mathbf{K}_c x_2 + \rho_0\mathbf{x}_2^H\mathbf{K}_c^H\mathbf{x}_1)\\ &= \Re(\mathbf{x}_1^H\mathbf{C}_s\mathbf{x}_1 + \rho_0\mathbf{x}_2^H\mathbf{C}_f\mathbf{x}_2) \geq 0\end{aligned}$$

Thus, the matrix $\mathbf{C}_{mu\phi}$ is semi-positive definite. The system (3.7) is then stable according to Lemma 3.1.3.

□

For exterior problem where the radiation condition is modelled by the BGT-1 method, the finite element model of the formulation in $(\mathbf{u}_s, \phi)$ is given by:

$$\begin{bmatrix}\mathbf{M}_s & \mathbf{0}\\ \mathbf{0} & -\rho_0\mathbf{M}_f\end{bmatrix}\begin{bmatrix}\ddot{\mathbf{U}}_s\\ \ddot{\mathbf{\Phi}}\end{bmatrix} + \begin{bmatrix}\mathbf{C}_s & -\rho_0\mathbf{K}_c\\ -\rho_0\mathbf{K}_c^T & -\rho_0(\mathbf{C}_f + \frac{\rho_0}{Z_C}\mathbf{Q})\end{bmatrix}\begin{bmatrix}\dot{\mathbf{U}}_s\\ \dot{\mathbf{\Phi}}\end{bmatrix} + \begin{bmatrix}\mathbf{K}_s & \mathbf{0}\\ \mathbf{0} & -\rho_0(\mathbf{K}_f + \frac{\rho_0}{Z_R}\mathbf{Q})\end{bmatrix}\begin{bmatrix}\mathbf{U}_s\\ \mathbf{\Phi}\end{bmatrix} = \begin{bmatrix}\mathbf{F}_s\\ \mathbf{F}_\phi\end{bmatrix} \tag{3.8}$$

Since the impedance matrix $\mathbf{Q}$ is symmetric and positive semi-definite, the stiffness matrix in the fluid part $\mathbf{K}_f^{ext} := \mathbf{K}_f + \frac{\rho_0}{Z_R}\mathbf{Q}$ remains symmetric and positive semi-definite and the total damping matrix in the fluid part $\mathbf{C}_f^{ext} := \mathbf{C}_f + \frac{\rho_0}{Z_C}\mathbf{Q}$ remains positive semi-definite. Thus, we can conclude that the system (3.8) is also stable. For exterior problem where the BGT-0 method is used to approximate the radiation condition, the finite element model remains also stable since we have in this case $\mathbf{K}_f^{ext} := \mathbf{K}_f$ and $\mathbf{C}_f^{ext} := \mathbf{C}_f + \frac{\rho_0}{Z_C}\mathbf{Q}$ which remains positive semi-definite.

3.1.2 Stability of full model in $(\mathbf{u}_s, p)$

In this section, we turn to the formulation in $(\mathbf{u}_s, p)$. We recall that the finite element model in $(\mathbf{u}_s, p)$ of an interior problem is given by:

$$\begin{bmatrix}\mathbf{M}_s & \mathbf{0}\\ -\rho_0\mathbf{K}_c^T & \mathbf{M}_f\end{bmatrix}\begin{bmatrix}\ddot{\mathbf{U}}_s\\ \ddot{\mathbf{P}}\end{bmatrix} + \begin{bmatrix}\mathbf{C}_s & \mathbf{0}\\ \mathbf{0} & \mathbf{C}_f\end{bmatrix}\begin{bmatrix}\ddot{\mathbf{U}}_s\\ \ddot{\mathbf{P}}\end{bmatrix} + \begin{bmatrix}\mathbf{K}_s & \mathbf{K}_c\\ \mathbf{0} & \mathbf{K}_f\end{bmatrix}\begin{bmatrix}\mathbf{U}_s\\ \mathbf{P}\end{bmatrix} = \begin{bmatrix}\mathbf{F}_s\\ \mathbf{F}_p\end{bmatrix} \tag{3.9}$$

where the matrices $\mathbf{C}_s$ and $\mathbf{C}_f$ which represent respectively the structural and the fluid damping terms, are introduced in the model in order to generalize our framework. We consider here only the case where these two damping matrices are positive semi-definite. The stability of the system (3.9) is achieved as a particular case (where all matrices have real coefficients) of the following lemma.

Lemma 3.1.5 *If the mass matrices $\boldsymbol{M}_s$, $\boldsymbol{M}_f$ are hermitian and positive definite, the stiffness matrices $\boldsymbol{K}_s$ et $\boldsymbol{K}_f$ are hermitian and positive semi-definite and the damping matrices $\boldsymbol{C}_s$ and $\boldsymbol{C}_f$ are positive semi-definite, the dynamical system*

$$\underbrace{\begin{bmatrix} \boldsymbol{M}_s & \boldsymbol{0} \\ -\rho_0 \boldsymbol{K}_c^H & \boldsymbol{M}_f \end{bmatrix}}_{\boldsymbol{M}_{up}} \begin{bmatrix} \ddot{\boldsymbol{U}}_s \\ \ddot{\boldsymbol{P}} \end{bmatrix} + \underbrace{\begin{bmatrix} \boldsymbol{C}_s & \boldsymbol{0} \\ \boldsymbol{0} & \boldsymbol{C}_f \end{bmatrix}}_{\boldsymbol{C}_{up}} \begin{bmatrix} \ddot{\boldsymbol{U}}_s \\ \ddot{\boldsymbol{P}} \end{bmatrix} + \underbrace{\begin{bmatrix} \boldsymbol{K}_s & \boldsymbol{K}_c \\ \boldsymbol{0} & \boldsymbol{K}_f \end{bmatrix}}_{\boldsymbol{K}_{up}} \begin{bmatrix} \boldsymbol{U}_s \\ \boldsymbol{P} \end{bmatrix} = \begin{bmatrix} \boldsymbol{F}_s \\ \boldsymbol{F}_p \end{bmatrix} \tag{3.10}$$

is stable.

Proof: We denote by P_{up} and $P_{u\phi}$ the characteristic polynomial (defined in the definition 3.1.2) of the system (3.10) and the system (3.6), respectively. By definition, the polynomial P_{up} of the system (3.10) is given by:

$$P_{up}(s) = \begin{vmatrix} s^2\mathbf{M}_s + s\mathbf{C}_s + \mathbf{K}_s & \mathbf{K}_c \\ -\rho_0 s^2 \mathbf{K}_c^H & s^2\mathbf{M}_f + s\mathbf{C}_f + \mathbf{K}_f \end{vmatrix}$$

and the polynomial $P_{u\phi}$ of the system (3.6) is given by:

$$P_{u\phi}(s) = \begin{vmatrix} s^2\mathbf{M}_s + s\mathbf{C}_s + \mathbf{K}_s & -\rho_0 s\mathbf{K}_c \\ -\rho_0 s\mathbf{K}_c^H & -\rho_0(s^2\mathbf{M}_f + s\mathbf{C}_f + \mathbf{K}_f) \end{vmatrix}$$

We denote by n_f the number of degrees of freedom in the fluid part. For $s \neq 0$, we have

$$\begin{aligned} P_{u\phi}(s) &= (-\rho_0 s)^{n_f} \begin{vmatrix} s^2\mathbf{M}_s + s\mathbf{C}_s + \mathbf{K}_s & \mathbf{K}_c \\ -\rho_0 s\mathbf{K}_c^H & \frac{1}{s}(s^2\mathbf{M}_f + s\mathbf{C}_f + \mathbf{K}_f) \end{vmatrix} \\ &= (-\rho_0)^{n_f} \begin{vmatrix} s^2\mathbf{M}_s + s\mathbf{C}_s + \mathbf{K}_s & \mathbf{K}_c \\ -\rho_0 s^2\mathbf{K}_c^H & s^2\mathbf{M}_f + s\mathbf{C}_f + \mathbf{K}_f \end{vmatrix} \\ &= (-\rho_0)^{n_f} P_{up}(s) \end{aligned}$$

The system (3.10) and the system (3.6) have the same non-zero poles which means that both systems have the same properties of stability. Since the system (3.6) is stable according to Lemma 3.1.4, we can then conclude that the system (3.10) is also stable.

□

For exterior problem where the radiation condition is modelled by the BGT-1 method, the finite element model of the formulation in $(\mathbf{u}_s, p)$ is given by:

$$\begin{bmatrix} \mathbf{M}_s & \mathbf{0} \\ -\rho_0 \mathbf{K}_c^T & \mathbf{M}_f \end{bmatrix} \begin{bmatrix} \ddot{\mathbf{U}}_s \\ \ddot{\mathbf{P}} \end{bmatrix} + \begin{bmatrix} \mathbf{C}_s & \mathbf{0} \\ \mathbf{0} & \mathbf{C}_f + \frac{\rho_0}{Z_C}\mathbf{Q} \end{bmatrix} \begin{bmatrix} \ddot{\mathbf{U}}_s \\ \ddot{\mathbf{P}} \end{bmatrix} + \begin{bmatrix} \mathbf{K}_s & \mathbf{K}_c \\ \mathbf{0} & \mathbf{K}_f + \frac{\rho_0}{Z_R}\mathbf{Q} \end{bmatrix} \begin{bmatrix} \mathbf{U}_s \\ \mathbf{P} \end{bmatrix} = \begin{bmatrix} \mathbf{F}_s \\ \mathbf{F}_p \end{bmatrix} \tag{3.11}$$

Since the impedance matrix $\mathbf{Q}$ is symmetric and positive semi-definite, the stiffness matrix in the fluid part $\mathbf{K}_f^{ext} := \mathbf{K}_f + \frac{\rho_0}{Z_R}\mathbf{Q}$ remains symmetric and positive semi-definite and the total damping matrix in the fluid part $\mathbf{C}_f^{ext} := \mathbf{C}_f + \frac{\rho_0}{Z_C}\mathbf{Q}$ remains positive semi-definite. Thus, we can conclude that the system (3.11) is also stable. For exterior problem where the BGT-0

method is used to approximate the radiation condition, the finite element model remains also stable since we have in this case $\mathbf{K}_f^{ext} := \mathbf{K}_f$ and $\mathbf{C}_f^{ext} := \mathbf{C}_f + \frac{\rho_0}{Z_C}\mathbf{Q}$ which remains positive semi-definite.

3.1.3 Stability of full model in $(\mathbf{u}_s, p, \varphi)$

Finally, let us put the focus on the formulation in $(\mathbf{u}_s, p, \varphi)$. We recall that the finite element model in $(\mathbf{u}_s, p, \varphi)$ of an interior problem is given by:

$$\begin{bmatrix} \mathbf{M}_s & \mathbf{0} & -\rho_0\mathbf{K}_c \\ \mathbf{0} & \mathbf{0} & \mathbf{M}_f \\ -\rho_0\mathbf{K}_c^T & \mathbf{M}_f & -\rho_0\mathbf{K}_f \end{bmatrix} \begin{bmatrix} \ddot{\mathbf{U}}_s \\ \ddot{\mathbf{P}} \\ \ddot{\boldsymbol{\varphi}} \end{bmatrix} + \begin{bmatrix} \mathbf{C}_s & \mathbf{0} & \mathbf{0} \\ \mathbf{0} & \mathbf{0} & \mathbf{0} \\ \mathbf{0} & \mathbf{C}_f & \mathbf{0} \end{bmatrix} \begin{bmatrix} \dot{\mathbf{U}}_s \\ \dot{\mathbf{P}} \\ \dot{\boldsymbol{\varphi}} \end{bmatrix} + \begin{bmatrix} \mathbf{K}_s & \mathbf{0} & \mathbf{0} \\ \mathbf{0} & \frac{1}{\rho_0}\mathbf{M}_f & \mathbf{0} \\ \mathbf{0} & \mathbf{0} & \mathbf{0} \end{bmatrix} \begin{bmatrix} \mathbf{U}_s \\ \mathbf{P} \\ \boldsymbol{\varphi} \end{bmatrix} = \begin{bmatrix} \mathbf{F}_s \\ \mathbf{0} \\ \mathbf{F}_p \end{bmatrix} \tag{3.12}$$

where the matrices $\mathbf{C}_s$ and $\mathbf{C}_f$ which represent respectively the structural and the fluid damping term, are introduced in order to generalize our framework. We consider here only the case where these two damping matrices are positive semi-definite. The stability of the system (3.12) is achieved as a particular case (where all matrices have real coefficients) of the following lemma.

Lemma 3.1.6 *If the mass matrices $\boldsymbol{M}_s$, $\boldsymbol{M}_f$ are hermitian and positive definite, the stiffness matrices $\boldsymbol{K}_s$ et $\boldsymbol{K}_f$ are hermitian and positive semi-definite and the damping matrices $\boldsymbol{C}_s$ and $\boldsymbol{C}_f$ are positive semi-definite, the dynamical system*

$$\begin{bmatrix} \boldsymbol{M}_s & \boldsymbol{0} & -\rho_0\boldsymbol{K}_c \\ \boldsymbol{0} & \boldsymbol{0} & \boldsymbol{M}_f \\ -\rho_0\boldsymbol{K}_c^H & \boldsymbol{M}_f & -\rho_0\boldsymbol{K}_f \end{bmatrix} \begin{bmatrix} \ddot{\boldsymbol{U}}_s \\ \ddot{\boldsymbol{P}} \\ \ddot{\boldsymbol{\varphi}} \end{bmatrix} + \begin{bmatrix} \boldsymbol{C}_s & \boldsymbol{0} & \boldsymbol{0} \\ \boldsymbol{0} & \boldsymbol{0} & \boldsymbol{0} \\ \boldsymbol{0} & \boldsymbol{C}_f & \boldsymbol{0} \end{bmatrix} \begin{bmatrix} \dot{\boldsymbol{U}}_s \\ \dot{\boldsymbol{P}} \\ \dot{\boldsymbol{\varphi}} \end{bmatrix} + \begin{bmatrix} \boldsymbol{K}_s & \boldsymbol{0} & \boldsymbol{0} \\ \boldsymbol{0} & \frac{1}{\rho_0}\boldsymbol{M}_f & \boldsymbol{0} \\ \boldsymbol{0} & \boldsymbol{0} & \boldsymbol{0} \end{bmatrix} \begin{bmatrix} \boldsymbol{U}_s \\ \boldsymbol{P} \\ \boldsymbol{\varphi} \end{bmatrix} = \begin{bmatrix} \boldsymbol{F}_s \\ \boldsymbol{0} \\ \boldsymbol{F}_p \end{bmatrix} \tag{3.13}$$

is stable.

Proof: We denote by P_{up} and $P_{up\varphi}$ the characteristic polynomial (defined in the definition 3.1.2) of the system (3.10) and the system (3.13), respectively. By definition, the polynomial P_{up} of the system (3.10) is given by:

$$P_{up}(s) = \begin{vmatrix} s^2\mathbf{M}_s + s\mathbf{C}_s + \mathbf{K}_s & \mathbf{K}_c \\ -\rho_0 s^2\mathbf{K}_c^H & s^2\mathbf{M}_f + s\mathbf{C}_f + \mathbf{K}_f \end{vmatrix}$$

and the polynomial $P_{up\varphi}$ of the system (3.13) is given by:

$$P_{up\varphi}(s) = \begin{vmatrix} s^2\mathbf{M}_s + s\mathbf{C}_s + \mathbf{K}_s & \mathbf{0} & -\rho_0 s^2\mathbf{K}_c \\ \mathbf{0} & \frac{1}{\rho_0}\mathbf{M}_f & s^2\mathbf{M}_f \\ -\rho_0 s^2\mathbf{K}_c^H & s^2\mathbf{M}_f + s\mathbf{C}_f & -\rho_0 s^2\mathbf{K}_f \end{vmatrix}$$

We denote by n_f the number of degrees of freedom of the pressure p which is equal to the number of degrees of freedom of the potential φ. We have:

$$\begin{aligned}
P_{up\varphi}(s) &= (-\rho_0 s^2)^{n_f} \begin{vmatrix} s^2\mathbf{M}_s + s\mathbf{C}_s + \mathbf{K}_s & 0 & \mathbf{K}_c \\ 0 & \frac{1}{\rho_0}\mathbf{M}_f & -\frac{1}{\rho_0}\mathbf{M}_f \\ -\rho_0 s^2 \mathbf{K}_c^H & s^2\mathbf{M}_f + s\mathbf{C}_f & \mathbf{K}_f \end{vmatrix} \\
&= (-\rho_0 s^2)^{n_f} \begin{vmatrix} s^2\mathbf{M}_s + s\mathbf{C}_s + \mathbf{K}_s & \mathbf{0} & \mathbf{K}_c \\ \mathbf{0} & \frac{1}{\rho_0}\mathbf{M}_f & \mathbf{0} \\ -\rho_0 s^2 \mathbf{K}_c^H & s^2\mathbf{M}_f + s\mathbf{C}_f & s^2\mathbf{M}_f + s\mathbf{C}_f + \mathbf{K}_f \end{vmatrix} \\
&= (-\rho_0 s^2)^{n_f} \det(\frac{1}{\rho_0}\mathbf{M}_f) \begin{vmatrix} s^2\mathbf{M}_s + s\mathbf{C}_s + \mathbf{K}_s & \mathbf{K}_c \\ -\rho_0 s^2 \mathbf{K}_c^H & s^2\mathbf{M}_f + s\mathbf{C}_f + \mathbf{K}_f \end{vmatrix} \\
&= (-s^2)^{n_f} \det(\mathbf{M}_f) \begin{vmatrix} s^2\mathbf{M}_s + s\mathbf{C}_s + \mathbf{K}_s & \mathbf{K}_c \\ -\rho_0 s^2 \mathbf{K}_c^H & s^2\mathbf{M}_f + s\mathbf{C}_f + \mathbf{K}_f \end{vmatrix} \\
&= (-s^2)^{n_f} \det(\mathbf{M}_f) P_{up}(s)
\end{aligned}$$

Since the matrix $\mathbf{M}_f$ is positive definite, we have $\det(\mathbf{M}_f) > 0$. Thus, the system (3.13) and the system (3.10) have the same non-zero poles which means that both systems have the same properties of stability. Since the system (3.10) is stable according to Lemma 3.1.5, we can then conclude that the system (3.13) is also stable.

□

For exterior problem where the radiation condition is modelled by the BGT-1 method, the finite element model of the formulation in $(\mathbf{u}_s, p, \varphi)$ is given by:

$$\begin{bmatrix} \mathbf{M}_s & \mathbf{0} & -\rho_0\mathbf{K}_c \\ \mathbf{0} & \mathbf{0} & \mathbf{M}_f \\ -\rho_0\mathbf{K}_c^T & \mathbf{M}_f & -\rho_0(\mathbf{K}_f + \frac{\rho_0}{Z_R}\mathbf{Q}) \end{bmatrix} \begin{bmatrix} \ddot{\mathbf{U}}_s \\ \ddot{\mathbf{P}} \\ \ddot{\boldsymbol{\varphi}} \end{bmatrix} + \begin{bmatrix} \mathbf{C}_s & \mathbf{0} & \mathbf{0} \\ \mathbf{0} & \mathbf{0} & \mathbf{0} \\ \mathbf{0} & \mathbf{C}_f + \frac{\rho_0}{Z_C}\mathbf{Q} & \mathbf{0} \end{bmatrix} \begin{bmatrix} \dot{\mathbf{U}}_s \\ \dot{\mathbf{P}} \\ \dot{\boldsymbol{\varphi}} \end{bmatrix}$$
$$+ \begin{bmatrix} \mathbf{K}_s & \mathbf{0} & \mathbf{0} \\ \mathbf{0} & \frac{1}{c_0^2}\mathbf{M}_f & \mathbf{0} \\ \mathbf{0} & \mathbf{0} & \mathbf{0} \end{bmatrix} \begin{bmatrix} \mathbf{U}_s \\ \mathbf{P} \\ \boldsymbol{\varphi} \end{bmatrix} = \begin{bmatrix} \mathbf{F}_s \\ \mathbf{0} \\ \mathbf{F}_p \end{bmatrix} \tag{3.14}$$

Since the impedance matrix $\mathbf{Q}$ is symmetric and positive semi-definite, the stiffness matrix in the fluid part $\mathbf{K}_f^{ext} := \mathbf{K}_f + \frac{\rho_0}{Z_R}\mathbf{Q}$ remains symmetric and positive semi-definite and the total damping matrix in the fluid part $\mathbf{C}_f^{ext} := \mathbf{C}_f + \frac{\rho_0}{Z_C}\mathbf{Q}$ remains positive semi-definite. Thus, we can conclude that the system (3.14) is also stable. For exterior problem where the BGT-0 method is used to approximate the radiation condition, the finite element model remains also stable since we have in this case $\mathbf{K}_f^{ext} := \mathbf{K}_f$ and $\mathbf{C}_f^{ext} := \mathbf{C}_f + \frac{\rho_0}{Z_C}\mathbf{Q}$ which remains positive semi-definite.

3.2 Reduced order modelling

As mentioned in introduction, the number of degrees of freedom in finite element model is often very large in industrial problems which limits the practical use of this so-called full

model in parametrized problems, due to the required computational cost. This problem can be overcome by using reduced order modelling techniques. In this section, we are interested in the Petrov-Galerkin projection-based model reduction techniques which consists to restrict the solution space to a subspace and enforce the orthogonality of the residual vector to a test subspace. We denote $\mathbf{V}$ and $\mathbf{W}$ the trial and the test subspace of dimension N which is much smaller than the dimension of the full model denoted by n, the reduced order model obtained by Petrov-Galerkin projection of the full model (3.1) on the couple $(\mathbf{V}, \mathbf{W})$ writes:

$$\begin{cases} \mathbf{M}_r\ddot{\mathbf{X}}_r(t) + \mathbf{C}_r\dot{\mathbf{X}}_r(t) + \mathbf{K}_r\mathbf{X}_r(t) = f(t)\mathbf{F}_r \\ \mathbf{X}_r(t=0) = \Pi_{\mathbf{V}}\mathbf{X}_0 \\ \dot{\mathbf{X}}_r(t=0) = \Pi_{\mathbf{V}}\dot{\mathbf{X}}_0 \end{cases} \tag{3.15}$$

where $\mathbf{M}_r = \mathbf{W}^H\mathbf{M}\mathbf{V}$, $\mathbf{C}_r = \mathbf{W}^H\mathbf{C}\mathbf{V}$, $\mathbf{K}_r = \mathbf{W}^H\mathbf{K}\mathbf{V} \in \mathbb{C}^{N\times N}$, $\mathbf{F}_r = \mathbf{W}^H\mathbf{F} \in \mathbb{C}^N$ and $\Pi_{\mathbf{V}}$ denotes the orthogonal projection on the space spanned by the reduced basis $\mathbf{V}$. The approximation of the solution of the full model (3.1) by the reduced order model (3.15) is given by: $\mathbf{X}^{rom}(t) = \mathbf{V}\mathbf{X}_r(t)$. In the case of $\mathbf{W} = \mathbf{V}$, the projection is well known as Galerkin projection.

The main challenge of projection based model reduction is to find the reduced basis $\mathbf{W}$ and $\mathbf{V}$ such that the reduced system (3.15) provides an accurate approximation of the output of interest over the desired ranges of inputs function f. One of necessary conditions to obtain such reduced order model is to ensure that the stability of the system is preserved. We recall that the definition of the stability used here states that the system (3.1) is stable if and only if all roots of the polynomial $P(s) := \det(s^2\mathbf{M} + s\mathbf{C} + \mathbf{K})$ have a negative real part. Preserving of the stability means that the reduced order models must have the same properties of stability as the full model. This condition is necessary in order to impose the solution of reduced order model (3.15) to have the same physical meaning as the original full model (3.1).

3.2.1 Offline/online decomposition

Before talking about the stability of the reduced order model, let us recall briefly an efficient offline/online procedure in the reduced order modelling framework. We remind that the complexity of computation in the offline phase may depend on the size of the full model. On the contrary, the complexity of computation in the online phase does not depend on the size of the full model. It depends only on the size of the reduced order model. We assume here that the mass, damping and stiffness matrices of the full model (3.1) do not depend on the parameter. The parameter that we seek to vary here is the time-dependent function f.

At offline phase, we begin by computing the reduced basis $\mathbf{V}$ and $\mathbf{W}$. The reduced mass, stiffness and damping matrices $\mathbf{M}_r, \mathbf{K}_r, \mathbf{C}_r$ as well as the reduced right-hand side vector $\mathbf{F}_r$ are then computed and saved. Once all the computations of $\mathbf{M}_r, \mathbf{K}_r, \mathbf{C}_r$ and $\mathbf{F}_r$ in offline phase are done, the solution $\mathbf{X}_r$ of the reduced order model (3.15) can be obtained with a complexity which depends only on the size of the reduced basis denoted by N and the number of time steps K considered in time-discretization. We should remark that the computation of the approximation of the full model's solution $\mathbf{X}^{rom}$ by the relation $\mathbf{X}^{rom}(t) = \mathbf{V}\mathbf{X}_r(t)$ is in complexity $O(nNK)$. Thus, it still depends on the size of the full model. However, if we are only interested in some physical quantities which can be expressed by a linear form:

$S_l(t) = \mathbf{L}^T\mathbf{X}(t)$, where $\mathbf{L}$ is a vector of $\mathbb{R}^n$ and $\mathbf{X}$ is the solution of the full model (3.1), then the prediction of this physical quantities by reduced order model can be obtained in complexity $O(NK)$. The idea is to pre-compute offline the reduced vector $\mathbf{L}_r^T = \mathbf{L}^T\mathbf{V} \in \mathbb{C}^{1\times N}$, and using online the relation $S_l^{rom}(t) = \mathbf{L}_r^T\mathbf{X}_r(t)$. The same technique is also applicable for the physical quantities which can be expressed by a quadratic form: $S_q(t) = \mathbf{X}^H(t)\mathbf{Q}\mathbf{X}(t)$, where $\mathbf{Q}$ is a matrix in $\mathbb{C}^{n\times n}$ and $\mathbf{X}$ is the solution of the full model (3.1), by pre-computing offline the reduced matrix $\mathbf{Q}_r = \mathbf{V}^H\mathbf{Q}\mathbf{V} \in \mathbb{C}^{N\times N}$, and using online the relation $S_q^{rom}(t) = \mathbf{X}_r^H(t)\mathbf{Q}_r\mathbf{X}_r(t)$. The complexity in online part for the latter case is in $O(N^2K)$.

3.2.2 Stability preserving reduced order model

In the most general cases, Petrov-Galerkin reduced order model does not preserve automatically the stability of the full model. It is possible to have a unstable Petrov-Galerkin projection reduced order model even if the original full model is stable, as we will see numerically in Section 3.4 for the case of vibro-acoustic problem. In some particular cases, the reduced order model based on Galerkin projection preserves automatically the stability of the full model as stated in the following lemma.

Lemma 3.2.1 *If the mass matrix $\boldsymbol{M}$ is positive definite and hermitian, the stiffness matrix $\boldsymbol{K}$ is positive semi-definite and hermitian and the damping matrix $\boldsymbol{C}$ is positive semi-definite, then the reduced order model obtained by Galerkin projection of the full model (3.1) preserves the stability for any choices of the reduced basis V.*

Proof: According to Lemma 3.1.3, it is sufficient to show that the reduced mass matrix $\mathbf{M}_r$ remains hermitian and positive definite, the reduced stiffness matrix $\mathbf{K}_r$ remains hermitian and positive semi-definite and the reduced damping matrix $\mathbf{C}_r$ remains positive semi-definite.

We denote in what follows by $\mathbf{A}_r = \mathbf{V}^H\mathbf{A}\mathbf{V} \in \mathbb{C}^{N\times N}$, where N is the dimension of the subspace spanned by the basis $\mathbf{V}$. Since $\mathbf{V}$ is a basis, the rank of the matrix $\mathbf{V}$ is maximum. Thus, for any $\mathbf{x}_r \in \mathbb{C}^N$, there exists an unique vector $\mathbf{x} \in \mathbb{C}^n$ such that $\mathbf{x} = \mathbf{V}\mathbf{x}_r$ and we have:

$$\Re(\mathbf{x}^H\mathbf{A}\mathbf{x}) = \Re((\mathbf{V}\mathbf{x}_r)^H\mathbf{A}(\mathbf{V}\mathbf{x}_r)) = \Re(\mathbf{x}_r^H(\mathbf{V}^H\mathbf{A}\mathbf{V})\mathbf{x}_r) = \Re(\mathbf{x}_r^H\mathbf{A}_r\mathbf{x}_r)$$

Clearly, we have $\mathbf{x} = \mathbf{V}\mathbf{x}_r \neq \mathbf{0}$ if $\mathbf{x}_r \neq \mathbf{0}$. The matrix $\mathbf{A}_r$ is then positive (semi-) definite if the matrix $\mathbf{A}$ is positive (semi-) definite. Thus, the reduced mass matrix $\mathbf{M}_r$ is positive definite and the reduced stiffness matrix $\mathbf{K}_r$ and reduced damping matrix $\mathbf{C}_r$ are positive semi-definite.

It remains to show that the reduced mass and stiffness matrices are hermitian. For any $\mathbf{x}_r, \mathbf{y}_r \in \mathbb{C}^N$ and $\mathbf{x} = \mathbf{V}\mathbf{x}_r, \mathbf{y} = \mathbf{V}\mathbf{y}_r \in \mathbb{C}^n$, we have:

$$\mathbf{y}^H\mathbf{A}\mathbf{x} = (\mathbf{V}\mathbf{y}_r)^H\mathbf{A}(\mathbf{V}\mathbf{x}_r) = \mathbf{y}_r^H(\mathbf{V}^H\mathbf{A}\mathbf{V})\mathbf{x}_r = \mathbf{y}_r^H\mathbf{A}_r\mathbf{x}_r$$

and

$$\mathbf{x}^H\mathbf{A}\mathbf{y} = (\mathbf{V}\mathbf{x}_r)^H\mathbf{A}(\mathbf{V}\mathbf{y}_r) = \mathbf{x}_r^H(\mathbf{V}^H\mathbf{A}\mathbf{V})\mathbf{y}_r = \mathbf{x}_r^H\mathbf{A}_r\mathbf{y}_r$$

If the matrix $\mathbf{A}$ is hermitian, we have $\mathbf{y}^H\mathbf{A}\mathbf{x} = \overline{\mathbf{x}^H\mathbf{A}\mathbf{y}}$. It implies that $\mathbf{y}_r^H\mathbf{A}_r\mathbf{x}_r = \overline{\mathbf{x}_r^H\mathbf{A}_r\mathbf{y}_r}$ which means that the reduced matrix $\mathbf{A}_r$ is also hermitian. The reduced mass and stiffness matrices are then hermitian.

□

According to Lemma 3.2.1, in the case of the full model resulting from the finite element discretization of structural dynamic or acoustic problem, where we have symmetric and positive definite mass matrix $\mathbf{M}$ and symmetric and positive semi-definite stiffness matrix $\mathbf{K}$, we can directly conclude that the reduced order model obtained by Galerkin projection is always stable. It remains true in the case where we also take into account a positive semi-definite damping matrix in the model. However, Lemma 3.2.1 can not be applied directly to vibro-acoustic coupling problem.

In the following, we present the stabilization reduced order modelling technique proposed in [121] for the time domain vibro-acoustic finite element model in $(\mathbf{u}_s, p)$ and $(\mathbf{u}_s, \phi)$ respectively in Section 3.2.3 and 3.2.4 and we will give a stabilization reduced order modelling technique for the finite element model in $(\mathbf{u}_s, p, \varphi)$ in Section 3.2.5.

3.2.3 Stable reduced order models for the formulation in $(\mathbf{u}_s, \phi)$

In the case of the full model in $(\mathbf{u}_s, \phi)$, a stable reduced order model can be obtained by Petrov-Galerkin projection using a particular form of the basis $\mathbf{W}$ of test subspace which depends on the choice of the basis of the trial subspace $\mathbf{V}$ as stated in Lemma 3.2.2. This stabilization technique is equivalent to the technique proposed in [121] which consists to construct a stable reduced order model by using Galerkin projection on the modified formulation in $(\mathbf{u}_s, \phi)$ (3.7). The stability of the reduced order model proposed in [121] is achieved since all the hypothesis of Lemma 3.2.1 is verified for the modified formulation (3.7) as shown in the demonstration of Lemma 3.1.4.

Lemma 3.2.2 *For any basis* $\boldsymbol{V} = \begin{bmatrix} \boldsymbol{V}_s \\ \boldsymbol{V}_f \end{bmatrix}$, *the Petrov-Galerkin projection of the full model in* $(\boldsymbol{u}_s, \phi)$ *on the* $(\boldsymbol{W}, \boldsymbol{V})$ *where* $\boldsymbol{W} = \begin{bmatrix} \boldsymbol{V}_s \\ -\boldsymbol{V}_f \end{bmatrix}$ *yields a stable reduced order model.*

Proof: The reduced order model obtained by Galerkin projection of modified formulation in $(\mathbf{u}_s, \phi)$ (3.7) on the basis $\mathbf{V} = \begin{bmatrix} \mathbf{V}_s \\ \mathbf{V}_f \end{bmatrix}$ is given by:

$$\mathbf{M}^r_{mu\phi}\ddot{\mathbf{X}}_r(t) + \mathbf{C}^r_{mu\phi}\dot{\mathbf{X}}_r(t) + \mathbf{K}^r_{mu\phi}\mathbf{X}_r(t) = \mathbf{F}^r_{mu\phi} \tag{3.16}$$

where

$$\begin{aligned}
\mathbf{M}^r_{mu\phi} &= \begin{bmatrix} \mathbf{V}_s^H & \mathbf{V}_f^H \end{bmatrix} \begin{bmatrix} \mathbf{M}_s & \mathbf{0} \\ \mathbf{0} & \rho_0\mathbf{M}_f \end{bmatrix} \begin{bmatrix} \mathbf{V}_s \\ \mathbf{V}_f \end{bmatrix} = \mathbf{V}_s^H\mathbf{M}_s\mathbf{V}_s + \rho_0\mathbf{V}_f^H\mathbf{M}_f\mathbf{V}_f \\
\mathbf{C}^r_{mu\phi} &= \begin{bmatrix} \mathbf{V}_s^H & \mathbf{V}_f^H \end{bmatrix} \begin{bmatrix} \mathbf{C}_s & -\rho_0\mathbf{K}_c \\ \rho_0\mathbf{K}_c^H & \rho_0\mathbf{C}_f \end{bmatrix} \begin{bmatrix} \mathbf{V}_s \\ \mathbf{V}_f \end{bmatrix} \\
&= \mathbf{V}_s^H\mathbf{C}_s\mathbf{V}_s + \rho_0\mathbf{V}_f^H\mathbf{C}_f\mathbf{V}_f - \rho_0\mathbf{V}_s^H\mathbf{K}_c\mathbf{V}_f + \rho_0\mathbf{V}_f^H\mathbf{K}_c^H\mathbf{V}_s \\
\mathbf{K}^r_{mu\phi} &= \begin{bmatrix} \mathbf{V}_s^H & \mathbf{V}_f^H \end{bmatrix} \begin{bmatrix} \mathbf{K}_s & \mathbf{0} \\ \mathbf{0} & \rho_0\mathbf{K}_f \end{bmatrix} \begin{bmatrix} \mathbf{V}_s \\ \mathbf{V}_f \end{bmatrix} = \mathbf{V}_s^H\mathbf{K}_s\mathbf{V}_s + \rho_0\mathbf{V}_f^H\mathbf{K}_f\mathbf{V}_f \\
\mathbf{F}^r_{mu\phi} &= \begin{bmatrix} \mathbf{V}_s^H & \mathbf{V}_f^H \end{bmatrix} \begin{bmatrix} \mathbf{F}_s \\ -\mathbf{F}_\phi \end{bmatrix} = \mathbf{V}_s^H\mathbf{F}_s - \mathbf{V}_f^H\mathbf{F}_\phi
\end{aligned}$$

The reduced order model obtained by Petrov-Galerkin projection of formulation in $(\mathbf{u}_s, \phi)$ (3.6) on $(\mathbf{V}, \mathbf{W})$ where $\mathbf{V} = \begin{bmatrix} \mathbf{V}_s \\ \mathbf{V}_f \end{bmatrix}$ and $\mathbf{W} = \begin{bmatrix} \mathbf{V}_s \\ -\mathbf{V}_f \end{bmatrix}$ is given by:

$$\mathbf{M}^r_{u\phi}\ddot{\mathbf{X}}_r(t) + \mathbf{C}^r_{u\phi}\dot{\mathbf{X}}_r(t) + \mathbf{K}^r_{u\phi}\mathbf{X}_r(t) = \mathbf{F}^r_{u\phi} \tag{3.17}$$

where

$$\begin{aligned}
\mathbf{M}^r_{u\phi} &= \begin{bmatrix} \mathbf{V}_s^H & -\mathbf{V}_f^H \end{bmatrix} \begin{bmatrix} \mathbf{M}_s & \mathbf{0} \\ \mathbf{0} & -\rho_0\mathbf{M}_f \end{bmatrix} \begin{bmatrix} \mathbf{V}_s \\ \mathbf{V}_f \end{bmatrix} = \mathbf{V}_s^H\mathbf{M}_s\mathbf{V}_s + \rho_0\mathbf{V}_f^H\mathbf{M}_f\mathbf{V}_f \\
\mathbf{C}^r_{u\phi} &= \begin{bmatrix} \mathbf{V}_s^H & -\mathbf{V}_f^H \end{bmatrix} \begin{bmatrix} \mathbf{C}_s & -\rho_0\mathbf{K}_c \\ -\rho_0\mathbf{K}_c^H & -\rho_0\mathbf{C}_f \end{bmatrix} \begin{bmatrix} \mathbf{V}_s \\ \mathbf{V}_f \end{bmatrix} \\
&= \mathbf{V}_s^H\mathbf{C}_s\mathbf{V}_s + \rho_0\mathbf{V}_f^H\mathbf{C}_f\mathbf{V}_f - \rho_0\mathbf{V}_s^H\mathbf{K}_c\mathbf{V}_f + \rho_0\mathbf{V}_f^H\mathbf{K}_c^H\mathbf{V}_s \\
\mathbf{K}^r_{u\phi} &= \begin{bmatrix} \mathbf{V}_s^H & -\mathbf{V}_f^H \end{bmatrix} \begin{bmatrix} \mathbf{K}_s & \mathbf{0} \\ \mathbf{0} & -\rho_0\mathbf{K}_f \end{bmatrix} \begin{bmatrix} \mathbf{V}_s \\ \mathbf{V}_f \end{bmatrix} = \mathbf{V}_s^H\mathbf{K}_s\mathbf{V}_s + \rho_0\mathbf{V}_f^H\mathbf{K}_f\mathbf{V}_f \\
\mathbf{F}^r_{u\phi} &= \begin{bmatrix} \mathbf{V}_s^H & -\mathbf{V}_f^H \end{bmatrix} \begin{bmatrix} \mathbf{F}_s \\ \mathbf{F}_\phi \end{bmatrix} = \mathbf{V}_s^H\mathbf{F}_s - \mathbf{V}_f^H\mathbf{F}_\phi
\end{aligned}$$

The reduced order model (3.16) and (3.17) are then equivalent. As a result, the reduced order model (3.17) is stable since the reduced order model (3.16) is stable according to Lemma 3.2.1

□

Remark 3.2.1 The reduced mass (stiffness) matrix of the reduced order model (3.17) is hermitian and positive (semi-) definite. The reduced damping matrix of the reduced order model (3.17) is positive semi-definite but not hermitian. Hence, even in case the basis is in $\mathbb{R}^{n\times N}$, the reduced order model (3.17) is then **not symmetric**.

Remark 3.2.2 For exterior problem where the BGT-1 method is used to approximate the radiation condition (3.8), it is obvious that the statement of Lemma 3.2.2 remains valid since the stiffness matrix of fluid part $\mathbf{K}_f^{ext} := \mathbf{K}_f + \frac{\rho_0}{Z_R}\mathbf{Q}$ remains symmetric and positive semi-definite and the total damping matrix of fluid part $\mathbf{C}_f^{ext} := \mathbf{C}_f + \frac{\rho_0}{Z_C}\mathbf{Q}$ remains positive semi-definite.

3.2.4 Stable reduced order models for the formulation in $(\mathbf{u}_s, p)$

For the formulation in $(\mathbf{u}_s, p)$, a stable reduced order model can be obtained by Galerkin projection on a particular form of reduced basis. The stabilization technique proposed in [121] is stated as in the following lemma.

Lemma 3.2.3 *The Galerkin projection of the full model in $(\boldsymbol{u}_s, p)$ on a basis*

$$\boldsymbol{V} = \begin{bmatrix} \boldsymbol{V}_s & \boldsymbol{0} \\ \boldsymbol{0} & \boldsymbol{V}_f \end{bmatrix} \tag{3.18}$$

where $\boldsymbol{V}_s$ and $\boldsymbol{V}_f$ are respectively a reduced basis of structural and fluid part, yields a stable reduced order model.

Proof: The reduced order model obtained by Galerkin projection of the full model in $(\mathbf{u}_s, p)$ (3.10) on the basis $\mathbf{V}$ is given by:

$$\mathbf{M}^r_{up}\ddot{\mathbf{X}}^r_{up}(t) + \mathbf{C}^r_{up}\dot{\mathbf{X}}^r_{up}(t) + \mathbf{K}^r_{up}\mathbf{X}^r_{up}(t) = \mathbf{F}^r_{up} \tag{3.19}$$

where

$$\mathbf{M}^r_{up} = \begin{bmatrix} \mathbf{V}_s^H\mathbf{M}_s\mathbf{V}_s & \mathbf{0} \\ -\rho_0 c_0^2\mathbf{V}_f^H\mathbf{K}_c^H\mathbf{V}_s & \mathbf{V}_f^H\mathbf{M}_f\mathbf{V}_f \end{bmatrix}, \mathbf{C}^r_{up} = \begin{bmatrix} \mathbf{V}_s^H\mathbf{C}_s\mathbf{V}_s & \mathbf{0} \\ \mathbf{0} & \mathbf{V}_f^H\mathbf{C}_f\mathbf{V}_f \end{bmatrix},$$

$$\mathbf{K}^r_{up} = \begin{bmatrix} \mathbf{V}_s^H\mathbf{K}_s\mathbf{V}_s & \mathbf{V}_s^H\mathbf{K}_c\mathbf{V}_f \\ \mathbf{0} & \mathbf{V}_f^H\mathbf{K}_f\mathbf{V}_f \end{bmatrix}$$

The reduced order model obtained by Petrov-Galerkin of the full model (3.6) of $(\mathbf{u}_s, \phi)$ formulation on $(\mathbf{V}, \mathbf{W})$ where $\mathbf{W} = \begin{bmatrix} \mathbf{V}_s & \mathbf{0} \\ \mathbf{0} & -\mathbf{V}_f \end{bmatrix}$, is given by:

$$\mathbf{M}^r_{u\phi}\ddot{\mathbf{X}}^r_{u\phi}(t) + \mathbf{C}^r_{u\phi}\dot{\mathbf{X}}^r_{u\phi}(t) + \mathbf{K}^r_{u\phi}\mathbf{X}^r_{u\phi}(t) = \mathbf{F}^r_{u\phi} \tag{3.20}$$

where

$$\mathbf{M}^r_{mu\phi} = \begin{bmatrix} \mathbf{V}_s^H\mathbf{M}_s\mathbf{V}_s & \mathbf{0} \\ \mathbf{0} & \rho_0\mathbf{V}_f^H\mathbf{M}_f\mathbf{V}_f \end{bmatrix}, \mathbf{C}^r_{u\phi} = \begin{bmatrix} \mathbf{V}_s^H\mathbf{C}_s\mathbf{V}_s & -\rho_0\mathbf{V}_s^H\mathbf{K}_c\mathbf{V}_f \\ \rho_0\mathbf{V}_f^H\mathbf{K}_c^T\mathbf{V}_s & \rho_0\mathbf{V}_f^H\mathbf{C}_f\mathbf{V}_f \end{bmatrix},$$

$$\mathbf{K}^r_{u\phi} = \begin{bmatrix} \mathbf{V}_s^H\mathbf{K}_s\mathbf{V}_s & \mathbf{0} \\ \mathbf{0} & \rho_0\mathbf{V}_f^H\mathbf{K}_f\mathbf{V}_f \end{bmatrix}$$

By computing the characteristic polynomial P^r_{up} and $P^r_{u\phi}$ of the system (3.19) and (3.20) using the same technique as in the demonstration of the stability of the full model in $(\mathbf{u}_s, p)$ in Lemma 3.1.5, we can show that these two reduced order models have the same properties of stability. Since the reduced order model (3.20) is stable according to Lemma 3.2.2, we can then conclude that the reduced order model (3.19) is also stable.

□

Remark 3.2.3 The reduced order model (3.19) has the same structure (in the sense that we have the same sparsity and we have hermitian positive (semi-) definite sub matrix) as the full model (3.10).

Remark 3.2.4 For exterior problem where the BGT-1 method is used to approximate the radiation condition (3.11), it is obvious that the statement of Lemma 3.2.3 remains valid since the stiffness matrix of fluid part $\mathbf{K}_f^{ext} := \mathbf{K}_f + \frac{\rho_0}{Z_R}\mathbf{Q}$ remains symmetric and positive semi-definite and the total damping matrix of fluid part $\mathbf{C}_f^{ext} := \mathbf{C}_f + \frac{\rho_0}{Z_C}\mathbf{Q}$ remains positive semi-definite.

3.2.5 Stable reduced order models for the formulation in $(\mathbf{u}_s, p, \varphi)$

As for the formulation in $(\mathbf{u}_s, p)$, a stable reduced order model of full model in $(\mathbf{u}_s, p, \varphi)$ can be obtained by Galerkin projection on a particular form of reduced basis.

Lemma 3.2.4 *The Galerkin projection of the full model in $(\boldsymbol{u}_s, p, \varphi)$ on a basis*

$$\boldsymbol{V} = \begin{bmatrix} \boldsymbol{V}_s & \boldsymbol{0} & \boldsymbol{0} \\ \boldsymbol{0} & \boldsymbol{V}_f & \boldsymbol{0} \\ \boldsymbol{0} & \boldsymbol{0} & \boldsymbol{V}_f \end{bmatrix} \tag{3.21}$$

where $\boldsymbol{V}_s$ and $\boldsymbol{V}_f$ are respectively the reduced basis of structural and fluid part, yields a stable reduced order model.

Proof: The proposed reduced order model is given by:

$$\mathbf{M}^r_{up\varphi}\ddot{\mathbf{X}}^r_{up\varphi}(t) + \mathbf{C}^r_{up\varphi}\dot{\mathbf{X}}^r_{up\varphi}(t) + \mathbf{K}^r_{up\varphi}\mathbf{X}^r_{up\varphi}(t) = \mathbf{F}^r_{up\varphi} \tag{3.22}$$

where

$$\mathbf{M}^r_{up\varphi} = \begin{bmatrix} \mathbf{V}_s^H\mathbf{M}_s\mathbf{V}_s & \mathbf{0} & -\rho_0\mathbf{V}_s^H\mathbf{K}_c\mathbf{V}_f \\ \mathbf{0} & \mathbf{0} & \mathbf{V}_f^H\mathbf{M}_f\mathbf{V}_f \\ -\rho_0\mathbf{V}_f^H\mathbf{K}_c^H\mathbf{V}_s & \mathbf{V}_f^H\mathbf{M}_f\mathbf{V}_f & -\rho_0\mathbf{V}_f^H\mathbf{K}_f\mathbf{V}_f \end{bmatrix}, \mathbf{C}^r_{up\varphi} = \begin{bmatrix} \mathbf{V}_s^H\mathbf{C}_s\mathbf{V}_s & \mathbf{0} & \mathbf{0} \\ \mathbf{0} & \mathbf{0} & \mathbf{0} \\ \mathbf{0} & \mathbf{V}_f^H\mathbf{C}_f\mathbf{V}_f & \mathbf{0} \end{bmatrix},$$

$$\mathbf{K}^r_{up\varphi} = \begin{bmatrix} \mathbf{V}_s^H\mathbf{K}_s\mathbf{V}_s & \mathbf{0} & \mathbf{0} \\ \mathbf{0} & \frac{1}{\rho_0}\mathbf{V}_f^H\mathbf{M}_f\mathbf{V}_f & \mathbf{0} \\ \mathbf{0} & \mathbf{0} & \mathbf{0} \end{bmatrix}$$

By computing the characteristic polynomial P^r_{up} and $P^r_{up\varphi}$ of the system (3.19) and (3.22) with the same manner as in the demonstration of the stability of the full model in $(\mathbf{u}_s, p, \varphi)$ in Lemma 3.1.6, we can show that these two reduced order models have the same properties of stability. Since the reduced order model (3.19) is stable according to Lemma 3.2.3, we can then conclude that the reduced order model (3.22) is also stable.

□

Remark 3.2.5 The reduced order model (3.22) has the same structure (in the sense that we have the same sparsity and we have hermitian positive (semi-) definite sub matrix) as the full model (3.13). Thus, in the case of an interior problem and the reduced basis V is in $\mathbb{R}^{n\times N}$, the reduced order model (3.22) is symmetric.

Not only that the reduced order models (3.19) and (3.22) have the same properties of stability, they are also equivalent since they both inherit the structure of the original full model.

Lemma 3.2.5 *The Galerkin reduced order model (3.19) of $(\boldsymbol{u}_s, p)$ formulation and the Galerkin reduced order model (3.22) of $(\boldsymbol{u}_s, p, \varphi)$ formulation are equivalent.*

Proof: We denote by $\mathbf{M}_{s,r} = \mathbf{V}_s^H\mathbf{M}_s\mathbf{V}_s, \mathbf{K}_{s,r} = \mathbf{V}_s^H\mathbf{K}_s\mathbf{V}_s, \mathbf{C}_{s,r} = \mathbf{V}_s^H\mathbf{C}_s\mathbf{V}_s, \mathbf{M}_{f,r} = \mathbf{V}_f^H\mathbf{M}_f\mathbf{V}_f$, $\mathbf{K}_{f,r} = \mathbf{V}_f^H\mathbf{K}_f\mathbf{V}_f$, $\mathbf{C}_{f,r} = \mathbf{V}_f^H\mathbf{C}_f\mathbf{V}_f$, $\mathbf{K}_{c,r} = \mathbf{V}_f^H\mathbf{K}_c\mathbf{V}_s$, $\mathbf{F}_{s,r} = \mathbf{V}_s^H\mathbf{F}_s$ and

$\mathbf{F}_{p,r} = \mathbf{V}_f^H \mathbf{F}_p$. The reduced order model (3.22) writes:

$$\begin{cases} \mathbf{M}_{s,r}\ddot{\mathbf{U}}_{s,r}(t) + \mathbf{C}_{s_r}\dot{\mathbf{U}}_{s,r}(t) + \mathbf{K}_{s,r}\mathbf{U}_{s,r}(t) - \rho_0 \mathbf{K}_{c,r}\ddot{\boldsymbol{\varphi}}_r = \mathbf{F}_{s,r} \\ \mathbf{M}_{f,r}\ddot{\boldsymbol{\varphi}}_r(t) + \dfrac{1}{\rho_0}\mathbf{M}_{f,r}\mathbf{P}_r(t) = \mathbf{0} \\ -\rho_0 \mathbf{K}_{c,r}^H \ddot{\mathbf{U}}_{s,r}(t) + \mathbf{M}_{f,r}\ddot{\mathbf{P}}_r(t) - \rho_0 \mathbf{K}_{f,r}\ddot{\boldsymbol{\varphi}}_r + \mathbf{C}_{f,r}\dot{\mathbf{P}}_r(t) = \mathbf{F}_{p,r} \end{cases} \tag{3.23}$$

From the second equation of the system (3.23), we have $\ddot{\boldsymbol{\varphi}}_r(t) = -\frac{1}{\rho_0}\mathbf{P}_r(t)$ (since the matrix $\mathbf{M}_{f,r}$ is invertible). Using this relation to eliminate the variable $\boldsymbol{\varphi}$ in the system (3.23) leads to the reduced order model (3.19) of $(\mathbf{u}_s, p)$ formulation.

□

Remark 3.2.6 For exterior problem where the BGT-1 method is used to approximate the radiation condition (3.14), it is obvious that the statement of Lemma 3.2.4 remains valid since the stiffness matrix of fluid part $\mathbf{K}_f^{ext} := \mathbf{K}_f + \frac{\rho_0}{Z_R}\mathbf{Q}$ remains symmetric and positive semi-definite and the total damping matrix of fluid part $\mathbf{C}_f^{ext} := \mathbf{C}_f + \frac{\rho_0}{Z_C}\mathbf{Q}$ remains positive semi-definite.

3.3 Construction of the reduced basis by Greedy Algorithm

The accuracy of reduced order model depends strongly on the choice of the reduced basis. Many reduced basis have been proposed in the literature such as $\mathcal{H}_2$ optimal model reduction (see [34, 63, 126]), Balanced Truncation method (see [36, 81, 96]) and Krylov subspace model reduction (see [14, 15]). In this chapter, we are only interested in the reduced basis used in the paper [83, 84] for parametrized frequency domain of vibro-acoustic problem. The main reason is that this approach can be extended easily in the case with parametric variation in the left-hand side of the problem (3.1) and can be accommodated to the stabilization technique proposed in the previous section by requiring only some small modifications of the original approach, on the contrary to all other methods mentioned above.

We recall that the frequency domain corresponding to the time-domain problem (3.1) is the following:

$$\underbrace{\left[-\omega^2\mathbf{M} + i\omega\mathbf{C} + \mathbf{K}\right]}_{\mathbf{A}(\omega)} \tilde{\mathbf{X}}(\omega) = \mathbf{F} \tag{3.24}$$

where ω is the pulsation and $\tilde{\mathbf{X}}(\omega)$ is the frequency mode of the given pulsation ω.

Considering the pulsation as a parameter in the problem (3.24), the Classical Greedy Algorithm is defined as follows. First, we propose to chose the smallest frequency of interest as the first frequency. The first vector of the reduced basis is then built by normalization of the solution at this frequency. Note that this choice of the minimum frequency of interest as the first frequency is not necessary. We could also use an alternative choice such as a highest frequency or choose randomly a value between the minimum and the maximum frequency of interest. After the initialization step, we enrich iteratively the reduced basis until a stopping criterion is verified. To select the next frequency rationally, we propose to use pieces of information from the error indicator based on the residual norm. At each iteration, we use the reduced basis of the previous iteration to built the reduced order model by Galerkin projection. We

compute then the norm of the corresponding residual vector for all values of the frequency in a training set and select the next frequency as the one who maximize the norm of the residual vector. The training set can be built only once for all iterations. However, its size can be very large in the case of high-dimensional parameter space in order to ensure that there is no important region forgotten in the parameter space. To avoid this problem, we propose to perform a new random training set in each iteration. At the end, it is important to note that enriching the new mode directly into the base may induce an ill-conditioned reduced problem. To ameliorate this, we can employ the Gram-Schmidt procedure to orthogonalize the reduced basis. We should also note that the classical Gram-Schmidt procedure suffers from numerical instability. Round-off errors can accumulate and destroy orthogonality of the resulting vectors. Many modified Gram-Schmidt procedures have been already proposed to cure this issue (see e.g [1, 44, 45, 59, 70]). The orthogonalization procedure of Kahan-Parlett [59, 104] is chosen in our work. A summary of the methodology is explicitly given in the following algorithm.

Algorithm 1 Classical Greedy Algorithm

Input: N_{max} (maximum number of iterations), N_{train} (size of training set to be performed in each iteration), the matrices $\mathbf{M}, \mathbf{C}, \mathbf{K}$ and the right-hand side $\mathbf{F}$ of the problem, ω_{min} (the minimum pulsation of interest), ω_{max} (the maximum pulsation of interest) and a tolerance ϵ

Output: A reduced basis $\mathbf{V}$

1: We choose $\tilde{\mathbf{X}}(\omega_{min})$ as the first vector of reduced basis:

$$\mathbf{V} = \{\frac{\tilde{\mathbf{X}}(\omega_{min})}{||\tilde{\mathbf{X}}(\omega_{min})||}\}$$

2: Set $k = 2$

3: **while** $(k \leq N_{max})$ **do**

4: Generate randomly a set of training sample $\mathcal{D}_k = \{\omega_1, \cdots, \omega_{N_{train}}\} \subset [\omega_{min}, \omega_{max}]$

5: Solve for every values of pulsation $\omega \in \mathcal{D}_k$, the reduced order model obtained by Galerkin projection on the basis $\mathbf{V}$ of dimension $k-1$:

$$\mathbf{A}_r(\omega)\tilde{\mathbf{X}}_r(\omega) = \mathbf{F}_r$$

where $\mathbf{A}_r(\omega) = \mathbf{V}^H\mathbf{A}(\omega)\mathbf{V}$ et $\mathbf{F}_r = \mathbf{V}^H\mathbf{F}$.

6: Find the value of ω_k^* which maximises the norm of residual divided by the norm of the right-hand side:

$$\omega_k^* = \text{argmax}_{\omega \in \mathcal{D}_k} ||\mathbf{F} - \mathbf{A}(\omega)\mathbf{V}\tilde{\mathbf{X}}_r(\omega)||/||\mathbf{F}||$$

7: **if** $(||\mathbf{F} - \mathbf{A}(\omega_k^*)\mathbf{V}\tilde{\mathbf{X}}_r(\omega_k^*)||/||\mathbf{F}|| \leq \epsilon)$ **then**

8: **break;**

9: **else**

10: Orthonormalization the new basis $\tilde{\mathbf{X}}(\omega_k^*)$ with the basis $\mathbf{V}$ of the previous iteration and enrich the basis:

$$\mathbf{V} = [\mathbf{V}, \text{ortho}(\tilde{\mathbf{X}}(\omega_k^*), \mathbf{V})]$$

11: **end if**

12: $k = k + 1$

13: **end while**

For the formulation in $(\mathbf{u}_s, \phi)$, it is not necessary to modify the Classical Greedy Algorithm 1 since we can obtain a stable reduced order model by using Petrov-Galerkin projection with a particular test subspace, which of course would depend on the obtained reduced basis as indicated in Lemma 3.2.2. In the following, we propose some improvements to the proposed Greedy Algorithm for the formulation in $(\mathbf{u}_s, p)$ and $(\mathbf{u}_s, p, \varphi)$ in order to obtain the reduced basis which can ensure the stability of the Galerkin reduced order model.

3.3.1 Case of the formulation in $(\mathbf{u}_s, p)$

Algorithm 2 Greedy Algorithm (stabilized version for the formulation in $(\mathbf{u}_s, p)$)

Input: N_{max} (maximum number of iterations), N_{train} (size of training set to be performed in each iteration), the matrices $\mathbf{M}_{up}, \mathbf{C}_{up}, \mathbf{K}_{up}$ and the right-hand side $\mathbf{F}_{up}$ of the problem, ω_{min} (the minimum pulsation of interest), ω_{max} (the maximum pulsation of interest) and a tolerance ϵ

Output: A reduced basis $\mathbf{V}$

1: We choose $\tilde{\mathbf{X}}(\omega_{min}) = \begin{bmatrix} \tilde{\mathbf{U}}^T(\omega_{min}) & \tilde{\mathbf{P}}^T(\omega_{min}) \end{bmatrix}^T$

2: Transform the reduced basis to the form:

$$\mathbf{V} = \begin{bmatrix} \frac{\mathbf{U}(\omega_{min})}{||\tilde{\mathbf{U}}(\omega_{min})||} & \mathbf{0} \\ \mathbf{0} & \frac{\tilde{\mathbf{P}}(\omega_{min})}{||\tilde{\mathbf{P}}(\omega_{min})||} \end{bmatrix}$$

3: Set $k = 2$

4: **while** $(k \leq N_{max})$ **do**

5: Generate randomly a set of training set $\mathcal{D}_k = \{\omega_1, \cdots, \omega_{N_{train}}\} \subset [\omega_{min}, \omega_{max}]$

6: Solve for every values of pulsation $\omega \in \mathcal{D}_k$, the reduced order model obtained by Galerkin projection on the basis $\mathbf{V}$ of dimension $2(k-1)$:

$$\mathbf{A}_r(\omega)\tilde{\mathbf{X}}_r(\omega) = \mathbf{F}_r$$

where $\mathbf{A}_r(\omega) = \mathbf{V}^H \mathbf{A}_{up}(\omega)\mathbf{V}$ et $\mathbf{F}_r = \mathbf{V}^H \mathbf{F}_{up}$.

7: Find the value ω_k^* which maximises the norm of residual divided by the norm of the right-hand side:

$$\omega_k^* = \text{argmax}_{\omega \in \mathcal{D}_k} ||\mathbf{F}_{up} - \mathbf{A}_{up}(\omega)\mathbf{V}\tilde{\mathbf{X}}_r(\omega)||/||\mathbf{F}_{up}||$$

8: **if** $(||\mathbf{F}_{up} - \mathbf{A}_{up}(\omega_k^*)\mathbf{V}\tilde{\mathbf{X}}_r(\omega_k^*)||/||\mathbf{F}_{up}|| \leq \epsilon)$ **then**

9: **break;**

10: **else**

11: Orthonormalization the two new vectors $\begin{bmatrix} \tilde{\mathbf{U}}^T(\omega_k^*) & \mathbf{0}^T \end{bmatrix}^T$, $\begin{bmatrix} \mathbf{0}^T & \tilde{\mathbf{P}}^T(\omega_k^*) \end{bmatrix}^T$ with the basis $\mathbf{V}$ of the previous iteration and enrich the basis:

$$\mathbf{V} = \begin{bmatrix} \mathbf{V} & \text{ortho}(\begin{bmatrix} \tilde{\mathbf{U}}^T(\omega_k^*) & \mathbf{0}^T \end{bmatrix}^T, \mathbf{V}) & \text{ortho}(\begin{bmatrix} \mathbf{0}^T & \tilde{\mathbf{P}}^T(\omega_k^*) \end{bmatrix}^T, \mathbf{V}) \end{bmatrix}$$

12: **end if**

13: $k = k + 1$

14: **end while**

According to Lemma 3.2.3, we propose to modify the Classical Greedy Algorithm 1 to ensure the stability of Galerkin reduced order model of $(\mathbf{u}_s, p)$ formulation as presented in Algorithm 2.

The only differences compared to Classical Greedy Algorithm 1 are the steps 2, 6 and 11. At the step 2, we transform the first frequency mode into two vectors and save these two independent vectors in the reduced basis $\mathbf{V}$. At the step 6, instead of having the reduced order model of size $k-1$ as in Classical Greedy Algorithm 1, we have a reduced order model of $2(k-1)$ degrees of freedom in the new Greedy Algorithm 2. At the step 11, instead of using directly the new solution of the frequency domain (where the frequency is selected as the one who maximizes the indicator error) for enriching the reduced basis $\mathbf{V}$, we first transform this new mode $\tilde{\mathbf{X}}(\omega_k^*)$ into two independent vectors: $\left[\tilde{\mathbf{U}}^T(\omega_k^*) \quad \mathbf{0}^T\right]^T$, $\left[\mathbf{0}^T \quad \tilde{\mathbf{P}}^T(\omega_k^*)\right]^T$ and use these two independent vectors to enrich the reduced basis $\mathbf{V}$.

Depending on the scalar product used in the orthogonalization procedure at the step 11 of Algorithm 2, the output reduced basis of Algorithm 2 may not be in the form of (3.18). However, the following lemma justifies that the output reduced basis of Greedy Algorithm 2 is in the form of (3.18), provided that we use a particular scalar product in the orthogonalization procedure.

Lemma 3.3.1 *The output reduced basis of Greedy Algorithm 2 is in the form of (3.18) if we use the scalar product defined by:*

$$\langle \left[\boldsymbol{U}_1^T \quad \boldsymbol{P}_1^T\right]^T, \left[\boldsymbol{U}_2^T \quad \boldsymbol{P}_2^T\right]^T \rangle = \boldsymbol{U}_2^H \boldsymbol{A}_u \boldsymbol{U}_1 + \boldsymbol{P}_2^H \boldsymbol{A}_p \boldsymbol{P}_1 \tag{3.25}$$

where $\boldsymbol{A}_u$ and $\boldsymbol{A}_p$ are two hermitian positive definite matrices, in the orthogonalization procedure. In particular, the output reduced basis of Greedy Algorithm 2 is in the form of (3.18) if we use euclidean scalar product in orthogonalization procedure.

Proof: The reduced basis $\mathbf{V}$ at the step 2 of Algorithm 2 is clearly in the form of (3.18). Suppose that at iteration $k-1$, the reduced basis $\mathbf{V}$ is in the form:

$$\mathbf{V}_{k-1} = \begin{bmatrix} \mathbf{v}_1^u & \mathbf{0} & \mathbf{v}_2^u & \mathbf{0} & \cdots & \mathbf{v}_{k-1}^u & \mathbf{0} \\ \mathbf{0} & \mathbf{v}_1^p & \mathbf{0} & \mathbf{v}_2^p & \cdots & \mathbf{0} & \mathbf{v}_{k-1}^p \end{bmatrix} \tag{3.26}$$

we will show that the reduced basis $\mathbf{V}_k$ of iteration k is in form:

$$\mathbf{V}_k = \begin{bmatrix} \mathbf{v}_1^u & \mathbf{0} & \mathbf{v}_2^u & \mathbf{0} & \cdots & \mathbf{v}_k^u & \mathbf{0} \\ \mathbf{0} & \mathbf{v}_1^p & \mathbf{0} & \mathbf{v}_2^p & \cdots & \mathbf{0} & \mathbf{v}_k^p \end{bmatrix} \tag{3.27}$$

Under the hypothesis of $\mathbf{V}_{k-1}$, we have

$$\begin{aligned}\text{ortho}(\begin{bmatrix}\tilde{\mathbf{U}}(\omega_k^*)\\ \mathbf{0}\end{bmatrix}, \mathbf{V}_{k-1}) &= \begin{bmatrix}\tilde{\mathbf{U}}(\omega_k^*)\\ \mathbf{0}\end{bmatrix} - \sum_{i=1}^{k-1} \langle \begin{bmatrix}\tilde{\mathbf{U}}(\omega_k^*)\\ \mathbf{0}\end{bmatrix}, \begin{bmatrix}\mathbf{v}_i^u\\ \mathbf{0}\end{bmatrix} \rangle \begin{bmatrix}\mathbf{v}_i^u\\ \mathbf{0}\end{bmatrix} \\ &\quad - \sum_{i=1}^{k-1} \underbrace{\langle \begin{bmatrix}\tilde{\mathbf{U}}(\omega_k^*)\\ \mathbf{0}\end{bmatrix}, \begin{bmatrix}\mathbf{0}\\ \mathbf{v}_i^p\end{bmatrix} \rangle}_{=0 \text{ according to the property of } \langle\cdot,\cdot\rangle} \begin{bmatrix}\mathbf{0}\\ \mathbf{v}_i^p\end{bmatrix} \\ &= \begin{bmatrix}\mathbf{v}_k^u\\ \mathbf{0}\end{bmatrix}\end{aligned}$$

where $\mathbf{v}_k^u = \tilde{\mathbf{U}}(\omega_k^*) - \sum_{i=1}^{k-1} \left(\mathbf{v}_i^{u,H} \mathbf{A}_u \tilde{\mathbf{U}}(\omega_k^*)\right) \mathbf{v}_i^u$.

With the same manner for $\text{ortho}(\begin{bmatrix}\mathbf{0}\\ \tilde{\mathbf{P}}(\omega_k^*)\end{bmatrix}, \mathbf{V}_{k-1})$, we have:

$$\text{ortho}(\begin{bmatrix}\mathbf{0}\\ \tilde{\mathbf{P}}(\omega_k^*)\end{bmatrix}, \mathbf{V}_{k-1}) = \begin{bmatrix}\mathbf{0}\\ \mathbf{v}_k^p\end{bmatrix}$$

where $\mathbf{v}_k^p = \tilde{\mathbf{P}}(\omega_k^*) - \sum_{i=1}^{k-1} \left(\mathbf{v}_i^{p,H} \mathbf{A}_p \tilde{\mathbf{P}}(\omega_k^*)\right) \mathbf{v}_i^p$.

□

3.3.2 Case of the formulation in $(\mathbf{u}_s, p, \varphi)$

According to Lemma 3.2.4, we propose to modify the Classical Greedy Algorithm 1 to ensure the stability of Galerkin reduced order model of $(\mathbf{u}_s, p, \varphi)$ formulation as outlined in Algorithm 3.

The only differences compared to Classical Greedy Algorithm 1 are the steps 2, 6 and 11. At the step 2, we transform the first frequency mode into three vectors and use these three independent vectors to enrich the reduced basis $\mathbf{V}$. At the step 6, instead of having the reduced order model of size $k-1$ as in Classical Greedy Algorithm 1, we have a reduced order model of $3(k-1)$ degrees of freedom in the new Greedy Algorithm 3. At the step 11, instead of using directly the new solution of the frequency domain (where the frequency is selected as the one who maximize the indicator error) for enriching the reduced basis $\mathbf{V}$, we first transform this new mode $\tilde{\mathbf{X}}(\omega_k^*)$ into three independent vectors: $\begin{bmatrix}\tilde{\mathbf{U}}(\omega_k^*) & \mathbf{0} & \mathbf{0}\end{bmatrix}^T$, $\begin{bmatrix}\mathbf{0} & \tilde{\mathbf{P}}(\omega_k^*) & \mathbf{0}\end{bmatrix}^T$, $\begin{bmatrix}\mathbf{0} & \mathbf{0} & \tilde{\mathbf{P}}(\omega_k^*)\end{bmatrix}^T$ and use these three independent vectors to enrich the reduced basis $\mathbf{V}$.

Algorithm 3 Greedy Algorithm (stabilized version for the formulation in $(\mathbf{u}_s, p, \varphi)$)

Input: N_{max} maximum number of iterations, N_{train} (size of training set to be performed in each iteration), the matrices $\mathbf{I}_{up\varphi}, \mathbf{M}_{up\varphi}, \mathbf{C}_{up\varphi}, \mathbf{K}_{up\varphi}$ and the right-hand side $\mathbf{F}_{up\varphi}$, ω_{min} (the minimum pulsation of interest), ω_{max} (the maximum pulsation of interest) and a tolerance ϵ

Output: A reduced basis $\mathbf{V}$

We choose $\tilde{\mathbf{X}}(\omega_{min}) = \begin{bmatrix} \tilde{\mathbf{U}}^T(\omega_{min}) & \tilde{\mathbf{P}}^T(\omega_{min}) & \tilde{\boldsymbol{\varphi}}^T(\omega_{min}) \end{bmatrix}^T$

Transform the reduced basis to the form:

$$\mathbf{V} = \begin{bmatrix} \frac{\mathbf{U}(\omega_{min})}{||\tilde{\mathbf{U}}(\omega_{min})||} & \mathbf{0} & \mathbf{0} \\ \mathbf{0} & \frac{\tilde{\mathbf{P}}(\omega_{min})}{||\tilde{\mathbf{P}}(\omega_{min})||} & \mathbf{0} \\ \mathbf{0} & \mathbf{0} & \frac{\tilde{\mathbf{P}}(\omega_{min})}{||\tilde{\mathbf{P}}(\omega_{min})||} \end{bmatrix}$$

Set $k = 2$

while $(k \leq N_{max})$ **do**

  Generate randomly a set of training sample $\mathcal{D}_k = \{\omega_1, \cdots, \omega_{N_{tr}}\} \subset [\omega_{min}, \omega_{max}]$

  Solve for every values of pulsation $\omega \in \mathcal{D}_k$, the reduced order model obtained by Galerkin projection on the basis $\mathbf{V}$ of dimension $3(k-1)$:

$$\mathbf{A}_r(\omega)\tilde{\mathbf{X}}_r(\omega) = \mathbf{F}_r$$

  where $\mathbf{A}_r(\omega) = \mathbf{V}^H \mathbf{A}_{up\varphi}(\omega)\mathbf{V}$ et $\mathbf{F}_r = \mathbf{V}^H \mathbf{F}_{up\varphi}$.

  Find the value of ω_k^* which maximises the norm of residual divided by the norm of the right-hand side:

$$\omega_k^* = \text{argmax}_{\omega \in \mathcal{D}_k} ||\mathbf{F}_{up\varphi} - \mathbf{A}_{up\varphi}(\omega)\mathbf{V}\tilde{\mathbf{X}}_r(\omega)||/||\mathbf{F}_{up\varphi}||$$

  if $(||\mathbf{F}_{up\varphi} - \mathbf{A}_{up\varphi}(\omega_k^*)\mathbf{V}\tilde{\mathbf{X}}_r(\omega_k^*)||/||\mathbf{F}_{up\varphi}|| \leq \epsilon)$ **then**

    break;

  else

    Orthonormalization the three new vectors $\begin{bmatrix} \tilde{\mathbf{U}}^T(\omega_k^*) & \mathbf{0}^T & \mathbf{0}^T \end{bmatrix}^T$, $\begin{bmatrix} \mathbf{0}^T & \tilde{\mathbf{P}}^T(\omega_k^*) & \mathbf{0}^T \end{bmatrix}^T$, $\begin{bmatrix} \mathbf{0}^T & \mathbf{0}^T & \tilde{\mathbf{P}}^T(\omega_k^*) \end{bmatrix}^T$ with the basis $\mathbf{V}$ of the previous iteration and enrich the basis:

$$\mathbf{V} = \begin{bmatrix} \mathbf{V} & \mathbf{v}_1^k & \mathbf{v}_2^k & \mathbf{v}_3^k \end{bmatrix}$$

    where

$$\mathbf{v}_1^k = \text{ortho}(\begin{bmatrix} \tilde{\mathbf{U}}^T(\omega_k^*) & \mathbf{0}^T & \mathbf{0}^T \end{bmatrix}^T, \mathbf{V})$$
$$\mathbf{v}_2^k = \text{ortho}(\begin{bmatrix} \mathbf{0}^T & \tilde{\mathbf{P}}^T(\omega_k^*) & \mathbf{0}^T \end{bmatrix}^T, \mathbf{V})$$
$$\mathbf{v}_3^k = \text{ortho}(\begin{bmatrix} \mathbf{0}^T & \mathbf{0}^T & \tilde{\mathbf{P}}^T(\omega_k^*) \end{bmatrix}^T, \mathbf{V})$$

  end if

  $k = k + 1$

end while

Depending on the scalar product used in the orthogonalization procedure at the step 11 of Algorithm 3, the output reduced basis of Algorithm 3 may not be in the form of (3.21). However, the following lemma justify that the output reduced basis of Greedy Algorithm 3 is in form of (3.21), provided that we use a particular scalar product in orthogonalization procedure.

Lemma 3.3.2 *The output reduced basis of Greedy Algorithm 3 is in the form of (3.21) if we use the scalar product defined by:*

$$\langle \begin{bmatrix} \boldsymbol{U}_1^T & \boldsymbol{P}_1^T & \boldsymbol{\varphi}_1^T \end{bmatrix}^T, \begin{bmatrix} \boldsymbol{U}_2^T & \boldsymbol{P}_2^T & \boldsymbol{\varphi}_2^T \end{bmatrix}^T \rangle = \boldsymbol{U}_2^H \boldsymbol{A}_u \boldsymbol{U}_1 + \boldsymbol{P}_2^H \boldsymbol{A}_p \boldsymbol{P}_1 + \boldsymbol{\varphi}_2^H \boldsymbol{A}_p \boldsymbol{\varphi}_1 \quad (3.28)$$

where $\boldsymbol{A}_u$ and $\boldsymbol{A}_p$ are two hermitian positive definite matrices, in the orthogonalization procedure. As a particular case, the output reduced basis of Greedy Algorithm 3 is in the form of (3.21) if we use euclidean scalar product in orthogonalization procedure.

Proof: The reduced basis $\mathbf{V}$ at the step 2 of Algorithm 3 is clearly in the form of (3.21). Suppose that at iteration $k-1$, the reduced basis $\mathbf{V}_{k-1}$ is in the form:

$$\mathbf{V}_{k-1} = \begin{bmatrix} \mathbf{v}_1^u & \mathbf{0} & \mathbf{0} & \mathbf{v}_2^u & \mathbf{0} & \mathbf{0} & \cdots & \mathbf{v}_{k-1}^u & \mathbf{0} & \mathbf{0} \\ \mathbf{0} & \mathbf{v}_1^p & \mathbf{0} & \mathbf{0} & \mathbf{v}_2^p & \mathbf{0} & \cdots & \mathbf{0} & \mathbf{v}_{k-1}^p & \mathbf{0} \\ \mathbf{0} & \mathbf{0} & \mathbf{v}_1^p & \mathbf{0} & \mathbf{0} & \mathbf{v}_2^p & \cdots & \mathbf{0} & \mathbf{0} & \mathbf{v}_{k-1}^p \end{bmatrix} \quad (3.29)$$

we will show that the reduced basis of iteration k is in form:

$$\mathbf{V}_k = \begin{bmatrix} \mathbf{v}_1^u & \mathbf{0} & \mathbf{0} & \mathbf{v}_2^u & \mathbf{0} & \mathbf{0} & \cdots & \mathbf{v}_k^u & \mathbf{0} & \mathbf{0} \\ \mathbf{0} & \mathbf{v}_1^p & \mathbf{0} & \mathbf{0} & \mathbf{v}_2^p & \mathbf{0} & \cdots & \mathbf{0} & \mathbf{v}_k^p & \mathbf{0} \\ \mathbf{0} & \mathbf{0} & \mathbf{v}_1^p & \mathbf{0} & \mathbf{0} & \mathbf{v}_2^p & \cdots & \mathbf{0} & \mathbf{0} & \mathbf{v}_k^p \end{bmatrix} \quad (3.30)$$

Under the hypothesis of $\mathbf{V}_{k-1}$, we have:

$$\begin{aligned} \text{ortho}(\begin{bmatrix} \tilde{\mathbf{U}}(\omega_k^*) \\ \mathbf{0} \\ \mathbf{0} \end{bmatrix}, \mathbf{V}_{k-1}) = \begin{bmatrix} \tilde{\mathbf{U}}(\omega_k^*) \\ \mathbf{0} \\ \mathbf{0} \end{bmatrix} &- \sum_{i=1}^{k-1} \langle \begin{bmatrix} \tilde{\mathbf{U}}(\omega_k^*) \\ \mathbf{0} \\ \mathbf{0} \end{bmatrix}, \begin{bmatrix} \mathbf{v}_i^u \\ \mathbf{0} \\ \mathbf{0} \end{bmatrix} \rangle \begin{bmatrix} \mathbf{v}_i^u \\ \mathbf{0} \\ \mathbf{0} \end{bmatrix} \\ &- \sum_{i=1}^{k-1} \underbrace{\langle \begin{bmatrix} \tilde{\mathbf{U}}(\omega_k^*) \\ \mathbf{0} \\ \mathbf{0} \end{bmatrix}, \begin{bmatrix} \mathbf{0} \\ \mathbf{v}_i^p \\ \mathbf{0} \end{bmatrix} \rangle}_{=0 \text{ according to the property of } \langle \cdot, \cdot \rangle} \begin{bmatrix} \mathbf{0} \\ \mathbf{v}_i^p \\ \mathbf{0} \end{bmatrix} \\ &- \sum_{i=1}^{k-1} \underbrace{\langle \begin{bmatrix} \tilde{\mathbf{U}}(\omega_k^*) \\ \mathbf{0} \\ \mathbf{0} \end{bmatrix}, \begin{bmatrix} \mathbf{0} \\ \mathbf{0} \\ \mathbf{v}_i^p \end{bmatrix} \rangle}_{=0 \text{ according to the property of } \langle \cdot, \cdot \rangle} \begin{bmatrix} \mathbf{0} \\ \mathbf{0} \\ \mathbf{v}_i^p \end{bmatrix} \\ &= \begin{bmatrix} \mathbf{v}_k^{u,T} & \mathbf{0}^T & \mathbf{0}^T \end{bmatrix}^T \end{aligned}$$

where $\mathbf{v}_k^u = \tilde{\mathbf{U}}(\omega_k^*) - \sum_{i=1}^{k-1} \left(\mathbf{v}_i^{u,H} \mathbf{A}_u \tilde{\mathbf{U}}(\omega_k^*) \right) \mathbf{v}_i^u$.

With the same manner for $\text{ortho}(\begin{bmatrix}\mathbf{0}\\ \tilde{\mathbf{P}}(\omega_k^*)\\ \mathbf{0}\end{bmatrix}, \mathbf{V}_{k-1})$ and $\text{ortho}(\begin{bmatrix}\mathbf{0}\\ \mathbf{0}\\ \tilde{\mathbf{P}}(\omega_k^*)\end{bmatrix}, \mathbf{V}_{k-1})$, we have:

$$\text{ortho}(\begin{bmatrix}\mathbf{0}\\ \tilde{\mathbf{P}}(\omega_k^*)\\ \mathbf{0}\end{bmatrix}, \mathbf{V}_{k-1}) = \begin{bmatrix}\mathbf{0}\\ \mathbf{v}_k^p\\ \mathbf{0}\end{bmatrix}, \quad \text{ortho}(\begin{bmatrix}\mathbf{0}\\ \mathbf{0}\\ \tilde{\mathbf{P}}(\omega_k^*)\end{bmatrix} \mathbf{V}_{k-1}) = \begin{bmatrix}\mathbf{0}\\ \mathbf{0}\\ \mathbf{v}_k^p\end{bmatrix}$$

where $\mathbf{v}_k^p = \tilde{\mathbf{P}}(\omega_k^*) - \sum_{i=1}^{k-1}\left(\mathbf{v}_i^{p,H}\mathbf{A}_p\tilde{\mathbf{P}}(\omega_k^*)\right)\mathbf{v}_i^p$.

□

Remark 3.3.1 For the formulation in $(\mathbf{u}_s, p, \varphi)$, we can write the frequency domain as a symmetric equation:

$$\underbrace{\left[-i\omega^3\mathbf{I} - \omega^2\mathbf{M} + \mathbf{K}\right]}_{\mathbf{A}^{sym}(\omega)}\tilde{\mathbf{X}}(\omega) = \mathbf{F} \tag{3.31}$$

and we can show that either we use the relation $\mathbf{A}^{sym}(\omega)$ defined in Equation (3.31) or the relation $\mathbf{A}(\omega)$ defined in Equation (3.24), in Algorithm 3, we obtain the same the evolution of residual norm in Algorithm 3 and the same output reduced basis.

Remark 3.3.2 If we use the same training set $\mathcal{D}_k$ in Algorithm 2 and Algorithm 3 at each iteration and we use the scalar product defined in (3.25) and (3.28) respectively for Algorithm 2 and Algorithm 3, we can show that the evolution of the residual norm in both algorithms is the same. Furthermore, according to Lemma 3.2.5, the Galerkin reduced order model in $(\mathbf{u}_s, p)$ formulation based on the output reduced basis of Greedy Algorithm 2 is equivalent to the Galerkin reduced order models in $(\mathbf{u}_s, p, \varphi)$ formulation based on the output reduced basis of Greedy Algorithm 3.

3.4 Numerical results

In this section, the stability of reduced order model proposed in Section 3.2 will be verified numerically in two examples. The first numerical model consists of a right cylindrical hull with square plate immersed in an acoustic fluid. The fist case is an academical example in which the geometry is very simple. The second case is an industrial problem which consists of a section of right cylindrical hull with stiffeners in T-form and a generic engine immersed in an acoustic fluid. In order to show that the proposed stabilization technique does not depend on the choice of finite element type, we intentionally chose different finite element type between these two study cases. In the first study case, we use linear finite element type. In the second study case, we use quadratic finite element type. In both cases, BGT-1 method is used to approximate the radiation condition. The accuracy of the reduced order model based on the reduced basis built by Greedy Algorithms applying on the corresponding frequency domain, will also be investigated.

3.4.1 Test case 1: a cylindrical hull with square plate immersed in an acoustic fluid

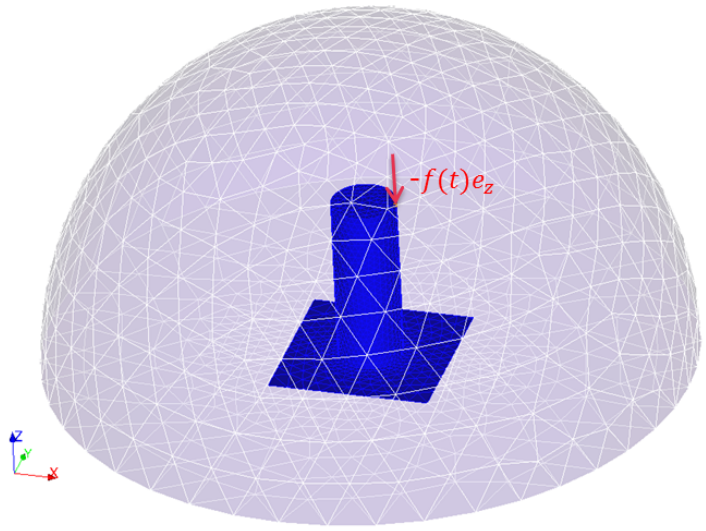

Figure 3.1: Graphical representation of the first study case

The vibro-acoustic system in this example consists of a cylindrical hull with square plate that is excited by a point force at $(0.1, 0, 0.5)$ m and radiates sound in an acoustic fluid. A graphical representation of this system is presented in Figure 3.1. The cylindrical hull has a height of 0.5 m and a radius of 0.1 m. The square plate has an edge length of 0.5 m. Both cylindrical hull and square plate have a thickness of 0.01 m. On the boundary of the square plate, a homogeneous Dirichlet condition is applied. To approximate the radiation condition by BGT-1 method (see Section 1.1.4), a truncated fluid domain in form of a half-spherical of radius $R_{bgt} = 1$ m is used. The physical properties of the structure and the fluid are given in Table 3.1.

Structure	Fluid
Young's modulus $E = 210$ GPa	Speed of sound $c_0 = 1500$ m/s
Poisson's ratio $\nu = 0.3$	Density $\rho_0 = 1000$ kg/m^3
Density $\rho_s = 7850$ kg/m^3	
Damping parameter $\alpha_s = 10^{-5}, \beta_s = 0$	

Table 3.1: Physical properties of the structure and the fluid in the first study case of Chapter 3

Finite element modelling

The finite element model or the full model is obtained by using a mesh in which the maximum size of element is chosen such that we have at least five elements per wavelength at 1 000 Hz. The cylindrical hull and square plate is modelled using linear Discrete Kirchhoff

Triangular (DKT) elements [20]. The acoustic fluid is modelled using linear tetrahedral elements. A structural damping is also considered in the system. We use Rayleigh damping model which represents the damping effect by a symmetric semi-positive definite matrix $\mathbf{C}_s = \alpha_s \mathbf{K}_s + \beta_s \mathbf{M}_s$, where the coefficient α_s and β_s are given in Table 3.1. On the boundary of the truncated fluid domain, the condition BGT-1 of Equation (1.35) is applied in order to approximate the outgoing sound wave by a spherical wave for which we use the value of impedance $Z_R = \rho_0 R_{bgt}, Z_C = \rho_0 c_0$.

For the formulation in $(\mathbf{u}_s, p)$ and in $(\mathbf{u}_s, \phi)$, the finite element model consists of 35 503 degrees of freedom, 12 132 of which correspond to the structural part and 23 371 of which correspond to the acoustic fluid part. For the formulation in $(\mathbf{u}_s, p, \varphi)$, the finite element model consists of 58 874 degrees of freedom, 12 132 of which correspond to the structural part and 46 742 of which correspond to the acoustic fluid part.

Numerical validation of the stability of the reduced order models

First, we propose to verify the stability properties of the Galerkin reduced order models in $(\mathbf{u}_s, p)$ and in $(\mathbf{u}_s, p, \varphi)$ formulation using respectively the reduced basis obtained by Greedy Algorithms 2 and 3 and the reduced order models in $(\mathbf{u}_s, \phi)$ formulation using Petrov-Galerkin projection as stated in Lemma 3.2.2. In order to show that this stability properties can not be achieved automatically without using the proposed techniques in Section 3.2, we will also be interested in the reduced order models of these three formulations using Galerkin projection with the reduced basis obtained by Classical Greedy Algorithm 1.

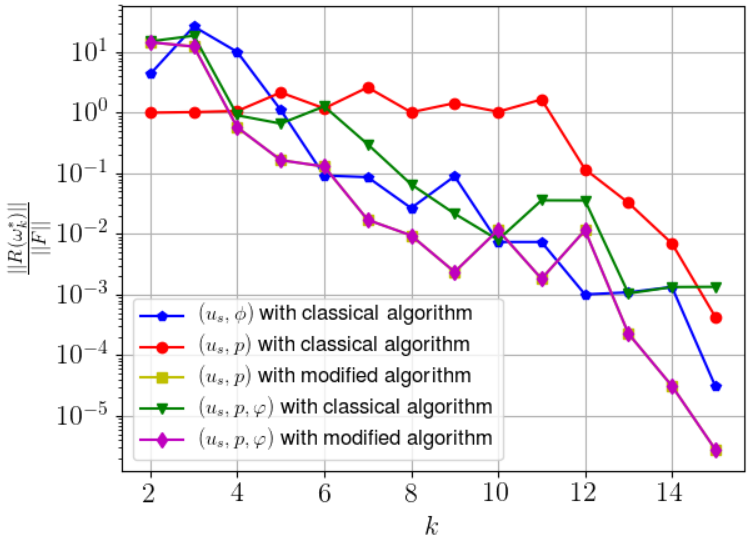

Figure 3.2: Evolution of error indicator in Greedy Algorithms in the first study case.

To run Greedy Algorithms, we use $f_{min} = 10$ Hz, $f_{max} = 1000$ Hz and $N_{max} = 15$. The same training samples $\mathcal{D}_k$, which are chosen randomly at each iteration such that $|\mathcal{D}_k| = 100$, are used for all versions of Greedy Algorithms. To orthogonalize the basis, we use the euclidean

scalar product. The evolution of the error indicator, defined as the norm of residual divided by the norm of the right-hand side, is shown in Figure 3.2.

In Figure 3.2, we see that the evolution of the error indicator in modified Greedy Algorithms 2 and 3 are the same as mentioned in Remark 3.3.2. We observe that the error indicator in the modified Greedy Algorithm 2 and 3 decrease faster than Classical Greedy Algorithm 1. This can be explained by the fact that the modified Greedy Algorithm 2 and 3 increase the size of reduced problem at the step 4. Even though the error indicator decreases well in both cases, we will see in the following that the Galerkin reduced order model based on the obtained reduced basis do not have the same stability properties.

To access to the stability, we can compute the poles of the reduced order model. We recall that the poles of a second order system (3.15) are the roots of the polynomial $P(s) := \det(s^2\mathbf{M}_r + s\mathbf{C}_r + \mathbf{K}_r)$ which are also the eigenvalues of the following Generalized Eigenvalue Problem:

$$\mathbf{A}\mathbf{v} = s\mathbf{E}\mathbf{v} \tag{3.32}$$

where $\mathbf{E} = \begin{bmatrix} \mathbf{I}_N & \mathbf{0} \\ \mathbf{0} & \mathbf{M}_r \end{bmatrix}$ et $\mathbf{A} = \begin{bmatrix} \mathbf{0} & \mathbf{I}_N \\ -\mathbf{K}_r & -\mathbf{C}_r \end{bmatrix}$.

Figure 3.3 shows the poles of the Galerkin and Petrov-Galerkin reduced order models of the formulation in $(\mathbf{u}_s, \phi)$. Figure 3.4 and 3.5 show respectively the poles of Galerkin reduced order models in $(\mathbf{u}_s, p)$ and $(\mathbf{u}_s, p, \varphi)$ based on the reduced basis of Classical Greedy Algorithm 1 and modified Greedy Algorithm 2 and 3. We remark that the Galerkin reduced order model of formulation in $(\mathbf{u}_s, p, \varphi)$ based on the reduced basis of Classical Greedy Algorithm 1 have some infinite poles which is due to the singularity of the reduced mass matrix $\mathbf{M}_r$. Only the finite poles are then illustrated in Figure 3.5 for this case.

Figure 3.3 confirms that the Petrov-Galerkin reduced order models of the formulation in $(\mathbf{u}_s, \phi)$ are always stable while the Galerkin reduced order model can be unstable, as we saw here in the case of $k = 3, 5, 10, 15$, there are some poles in the right-half of the complex plane. For the formulation in $(\mathbf{u}_s, p)$, we observe in Figure 3.4 that Galerkin reduced order model is always stable if we use the reduced basis obtained by modified Greedy Algorithm 2 and that using the reduced basis of Classical Greedy Algorithm 1 might yield unstable reduced order model, as we saw here in the case of $k = 3, 5, 10, 15$. A closer look at Figure 3.4 and 3.5 reveals that the reduced order models in $(\mathbf{u}_s, p, \varphi)$ using the output reduced basis of Greedy Algorithm 3 has the same non-zeros poles as the reduced order models in $(\mathbf{u}_s, p)$ using the output reduced basis of Greedy Algorithm 2. Finally, the position of the finite poles in complex plane in Figure 3.5 shows clearly that the Galerkin reduced order models based on the reduced basis of Classical Greedy Algorithm 1 are unstable for $k = 5, 10, 15$.

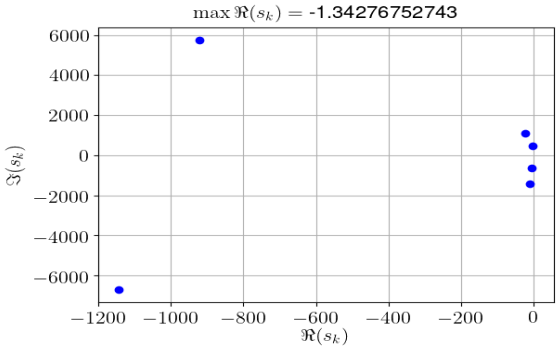

(a) $k = 3$

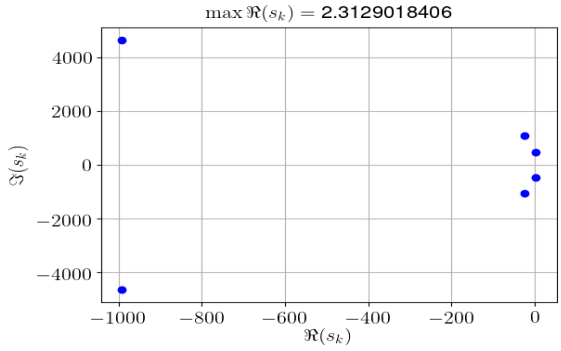

(b) $k = 3$

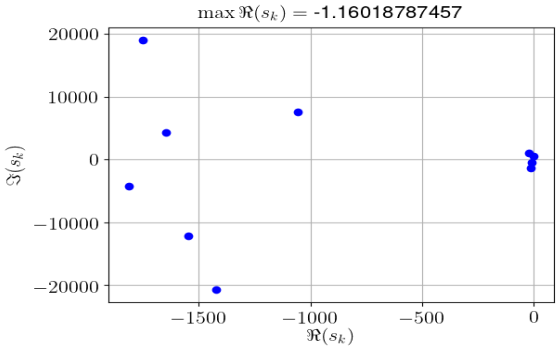

(c) $k = 5$

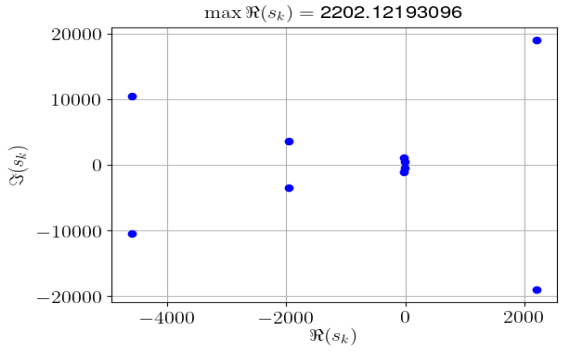

(d) $k = 5$

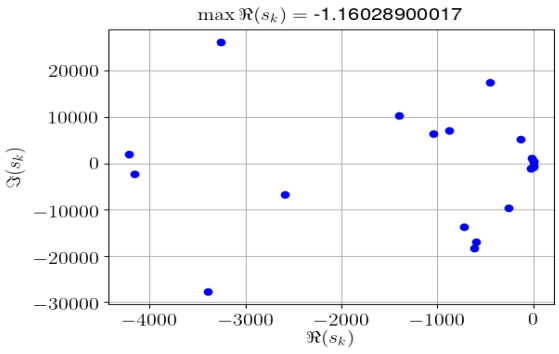

(e) $k = 10$

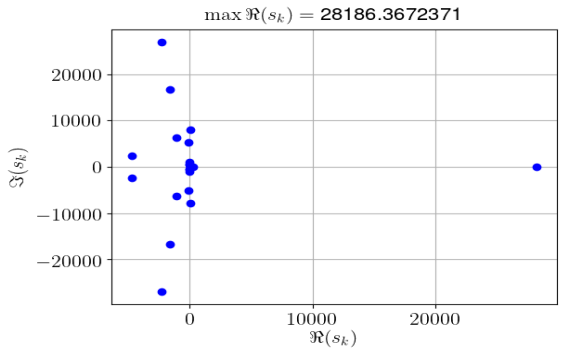

(f) $k = 10$

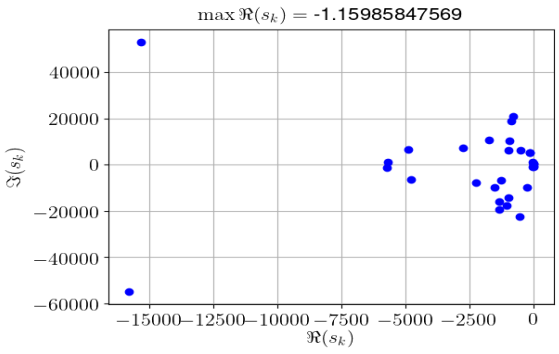

(g) $k = 15$

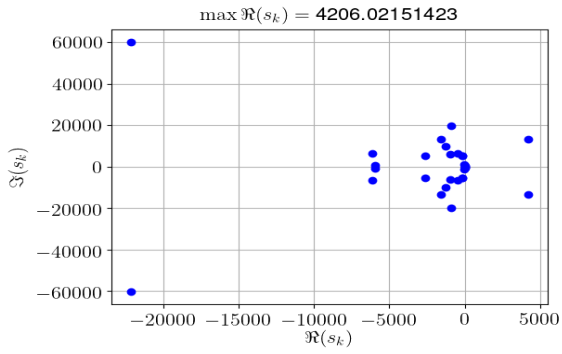

(h) $k = 15$

Figure 3.3: The poles of reduced order models in $(\mathbf{u}_s, \phi)$ using the reduced basis of iteration k of Greedy Algorithm 1. Left: *case of Petrov-Galerkin projection of Lemma 3.2.2.* Right: *case of Galerkin projection.*

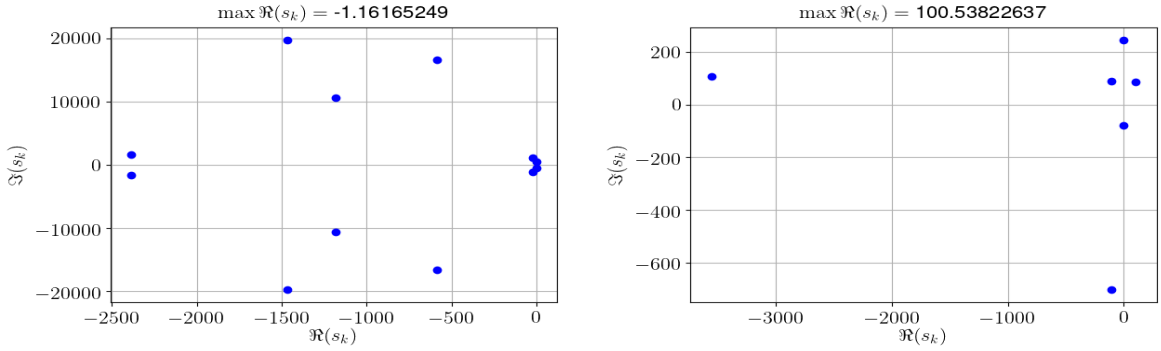

(a) $k = 3$

(b) $k = 3$

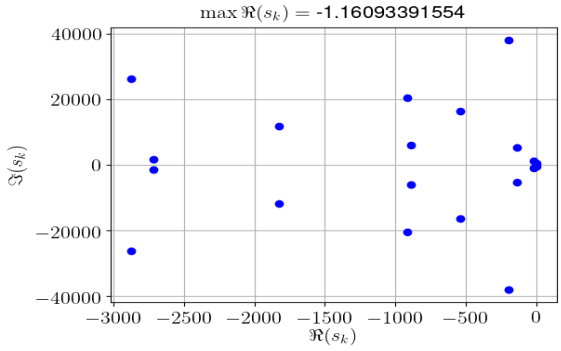

(c) $k = 5$

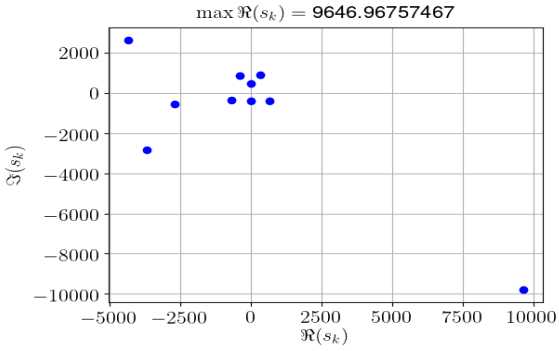

(d) $k = 5$

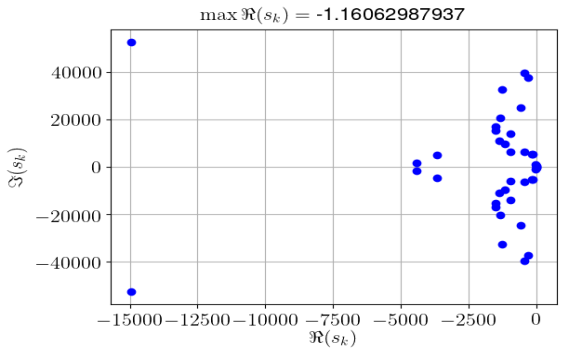

(e) $k = 10$

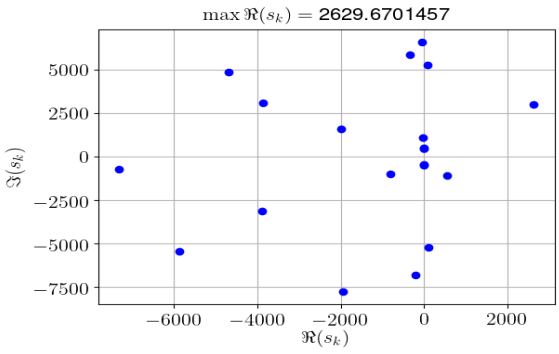

(f) $k = 10$

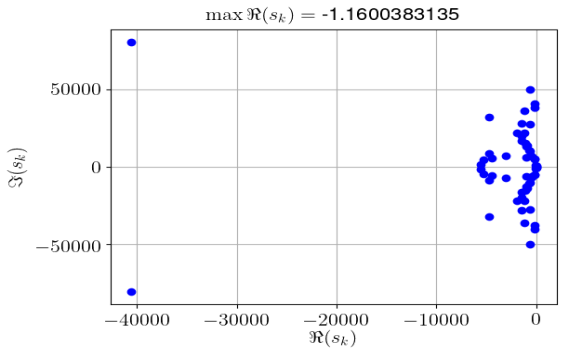

(g) $k = 15$

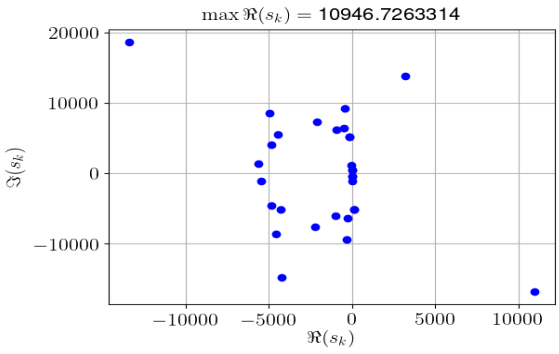

(h) $k = 15$

Figure 3.4: The poles of Galerkin reduced order models in $(\mathbf{u}_s, p)$ using the reduced basis of iteration k of Greedy Algorithm. Left: *case of modified Greedy Algorithm 2.* Right: *case of Classical Greedy Algorithm 1*

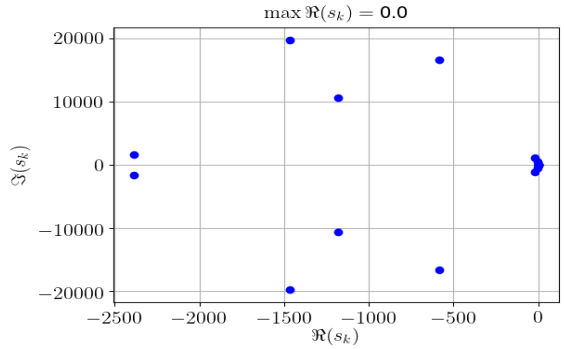

(a) $k = 3$

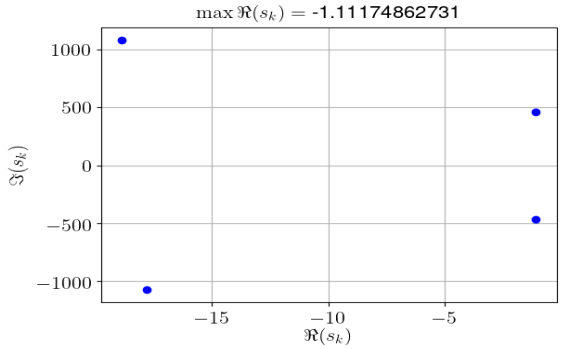

(b) $k = 3$

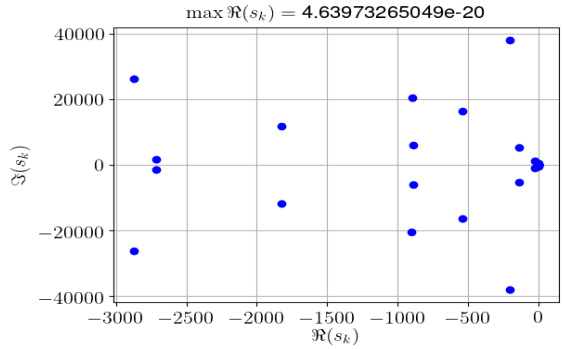

(c) $k = 5$

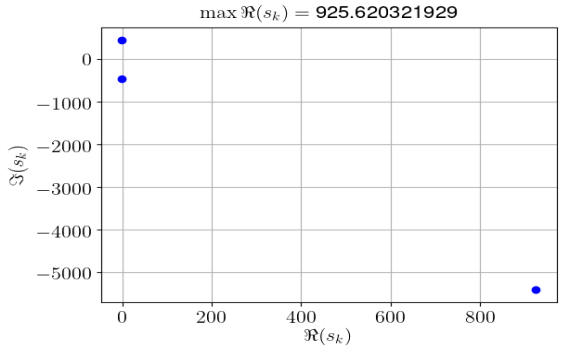

(d) $k = 5$

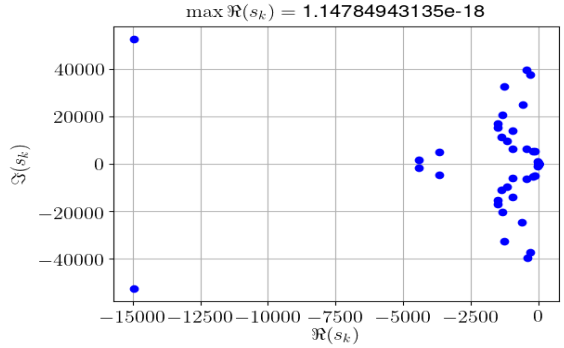

(e) $k = 10$

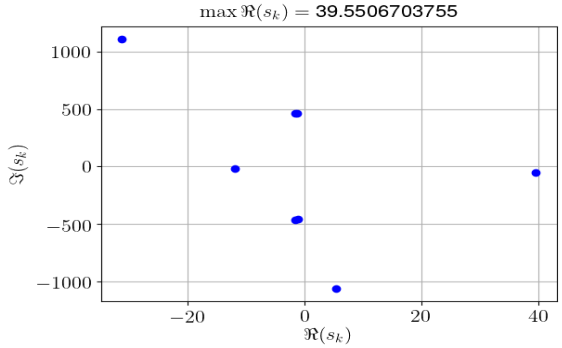

(f) $k = 10$

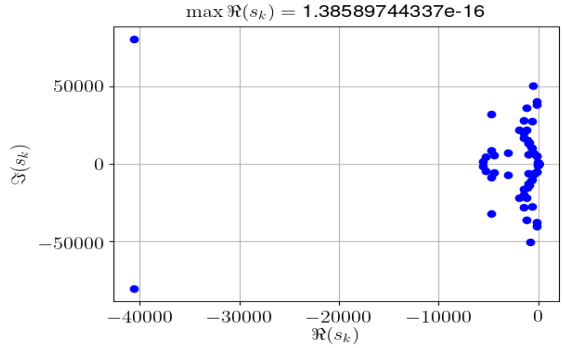

(g) $k = 15$

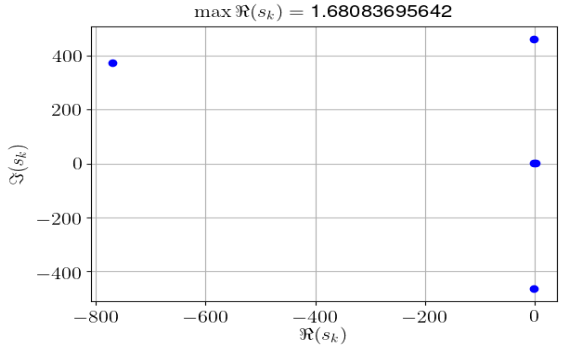

(h) $k = 15$

Figure 3.5: The poles of Galerkin reduced order models in $(\mathbf{u}_s, p, \varphi)$ using the reduced basis of iteration k of Greedy Algorithms. Left: *case of Classical Greedy Algorithm 1.* Right: *case of the modified Greedy Algorithm 3.*

Numerical study of the accuracy of the reduced order models

Now, let us turn to the accuracy of the proposed reduced order models. We recall that the Galerkin reduced order models in $(\mathbf{u}_s, p, \varphi)$ formulation based on the reduced basis obtained by Greedy Algorithm 3 is equivalent to the Galerkin reduced order models in $(\mathbf{u}_s, p)$ formulation based on the reduced basis obtained by Greedy Algorithm 2 (see Remark 3.3.2). Hence, only the Galerkin reduced order models in $(\mathbf{u}_s, p)$ formulation and the Petrov-Galerkin reduced order models in $(\mathbf{u}_s, \phi)$ formulation are considered here.

In the following, we set $f_{min} = 1$ Hz, $N_{train} = 100$, and the stopping criteria $\epsilon = 10^{-8}$ in order to run Classical Greedy Algorithm 1 and modified Greedy Algorithm 2. At each iteration k, the same training samples $\mathcal{D}_k$ are used for both Greedy Algorithms. Depending on the value of f_{max}, the evolution of the error indicators in Classical Greedy Algorithm 1 for the formulation in $(\mathbf{u}_s, \phi)$ and in modified Greedy Algorithm 2 for the formulation in $(\mathbf{u}_s, p)$ are illustrated in Figure 3.6.

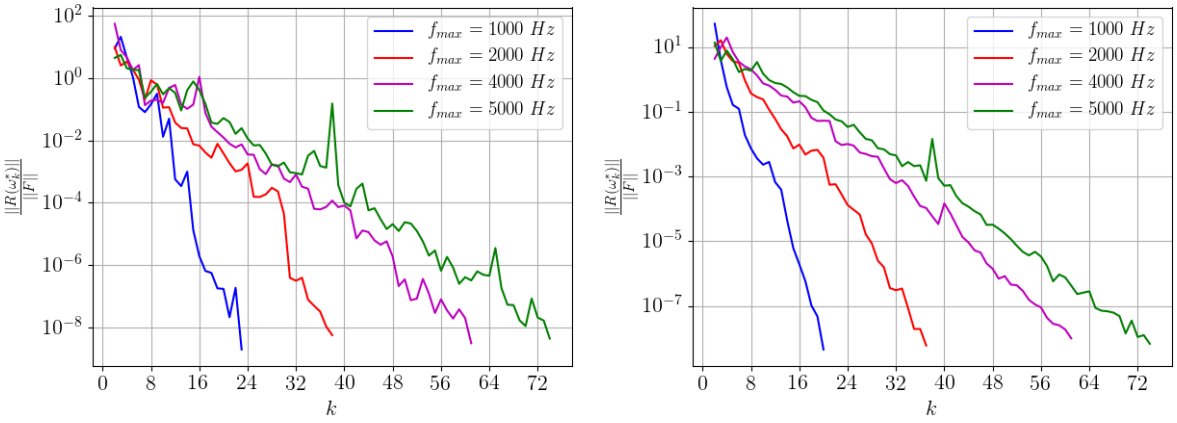

(a) Case of formulation in $(\mathbf{u}_s, \phi)$ with Algorithm 1 (b) Case of formulation in $(\mathbf{u}_s, p)$ with Algorithm 2

Figure 3.6: Evolution of error indicator in Greedy Algorithm in the first study case

In Figure 3.6, we observe that the number of iterations required increase as we increase the value of f_{max}. Although the size of the reduced basis in Algorithm 2 is two times bigger than in Algorithm 1 at each iteration, we remark that both algorithms need around the same number of iterations to achieve the stopping criteria $\epsilon = 10^{-8}$. The size of the reduced basis of these two algorithms is given in Table 3.2.

f_{max}	Formulation in $(\mathbf{u}_s, \phi)$	Formulation in $(\mathbf{u}_s, p)$
1000 Hz	22	38
2000 Hz	37	72
4000 Hz	60	120
5000 Hz	73	146

Table 3.2: Size of the reduced basis in function of f_{max} for the first study case

To compute the accuracy of the reduced order models, we consider an input function f defined by:

$$f(t) = \begin{cases} 10^5 \sin(2\pi f_d t) \text{ , for } 0 \leq t \leq 1/f_d \\ 0 \text{ , for } t > 1/f_d \end{cases} \tag{3.33}$$

Newmark scheme with $\gamma = 1/2 - \alpha$, $\beta = (1-\alpha)^2/4$, where $\alpha = -0.1$, is employed as time integration scheme for both full model and reduced order models. The time step is chosen by $\Delta t = 1/(100 f_d)$ which is sufficiently small for our frequency of interest f_d. The final times in our study is $T_f = 10/f_d$. To access to the accuracy of reduced order models, we compute the relative errors of the structural displacement and the pressure, which are defined by:

$$err_u(t) = \frac{||\mathbf{U}_s^{fom}(t) - \mathbf{U}_s^{rom}(t)||}{||\mathbf{U}_s^{fom}(t)||} \text{ , } err_p(t) = \frac{||\mathbf{P}^{fom}(t) - \mathbf{P}_s^{rom}(t)||}{||\mathbf{P}_s^{fom}(t)||} \tag{3.34}$$

where $||\cdot||$ denotes the euclidean norm and $\mathbf{U}_s$ and $\mathbf{P}$ are two vectors which contain respectively the nodal displacement and nodal pressure, and where the superscript ^{fom} refers to the solution of the full model and the superscript ^{rom} refers to its approximation by the reduced order models.

We recall that for the case of the formulation in $(\mathbf{u}_s, \phi)$, the value of the pressure is obtained by the relation (1.17).

Here, we are interested in the case where $f_d \in \{100 \text{ Hz}, 300 \text{ Hz}, 750 \text{ Hz}, 1000 \text{ Hz}\}$. Figure 3.7 shows the evolution of these errors in the case of the Petrov-Galerkin reduced order model of the formulation in $(\mathbf{u}_s, \phi)$. The case of Galerkin reduced order models of the formulation in $(\mathbf{u}_s, p)$ are reported in Figure 3.8. In both cases, we observe that the errors between the full model and the reduced order models are significant at first and decrease as the times increase. In addition, the errors increase while we increase the frequency f_d of the input function. In all the cases, we remark that the reduced order models approximate the structural displacement better than the fluid pressure. When we increase the value of f_{max} in the construction of the basis by Greedy Algorithms, we observe that it can slightly improve the accuracy of the reduced order models. However, the errors are still large at the beginning of the simulation especially for the case of high frequency.

Recall that the size of Galerkin reduced order model of the formulation in $(\mathbf{u}_s, p)$ is almost two times bigger than the Petrov-Galerkin reduced order model of the formulation in $(\mathbf{u}_s, \phi)$ even though we use almost the same number of modes to built the reduced basis. As compensation, we observe here that Galerkin reduced order model of the formulation in $(\mathbf{u}_s, p)$ has a better accuracy than the Petrov-Galerkin reduced order model of the formulation in $(\mathbf{u}_s, \phi)$.

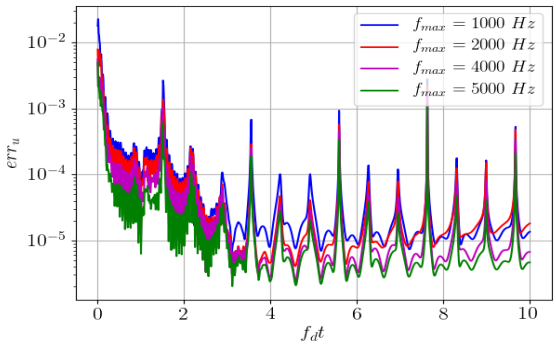

(a) Error on $\mathbf{u}_s$ for the case $f_d = 100$ Hz

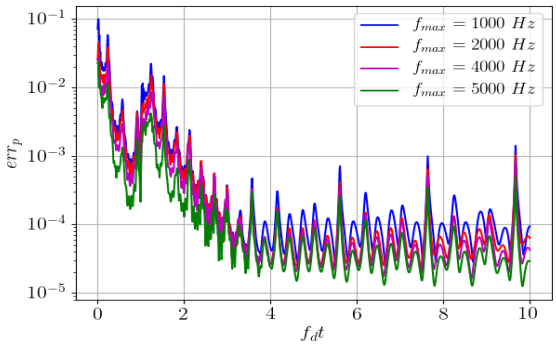

(b) Error on p for the case $f_d = 100$ Hz

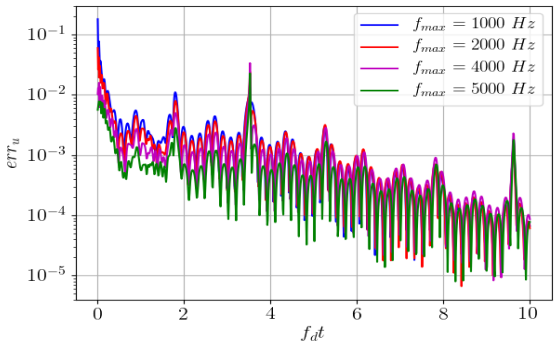

(c) Error on $\mathbf{u}_s$ for the case $f_d = 300$ Hz

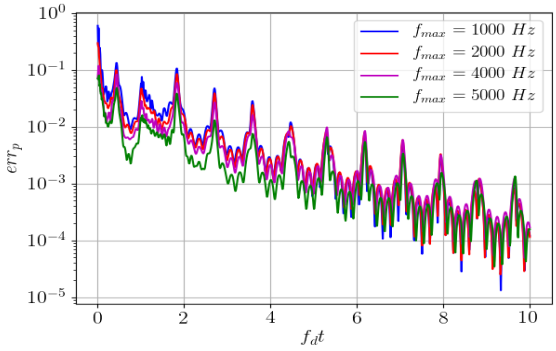

(d) Error on p for the case $f_d = 300$ Hz

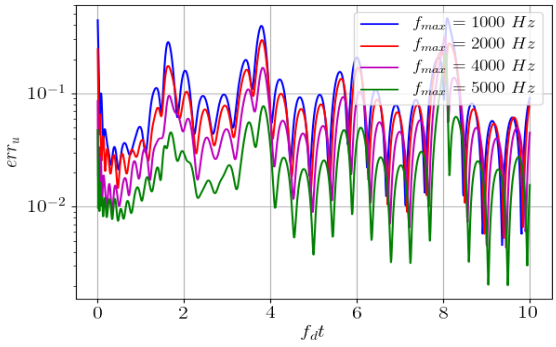

(e) Error on $\mathbf{u}_s$ for the case $f_d = 750$ Hz

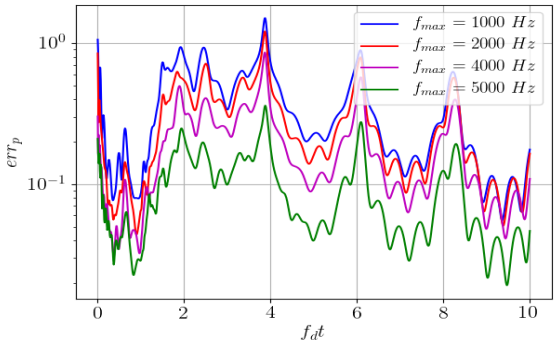

(f) Error on p for the case $f_d = 750$ Hz

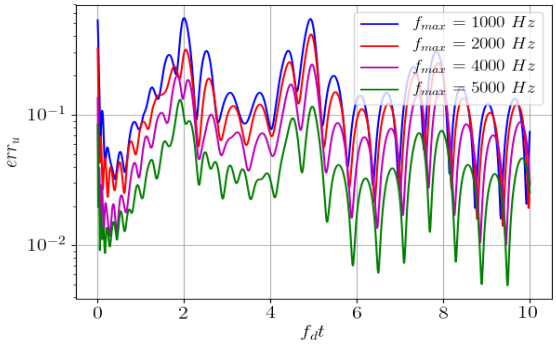

(g) Error on $\mathbf{u}_s$ for the case $f_d = 1000$ Hz

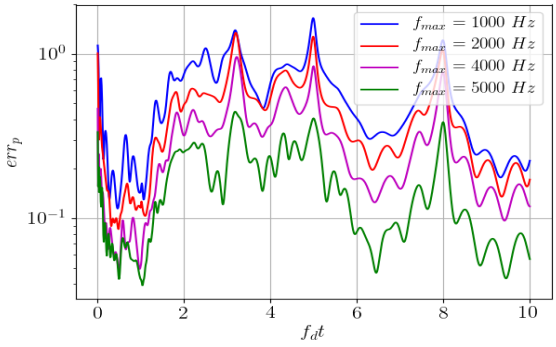

(h) Error on p for the case $f_d = 1000$ Hz

Figure 3.7: Relative errors between the solution of the full model and the Petrov-Galerkin reduced order models in $(\mathbf{u}_s, \phi)$ in the first study case

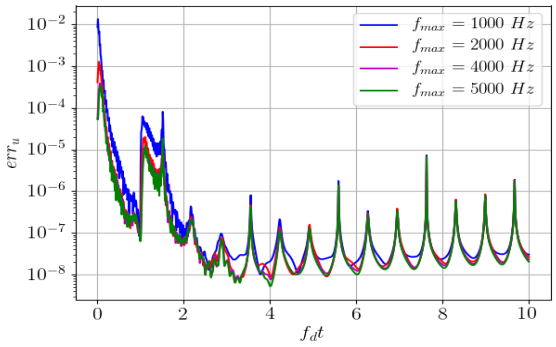

(a) Error of $\mathbf{u}_s$ for the case $f_d = 100$ Hz

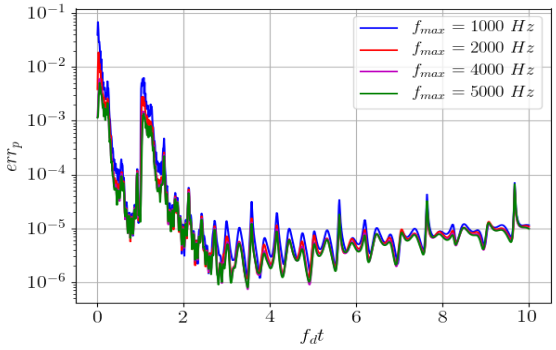

(b) Error of p for the case $f_d = 100$ Hz

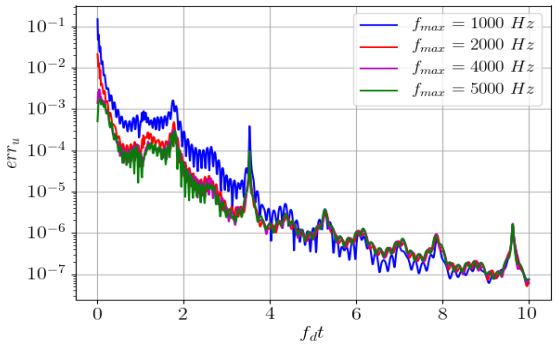

(c) Error of $\mathbf{u}_s$ for the case $f_d = 300$ Hz

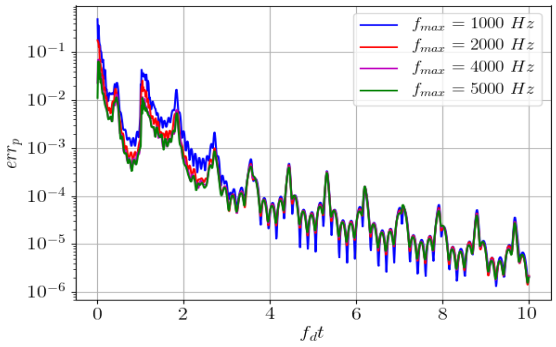

(d) Error of p for the case $f_d = 300$ Hz

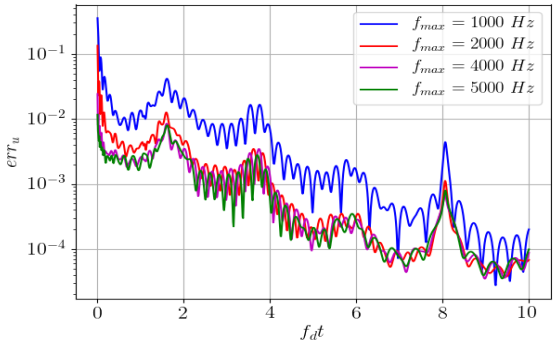

(e) Error of $\mathbf{u}_s$ for the case $f_d = 750$ Hz

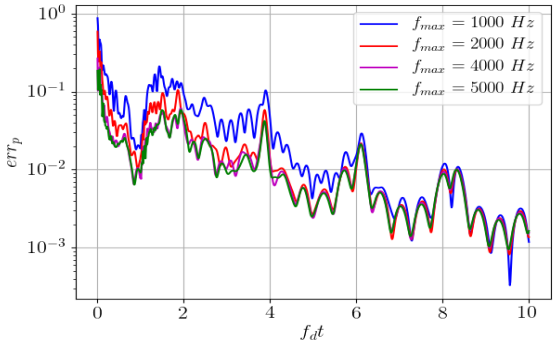

(f) Error of p for the case $f_d = 750$ Hz

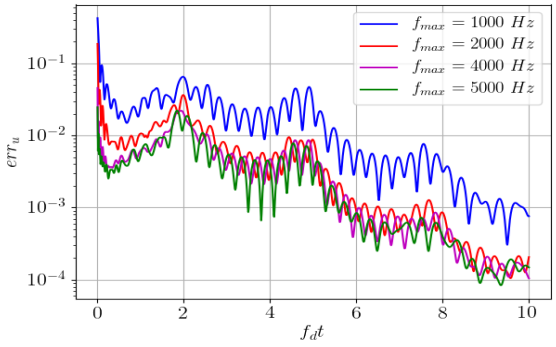

(g) Error of $\mathbf{u}_s$ for the case $f_d = 1000$ Hz

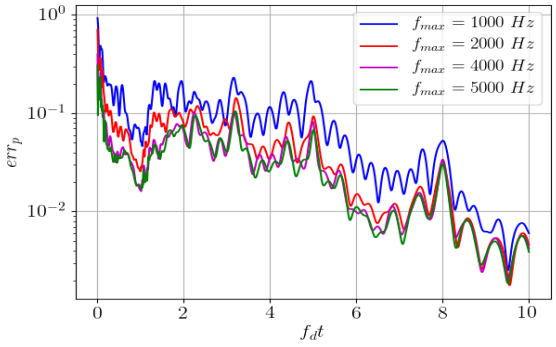

(h) Error of p for the case $f_d = 1000$ Hz

Figure 3.8: Relative errors between the solution of the full model and the Galerkin reduced order models in $(\mathbf{u}_s, p)$ in the first study case

3.4.2 Test case 2: a section of cylindrical hull with stiffeners in T-form and a generic structure immersed in an acoustic fluid

In the second study case, we consider the case where the structure has a more complex geometry (sourced from [84]). A graphical representation of this study case is illustrated in Figure 3.9 in which the structure part are marked in blue. The vibro-acoustic system consists of a section of a cylindrical hull with stiffeners in form of T and an structure immersed in an acoustic fluid. The excitation are introduced by a point force acting on the plate of the structure (marked in red in Figure 3.9). On the top and bottom boundary of the cylindrical hull, a homogeneous Dirichlet condition is applied. To approximate the radiation condition by BGT-1 method, a truncated fluid domain in form of a sphere of with a radius equal to two times the radius of cylindrical hull, is used. The physical properties of the structure and the fluid in this study case are given in Table 3.3.

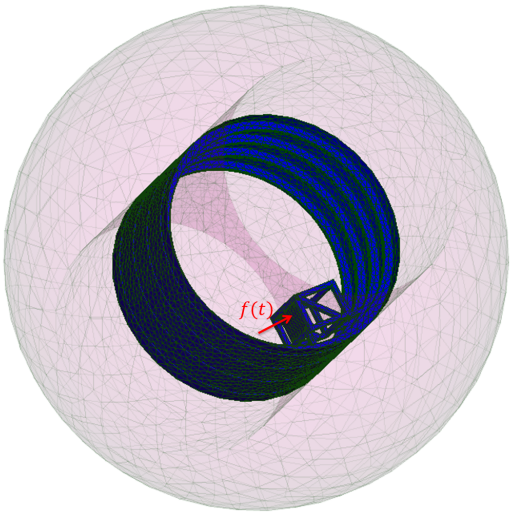

Figure 3.9: Graphical representation of the second study case

Finite element modelling

The finite element model or the full model is obtained by using a mesh in which the maximum size of element is chosen such that we have at least six elements per wavelength at 500 Hz. The structural part is modelled using quadratic triangular shell elements [21]. The acoustic fluid is modelled using quadratic tetrahedral elements. A structural damping is introduced in the system by using the Rayleigh damping model in which the damping effect are represented by a symmetric semi-positive definite matrix $\mathbf{C}_s = \alpha_s \mathbf{K}_s + \beta_s \mathbf{M}_s$. The value of the coefficients α_s and β_s are given in Table 3.3. On the boundary of the truncated fluid domain, the condition BGT-1 of Equation (1.35) is applied in order to approximate the outgoing sound wave by a spherical wave for which we use the value of impedance $Z_R = \rho_0 R_{bgt}, Z_C = \rho_0 c_0$.

For the formulation in $(\mathbf{u}_s, p)$ and in $(\mathbf{u}_s, \phi)$, the finite element model consists of 146 385 degrees of freedom, 106 442 of which correspond to the structural part and 39 963 of which correspond to the acoustic fluid part. For the formulation in $(\mathbf{u}_s, p, \varphi)$, the finite element model

consists of 186 348 degrees of freedom, 106 442 of which correspond to the structural part and 79 926 of which correspond to the acoustic fluid part.

Structure	Fluid
Young's modulus $E = 210$ GPa Poisson's ratio $\nu = 0.3$ Density $\rho_s = 7850$ kg/m^3 Damping parameter $\alpha_s = 10^{-4}, \beta_s = 0$	Speed of sound $c_0 = 1500$ m/s Density $\rho_0 = 1000$ kg/m^3

Table 3.3: Physical properties of the structure and the fluid in the second study case

Numerical validation of the stability of reduced order models

First, we propose to verify the stability properties of the Galerkin reduced order models in $(\mathbf{u}_s, p)$ and in $(\mathbf{u}_s, p, \varphi)$ formulation using respectively the reduced basis obtained by Greedy Algorithms 2 and 3 and the reduced order models in $(\mathbf{u}_s, \phi)$ formulation using Petrov-Galerkin projection as indicated in Lemma 3.2.2. In order to show that this stability properties can not be achieved automatically without using the proposed techniques in Section 3.2, we will also investigate the reduced order models of these three formulations using Galerkin projection with the reduced basis obtained by Classical Greedy Algorithm 1.

To run the Greedy Algorithms, we use $f_{min} = 10$ Hz, $f_{max} = 150$ Hz and $N_{max} = 40$. The same training samples $\mathcal{D}_k$, which are chosen randomly at each iteration such that $|\mathcal{D}_k| = 50$, are used for all versions of Greedy Algorithms. To orthogonalize the basis, we use the euclidean scalar product. The evolution of the error indicator, defined as the norm of residual divided by the norm of the right-hand side, is shown in Figure 3.10.

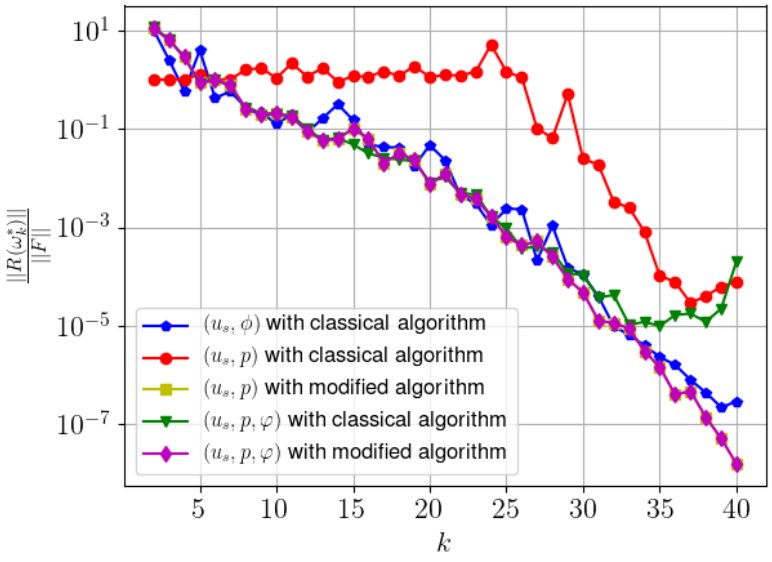

Figure 3.10: Evolution of error indicator in Greedy Algorithms in the second study case.

As expected, we observe that the evolution of the error indicator in modified Greedy Algorithm 2 and 3 are the same, which confirms the statement in Remark 3.3.2. As in the first study case, we see that the error indicators of modified Greedy Algorithm 2 and 3 decrease asymptotically faster than Classical Greedy Algorithm 1. For the case of the formulation in $(\mathbf{u}_s, \phi)$, it should be pointed out that the error indicator in the Classical Greedy Algorithm 1 seems to decrease as well as in the case of the formulation in $(\mathbf{u}_s, p)$ and $(\mathbf{u}_s, p, \varphi)$ with the modified Greedy Algorithm, despite that the size of the reduced basis in this case is smaller.

Let us put the focus on the stability of the reduced order model. To access to the stability, we compute the poles of the reduced order model. We recall that the poles of a second order system (3.15) are the roots of the polynomial $P(s) := \det(s^2\mathbf{M}_r + s\mathbf{C}_r + \mathbf{K}_r)$ which are also the eigenvalues of the Generalized Eigenvalue Problem (3.32).

Figure 3.11 shows the poles of the Galerkin and Petrov-Galerkin reduced order models of the formulation in $(\mathbf{u}_s, \phi)$. Figure 3.12 and 3.13 show respectively the poles of Galerkin reduced order models in $(\mathbf{u}_s, p)$ and $(\mathbf{u}_s, p, \varphi)$ formulation using the reduced basis obtained by Classical Greedy Algorithm 1 and modified Greedy Algorithms 2 and 3. We also remark in this study case that the Galerkin reduced order model of formulation in $(\mathbf{u}_s, p, \varphi)$ using the reduced basis of Classical Greedy Algorithm 1 have some infinite poles which is due to the singularity of the reduced mass matrix $\mathbf{M}_r$. Only the finite poles are then illustrated in Figure 3.13 for this case.

Figure 3.11 confirms that the Petrov-Galerkin reduced order models of the formulation in $(\mathbf{u}_s, \phi)$ are always stable while the corresponding Galerkin reduced order models can be unstable, as we see here in the case of $k = 10, 30, 40$, there are poles in the right-half of the complex plane. We remark that the Galerkin reduced order model can also be stable as shown in the case $k = 20$. For the formulation in $(\mathbf{u}_s, p)$, we can see in Figure 3.12 that Galerkin reduced order models are always stable if we use the reduced basis obtained by modified Greedy Algorithm 2 and that using the reduced basis of Classical Greedy Algorithm 1 might yield unstable reduced order models, as we see here in the case of $k = 10, 20, 30, 40$. A closer look at Figure 3.12 and 3.13 reveals that the reduced order models in $(\mathbf{u}_s, p, \varphi)$ formulation using the output reduced basis of Greedy Algorithm 3 has the same non-zeros poles as the reduced order models in $(\mathbf{u}_s, p)$ formulation using the reduced basis of Greedy Algorithm 2. Finally, the position of the finite poles in complex plane in Figure 3.13 shows clearly that the Galerkin reduced order models based on the reduced basis of Classical Greedy Algorithm 1 are unstable for $k = 30$ and $k = 40$.

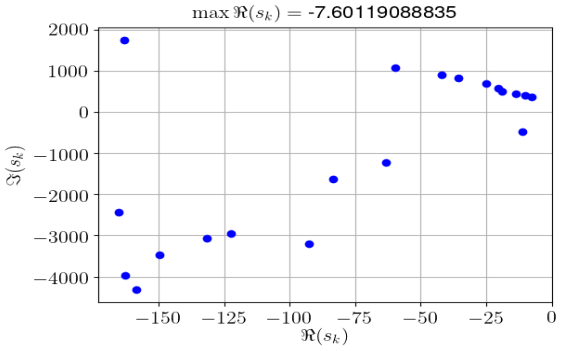

(a) $k = 10$

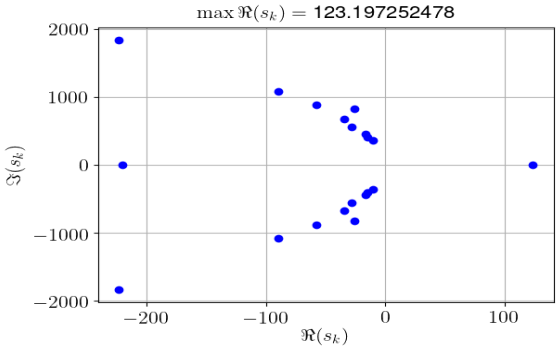

(b) $k = 10$

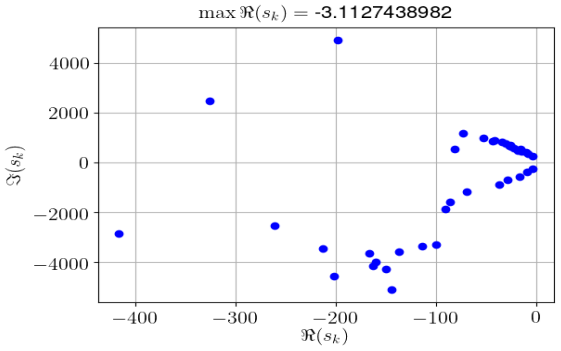

(c) $k = 20$

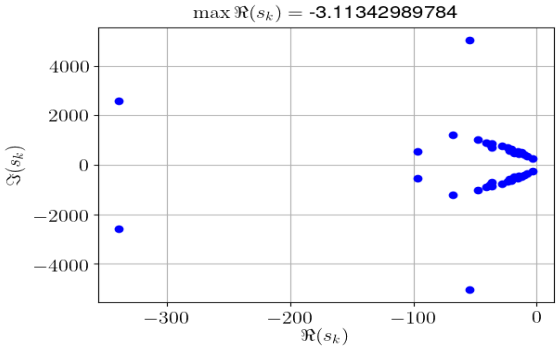

(d) $k = 20$

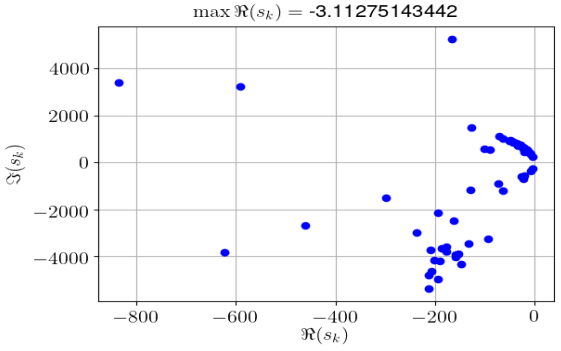

(e) $k = 30$

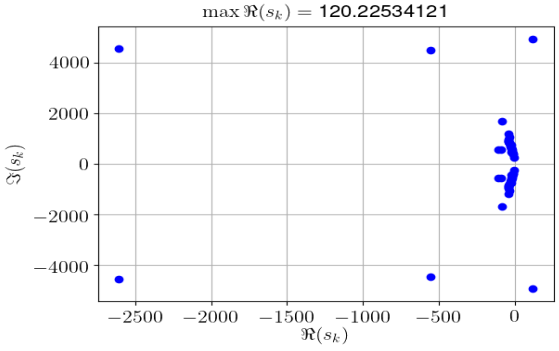

(f) $k = 30$

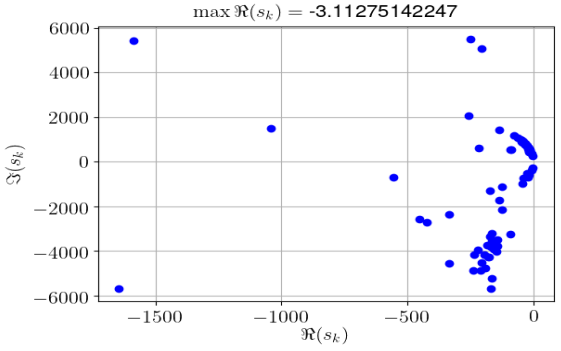

(g) $k = 40$

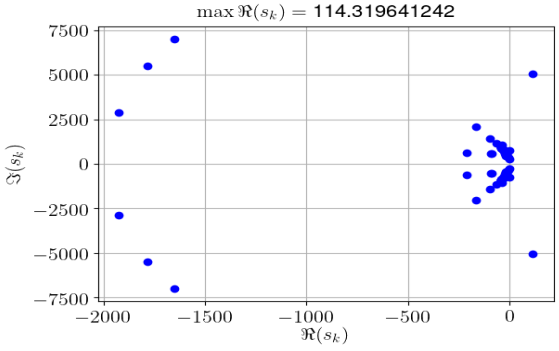

(h) $k = 40$

Figure 3.11: The poles of reduced order models in $(\mathbf{u}_s, \phi)$ using the reduced basis of iteration k of Classical Greedy Algorithm 1. Left: *case of Petrov-Galerkin projection of Lemma 3.2.2.* Right: *case of Galerkin projection.*

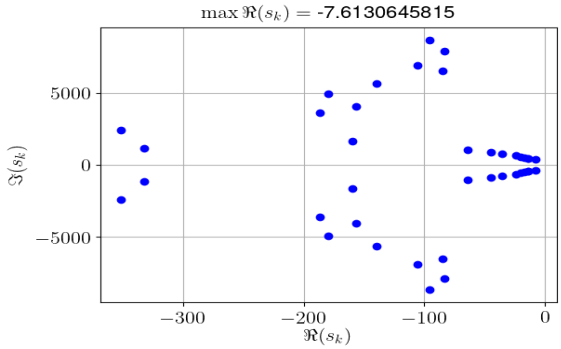

(a) $k = 10$

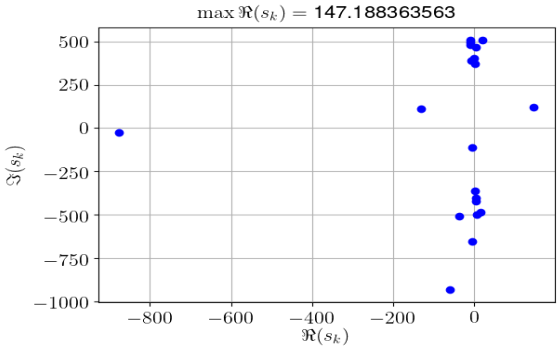

(b) $k = 10$

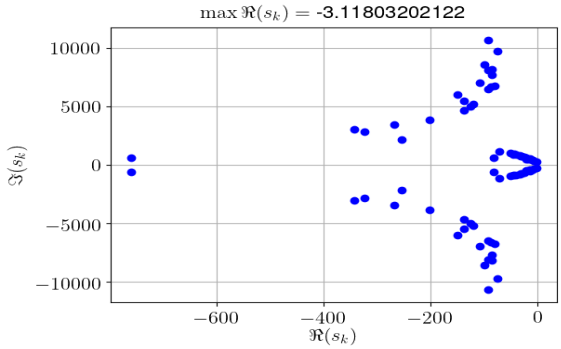

(c) $k = 20$

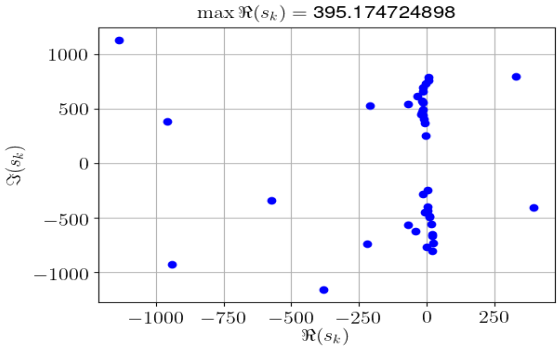

(d) $k = 20$

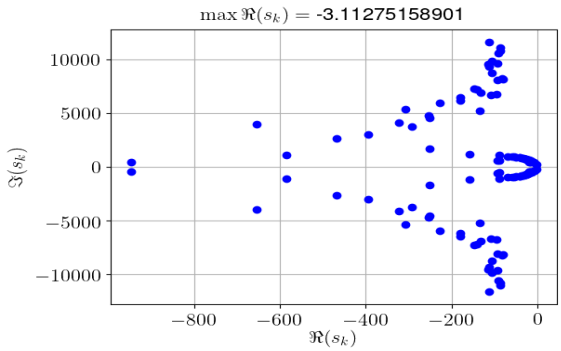

(e) $k = 30$

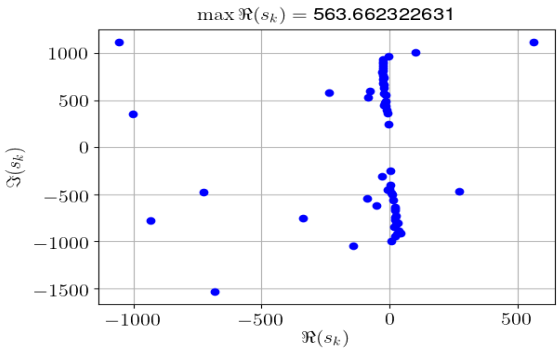

(f) $k = 30$

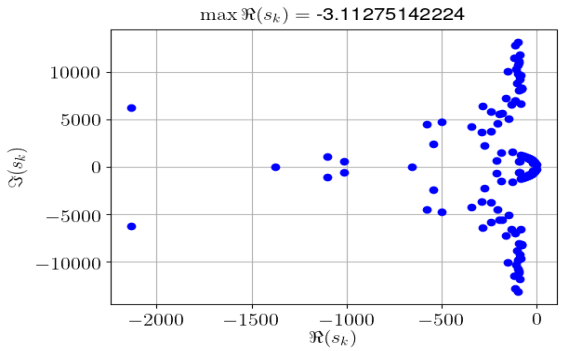

(g) $k = 40$

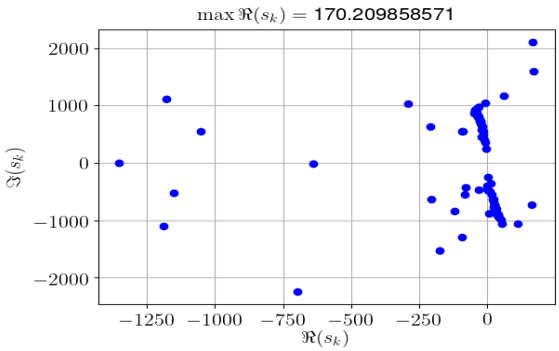

(h) $k = 40$

Figure 3.12: The poles of Galerkin reduced order models in $(\mathbf{u}_s, p)$ using the reduced basis of iteration k of Greedy Algorithms. Left: *case of modified Greedy Algorithm 2.* Right: *case of Classical Greedy Algorithm 1*

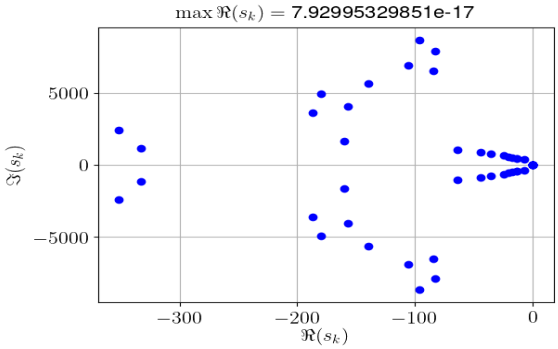

(a) $k = 10$

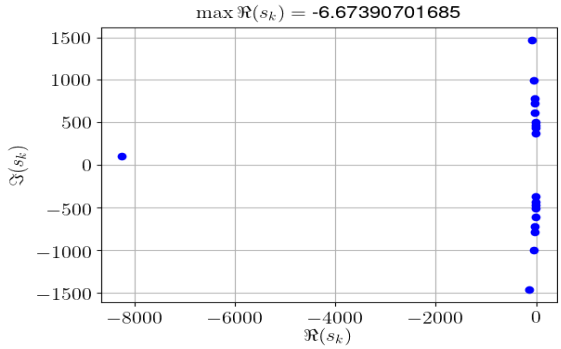

(b) $k = 10$

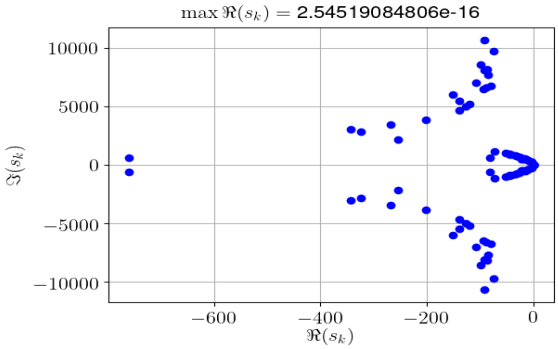

(c) $k = 20$

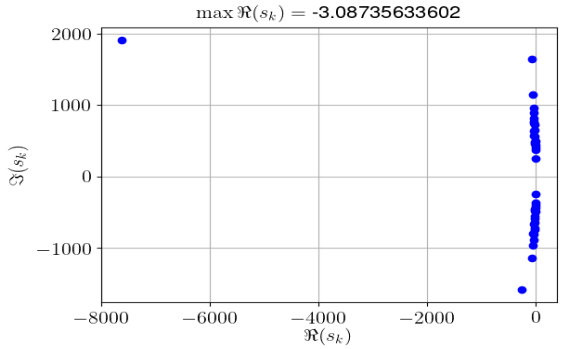

(d) $k = 20$

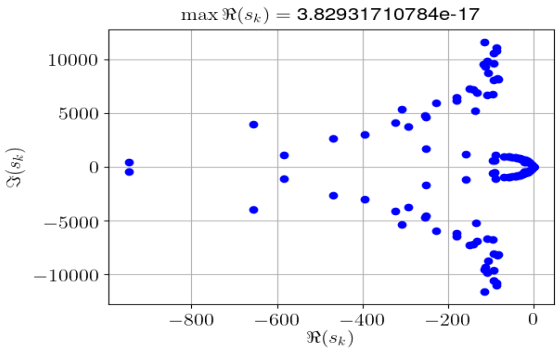

(e) $k = 30$

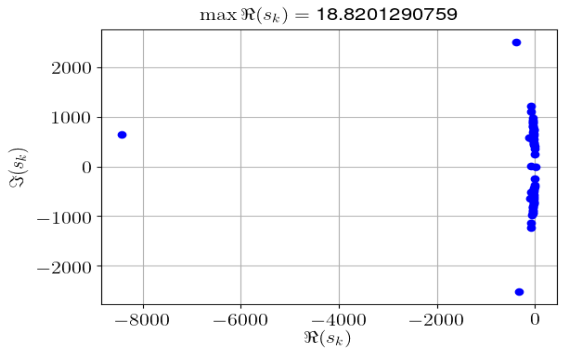

(f) $k = 30$

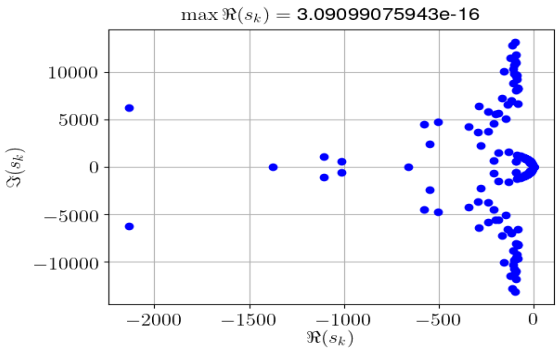

(g) $k = 40$

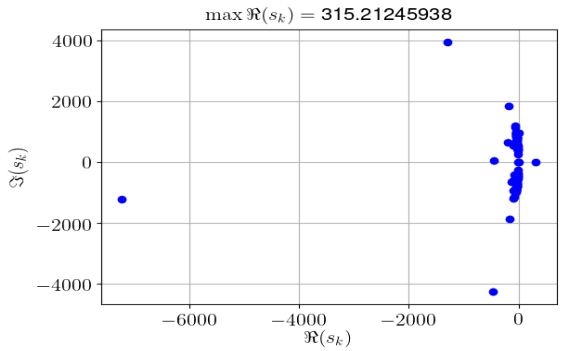

(h) $k = 40$

Figure 3.13: The poles of Galerkin reduced order models in $(\mathbf{u}_s, p, \varphi)$ using the reduced basis of iteration k of Greedy Algorithms. Left: *case of Classical Greedy Algorithm 1.* Right: *case of modified Greedy Algorithm 3.*

Numerical study of the accuracy of reduced order models

We now turn to the accuracy of the obtained reduced order models. We recall that the Galerkin reduced order models in $(\mathbf{u}_s, p, \varphi)$ formulation based on the reduced basis obtained by modified Greedy Algorithm 3 is equivalent to the Galerkin reduced order models in $(\mathbf{u}_s, p)$ formulation based on the reduced basis obtained by modified Greedy Algorithm 2 (see Remark 3.3.2). Hence, only the Galerkin reduced order models in $(\mathbf{u}_s, p)$ formulation and the Petrov-Galerkin reduced order models in $(\mathbf{u}_s, \phi)$ formulation will be considered here.

In the following, we set $f_{min} = 1$ Hz, $N_{train} = 100$, and the stopping criteria $\epsilon = 10^{-6}$ in order to run Classical Greedy Algorithm 1 and modified Greedy Algorithm 2. At each iteration k, the same training samples $\mathcal{D}_k$ are used in both versions of Greedy Algorithms. Depending on the value of f_{max}, the evolution of the error indicators in Classical Greedy Algorithm 1 for the formulation in $(\mathbf{u}_s, \phi)$ and in modified Greedy Algorithm 2 for the formulation in $(\mathbf{u}_s, p)$ are reported by Figure 3.14.

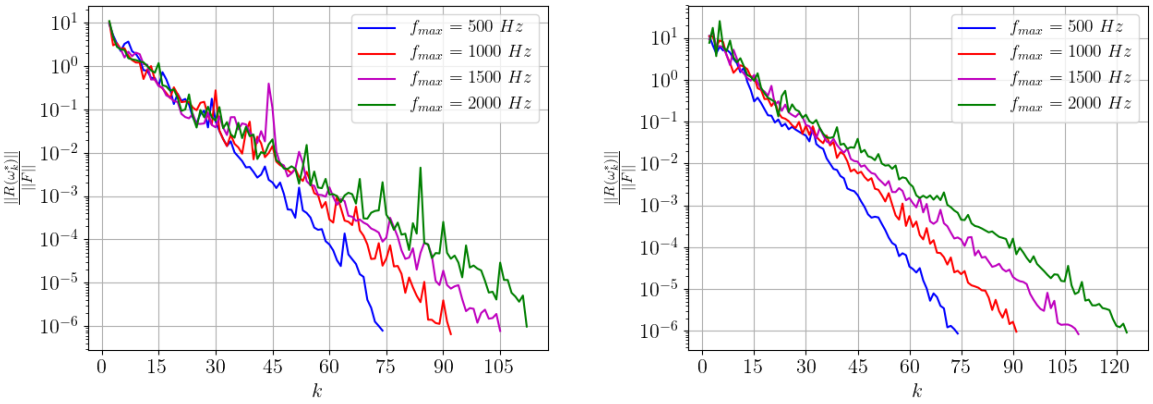

(a) Case of formulation in $(\mathbf{u}_s, \phi)$ with Algorithm 1 (b) Case of formulation in $(\mathbf{u}_s, p)$ with Algorithm 2

Figure 3.14: Evolution of error indicator in Greedy Algorithm in the second study case

In Figure 3.14, we observe that the number of iterations required increase as we increase the value of f_{max}. Although the size of the reduced basis in Algorithm 2 is two times bigger than in Algorithm 1 at each iteration, we remark, as in the first study case, that both algorithms need roughly the same number of iterations to achieve the stopping criteria $\epsilon = 10^{-6}$. The size of the reduced basis of these two algorithms is given in Table 3.4.

f_{max}	Formulation in $(\mathbf{u}_s, \phi)$	Formulation in $(\mathbf{u}_s, p)$
500 Hz	73	146
1000 Hz	91	180
1500 Hz	104	216
2000 Hz	111	244

Table 3.4: Size of the reduced basis in function of f_{max} for the second study case

To compute the accuracy of the reduced order models, we consider the case where input function f is defined by:

$$f(t) = \begin{cases} 10^5 \sin(2\pi f_d t) \text{ , for } 0 \leq t \leq 1/f_d \\ 0 \text{ , for } t > 1/f_d \end{cases} \tag{3.35}$$

Newmark scheme with $\gamma = 1/2 - \alpha$, $\beta = (1-\alpha)^2/4$, where $\alpha = -0.1$, is employed as time integration scheme for both of full model and reduced order models. The time step is chosen by $\Delta t = 1/(100 f_d)$ which is sufficiently small for our frequency of interest f_d. The final times in our study is $T_f = 10/f_d$. To access to the accuracy of the reduced order models, we compute the relative errors of the structural displacement and the pressure which are defined in Equation (3.34). We recall that for the case of the formulation in $(\mathbf{u}_s, \phi)$, the value of the pressure is obtained by the relation (1.17).

We are interested here in the case where $f_d \in \{100 \text{ Hz}, 200 \text{ Hz}, 300 \text{ Hz}, 500 \text{ Hz}\}$. Figure 3.7 shows the evolution of these errors in the case of the Petrov-Galerkin reduced order models of the formulation in $(\mathbf{u}_s, \phi)$. The case of Galerkin reduced order models for the formulation in $(\mathbf{u}_s, p)$ are illustrated in Figure 3.8. In both cases, we observe that the errors of pressure between the full model and the reduced order model are larger at the beginning and decrease rapidly to a minimum value before oscillating around that value. For the displacement, the errors are also larger at short times. Then, the errors decrease rapidly to a minimum value before increase rapidly to a maximum value and oscillate around that value afterwards in exception of the case of Galerkin reduced order models in $(\mathbf{u}_s, p)$ formulation with $f_d = 100$ Hz where the error seem to decrease as time increase. When we increase the value of f_{max} in the construction of the basis by greedy algorithm, we observe that it improves very slightly the accuracy of the reduced order model and it reveals the same phenomena as discussed above.

We recall that the size of Galerkin reduced order models in the formulation in $(\mathbf{u}_s, p)$ is almost two times bigger than the Petrov-Galerkin reduced order models of the formulation in $(\mathbf{u}_s, \phi)$ even though we use almost the same number of modes to built the reduced basis. Despite their bigger size, we do not observe in this study case that Galerkin reduced order models of the formulation in $(\mathbf{u}_s, p)$ could provide significantly a better accuracy than the Petrov-Galerkin reduced order models of the formulation in $(\mathbf{u}_s, \phi)$.

3.4.3 Conclusions

In both study cases, numerical results confirm that the reduced order models built by the proposed stabilization techniques are all stable. Concerning the accuracy, the reduced basis based on the frequency mode alone does not seem to be an appropriate basis for time-domain analysis. This is particularly the case when the system converges to its stationary regime slowly as in the second example and when the excitation is of high frequency.

It nevertheless provides a good approximation for the stationary regime when the excitation consists of low frequencies, as we saw in the first example. As a result, it could be employed to concatenate with an other reduced basis which can approximate accurately the full order model for the transient regime.

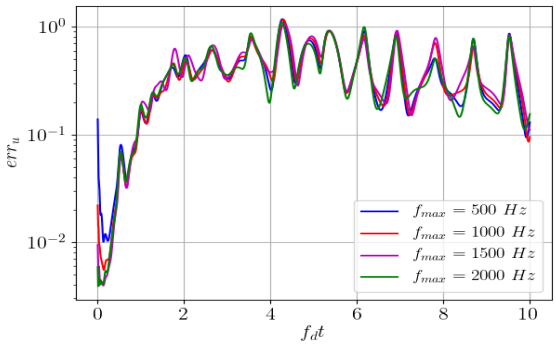

(a) Error on $\mathbf{u}_s$ for the case $f_d = 100$ Hz

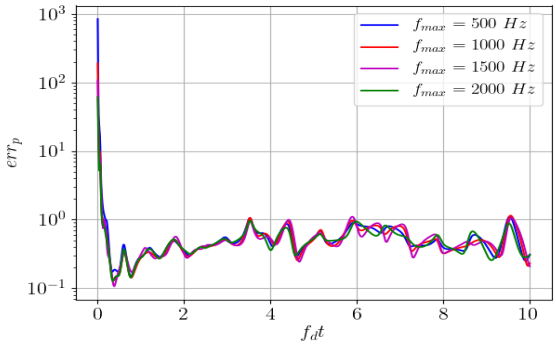

(b) Error on p for the case $f_d = 100$ Hz

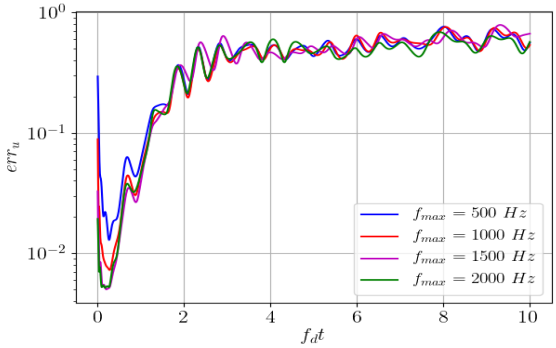

(c) Error on $\mathbf{u}_s$ for the case $f_d = 200$ Hz

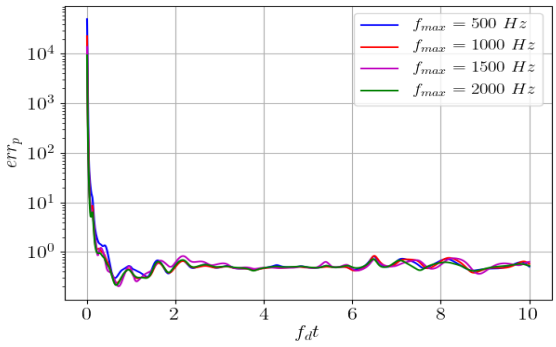

(d) Error on p for the case $f_d = 200$ Hz

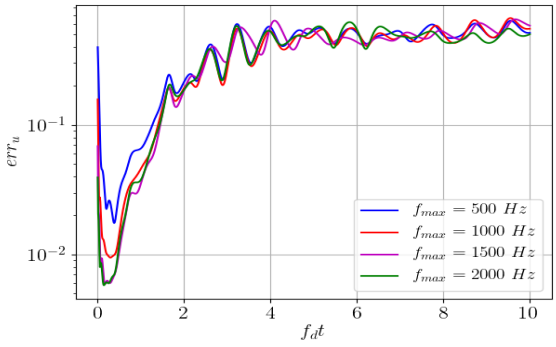

(e) Error on $\mathbf{u}_s$ for the case $f_d = 300$ Hz

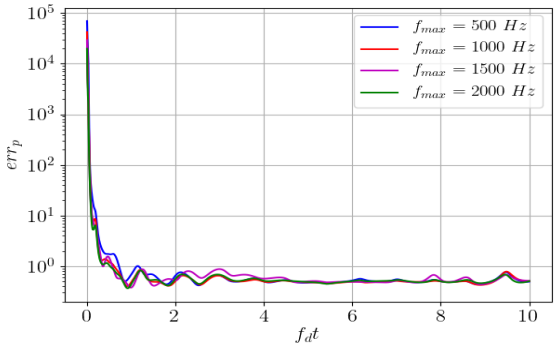

(f) Error on p for the case $f_d = 300$ Hz

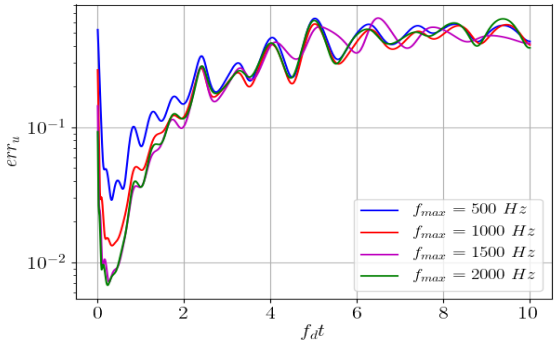

(g) Error on $\mathbf{u}_s$ for the case $f_d = 500$ Hz

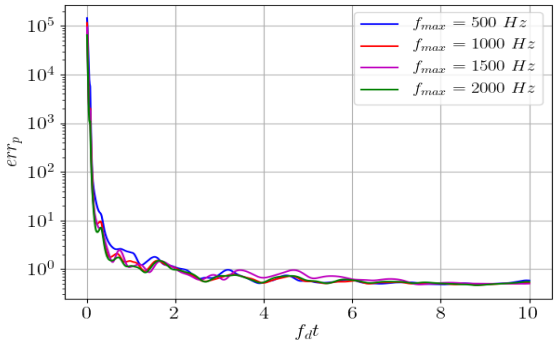

(h) Error on p for the case $f_d = 500$ Hz

Figure 3.15: Relative errors between the solution of the full model and the Petrov-Galerkin reduced order models in $(\mathbf{u}_s, \phi)$ formulation in the second study case

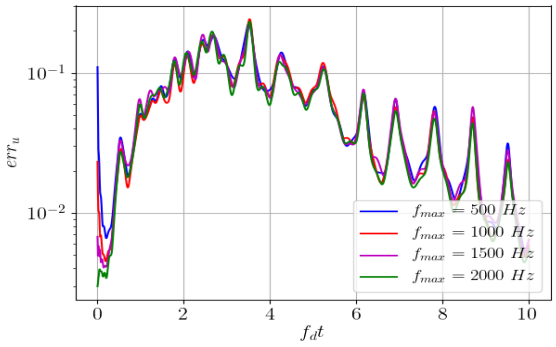

(a) Error on $\mathbf{u}_s$ for the case $f_d = 100$ Hz

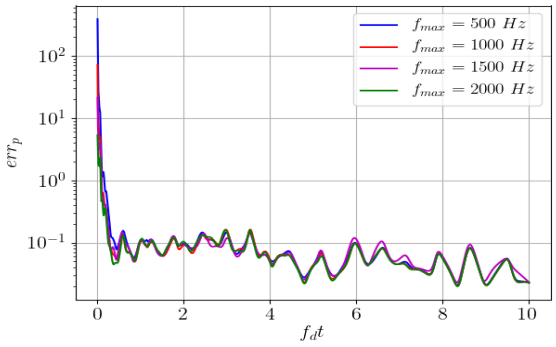

(b) Error on p for the case $f_d = 100$ Hz

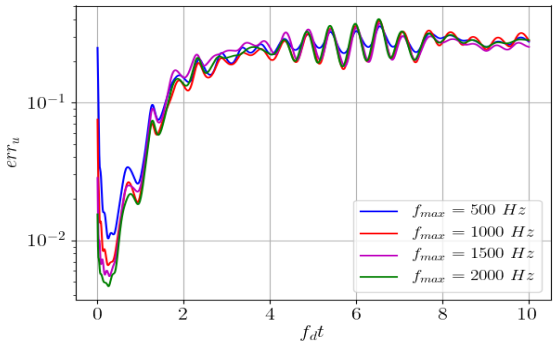

(c) Error on $\mathbf{u}_s$ for the case $f_d = 200$ Hz

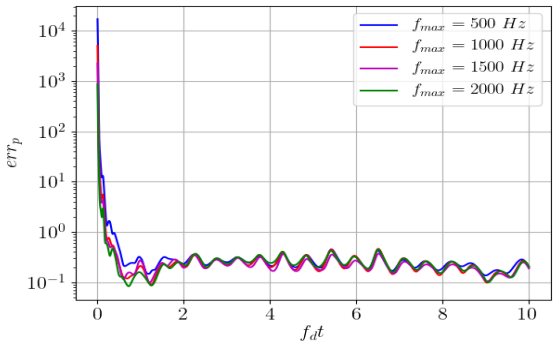

(d) Error on p for the case $f_d = 200$ Hz

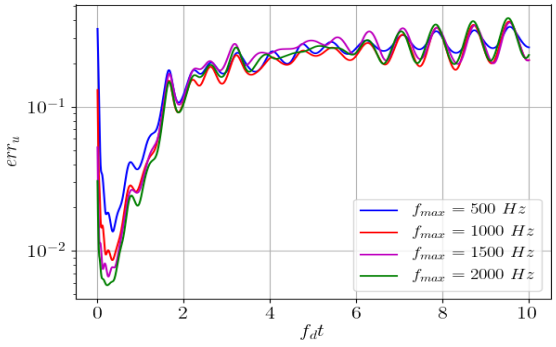

(e) Error on $\mathbf{u}_s$ for the case $f_d = 300$ Hz

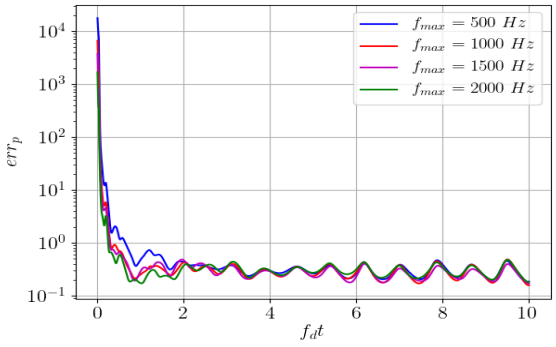

(f) Error on p for the case $f_d = 300$ Hz

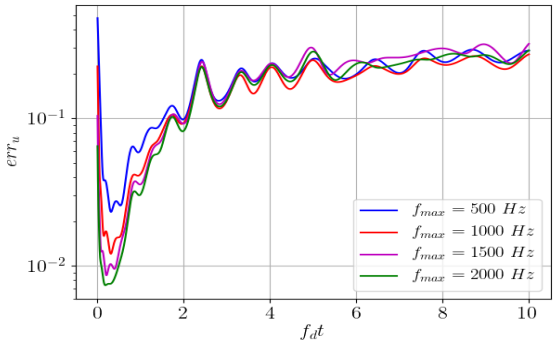

(g) Error on $\mathbf{u}_s$ for the case $f_d = 500$ Hz

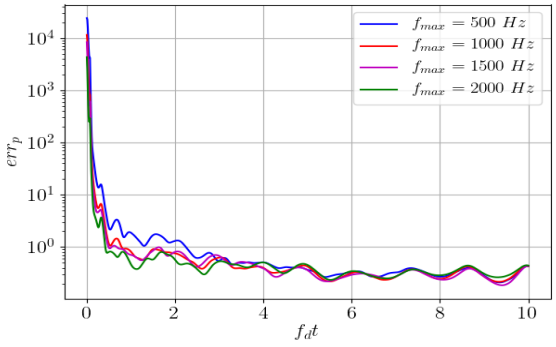

(h) Error on p for the case $f_d = 500$ Hz

Figure 3.16: Relative errors between the solution of the full model and the Galerkin reduced order models in $(\mathbf{u}_s, p)$ formulation in the second study case

3.5 Conclusions

In this chapter, we give a stabilization reduced order modelling technique for the three formulation of time domain vibro-acoustic problem presented in the previous chapters. For the formulation in $(\mathbf{u}_s, \phi)$, we can obtain a stable reduced order model by using a Petrov-Galerkin projection on a particular test subspace which depends on the choice of the trial subspace. Even though the full model in $(\mathbf{u}_s, \phi)$ is symmetric, using this stabilization technique results in a **non-symmetric** reduced order models. For the formulation in $(\mathbf{u}_s, p)$ and $(\mathbf{u}_s, p, \varphi)$, we can obtain a stable reduced order model by using a Galerkin projection on a particular form of reduced basis. In both cases, the reduced order models have the same structure, in the sense that we have the same sparsity and the same hermitian (semi-) definite sub matrices, as the original full model. The proposed reduced order models in $(\mathbf{u}_s, p)$ formulation are always **non-symmetric**. For the formulation in $(\mathbf{u}_s, p, \varphi)$, the reduced order models are **symmetric** only in the case of an interior problem without any damping in the fluid part and by using a real reduced basis, *i.e* $\mathbf{V} \in \mathbb{R}^{n \times N}$.

We proposed to construct the reduced basis based on a Greedy Algorithm in the corresponding frequency domain problem by considering the frequency as the parameter. In order to achieve the stability in Galerkin reduced order models, some modifications are introduced in the Classical Greedy Algorithm for the formulation in $(\mathbf{u}_s, p)$ and $(\mathbf{u}_s, p, \varphi)$. Two numericals study cases are presented in order to check the stability properties and the accuracy of the proposed reduced order models. The first study case is an academical study case with a simple geometry. The second study case is of industrial complexity. Between the two study cases, we used intentionally different finite element type to built the full model in order to show that the proposed stabilization technique does not depend on the choice of finite element type. In both study cases, numerical results confirm the stability of the proposed reduced order models.

Concerning the accuracy, we observed that the proposed reduced basis results in significant error especially for the case where the solicitation is of high frequency. As detailed in Chapter 2, in «*interaction of submerged structure and shock wave problems*», which is a problem of interest in this thesis, the loading contains high frequency components due to its discontinuity. Hence, the reduced basis proposed in this chapter may not be the most appropriate for this problem. As a result, we will propose in the next chapters another approach to built the reduced basis, in order to improve the reduced order model accuracy for parametrized problem.

Chapter 4

Reduced order modelling for parametrized time-domain vibro-acoustic FE model

This chapter is devoted to a framework for constructing an accurate parametrized reduced order model in the case where both the operators in the left hand-side of the full order model and the solicitation depend on the parameter.

Two main classes of reduced order modelling techniques for the parametrized time-domain problem can be found in the literature. In the first class of approaches, the main idea is to sample offline the reduced order models for some selected values of parameter and to approximate the reduced order model for the new values of the parameter by interpolating at the online stage the corresponding reduced operators. For this class of framework, we refer to [4, 5, 6, 46, 98, 99] and the references therein.

In the second class of approaches which are chosen in our work, we aim at constructing an accurate reduced basis over the desired ranges of the parameter values and using the Petrov-Galerkin projection to built an appropriate parametrized reduced order model. We do not extend the stabilized greedy algorithm presented in the previous chapter for parametrized time dependent problem, since we observed numerically in the previous chapter that it yields inaccurate reduced order models for high frequency solicitation. We propose in this chapter to use an alternative approach in order to construct an accurate reduced basis. More precisely, we put here the focus on the POD-Greedy algorithm [62, 64], which can be viewed as a combination of a classical greedy algorithm on parameters and a temporal compression by performing a proper orthogonal decomposition (POD, see for instance [96]). We will restrict ourselves to the case where all the operators in the problem can be written as affine parametric dependences. The case of non-affine parametric dependence will be the main subject of the next chapter.

The structure of this chapter is as follows. In the first section, we reformulate our problem into a purely algebraic way. In the second section, we introduce some elements on the Petrov-Galerkin projection based model order reduction. An error indicator based on the residual norm and an efficient offline-online decomposition strategy are also discussed in this section. In the third section, we are interested in the construction of the reduced basis by the POD-Greedy algorithm. According to the stabilization techniques presented in the previous chapter, some modifications in the classical POD-Greedy algorithm are required. Further remarks and

the limits of the proposed reduced order modelling framework are discussed in Section 4.5. In order to illustrate the performance of the proposed methodology, numerical results on a simple study case of shock wave/submerged structures interaction problems are presented in Section 4.6. In Section 4.7, we propose to apply the developed methodology in two industrial cases. Finally, concluding remarks are given in the last section.

4.1 Problem setting

In this chapter, we consider that the full model is described by a parametrized second-order ordinary differential equation:

$$\mathbf{M}(\boldsymbol{\mu})\ddot{\mathbf{X}}(t;\boldsymbol{\mu}) + \mathbf{C}(\boldsymbol{\mu})\dot{\mathbf{X}}(t;\boldsymbol{\mu}) + \mathbf{K}(\boldsymbol{\mu})\mathbf{X}(t;\boldsymbol{\mu}) = \mathbf{F}(t;\boldsymbol{\mu}) \tag{4.1}$$

where $\boldsymbol{\mu} \in \mathcal{D}$ ($P \geq 1$) is the parameter vector, whose components represent physical feature of interest; $\mathcal{D} \subset \mathbb{R}^P$ denotes the corresponding parameter space. The matrices $\mathbf{M}$, $\mathbf{C}$, $\mathbf{K} \in \mathbb{R}^{n\times n}$ represent respectively mass, damping and stiffness matrices of the problem which are supposed to be parameter dependent and $\mathbf{F} \in \mathbb{R}^n$ is the right-hand side vector of the problem which is time and parameter dependent. For simplify our presentation, we assume that the initial condition is given by $\mathbf{X}(t=0,\boldsymbol{\mu}) = \dot{\mathbf{X}}(t=0,\boldsymbol{\mu}) = \mathbf{0}$.

In this chapter, we restrict ourselves to the case where the geometry of the domain is not considered as a parameter of the problem and all operators of the left and right-hand sides of the problem can be written as an affine dependent form in parameter $\boldsymbol{\mu} \in \mathcal{D}$ as following:

$$\mathbf{F}(t;\boldsymbol{\mu}) = \sum_{i=1}^{N_F} \theta_i^F(t;\boldsymbol{\mu})\mathbf{F}_i \ , \ \mathbf{A}(\boldsymbol{\mu}) = \sum_{i=1}^{N_A} \theta_i^A(\boldsymbol{\mu})\mathbf{A}_i \ , \ \forall \mathbf{A} \in \{\mathbf{M},\mathbf{C},\mathbf{K}\} \tag{4.2}$$

where $\mathbf{A}_i$ are given constant matrices of $\mathbb{R}^{n\times n}$, $\mathbf{F}_i$ are given constants vectors of $\mathbb{R}^n$ and θ_i^A, θ_i^F are given parameter dependent functions. We assume here that the full model (4.1) is stable for any value of parameter $\boldsymbol{\mu} \in \mathcal{D}$.

We consider that our output of interest can be written as a linear form $S_l(t;\boldsymbol{\mu}) = \mathbf{L}^T\mathbf{X}(t;\boldsymbol{\mu})$, where $\mathbf{L}$ is a vector in $\mathbb{R}^n$, or as a quadratic form $S_q(t;\boldsymbol{\mu}) = \mathbf{X}^T(t;\boldsymbol{\mu})\mathbf{Q}\mathbf{X}(t;\boldsymbol{\mu})$ where $\mathbf{Q}$ is a matrix of $\mathbb{R}^{n\times n}$.

To make this chapter self contained, let us briefly recall the expression of the matrices $\mathbf{M},\mathbf{C},\mathbf{K}$ of the full model (4.1) for a parametrized time domain vibro-acoustic problem. For the case where the formulation in $(\mathbf{u}_s,\phi)$ is employed, we have:

$$\begin{aligned}
\mathbf{M}_{u\phi}(\boldsymbol{\mu}) &= \begin{bmatrix} \mathbf{M}_s(\boldsymbol{\mu}) & \mathbf{0} \\ \mathbf{0} & -\rho_0(\boldsymbol{\mu})\mathbf{M}_f(\boldsymbol{\mu}) \end{bmatrix}, \mathbf{C}_{u\phi}(\boldsymbol{\mu}) = \begin{bmatrix} \mathbf{C}_s(\boldsymbol{\mu}) & -\rho_0(\boldsymbol{\mu})\mathbf{K}_c \\ -\rho_0(\boldsymbol{\mu})\mathbf{K}_c^T & -\rho_0(\boldsymbol{\mu})\mathbf{C}_f(\boldsymbol{\mu}) \end{bmatrix} \\
\mathbf{K}_{u\phi}(\boldsymbol{\mu}) &= \begin{bmatrix} \mathbf{K}_s(\boldsymbol{\mu}) & \mathbf{0} \\ \mathbf{0} & -\rho_0(\boldsymbol{\mu})\mathbf{K}_f \end{bmatrix}, \text{ and } \mathbf{X}_{u\phi}(t;\boldsymbol{\mu}) = \begin{bmatrix} \mathbf{U}_s(t;\boldsymbol{\mu}) \\ \boldsymbol{\Phi}(t;\boldsymbol{\mu}) \end{bmatrix}
\end{aligned} \tag{4.3}$$

where ρ_0 denotes the fluid density, the matrices $\mathbf{M}_s$ and $\mathbf{M}_f$ are known respectively as the mass matrices of the structural part and the fluid part, the matrices $\mathbf{K}_s$ and $\mathbf{K}_f$ are known respectively as the stiffness matrices of the structural part and the fluid part, the matrix $\mathbf{K}_c$ represents the vibro-acoustic coupling matrix, the matrices $\mathbf{C}_s$ and $\mathbf{C}_f$ represent respectively the damping matrix in structural part and the fluid part and the vector $\mathbf{U}_s$ and $\boldsymbol{\Phi}$ contain

respectively the nodal values of structural displacement and velocity potential in the fluid. By their definitions in (1.39), the matrices $\mathbf{M}_s$ and $\mathbf{M}_f$ are symmetric positive definite, the matrices $\mathbf{K}_s$ and $\mathbf{K}_f$ are symmetric positive semi-definite. In our work, we assume that the matrices $\mathbf{C}_s$ and $\mathbf{C}_f$ are positive semi-definite which are sufficient conditions for the stability of the full order model (see Lemma 3.1.4). As a remark, the matrices $\mathbf{K}_c$ and $\mathbf{K}_f$ depend only on the geometry of the fluid domain. Thus, they are $\boldsymbol{\mu}$ independent through this chapter since the geometry of the domain is not considered here as a parameter of the problem.

With the same notations, the expression of the matrices $\mathbf{M}, \mathbf{C}, \mathbf{K}$ of the full model (4.1) for a parametrized time domain vibro-acoustic problem formulated in $(\mathbf{u}_s, p)$ is defined by:

$$\begin{aligned} \mathbf{M}_{up}(\boldsymbol{\mu}) &= \begin{bmatrix} \mathbf{M}_s(\boldsymbol{\mu}) & \mathbf{0} \\ -\rho_0(\boldsymbol{\mu})\mathbf{K}_c^T & \mathbf{M}_f(\boldsymbol{\mu}) \end{bmatrix}, \mathbf{C}_{up}(\boldsymbol{\mu}) = \begin{bmatrix} \mathbf{C}_s(\boldsymbol{\mu}) & \mathbf{0} \\ \mathbf{0} & \mathbf{C}_f(\boldsymbol{\mu}) \end{bmatrix} \\ \mathbf{K}_{up}(\boldsymbol{\mu}) &= \begin{bmatrix} \mathbf{K}_s(\boldsymbol{\mu}) & \mathbf{K}_c \\ \mathbf{0} & \mathbf{K}_f \end{bmatrix} \text{ and } \mathbf{X}_{up}(t;\boldsymbol{\mu}) = \begin{bmatrix} \mathbf{U}_s(t;\boldsymbol{\mu}) \\ \mathbf{P}(t;\boldsymbol{\mu}) \end{bmatrix} \end{aligned} \tag{4.4}$$

and in $(\mathbf{u}_s, p, \varphi)$ is defined by:

$$\begin{aligned} \mathbf{M}_{up\varphi}(\boldsymbol{\mu}) &= \begin{bmatrix} \mathbf{M}_s(\boldsymbol{\mu}) & \mathbf{0} & -\rho_0(\boldsymbol{\mu})\mathbf{K}_c \\ \mathbf{0} & \mathbf{0} & \mathbf{M}_f(\boldsymbol{\mu}) \\ -\rho_0(\boldsymbol{\mu})\mathbf{K}_c^T & \mathbf{M}_f(\boldsymbol{\mu}) & -\rho_0(\boldsymbol{\mu})\mathbf{K}_f \end{bmatrix}, \mathbf{C}_{up\varphi}(\boldsymbol{\mu}) = \begin{bmatrix} \mathbf{C}_s(\boldsymbol{\mu}) & \mathbf{0} & \mathbf{0} \\ \mathbf{0} & \mathbf{0} & \mathbf{0} \\ \mathbf{0} & \mathbf{C}_f(\boldsymbol{\mu}) & \mathbf{0} \end{bmatrix} \\ \mathbf{K}_{up\varphi}(\boldsymbol{\mu}) &= \begin{bmatrix} \mathbf{K}_s(\boldsymbol{\mu}) & \mathbf{0} & \mathbf{0} \\ \mathbf{0} & \frac{1}{\rho_0(\boldsymbol{\mu})}\mathbf{M}_f(\boldsymbol{\mu}) & \mathbf{0} \\ \mathbf{0} & \mathbf{0} & \mathbf{0} \end{bmatrix} \text{ and } \mathbf{X}_{up\varphi}(t;\boldsymbol{\mu}) = \begin{bmatrix} \mathbf{U}_s(t;\boldsymbol{\mu}) \\ \mathbf{P}(t;\boldsymbol{\mu}) \\ \boldsymbol{\varphi}(t;\boldsymbol{\mu}) \end{bmatrix} \end{aligned} \tag{4.5}$$

where the vectors $\mathbf{P}$ and $\boldsymbol{\varphi}$ contain respectively the nodal values of pressure and displacement potential in the fluid.

We also recall the expression of the right-hand side vector of full order model (4.1) for the case of shock wave/submerged structure interaction problem. Assuming that the shock wave is characterized by a incident pressure p^{inc} and an incident velocity $\mathbf{v}^{inc}$, the right-hand side vector of the problem formulated in $(\mathbf{u}_s, \phi^{sca})$ are given by $\mathbf{F}_{u\phi}^{sca}(t;\boldsymbol{\mu}) = \begin{bmatrix} \mathbf{F}_s^{sca}(t;\boldsymbol{\mu})^T & \mathbf{F}_\phi^{sca}(t;\boldsymbol{\mu})^T \end{bmatrix}^T$ where the vectors $\mathbf{F}_s^{sca}(t;\boldsymbol{\mu})$ and $\mathbf{F}_\phi^{sca}(t;\boldsymbol{\mu})$ are defined by $\mathbf{F}_{s,j}^{sca}(t;\boldsymbol{\mu}) := -\int_\Gamma p^{inc}(\mathbf{x},t;\boldsymbol{\mu})[\mathbf{N}_j^s(\mathbf{x}) \cdot \mathbf{n}_s(\mathbf{x})]d\mathbf{x}$, $\mathbf{F}_{\phi,j}^{sca}(t;\boldsymbol{\mu}) := -\int_\Gamma \rho_0(\boldsymbol{\mu})[\mathbf{v}^{inc}(\mathbf{x},t;\boldsymbol{\mu}) \cdot \mathbf{n}_s(\mathbf{x})]N_j^f(\mathbf{x})d\mathbf{x}$ with $\mathbf{N}^s$ and N^f denote respectively the finite element basis of the structural and the fluid part.

With the same notations, the right-hand side vector of the formulation in $(\mathbf{u}_s, \phi^{rad})$ and in $(\mathbf{u}_s, p^{rad})$ are given by $\mathbf{F}_{up}^{rad}(t;\boldsymbol{\mu}) = \begin{bmatrix} \mathbf{F}_s^{rad}(t;\boldsymbol{\mu})^T & \mathbf{0}^T \end{bmatrix}^T$, where the vector $\mathbf{F}_s^{rad}(t;\boldsymbol{\mu})$ are defined by $\mathbf{F}_{s,j}^{rad}(t;\boldsymbol{\mu}) = -\int_\Gamma (p^{inc}+p^{ref})(\mathbf{x},t;\boldsymbol{\mu})[\mathbf{N}_j^s(\mathbf{x}) \cdot \mathbf{n}_s(\mathbf{x})]d\mathbf{x}$. Finally, the right-hand side vector for the case of the formulation in $(\mathbf{u}_s, p^{rad}, \varphi^{rad})$ is given by $\mathbf{F}_{up\varphi}^{rad}(t;\boldsymbol{\mu}) = \begin{bmatrix} \mathbf{F}_s^{rad}(t;\boldsymbol{\mu})^T & \mathbf{0}^T & \mathbf{0}^T \end{bmatrix}^T$. We recall that the reflected pressure p^{ref} has to be pre-computed (see Section 2.4.5) in order to employ these three formulations. As a remark, the reflected pressure p^{ref} depends only on the incident velocity $\mathbf{v}^{inc}$ and the properties of the fluid.

4.2 Reduced order modelling

Solving the full model (4.1) is often computationally intractable for parametrized problems. The aim of this section is to develop a suitable inexpensive and fast reduced-order model to overcome this computational burden. Here, we are only interested in the Petrov-Galerkin projection based ROM. The idea of Petrov-Galerkin projection based reduced order modelling is to approximate the solution of the full model (4.1) in a reduced basis $\mathbf{V} \in \mathbb{R}^{n\times N}$ of dimension N, which is much smaller than the dimension of the full model, and enforce the orthogonality of the residual vector to a test subspace spanned by a suitable basis $\mathbf{W} \in \mathbb{R}^{n\times N}$. The Petrov-Galerkin reduced order model writes:

$$\mathbf{M}_r(\boldsymbol{\mu})\ddot{\mathbf{X}}_r(t;\boldsymbol{\mu}) + \mathbf{C}_r(\boldsymbol{\mu})\dot{\mathbf{X}}_r(t;\boldsymbol{\mu}) + \mathbf{K}_r(\boldsymbol{\mu})\mathbf{X}_r(t;\boldsymbol{\mu}) = \mathbf{F}_r(t;\boldsymbol{\mu}) \tag{4.6}$$

where the reduced matrices and vectors are given by:

$$\begin{aligned} \mathbf{M}_r(\boldsymbol{\mu}) &= \mathbf{W}^T\mathbf{M}(\boldsymbol{\mu})\mathbf{V}, \quad & \mathbf{C}_r(\boldsymbol{\mu}) &= \mathbf{W}^T\mathbf{C}(\boldsymbol{\mu})\mathbf{V} \\ \mathbf{K}_r(\boldsymbol{\mu}) &= \mathbf{W}^T\mathbf{K}(\boldsymbol{\mu})\mathbf{V}, \quad & \mathbf{F}_r(t;\boldsymbol{\mu}) &= \mathbf{W}^T\mathbf{F}(t;\boldsymbol{\mu}) \end{aligned} \tag{4.7}$$

and the initial condition is given by $\mathbf{X}_r(t=0,\boldsymbol{\mu}) = \dot{\mathbf{X}}_r(t=0,\boldsymbol{\mu}) = \mathbf{0}$.

The approximation of the solution of full model (4.1) given by the reduced order model (4.6) is defined by $\mathbf{X}^{rom}(t;\boldsymbol{\mu}) = \mathbf{V}\mathbf{X}_r(t;\boldsymbol{\mu})$. For the case where the output of interest can be written as a linear (quadratic) form, its approximation by the reduced order model (4.6) is given by $S_l^{rom}(t;\boldsymbol{\mu}) = \mathbf{L}_r^T\mathbf{X}_r(t;\boldsymbol{\mu})$ ($S_q^{rom}(t;\boldsymbol{\mu}) = \mathbf{X}_r^T(t;\boldsymbol{\mu})\mathbf{Q}_r\mathbf{X}_r(t;\boldsymbol{\mu})$), where the reduced vector $\mathbf{L}_r \in \mathbb{R}^N$ is defined by $\mathbf{L}_r^T = \mathbf{L}^T\mathbf{V}$ (the reduced matrix $\mathbf{Q}_r \in \mathbb{R}^{N\times N}$ is defined by $\mathbf{Q}_r = \mathbf{V}^T\mathbf{Q}\mathbf{V}$).

4.2.1 Stability preserving model order reduction

For time-dependent problem, it has been shown in Chapter 3 that the reduced order modelling has to ensure that the stability of the full model is preserved. In the most general cases, the Petrov-Galerkin projection based ROM can be unstable even if the original full model is stable. We recall that the dynamical system (4.1) is called *stable* if and only if all roots of the polynomial $P(s) := \det(s^2\mathbf{M} + s\mathbf{C} + \mathbf{K})$ have negative real part. In other words, the system (4.1) is *stable* if and only if the state of the system remains bounded for any initial condition in the absence of external force. With this definition, the full model (4.1) is stable for the case where the mass matrix $\mathbf{M}$ is symmetric positive definite, the stiffness matrix $\mathbf{K}$ symmetric positive semi-definite and the damping matrix $\mathbf{C}$ is positive semi-definite (see Lemma 3.1.3). As example, it is the case when the full model (4.1) represents the finite element model of an acoustic wave or a structural dynamic equation. For this case, a stable reduced order model can be obtained by using Galerkin projection on any reduced basis (see Lemma 3.2.1).

For vibro-acoustic problem, the finite element model in $(\mathbf{u}_s, \phi)$, in $(\mathbf{u}_s, p)$ and in $(\mathbf{u}_s, p, \varphi)$ are all stable thanks to the symmetric positive definiteness of the mass matrices $\mathbf{M}_s$, $\mathbf{M}_f$ and the symmetric positive semi-definiteness of stiffness matrices $\mathbf{K}_s$, $\mathbf{K}_f$ and of the impedance matrix $\mathbf{Q}$ (for the case of exterior problem). For the formulation in $(\mathbf{u}_s, \phi)$, it has been shown in Lemma 3.2.2 that we can obtain a stable reduced order model by using a Petrov-Galerkin projection on a particular test subspace which depends on the choice of the trial subspace.

More precisely, using a Petrov-Galerkin projection on the trial subspace $\mathbf{V} = \begin{bmatrix} \mathbf{V}_s \\ \mathbf{V}_f \end{bmatrix} \in \mathbb{R}^{n\times N}$ with the test subspace defined by $\mathbf{W} = \begin{bmatrix} \mathbf{V}_s \\ -\mathbf{V}_f \end{bmatrix} \in \mathbb{R}^{n\times N}$ yields a stable reduced order model for any choices of $\mathbf{V}_s$ and $\mathbf{V}_f$. For the formulation in $(\mathbf{u}_s, p)$, it has been shown in Lemma 3.2.3 that using Galerkin projection on the reduced basis with a particular form $\mathbf{V} = \begin{bmatrix} \mathbf{V}_s & \mathbf{0} \\ \mathbf{0} & \mathbf{V}_f \end{bmatrix}$ yields a stable ROM for any choices of the reduced basis in structural part $\mathbf{V}_s$ and the fluid part $\mathbf{V}_f$. For the formulation in $(\mathbf{u}_s, p, \varphi)$, it has been shown in Lemma 3.2.4 that using Galerkin projection on the reduced basis with a particular form $\mathbf{V} = \begin{bmatrix} \mathbf{V}_s & \mathbf{0} & \mathbf{0} \\ \mathbf{0} & \mathbf{V}_f & \mathbf{0} \\ \mathbf{0} & \mathbf{0} & \mathbf{V}_f \end{bmatrix}$ yields a stable ROM for any choice of the reduced basis in structural part $\mathbf{V}_s$ and the fluid part $\mathbf{V}_f$.

4.2.2 Error indicator

An error indicator can provide information on the accuracy of reduced order model. It also plays an important role in the construction of the reduced basis with a greedy algorithm as we will see in Section 4.3. In this work, we propose to use the error indicator based on the norm of residual vector since it is relatively inexpensive to compute. The residual vector corresponding to the reduced order model (4.6) of the full model (4.1) writes:

$$\mathbf{R}(t;\boldsymbol{\mu}) := \mathbf{F}(t;\mu) - \mathbf{M}(\boldsymbol{\mu})\mathbf{V}\ddot{\mathbf{X}}_r(t;\boldsymbol{\mu}) - \mathbf{C}(\boldsymbol{\mu})\mathbf{V}\dot{\mathbf{X}}_r(t;\boldsymbol{\mu}) - \mathbf{K}(\boldsymbol{\mu})\mathbf{V}\mathbf{X}_r(t;\boldsymbol{\mu}) \tag{4.8}$$

The error indicator used in this work is defined by:

$$\Delta(\boldsymbol{\mu}) = \max_{t\in[0,T]} \frac{||\mathbf{R}(t;\mu)||}{||\mathbf{F}(t;\mu)||} \tag{4.9}$$

where T is the final time of interest in the problem and $||\cdot||$ denotes the euclidean norm.

Under the hypothesis that all operators of both left and the right-hand sides of the problem can be written in an affine dependence form in parameter, characterized by Equation (4.2), the norm of right-hand side and residual vectors can be written as (see Appendix C):

$$\begin{aligned}
||\mathbf{F}(t;\boldsymbol{\mu})||^2 &= \boldsymbol{\Theta}_F^T(t;\boldsymbol{\mu})\mathbf{M}_{FF}\boldsymbol{\Theta}_F(t;\boldsymbol{\mu}) \\
||\mathbf{R}(t;\boldsymbol{\mu})||^2 &= \boldsymbol{\Theta}_F^T(t;\boldsymbol{\mu})\mathbf{M}_{FF}\boldsymbol{\Theta}_F(t;\boldsymbol{\mu}) \\
&\quad + \ddot{\mathbf{X}}_r^T(t;\boldsymbol{\mu})\mathbf{M}_{MM}(\boldsymbol{\mu})\ddot{\mathbf{X}}_r(t;\boldsymbol{\mu}) + \dot{\mathbf{X}}_r^T(t;\boldsymbol{\mu})\mathbf{M}_{CC}(\boldsymbol{\mu})\dot{\mathbf{X}}_r(t;\boldsymbol{\mu}) + \mathbf{X}_r^T(t;\boldsymbol{\mu})\mathbf{M}_{KK}(\boldsymbol{\mu})\mathbf{X}_r(t;\boldsymbol{\mu}) \\
&\quad + 2\left(\ddot{\mathbf{X}}_r^T(t;\boldsymbol{\mu})\mathbf{M}_{MC}(\boldsymbol{\mu})\dot{\mathbf{X}}_r(t;\boldsymbol{\mu}) + \ddot{\mathbf{X}}_r^T(t;\boldsymbol{\mu})\mathbf{M}_{MK}(\boldsymbol{\mu})\mathbf{X}_r(t;\boldsymbol{\mu}) + \dot{\mathbf{X}}_r^T(t)\mathbf{M}_{CK}(\boldsymbol{\mu})\mathbf{X}_r(t)\right) \\
&\quad - 2\left(\boldsymbol{\Theta}_F^T(t;\boldsymbol{\mu})\mathbf{M}_{MF}(\boldsymbol{\mu})\ddot{\mathbf{X}}_r(t;\boldsymbol{\mu}) + \boldsymbol{\Theta}_F^T(t;\boldsymbol{\mu})\mathbf{M}_{CF}(\boldsymbol{\mu})\dot{\mathbf{X}}_r(t;\boldsymbol{\mu}) + \boldsymbol{\Theta}_F^T(t;\boldsymbol{\mu})\mathbf{M}_{KF}(\boldsymbol{\mu})\mathbf{X}_r(t;\boldsymbol{\mu})\right)
\end{aligned} \tag{4.10}$$

The vector $\boldsymbol{\Theta}_F(t;\boldsymbol{\mu}) \in \mathbb{R}^{N_F}$ is defined by $\boldsymbol{\Theta}_F(t;\boldsymbol{\mu}) = \left[\theta_1^F(t;\boldsymbol{\mu}), \cdots, \theta_{N_F}^F(t;\boldsymbol{\mu})\right]^T \in \mathbb{R}^{N_F}$. Here, we denote by $\langle\cdot,\cdot\rangle$ the euclidean scalar product. The matrix $\mathbf{M}_{FF} \in \mathbb{R}^{N_F\times N_F}$ is independent of $\boldsymbol{\mu}$ and is defined by $(\mathbf{M}_{FF})_{ij} = \langle \mathbf{F}_i, \mathbf{F}_j\rangle$ and the matrices $\mathbf{M}_{AB} \in \mathbb{R}^{N\times N}$ and

$\mathbf{M}_{AF} \in \mathbb{R}^{N_F \times N}$, for $A, B \in \{M, C, K\}$, are $\boldsymbol{\mu}$-dependent and defined by:

$$\begin{aligned} \mathbf{M}_{AB}(\boldsymbol{\mu}) &= \sum_{l=1}^{N_A} \sum_{k=1}^{N_B} \theta_l^A(\boldsymbol{\mu}) \theta_k^B(\boldsymbol{\mu}) \mathbf{M}_{A_l B_k} \\ \mathbf{M}_{AF}(\boldsymbol{\mu}) &= \sum_{l=1}^{N_A} \theta_l^A(\boldsymbol{\mu}) \mathbf{M}_{A_l F} \end{aligned} \tag{4.11}$$

where the matrices $\mathbf{M}_{A_l B_k} \in \mathbb{R}^{N \times N}$ and $\mathbf{M}_{A_l F} \in \mathbb{R}^{N \times N_F}$, for $l \in \{1, \cdots, N_A\}$ and $k \in \{1, \cdots, N_B\}$, are $\boldsymbol{\mu}$-independent and respectively defined by $(\mathbf{M}_{A_l B_k})_{ij} = \langle \mathbf{A}_l \mathbf{v}_i, \mathbf{B}_k \mathbf{v}_j \rangle$ and $(\mathbf{M}_{A_l F})_{ij} = \langle \mathbf{A}_l \mathbf{v}_i, \mathbf{F}_j \rangle$. Here, we denote by $\mathbf{v}_i \in \mathbb{R}^n$ the i^{th} column of the reduced basis $\mathbf{V} \in \mathbb{R}^{n \times N}$. Finally, it should be noticed that for any $A \in \{M, C, K\}$ and any $l, k \in \{1, \cdots, N_A\}$, the matrices $\mathbf{M}_{A_l A_l}$ are symmetric and that $\mathbf{M}_{A_l A_k} = \mathbf{M}_{A_k A_l}^T$.

Remark 4.2.1 By definition of residual vector in Equation (4.8), the dynamic of the error of the solution of the full model (4.1) and its approximation by the reduced order model (4.6), $\mathbf{e}(t; \boldsymbol{\mu}) := \mathbf{X}(t; \boldsymbol{\mu}) - \mathbf{V}\mathbf{X}_r(t; \boldsymbol{\mu})$, writes:

$$\mathbf{M}(\boldsymbol{\mu}) \ddot{\mathbf{e}}(t; \boldsymbol{\mu}) + \mathbf{C}(\boldsymbol{\mu}) \dot{\mathbf{e}}(t; \boldsymbol{\mu}) + \mathbf{K}(\boldsymbol{\mu}) \mathbf{e}(t; \boldsymbol{\mu}) = \mathbf{R}(t; \boldsymbol{\mu}) \tag{4.12}$$

with initial condition $\mathbf{e}(t; \boldsymbol{\mu}) = \dot{\mathbf{e}}(t; \boldsymbol{\mu}) = \mathbf{0}$. In the case where we have $\mathbf{R}(t; \boldsymbol{\mu}) = \epsilon \mathbf{F}(t; \boldsymbol{\mu})$, the linearity of the problem implies that: $\mathbf{e}(t; \boldsymbol{\mu}) = \epsilon \mathbf{X}(t; \boldsymbol{\mu})$ which means that the relative error between the solution of the full model (4.1) and its approximation by the reduced order model (4.6) is ϵ. We note that when $\Delta(\boldsymbol{\mu}) = \epsilon$, it implies that we have $||\mathbf{R}(t; \boldsymbol{\mu})|| \leq \epsilon ||\mathbf{F}(t; \boldsymbol{\mu})||, \forall t \in [0, T]$. Thus, the smaller the value of error indicator, the more accurate reduced order model is expected.

Remark 4.2.2 We remark that using the relation (4.10) implies that $||\mathbf{R}(t; \mu)||/||\mathbf{F}(t; \mu)||$ is equivalent to a relation in form $\sqrt{(a+b)/a}$, where a is the square of the norm of the right-hand side and b is the sum of the second term to the last term of the second equation of (4.10). Because of round-off error, the result of the operation $a + b$ returned by the computer can be different from its theoretical value, especially when a and b are almost opposite numbers. As a result, even in the case where $a = -b$ theoretically, when the maximal accumulation of round-off errors occurs in the computation of $a + b$, the computer would return a value $\approx \epsilon_{machine}|a|$, where $\epsilon_{machine}$ is machine precision. Therefore, the result of $\sqrt{(a+b)/a}$ provided by the computer has a lower bound $\approx \sqrt{\epsilon_{machine}}$.

As consequence of the above remark, the computation of the error indicator $\Delta(\boldsymbol{\mu})$ defined in Equation (4.9) by using the relations (4.10)-(4.11) with an expected value smaller than $\sqrt{\epsilon_{machine}}$ does not make sense (see Section 4.5.1 for some alternatives to remedy this). We will see, in the next section, that the relations (4.10)-(4.11) allow us to built an efficient offline/online strategy for computing the indicator error $\Delta(\boldsymbol{\mu})$ defined in Equation (4.9).

4.2.3 Offline-online computational procedures

In this section, we present an offline-online computational procedure which allows us to fully exploit the small dimension of the reduced problem. We should note that the offline stage

whose complexity can depend on the size of the full model, is performed only once. On the contrary, the online stage whose complexity can depend only the size of the reduced order model, is performed many times, for each parameter value $\boldsymbol{\mu} \in \mathcal{D}$.

Assuming that appropriate trial and test spaces $\mathbf{V}, \mathbf{W} \in \mathbb{R}^{n \times N}$ ($N << n$) are known and all operators of the left and the right-hand sides of the problem can be written in an affine dependent form in parameter (4.2), an efficient strategy of offline-online decomposition can be defined as follows.

Offline stage

In order to construct the reduced matrices $\mathbf{M}_r(\boldsymbol{\mu}), \mathbf{C}_r(\boldsymbol{\mu}), \mathbf{K}_r(\boldsymbol{\mu})$ and reduced vector $\mathbf{F}_r(t; \boldsymbol{\mu})$ in the online stage with a complexity which depends only on the size of the reduced order model, we need to compute and save the reduced matrices $\mathbf{A}_{l,r} = \mathbf{W}^T \mathbf{A}_l \mathbf{V} \in \mathbb{R}^{N \times N}$, for $A \in \{M, C, K\}, l \in \{1, \cdots, N_A\}$, and the reduced vectors $\mathbf{F}_{l,r} = \mathbf{W}^T \mathbf{F}_l \in \mathbb{R}^N, l \in \{1, \cdots, N_F\}$. In order to predict the output of interest by the reduced order model with a complexity independent of the size of the full model, we also need to compute and save during the offline stage the reduced vector $\mathbf{L}_r^T = \mathbf{L}^T \mathbf{V} \in \mathbb{R}^{1 \times N}$ (for a linear form output) and the reduced matrix $\mathbf{Q}_r = \mathbf{V}^T \mathbf{Q} \mathbf{V} \in \mathbb{R}^{N \times N}$ (for a quadratic form output).

For the computation of the error indicator defined in Equation (4.9), by using the relations (4.10)-(4.11, with a complexity which depends only on the size of the reduced order model in the online stage, we need to compute and save in the offline stage the following $\boldsymbol{\mu}$-independent quantities: $\mathbf{M}_{FF} \in \mathbb{R}^{N_F \times N_F}$, $\mathbf{M}_{A_l B_k} \in \mathbb{R}^{N \times N}$ for $A \geq B \in \{M, C, K\}$ (with the convention $K < C < M$), $l \in \{1, \cdots, N_A\}$ and $k \in \{1, \cdots N_B\}$ and $\mathbf{M}_{A_l F} \in \mathbb{R}^{N_F \times N}$ for $A \in \{M, C, K\}$ and $l \in \{1, \cdots N_A\}$.

In practice, we begin by computing the product of matrices and the trial space $\mathbf{A}_l \mathbf{V} \in \mathbb{R}^{n \times N}, A \in \{M, C, K\}, l = 1, \cdots, N_A$, before the computation of the reduced matrices and the data for the error indicator. The complexity of this first step is in $O(n^2 N(N_M + N_C + N_K))$. Using the results of the product matrices and the trial reduced basis, the complexity of the computation of the reduced matrices is in $O(nN^2(N_M + N_C + N_K))$. The complexity in the computation of the reduced vector is in $O(nNN_F)$. For the data of output of interest, the complexity is in $O(nN)$ for the linear form case, and in $O(n^2 N)$ for the quadratic form case. For the error indicator, the complexity in the computation of the matrix $\mathbf{M}_{FF}$ is in $O(nN_F^2)$. Using the results of the product matrices and the trial reduced basis, the complexity in the computation of the matrices $\mathbf{M}_{A_l F}, A \in \{M, C, K\}, l \in \{1, \cdots, N_A\}$, is in $O(nNN_F(N_M + N_C + N_K))$ and of the matrices $\mathbf{M}_{A_l B_k}$, for $A \geq B \in \{M, C, K\}$ (with the convention $K < C < M$), $l \in \{1, \cdots, N_A\}$ and $k \in \{1, \cdots N_B\}$, is in $O(nN^2(N_M(N_M + N_C + N_K) + N_C(N_C + N_K)))$.

It should be noticed that the data to be computed in the offline part for error indicator and the linear or quadratic output of interest depend only on the trial subspace $\mathbf{V}$ and not on the test subspace $\mathbf{W}$. The offline stage is summarized by Algorithm 4.

Remark 4.2.3 In the full model (4.1) the matrices $\mathbf{M}, \mathbf{C}, \mathbf{K}$ are sparse. Thus, the complexity of the product of matrices and the basis $\mathbf{V}$ is in $O(n_z N(N_M + N_C + N_K))$ instead of $O(n^2 N(N_M + N_C + N_K))$, where n_z is the number of non-zeros entries in the matrix.

Algorithm 4 Offline stage of the reduced order modelling framework in case of affine parametric dependence

Input: A test and trial reduced basis $\mathbf{W}, \mathbf{V} \in \mathbb{R}^{n\times N}$
Output: The data to be saved for online stage

// Compute the product of matrices and the basis $\boldsymbol{V}$, complexity $O(n^2N(N_M+N_C+N_K))$
for $A = M, C, K$ **do**
  for $l = 1, \cdots, N_A$ **do**
    Compute $\mathbf{A}_l\mathbf{V} \in \mathbb{R}^{n\times N}$
  end for
end for
// Data for the reduced matrices, complexity $O(nN^2(N_M+N_C+N_K))$
for $A = M, C, K$ **do**
  for $l = 1, \cdots, N_A$ **do**
    Compute and save $\mathbf{A}_{l,r} = \mathbf{W}^T(\mathbf{A}_l\mathbf{V}\ ) \in \mathbb{R}^{N\times N}$
  end for
end for
// Compute and save the data for the reduced vectors, complexity $O(nNN_F)$
for $l = 1, \cdots, N_F$ **do**
  Compute and save $\mathbf{F}_{l,r} = \mathbf{W}^T\mathbf{F}_l$
end for
// Compute and save the data for the linear output, complexity $O(nN)$
Compute and save $\mathbf{L}_r^T = \mathbf{L}^T\mathbf{V} \in \mathbb{R}^{1\times N}$
// Compute and save the data for the quadratic output, complexity $O(n^2N)$
Compute and save $\mathbf{Q}_r = \mathbf{V}^T\mathbf{Q}\mathbf{V} \in \mathbb{R}^{N\times N}$
// Compute and save the data for the error indicator, complexity $O(nN_F^2 + nNN_F(N_M+N_C+N_K) + nN^2(N_M(N_M+N_C+N_K)+N_C(N_C+N_K)))$
Compute $\mathbf{M}_{FF} \in \mathbb{R}^{N_F\times N_F}$ defined by $(\mathbf{M}_{FF})_{ij} = \langle \mathbf{F}_i, \mathbf{F}_j\rangle$
for $A = M, C, K$ **do**
  for $l = 1, \cdots, N_A$ **do**
    Compute and save $\mathbf{M}_{A_lF} \in \mathbb{R}^{N_F\times N}$ defined by $(\mathbf{M}_{A_lF})_{ij} = \langle \mathbf{A}_l\mathbf{v}_i, \mathbf{F}_j\rangle$, where $\mathbf{v}_i$ is i^{th} column of $\mathbf{V}$
  end for
end for
for $A = M, C, K$ **do**
  for $B = M, C, K$ **do**
    if $B \leq A$ (with the convention $K < C < M$) **then**
      for $l = 1, \cdots, N_A$ **do**
        for $k = 1, \cdots, N_B$ **do**
          Compute and save $\mathbf{M}_{A_lB_k} \in \mathbb{R}^{N\times N}$ defined by $(\mathbf{M}_{A_lB_k})_{ij} = \langle \mathbf{A}_l\mathbf{v}_i, \mathbf{B}_k\mathbf{v}_j\rangle$
        end for
      end for
    end if
  end for
end for

Online stage

Once all calculations at the offline stage are done, the computation of the output of interest $S_l^{rom}(t;\boldsymbol{\mu})$, $S_q^{rom}(t;\boldsymbol{\mu})$ and error indicator $\Delta(\boldsymbol{\mu})$, for any new value parameter value $\boldsymbol{\mu} \in \mathcal{D}$,

can be performed with a complexity which depends only on the small size of the reduced order model.

Using the affine decomposition (4.2) and the data saved in offline stage, we can compute for any new value parameter value $\boldsymbol{\mu} \in \mathcal{D}$ the reduced matrices $\mathbf{M}_r(\boldsymbol{\mu}), \mathbf{C}_r(\boldsymbol{\mu}), \mathbf{K}_r(\boldsymbol{\mu})$ with a complexity in $O(NN_A^2)$, $A \in \{M, C, K\}$, by using relation $\mathbf{A}_r(\boldsymbol{\mu}) = \sum_{i=1}^{N_A} \theta_i^A(\boldsymbol{\mu})(\mathbf{A}_i)_r$. The cost of resolution of the reduced problem (4.6) depends then only on N, N_F, the number of time steps N_t and the choice of time-discretization scheme. The cost of computation of the output of interest $S_l^{rom}(t;\boldsymbol{\mu})$ ($S_q^{rom}(t;\boldsymbol{\mu})$) with the relation $S_l^{rom}(t;\boldsymbol{\mu}) = \mathbf{L}_r^T \mathbf{X}_r(t;\boldsymbol{\mu})$ ($S_q^{rom}(t;\boldsymbol{\mu}) = \mathbf{X}_r^T(t;\boldsymbol{\mu})\mathbf{Q}_r\mathbf{X}_r(t;\boldsymbol{\mu})$), where $\mathbf{L}_r \in \mathbb{R}^{1\times N}$ ($\mathbf{Q}_r \in \mathbb{R}^{N\times N}$) are already computed at offline stage, are in $O(N_t N)$ (in $O(N_t N^2)$).

Algorithm 5 Online stage of the reduced order modelling framework in case of affine parametric dependence

Input: The data of offline stage and a new value parameter value $\boldsymbol{\mu} \in \mathcal{D}$

Output: The output of interest $S_l^{rom}(t;\boldsymbol{\mu})$, $S_q^{rom}(t;\boldsymbol{\mu})$ and the error indicator $\Delta(\boldsymbol{\mu})$

1: *// Overall complexity* $O(N^2(N_M + N_C + N_K))$

2: Compute the reduced mass, damping and stiffness matrices by the relation:

$$\mathbf{A}_r(\boldsymbol{\mu}) = \sum_{i=1}^{N_A} \theta_i^A(\boldsymbol{\mu})(\mathbf{A}_i)_r \ , \ A \in \{M, C, K\} \tag{4.13}$$

3: *// Complexity depends only on* N, N_F *and the number of time step* N_t

4: Solve the reduced problem

$$\mathbf{M}_r(\boldsymbol{\mu})\ddot{\mathbf{X}}_r(t;\boldsymbol{\mu}) + \mathbf{C}_r(\boldsymbol{\mu})\dot{\mathbf{X}}_r(t;\boldsymbol{\mu}) + \mathbf{K}_r(\boldsymbol{\mu})\mathbf{X}_r(t;\boldsymbol{\mu}) = \sum_{i=1}^{N_F} \theta_i^F(t;\boldsymbol{\mu})(\mathbf{F}_i)_r \tag{4.14}$$

5: *// Complexity in* $O(NN_t)$ *for linear case and in* $O(N^2N_t)$ *for quadratic case*

6: Compute the output of interest

$$S_l^{rom}(t;\boldsymbol{\mu}) = \mathbf{L}_r^T\mathbf{X}_r(t;\boldsymbol{\mu}), S_q^{rom}(t;\boldsymbol{\mu}) = \mathbf{X}_r^T(t;\boldsymbol{\mu})\mathbf{Q}_r\mathbf{X}_r^T(t;\boldsymbol{\mu}) \tag{4.15}$$

7: *// Complexity in* $O(N^2(N_M(N_M + N_C + N_K) + N_C(N_C + N_K)) + NN_F(N_M + N_C + N_K))$

8: Compute the data for error indicator: $\mathbf{M}_{AF}(\boldsymbol{\mu}) \in \mathbb{R}^{N_F\times N}$, $\mathbf{M}_{AB}(\boldsymbol{\mu}) \in \mathbb{R}^{N\times N}$, for $A, B \in \{M, C, K\}$ and $B \leq A$ (with the convention $K < C < M$), by the relation:

$$\begin{aligned} \mathbf{M}_{AB}(\boldsymbol{\mu}) &= \sum_{l=1}^{N_A}\sum_{k=1}^{N_B} \theta_l^A(\boldsymbol{\mu})\theta_k^B(\boldsymbol{\mu})\mathbf{M}_{A_lB_k} \\ \mathbf{M}_{AF}(\boldsymbol{\mu}) &= \sum_{l=1}^{N_A} \theta_l^A(\boldsymbol{\mu})\mathbf{M}_{A_lF} \end{aligned} \tag{4.16}$$

9: *// Complexity in* $O(N_t(N_F^2 + N^2 + NN_F))$

10: Compute the error indicator $\Delta(\boldsymbol{\mu})$ by the relations (4.9)-(4.10)

Concerning the error indicator $\Delta(\boldsymbol{\mu})$, the first step consists of computing the matrices $\mathbf{M}_{AB}(\boldsymbol{\mu}) \in \mathbb{R}^{N\times N}$ and $\mathbf{M}_{AF}(\boldsymbol{\mu}) \in \mathbb{R}^{N_F\times N}$, for $A \geq B \in \{M, C, K\}$ (with the convention $K < C < M$). Using the relation (4.11) and the data of $\mathbf{M}_{A_lB_k}$ and $\mathbf{M}_{A_lF}$, $A \geq B \in \{M, C, K\}$, $l \in \{1, \cdots, N_A\}$, $k \in \{1, \cdots, N_B\}$ which are already computed at offline stage, the cost of computation of $\mathbf{M}_{AB}(\boldsymbol{\mu})$ et $\mathbf{M}_{AF}(\boldsymbol{\mu})$ are respectively in $O(N^2 N_A N_B)$ and in $O(NN_F N_A)$. Once the computation of $\mathbf{M}_{AB}(\boldsymbol{\mu}) \in \mathbb{R}^{N\times N}$ and $\mathbf{M}_{AF}(\boldsymbol{\mu}) \in \mathbb{R}^{N_F\times N}$, for $A, B \in \{M, C, K\}$, are done, we can now compute the error indicator $\Delta(\boldsymbol{\mu})$ of Equation (4.9) by using the relation (4.10) with a complexity in $O(N_t(N_F^2 + N^2 + NN_F))$. Note that there are no additional computation cost of $\dot{\mathbf{X}}_r(t;\boldsymbol{\mu})$ and $\ddot{\mathbf{X}}_r(t;\boldsymbol{\mu})$ in the common used time-integration schemes (such as Newmark scheme, Wilson scheme, ...) which also explicitly compute the time derivate of the primal variables. The online stage is summarized by Algorithm 5.

4.3 Construction of the reduced basis by POD-Greedy algorithm

The most common way to generate an appropriate reduced basis $\mathbf{V}$ for a parametrized unsteady problem is based on the well known Proper Orthogonal Decomposition (POD) technique, which is also known as Principal Component Analysis (PCA) in statistics [71, 105], Karhunen-Loève expansion in stochastic application [87, 77], Hotelling Transformation in image processing, Principal Orthogonal Direction (POD) in geophysics and Empirical Orthogonal Functions (EOFs) in meteorology and geophysics. In the context of model reduction, Proper Orthogonal Decomposition has been applied successfully for generating an appropriate reduced basis in various domains of application: in turbulent flow in [12, 74, 56, 125], in Navier-Stokes equations in [43], in parabolic partial differential equations [80].

In algebraic way, Proper Orthogonal Decomposition can be viewed as a technique for finding a low-dimension approximation space by exploiting the singular value decomposition (SVD) of a suitable snapshot matrix. Considering in our case a set of N_μ well chosen instances of the parameters $\{\boldsymbol{\mu}_1^*, \cdots, \boldsymbol{\mu}_{N_\mu}^*\} \in \mathcal{D}$, we introduce the snapshot matrix $\mathbf{S} \in \mathbb{R}^{n\times N_s}$ defined as:

$$\mathbf{S} = \begin{bmatrix} \mathbf{X}(t^1;\boldsymbol{\mu}_1^*) & \cdots & \mathbf{X}(t^{N_t};\boldsymbol{\mu}_1^*) & \cdots & \mathbf{X}(t^1;\boldsymbol{\mu}_{N_\mu}^*) & \cdots & \mathbf{X}(t^{N_t};\boldsymbol{\mu}_{N_\mu}^*) \end{bmatrix} \tag{4.17}$$

where we have introduced a partition of the time interval $[0, T]$ in N_t time step $\{t^k\}_{k=1}^{N_t}$, $t^k = k\Delta t$, of size $\Delta t = T/N_t$ and $N_s = N_t N_\mu$. By computing the singular value decomposition (SVD) of the matrix $\mathbf{S}$,

$$\mathbf{S} = \mathbf{U}\boldsymbol{\Sigma}\mathbf{Z}^T \tag{4.18}$$

where $\boldsymbol{\Sigma} = \mathrm{diag}(\sigma_1, \cdots, \sigma_{N_s})$, being $\sigma_1 \geq \sigma_2 \geq \cdots, \sigma_{N_s} \geq 0$ the N_s singular values of $\mathbf{S}$, the POD reduced basis $\mathbf{V}_N$ of dimension $N \leq \min\{n, N_s\}$ is obtained by selecting the first N columns of the left singular vector $\mathbf{U}$, corresponding to the first N largest singular values, that is $\mathbf{V}_N = \begin{bmatrix} \mathbf{u}_1 & \cdots, \mathbf{u}_N \end{bmatrix} \in \mathbb{R}^{n\times N}$. The vector $\mathbf{u}_i$ is also known as i^{th} *principal component* or i^{th} *POD mode* of the snapshot matrix $\mathbf{S}$.

By construction, the columns of $\mathbf{V}_N$ are orthonormal with respect to the euclidean scalar product. The reduced basis provided by POD is optimal in the sense that for all possible N dimensional subspaces W spanned by any set $\{\mathbf{w}_1, \cdots, \mathbf{w}_N\}$ of N orthonormal vectors in $\mathbb{R}^n$, the subspace spanned by the columns of $\mathbf{V}_N$ provides the best reconstruction of snapshots,

that is,

$$\sum_{i=1}^{N_\mu}\sum_{k=1}^{N_t}||\mathbf{X}(t^k;\boldsymbol{\mu}_k^*)-\Pi_V\mathbf{X}(t^k;\boldsymbol{\mu}_i^*)||^2=\min_{\mathbf{w}_1,\cdots,\mathbf{w}_N\in\mathbb{R}^n}\sum_{i=1}^{N_\mu}\sum_{k=1}^{N_t}||\mathbf{X}(t^k;\boldsymbol{\mu}_k^*)-\Pi_W\mathbf{X}(t^k;\boldsymbol{\mu}_i^*)||^2 \quad (4.19)$$

where $\Pi_W\mathbf{X}$ denotes the orthogonal projection of the vector $\mathbf{X}\in\mathbb{R}^n$ onto the subspace spanned by the orthonormal vectors $\{\mathbf{w}_1,\cdots,\mathbf{w}_N\}$ with respect to the euclidean scalar product. In other words, the POD reduced basis minimizes the sum of the squared distances between each snapshot and the corresponding orthogonal projection onto the subspace. Moreover, the corresponding minimum value can be expressed explicitly by:

$$\sum_{i=1}^{N_\mu}\sum_{k=1}^{N_t}||\mathbf{X}(t^k;\boldsymbol{\mu}_k^*)-\Pi_V\mathbf{X}(t^k;\boldsymbol{\mu}_i^*)||^2=\sum_{i=N+1}^{N_s}\sigma_i^2 \quad (4.20)$$

With this result, POD is commonly performed with a given tolerance ϵ, in order to control the relative error on the approximation of snapshots, by setting the reduced basis dimension N as the smallest integer such that:

$$\frac{\sum_{i=N+1}^{N_s}\sigma_i^2}{\sum_{i=1}^{N_s}\sigma_i^2}\leq\epsilon^2 \quad (4.21)$$

As summarized, for a given snapshot matrix $\mathbf{S}\in\mathbb{R}^{n\times N_s}$ and a tolerance ϵ, the POD reduced basis $\mathbf{V}_N\in\mathbb{R}^{n\times N}$, denoted by $\mathrm{POD}(\mathbf{S};\epsilon)$, are constructed by Algorithm 6.

Algorithm 6 POD algorithm based on SVD decomposition

Input: A snapshot matrix $\mathbf{S}$ and a tolerance ϵ

Output: A reduced basis $\mathbf{V}_N=\mathrm{POD}(\mathbf{S};\epsilon)$

1: Compute the singular value decomposition of $\mathbf{S}$: $\mathbf{S}=\mathbf{U}\boldsymbol{\Sigma}\mathbf{Z}^T$

2: Set the basis dimension N as the smallest integer such that

$$\frac{\sum_{i=N+1}^{N_s}\sigma_i^2}{\sum_{i=1}^{N_s}\sigma_i^2}\leq\epsilon^2$$

3: Construct the reduced basis by collecting the first N columns of the left sigular vector $\mathbf{U}$:

$$\mathbf{V}_N=\begin{bmatrix}\mathbf{u}_1 & \cdots,\mathbf{u}_N\end{bmatrix}\in\mathbb{R}^{n\times N}$$

Remark 4.3.1 Different norms can also be used in the minimization problem (4.19) instead of the euclidean norm. If the norm is encoded by a symmetric and positive definite matrix $\mathbf{A}\in\mathbb{R}^{n\times n}$ ($||\mathbf{v}||_A=\langle\mathbf{v},\mathbf{A}\mathbf{v}\rangle^{1/2}$) which admits a Cholesky factorisation $\mathbf{A}=\mathbf{L}\mathbf{L}^T$, the POD reduced basis which minimizes the problem (4.19) with respect to the norm $||\cdot||_A$ is given by $\mathbf{V}_N=\begin{bmatrix}(\mathbf{L}^T)^{-1}\mathbf{u}_1\cdots(\mathbf{L}^T)^{-1}\mathbf{u}_N\end{bmatrix}\in\mathbb{R}^{n\times N}$ where $\mathbf{u}_i$ denotes the i^{th} column of the left singular matrix $\mathbf{U}$ of the matrix $\mathbf{L}^T\mathbf{S}$; $\mathbf{L}^T\mathbf{S}=\mathbf{U}\boldsymbol{\Sigma}\mathbf{Z}^T$.

Remark 4.3.2 An alternative way to built POD reduced basis from the snapshot matrix $\mathbf{S}=[\mathbf{s}_1,\cdots,\mathbf{s}_{N_s}]$ relies on computing the eigenvector of the symmetric Gramian matrix (which also known as Kernel or Correlation matrix) $\mathbf{G}\in\mathbb{R}^{N_s\times N_s}$ defined by $G_{ij}=\langle\mathbf{s}_i,\mathbf{s}_j\rangle_A$, where

$\langle \cdot, \cdot \rangle_A$ denotes a scalar product of interest. The k^{th} POD basis $\mathbf{v}_k$ is then obtained as:

$$\mathbf{v}_k = \frac{1}{\sqrt{\lambda_k}} \sum_{i=1}^{N_s} \psi_{k,i} \mathbf{s}_k \tag{4.22}$$

where $\psi_{k,i}$ the i^{th} component of the eigenvector corresponding to k^{th} largest eigenvalue λ_k of $\mathbf{G}$. The eigenvalues of $\mathbf{G}$ directly provide the singular values of the snapshot matrix $\mathbf{S}$, that is $\lambda_i = \sigma_i^2, i = 1, \cdots, N_s$. This approach is well known as "*method of snapshots*". The complexity of this approach is dominated by the step of construction of the Gramian matrix $\mathbf{G}$. The complexity can be approximated by $O(nN_s^2)$ for the case of the euclidean norm and by $O(n^2 N_s + nN_s^2)$ for other cases (only in $O(n_z N_s + nN_s^2)$ if the matrix encoding the norm is a sparse matrix with n_z non-zeros entries). Using this approach to build POD reduced basis can avoid the difficult task of computing a Cholesky factorization for the case where the norm of interest is not the euclidean one, and SVD decomposition of the snapshot matrix by computing the eigenvalue decomposition of a much smaller symmetric matrix $\mathbf{G}$. However, it should be pointed out that the conditioning number of the Gramian matrix $\mathbf{G}$ is the square of the conditioning number of the snapshot matrix $\mathbf{S}$. This limits the numerical accuracy of this approach in comparison to SVD algorithm. For this reason, we employ in our work Algorithm 6 to generate POD reduced basis.

For the case of the euclidean scalar product, the complexity of computation of POD reduced basis with Algorithm 6 can be approximated by $O(nN_s^2)$ where n is the size of the full model and $N_s = N_\mu N_t$. As remark, the complexity increases quadratically in N_t and N_μ. We should also note that a sufficient large number N_μ of solutions of the full model (4.1) is required in order to ensure that the obtained reduced basis is accurate. Hence, computing the POD reduced basis by Algorithm 6 can become prohibitively expensive. To reduce the computation cost, we can employ Hierarchical Approximate Proper Orthogonal Decomposition (HAPOD, [69]) in which the main idea is to compute POD of several small subsets of $\mathbf{S}$ instead of computing a POD of a given large snapshot set $\mathbf{S}$. Two particular cases of HAPOD namely Distributed and Incremental HAPOD are outlined in Algorithm 7 and 8, respectively.

Algorithm 7 Distributed HAPOD algorithm

Input: A snapshot matrix $\mathbf{S} = [\mathbf{S}_1 \cdots \mathbf{S}_N]$ and a tolerance ϵ

Output: A reduced basis $\mathbf{V}$

1: **for** $i = 1, \cdots, N$ **do**
2: Set $\mathbf{Z}_i = \mathrm{POD}(\mathbf{S}_i, \epsilon)$
3: **end for**
4: Set $\mathbf{V} = \mathrm{POD}([\mathbf{Z}_1 \cdots \mathbf{Z}_N], \epsilon)$

Algorithm 8 Incremental HAPOD algorithm

Input: A snapshot matrix $\mathbf{S} = [\mathbf{S}_1 \cdots \mathbf{S}_N]$ and a tolerance ϵ

Output: A reduced basis $\mathbf{V}$

1: Set $\mathbf{V} = \mathrm{POD}(\mathbf{S}_1, \epsilon)$
2: **for** $i = 2, \cdots, N$ **do**
3: Set $\mathbf{Z} = \mathrm{POD}(\mathbf{S}_i, \epsilon)$
4: Set $\mathbf{V} = \mathrm{POD}([\mathbf{V}\ \mathbf{Z}], \epsilon)$
5: **end for**

It is worth mentioning that one of the advantages of the Distributed HAPOD algorithm is that it opens a very easy way in parallelization since the computation of local PODs of each subset $\mathbf{S}_i$ can be done independently. For the Incremental HAPOD, the main advantage is that it can reduce the required memory since in each iteration, the procedure only requires the current subset $\mathbf{S}_i$ and the POD reduced basis of the previous iteration, so that the current subset $\mathbf{S}_i$ does not need to be saved for the next iteration.

Even though the complexity in the computation of POD reduced basis for the case where N_μ is large can be overcome by employing HAPOD, a proper choice of N_μ and the set $\{\boldsymbol{\mu}_1^*, \cdots, \boldsymbol{\mu}_{N_\mu}^*\}$ is not known or predictable in a general case. A too large number of N_μ leads to a very substantial computation overhead by having to compute too many solutions of the full model where the majority of these solutions do not contribute to the reduced basis. A too small number of N_μ leads to an inaccurate reduced basis. To overcome this problem, we can use the information of the error indicator, which can be computed with a complexity relatively inexpensive, to propose an iterative procedure in the selection of the number N_μ of the solution of the full model (4.1) and the corresponding parameter values $\boldsymbol{\mu}_1^*, \cdots, \boldsymbol{\mu}_{N_\mu}^*$ in a greedy way. Combining the Proper Orthogonal Decomposition (POD) to compress the time-trajectories, with the greedy procedure in the parameter space gives an efficient algorithm, namely POD-Greedy algorithm, to construct an accurate reduced basis.

4.3.1 POD-Greedy algorithms

With a given tolerance ϵ_{POD} for POD compression, a naive POD-Greedy approach can be defined as follows. We can start with a first value of parameter $\boldsymbol{\mu}_1^*$ by choosing randomly in the parameter space $\mathcal{D}$ or by using knowledge of the problem at hand. The first reduced basis is then obtained by Algorithm 6 by using the snapshot matrix consisting of the solution of the full model for this value of parameter; $\mathbf{V}_1 = \text{POD}(\mathbf{S}_1, \epsilon_{POD})$ where $\mathbf{S}_1 = [\mathbf{X}(t_1, \boldsymbol{\mu}_1^*) \cdots \mathbf{X}(t_{N_t}, \boldsymbol{\mu}_1^*)] \in \mathbb{R}^{n \times N_t}$. After the initialization step, we can now update the reduced basis iteratively until it is sufficiently accurate. At iteration k, we use the reduced basis $\mathbf{V}_k \in \mathbb{R}^{n \times N_k}$ of the previous iteration to built an appropriate parametrized reduced order model (4.6). The new value of parameter $\boldsymbol{\mu}_{k+1}^*$ is then chosen as the one who maximizes the error indicator of the reduced order model over the parameter space $\mathcal{D}$. Next, we update the snapshot matrix by enriching the solution of the full model for the new value of parameter and compute the new reduced basis by using Algorithm 6 with the new snapshot matrix $\mathbf{S}_{k+1} = [\mathbf{S}_1 \cdots \mathbf{S}_{k+1}]$, where $\mathbf{S}_l = [\mathbf{X}(t_1, \boldsymbol{\mu}_l^*) \cdots \mathbf{X}(t_{N_t}, \boldsymbol{\mu}_l^*)]$, $l = 1, \cdots, k+1$. The procedure is iterated until the value of the error indicator is sufficiently small. The summary of this naive approach is outlined in Algorithm 9.

Algorithm 9 Construction of the reduced basis by a POD-Greedy algorithm (naive version)

Input: A partition $\{t_n\}_{n=1}^{N_t}$ of the time interval $[0,T]$, tolerance $\epsilon_{POD}, \epsilon_{algo}$, maximum number of iterations N_{max}

Output: A reduced basis $\mathbf{V}$

1: Choose randomly $\boldsymbol{\mu}_1^* \in \mathcal{D}$ and compute the solution of the full model (4.1) for $\boldsymbol{\mu} = \boldsymbol{\mu}_1^*$
2: Construct the basis by POD using the snapshot matrix $\mathbf{S}_1 = [\mathbf{X}(t_1, \boldsymbol{\mu}_1^*) \cdots \mathbf{X}(t_{N_t}, \boldsymbol{\mu}_1^*)]$ and $\epsilon = \epsilon_{POD}$ with Algorithm 6

$$\mathbf{V} = \mathrm{POD}(\mathbf{S}_1, \epsilon_{POD})$$

3: Set $k = 1$
4: **while** $(k \leq N_{max})$ **do**
5: Perform the offline stage for an appropriate couple $(\mathbf{W}, \mathbf{V})$ with Algorithm 4
6: Compute the error indicator $\Delta(\boldsymbol{\mu})$ of an appropriate parametrized reduced order model based on the reduced basis $\mathbf{V}$ for all $\boldsymbol{\mu} \in \mathcal{D}$
7: Set $\boldsymbol{\mu}_{k+1}^* = \arg\max_{\boldsymbol{\mu} \in \mathcal{D}} \Delta(\boldsymbol{\mu})$
8: **if** $\Delta(\boldsymbol{\mu}_{k+1}^*) \leq \epsilon_{algo}$ **then**
9: **break**
10: **else**
11: Compute the solution of the full model (4.1) for $\boldsymbol{\mu} = \boldsymbol{\mu}_{k+1}^*$
12: Set the snapshot matrix

$$\mathbf{S}_{k+1} = \begin{bmatrix} \mathbf{X}(t_1; \boldsymbol{\mu}_1^*) & \cdots & \mathbf{X}(t_{N_t}; \boldsymbol{\mu}_1^*) & \cdots & \mathbf{X}(t_1; \boldsymbol{\mu}_{k+1}^*) & \cdots & \mathbf{X}(t_{N_t}; \boldsymbol{\mu}_{k+1}^*) \end{bmatrix} \in \mathbb{R}^{n \times (k+1)N_t}$$

13: Construct the basis by POD using the snapshot matrix $\mathbf{S}_{k+1}$ with the given tolerance ϵ_{POD} with Algorithm (6)

$$\mathbf{V} = \mathrm{POD}(\mathbf{S}_{k+1}, \epsilon_{POD})$$

14: **end if**
15: Set $k = k + 1$
16: **end while**

Two major drawbacks should be pointed out in the naive POD-Greedy algorithm. First, the computation complexity of the new reduced basis at the step 13 of Algorithm 9 increases quadratically in k. This issue can be overcome by employing HAPOD [69] (such as Distributed or Incremental HAPOD, see Algorithm 7 and 8). The second default is that the algorithm does not generate a hierarchical reduced basis which is computationally disadvantageous (see Section 4.3.6).

To remedy this, we propose to modify the step 12-13 of Algorithm 9, by inspiring the POD-Greedy Algorithm proposed in [107]. After identifying the new value of parameter $\boldsymbol{\mu}_{k+1}^*$, we apply POD Algorithm 6 on the snapshot matrix $\mathbf{S}_{k+1} := \left[\mathbf{X}(t_1, \boldsymbol{\mu}_{k+1}^*) \cdots \mathbf{X}(t_{N_t}, \boldsymbol{\mu}_{k+1}^*)\right] \in \mathbb{R}^{n \times N_t}$, which is made up of the solution of the full model (4.1) for this new value of parameter $\boldsymbol{\mu}_{k+1}^*$ with the given value of tolerance ϵ_{POD} and let $\mathbf{Z}_{k+1} = \mathrm{POD}(\mathbf{S}_{k+1}, \epsilon_{POD}) \in \mathbb{R}^{n \times M_{k+1}}$. The new reduced basis is then obtained as the concatenation of $\mathbf{Z}_{k+1}$ with the previous reduced basis $\mathbf{V}_k$. In order to avoid the duplication with the existing reduced basis $\mathbf{V}_k$, we can apply POD Algorithm 6 on the snapshot matrix $[\mathbf{Z}_{k+1}\ \mathbf{V}_k] \in \mathbb{R}^{n \times (N_k + M_{k+1})}$ with $\epsilon = \epsilon_{POD}$, to obtain the new reduced basis $\mathbf{V}_{k+1}$. This procedure is equivalent to the computation of the reduced basis

$\mathbf{V}$ from the well chosen sample $\{\boldsymbol{\mu}_1^*, \cdots, \boldsymbol{\mu}_k^*\}$ at iteration $k \geq 2$ by using incremental HAPOD Algorithm 8 on a large snapshot matrix $\mathbf{S} = [\mathbf{S}_1 \cdots \mathbf{S}_{k+1}]$, where $\mathbf{S}_l = [\mathbf{X}(t_1, \boldsymbol{\mu}_l^*) \cdots \mathbf{X}(t_{N_t}, \boldsymbol{\mu}_l^*)]$, $l = 1, \cdots, k+1$. With this solution, the obtained reduced basis is not hierarchical which is disadvantageous in the computation procedure (see Section 4.3.6). Hence, we propose to employ Algorithm 11 in order to concatenate the basis $\mathbf{V}_k$ and $\mathbf{Z}_{k+1}$ with respect to the given tolerance ϵ_{POD}. The methodology is summarized in Algorithm 10.

Algorithm 10 Construction of the reduced basis by a POD-Greedy algorithm

Input: A partition $\{t_n\}_{n=1}^{N_t}$ of the time interval $[0, T]$, tolerance $\epsilon_{POD}, \epsilon_{algo}$, maximum number of iterations N_{max}

Output: A reduced basis $\mathbf{V}$

Choose randomly $\boldsymbol{\mu}_1^* \in \mathcal{D}$ and compute the solution of the full model (4.1) for $\boldsymbol{\mu} = \boldsymbol{\mu}_1^*$

Construct the basis by POD using the snapshot matrix $\mathbf{S}_1 = [\mathbf{X}(t_1, \boldsymbol{\mu}_1^*) \cdots \mathbf{X}(t_{N_t}, \boldsymbol{\mu}_1^*)]$ and $\epsilon = \epsilon_{POD}$ with Algorithm 6

$$\mathbf{V} = \text{POD}(\mathbf{S}_1, \epsilon_{POD})$$

Set $k = 1$

while $(k \leq N_{max})$ **do**

  Perform the offline stage for an appropriate couple $(\mathbf{W}, \mathbf{V})$ with Algorithm 4

  Compute the error indicator $\Delta(\boldsymbol{\mu})$ of an appropriate parametrized reduced order model based on the reduced basis $\mathbf{V}$ for all $\boldsymbol{\mu} \in \mathcal{D}$

  Set $\boldsymbol{\mu}_{k+1}^* = \arg\max_{\boldsymbol{\mu} \in \mathcal{D}} \Delta(\boldsymbol{\mu})$

  if $\Delta(\boldsymbol{\mu}_{k+1}^*) \leq \epsilon_{algo}$ **then**

    break

  else

    Compute the solution of the full model (4.1) for $\boldsymbol{\mu} = \boldsymbol{\mu}_{k+1}^*$

    Compute $\mathbf{Z}_{k+1} = \text{POD}(\mathbf{S}_{k+1}, \epsilon_{POD})$ using Algorithm 6 with $\mathbf{S}_{k+1} = \left[\mathbf{X}(t_1, \boldsymbol{\mu}_{k+1}^*) \cdots \mathbf{X}(t_{N_t}, \boldsymbol{\mu}_{k+1}^*)\right]$

    Compute the new reduced basis $\mathbf{V}$ with Algorithm 11

$$\mathbf{V} = \text{concatenate}(\mathbf{V}, \mathbf{Z}_{k+1}; \epsilon_{POD})$$

  end if

  Set $k = k + 1$

end while

Algorithm 11 A procedure for concatenating two basis with respect to a given tolerance

Input: Two orthogonal basis $\mathbf{V}_1 \in \mathbb{R}^{n \times N_1}$, $\mathbf{V}_2 \in \mathbb{R}^{n \times N_2}$, a tolerance ϵ

Output: A concatenated basis $\mathbf{V} = \text{concatenate}(\mathbf{V}_1, \mathbf{V}_2; \epsilon)$

Set $\mathbf{V} = \mathbf{V}_1$

for $i = 1, \cdots, N_2$ **do**

  Compute the error $\mathbf{e}_i := \mathbf{v}_{2,i} - \Pi_V \mathbf{v}_{2,i}$ where $\mathbf{v}_{2,i}$ is i^{th} column of $\mathbf{V}_2$ and Π_V denotes the orthogonal projection on the subspace spanned by $\mathbf{V}$

  if $||\mathbf{e}_i|| \geq \epsilon ||\mathbf{v}_{2,i}||$ **then**

    Enrich the basis $\mathbf{V}$ as $\mathbf{V} = \mathbf{V} \oplus [\mathbf{e}_i / ||\mathbf{e}_i||]$

  end if

end for

Remark 4.3.3 In practical use, the parameter space $\mathcal{D} \subset \mathcal{R}^P$ is replaced by a finite training set $\mathcal{D}_{train}$ which has to be chosen sufficiently large in order to ensure that there is no important forgotten regions in the parameter space. In the case of high-dimensional parameter space ($P >> 1$), the size of the training set can be prohibitive even if we use a sparse uniform grid in each direction. A very simple way avoid this is to built randomly new training set at each iteration of POD-Greedy algorithm which allows us to not have too large regions without point in parameter space with a reasonable probability.

Remark 4.3.4 Instead of using the stopping criterion for the step 8 of Algorithm 10 based on the value of error indicator, we can use the information on the error of an output of interest between the full model and the reduced order model, based on the worst case predicted by the error indicator (*i.e* for the value of parameter $\boldsymbol{\mu}_{k+1} = \arg\max_{\boldsymbol{\mu}\in\mathcal{D}}\Delta(\boldsymbol{\mu})$). This requires only one resolution of the full model whose solution will be used to enrich the reduced basis in the next iteration if the stopping criterion is not yet verified. Another alternative is to pre-compute the output of interest by the full model over a test sample $\mathcal{D}_{test}$, whose cardinal is relatively small, and define the stopping criterion based on the error of the output of interest over the selected values of the parameters in $\mathcal{D}_{test}$.

Remark 4.3.5 Another version of POD-Greedy algorithm which is proposed in [64] and whose convergence rate has been analysed in [65], differs from our POD-Greedy algorithm 10 at the steps 12-13. In [64, 65], it has been proposed to construct the new reduced basis by computing at first the error of orthogonal projection of the solution of the full model (4.1) for the new value of parameter $\boldsymbol{\mu} = \boldsymbol{\mu}^*_{k+1}$, onto the reduced basis of previous iteration. We perform then POD on the snapshot matrix, which is made up of these error vectors, and chose the first N_m principal components to enrich the reduced basis. By construction, these N_m principal components are orthogonal with the reduced basis of the previous iteration. In practice N_m can be chosen as the smallest integer which verifies the inequality (4.21) with the same given tolerance for temporal compression, $\epsilon = \epsilon_{POD}$. This alternative approach is outlined in Algorithm 12.

Remark 4.3.6 As explained in [64], one of the main advantages of Algorithm 12 is that it generates hierarchical spaces which is computationally advantageous (we will discuss on this matter in Section 4.3.6). However, it should be pointed out that the accumulation of round-off errors in the computation of error projection vectors, at the step 12, and numerical errors in the computation POD of snapshot $\mathbf{E}_k$ can destroy the orthogonality of the reduced basis obtained at step 13 of Algorithm 12. Because of the loss of orthogonality, the computation of error vectors at the next iteration would require N_t resolutions of the linear system, whose size is equal to the dimension of the current reduced basis. This represents an other potential source of numerical errors which may be accumulated in the computation of POD at the step 13. For this reason, we prefer to work with the POD-Greedy algorithm inspired by [107].

Algorithm 12 Construction of the reduced basis by a POD-Greedy algorithm version of Ref [64]

Input: A partition $\{t_n\}_{n=1}^{N_t}$ of the time interval $[0,T]$, tolerance $\epsilon_{POD}, \epsilon_{algo}$, maximum number of iterations N_{max}

Output: A reduced basis $\mathbf{V}$

1: Choose randomly $\boldsymbol{\mu}_1^* \in \mathcal{D}$ and compute the solution of the full model (4.1) for $\boldsymbol{\mu} = \boldsymbol{\mu}_1^*$
2: Construct the basis by POD using the snapshot matrix $\mathbf{S}_1 = [\mathbf{X}(t_1, \boldsymbol{\mu}_1^*) \cdots \mathbf{X}(t_{N_t}, \boldsymbol{\mu}_1^*)]$ and $\epsilon = \epsilon_{POD}$ with Algorithm 6

$$\mathbf{V} = \mathrm{POD}(\mathbf{S}_1, \epsilon_{POD})$$

3: Set $k = 1$
4: **while** $(k \leq N_{max})$ **do**
5: Perform the offline stage for an appropriate couple $(\mathbf{W}, \mathbf{V})$ with Algorithm 4
6: Compute the error indicator $\Delta(\boldsymbol{\mu})$ of an appropriate parametrized reduced order model based on the reduced basis $\mathbf{V}$ for all $\boldsymbol{\mu} \in \mathcal{D}$
7: Set $\boldsymbol{\mu}_{k+1}^* = \arg\max_{\boldsymbol{\mu} \in \mathcal{D}} \Delta(\boldsymbol{\mu})$
8: **if** $\Delta(\boldsymbol{\mu}_{k+1}^*) \leq \epsilon_{algo}$ **then**
9: **break**
10: **else**
11: Compute the solution of the full model (4.1) for $\boldsymbol{\mu} = \boldsymbol{\mu}_{k+1}^*$
12: Compute the snapshot matrix

$$\mathbf{E}_k = \left[\mathbf{X}(t_1; \boldsymbol{\mu}_k^*) - \Pi_V \mathbf{X}(t_1; \boldsymbol{\mu}_k^*) \quad \cdots \quad \mathbf{X}(t_{N_t}; \boldsymbol{\mu}_k^*) - \Pi_V \mathbf{X}(t_{N_t}; \boldsymbol{\mu}_k^*)\right] \in \mathbb{R}^{n \times N_t}$$

where Π_V denotes the orthogonal projection on the subspace $\mathbf{V}$
13: Enrich the reduced basis

$$\mathbf{V} = \mathbf{V} \oplus \mathrm{POD}(\mathbf{E}_k, \epsilon_{POD})$$

14: **end if**
15: Set $k = k + 1$
16: **end while**

In what follows, we present different versions of the POD-Greedy algorithm based on Algorithm 10 for the three finite element models of vibro-acoustic problem given in Chapter 1, together with the stabilization techniques presented in Chapter 3.

4.3.2 POD-Greedy algorithm for formulation in $(\mathbf{u}_s, \phi)$

For the formulation in $(\mathbf{u}_s, \phi)$, we recall that a stable reduced order model can be obtained by using Petrov-Galerkin projection on any trial subspace $\mathbf{v} = \begin{bmatrix} \mathbf{V}_s \\ \mathbf{V}_f \end{bmatrix}$ with an test subspace $\mathbf{w}$ defined by $\mathbf{w} = \begin{bmatrix} \mathbf{V}_s \\ -\mathbf{V}_f \end{bmatrix}$ (see Lemma 3.2.2). As consequence, it should be emphasised that the parametrized reduced order model of the step 6 of Algorithm 10 is constructed by using Petrov-Galerkin projection with this particular test subspace. The POD-Greedy algorithm for formulation in $(\mathbf{u}_s, \phi)$ is outlined in Algorithm 13.

Algorithm 13 Construction of the basis by a POD-Greedy algorithm for a parametrized time-domain vibro-acoustic formulated in $(\mathbf{u}_s, \phi)$

Input: A partition $\{t_n\}_{n=1}^{N_t}$ of the time interval $[0, T]$, tolerance $\epsilon_{POD}, \epsilon_{algo}$, maximum number of iterations N_{max}

Output: A reduced basis $\mathbf{V}$

1: Choose randomly $\boldsymbol{\mu}_1^* \in \mathcal{D}$ and compute the solution of the full model (4.1) for $\boldsymbol{\mu} = \boldsymbol{\mu}_1^*$
2: Construct the basis by POD using the snapshot matrix $\mathbf{S}_1 = [\mathbf{X}(t_1, \boldsymbol{\mu}_1^*) \cdots \mathbf{X}(t_{N_t}, \boldsymbol{\mu}_1^*)]$ and $\epsilon = \epsilon_{POD}$ with Algorithm 6

$$\mathbf{V} = \mathrm{POD}(\mathbf{S}_1, \epsilon_{POD})$$

3: Set $k = 1$
4: **while** $(k \leq N_{max})$ **do**
5: Perform the offline stage for the couple $(\mathbf{W}, \mathbf{V})$ where $\mathbf{W} = \begin{bmatrix} \mathbf{V}_s^T & -\mathbf{V}_f^T \end{bmatrix}^T$ with Algorithm 4
6: Using Petrov-Galerkin projection on the couple $(\mathbf{W}, \mathbf{V})$ to built the parametrized reduced order model (4.6) and compute the error indicator $\Delta(\boldsymbol{\mu})$, for all $\boldsymbol{\mu} \in \mathcal{D}$
7: Set $\boldsymbol{\mu}_{k+1}^* = \arg\max_{\boldsymbol{\mu} \in \mathcal{D}} \Delta(\boldsymbol{\mu})$
8: **if** $\Delta(\boldsymbol{\mu}_{k+1}^*) \leq \epsilon_{algo}$ **then**
9: **break**
10: **else**
11: Compute the solution of the full model (4.1) for $\boldsymbol{\mu} = \boldsymbol{\mu}_{k+1}^*$
12: Compute $\mathbf{Z}_{k+1} = \mathrm{POD}(\mathbf{S}_{k+1}, \epsilon_{POD})$ using Algorithm 6 with $\mathbf{S}_{k+1} = \left[\mathbf{X}(t_1, \boldsymbol{\mu}_{k+1}^*) \cdots \mathbf{X}(t_{N_t}, \boldsymbol{\mu}_{k+1}^*)\right]$
13: Compute the new reduced basis $\mathbf{V}$ with Algorithm 11

$$\mathbf{V} = \mathrm{concatenate}(\mathbf{V}, \mathbf{Z}_{k+1}; \epsilon_{POD})$$

14: **end if**
15: Set $k = k + 1$
16: **end while**

4.3.3 POD-Greedy algorithm for formulation in $(\mathbf{u}_s, p)$

For the formulation in $(\mathbf{u}_s, p)$, we recall that a stable reduced order model can be obtained by a Galerkin projection on any basis in form $\mathbf{V} = \begin{bmatrix} \mathbf{V}_s & \mathbf{0} \\ \mathbf{0} & \mathbf{V}_f \end{bmatrix}$, where $\mathbf{V}_s$ and $\mathbf{V}_f$ can be viewed as the reduced basis for the structural and fluid part, respectively (see Lemma 3.2.3). Hence, we propose to enrich these two reduced basis separately at each iteration of POD-Greedy algorithm. The POD-Greedy algorithm for formulation in $(\mathbf{u}_s, p)$ is outlined in Algorithm 14.

Algorithm 14 Construction of the basis by Greedy-POD for a parametrized time-domain vibro-acoustic formulated in $(\mathbf{u}_s, p)$

Input: A partition $\{t_n\}_{n=1}^{N_t}$ of the time interval $[0,T]$, tolerance $\epsilon_{POD}, \epsilon_{algo}$, maximum number of iterations N_{max}

Output: A reduced basis $\mathbf{V}$

1: Choose randomly $\boldsymbol{\mu}_1^* \in \mathcal{D}$ and compute the solution of the full model (4.1) for $\boldsymbol{\mu} = \boldsymbol{\mu}_1^*$

2: Construct the basis by POD for the structural part using the snapshot matrix $\mathbf{S}_1^u = [\mathbf{U}(t_1, \boldsymbol{\mu}_1^*) \cdots \mathbf{U}(t_{N_t}, \boldsymbol{\mu}_1^*)]$ and $\epsilon = \epsilon_{POD}$ with Algorithm 6

$$\mathbf{V}_s = \mathrm{POD}(\mathbf{S}_1^u, \epsilon_{POD})$$

3: Construct the basis by POD for the fluid part using the snapshot matrix $\mathbf{S}_1^p = [\mathbf{P}(t_1, \boldsymbol{\mu}_1^*) \cdots \mathbf{P}(t_{N_t}, \boldsymbol{\mu}_1^*)]$ and $\epsilon = \epsilon_{POD}$ with Algorithm 6

$$\mathbf{V}_f = \mathrm{POD}(\mathbf{S}_1^p, \epsilon_{POD})$$

4: Set $k = 1$

5: **while** $(k \leq N_{max})$ **do**

6: Perform the offline stage for the couple $(\mathbf{W}, \mathbf{V})$, where $\mathbf{W} = \mathbf{V} = \begin{bmatrix} \mathbf{V}_s & \mathbf{0} \\ \mathbf{0} & \mathbf{V}_f \end{bmatrix}$, with Algorithm 4

7: Using Galerkin projection on the reduced basis $\mathbf{V}$ to built the parametrized reduced order model (4.6) and compute the error indicator $\Delta(\boldsymbol{\mu})$, for all $\boldsymbol{\mu} \in \mathcal{D}$

8: Set $\boldsymbol{\mu}_{k+1}^* = \arg\max_{\boldsymbol{\mu} \in \mathcal{D}} \Delta(\boldsymbol{\mu})$

9: **if** $\Delta(\boldsymbol{\mu}_{k+1}^*) \leq \epsilon_{algo}$ **then**

10: **break**

11: **else**

12: Compute the solution of the full model (4.1) for $\boldsymbol{\mu} = \boldsymbol{\mu}_{k+1}^*$

13: Compute $\mathbf{Z}_{k+1}^u = \mathrm{POD}(\mathbf{S}_{k+1}^u, \epsilon_{POD})$ using Algorithm 6 with $\mathbf{S}_{k+1}^u = \left[\mathbf{U}(t_1, \boldsymbol{\mu}_{k+1}^*) \cdots \mathbf{U}(t_{N_t}, \boldsymbol{\mu}_{k+1}^*)\right]$

14: Compute $\mathbf{Z}_{k+1}^p = \mathrm{POD}(\mathbf{S}_{k+1}^p, \epsilon_{POD})$ using Algorithm 6 with $\mathbf{S}_{k+1}^p = \left[\mathbf{P}(t_1, \boldsymbol{\mu}_{k+1}^*) \cdots \mathbf{P}(t_{N_t}, \boldsymbol{\mu}_{k+1}^*)\right]$

15: Compute the new reduced basis for the structural part $\mathbf{V}_p$ as

$$\mathbf{V}_s = \mathrm{concatenate}(\mathbf{V}_s, \mathbf{Z}_{k+1}^u; \epsilon_{POD})$$

16: Compute the new reduced basis for the fluid part $\mathbf{V}_f$ as

$$\mathbf{V}_f = \mathrm{concatenate}(\mathbf{V}_f, \mathbf{Z}_{k+1}^p; \epsilon_{POD})$$

17: **end if**

18: Set $k = k + 1$

19: **end while**

4.3.4 POD-Greedy algorithm for formulation in $(\mathbf{u}_s, p, \varphi)$

For the formulation in $(\mathbf{u}_s, p, \varphi)$, we recall that a stable reduced order model can be obtained by a Galerkin projection on any basis in form $\mathbf{V} = \begin{bmatrix} \mathbf{V}_s & \mathbf{0} & \mathbf{0} \\ \mathbf{0} & \mathbf{V}_f & \mathbf{0} \\ \mathbf{0} & \mathbf{0} & \mathbf{V}_f \end{bmatrix}$, where $\mathbf{V}_s$ and $\mathbf{V}_f$ can be viewed as the reduced basis for the structural and fluid part, respectively (see Lemma 3.2.4).

Similarly to the case of the formulation in $(\mathbf{u}_s, p)$, we propose to enrich these two reduced basis separately at each iteration of POD-Greedy algorithm. The POD-Greedy algorithm for formulation in $(\mathbf{u}_s, p, \varphi)$ is outlined in Algorithm 15.

Algorithm 15 Construction of the basis by a POD-Greedy algorithm for a parametrized time-domain vibro-acoustic formulated in $(\mathbf{u}_s, p, \varphi)$

Input: A partition $\{t_n\}_{n=1}^{N_t}$ of the time interval $[0, T]$, tolerance $\epsilon_{POD}, \epsilon_{algo}$, maximum number of iterations N_{max}

Output: A reduced basis $\mathbf{V}$

1: Choose randomly $\boldsymbol{\mu}_1^* \in \mathcal{D}$ and compute the solution of the full model (4.1) for $\boldsymbol{\mu} = \boldsymbol{\mu}_1^*$

2: Construct the basis by POD for the structural part using the snapshot matrix $\mathbf{S}_1^u = [\mathbf{U}(t_1, \boldsymbol{\mu}_1^*) \cdots \mathbf{U}(t_{N_t}, \boldsymbol{\mu}_1^*)]$ and $\epsilon = \epsilon_{POD}$ with Algorithm 6

$$\mathbf{V}_s = \mathrm{POD}(\mathbf{S}_1^u, \epsilon_{POD})$$

3: Construct the basis by POD for the fluid part using the snapshot matrix $\mathbf{S}_1^p = [\mathbf{P}(t_1, \boldsymbol{\mu}_1^*) \cdots \mathbf{P}(t_{N_t}, \boldsymbol{\mu}_1^*)]$ and $\epsilon = \epsilon_{POD}$ with Algorithm 6

$$\mathbf{V}_f = \mathrm{POD}(\mathbf{S}_1^p, \epsilon_{POD})$$

4: Set $k = 1$

5: **while** $(k \leq N_{max})$ **do**

6: Perform the offline stage for the couple $(\mathbf{W}, \mathbf{V})$, where $\mathbf{W} = \mathbf{V} = \begin{bmatrix} \mathbf{V}_s & \mathbf{0} & \mathbf{0} \\ \mathbf{0} & \mathbf{V}_f & \mathbf{0} \\ \mathbf{0} & \mathbf{0} & \mathbf{V}_f \end{bmatrix}$, with Algorithm 4

7: Using Galerkin projection on the reduced basis $\mathbf{V}$ to built the parametrized reduced order model (4.6) and compute the error indicator $\Delta(\boldsymbol{\mu})$, for all $\boldsymbol{\mu} \in \mathcal{D}$

8: Set $\boldsymbol{\mu}_{k+1}^* = \arg\max_{\boldsymbol{\mu} \in \mathcal{D}} \Delta(\boldsymbol{\mu})$

9: **if** $\Delta(\boldsymbol{\mu}_{k+1}^*) \leq \epsilon_{algo}$ **then**

10: **break**

11: **else**

12: Compute the solution of the full model (4.1) for $\boldsymbol{\mu} = \boldsymbol{\mu}_{k+1}^*$

13: Compute $\mathbf{Z}_{k+1}^u = \mathrm{POD}(\mathbf{S}_{k+1}^u, \epsilon_{POD})$ using Algorithm 6 with $\mathbf{S}_{k+1}^u = \left[\mathbf{U}(t_1, \boldsymbol{\mu}_{k+1}^*) \cdots \mathbf{U}(t_{N_t}, \boldsymbol{\mu}_{k+1}^*)\right]$

14: Compute $\mathbf{Z}_{k+1}^p = \mathrm{POD}(\mathbf{S}_{k+1}^p, \epsilon_{POD})$ using Algorithm 6 with $\mathbf{S}_{k+1}^p = \left[\mathbf{P}(t_1, \boldsymbol{\mu}_{k+1}^*) \cdots \mathbf{P}(t_{N_t}, \boldsymbol{\mu}_{k+1}^*)\right]$

15: Compute the new reduced basis for the structural part $\mathbf{V}_p$ as

$$\mathbf{V}_s = \mathrm{concatenate}(\mathbf{V}_s, \mathbf{Z}_{k+1}^u; \epsilon_{POD})$$

16: Compute the new reduced basis for the fluid part $\mathbf{V}_f$ as

$$\mathbf{V}_f = \mathrm{concatenate}(\mathbf{V}_f, \mathbf{Z}_{k+1}^p; \epsilon_{POD})$$

17: **end if**

18: Set $k = k + 1$

19: **end while**

4.3.5 Equivalence of the POD-Greedy algorithm for the formulation in $(\mathbf{u}_s, p)$ and in $(\mathbf{u}_s, p, \varphi)$

In the case where we employ the norm of the residual vector as error indicator, the POD-Greedy algorithm for the formulation in $(\mathbf{u}_s, p)$ and in $(\mathbf{u}_s, p, \varphi)$ are equivalent.

Lemma 4.3.1 *With the error indicator defined in Equation (4.9), the POD-Greedy algorithm 14 for the formulation in $(\boldsymbol{u}_s, p)$ and the POD-Greedy algorithm 15 for the formulation in $(\boldsymbol{u}_s, p, \varphi)$ are equivalent.*

Proof: First, we recall that the Galerkin reduced order model in $(\mathbf{u}_s, p)$ based on the reduced basis $\mathbf{V}_{up} = \begin{bmatrix} \mathbf{V}_s & \mathbf{0} \\ \mathbf{0} & \mathbf{V}_f \end{bmatrix}$ and the Galerkin reduced order model in $(\mathbf{u}_s, p, \varphi)$ based on the reduced basis $\mathbf{V}_{up\varphi} = \begin{bmatrix} \mathbf{V}_s & \mathbf{0} & \mathbf{0} \\ \mathbf{0} & \mathbf{V}_f & \mathbf{0} \\ \mathbf{0} & \mathbf{0} & \mathbf{V}_f \end{bmatrix}$ are equivalent (see Lemma 3.2.5). It remains now to show that both reduced order models have the same values of error indicator. For the formulation in $(\mathbf{u}_s, p)$, we have:

$$
\begin{aligned}
\mathbf{R}_{up}(t;\boldsymbol{\mu}) &:= \mathbf{F}_{up}(t;\boldsymbol{\mu}) - \mathbf{M}_{up}(\boldsymbol{\mu})\mathbf{V}_{up}\ddot{\mathbf{X}}_{up,r}(t;\boldsymbol{\mu}) - \mathbf{C}_{up}(\boldsymbol{\mu})\mathbf{V}_{up}\dot{\mathbf{X}}_{up,r}(t;\boldsymbol{\mu}) - \mathbf{K}_{up}(\boldsymbol{\mu})\mathbf{V}_{up}\mathbf{X}_{up,r}(t;\boldsymbol{\mu}) \\
&= \begin{bmatrix} \mathbf{F}_s(t;\boldsymbol{\mu}) \\ \mathbf{F}_p(t;\boldsymbol{\mu}) \end{bmatrix} - \begin{bmatrix} \mathbf{M}_s(\boldsymbol{\mu}) & \mathbf{0} \\ -\rho_0(\boldsymbol{\mu})\mathbf{K}_c^T & \mathbf{M}_f(\boldsymbol{\mu}) \end{bmatrix} \begin{bmatrix} \mathbf{V}_s\ddot{\mathbf{U}}_{s,r}(t;\boldsymbol{\mu}) \\ \mathbf{V}_f\ddot{\mathbf{P}}_r(t;\boldsymbol{\mu}) \end{bmatrix} - \begin{bmatrix} \mathbf{C}_s(\boldsymbol{\mu}) & \mathbf{0} \\ \mathbf{0} & \mathbf{C}_f(\boldsymbol{\mu}) \end{bmatrix} \begin{bmatrix} \mathbf{V}_s\dot{\mathbf{U}}_{s,r}(t;\boldsymbol{\mu}) \\ \mathbf{V}_f\dot{\mathbf{P}}_r(t;\boldsymbol{\mu}) \end{bmatrix} \\
&\quad - \begin{bmatrix} \mathbf{K}_s(\boldsymbol{\mu}) & \mathbf{K}_c \\ \mathbf{0} & \mathbf{K}_f \end{bmatrix} \begin{bmatrix} \mathbf{V}_s\mathbf{U}_{s,r}(t;\boldsymbol{\mu}) \\ \mathbf{V}_f\mathbf{P}_r(t;\boldsymbol{\mu}) \end{bmatrix} \\
&= \begin{bmatrix} \mathbf{F}_s(t;\boldsymbol{\mu}) - \mathbf{M}_s(\boldsymbol{\mu})\mathbf{V}_s\ddot{\mathbf{U}}_{s,r}(t;\boldsymbol{\mu}) - \mathbf{C}_s(\boldsymbol{\mu})\mathbf{V}_s\dot{\mathbf{U}}_{s,r}(t;\boldsymbol{\mu}) - \mathbf{K}_s(\boldsymbol{\mu})\mathbf{V}_s\mathbf{U}_{s,r}(t;\boldsymbol{\mu}) - \mathbf{K}_c\mathbf{V}_f\mathbf{P}_r(t;\boldsymbol{\mu}) \\ \mathbf{F}_p(t;\boldsymbol{\mu}) + \rho_0(\boldsymbol{\mu})\mathbf{K}_c^T\mathbf{V}_s\ddot{\mathbf{U}}_{s,r}(t;\boldsymbol{\mu}) - \mathbf{M}_f(\boldsymbol{\mu})\mathbf{V}_f\ddot{\mathbf{P}}_r(t;\boldsymbol{\mu}) - \mathbf{C}_f(\boldsymbol{\mu})\mathbf{V}_f\dot{\mathbf{P}}_r(t;\boldsymbol{\mu}) - \mathbf{K}_f\mathbf{V}_f\mathbf{P}_r(t;\boldsymbol{\mu}) \end{bmatrix}
\end{aligned}
$$

For the formulation in $(\mathbf{u}_s, p, \varphi)$, we have:

$$
\begin{aligned}
\mathbf{R}_{up\varphi}(t;\boldsymbol{\mu}) &:= \mathbf{F}_{up\varphi}(t;\boldsymbol{\mu}) - \mathbf{M}_{up\varphi}(\boldsymbol{\mu})\mathbf{V}_{up\varphi}\ddot{\mathbf{X}}_{up\varphi,r}(t;\boldsymbol{\mu}) - \mathbf{C}_{up\varphi}(\boldsymbol{\mu})\mathbf{V}_{up\varphi}\dot{\mathbf{X}}_{up\varphi,r}(t;\boldsymbol{\mu}) - \mathbf{K}_{up\varphi}(\boldsymbol{\mu})\mathbf{V}_{up\varphi}\mathbf{X}_{up\varphi,r}(t;\boldsymbol{\mu}) \\
&= \begin{bmatrix} \mathbf{F}_s(t;\boldsymbol{\mu}) \\ \mathbf{0} \\ \mathbf{F}_p(t;\boldsymbol{\mu}) \end{bmatrix} - \begin{bmatrix} \mathbf{M}_s(\boldsymbol{\mu}) & \mathbf{0} & -\rho_0(\boldsymbol{\mu})\mathbf{K}_c \\ \mathbf{0} & \mathbf{0} & \mathbf{M}_f(\boldsymbol{\mu}) \\ -\rho_0(\boldsymbol{\mu})\mathbf{K}_c^T & \mathbf{M}_f(\boldsymbol{\mu}) & -\rho_0(\boldsymbol{\mu})\mathbf{K}_f \end{bmatrix} \begin{bmatrix} \mathbf{V}_s\ddot{\mathbf{U}}_{s,r}(t;\boldsymbol{\mu}) \\ \mathbf{V}_f\ddot{\mathbf{P}}_r(t;\boldsymbol{\mu}) \\ \mathbf{V}_f\ddot{\boldsymbol{\varphi}}_r(t;\boldsymbol{\mu}) \end{bmatrix} \\
&\quad - \begin{bmatrix} \mathbf{C}_s(\boldsymbol{\mu}) & \mathbf{0} & \mathbf{0} \\ \mathbf{0} & \mathbf{0} & \mathbf{0} \\ \mathbf{0} & \mathbf{C}_f(\boldsymbol{\mu}) & \mathbf{0} \end{bmatrix} \begin{bmatrix} \mathbf{V}_s\dot{\mathbf{U}}_{s,r}(t;\boldsymbol{\mu}) \\ \mathbf{V}_f\dot{\mathbf{P}}_r(t;\boldsymbol{\mu}) \\ \mathbf{V}_f\dot{\boldsymbol{\varphi}}_r(t;\boldsymbol{\mu}) \end{bmatrix} - \begin{bmatrix} \mathbf{K}_s(\boldsymbol{\mu}) & \mathbf{0} & \mathbf{0} \\ \mathbf{0} & \frac{1}{\rho_0(\boldsymbol{\mu})}\mathbf{M}_f(\boldsymbol{\mu}) & \mathbf{0} \\ \mathbf{0} & \mathbf{0} & \mathbf{0} \end{bmatrix} \begin{bmatrix} \mathbf{V}_s\mathbf{U}_{s,r}(t;\boldsymbol{\mu}) \\ \mathbf{V}_f\mathbf{P}_r(t;\boldsymbol{\mu}) \\ \mathbf{V}_f\boldsymbol{\varphi}_r(t;\boldsymbol{\mu}) \end{bmatrix} \\
&= \begin{bmatrix} \mathbf{F}_s(t;\boldsymbol{\mu}) - \mathbf{M}_s(\boldsymbol{\mu})\mathbf{V}_s\ddot{\mathbf{U}}_{s,r}(t;\boldsymbol{\mu}) - \mathbf{C}_s(\boldsymbol{\mu})\mathbf{V}_s\dot{\mathbf{U}}_{s,r}(t;\boldsymbol{\mu}) - \mathbf{K}_s(\boldsymbol{\mu})\mathbf{V}_s\mathbf{U}_{s,r}(t;\boldsymbol{\mu}) + \rho_0(\boldsymbol{\mu})\mathbf{K}_c\mathbf{V}_f\ddot{\boldsymbol{\varphi}}_r(t;\boldsymbol{\mu}) \\ -\mathbf{M}_f(\boldsymbol{\mu})\mathbf{V}_f\ddot{\boldsymbol{\varphi}}_r(t;\boldsymbol{\mu}) - \frac{1}{\rho_0(\boldsymbol{\mu})}\mathbf{M}_f\mathbf{V}_f\mathbf{P}_r(t;\boldsymbol{\mu}) \\ \mathbf{F}_p(t;\boldsymbol{\mu}) + \rho_0(\boldsymbol{\mu})\mathbf{K}_c^T\mathbf{V}_s\ddot{\mathbf{U}}_{s,r}(t;\boldsymbol{\mu}) - \mathbf{M}_f(\boldsymbol{\mu})\mathbf{V}_f\ddot{\mathbf{P}}_r(t;\boldsymbol{\mu}) - \mathbf{C}_f(\boldsymbol{\mu})\mathbf{V}_f\dot{\mathbf{P}}_r(t;\boldsymbol{\mu}) + \rho(\boldsymbol{\mu})\mathbf{K}_f\mathbf{V}_f\ddot{\boldsymbol{\varphi}}_r(t;\boldsymbol{\mu}) \end{bmatrix}
\end{aligned}
$$

We recall that $\ddot{\boldsymbol{\varphi}}_r(t;\boldsymbol{\mu}) = -\frac{1}{\rho(\boldsymbol{\mu})}\mathbf{P}_r(t;\boldsymbol{\mu})$ (see the demonstration of Lemma 3.2.5). Using this relation to eliminate the variable $\boldsymbol{\varphi}$ leads to:

$$
\mathbf{R}_{up\varphi}(t;\boldsymbol{\mu}) = \begin{bmatrix} \mathbf{F}_s(t;\boldsymbol{\mu}) - \mathbf{M}_s(\boldsymbol{\mu})\mathbf{V}_s\ddot{\mathbf{U}}_{s,r}(t;\boldsymbol{\mu}) - \mathbf{C}_s(\boldsymbol{\mu})\mathbf{V}_s\dot{\mathbf{U}}_{s,r}(t;\boldsymbol{\mu}) - \mathbf{K}_s(\boldsymbol{\mu})\mathbf{V}_s\mathbf{U}_{s,r}(t;\boldsymbol{\mu}) - \mathbf{K}_c\mathbf{V}_f\mathbf{P}_r(t;\boldsymbol{\mu}) \\ \mathbf{0} \\ \mathbf{F}_p(t;\boldsymbol{\mu}) + \rho_0(\boldsymbol{\mu})\mathbf{K}_c^T\mathbf{V}_s\ddot{\mathbf{U}}_{s,r}(t;\boldsymbol{\mu}) - \mathbf{M}_f(\boldsymbol{\mu})\mathbf{V}_f\ddot{\mathbf{P}}_r(t;\boldsymbol{\mu}) - \mathbf{C}_f(\boldsymbol{\mu})\mathbf{V}_f\dot{\mathbf{P}}_r(t;\boldsymbol{\mu}) - \mathbf{K}_f\mathbf{V}_f\mathbf{P}_r(t;\boldsymbol{\mu}) \end{bmatrix}
$$

Hence, we have $||\mathbf{R}_{up}(t;\boldsymbol{\mu})|| = ||\mathbf{R}_{up\varphi}(t;\boldsymbol{\mu})||$. This implies that the value of error indicator defined in Equation (4.9) is the same for both reduced order models; $\Delta_{up}(\boldsymbol{\mu}) = \Delta_{up\varphi}(\boldsymbol{\mu})$.

□

4.3.6 An efficient computation procedure for the case where POD-Greedy algorithm generates a hierarchical reduced basis

We say that POD-Greedy algorithm generates a hierarchical reduced basis if, at each iterations, the current reduced basis contains the reduced basis of the previous section, that is $\mathbf{V}_k = \left[\mathbf{V}_{k-1}\ \mathbf{v}_{N_{k-1}+1}\cdots\mathbf{v}_{N_k}\right] \in \mathbb{R}^{n\times N_k}$, where N_k denotes the size of the reduced basis at iteration k. In the case that the test subspace $\mathbf{W}_k$ is also hierarchical (*which is the case for POD-Greedy Algorithm 13, 14 and 15*), we remark that the data to be computed by Algorithm 4 at the step 5 of the POD-Greedy Algorithm 10 are partially computed in the previous iteration.

At iteration $k \geq 2$, the product of matrices and the basis $\mathbf{A}_l\mathbf{V}_{k-1}$, for $A \in \{M, C, K\}$ and $l = 1, \cdots, N_A$, are already computed in the previous iteration. Hence, we only need to compute $\mathbf{A}_l\mathbf{v}_j$ for $j = N_{k-1}+1, \cdots, N_k$. This requires a total complexity in $O(n^2(N_k - N_{k-1})(N_M + N_C + N_K))$ instead of $O(n^2N_k(N_M + N_C + N_K))$. For the case of sparse matrices with n_z non-zeros entries, it is in $O(n_z(N_k - N_{k-1})(N_M + N_C + N_K))$ instead of in $O(n_zN_k(N_M + N_C + N_K))$.

In what follows, we use the superscript ^{k} for the quantity corresponding to the iteration k of POD-Greedy Algorithm. We remark that the relation of the reduced matrices $\mathbf{A}_{l,r}^k$ and $\mathbf{A}_{l,r}^{k-1}$ writes:

$$\mathbf{A}_{l,r}^k = \begin{bmatrix} \mathbf{A}_{l,r}^{k-1} & \left[\mathbf{w}_1\cdots\mathbf{w}_{N_{k-1}}\right]^T\mathbf{A}_l\left[\mathbf{v}_{N_{k-1}+1}\cdots\mathbf{v}_{N_k}\right] \\ \left[\mathbf{w}_{N_{k-1}+1}\cdots\mathbf{w}_{N_k}\right]^T\mathbf{A}_l\left[\mathbf{v}_1\cdots\mathbf{v}_{N_{k-1}}\right] & \left[\mathbf{w}_{N_{k-1}+1}\cdots\mathbf{w}_{N_k}\right]^T\mathbf{A}_l\left[\mathbf{v}_{N_{k-1}+1}\cdots\mathbf{v}_{N_k}\right] \end{bmatrix} \tag{4.23}$$

Then, we only need to compute $\left[\mathbf{w}_1\cdots\mathbf{w}_{N_{k-1}}\right]^T\mathbf{A}_l\left[\mathbf{v}_{N_{k-1}+1}\cdots\mathbf{v}_{N_k}\right]$ and $\left[\mathbf{w}_{N_{k-1}+1}\cdots\mathbf{w}_{N_k}\right]^T\mathbf{A}_l\mathbf{V}_k$, which requires a total complexity in $O(n(N_k^2 - N_{k-1}^2)(N_M + N_C + N_K))$ instead of in $O(nN_k^2(N_M + N_C + N_K))$. The same observation holds for the reduced vectors. We have the relation of the reduced vectors $\mathbf{F}_{l,r}^k$ and $\mathbf{F}_{l,r}^{k-1}$:

$$\mathbf{F}_{l,r}^k = \begin{bmatrix} \mathbf{F}_{l,r}^{k-1} \\ \left[\mathbf{w}_{N_{k-1}+1}\cdots\mathbf{w}_{N_k}\right]^T\mathbf{F}_l \end{bmatrix} \tag{4.24}$$

which allows us to compute only $\left[\mathbf{w}_{N_{k-1}+1}\cdots\mathbf{w}_{N_k}\right]^T\mathbf{F}_l$ to obtain $\mathbf{F}_{l,r}^k$. The total complexity of the computation of the reduced vectors is then in $O(n(N_k - N_{k-1})N)$ instead of $O(nN_kN)$.

We now turn to the data for error indicator. To start, we note that the matrix $\mathbf{M}_{FF}$ is independent of $\mathbf{V}$. For the matrices $\mathbf{M}_{A_lF}$, for $A \in \{M, C, K\}$ and $l \in 1, \cdots, N_A$, we have the relation:

$$\mathbf{M}_{A_lF}^k = \begin{bmatrix} \mathbf{M}_{A_lF}^{k-1} & \left[\mathbf{A}_l\mathbf{v}_{N_{k-1}+1}\cdots\mathbf{A}_l\mathbf{v}_{N_k}\right]^T\begin{bmatrix}\mathbf{F}_1 & \cdots & \mathbf{F}_{N_F}\end{bmatrix} \end{bmatrix} \tag{4.25}$$

Then, we only need to compute $(\mathbf{A}_l\mathbf{v}_i)^T\mathbf{F}_j$, for $i = N_{k-1}+1, \cdots, N_k$ and $j = 1, \cdots, N_F$. The total complexity of the computation of the matrices $\mathbf{M}_{A_lF}$, for $A \in \{M, C, K\}$ and $l \in 1, \cdots, N_A$, is in $O(n(N_k - N_{k-1})N_F(N_M + N_C + N_K))$ instead of $O(nN_kN_F(N_M + N_C + N_K))$. Finally, for the matrices $\mathbf{M}_{A_lB_k}$, where $A \geq B \in \{M, C, K\}$ (with convention $M > C > K$), $l = 1, \cdots, N_A$ and $k = 1, \cdots, N_B$, we have the relation:

$$\mathbf{M}_{A_lB_k}^k = \begin{bmatrix} \mathbf{M}_{A_lB_k}^{k-1} & \left[\mathbf{A}_l\mathbf{v}_1\cdots\mathbf{A}_l\mathbf{v}_{N_{k-1}}\right]^T\left[\mathbf{B}_k\mathbf{v}_{N_{k-1}+1}\cdots\mathbf{B}_k\mathbf{v}_{N_k}\right] \\ \left[\mathbf{A}_l\mathbf{v}_{N_{k-1}+1}\cdots\mathbf{A}_l\mathbf{v}_{N_k}\right]^T\left[\mathbf{B}_k\mathbf{v}_1\cdots\mathbf{B}_k\mathbf{v}_{N_{k-1}}\right] & \left[\mathbf{A}_l\mathbf{v}_{N_{k-1}+1}\cdots\mathbf{A}_l\mathbf{v}_{N_k}\right]^T\left[\mathbf{B}_k\mathbf{v}_{N_{k-1}+1}\cdots\mathbf{B}_k\mathbf{v}_{N_k}\right] \end{bmatrix} \tag{4.26}$$

which allows us to obtain $\mathbf{M}_{A_lB_k}^k$ by computing only $\left[\mathbf{A}_l\mathbf{v}_1\cdots\mathbf{A}_l\mathbf{v}_{N_{k-1}}\right]^T\left[\mathbf{B}_k\mathbf{v}_{N_{k-1}+1}\cdots\mathbf{B}_k\mathbf{v}_{N_k}\right]$ and $\left[\mathbf{A}_l\mathbf{v}_{N_{k-1}+1}\cdots\mathbf{A}_l\mathbf{v}_{N_k}\right]^T\mathbf{B}_k\mathbf{V}_k$. The total complexity in the computation of $\mathbf{M}_{A_lB_k}$, where

$A \geq B \in \{M, C, K\}$ (with convention $M > C > K$), $l = 1, \cdots, N_A$ and $k = 1, \cdots, N_B$ is in $O(n(N_k^2 - N_{k-1}^2)(N_M(N_M + N_C + N_K) + N_C(N_C + N_K))$ instead of $O(nN_k^2(N_M(N_M + N_C + N_K) + N_C(N_C + N_K)))$.

To summary, Table 4.1 presents the complexity of the proposed computation procedure in the case of a hierarchical reduced basis in compared with the general case.

Data	Case of a hierarchical reduced basis	Case general
$\mathbf{A}_l\mathbf{V}_k$	$O(n^2(N_k - N_{k-1})(N_M + N_C + N_K))$	$O(n^2N_k(N_M + N_C + N_K))$
$\mathbf{A}_{l,r}$	$O(n(N_k^2 - N_{k-1}^2)(N_M + N_C + N_K))$	$O(nN_k^2(N_M + N_C + N_K))$
$\mathbf{F}_{l,r}$	$O(n(N_k - N_{k-1})N_F)$	$O(nN_kN_F)$
$\mathbf{M}_{A_lF}$	$O(n(N_k - N_{k-1})N_F(N_M + N_C + N_K))$	$O(nN_kN_F(N_M + N_C + N_K))$
$\mathbf{M}_{A_lB_k}$	$O(n(N_k^2 - N_{k-1}^2)(N_M(N_M + N_C + N_K) + N_C(N_C + N_K)))$	$O(nN_k^2(N_M(N_M + N_C + N_K) + N_C(N_C + N_K)))$

Table 4.1: Complexity of the computation of the offline data (step 5) of POD-Algorithm 10 at iteration $k \geq 2$

Remark 4.3.7 Assuming that the POD-Greedy Algorithm 10 achieves the stopping criterion in K iterations, the total complexity in the computation of the products of matrices and the basis $\mathbf{A}_l\mathbf{V}_k$, the reduced vectors $\mathbf{F}_{l,r}$ and the matrices $\mathbf{M}_{A_lF}$ for the case where the reduced basis is not hierarchical is $(\sum_{k=1}^{K} N_k)/N_K$ times bigger than the case of hierarchical reduced basis. For the reduced matrices $\mathbf{A}_{l,r}$ and the matrices $\mathbf{M}_{A_lB_k}$, the complexity of the case where the reduced basis is not hierarchical is $(\sum_{k=1}^{K} N_k^2)/N_K^2$ times bigger than the case of hierarchical reduced basis.

4.4 Workflow

In this section, we condense the results from the previous sections into a structured workflow for performing efficient parametrized time-domain simulation of vibro-acoustic finite element models by using the stabilization reduced order modelling technique presented in Chapter 3, combined with a POD-Greedy algorithm. A schematic of this workflow is depicted in Figure 4.1.

The first step is to choose the formulation and to write the corresponding left hand-side operators $\mathbf{M}(\boldsymbol{\mu})$, $\mathbf{C}(\boldsymbol{\mu})$, $\mathbf{K}(\boldsymbol{\mu})$ and the vector $\mathbf{F}(t; \boldsymbol{\mu})$ of the right-hand side in an affine dependent form in parameter $\boldsymbol{\mu} \in \mathcal{D}$ as in Equation (4.2). To obtain such decomposition, it requires a knowledge on the definition of each sub-matrices of the problem (we will see in Section 5.2.4 that the Empirical Interpolation Method (EIM) [17] can be employed to avoid this constraint).

The second step consists of the construction of the reduced basis with a POD-Greedy algorithm which depends on the choice of formulation. For the formulation in $(\mathbf{u}_s, \phi)$, the POD-Greedy Algorithm 13 is employed. For the formulation in $(\mathbf{u}_s, p)$ and in $(\mathbf{u}_s, p, \varphi)$, we use respectively the POD-Greedy Algorithm 14 and 15 which are equivalent (see Lemma 4.3.1). The last step of the offline stage is to pre-compute the data for the online stage outlined by Algorithm 5.

Now that we have computed all the data of the offline stage, it becomes possible to compute the physical output of interest predicted by reduced order model for any values of the parameter

$\boldsymbol{\mu} \in \mathcal{D}$ by Algorithm 5 with a complexity relatively small compared to the finite element model.

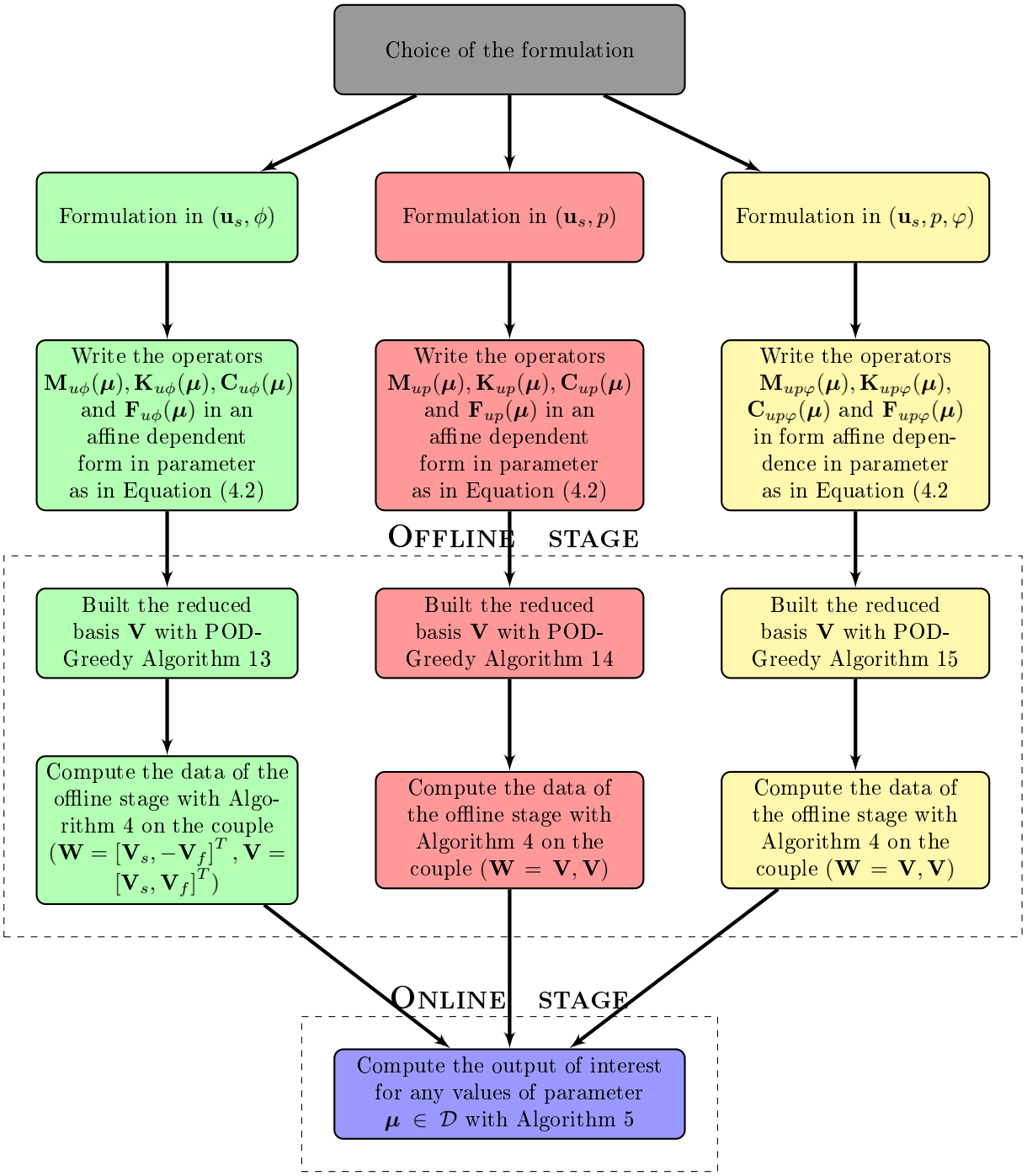

Figure 4.1: Workflow for the case of an affine dependency in parameter

4.5 Further remarks and open issues

Before presenting some numerical experiments on the efficiency of the proposed framework, we would like to point out the limits of our approach and some ideas to overcome these limits.

4.5.1 On the numerical lower bound of error indicator

First of all, we recall that the computation of error indicator Δ defined in Equation (4.9) using the relation (4.10) suffers from the round-off errors. This implies that it has a numerical lower bound of order of magnitude $\sqrt{\epsilon_{machine}} \approx 10^{-7}$ (see Remark 4.2.2), where $\epsilon_{machine}$ denotes the machine precision. Despite that, it should be noted that this lower bound is acceptable in practice since the full model is not so accurate for the PDE model (which is known as errors of finite element discretization) and the PDE model is not so accurate compared to the real physical problem (which is known as errors of modelling). In addition, the numerical resolution of the finite element model can also introduce another source of errors, for instance by the linear system solver and the time-discretization scheme. As a result, a stopping criterion ϵ_{algo} in POD-Greedy Algorithm 10 is usually fixed with a value greater than 10^{-7} so that this numerical lower bound has no impact in the practice.

However, it should be mentioned that three alternatives can be used to avoid this numerical lower bound of the error indicator Δ of Equation (4.9):

- The first one is not online efficient in the sense that the computation cost in online phase depends on the size of the full model. The idea is to compute first the residual vector $\mathbf{R}(t, \boldsymbol{\mu})$ defined in Equation (4.8) rather than computing directly its norm using Equation (4.10). To reduced some computational costs in online part, we can pre-compute and save in the offline stage the product of matrices A_l, where $A \in \{M, C, K\}, l \in \{1, \cdots N_A\}$, and the reduced basis $\mathbf{V}$. By doing so, the complexity of the computation of Δ in online stage is in $O(nN(N_M + N_C + N_K)N_t)$, where n and N are the size of the full model and the reduced model respectively, N_t is the number of time steps and N_A is the number of terms in the affine decomposition assumption of the matrix $A \in \{M, C, K\}$ of Equation (4.2). This procedure is mathematically equivalent to our approach but it has a numerical lower bound due to the round-off errors in order of $\epsilon_{machine}$, and not $\sqrt{\epsilon_{machine}}$.

- The second alternative, exploited from [31], is not only equivalent to our approach but also is online efficient. The key idea is to rewrite the norm of the residual of Equation (4.10) as:

$$||\mathbf{R}(t, \boldsymbol{\mu})||^2 = \sum_{i=1}^{d_R} \alpha_i^R(t; \boldsymbol{\mu}) ||\mathbf{R}(t, \boldsymbol{\mu}_i)||^2 \tag{4.27}$$

  where the coefficient $(\alpha_i^R(t; \boldsymbol{\mu}))_{1 \leq i \leq d_F}$ is the solution of a linear system of $d_R \times d_R$, and $(\boldsymbol{\mu}_i)_{1 \leq i \leq d_R}$ could be chosen randomly. To simplify our presentation, let us consider in the case of $||\mathbf{F}(t, \boldsymbol{\mu})||^2$ defined in the first equation of (4.10). Let us denote by $d_F = N_F(N_F + 1)/2$ and define $\mathbf{X}^F(t; \boldsymbol{\mu}) \in \mathbb{R}^{d_F}$ as a vector with the component $\left[\theta_i^F(t; \boldsymbol{\mu})\theta_j^F(t; \boldsymbol{\mu})\right]_{1 \leq i \leq j \leq N_F}$ and $\mathbf{q}^F \in \mathbb{R}^{d_F}$ as a vector with the component $[c_{ij}(M_{FF})_{ij}]_{1 \leq i \leq j \leq N_F}$, where $c_{ij} = 1$ if $i = j$ and $c_{ij} = 2$ if $i \neq j$. Using the symmetry of the matrix $\mathbf{M}_{FF}$, the norm of the right-hand side vector can also be written as:

$$||\mathbf{F}(t, \boldsymbol{\mu})||^2 = \sum_{i=1}^{N_F} \theta_i^F(t; \boldsymbol{\mu})^2 (\mathbf{M}_{FF})_{ii} + \sum_{1 \leq i < j \leq N_F} 2\theta_i^F(t; \boldsymbol{\mu})\theta_j^F(t; \boldsymbol{\mu})(\mathbf{M}_{FF})_{ij} \tag{4.28}$$

$$= \sum_{i=1}^{d_F} q_p^F X_p^F(t; \boldsymbol{\mu}) \tag{4.29}$$

where q_p^F, X_p^F is the p^{th} component of the vector $\mathbf{q}^F$ and $\mathbf{X}^F \in \mathbb{R}^{d_F}$ respectively. By taking d_F values, possibly random, $(\boldsymbol{\mu}_i)_{1\leq i\leq d_F}$ of the parameter $\boldsymbol{\mu} \in \mathcal{D}$, so that the dimension of span$\{\mathbf{X}^F(t;\boldsymbol{\mu}_i), 1 \leq i \leq d_F\}$ is equal to d_F for all $t \in [0,T]$, we can write $\mathbf{X}^F(t;\boldsymbol{\mu})$ as:

$$\mathbf{X}^F(t;\boldsymbol{\mu}) = \sum_{i=1}^{d_F} \alpha_i^F(t;\boldsymbol{\mu})\mathbf{X}^F(t;\boldsymbol{\mu}_i) \tag{4.30}$$

where the coefficient $(\alpha_i^F(t;\boldsymbol{\mu}))_{1\leq i\leq d_F}$ is the solution of the linear system $\sum_{j=1}^{d_F} A_{ij}^F \alpha_j^F(t;\boldsymbol{\mu}) = X_i^F(t;\boldsymbol{\mu}), i = 1,\cdots,N_F$, where $A_{ij}^F := X_i^F(t;\boldsymbol{\mu}_j)$. Injecting the expression of Equation (4.30) into Equation(4.29) yields:

$$||\mathbf{F}(t,\boldsymbol{\mu})||^2 = \sum_{p=1}^{d_F}\sum_{i=1}^{d_F} q_p^F \alpha_i^F(t;\boldsymbol{\mu}) X_p^F(t;\boldsymbol{\mu}_i) \tag{4.31}$$

$$= \sum_{i=1}^{d_F} \alpha_i^F(t;\boldsymbol{\mu}) \sum_{p=1}^{d_F} q_p^F X_p^F(t;\boldsymbol{\mu}_i) \tag{4.32}$$

$$= \sum_{i=1}^{d_F} \alpha_i^F(t;\boldsymbol{\mu}) ||\mathbf{F}(t,\boldsymbol{\mu}_i)||^2 \tag{4.33}$$

The idea is straightforward for the case of residual norm. With Equation (4.27), we can compute at the online stage the norm of the residual norm with a complexity independent of the size of the full model. Thus, it is online efficient provided that the value of residual norm for $\boldsymbol{\mu} \in \{\boldsymbol{\mu}_i, 1 \leq i \leq d_R\}$ are pre-computed during the offline stage. Since the value of residual norm for $\boldsymbol{\mu} \in \{\boldsymbol{\mu}_i, 1 \leq i \leq d_R\}$ is evaluated in the offline stage, we can use the accurate formula as proposed in the first alternative. Assuming that the resolution of a linear system $d_R \times d_R$ is in $O(d_R^3)$, the complexity in the online stage of this approach is in $O(N_t d_R^3)$ where N_t is the number of time step.

- A drawback of the second alternative is on the choice of the value parameters $\{\boldsymbol{\mu}_i, 1 \leq i \leq d_R\}$. Even though a random selection could work well in practice, it has been observed in [32] that the matrix representing the linear system to be solved exhibits large condition numbers especially when the chosen values of the parameters are very close. To remedy this, the third alternative consists of exploiting the Empirical Interpolation method (EIM) [17], see Section 5.2.1 for a short presentation of EIM, in order to obtain an approximation of the vector $\mathbf{X}^R(t;\boldsymbol{\mu})$ representing the residual norm (in analogue with the vector $\mathbf{X}^R(t;\boldsymbol{\mu})$ mentioned in the second alternative) as $\sum_{i=1}^{d_R^{EIM}} \alpha_i^R(t;\boldsymbol{\mu})\mathbf{X}^R(t;\boldsymbol{\mu}_i)$. This implies that $||\mathbf{R}(t;\boldsymbol{\mu})||^2 \approx \sum_{i=1}^{d_R^{EIM}} \alpha_i^F(t;\boldsymbol{\mu})||\mathbf{R}(t;\boldsymbol{\mu}_i)||^2$, where $d_R^{EIM} \leq d_R$ and such that the coefficient $(\alpha_i^R(t;\boldsymbol{\mu}))_{1\leq i\leq d_R^{EIM}}$ is the solution of a better conditioned linear system.

For the presentation in more detail and numerical experiments of the last two alternative approaches in the case of parametrized stationary problem, we refer to [31, 32].

4.5.2 On the a posteriori error estimator

Instead of using the error indicator in the construction of the reduced basis by the POD-Greedy Algorithm 10, a more rigorous way is to use the posteriori error estimator of either the state

error or quantity of interest error, see for instance [62, 100] for the case of a parametrized parabolic equation. For the parametrized time-domain vibro-acoustic formulated in $(\mathbf{u}_s, p)$, we propose a posteriori error bound of the state error in energy norm as stated in the following theorem.

Theorem 4.5.1 *We denote by* $\left[\boldsymbol{R}_s(t;\mu)^T \quad \boldsymbol{R}_\phi(t;\mu)^T\right]^T = \boldsymbol{F}_{u\phi}(t;\boldsymbol{\mu}) - \boldsymbol{M}_{u\phi}(\boldsymbol{\mu})\boldsymbol{V}\ddot{\boldsymbol{X}}_r(t;\boldsymbol{\mu}) - \boldsymbol{C}_{u\phi}(\boldsymbol{\mu})\boldsymbol{V}\dot{\boldsymbol{X}}_r(t;\boldsymbol{\mu}) - \boldsymbol{K}_{u\phi}(\boldsymbol{\mu})\boldsymbol{V}\boldsymbol{X}_r(t;\boldsymbol{\mu})$ *the residual vector,* $\boldsymbol{e}_s := \boldsymbol{U}_s - \boldsymbol{U}_s^{rom}$ *the error of the structural part and* $\boldsymbol{e}_f := \boldsymbol{\Phi}_f - \boldsymbol{\Phi}_f^{rom}$ *the error of the fluid part. We introduce an energy norm* $||\cdot||_{\boldsymbol{\mu}}$ *defined by:*

$$||\begin{bmatrix}\boldsymbol{v}_s^T & \boldsymbol{v}_f^T\end{bmatrix}^T||_{\boldsymbol{\mu}} := \sqrt{\dot{\boldsymbol{v}}_s^T\boldsymbol{M}_s(\boldsymbol{\mu})\dot{\boldsymbol{v}}_s + \boldsymbol{v}_s^T\boldsymbol{K}_s(\boldsymbol{\mu})\boldsymbol{v}_s + \dot{\boldsymbol{v}}_f^T\tilde{\boldsymbol{M}}_f(\boldsymbol{\mu})\dot{\boldsymbol{v}}_f + \boldsymbol{v}_f^T\tilde{\boldsymbol{K}}_f(\boldsymbol{\mu})\boldsymbol{v}_f} \tag{4.34}$$

where $\tilde{\boldsymbol{M}}_f(\boldsymbol{\mu}) = \rho_0(\boldsymbol{\mu})\boldsymbol{M}_f(\boldsymbol{\mu})$ *and* $\tilde{\boldsymbol{K}}_f(\boldsymbol{\mu}) = \rho_0(\boldsymbol{\mu})\boldsymbol{K}_f(\boldsymbol{\mu})$*. The error between the solution of ROM and the full model in norm* $||\cdot||_{\boldsymbol{\mu}}$ *is bounded by:*

$$||\begin{bmatrix}\boldsymbol{e}_s^T(t;\boldsymbol{\mu}) & \boldsymbol{e}_f^T(t;\boldsymbol{\mu})\end{bmatrix}^T||_{\boldsymbol{\mu}} \leq \sqrt{\int_0^t e^{t-u}\left(\frac{1}{\alpha_{M_s}(\boldsymbol{\mu})}||\boldsymbol{R}_s(u;\boldsymbol{\mu})||^2 + \frac{1}{\alpha_{\tilde{M}_f}(\boldsymbol{\mu})}||\boldsymbol{R}_\phi(u;\boldsymbol{\mu})||^2\right)du} \tag{4.35}$$

for $t \geq 0$ *and* $\boldsymbol{\mu} \in \mathcal{D}$*, where* $\alpha_{M_s}(\boldsymbol{\mu})$ *and* $\alpha_{\tilde{M}_f}(\boldsymbol{\mu})$ *are respectively coercivity constant of the matrices* $M_s(\boldsymbol{\mu})$ *and* $\tilde{M}_f(\boldsymbol{\mu})$*.*

Proof: By definition of residual vector, we have:

$$\begin{cases}\mathbf{M}_s\ddot{\mathbf{e}}_s - \rho_0\mathbf{K}_c\dot{\mathbf{e}}_f + \mathbf{C}_s\dot{\mathbf{e}}_s + \mathbf{K}_s\mathbf{e}_s = \mathbf{R}_s \\ \tilde{\mathbf{M}}_f\ddot{\mathbf{e}}_f + \rho_0\mathbf{K}_c^T\dot{\mathbf{e}}_s + \rho_0\mathbf{C}_f\dot{\mathbf{e}}_f + \tilde{\mathbf{K}}_f\mathbf{e}_f = -\mathbf{R}_\phi\end{cases} \tag{4.36}$$

By left multiplying with $\dot{\mathbf{e}}_s^T$ and $\dot{\mathbf{e}}_f^T$ in the first and the second equation of (4.36), we have:

$$\begin{cases}\dot{\mathbf{e}}_s^T\mathbf{M}_s\ddot{\mathbf{e}}_s - \rho_0\dot{\mathbf{e}}_s^T\tilde{\mathbf{K}}_c\dot{\mathbf{e}}_f + \dot{\mathbf{e}}_s^T\mathbf{C}_s\dot{\mathbf{e}}_s + \dot{\mathbf{e}}_s^T\mathbf{K}_s\mathbf{e}_s = \dot{\mathbf{e}}_s^T\mathbf{R}_s \\ \dot{\mathbf{e}}_f^T\tilde{\mathbf{M}}_f\ddot{\mathbf{e}}_f + \rho_0\dot{\mathbf{e}}_f^T\tilde{\mathbf{K}}_c^T\dot{\mathbf{e}}_s + \rho_0\dot{\mathbf{e}}_f^T\mathbf{C}_f\dot{\mathbf{e}}_f + \dot{\mathbf{e}}_f^T\tilde{\mathbf{K}}_f\mathbf{e}_f = -\dot{\mathbf{e}}_f^T\mathbf{R}_\phi\end{cases} \tag{4.37}$$

Combining the two equations of (4.37), we have:

$$\dot{\mathbf{e}}_s^T\mathbf{M}_s\ddot{\mathbf{e}}_s + \dot{\mathbf{e}}_s^T\mathbf{K}_s\mathbf{e}_s + \dot{\mathbf{e}}_f^T\tilde{\mathbf{M}}_f\ddot{\mathbf{e}}_f + \dot{\mathbf{e}}_f^T\tilde{\mathbf{K}}_f\mathbf{e}_f + \underbrace{\dot{\mathbf{e}}_s^T\mathbf{C}_s\dot{\mathbf{e}}_s + \rho_0\dot{\mathbf{e}}_f^T\mathbf{C}_f\dot{\mathbf{e}}_f}_{\geq 0} = \dot{\mathbf{e}}_s^T\mathbf{R}_s - \dot{\mathbf{e}}_f^T\mathbf{R}_\phi \tag{4.38}$$

$$\Rightarrow \frac{d}{dt}\left(\dot{\mathbf{e}}_s^T\mathbf{M}_s\dot{\mathbf{e}}_s + \mathbf{e}_s^T\mathbf{K}_s\mathbf{e}_s + \dot{\mathbf{e}}_f^T\tilde{\mathbf{M}}_f\dot{\mathbf{e}}_f + \mathbf{e}_f^T\tilde{\mathbf{K}}_f\mathbf{e}_f\right) \leq 2\left(\dot{\mathbf{e}}_s^T\mathbf{R}_s - \dot{\mathbf{e}}_f^T\mathbf{R}_\phi\right) \tag{4.39}$$

Using the Cauchy-Schwarz inequality in the right-hand side of the inequality (4.39) yields:

$$\frac{d}{dt}\left(\dot{\mathbf{e}}_s^T\mathbf{M}_s\dot{\mathbf{e}}_s + \mathbf{e}_s^T\mathbf{K}_s\mathbf{e}_s + \dot{\mathbf{e}}_f^T\tilde{\mathbf{M}}_f\dot{\mathbf{e}}_f + \mathbf{e}_f^T\tilde{\mathbf{K}}_f\mathbf{e}_f\right) \leq 2\left(||\dot{\mathbf{e}}_s||||\mathbf{R}_s|| + ||\dot{\mathbf{e}}_f||||\mathbf{R}_\phi||\right) \tag{4.40}$$

We now recall the Young inequality (for $a, b \in \mathbb{R}$ and $\rho > 0$):

$$2|a||b| \leq \frac{a^2}{\rho^2} + \rho^2 b^2 \tag{4.41}$$

which we apply twice: first choosing $a = ||\mathbf{R}_s||$, $b = ||\dot{\mathbf{e}}_s||$ and $\rho = \sqrt{\alpha_{M_s}}$ to obtain:

$$||\dot{\mathbf{e}}_s||||\mathbf{R}_s|| \leq \frac{||\mathbf{R}_s||^2}{\alpha_{M_s}} + \alpha_{M_s}||\dot{\mathbf{e}}_s||^2 \tag{4.42}$$

and second, choosing $a = ||\mathbf{R}_\phi||$, $b = ||\dot{\mathbf{e}}_f||$ and $\rho = \sqrt{\alpha_{\tilde{M}_f}}$ to obtain:

$$||\dot{\mathbf{e}}_f||||\mathbf{R}_\phi|| \leq \frac{||\mathbf{R}_\phi||^2}{\alpha_{\tilde{M}_f}} + \alpha_{\tilde{M}_f}||\dot{\mathbf{e}}_f||^2 \tag{4.43}$$

Injecting the inequalities (4.42)-(4.43) in (4.40), we obtain:

$$\frac{d}{dt}\left(\dot{\mathbf{e}}_s^T\mathbf{M}_s\dot{\mathbf{e}}_s + \mathbf{e}_s^T\mathbf{K}_s\mathbf{e}_s + \dot{\mathbf{e}}_f^T\tilde{\mathbf{M}}_f\dot{\mathbf{e}}_f + \mathbf{e}_f^T\tilde{\mathbf{K}}_f\mathbf{e}_f\right) \leq \alpha_{M_s}||\dot{\mathbf{e}}_s||^2 + \alpha_{\tilde{M}_f}||\dot{\mathbf{e}}_f||^2 + \frac{1}{\alpha_{M_s}}||\mathbf{R}_s||^2 + \frac{1}{\alpha_{\tilde{M}_f}}||\mathbf{R}_\phi||^2 \tag{4.44}$$

By definition of coercivity constants α_{M_s} and $\alpha_{\tilde{M}_f}$, we have $\mathbf{v}_s^T\mathbf{M}_s\mathbf{v}_s \geq \alpha_{M_s}||\mathbf{v}_s||^2$, $\mathbf{v}_f^T\tilde{\mathbf{M}}_f\mathbf{v}_f \geq \alpha_{\tilde{M}_f}||\mathbf{v}_f||^2$, for all $\mathbf{v}_s \in \mathbb{R}^{n_s}$ and $\mathbf{v}_f \in \mathbb{R}^{n_f}$, so that:

$$\frac{d}{dt}\left(\dot{\mathbf{e}}_s^T\mathbf{M}_s\dot{\mathbf{e}}_s + \mathbf{e}_s^T\mathbf{K}_s\mathbf{e}_s + \dot{\mathbf{e}}_f^T\tilde{\mathbf{M}}_f\dot{\mathbf{e}}_f + \mathbf{e}_f^T\tilde{\mathbf{K}}_f\mathbf{e}_f\right) \leq \dot{\mathbf{e}}_s^T\mathbf{M}_s\dot{\mathbf{e}}_s + \dot{\mathbf{e}}_f^T\tilde{\mathbf{M}}_f\dot{\mathbf{e}}_f + \frac{1}{\alpha_{M_s}}||\mathbf{R}_s||^2 + \frac{1}{\alpha_{\tilde{M}_f}}||\mathbf{R}_\phi||^2 \tag{4.45}$$

Since the matrices $\mathbf{K}_s$ and $\tilde{\mathbf{K}}_f$ are positive semi-definite, we have $\mathbf{e}_s^T\mathbf{K}_s\mathbf{e}_s + \mathbf{e}_f^T\tilde{\mathbf{K}}_f\mathbf{e}_f \geq 0$. By adding $\mathbf{e}_s^T\mathbf{K}_s\mathbf{e}_s + \mathbf{e}_f^T\tilde{\mathbf{K}}_f\mathbf{e}_f$ in the right-hand side of the inequality (4.45), we obtain:

$$\frac{d}{dt}\mathbf{E}(t;\boldsymbol{\mu}) \leq \mathbf{E}(t;\boldsymbol{\mu}) + \frac{1}{\alpha_{M_s}(\boldsymbol{\mu})}||\mathbf{R}_s(t;\boldsymbol{\mu})||^2 + \frac{1}{\alpha_{\tilde{M}_f}(\boldsymbol{\mu})}||\mathbf{R}_\phi(t;\boldsymbol{\mu})||^2 \tag{4.46}$$

where $\mathbf{E}(t;\boldsymbol{\mu}) := \dot{\mathbf{e}}_s^T\mathbf{M}_s\dot{\mathbf{e}}_s + \mathbf{e}_s^T\mathbf{K}_s\mathbf{e}_s + \dot{\mathbf{e}}_f^T\tilde{\mathbf{M}}_f\dot{\mathbf{e}}_f + \mathbf{e}_f^T\tilde{\mathbf{K}}_f\mathbf{e}_f$. Thus, we have:

$$\begin{aligned}
\frac{d}{du}\left(e^{-u}\mathbf{E}(u;\boldsymbol{\mu})\right) &= -e^{-u}\mathbf{E}(u;\boldsymbol{\mu}) + e^{-u}\frac{d}{du}\mathbf{E}(u;\boldsymbol{\mu}) && (4.47)\\
&\leq -e^{-u}\mathbf{E}(u;\boldsymbol{\mu}) + e^{-u}\mathbf{E}(u;\boldsymbol{\mu}) && (4.48)\\
&\quad + e^{-u}\left(\frac{1}{\alpha_{M_s}(\boldsymbol{\mu})}||\mathbf{R}_s(u;\boldsymbol{\mu}||^2 + \frac{1}{\alpha_{\tilde{M}_f}(\boldsymbol{\mu})}||\mathbf{R}_\phi(u;\boldsymbol{\mu})||^2\right) && (4.49)\\
&\leq e^{-u}\left(\frac{1}{\alpha_{M_s}(\boldsymbol{\mu})}||\mathbf{R}_s(u;\boldsymbol{\mu}||^2 + \frac{1}{\alpha_{\tilde{M}_f}(\boldsymbol{\mu})}||\mathbf{R}_\phi(u;\boldsymbol{\mu})||^2\right) && (4.50)\\
\Rightarrow e^{-t}\mathbf{E}(t;\boldsymbol{\mu}) - \mathbf{E}(0;\boldsymbol{\mu}) &\leq \int_0^t e^{-u}\left(\frac{1}{\alpha_{M_s}(\boldsymbol{\mu})}||\mathbf{R}_s(u;\boldsymbol{\mu})||^2 + \frac{1}{\alpha_{\tilde{M}_f}(\boldsymbol{\mu})}||\mathbf{R}_\phi(u;\boldsymbol{\mu})||^2\right)du && (4.51)
\end{aligned}$$

Which is the result of the theorem since we have $\mathbf{E}(0;\boldsymbol{\mu}) = 0$.

□

From our current numerical experiments, the aposteriori error bound proposed in the above theorem is too pessimist even in the context of the interaction of submerged structure and shock wave where the final time of interest is a few milliseconds. A sharp a posteriori error bound for parametrized time-domain vibro-acoustic problem is still an open issue.

4.5.3 On the convergence of POD-Greedy algorithm

To give a good answer to the question: *when can we expect that the error indicator in POD-Greedy algorithm 10 decreases rapidly ?*, it is worth to recall a mathematical notion of the Kolmogorov N-width of a given manifold [79].

Definition 4.5.1 Let V be a normed linear space, S be a subset of V and V_N be a generic N-dimensional subspace of V. The deviation of S from V_N is:

$$E(S;V_N) = \sup_{s\in S}\inf_{v_N\in V_N}||s-v_N||_V \tag{4.52}$$

The *Kolmogorov N-width* of S in V is defined by

$$d_N(S,V) = \inf_{V_N} E(S;V_N) \tag{4.53}$$

By definition, Kolmogorov N-width of S measures how well the subset S can be approximated by a N-dimensional subspace of X. Here, the subset S is the solution manifold $\mathcal{M}_{t,\boldsymbol{\mu}} := \{\mathbf{X}(t;\boldsymbol{\mu}), t\in[0,T], \boldsymbol{\mu}\in\mathcal{D}\} \subset \mathbb{R}^n$, where $\mathbf{X}$ is the solution of the full model (4.1). When the Kolmogorov N-width $d_N(\mathcal{M}_{t,\boldsymbol{\mu}},\mathbb{R}^n)$ is small, it means that the manifold $\mathcal{M}_{t,\boldsymbol{\mu}}$ can be well approximated by a N-dimensional subspace of $\mathbb{R}^n$. However, the N-dimensional subspace V_N which is the solution of the minimization problem in the definition (4.53) is not attainable. For this reason, we proposed in Section 4.3 to construct an appropriate reduced subspace by the POD-Greedy algorithm 10.

The convergence rate of the POD-Greedy algorithm 10 depends strongly on how well the Kolmogorov N-width of solution manifolds $\mathcal{M}_{t,\boldsymbol{\mu}}$ decays as a function of N. The faster $d_N(\mathcal{M}_{t,\boldsymbol{\mu}},\mathbb{R}^n)$ decreases as a function of N, the better convergence rate in POD-Greedy algorithm 10 can be expected. A rigorous analysis on the convergence rate has also been investigated in [65] for the POD-Greedy algorithm 12. For the case of stationary problem, we refer to [24] for a rigorous analysis on the convergence rate of the Greedy algorithm.

Despite numerous numerical evidences in many parametrized elliptic problems showing that the Kolmogorov N-width of the solution manifold may decay exponentially (see for instance [124]), there are still very few rigorous mathematical analysis on this matter, see for instance [39, 95]. A numerical way to access to the decay of the Kolmogorov N-width of a manifold $S\subset X$ is to compute the singular values of a finite subset $S_{train}\subset S$ whose cardinal is sufficiently large for representing the manifold S. The decay of the Kolmogorov N-width of S can be then characterized by the decay of these singular values.

We recall that the singular values of $S_{train} = \{\mathbf{s}_1,\cdots,\mathbf{s}_N\}$, where N denotes the cardinal of S, are the square root of the eigenvalues of the symmetric (hermitian in complex case) Grammian matrix $\mathbf{G}\in\mathbb{R}^{N\times N}$ which is defined by $G_{ij} = \langle \mathbf{s}_i,\mathbf{s}_j\rangle_X$ (see Remark 4.3.2). The more the vector $(\mathbf{s}_i)_{1\leq i\leq N}$ is correlated, which also means that the more the Grammian matrix is ill-conditioned, the faster the singular values and the Kolmogorov N-width decay, can be ex-

pected. Hence, the best case occurs when $(\mathbf{s}_i)_{1\leq i\leq N}$ are collinear where the Grammian matrix $\mathbf{G}$ has only one non zero eigenvalue. The worst case occurs when $(\mathbf{s}_i)_{1\leq i\leq N}$ are orthonormal which implies that the Grammian matrix $\mathbf{G}$ is the unity matrix so that there is no decay in the eigenvalue spectrum.

In fact, most of the works in the reduced order modelling of the parametrized problem is under the assumption of a small Kolmogorov N-width of the solution manifold. Even though this assumption can be expected or verified in many cases, for instance because of the regularity of the solution in parameter $\boldsymbol{\mu}$ and time t, this assumption may not be verified in some cases such as in the pure transport and in the pure propagation problem. For the cases of large Kolmogorov N-width, we refer to [30] and the references therein for some propositions to overcome this issue.

4.5.4 On the need of the local ROMs

When the parameter space $\mathcal{D}$ and the time interval of interest $[0,T]$ are too large, it implies a widening of the Kolmogorov N-width of solution manifold so that the size of the reduced basis required to approximate accurately the solution of full model can be too large, which yields inefficient reduced order model approximations. This happens when it has too many different physical regimes in the solution manifold while varying the parameter values in $\mathcal{D}$ and the time in an interval of interest $[0,T]$. A solution to overcome this issue is to built a suitable partition of the parameter space $\mathcal{D}=\mathcal{D}_1\cup\cdots\mathcal{D}_{N_\mathcal{D}}$, where $\mathcal{D}_i\cap\mathcal{D}_j=\emptyset,\forall i\neq j$, and construct a local reduced order model for each subset $\mathcal{D}_i, i=1,\cdots,N_\mathcal{D}$. We can also use an alternative by subdividing the time interval of interest $[0,T]$ into $[0,T]=[T_0,T_1]\cup[T_1,T_2]\cdots\cup[T_{N_{D_t}-1},T_{N_{D_t}}]$, where $T_0=0$, $T_{N_{D_t}}=T$, and constructing a local reduced order model for each time interval $[T_i,T_{i+1}], i=0,\cdots,N_{D_t}-1$.

In the latter case, it should be noted that switching from the local reduced order model for $[T_{i-1},T_i]$ to the local reduced order model for $[T_i,T_{i+1}]$ must be done inexpensively during the online stage. In what follows, we denote by $\mathbf{V}_{i,i+1}\in\mathbb{R}^{n\times N_{i,i+1}}$ and $\mathbf{X}_r^{i,i+1}$ the reduced basis and the state corresponding to $\mathrm{ROM}_{T_i,T_{i+1}}$ (the local reduced order model for $[T_i,T_{i+1}]$). We remark that the values of $\mathbf{X}_{t=T_i},\dot{\mathbf{X}}_{t=T_i}\in\mathbb{R}^n$ are required in order to determine the initial conditions for $\mathrm{ROM}_{T_i,T_{i+1}}$, $\forall i\geq 1$. For the given $\mathbf{X}_{t=T_i},\dot{\mathbf{X}}_{t=T_i}$, the initial condition of $\mathrm{ROM}_{T_i,T_{i+1}}$ can be defined as the orthogonal projection of $\mathbf{X}_{t=T_i}$ and $\dot{\mathbf{X}}_{t=T_i}$ on the subspace spanned by $\mathbf{V}_{i,i+1}$. Assuming that the reduced basis $\mathbf{V}_{i,i+1}$ is orthonormal, the initial condition of $\mathrm{ROM}_{T_i,T_{i+1}}$ can be defined by $\mathbf{X}_{r,t=T_i}^{i,i+1}=\mathbf{V}_{i,i+1}^T\mathbf{X}_{t=T_i}$ and $\dot{\mathbf{X}}_{r,t=T_i}^{i,i+1}=\mathbf{V}_{i,i+1}^T\dot{\mathbf{X}}_{t=T_i}$. We note that the approximation of $\mathbf{X}_{t=T_i}$ and $\dot{\mathbf{X}}_{t=T_i}$ provided by the $\mathrm{ROM}_{T_{i-1},T_i}$ are $\mathbf{X}_{t=T_i}=\mathbf{V}_{i-1,i}^T\mathbf{X}_{r,t=T_i}^{i-1,i}, \dot{\mathbf{X}}_{t=T_i}=\mathbf{V}_{i-1,i}^T\dot{\mathbf{X}}_{r,t=T_i}^{i-1,i}$. Hence, the initial condition of $\mathrm{ROM}_{T_i,T_{i+1}}$ can be computed with a complexity independent of the size of full model as $\mathbf{X}_{r,t=T_i}^{i,i+1}=(\mathbf{V}_{i,i+1}^T\mathbf{V}_{i-1,i}^T)\mathbf{X}_{t=T_i}^{i-1,i}$ and $\dot{\mathbf{X}}_{r,t=T_i}^{i,i+1}=(\mathbf{V}_{i,i+1}^T\mathbf{V}_{i-1,i}^T)\dot{\mathbf{X}}_{t=T_i}^{i-1,i}$ provided that the matrix $\mathbf{V}_{i,i+1}^T\mathbf{V}_{i-1,i}^T\in\mathbb{R}^{N_{i,i+1}\times N_{i-1,i}}$ is pre-computed at the offline stage.

The idea of local reduced order modelling is not new. It has been already investigated in various contexts, see for instance [8, 48, 88, 103].

4.6 Numerical results

In this section, we propose to study numerically the efficiency of our reduced order modelling framework in a study case which aims to deal with the study case proposed in Section 2.5.1 by taking into account a *spring-mass* system in the model. This can be viewed as a representative study case for the industrial application considered in the next section. In this study case, the four formulations presented in Section 2.4 of Chapter 2 are employed for the reduced order modelling. The comparison of the efficiency of the reduced order modelling between each formulations will also be investigated.

Presentation of the study case

Here, we are interested in an elastic ring with a *spring-mass* system submitted to an underwater explosion's shock wave. A graphical representation of this study case is given by Figure 4.2. Here, we consider that the elastic ring has a radius $R = 1$ m, a thickness $h = 0.01$ m and Poisson's ration $\nu = 0.28$. The excitation is induced by an acoustic shock wave generated by an underwater explosion of 1 000 kg of Trinitrotoluene (TNT) located at $(d, 0)$ where $d = 100$ m. The profile of the considered shock wave is modelled by Equation (2.12) for the pressure and Equation (2.15) for the fluid particle's velocity using the value of constants P_c, v_c, A and B of Equation (2.10) provided by [40]. At $t = 0$, we assume that the shock wave arrives at the stand-off point $(0, R + h/2)$ of the structure. The density and the speed of sound of the fluid are given by $\rho_0 = 1\ 000$ kg/m^3, $c_0 = 1\ 500$ m/s. The *spring-mass* system is suspended at the point $(R - h/2, 0)$ which represents the closest point in the interior part of the ring to the explosion.

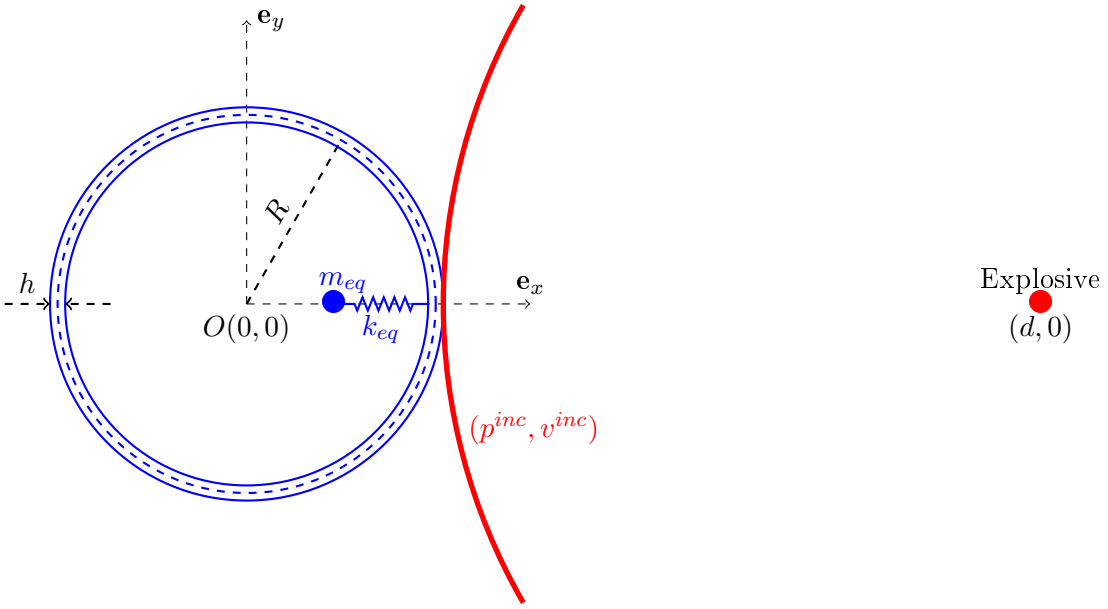

Figure 4.2: Graphical representation of the first study case

The parameter vector in the problem is defined by $\boldsymbol{\mu} := (m_{eq}, f_{eq}, E, \rho_s)$ where m_{eq}, $f_{eq} := \frac{1}{2\pi}\sqrt{\frac{k_{eq}}{m_{eq}}}$ are respectively the mass and the frequency of the *spring-mass* system , E and ρ_s are respectively Young's modulus and the density of the elastic ring. The parameter spaces is set

by $\mathcal{D} := [10, 500] \times [100, 250] \times [0.95\bar{E}, 1.05\bar{E}] \times [0.95\bar{\rho}_s, 1.05\bar{\rho}_s] \subset \mathbb{R}^4$ where $\bar{E} = 200$ GPa and $\bar{\rho}_s = 7\,850$ kg/m^3 are nominal value of Young's modulus and the density of the elastic ring.

Full model and quantity of interest

In order to approximate the Sommerfeld radiation condition, a truncated fluid domain in form of a circle of radius $R_{bgt} = 3$ m is employed. On the boundary of the truncated fluid domain, the BGT-1 boundary condition (1.35) is applied in order to approximate the outgoing sound wave by a cylindrical wave for which we use the value of impedance $Z_R = 2\rho_0 R_{bgt}, Z_C = \rho_0 c_0$. In finite element modelling, we use **quadratic triangular elements** both for the elastic ring and the fluid. The largest element size in the fluid part of the mesh is 0.06 m and there are 4 elements in the thickness of the ring. The using mesh is illustrated in Figure 2.7.

In the finite element model, we have 172 475 degrees of freedom, 91 030 of which correspond to the structural part (one of which corresponds to the point mass in the spring-mass system) and 81 445 of which correspond to the acoustic fluid part for the formulation in $(\mathbf{u}_s, \phi^{sca})$, in $(\mathbf{u}_s, \phi^{rad})$ and in $(\mathbf{u}_s, p^{rad})$. For the formulation in $(\mathbf{u}_s, p^{rad}, \varphi^{rad})$, we have 253 920 degrees of freedom 91 030 of which correspond to the structural part and 162 890 of which correspond to the acoustic fluid part and the non-symmetric finite element model (2.37) will be used in this study. For the time-discretization of the finite element models, Newmark scheme (with $\beta = \frac{1}{4}(1-\alpha)^2$, $\gamma = 1/2 - \alpha$ where $\alpha = -0.1$) is employed by using the time step $\Delta t = 4 \cdot 10^{-5}$ s which means that the shock wave needs 100 times step in order to travel the distance of $6R$. The final time of interest is set by $T = 6R/c_0$ so that the total number of time steps is $N_t = 100$.

In this study case, the acceleration $a_{m_{eq}}$ of the point mass in the *spring-mass* system represents the output of interest. Therefore, we define the accuracy of the reduced order model by the following quantity:

$$\Delta_l(\boldsymbol{\mu}) := \frac{\left(\int_0^T \left| a_{m_{eq}}^{fom}(t;\boldsymbol{\mu}) - a_{m_{eq}}^{rom}(t;\boldsymbol{\mu}) \right|^2 dt \right)^{1/2}}{\left(\int_0^T \left| a_{m_{eq}}^{fom}(t;\boldsymbol{\mu}) \right|^2 dt \right)^{1/2}} \tag{4.54}$$

where the superscripts ^{fom} and ^{rom} refer respectively to the values provided by the full model and the reduced order model.

Influence of the parameter ϵ_{POD} in POD-Greedy Algorithm 10

First of all, we propose to study the influence of the parameter ϵ_{POD} in POD-Greedy Algorithm 10. To do so, we run the POD-Greedy Algorithm 13 with the formulation in $(\mathbf{u}_s, \phi^{sca})$ by varying the value of the $\epsilon_{POD} \in \{10^{-2}, 10^{-3}, 10^{-4}, 10^{-5}, 10^{-6}\}$. For each value of ϵ_{POD}, we use the same training sample $\mathcal{D}_{train}^k$ which is chosen randomly at each iteration with $|\mathcal{D}_{train}^k| = 50$. In our study, we employ the same time-integration scheme as the full model for the reduced order model. We plot in Figure 4.3a the evolution of the maximum value of error indicator Δ defined in Equation (4.9) over the parameter values in $\mathcal{D}_{train}^k$. Figure 4.3b plots the evolution of the error of the output of interest Δ_l defined in Equation (4.54) for the parameter value $\boldsymbol{\mu}_{k+1}^*$ which maximizes the error indicator Δ over the parameter values in $\mathcal{D}_{train}^k$.

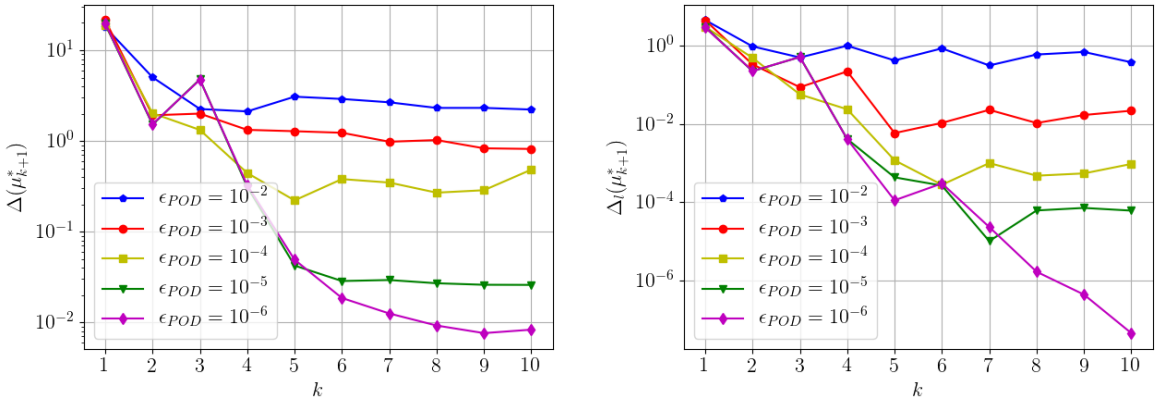

(a) On the error indicator Δ based on the residual norm

(b) On the error on the output of interest Δ_l defined in 4.54

Figure 4.3: Convergences of the POD-Greedy Algorithm 13 with the formulation in $(\mathbf{u}_s, \phi^{sca})$ in the first study case

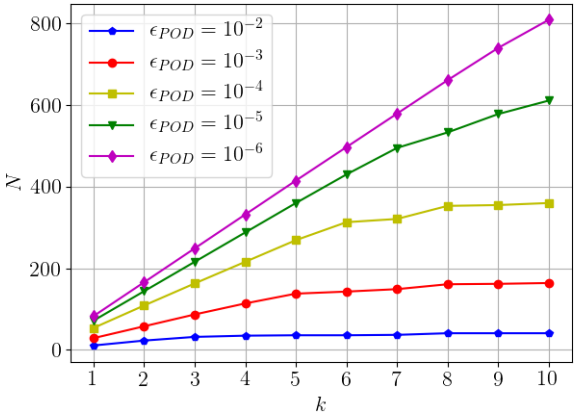

Figure 4.4: The dimension of the reduced basis during the iteration of the POD-Greedy Algorithm 13 with the formulation in $(\mathbf{u}_s, \phi^{sca})$ in the first study case

In the figure 4.3, we see that the smaller ϵ_{POD}, the better convergence rate of the POD-Greedy Algorithm we have. Except for the case of $\epsilon_{POD} = 10^{-6}$, we see clearly that both the error indicator Δ and the error on the output of interest Δ_l are stabilized after some iterations. This can be explained by the fact that there is relatively only few new basis vectors be added in the old reduced basis at the procedure of the concatenation at the step 13 of Algorithm 13. More precisely, after 3 iterations for the case of $\epsilon_{POD} = 10^{-2}$, after 5 iterations for the case of $\epsilon_{POD} \in \{10^{-3}, 10^{-4}\}$ and after 7 iterations for the case of $\epsilon_{POD} = 10^{-5}$ as we can observe in Figure 4.4 which plots the dimension of the reduced basis during the iteration. Figure 4.4 also indicates that the smaller ϵ_{POD}, the bigger dimension of the reduced basis, which is the reason why we have the better convergence rate.

As a first conclusion, too small values of ϵ_{POD} may require small number of iterations (thus small number of the full model to be solved in offline stage) of POD-Greedy Algorithm but

it could lead to an inefficient reduced order model for the online stage. On the contrary, too large values of ϵ_{POD} could lead to an inaccurate reduced order model.

Comparison of the convergence in POD-Greedy Algorithms for the different formulations

Now, let us compare the convergence in POD-Greedy Algorithm for the different formulations. Here, we have four formulations: in $(\mathbf{u}_s, \phi^{sca})$, in $(\mathbf{u}_s, \phi^{rad})$, in $(\mathbf{u}_s, p^{rad})$ and $(\mathbf{u}_s, p^{rad}, \varphi^{rad})$ (see Section 2.4 for the presentation of each formulation). We recall that for the formulation in $(\mathbf{u}_s, p^{rad})$ and in $(\mathbf{u}_s, p^{rad}, \varphi^{rad})$, we use respectively the stabilized POD-Greedy Algorithm 14 and 15. The case of formulation in $(\mathbf{u}_s, \phi^{sca})$ and $(\mathbf{u}_s, \phi^{rad})$ are both based on the same POD-Greedy Algorithm 13. Again, we will use the same training sample $\mathcal{D}^k_{train}$ of 50 values (which are chosen randomly at each iteration) in the POD-Greedy algorithm of each formulation.

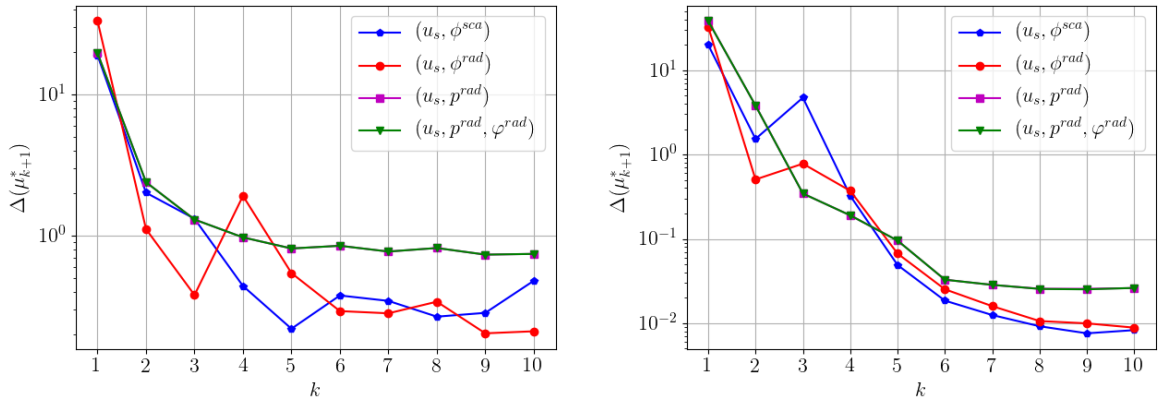

(a) Case of $\epsilon_{POD} = 10^{-4}$ (b) Case of $\epsilon_{POD} = 10^{-6}$

Figure 4.5: Evolution of the error indicator Δ based on the residual norm of the POD-Algorithm for the different formulations in the first study case

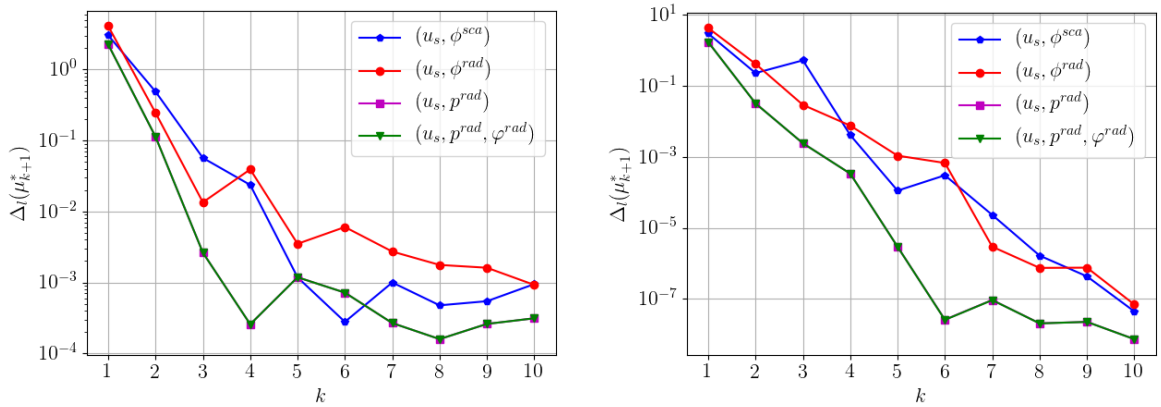

(a) Case of $\epsilon_{POD} = 10^{-4}$ (b) Case of $\epsilon_{POD} = 10^{-6}$

Figure 4.6: Evolution of the error of the output of interest Δ_l defined in Equation (4.54) in the POD-Greedy Algorithm for the different formulations in the first study case

Figure 4.5 illustrates the evolution of the error indicator Δ defined in Equation (4.9) during the iteration of the POD-Greedy Algorithm for the different formulations. The evolution of the error on the output of interest $\Delta_l(\boldsymbol{\mu}^*_{k+1})$ defined in Equation (4.54) are reported in Figure 4.6.

As could be expected, we see that the same evolution of the error indicator Δ and the error on the output of interest Δ_l for the formulation in $(\mathbf{u}_s, p^{rad})$ and in $(\mathbf{u}_s, p^{rad}, \varphi^{rad})$. This results confirm numerically the equivalence of the POD-Greedy Algorithm 14 and 15 as mentioned in Lemma 4.3.1. We also remark in Figure 4.6 that the formulation in $(\mathbf{u}_s, p^{rad})$ and in $(\mathbf{u}_s, p^{rad}, \varphi^{rad})$ has the better convergence rate for Δ_l compared to the formulation in $(\mathbf{u}_s, \phi^{sca})$ and in $(\mathbf{u}_s, \phi^{rad})$. This is because the dimension of the reduced basis in the former cases is bigger than the latter cases (as shown in Figure 4.7) due to the requirement imposed by the stabilization technique of Lemma 3.2.3.

Even though the formulation in $(\mathbf{u}_s, p^{rad}, \varphi^{rad})$ and the formulation in $(\mathbf{u}_s, p^{rad})$ are equivalent, we see in Figure 4.7 that the dimension of the reduced basis for the former case is larger than the latter case. It is because the stabilized reduced order model in $(\mathbf{u}_s, p^{rad}, \varphi^{rad})$ formulation proposed in Lemma 3.2.4, we have two degrees of freedom for the fluid part (p and φ) instead of one as in the stabilized reduced order model in $(\mathbf{u}_s, p^{rad})$ formulation proposed in Lemma 3.2.3.

It should also be pointed out, as illustrated in Figure 4.5 and 4.6, that the formulation in $(\mathbf{u}_s, \phi^{sca})$ have a slightly better convergence rate for Δ_l than the formulation in $(\mathbf{u}_s, \phi^{rad})$ while Figure 4.7 shows that this can be essentially due to the dimension of the reduced basis in the case of $(\mathbf{u}_s, \phi^{rad})$ increases slower than in the case of $(\mathbf{u}_s, \phi^{sca})$.

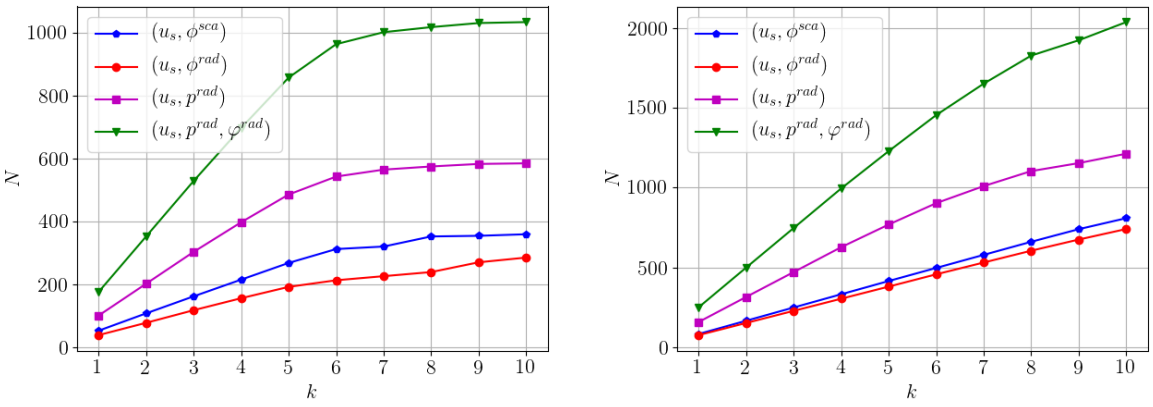

(a) Case of $\epsilon_{POD} = 10^{-4}$ (b) Case of $\epsilon_{POD} = 10^{-6}$

Figure 4.7: Evolution of the dimension of the reduced basis in the POD-Greedy Algorithm for the different formulations in the first study case

As observed in the previous section for the formulation in $(\mathbf{u}_s, \phi^{rad})$, it can also be seen in the case of the other three formulations that the smaller ϵ_{POD}, the bigger dimension of the reduced basis, which leads to a better convergence rate for the error on the output Δ_l as compensation.

On the efficiency of the reduced order models

We now turn to the efficiency of the proposed reduced order model. First, let us put the focus on the accuracy. To do so, we compute the maximum error of the output of interest defined in Equation (4.54) over a test sample $\mathcal{D}_{test}$ which consists of $n_{test} = 30$ values of parameters chosen randomly.

Figure 4.8 shows the evolution of the accuracy of the reduced order model during the iteration of the POD-Greedy algorithm for the different formulations. Since the reduced order model in $(\mathbf{u}_s, p^{rad})$ formulation and in $(\mathbf{u}_s, p^{rad}, \varphi^{rad})$ are equivalent, it is expected that they have the same accuracy, as observed in Figure 4.8. For the formulation in $(\mathbf{u}_s, \phi^{rad})$ which yields a smaller dimension of the reduced basis compared to the case of the formulation in $(\mathbf{u}_s, \phi^{sca})$ (as shown in Figure 4.7), we see in Figure 4.8a that the formulation in $(\mathbf{u}_s, \phi^{sca})$ displays a slightly better accuracy than the formulation in $(\mathbf{u}_s, \phi^{rad})$. For the formulations in $(\mathbf{u}_s, p^{rad})$ and in $(\mathbf{u}_s, p^{rad}, \varphi^{rad})$, the accuracy of the reduced basis seem be limited after 4 iterations in the case of $\epsilon_{POD} = 10^{-4}$ and after 6 iterations in the case of $\epsilon_{POD} = 10^{-6}$. This can be explained by the fact that the accuracy of reduced order models have already reached a value close to ϵ_{POD}.

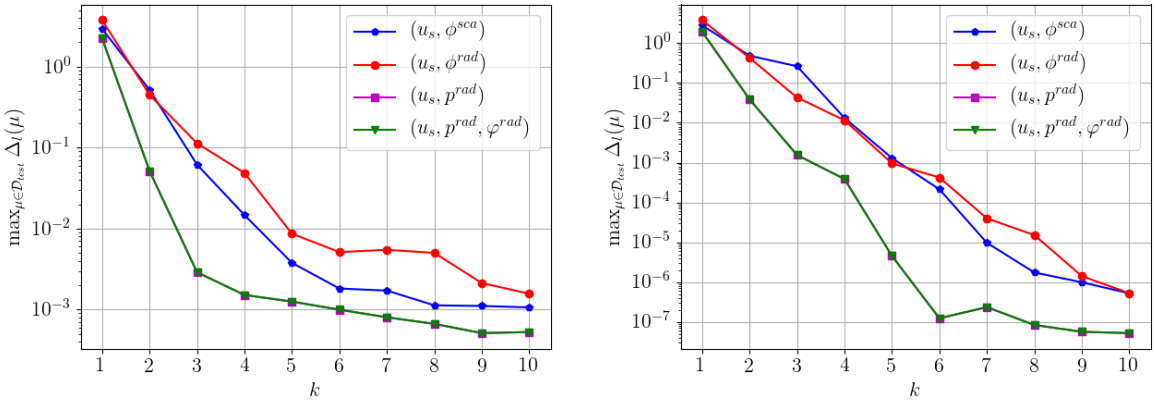

(a) Case of $\epsilon_{POD} = 10^{-4}$

(b) Case of $\epsilon_{POD} = 10^{-6}$

Figure 4.8: Evolution of the accuracy of the reduced basis in the POD-Greedy Algorithm for the different formulations in the first study case

In order to show the performance of the reduced order modelling, we are interested in the time speed-up which is defined as the ratio of the time required for the full model to the time required for its corresponding reduced order model. Here, only the smallest reduced order models satisfying the criterion: $\max_{\boldsymbol{\mu} \in \mathcal{D}_{test}} \Delta_l(\boldsymbol{\mu}) < 10^{-2}$, are considered. In both cases $\epsilon_{POD} = 10^{-4}$ and $\epsilon_{POD} = 10^{-6}$, Figure 4.8 indicates that it corresponds to the reduced order models obtained after 5 iterations of the POD-Greedy Algorithm 13, for the formulation in $(\mathbf{u}_s, p^{sca})$ and $(\mathbf{u}_s, p^{rad})$ and after 3 iterations the POD-Greedy Algorithm 14 and 15 for the formulations in $(\mathbf{u}_s, p^{rad})$ and in $(\mathbf{u}_s, p^{rad}, \varphi^{rad})$.

Table 4.2 and 4.3 present respectively the time speed up of the considered reduced order models of each formulation constructed by POD-Greedy algorithm with $\epsilon_{POD} = 10^{-4}$ and $\epsilon_{POD} = 10^{-6}$.

Formulation	Number of dofs		Time consumption		Time Speed-up
	FE Model	ROM	FE Model	ROM	
$(\mathbf{u}_s, \phi^{sca})$	172 475	269	123.21 s	1.63 s	75,59
$(\mathbf{u}_s, \phi^{rad})$	172 475	193	131.49 s	1.47 s	89.45
$(\mathbf{u}_s, p^{rad})$	172 475	304	132.20 s	1.74 s	75.98
$(\mathbf{u}_s, p, \varphi^{rad})$	253 920	529	145.08 s	2.11 s	68,76

Table 4.2: The speed-up of the reduced order model (for $\epsilon_{POD} = 10^{-4}$) for the different formulations in the first study case

Formulation	Number of dofs		Time consumption		Time Speed-up
	FE Model	ROM	FE Model	ROM	
$(\mathbf{u}_s, \phi^{sca})$	172 475	415	123.21 s	1.91 s	64,50
$(\mathbf{u}_s, \phi^{rad})$	172 475	380	131.49 s	1.82 s	72.25
$(\mathbf{u}_s, p^{rad})$	172 475	471	132.20 s	2.08 s	63,56
$(\mathbf{u}_s, p, \varphi^{rad})$	253 920	747	145.08 s	2.70 s	53,73

Table 4.3: The speed-up of the reduced order model (for $\epsilon_{POD} = 10^{-6}$) for the different formulations in the first study case

To construct a reduced order model with 99% accuracy, Table 4.2 and 4.3 show that the case of $\epsilon_{POD} = 10^{-4}$ is more efficient than the case of $\epsilon_{POD} = 10^{-6}$. On the other hand, we can see in Figure 4.8 that the case of $\epsilon_{POD} = 10^{-6}$ could be employed to construct a reduced order model with 99.99 % accuracy (in the sense that it verifies: $\max_{\boldsymbol{\mu} \in \mathcal{D}_{test}} \Delta_l(\boldsymbol{\mu}) < 10^{-4}$) which might be not the case of $\epsilon_{POD} = 10^{-4}$.

Finally, we present in Figure 4.9 the time evolution of the acceleration of the point mass in the *spring-mass* system given by the finite element model and the reduced order model obtained by POD-Greedy algorithm (with $\epsilon_{POD} = 10^{-4}$ at $k = 5$) of the formulation in $(\mathbf{u}_s, \phi^{sca})$ for some selected values of the parameters.

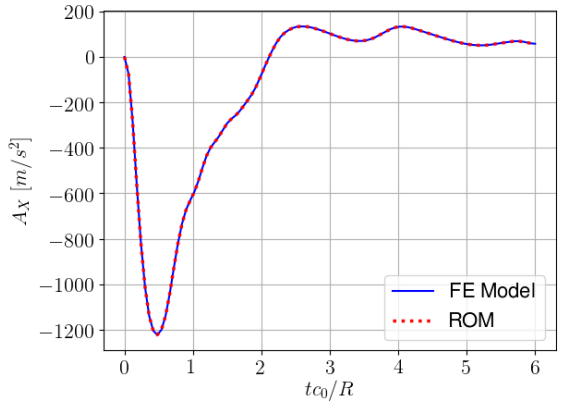

(a) Case of $\boldsymbol{\mu} = (320, 250, 1.03\bar{E}, 0.98\bar{\rho}_s)$

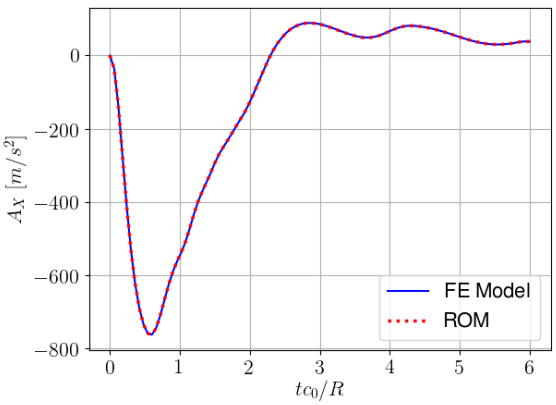

(b) Case of $\boldsymbol{\mu} = (450, 170, 0.97\bar{E}, 1.01\bar{\rho}_s)$

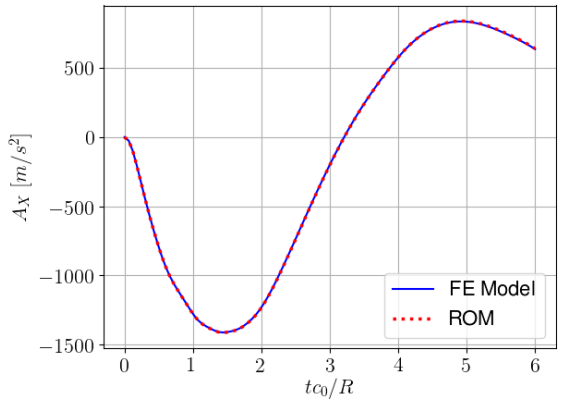

(c) Case of $\boldsymbol{\mu} = (100, 140, 1.02\bar{E}, 1.04\bar{\rho}_s)$

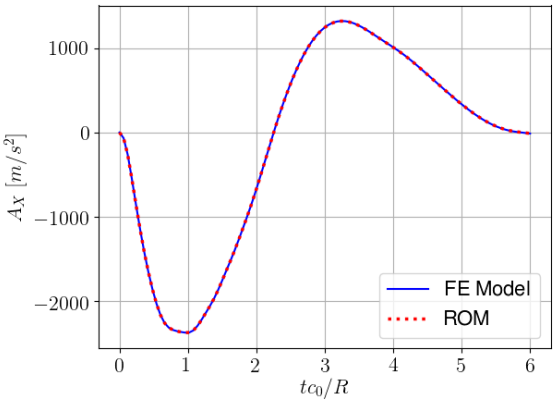

(d) Case of $\boldsymbol{\mu} = (80, 230, 0.99\bar{E}, 1.02\bar{\rho}_s)$

Figure 4.9: The acceleration of the point mass in the *spring-mass* system given by the full model and the reduced order model in $(\mathbf{u}_s, \phi^{sca})$ in the first study case

Concluding remarks

In this study case, numerical results show that the choice of value of ϵ_{POD} in POD-Greedy algorithm has an influence both on the accuracy and on the performance of the reduced order model. Small values of ϵ_{POD} tend to ameliorate the accuracy of the reduced order model at the price of a degradation of its performance. Hence, in order to construct a reduced order model with a desired accuracy ϵ, the parameter ϵ_{POD} of the POD-Greedy algorithm should be fixed with a value which is not too small compared to ϵ.

In all formulations considered in this study, we also note that the error indicator Δ based on the norm of the residual is very pessimist in the prediction of the error of the acceleration of the point mass in the *spring-mass* system, which is considered here as the output of interest. Therefore, for this type of problem, another alternatives for the stopping criterion in the POD-Greedy algorithm (as mentioned in Remark 4.3.4) should be used.

4.7 Industrial application

In this section, we aim to apply our reduced order modelling framework in the industrial problems. More precisely, this parametric study may contribute to the technical justification of the shock resistance of the equipment subjected to the primary shock wave, in pre-project phase of submarine design.

Presentation of the study case

We divide our study into two scenarios. In the first study case, we consider that the equipment is suspended directly on the hull of a submarine. The second study case deals with the situation where the equipment is suspended on a stiffener in T-form attached on the hull of a submarine.

For simplifying our problem, we model the equipment as a one degree of freedom system with equivalent mass and spring whose properties are calibrated by its first mode of vibration in the direction perpendicular to the hull. By doing so, different types of equipments can be simply characterized by their equivalent point mass and stiffness in the *spring-mass* system.

Here, we only consider a section of the resistance hull. The geometry of the hull is defined by $\Omega_{hull} := \{(x,y,z) \in \mathbb{R}^3, R_h - e_h/2 < x^2+y^2 < R_h + e_h/2, -h_h/2 < z < h_h/2\}$ where R_h, e_h and h_h denote respectively the radius, the thickness and the height of the cylindrical hull. In the first study case where there is no stiffener attached to the hull, the *spring-mass* system is suspended at the point $(R_h - e_h/2, 0, 0)$. In the second study case, the domain occupied by the stiffener in T-form is $\Omega_T = \Omega_{T_1} \cup \Omega_{T_2}$ where $\Omega_{T_1} := \{(x,y,z) \in \mathbb{R}^3, R_h - e_h/2 - l_1 < x^2+y^2 < R_h - e_h/2, -e_1/2 < z < e_1/2\}$ is the part perpendicular to the cylindrical hull and $\Omega_{T_2} := \{(x,y,z) \in \mathbb{R}^3, R_h - e_h/2 - l_1 - e_2 < x^2+y^2 < R_h - e_h/2 - l_1, -l_2/2 < z < l_2/2\}$ is the part parallel to the cylindrical hull. Here, we denote by l_i and e_i the length and the thickness of T_i, with $i \in \{1,2\}$. In the second case, the *spring-mass* system is suspended at the point $(R_h - e_h/2 - l_1 - e_2, 0, 0)$. The geometry of the structure part in the problem is illustrated by Figure 4.10 for the first study case and by Figure 4.11 for the second study case.

The excitation is created by an underwater explosion detonated at $(R_h + e_h/2 + d, 0, 0)$, where d denotes the distance of the charge to the the stand-off point $(R_h + e_h/2, 0, 0)$. The primary shock wave characterized by the Equation (2.12) and (2.15) with the value of constants P_c, v_c, A and B given by [40] (see Equation (2.10)), is used in our study.

Finite element modelling

In order to approximate the Sommerfeld radiation condition, a truncated fluid domain in form of a cylindrical of radius $R_{bgt} = 4R_h$ and of the same height as the hull is employed. On the boundary of the truncated fluid domain, the BGT-1 boundary condition (1.35) is applied in order to approximate the outgoing sound wave by a cylindrical wave for which we use the value of impedance $Z_R = 2\rho_0 R_{bgt}, Z_C = \rho_0 c_0$, where ρ_0 and c_0 are respectively the density and the sound speed in the fluid. On the boundary $z = -h_h/2$ and $z = h_h/2$ of the cylindrical hull Ω_{hull}, a homogeneous Dirichlet condition is applied.

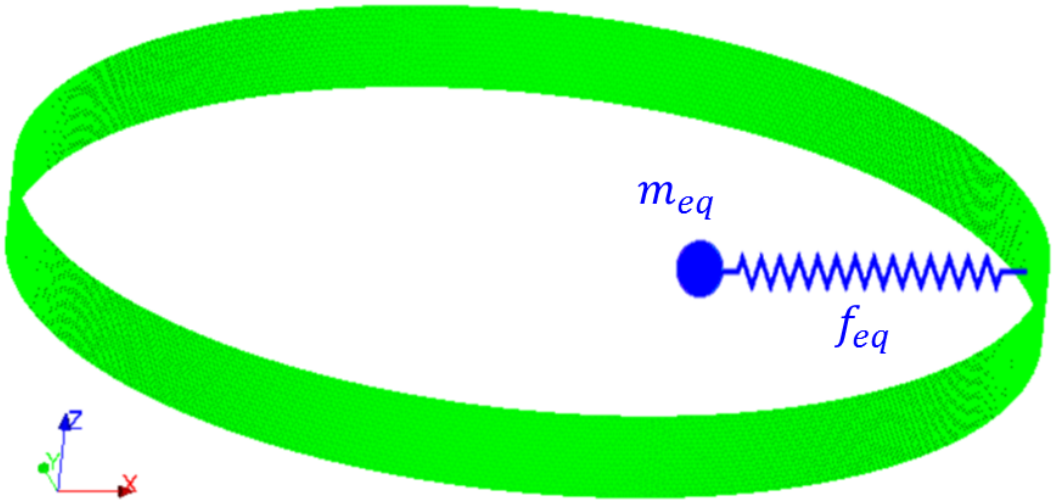

Figure 4.10: Geometrical representation of the structure part in the first study case of the industrial application: a section of cylindrical hull (in green) and a *spring-mass* system submitted to an underwater explosion's primary shock wave

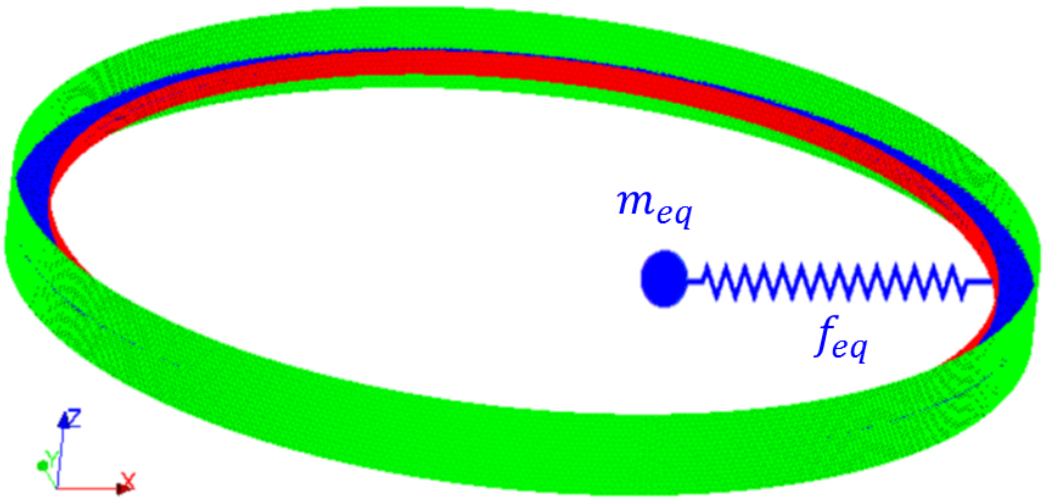

Figure 4.11: Geometrical representation of the structure part in the second study case of the industrial application: a section of cylindrical hull (in green) with a stiffness in T-form (in red and blue) and a *spring-mass* system submitted to an underwater explosion's primary shock wave

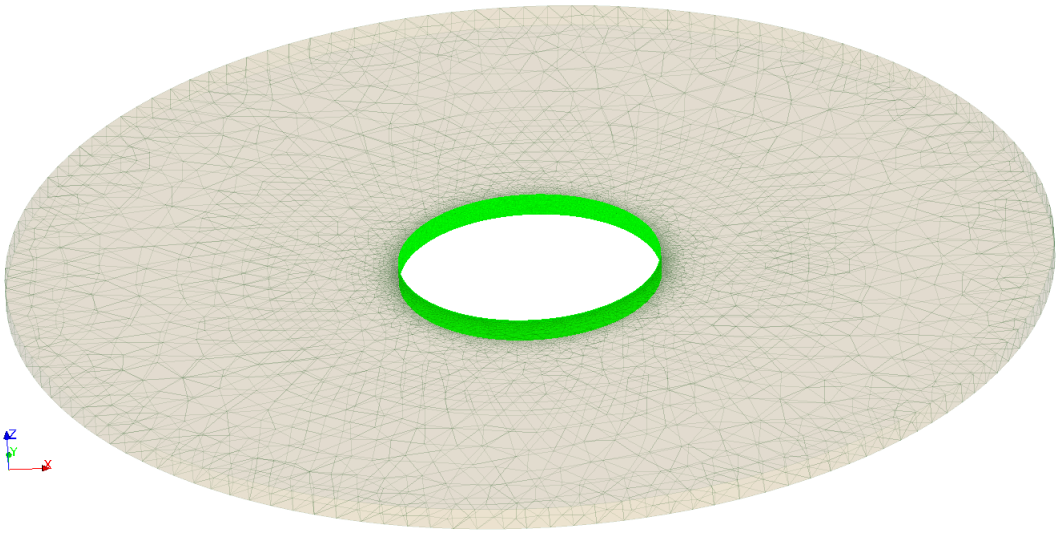

Figure 4.12: The mesh used for finite element modelling in the first study case of the industrial application: a section of cylindrical hull (in green) and a *spring-mass* system submitted to an underwater explosion's primary shock wave

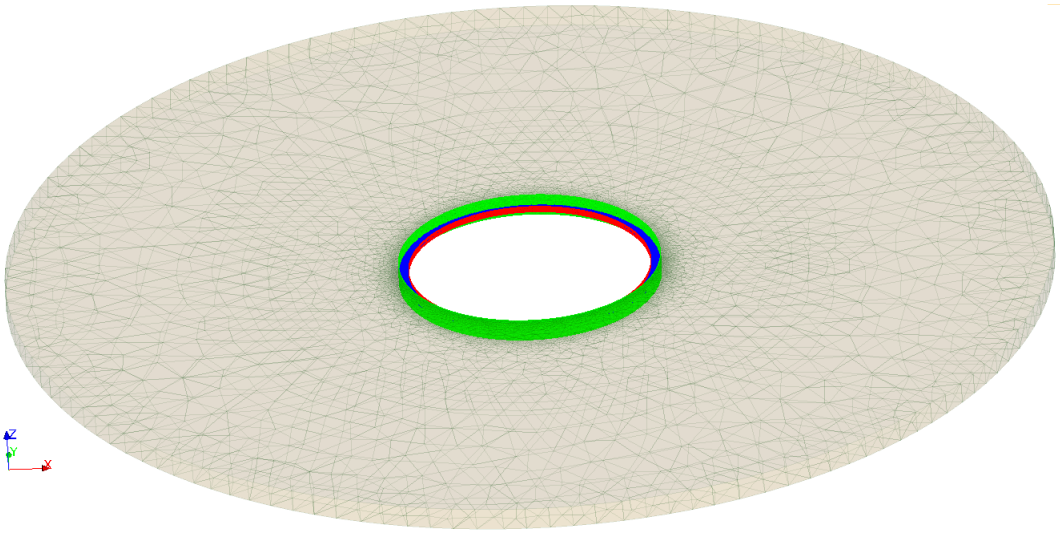

Figure 4.13: The mesh used for finite element modelling in the second study case of the industrial application: a section of cylindrical hull (in green) with a stiffness in T-form (in red and blue) and a *spring-mass* system submitted to an underwater explosion's primary shock wave

In numerical application, we use $R_h = 4$ m and $e_h = 0.03$ m. Both the stiffener and the hull are supposed to be constituted by a linear elastic material with the density $\rho_s = 7\ 800$ kg/m^3, Young's modulus $E_s = 2.0 \cdot 10^{11}$ Pa and Poisson's ratio $\nu = 0.3$. The underwater explosion under consideration is generated by $M_{tnt} = 1\ 000$ kg of Trinitrotoluene (TNT). The density and the sound speed in the fluid are given by $\rho_0 = 1\ 000$ kg/m^3, $c_0 = 1\ 500$ m/s.

The formulation in $(\mathbf{u}_s, \phi^{sca})$ is employed for our study. In the finite element modelling, we employ the quadratic tetrahedral elements for the fluid part. The structural part is modelled by the quadratic triangular shell elements [21]. The underlying mesh are presented in Figure 4.12 for the first study case and by Figure 4.13 for the second study case. The number of degrees of freedom in the fluid part and the structure part of the finite element model is summarized in the Table 4.4.

Study case	Number of dofs in FE model		
	Structural part	Fluid part	Total
Without stiffener	236 421	215 648	452 069
With a stiffener in T-form	392 781	215 648	608 429

Table 4.4: Characteristics of the finite element model in the industrial case

For the time-discretization of the finite element model, Newmark scheme (with $\beta = \frac{1}{4}(1-\alpha)^2$, $\gamma = 1/2 - \alpha$ where $\alpha = -0.2$) is employed by using the time step $\Delta t = 2.67 \cdot 10^{-4}$ s which means that the shock wave needs 600 times steps in order to travel the distance of $6R_h$. The final time of interest is set by $T = 6R_h/c_0$ so that the total number of time steps is $N_t = 600$.

Variability of parameters and output of interest

The output of interest in our problem is the acceleration $a_{m_{eq}}$ of the point mass in the *spring-mass* system. The main parameters considered in the problem are the equivalent mass m_{eq} and the equivalent frequency f_{eq} of the *spring-mass* system. The domain of variability is set by $\mathcal{D} := [1 \text{ kg}, 10\,000 \text{ kg}] \times [1 \text{ Hz}, 10\,000 \text{ Hz}] \subset \mathbb{R}^2$.

Reduced order modelling

We start by generating randomly a test sample $\mathcal{D}_{test}$ of $n_{test} = 25$ values of the parameter. Next, we compute and save the quantity of interest, the acceleration $a_{m_{eq}}$ of the point mass, for all values in the test sample $\mathcal{D}_{test}$ using the full order model. To construct the reduced order model, we run the POD-Greedy Algorithm 13 with the training set $\mathcal{D}_{train}$ of 30 values generated randomly at each iterations, and the stopping criterion defined by: $\max_{\boldsymbol{\mu} \in \mathcal{D}_{test}} \Delta_l(\boldsymbol{\mu}) < 10^{-2}$, where the error on the output of interest Δ_l is defined by Equation (4.54) as the study case of the previous section. The value of tolerance for the POD process at the step 12 and the concatenation of the basis by Algorithm 11 at the step 13 of the POD-Greedy Algorithm 13 is fixed by $\epsilon_{POD} = 10^{-4}$.

The evolutions of the error indicator Δ of Equation (4.9), of the error on the output of interest evaluated at the value of the parameter which maximize the error indicator and of the value of $\max_{\boldsymbol{\mu} \in \mathcal{D}_{test}} \Delta_l(\boldsymbol{\mu})$ during the iteration of the POD-Greedy Algorithm 13 are reported in Figure 4.14. The dimension of the corresponding reduced basis during the iteration are shown in Figure 4.15.

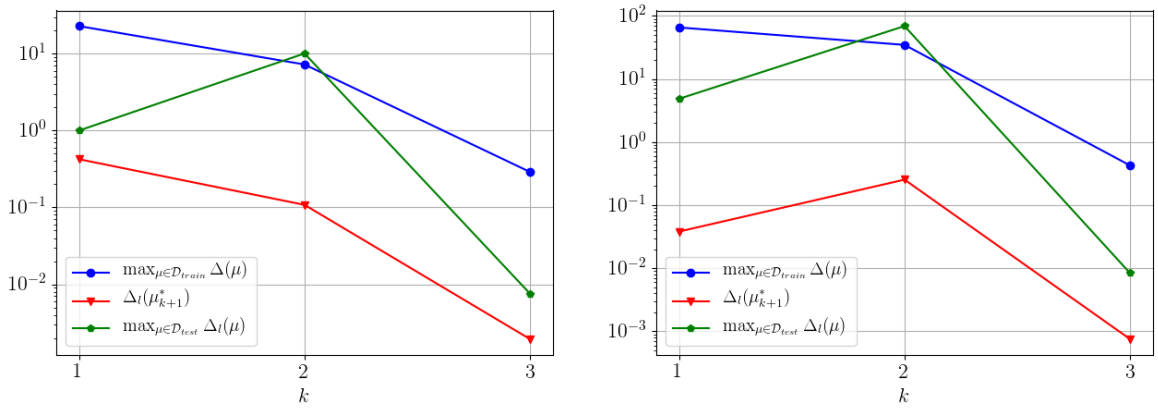

(a) Case without stiffener (b) Case with a T-form stiffener

Figure 4.14: Evolution of the accuracy of the reduced basis in the POD-Greedy Algorithm in the industrial cases

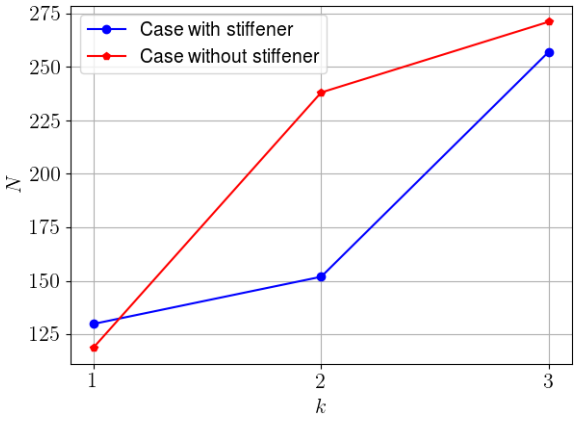

Figure 4.15: The dimension of the reduced basis during the iteration of the POD-Greedy Algorithm 13 with the formulation in $(\mathbf{u}_s, \phi^{sca})$ in the industrial cases

To achieve the stopping criterion, Figure 4.14a and 4.14b indicate that it only need 3 iterations for both cases. In order to show the performance of the proposed reduced order model, we present in Table 4.5 the comparison of the number of degrees of freedom and the time-speed up in the two study cases.

Study case	Number of dofs		Time consumption		Time Speed-up
	FE Model	ROM	FE Model	ROM	
Without stiffener	452 069	271	14 mins	21 s	40
With a T-form stiffener	608 429	257	17 mins	20 s	51

Table 4.5: The speed-up of the reduced order models in the industrial case

Application of the reduced order models

In order to illustrate a possible industrial application of the obtained reduced order models, whose time complexity is approximately 40 times cheaper than the full model for the first case and approximately 51 times cheaper than the full model for the second case, we put the focus here on the computation of the so called « *real spectrum* » of the equipment which is defined, for a fixed mass m_{eq}, by a function: $f_{eq} \rightarrow \max_{t\in[0,T]} a_{m_{eq}}(t; f_{eq})$ where $a_{m_{eq}}$ is the acceleration of the equipment for the mass m_{eq}. For a given equipment, this « *real spectrum* » curve yields its acceleration level as a function of its suspension frequency. It may for instance help to specify the acceleration levels that the equipment must withstand. It may also help to design architects to find a frequency at which an equipment must be suspended to stay below a given level of acceleration.

Figure 4.16 plots the « *real spectrum* » for different values of mass of equipment. For the first case where the equipment is suspended directly on the hull, the results are represented by dashed lines. For the second case where the equipment is suspended on the stiffener of the hull, the results are represented by full lines. To construct a « *real spectrum* » curve for a fixed mass of equipment, we divide uniformly the interval $[f_{min}, f_{max}]$ into 200 equidistant points in logarithm scale. Using the reduced order model requires in both case approximately 1 hour to obtain a « *real spectrum* » curve which would requires approximately 2.5 days for the first study case and 3 days for the second study case if the full model is employed.

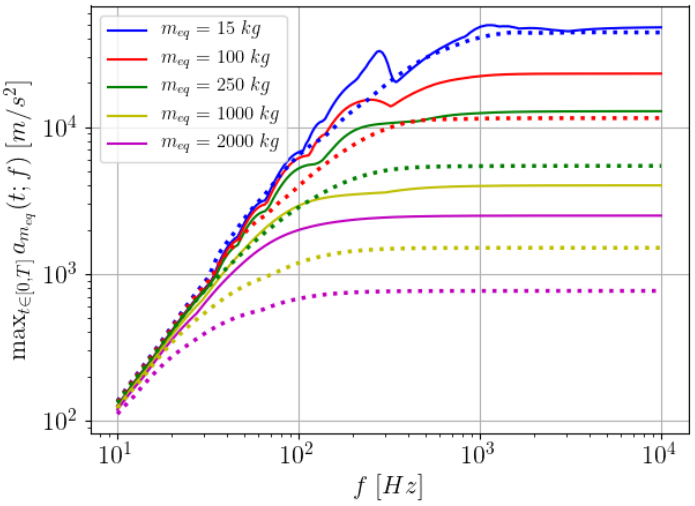

Figure 4.16: The real spectrum of the equipment for different values of mass of equipment in the case with (in full lines) and without the T-form stiffener (in dashed lines).

We can remark that the case with a stiffener implies a higher level of acceleration on the equipment than the case where the equipment is suspended directly on the resistance hull. This can be explained by the fact that the presence of the stiffener induces logically a local stiffening of the structure, which reduces the spectrum dip effect [109, 112].

At the end, we present in Figure 4.17 the time-evolution of the acceleration of equipment for some selected values of mass and frequency of suspension provided by the reduced order model (in dashed lines) and the full model (in full line).

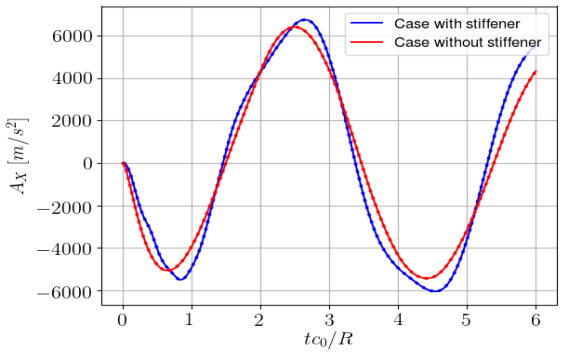

(a) Case of $m_{eq} = 15$ kg and $f_{eq} = 100$ Hz

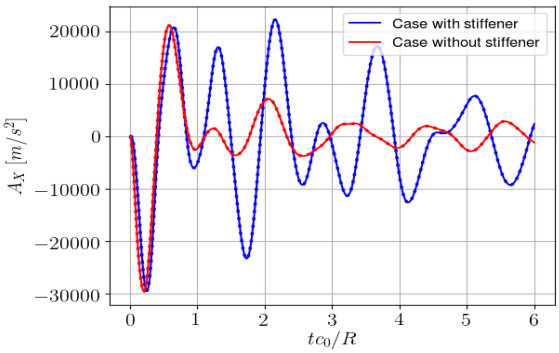

(b) Case of $m_{eq} = 15$ kg and $f_{eq} = 500$ Hz

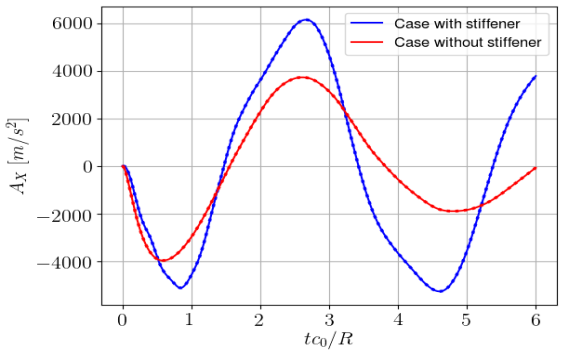

(c) Case of $m_{eq} = 100$ kg and $f_{eq} = 100$ Hz

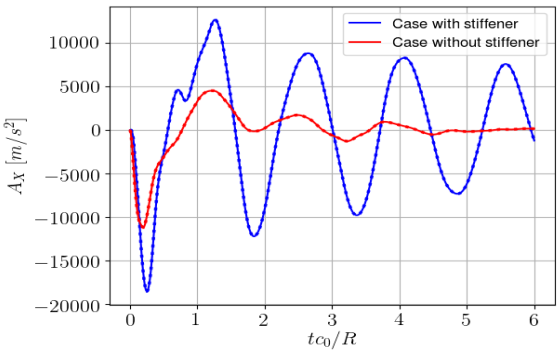

(d) Case of $m_{eq} = 100$ kg and $f_{eq} = 500$ Hz

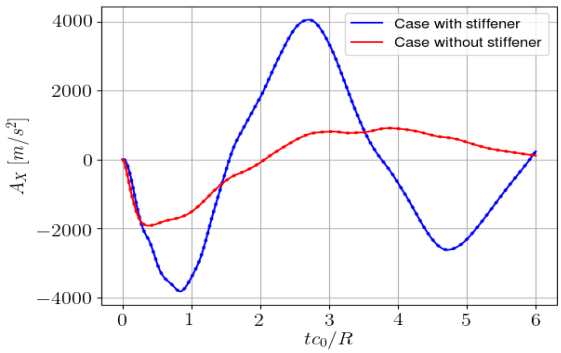

(e) Case of $m_{eq} = 500$ kg and $f_{eq} = 100$ Hz

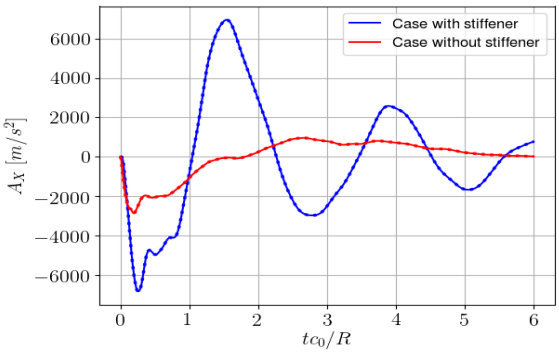

(f) Case of $m_{eq} = 500$ kg and $f_{eq} = 500$ Hz

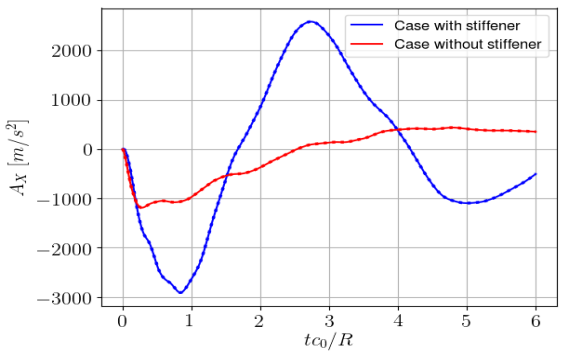

(g) Case of $m_{eq} = 1\ 000$ kg and $f_{eq} = 100$ Hz

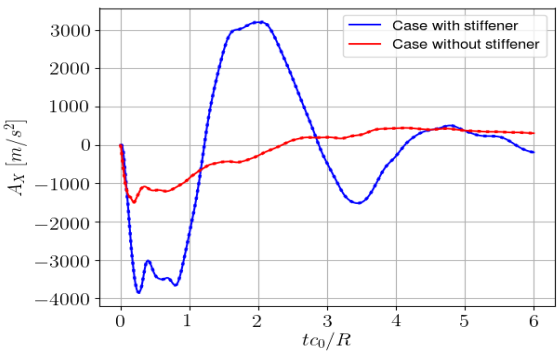

(h) Case of $m_{eq} = 1\ 000$ kg and $f_{eq} = 500$ Hz

Figure 4.17: Time evolution of acceleration of equipment in the two industrial study cases

4.8 Conclusions

In this chapter, we present a reduced order modelling framework for parametrized time-domain vibro-acoustic problem. For the construction of the reduced basis, we derive an algorithm based on the idea of the well-known POD-Greedy algorithm for all the formulations given in Chapter 1 and 2 by integrating the stabilization techniques proposed in Chapter 3. In order to get an advantage in the computation procedure at the offline stage, we ensured that the POD-Greedy algorithm generates a hierarchical reduced basis. We proposed here to use the norm of the residual vector as an indicator error, for which it can be shown that the proposed reduced order models for the formulation in $(\mathbf{u}_s, p)$ and in $(\mathbf{u}_s, p, \varphi)$ are equivalent.

A simple numerical study and two industrial applications are given in order to show the efficiency of the proposed reduced order modelling framework. Numerical results on the simple case show that our error indicator based on the norm of the residual vector seems very pessimist. As a result, we proposed to use the error of the output of interest evaluated on a test sample as the stopping criterion of the POD-Greedy in the industrial cases. The time speed-up gain compared to the finite element model is one to two orders of magnitude, which opens a way for parametric analysis as required in industrial applications.

The efficiency of the proposed reduced order modelling framework relies on the assumption of affine-dependencies in parameter. This requirement can not be verified in some applications, for instance in the case where we aim to consider the shape of the domain as the parameter in the problem. Since the accuracy and the performance of the resulting reduced order model are promising, we extend this framework into the case non-affine dependencies in parameter, which is the objective of the next chapter.

Chapter 5

Reduced order modelling for non-affinely parametrized time-domain vibro-acoustic FE model

In the previous chapter, we introduced an efficient reduced order modelling framework for parametrized time-domain vibro-acoustic problems. The framework proposed in Chapter 4 deals only with the case where all operators and the right hand side can be written as affine parametric dependences. In this chapter, we aim at extending the proposed framework to the case where this assumption is not verified. For instance, it occurs when the geometry of the fluid or the structure domain or the mass of TNT (Trinitrotoluene) in the explosion in the interaction of submerged structure and underwater explosion's shock wave problem are varied.

In this context, the Empirical Interpolation Method (EIM) [17] is classically employed to obtain an approximation in form of affine parametric dependence. This enables to recover the efficiency of the reduced order modelling framework based on an offline/online decomposition. For stationary problems, the integration of Empirical Interpolation Method (EIM) in the reduced order modelling framework for tackling non-affine dependencies has been already investigated in the different contexts, see for instance [61, 90, 124]. At first, EIM has been widely applied on the non-affinely parametrized function appearing in the definition of the left-hand side operators and the right-hand side vector of the full order model. In the case where the full order model results from a finite element discretization, EIM can also be applied directly and efficiently on the parametrized matrix/vector by exploiting the local support of finite element basis, see for instance [43, 92, 100, 120].

For the case where the geometry of the domain is considered as the parameter in the problem, one of the main challenges in model order reduction is the parametrization of the varying shape. Here, we restrict ourselves to the case where the parameter dependent domain can be described by a flexible boundary parametrizations of a reference domain. In our work, we choose to employ the so-called Solid Extension Mesh Moving Technique (SEMMT) which aims at generating the mesh for a new geometry by deforming a reference mesh via the displacement fields obtained by an elasticity problem [115, 117] (alternatively by an analytical formulation for the simplest case or by a Laplacian [16, 35] or bi-Laplacian [68] problem).

The goal of this chapter is to exploit the EIM and the SEMMT for extending the reduced order modelling framework proposed in the previous chapter into the case of non-affinely parametrized time-domain vibro-acoustic problem. This chapter is structured as follows. In the first section, we give a short presentation of the EIM and its potential applications in the context of model order reduction. In this section, we will also introduce an application of EIM for approximating the solution of the interaction of submerged structure and underwater explosion's shock wave problem when the mass of TNT is the only parameter of the problem. Numerical results on a simple case are also given for illustrating the accuracy of the proposed approximations. In Section 5.3, we give a presentation of Solid Extension Mesh Moving Technique (SEMMT). An application of EIM for reducing the computational cost of the parametrized displacement fields of SEMMT are also pointed out in this section. The integration of EIM and SEMMT non-affinely parametrized time-domain vibro-acoustic problem is described in Section 5.4. To show the efficiency of the proposed framework, numerical results are then presented in Section 5.5. Finally, conclusions are offered in Section 5.6.

5.1 Problem setting

In this chapter, we consider that the full model is described by a parametrized ordinary differential equation of second order:

$$\mathbf{M}(\boldsymbol{\mu})\ddot{\mathbf{X}}(t;\boldsymbol{\mu}) + \mathbf{C}(\boldsymbol{\mu})\dot{\mathbf{X}}(t;\boldsymbol{\mu}) + \mathbf{K}(\boldsymbol{\mu})\mathbf{X}(t;\boldsymbol{\mu}) = \mathbf{F}(t;\boldsymbol{\mu}) \tag{5.1}$$

where $\boldsymbol{\mu} \in \mathcal{D}$ ($P \geq 1$) is the parameter vector and $\mathcal{D} \subset \mathbb{R}^P$ denotes the corresponding parameter space. The matrices $\mathbf{M}$, $\mathbf{C}$, $\mathbf{K} \in \mathbb{R}^{n\times n}$ represent respectively the mass, damping and stiffness matrices of the problem which are supposed to be parameter dependent and $\mathbf{F} \in \mathbb{R}^n$ is the right-hand side vector of the problem which is time and parameter dependent. As in the previous chapter, we consider that our output of interest can be written as a linear form $S_l(t;\boldsymbol{\mu}) = \mathbf{L}^T\mathbf{X}(t;\boldsymbol{\mu})$, where $\mathbf{L}$ is a vector in $\mathbb{R}^n$, or as a quadratic form $S_q(t;\boldsymbol{\mu}) = \mathbf{X}^T(t;\boldsymbol{\mu})\mathbf{Q}\mathbf{X}(t;\boldsymbol{\mu})$ where $\mathbf{Q}$ is a matrix of $\mathbb{R}^{n\times n}$.

In the opposition to the previous chapter, we do not restrict ourselves here to the case where all operators of the left and the right-hand side of the problem can be expressed in a form affine parametric dependence. In addition, we will also consider the case where the geometry of the domain represents the parameter in the problem.

To make this chapter self contained, let us briefly recall the expressions of the matrices $\mathbf{M}, \mathbf{C}, \mathbf{K}$ of the full model (5.1) for a parametrized time domain vibro-acoustic problem. For the case where the formulation in $(\mathbf{u}_s, \phi)$ is employed, we have:

$$\begin{aligned}
\mathbf{M}_{u\phi}(\boldsymbol{\mu}) &= \begin{bmatrix} \mathbf{M}_s(\boldsymbol{\mu}) & \mathbf{0} \\ \mathbf{0} & -\rho_0(\boldsymbol{\mu})\mathbf{M}_f(\boldsymbol{\mu}) \end{bmatrix}, \mathbf{C}_{u\phi}(\boldsymbol{\mu}) = \begin{bmatrix} \mathbf{C}_s(\boldsymbol{\mu}) & -\rho_0(\boldsymbol{\mu})\mathbf{K}_c(\boldsymbol{\mu}) \\ -\rho_0(\boldsymbol{\mu})\mathbf{K}_c^T(\boldsymbol{\mu}) & -\rho_0(\boldsymbol{\mu})\mathbf{C}_f(\boldsymbol{\mu}) \end{bmatrix} \\
\mathbf{K}_{u\phi}(\boldsymbol{\mu}) &= \begin{bmatrix} \mathbf{K}_s(\boldsymbol{\mu}) & \mathbf{0} \\ \mathbf{0} & -\rho_0(\boldsymbol{\mu})\mathbf{K}_f(\boldsymbol{\mu}) \end{bmatrix}, \text{ and } \mathbf{X}_{u\phi}(t;\boldsymbol{\mu}) = \begin{bmatrix} \mathbf{U}_s(t;\boldsymbol{\mu}) \\ \boldsymbol{\Phi}(t;\boldsymbol{\mu}) \end{bmatrix}
\end{aligned} \tag{5.2}$$

where ρ_0 denotes the fluid density, the matrices $\mathbf{M}_s$ and $\mathbf{M}_f$ are known respectively as the

mass matrices of the structural part and the fluid part, the matrices $\mathbf{K}_s$ and $\mathbf{K}_f$ are known respectively as the stiffness matrices of the structural part and the fluid part, the matrix $\mathbf{K}_c$ represents the vibro-acoustic coupling matrix, the matrices $\mathbf{C}_s$ and $\mathbf{C}_f$ represent respectively the damping in structural part and the fluid part and the vector $\mathbf{U}_s$ and $\mathbf{\Phi}$ contain respectively the nodal values of structural displacement and velocity potential in the fluid. From their definitions in (1.39), the matrices $\mathbf{M}_s$ and $\mathbf{M}_f$ are symmetric positive definite, the matrices $\mathbf{K}_s$ and $\mathbf{K}_f$ are symmetric positive semi-definite. In our work, we assume that the matrices $\mathbf{C}_s$ and $\mathbf{C}_f$ are positive semi-definite which are sufficient conditions for the stability of the finite element model (see Lemma 3.1.4). As a remark, the matrices $\mathbf{K}_c$ and $\mathbf{K}_f$ depend only on the geometry of the fluid domain. Thus, they are $\boldsymbol{\mu}$-dependent only in the case when the geometry of the fluid domain is considered as the parameter of the problem.

With the same notations, the expression of the matrices $\mathbf{M}, \mathbf{C}, \mathbf{K}$ of the full model (5.1) for a parametrized time domain vibro-acoustic problem formulated in $(\mathbf{u}_s, p)$ is defined by:

$$\begin{aligned}
\mathbf{M}_{up}(\boldsymbol{\mu}) &= \begin{bmatrix} \mathbf{M}_s(\boldsymbol{\mu}) & \mathbf{0} \\ -\rho_0(\boldsymbol{\mu})\mathbf{K}_c^T(\boldsymbol{\mu}) & \mathbf{M}_f(\boldsymbol{\mu}) \end{bmatrix}, \mathbf{C}_{up}(\boldsymbol{\mu}) = \begin{bmatrix} \mathbf{C}_s(\boldsymbol{\mu}) & \mathbf{0} \\ \mathbf{0} & \mathbf{C}_f(\boldsymbol{\mu}) \end{bmatrix} \\
\mathbf{K}_{up}(\boldsymbol{\mu}) &= \begin{bmatrix} \mathbf{K}_s(\boldsymbol{\mu}) & \mathbf{K}_c(\boldsymbol{\mu}) \\ \mathbf{0} & \mathbf{K}_f(\boldsymbol{\mu}) \end{bmatrix} \text{ and } \mathbf{X}_{up}(t;\boldsymbol{\mu}) = \begin{bmatrix} \mathbf{U}_s(t;\boldsymbol{\mu}) \\ \mathbf{P}(t;\boldsymbol{\mu}) \end{bmatrix}
\end{aligned} \tag{5.3}$$

and in $(\mathbf{u}_s, p, \varphi)$ is defined by:

$$\begin{aligned}
\mathbf{M}_{up\varphi}(\boldsymbol{\mu}) &= \begin{bmatrix} \mathbf{M}_s(\boldsymbol{\mu}) & \mathbf{0} & -\rho_0(\boldsymbol{\mu})\mathbf{K}_c(\boldsymbol{\mu}) \\ \mathbf{0} & \mathbf{0} & \mathbf{M}_f(\boldsymbol{\mu}) \\ -\rho_0(\boldsymbol{\mu})\mathbf{K}_c^T(\boldsymbol{\mu}) & \mathbf{M}_f(\boldsymbol{\mu}) & -\rho_0(\boldsymbol{\mu})\mathbf{K}_f(\boldsymbol{\mu}) \end{bmatrix}, \mathbf{C}_{up\varphi}(\boldsymbol{\mu}) = \begin{bmatrix} \mathbf{C}_s(\boldsymbol{\mu}) & \mathbf{0} & \mathbf{0} \\ \mathbf{0} & \mathbf{0} & \mathbf{0} \\ \mathbf{0} & \mathbf{C}_f(\boldsymbol{\mu}) & \mathbf{0} \end{bmatrix} \\
\mathbf{K}_{up\varphi}(\boldsymbol{\mu}) &= \begin{bmatrix} \mathbf{K}_s(\boldsymbol{\mu}) & \mathbf{0} & \mathbf{0} \\ \mathbf{0} & \frac{1}{\rho_0(\boldsymbol{\mu})}\mathbf{M}_f(\boldsymbol{\mu}) & \mathbf{0} \\ \mathbf{0} & \mathbf{0} & \mathbf{0} \end{bmatrix} \text{ and } \mathbf{X}_{up\varphi}(t;\boldsymbol{\mu}) = \begin{bmatrix} \mathbf{U}_s(t;\boldsymbol{\mu}) \\ \mathbf{P}(t;\boldsymbol{\mu}) \\ \boldsymbol{\varphi}(t;\boldsymbol{\mu}) \end{bmatrix}
\end{aligned} \tag{5.4}$$

where the vector $\mathbf{P}$ and $\boldsymbol{\varphi}$ contain respectively the nodal values of pressure and displacement potential in the fluid.

We would also like to recall the expression of the right-hand side vector of the full model (5.1) for the case of an interaction of submerged structure and shock wave problem. Assuming that the shock wave is characterized by a incident pressure p^{inc} and an incident velocity $\mathbf{v}^{inc}$, the right-hand side of the problem formulated in $(\mathbf{u}_s, \phi^{sca})$ are given by $\mathbf{F}_{u\phi}^{sca}(t;\boldsymbol{\mu}) = \begin{bmatrix} \mathbf{F}_s^{sca}(t;\boldsymbol{\mu})^T & \mathbf{F}_\phi^{sca}(t;\boldsymbol{\mu})^T \end{bmatrix}^T$ where the vectors $\mathbf{F}_s^{sca}(t;\boldsymbol{\mu})$ and $\mathbf{F}_\phi^{sca}(t;\boldsymbol{\mu})$ are defined by $\mathbf{F}_{s,j}^{sca}(t;\boldsymbol{\mu}) := -\int_{\Gamma(\boldsymbol{\mu})} p^{inc}(\mathbf{x},t;\boldsymbol{\mu})[\mathbf{N}_j^s(\mathbf{x})\cdot\mathbf{n}_s(\mathbf{x})]d\mathbf{x}$, $\mathbf{F}_{\phi,j}^{sca}(t;\boldsymbol{\mu}) := -\int_{\Gamma(\boldsymbol{\mu})} \rho_0(\boldsymbol{\mu})[\mathbf{v}^{inc}(\mathbf{x},t;\boldsymbol{\mu})\cdot\mathbf{n}_s(\mathbf{x})]N_j^f(\mathbf{x})d\mathbf{x}$ with $\mathbf{N}^s$ and N^f denote respectively the finite element basis of the structural and the fluid part.

With the same notation, the right-hand side vector of the formulation in $(\mathbf{u}_s, \phi^{rad})$ and in $(\mathbf{u}_s, p^{rad})$ are given by $\mathbf{F}_{up}^{rad}(t;\boldsymbol{\mu}) = \begin{bmatrix} \mathbf{F}_s^{rad}(t;\boldsymbol{\mu})^T & \mathbf{0}^T \end{bmatrix}^T$, where the vector $\mathbf{F}_s^{rad}(t;\boldsymbol{\mu})$ is defined by $\mathbf{F}_{s,j}^{rad}(t;\boldsymbol{\mu}) = -\int_{\Gamma(\boldsymbol{\mu})}(p^{inc}+p^{ref})(\mathbf{x},t;\boldsymbol{\mu})[\mathbf{N}_j^s(\mathbf{x})\cdot\mathbf{n}_s(\mathbf{x})]d\mathbf{x}$. Finally, the right-hand side for the case of the formulation in $(\mathbf{u}_s, p^{rad}, \varphi^{rad})$ is given by $\mathbf{F}_{up\varphi}^{rad}(t;\boldsymbol{\mu}) = \begin{bmatrix} \mathbf{F}_s^{rad}(t;\boldsymbol{\mu})^T & \mathbf{0}^T & \mathbf{0}^T \end{bmatrix}^T$.

We recall that the reflected pressure p^{ref} has to be pre-computed (see Section 2.4.5) in order to employ these three formulations. Since the reflected pressure p^{ref} depends on the incident velocity $\mathbf{v}^{inc}$ and the properties of the fluid, it becomes $\boldsymbol{\mu}$-dependent when the geometry of fluid domain represents the parameter of the problem and when the incident velocity $\mathbf{v}^{inc}$ is $\boldsymbol{\mu}$-dependent, for instance in the case where the shock wave comes from an underwater explosion with a varying mass of explosive material.

5.2 Empirical Interpolation Method (EIM) and its applications

As exposed in the previous chapter, the affine parametric dependence assumption is a key for the offline-online efficiency of the procedure and in construction of the reduced basis by a POD-Greedy algorithm. In the case where this assumption is not valid, we can rely on the Empirical Interpolation Method (EIM) [17] to recover this assumption approximately. The aim of this section is to recall the EIM and give an overview of its applications in the context of the reduced order modelling.

5.2.1 A short presentation of EIM

To begin, we give a short presentation of the original version of EIM proposed in [17]. The aim of EIM is to seek an approximation of any function $g(\mathbf{x}, \boldsymbol{\mu}) : \Omega \times \mathcal{D} \to \mathbb{R}$ depending on both the spatial variable $\mathbf{x}$ and the parameter vector $\boldsymbol{\mu}$ in a non affine way, in a separated form with respect to $\mathbf{x}$ and $\boldsymbol{\mu}$:

$$g(\mathbf{x}, \boldsymbol{\mu}) \approx g_M^{EIM}(\mathbf{x}, \boldsymbol{\mu}) := \sum_{i=1}^{M} \beta_i(\boldsymbol{\mu}) q_i(\mathbf{x}) \tag{5.5}$$

by choosing on a greedy manner the nested sets interpolation points $\{\mathbf{x}_1^g, \cdots, \mathbf{x}_M^g\} \subset \Omega$ (also called magic points) and the nested set of basis functions $\{q_1, \cdots, q_M\}$. Being an interpolation method, the coefficients $(\beta_i(\boldsymbol{\mu}))_{1 \leq i \leq M}$ are determined by solving the following linear system:

$$\sum_{j=1}^{M} q_j(\mathbf{x}_i^g) \beta_j(\boldsymbol{\mu}) = g(\mathbf{x}_i^g, \boldsymbol{\mu}), \forall i = 1, \cdots, M \tag{5.6}$$

Let us denote by $\mathcal{D}_{train}^{EIM} \subset \mathcal{D}$ a finite training set, ϵ_{EIM} a given tolerance, M_{max} the maximum number of terms and $\boldsymbol{\mu}_1^g$ an initial parameter value which can be determined randomly or by using knowledge of the problem at hand, the EIM procedure for finding the magic points $(\mathbf{x}_i^g)_{1 \leq i \leq M}$ and the basis functions $(q_i)_{1 \leq i \leq M}$ is as follows. The first interpolation point $\mathbf{x}_1^g$ and the first basis function q_1 are defined by:

$$\mathbf{x}_1^g = \text{argmax}_{\mathbf{x} \in \Omega} |g(\mathbf{x}, \boldsymbol{\mu}_1^g)|, q_1(\mathbf{x}) = \frac{g(\mathbf{x}, \boldsymbol{\mu}_1^g)}{g(\mathbf{x}_1^g, \boldsymbol{\mu}_1^g)} \tag{5.7}$$

Then, for $2 \leq M \leq M_{max}$, we set $\boldsymbol{\mu}_M^g$ as the solution of following minimization problem:

$$\boldsymbol{\mu}_M^g = \text{argmax}_{\boldsymbol{\mu} \in \mathcal{D}_{train}^{EIM}} ||g(\cdot, \boldsymbol{\mu}) - g_{M-1}^{EIM}(\cdot, \boldsymbol{\mu})||_{L^\infty(\Omega)} \tag{5.8}$$

where $g_{M-1}^{EIM}(\mathbf{x}, \boldsymbol{\mu})$ defined by $g_{M-1}^{EIM}(\mathbf{x}, \boldsymbol{\mu}) = \sum_{j=1}^{M-1} \beta_j^{M-1} q_j(\mathbf{x})$ with $(\beta_j^{M-1}(\boldsymbol{\mu}))_{1 \leq j \leq M-1}$ being the solution of linear system $\sum_{j=1}^{M-1} \beta_j^{M-1}(\boldsymbol{\mu}) q_j(\mathbf{x}_i^g) = g(\mathbf{x}_i^g, \boldsymbol{\mu}), i = 1, \cdots, M-1$. We compute

then the residual for this new value of parameter $r_M(\mathbf{x}) := g(\mathbf{x}, \boldsymbol{\mu}_M^g) - g_{M-1}^{EIM}(\cdot, \boldsymbol{\mu}_M^g)$ and set the next interpolation points and the basis functions q_M as

$$\mathbf{x}_M^g = \text{argmax}_{\mathbf{x}\in\Omega}|r_M(\mathbf{x})|, q_M(\mathbf{x}) = \frac{r_M(\mathbf{x})}{r_M(\mathbf{x}_M^g)} \tag{5.9}$$

The procedure is iterated until the stopping criterion is verified or the maximal number of iteration is reached. The summary of EIM [17] procedure is outlined in Algorithm 16.

Algorithm 16 Greedy EIM algorithm [17]

Input: A function $g : \Omega \times \mathcal{D} \to$, a fixed tolerance ϵ_{EIM}, a maximal number of terms M_{max}, a finite training set $\mathcal{D}_{train}^{EIM} \subset \mathcal{D}$ and a selection of $\boldsymbol{\mu}_1^g \in \mathcal{D}_{train}^{EIM}$

Output: The interpolations points $\{\mathbf{x}_1^g, \cdots, \mathbf{x}_M^g\} \subset \Omega$ and the basis functions $\{q_1, \cdots, q_M\}$

1: Set $\mathbf{x}_1^g = \text{argmax}_{\mathbf{x}\in\Omega}|g(\mathbf{x}, \boldsymbol{\mu}_1^g)|$, and $q_1(\mathbf{x}) = \frac{g(\mathbf{x}, \boldsymbol{\mu}_1^g)}{g(\mathbf{x}_1^g, \boldsymbol{\mu}_1^g)}$
2: Set $M = 2$
3: **while** $(M \leq M_{max})$ **do**
4: Compute for all $\boldsymbol{\mu} \in \mathcal{D}_{train}^{EIM}$, $g_{M-1}^{EIM}(\cdot, \boldsymbol{\mu}) := \sum_{j=1}^{M-1} \beta_j^{M-1}(\boldsymbol{\mu}) q_j(\mathbf{x})$ where $(\beta_j^{M-1}(\boldsymbol{\mu}))_{1\leq j\leq M-1}$ is the solution of linear system

$$\sum_{j=1}^{M-1} \beta_j^{M-1}(\boldsymbol{\mu}) q_j(\mathbf{x}_i^g) = g(\mathbf{x}_i^g, \boldsymbol{\mu}), i = 1, \cdots, M-1 \tag{5.10}$$

5: Set $\boldsymbol{\mu}_M^g = \text{argmax}_{\boldsymbol{\mu}\in\mathcal{D}_{train}^{EIM}} ||g(\cdot, \boldsymbol{\mu}) - g_{M-1}^{EIM}(\cdot, \boldsymbol{\mu})||_{L^\infty(\Omega)}$
6: **if** $(||g(\cdot, \boldsymbol{\mu}_M^g) - g_{M-1}^{EIM}(\cdot, \boldsymbol{\mu}_M^g)||_{L^\infty(\Omega)} \leq \epsilon_{EIM} ||g(\cdot, \boldsymbol{\mu}_M^g)||_{L^\infty(\Omega)})$ **then**
7: **break;**
8: **else**
9: Compute the residual $r_M(\mathbf{x}) = g(\mathbf{x}, \boldsymbol{\mu}_M^g) - g_{M-1}^{EIM}(\cdot, \boldsymbol{\mu}_M^g)$
10: Set $\mathbf{x}_M^g = \text{argmax}_{\mathbf{x}\in\Omega}|r_M(\mathbf{x})|$ and $q_M(\mathbf{x}) = \frac{r_M(\mathbf{x})}{r_M(\mathbf{x}_M^g)}$
11: **end if**
12: Set $M = M + 1$
13: **end while**

By the construction of the interpolation points $\{\mathbf{x}_1^g, \cdots, \mathbf{x}_M^g\}$ and the basis function $(q_i)_{1\leq i\leq M}$, the matrix $\mathbf{B}^{M-1} \in \mathbb{R}^{(M-1)\times(M-1)}$ (defined by $\mathbf{B}_{ij}^{M-1} = q_j(\mathbf{x}_i^g)$) representing the linear system of the step 4 of Algorithm 16 is a lower triangular matrix with unity diagonal. Hence, the procedure of EIM is well defined. We note that $\text{span}\{q_1, \cdots, q_M\} = \text{span}\{g(\cdot, \boldsymbol{\mu}_1^g), \cdots, g(\cdot, \boldsymbol{\mu}_M^g)\}$, so the approximation g_M^{EIM} of g in Equation (5.5) can be written in a equivalent way as:

$$g_M^{EIM}(\mathbf{x}, \boldsymbol{\mu}) := \sum_{i=1}^{M} \alpha_i(\boldsymbol{\mu}) g(\mathbf{x}, \boldsymbol{\mu}_i^g) \tag{5.11}$$

where the coefficient $(\alpha_i(\boldsymbol{\mu}))_{1\leq i\leq M}$ is the solution of the linear system:

$$\sum_{j=1}^{M} g(\mathbf{x}_j^g, \boldsymbol{\mu}_i^g) \alpha_j(\boldsymbol{\mu}) = g(\mathbf{x}_i^g, \boldsymbol{\mu}), \forall i = 1, \cdots, M \tag{5.12}$$

It is worth mentioning a conservation property of the approximation g by g_M^{EIM} as stated in the following lemma.

Lemma 5.2.1 *[66] Let L a linear form over the functional space span$\{g(\cdot,\boldsymbol{\mu}), \boldsymbol{\mu}\in\mathcal{D}\}$ and let $L(g(\cdot,\boldsymbol{\mu}))=0, \forall\boldsymbol{\mu}\in\mathcal{D}$, then we also have*

$$L(g_M^{EIM}(\cdot,\boldsymbol{\mu}))=0, \forall\boldsymbol{\mu}\in\mathcal{D} \tag{5.13}$$

Proof: Combining the linearity of L and the definition of g_M^{EIM} in Equation (5.11), we have for any $\boldsymbol{\mu}\in\mathcal{D}$: $L(g_M^{EIM}(\cdot,\boldsymbol{\mu}))=\sum_{i=1}^{M}\alpha_i(\boldsymbol{\mu})L(g(\mathbf{x},\boldsymbol{\mu}_i^g))=0$.

□

A particular case of Lemma 5.2.1 is that if $\mathbf{x}^*\in\Omega$ is a zero/root of the function $g(\cdot,\boldsymbol{\mu})$, for any $\boldsymbol{\mu}\in\mathcal{D}$, then $\mathbf{x}^*$ is also zero/root of its approximation by EIM $g_M^{EIM}(\cdot,\boldsymbol{\mu})$. An other particular case is the case of zero-mean functions: if $\int_\Omega g(x,\boldsymbol{\mu})dx=0$ for any $\boldsymbol{\mu}\in\mathcal{D}$, then its approximation by EIM is also a zero-mean function: $\int_\Omega g_M^{EIM}(x,\boldsymbol{\mu})dx=0, \forall\boldsymbol{\mu}\in\mathcal{D}$.

Finally, it should be noted that in the case where the dimension of the space $W_g=$ span$\{g(\cdot,\boldsymbol{\mu}),\boldsymbol{\mu}\in\mathcal{D}\}$ is equal to M the number of terms used in EIM approximation, then we have $g=g_M^{EIM}$.

5.2.2 Application of EIM to obtain an approximation in form affine parametric dependence

One of the most powerful application of EIM is that it allows to approximate any operator $\mathbf{A}(\boldsymbol{\mu})$ which is nonaffine parametric dependence into an affine parametric dependence form:

$$\mathbf{A}(\boldsymbol{\mu})\approx\mathbf{A}_M^{EIM}(\boldsymbol{\mu}):=\sum_{i=1}^{M}\theta_i^A(\boldsymbol{\mu})\mathbf{A}_i \tag{5.14}$$

where the matrices $\mathbf{A}_i$ are $\boldsymbol{\mu}$-independent. This allows us to recover the efficient offline-online computation procedure in the context of the reduced order modelling. As an example, assuming that the operator $\mathbf{A}(\mu)$ arises from the finite element discretization of the bilinear form:

$$a(\mathbf{u},\mathbf{v};\boldsymbol{\mu}):=\int_\Omega\left[g(\mathbf{x},\boldsymbol{\mu})\mathbf{u}(\mathbf{x})\mathbf{v}(\mathbf{x})+\boldsymbol{\nabla}\mathbf{u}(\mathbf{x})\cdot\boldsymbol{\nabla}\mathbf{v}(\mathbf{x})\right]d\mathbf{x} \tag{5.15}$$

then replacing the function g by its approximation g_M^{EIM} of Equation (5.11) by the EIM, leads to:

$$\mathbf{A}(\boldsymbol{\mu})\approx\sum_{i=1}^{M}\alpha_i^g(\boldsymbol{\mu})\mathbf{A}_i+\mathbf{A}_0 \tag{5.16}$$

where the matrices $\mathbf{A}_i$ correspond to the bilinear form $a_i(\mathbf{u},\mathbf{v}):=\int_\Omega\left[g(\mathbf{x},\boldsymbol{\mu}_i^g)\mathbf{u}(\mathbf{x})\mathbf{v}(\mathbf{x})\right]d\mathbf{x}$, for $i=1,\cdots,M$ and the matrix $\mathbf{A}_0$ corresponds to the bilinear form $a_0(\mathbf{u},\mathbf{v}):=\int_\Omega\boldsymbol{\nabla}\mathbf{u}(\mathbf{x})\cdot\boldsymbol{\nabla}\mathbf{v}(\mathbf{x})d\mathbf{x}$ which are $\boldsymbol{\mu}$-independent.

5.2.3 Application of EIM for an nonintrusive procedure

Another potential application of EIM is in the construction of an nonintrusive procedure [33] in the sense that it should not require to construct the matrices $\mathbf{A}_i$ in the affine parametric dependence assumption:

$$\mathbf{A}(\boldsymbol{\mu}) = \sum_{i=1}^{N_A} \theta_i(\boldsymbol{\mu}) \mathbf{A}_i \tag{5.17}$$

but only the matrices $\mathbf{A}(\boldsymbol{\mu})$ for some selected values of the parameter $\{\boldsymbol{\mu}_1^*, \cdots, \boldsymbol{\mu}_M^*\}$, that is:

$$\mathbf{A}(\boldsymbol{\mu}) \approx \sum_{m=1}^{M} \alpha_m(\boldsymbol{\mu}) \mathbf{A}(\boldsymbol{\mu}_m^*) \tag{5.18}$$

The construction of a non-intrusive procedure is motivated by the fact that in the most general cases it requires to modify the assembling routines in the computational code to obtain the matrices $\mathbf{A}_i$, for $i = 1, \cdots, N_A$, of Equation (5.17). The main idea to obtain such a non-intrusive form of Equation (5.18) is to apply the EIM to approximate the function $\theta_i(\boldsymbol{\mu})$ seen as a function depending on two variables $i \in \Omega := \{1, \cdots, N_A\}$ and $\boldsymbol{\mu} \in \mathcal{D}$:

$$\theta(i, \boldsymbol{\mu}) \approx \theta_M^{EIM}(i, \boldsymbol{\mu}) = \sum_{m=1}^{M} \alpha_m(\boldsymbol{\mu}) \theta_i(\boldsymbol{\mu}_m^\theta) \tag{5.19}$$

Then, injecting the approximation (5.19) into the Equation (5.17) yields:

$$\mathbf{A}(\boldsymbol{\mu}) \approx \sum_{i=1}^{N_A} \left[\sum_{m=1}^{M} \alpha_m(\boldsymbol{\mu}) \theta_i(\boldsymbol{\mu}_m^\theta) \right] \mathbf{A}_i = \sum_{m=1}^{M} \alpha_m(\boldsymbol{\mu}) \sum_{i=1}^{N_A} \theta_i(\boldsymbol{\mu}_m^\theta) \mathbf{A}_i = \sum_{m=1}^{M} \alpha_m(\boldsymbol{\mu}) \mathbf{A}(\boldsymbol{\mu}_m^\theta) \tag{5.20}$$

It should be remarked that an EIM algorithm applied on the function $\theta_i(\boldsymbol{\mu})$ can stop before $M = N_A$. It occurs when the dimension of $\text{span}\{\theta(\cdot, \boldsymbol{\mu}), \boldsymbol{\mu} \in \mathcal{D}\}$ is less than M. In the case where $\theta(i, \boldsymbol{\mu}) = \theta_M^{EIM}(i, \boldsymbol{\mu})$ (when $M = N_A$ or when the dimension of $\text{span}\{\theta(\cdot, \boldsymbol{\mu}), \boldsymbol{\mu} \in \mathcal{D}\}$ is equal to the dimension of $\text{span}\{\theta_M^{EIM}(\cdot, \boldsymbol{\mu}), \boldsymbol{\mu} \in \mathcal{D}\}$), there is no loss of accuracy to obtain a non-intrusive procedure. The proposed technique can also be extended to the case where the operator $\mathbf{A}(\boldsymbol{\mu})$ depends on $\boldsymbol{\mu}$ in a non-affine way by seeking at first its approximation in form of affine dependence in $\boldsymbol{\mu}$ as presented in Section 5.2.2.

5.2.4 Application of EIM Algorithm with a black box way in context of finite element model

In order to apply the EIM to obtain an approximation in an affine parametric dependence form with a non-intrusive way as presented in Section 5.2.3, we remark that it requires the knowledge on the definition of the bilinear form of which the operator $\mathbf{A}$ arises from the finite element discretization. In this section, we propose to exploit the idea of EIM to develop an algorithm for finding an approximation of any matrix $\mathbf{A}(\boldsymbol{\mu}) : \boldsymbol{\mu} \in \mathcal{D} \to \mathbb{R}^{n \times n}$ or vector $\mathbf{F}(\boldsymbol{\mu}) : \boldsymbol{\mu} \in \mathcal{D} \to \mathbb{R}^n$ resulting from a finite element discretization of a parametrized bilinear or linear form and being

non-affine dependence in $\boldsymbol{\mu}$ into an affine parametric dependence form:

$$\mathbf{A}(\boldsymbol{\mu}) \approx \mathbf{A}^{EIM}(\boldsymbol{\mu}) := \sum_{i=1}^{N_A^{EIM}} \theta_i^A(\boldsymbol{\mu})\mathbf{A}(\boldsymbol{\mu}_i^A),\ \mathbf{F}(\boldsymbol{\mu}) \approx \mathbf{F}^{EIM}(\boldsymbol{\mu}) := \sum_{i=1}^{N_F^{EIM}} \theta_i^F(\boldsymbol{\mu})\mathbf{F}(\boldsymbol{\mu}_i^F) \quad (5.21)$$

purely in algebraic way without any knowledge on the definition of the matrix $\mathbf{A}$ and the vector $\mathbf{F}$. In our work, the matrix $\mathbf{A}$ refers, as a particular case, to the mass matrix $\mathbf{M}$ or the damping matrix $\mathbf{C}$ or the stiffness matrix $\mathbf{K}$ of a finite element vibro-acoustic model, whose definitions are given by Equation (5.2) for the formulation in $(\mathbf{u}_s, \phi)$, by Equation (5.3) for the formulation in $(\mathbf{u}_s, p)$ and by Equation (5.4) for the formulation in $(\mathbf{u}_s, p, \varphi)$. The vector $\mathbf{F}$ refers to the right-hand side vector of the interaction of submerged structure and shock wave problem whose definition is given in Section 5.1.

The key idea is not to apply EIM algorithm on the continuous function depending on two parameters $g : (\mathbf{x}, \boldsymbol{\mu}) \in \Omega \times \mathcal{D}$, underlying in the definition of the bilinear form of the matrix $\mathbf{A}$ or the linear form of the vector $\mathbf{F}$, but to apply directly on the matrix $\mathbf{A}$ or the vector $\mathbf{F}$. To begin, we consider the case of the vector $\mathbf{F}(\boldsymbol{\mu})$. The first step consists in the construction of the vectors $\mathbf{F}$ for all values of the parameter in a finite training set $\mathcal{D}_{train}$. By applying EIM algorithm 16 on the function $f : (i, \boldsymbol{\mu}) \in \{1, \cdots, n\} \times \mathcal{D}_{train} \to \mathbb{R}$ defined by $f(i, \boldsymbol{\mu}) = F_i(\boldsymbol{\mu})$ where F_i is i^{th} component of the vector $\mathbf{F}$, we obtain then a set of magical indices $(i_l^F)_{1 \leq l \leq N_F^{EIM}}$ and a set of the selected values of parameter $(\boldsymbol{\mu}_l^F)_{1 \leq l \leq N_F^{EIM}}$ such that:

$$\mathbf{F}(\boldsymbol{\mu}) \approx \sum_{l=1}^{N_F^{EIM}} \theta_l^F(\boldsymbol{\mu})\mathbf{F}(\boldsymbol{\mu}_l^F), \forall \boldsymbol{\mu} \in \mathcal{D} \quad (5.22)$$

where the coefficients $(\theta_l^F(\boldsymbol{\mu}))_{1 \leq l \leq N_F^{EIM}}$ are determined by Lagrange interpolation at magical indices $(i_l^F)_{1 \leq l \leq N_F^{EIM}}$:

$$\sum_{l=1}^{N_F^{EIM}} \theta_l^F(\boldsymbol{\mu})F_{i_l^F}(\boldsymbol{\mu}_l^F) = F_{i_l^F}(\boldsymbol{\mu}), \forall l = 1, \cdots, N_F^{EIM} \quad (5.23)$$

In order to obtain the value of the coefficients $(\theta_l^F(\boldsymbol{\mu}))_{1 \leq l \leq N_F^{EIM}}$ for any new value of $\boldsymbol{\mu} \in \mathcal{D}$ by Equation (5.23), it should not require to construct the whole vector $\mathbf{F}(\boldsymbol{\mu})$ but only to access to its values at the magical indices: $\{i_l^F, 1 \leq l \leq N_F^{EIM}\} \subset \{1, \cdots, n\}$ chosen by EIM. In the context of the finite element model, these values can be obtained with an complexity independent of n thanks to the property of the local support of the finite element basis functions.

The strategy [100] consists of computing and assembling only the elementary terms which have a non-zero contribution on the values of the vector $\mathbf{F}$ at the magical indices. To do so, it suffices to identify such a group of elements in the mesh and to restrict the loop of the vector assembly over those elements. From the data structures defining the mesh and the procedure of assembling, we can identify a set of the nodes $\{n_l^F, 1 \leq l \leq N_F^{EIM}\}$, whose degree of freedom corresponds to magical indices $(i_l^F)_{1 \leq l \leq N_F^{EIM}}$. In the case of vectorial problem where each node can have more than one degree of freedom, it is possible that the total number of these nodes is less than N_F^{EIM}. The group of elements, namely *reduced elements*, which provide a non-zero contribution to the value of the vector $\mathbf{F}(\boldsymbol{\mu})$ at the magical indices $(i_l^F)_{1 \leq l \leq N_F^{EIM}}$ is

then defined as the union of the element in the mesh which contains at least one node of the set $\{n_l^F, 1 \leq l \leq N_F^{EIM}\}$. The summary of the methodology for the case of vector is outlined by Algorithm 17 and 18.

Algorithm 17 Greedy EIM algorithm in a black box way for the case of vectors

Input: A fixed tolerance ϵ_{EIM}, a maximal number of terms M_{max}, $[\mathbf{F}(\boldsymbol{\mu}_1), \cdots, \mathbf{F}(\boldsymbol{\mu}_{n_{train}})] \in \mathbb{R}^{n \times n_{train}}$ and a selection of $\boldsymbol{\mu}_1^F \in \{\boldsymbol{\mu}_1, \cdots, \boldsymbol{\mu}_{n_{train}}\}$

Output: The magical indices $\{i_l^F, 1 \leq l \leq N_F^{EIM}\} \subset \{1, \cdots, n\}$ and the chosen value parameters $\{\boldsymbol{\mu}_l^F, 1 \leq l \leq N_F^{EIM}\} \subset \mathcal{D}_{train} := \{\boldsymbol{\mu}_1, \cdots, \boldsymbol{\mu}_{n_{train}}\}$

1: Define the function $f : (i, \boldsymbol{\mu}) \in \{1, \cdots, n\} \times \mathcal{D}_{train} \to \mathbb{R}$ as

$$f(i, \boldsymbol{\mu}) = F_i(\boldsymbol{\mu}) \tag{5.24}$$

where F_i is i^{th} component of the vector $\mathbf{F}$

2: Run the EIM Algorithm 16 with the function f seen as a function depending on two variables $i \in \Omega := \{1, \cdots, n\}$ and $\boldsymbol{\mu} \in \mathcal{D}_{train}$

Algorithm 18 Construction of the reduced elements in the mesh which have a non-zero contribution on the values of the vector $\mathbf{F}$ at the magical indices

Input: The magical indices $(i_l^F)_{1 \leq l \leq N_F^{EIM}}$ provided by EIM algorithm 17

Output: A group of elements e^F which have a non-zero contribution on the values of the vector $\mathbf{F}$ at the magical indices $(i_l^F)_{1 \leq l \leq N_F^{EIM}}$

1: Identify the set of nodes $\{n_l^F, 1 \leq l \leq N_F^{EIM}\}$ whose degree of freedom correspond to magical indices $\{i_l^F, 1 \leq l \leq N_F^{EIM}\}$

2: Set e^F as the union of the element in the mesh which contains at least one node of the set $\{n_l^F, 1 \leq l \leq N_F^{EIM}\}$

The same approach can also be applied to the case of the matrix $\mathbf{A}$ by vectorizing at first the matrix $\mathbf{A}$ to obtain its representation $\text{vec}(\mathbf{A})$ as a vector of $\mathbb{R}^{n^2}$, for instance by stacking the columns of $\mathbf{A}$ (see Remark 5.2.1 for some optimisation). By running the Algorithm 17, we obtain the set of chosen values of parameter $\{\boldsymbol{\mu}_l^A, 1 \leq l \leq N_A^{EIM}\} \subset \mathcal{D}_{train} := \{\boldsymbol{\mu}_1, \cdots, \boldsymbol{\mu}_{n_{train}}\}$ and the set of magical indices $\{i_l^A, 1 \leq l \leq N_A^{EIM}\} \subset \{1, \cdots, n^2\}$. To construct the group element which have a non-zero contribution on the value of $\text{vec}(\mathbf{A})$ at the magical indices $(i_l^A)_{1 \leq l \leq N_A^{EIM}}$, we seek the set of pair of row-columns index $\{(j_l, k_l), 1 \leq l \leq N_A^{EIM}\} \subset \{1, \cdots, n\} \times \{1, \cdots, n\}$ corresponding to the magical indices $(i_l^A)_{1 \leq l \leq N_A^{EIM}}$ in vector format. We identify then a group of nodes: $\{n_l^A, 1 \leq l \leq 2N_A^{EIM}\}$ whose degree of freedom corresponds to the set of indices $\{j_l, 1 \leq l \leq N_A^{EIM}\} \cup \{k_l, 1 \leq l \leq N_A^{EIM}\}$. Note that if the index i_l^A of $\text{vec}(\mathbf{A})$ corresponds to a diagonal term of the matrix $\mathbf{A}$, it corresponds to only one node in the mesh. On the contrary, it can correspond to two nodes in the mesh. The group of elements, so called *reduced elements*, which provide a non-zero contribution to the value of $\text{vec}(\mathbf{F})(\boldsymbol{\mu})$ at the magical indices $(i_l^A)_{1 \leq l \leq N_A^{EIM}}$ is then defined as the union of the element in the mesh which contains at least one node of the set $\{n_l^A, 1 \leq l \leq 2N_A^{EIM}\}$. The summary of the methodology for the case of matrix is outlined by Algorithm 17 and 18.

Algorithm 19 Greedy EIM algorithm in a black box way for the case of matrices

Input: A fixed tolerance ϵ_{EIM}, a maximal number of terms M_{max}, $[\mathbf{A}(\boldsymbol{\mu}_1), \cdots, \mathbf{A}(\boldsymbol{\mu}_{n_{train}})] \in \mathbb{R}^{n\times n}$ and a selection of $\boldsymbol{\mu}_1^A \in \{\boldsymbol{\mu}_1, \cdots, \boldsymbol{\mu}_{n_{train}}\}$

Output: The magical indices $\{i_l^A, 1 \leq l \leq N_A^{EIM}\} \subset \{1, \cdots, n^2\}$ and the chosen value parameters $\{\boldsymbol{\mu}_l^A, 1 \leq l \leq N_A^{EIM}\} \subset \mathcal{D}_{train} := \{\boldsymbol{\mu}_1, \cdots, \boldsymbol{\mu}_{n_{train}}\}$

1: Define an application for transforming the matrix $\mathbf{A}(\boldsymbol{\mu}) \in \mathbb{R}^{n\times n}$ to a vector format $\text{vec}(\mathbf{A})(\boldsymbol{\mu}) \in \mathbb{R}^{n^2}$

2: Define the function $f : (i, \boldsymbol{\mu}) \in \{1, \cdots, n^2\} \times \mathcal{D}_{train} \to \mathbb{R}$ as

$$f(i, \boldsymbol{\mu}) = \text{vect}(\mathbf{A})_i(\boldsymbol{\mu}) \tag{5.25}$$

where $\text{vect}(\mathbf{A})_i$ is i^{th} component of the vector $\text{vec}(\mathbf{A}) \in \mathbb{R}^{n^2}$

3: Run the EIM Algorithm 16 with the function f seen as a function depending on two variables $i \in \Omega := \{1, \cdots, n^2\}$ and $\boldsymbol{\mu} \in \mathcal{D}_{train}$

Algorithm 20 Construction of the reduced elements in the mesh which have a non-zero contribution on the value of the vector $\text{vec}(\mathbf{A})$ at the magical indices

Input: The magical indices $(i_l^A)_{1\leq l\leq N_A^{EIM}}$ provided by EIM algorithm 19

Output: A group of elements e^A which have a non-zero contribution on the value of the vector $\text{vec}(\mathbf{A})$ at the magical indices $(i_l^A)_{1\leq l\leq N_A^{EIM}}$

1: Identify the set of pair of row-columns index $\{(j_l, k_l), 1 \leq l \leq N_A^{EIM}\} \subset \{1, \cdots, n\} \times \{1, \cdots, n\}$ corresponding to the magical indices $(i_l^A)_{1\leq 1\leq N_A^{EIM}}$ in vector format

2: Identify the set of node $\{n_l^A, 1 \leq l \leq 2N_A^{EIM}\}$ whose degree of freedom correspond to the set of indices $\{j_l, 1 \leq l \leq N_A^{EIM}\} \cup \{k_l, 1 \leq l \leq N_A^{EIM}\}$

3: Set e^A as the union of the element in the mesh which contains at least one node of the set $\{n_l^A, 1 \leq l \leq 2N_A^{EIM}\}$

An illustration of the procedure of identification of the reduced elements for the case of matrix, resulting from a P^1 finite element discretization, is given by Figure 5.1.

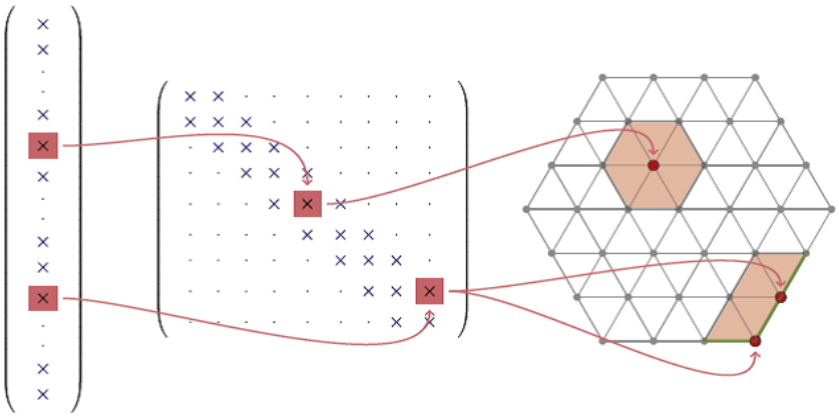

Figure 5.1: On the left: red boxes represent the magical indices chosen by EIM. In the middle: red boxes represent to the pairs of row-column index in the matrix format corresponding to the chosen magical indices. On the right, the obtained reduced elements in the mesh. (source from [100])

Remark 5.2.1 In the case where the matrices $\mathbf{A}(\boldsymbol{\mu})$ have the same sparse structure for any $\boldsymbol{\mu} \in \mathcal{D}$, the procedure of the matrix case can be implemented by exploiting its sparse format so that the actual dimension of the vector vec($\mathbf{A}$) is n_z rather than n, where n_z is the number of non-zero entries in the matrix $\mathbf{A}$. Furthermore, if the matrices $\mathbf{A}(\boldsymbol{\mu})$ are all symmetric then the dimension of the vector vec($\mathbf{A}$) is the number of non-zero entries in the superior (or inferior) block.

Remark 5.2.2 We note that the property of symmetry is automatically inherited in the approximation by the EIM. In the opposition, this might be not the case for the definite definiteness. On this matter, it is worth to recall a general result of perturbation of theory of eigenvalue problem, proposed by Bauer-Fike theorem (see for instance in [60]), which states that: the deviation between the singular values σ_i^{EIM} of the approximation matrix $\mathbf{A}^{EIM}$ and the singular values σ_i of the original matrix $\mathbf{A}$ is bounded by:

$$|\sigma_i^{EIM} - \sigma_i| \leq ||\mathbf{A} - \mathbf{A}^{EIM}||_2 \tag{5.26}$$

where $||\cdot||_2$ denotes the Frobenius norm. As a result, it should be sufficient by increasing the number of terms N_A^{EIM} in the EIM's approximation (5.21) to recover this definiteness properties.

Remark 5.2.3 For the case where the matrices $\mathbf{A}(\boldsymbol{\mu})$ are positive semi-definiteness, for all $\boldsymbol{\mu} \in \mathcal{D}$, with the kernel Ker($\mathbf{A}(\boldsymbol{\mu})$) := $\{\mathbf{x} \in \mathbb{R}^n | \mathbf{A}(\boldsymbol{\mu})\mathbf{x} = \mathbf{0}\}$ is $\boldsymbol{\mu}$-independent, as a particular case of Lemma 5.2.1, we can show that that the kernel of the matrix $\mathbf{A}(\boldsymbol{\mu})$ is a subset of the kernel of its EIM approximation $\mathbf{A}^{EIM}(\boldsymbol{\mu})$. This result implies that in the case where the matrix $\mathbf{A}$ represents the structural stiffness matrix $\mathbf{K}_s$, its EIM approximation $\mathbf{K}_s^{EIM}$ has the same rigid body modes as the original matrix $\mathbf{K}_s$ and it ensures that this mode corresponds well to the eigenvalue $\lambda = 0$, not $\lambda \approx \pm\epsilon_{EIM}$ which would destroy the positive semi-definiteness property of $\mathbf{A}^{EIM}(\boldsymbol{\mu})$. The same conclusion can also be valid for the case of the fluid stiffness matrix $\mathbf{K}_f$ where its kernel represents the pressure constant mode. As a conclusion, for the case the matrices $\mathbf{A}(\boldsymbol{\mu})$ are positive semi-definiteness with a $\boldsymbol{\mu}$-independent kernel, we believe that it could be recover the positive semi-definiteness property for $\mathbf{A}^{EIM}(\boldsymbol{\mu})$ by increasing the number of terms N_A^{EIM} in the EIM's approximation (5.21).

Remark 5.2.4 An alternative way to obtain an approximation in affine parametric dependence form of any nonaffine parametric dependence vector or matrix in a purely algebraic and black box way is to construct the basis by applying the POD on the snapshot matrix $\mathbf{S} = [\mathbf{F}(\boldsymbol{\mu}_1), \cdots, \mathbf{F}(\boldsymbol{\mu}_{n_{train}})] \in \mathbb{R}^{n \times n_{train}}$ with respect to a given tolerance instead of choosing with a greedy procedure the basis as: $\mathbf{F}(\boldsymbol{\mu}_1^F), \cdots, \mathbf{F}(\boldsymbol{\mu}_{N_F^{EIM}}^F)$, see for instance [37, 100]. The interpolation points are then defined using a greedy procedure from the resulting basis $\mathbf{F}_1, \cdots, \mathbf{F}_N$. The complexity of this alternative is dominated by the computation of the basis by POD, thus in $O(nn_{train}^2)$ while the complexity of our approach is only in $O(nn_{train}N_F^{EIM})$.

5.2.5 Application of EIM to approximate the solution of the linear problem with non-affine parameter dependent right-hand side

EIM can also be employed to approximate the solution of the linear problem with non-affine parameter dependent right-hand side:

$$\mathbf{M}\ddot{\mathbf{X}}(t;\boldsymbol{\mu}) + \mathbf{C}\dot{\mathbf{X}}(t;\boldsymbol{\mu}) + \mathbf{K}\mathbf{X}(t;\boldsymbol{\mu}) = \mathbf{F}(t;\boldsymbol{\mu}) \tag{5.27}$$

over the parameter value range $\boldsymbol{\mu} \in \mathcal{D}$. Here, we consider that the left hand-side operator of the problem is $\boldsymbol{\mu}$-independent. Assuming that the right-hand side of the problem (5.27) is defined by:

$$[\mathbf{F}(t;\boldsymbol{\mu})]_j = \int_\Omega g(\mathbf{x},t;\boldsymbol{\mu}) v_j(\mathbf{x}) d\mathbf{x}, j = 1, \cdots, n \tag{5.28}$$

which is for instance the case of a finite element discretization of a linear form, then applying the EIM to obtain an approximation for g as: $g(\mathbf{x},t;\boldsymbol{\mu}) \approx g_M^{EIM}(\mathbf{x},t;\boldsymbol{\mu}) := \sum_{i=1}^M \alpha_i(\boldsymbol{\mu}) g(\mathbf{x},t;\boldsymbol{\mu}_i^g)$ leads to $\mathbf{F}(t;\boldsymbol{\mu}) \approx \sum_{i=1}^M \alpha_i(\boldsymbol{\mu}) \mathbf{F}(t;\boldsymbol{\mu}_i^g)$. By linearity, the solution of the problem (5.27) can then be approximated by:

$$\mathbf{X}(t;\boldsymbol{\mu}) \approx \sum_{i=1}^M \alpha_i(\boldsymbol{\mu}) \mathbf{X}(t;\boldsymbol{\mu}_i^g), \forall \boldsymbol{\mu} \in \mathcal{D} \tag{5.29}$$

Remark 5.2.5 It can be used with the same approach for the parametrized stationary problem:

$$\mathbf{A}\mathbf{X}(\boldsymbol{\mu}) = \mathbf{F}(\boldsymbol{\mu}) \tag{5.30}$$

where the matrix $\mathbf{A}$ is $\boldsymbol{\mu}$-independent and the right-hand side vector $\mathbf{F}$ depends on the parameter $\boldsymbol{\mu}$ in a non-affine way, for instance via a relation $[\mathbf{F}(\boldsymbol{\mu})]_j = \int_\Omega g(\mathbf{x},\boldsymbol{\mu}) v_j(\mathbf{x}) d\mathbf{x}, j \in \{1, \cdots, n\}$. The approximation of the solution of Equation (5.30) can be obtained as follows:

$$\mathbf{X}(\boldsymbol{\mu}) \approx \sum_{i=1}^M \alpha_i(\boldsymbol{\mu}) \mathbf{X}(\boldsymbol{\mu}_i^g) \tag{5.31}$$

where $(\alpha_i(\boldsymbol{\mu}))_{1\leq i\leq M}$ and $(\boldsymbol{\mu})_i^g$ are defined in the definition of the approximation of g by g_M^{EIM} of Equation (5.11).

Remark 5.2.6 The computation of the approximation of $\mathbf{X}(t;\boldsymbol{\mu})$ by the relation (5.29) for any new values of parameter $\boldsymbol{\mu} \in \mathcal{D}$ has a complexity in $O(nMN_t)$ where N_t is the number of time step and n is the number of degrees of freedom in the problem. It is worth to mention that in the case where we are only interested in a linear physical output of interest, $S_l(t;\boldsymbol{\mu}) := \mathbf{L}^T\mathbf{X}(t;\boldsymbol{\mu})$ with $\mathbf{L}$ is a vector of $\mathbb{R}^n$, we can obtain an approximation of $S_l(t;\boldsymbol{\mu})$ for any new value of the parameter $\boldsymbol{\mu} \in \mathcal{D}$ with a complexity independent of n via the relation $S_l(t;\boldsymbol{\mu}) \approx \sum_{i=1}^M \alpha_i(\boldsymbol{\mu}) S_l(t;\boldsymbol{\mu}_i^g)$ provided that $[S_l(t;\boldsymbol{\mu}_i^g)]_{1\leq i\leq M}$ are pre-computed in an offline stage. The same holds for the case of a quadratic output $S_q(t;\boldsymbol{\mu}) = \mathbf{X}^T(t;\boldsymbol{\mu})\mathbf{Q}\mathbf{X}(t;\boldsymbol{\mu})$, where $\mathbf{Q}$ is a matrix in $\mathbb{R}^{n\times n}$. An approximation of $S_q(t;\boldsymbol{\mu})$ can be obtained with a complexity independent of n via the relation $S_q(t;\boldsymbol{\mu}) \approx \sum_{i=1}^M \sum_{j=1}^M \alpha_i(\boldsymbol{\mu})\alpha_j(\boldsymbol{\mu}) S_q^{ij}(t)$ provided that the quantities $\left[S_q^{ij}(t) := \mathbf{X}^T(t;\boldsymbol{\mu}_j^g)\mathbf{Q}\mathbf{X}(t;\boldsymbol{\mu}_i^g)\right]_{1\leq i,j\leq M}$ are pre-computed in an offline stage.

Application in the interaction of submerged structure and underwater explosion shock wave problem

In what follows, we illustrate this application of EIM in the context of the interaction structure and underwater explosion's shock wave problem when the mass of explosion in Trinitrotoluene (TNT) represents the only parameter in the problem. We only consider here the case of the formulation in $(\mathbf{u}_s, \phi^{sca})$. For the other formulations presented in Section 2.4, the application of the approach is straightforward. To begin, we recall that the loading induced by a shock wave in the finite element model formulated in $(\mathbf{u}_s, \phi^{sca})$ reads (see Section 2.4.1):

$$\mathbf{F}^{sca}_{u\phi}(t;\boldsymbol{\mu}) = \begin{bmatrix} \mathbf{F}^{sca}_{s}(t;\boldsymbol{\mu}) \\ \mathbf{F}^{sca}_{\phi}(t;\boldsymbol{\mu}) \end{bmatrix} \tag{5.32}$$

where the vectors $\mathbf{F}^{sca}_{s}(t;\boldsymbol{\mu})$ and $\mathbf{F}^{sca}_{\phi}(t;\boldsymbol{\mu})$ are defined by $\mathbf{F}^{sca}_{s,j}(t;\boldsymbol{\mu}) := -\int_\Gamma p^{inc}(\mathbf{x},t;\boldsymbol{\mu})[\mathbf{N}^s_j(\mathbf{x})\cdot \mathbf{n}_s(\mathbf{x})]d\mathbf{x}$ and $\mathbf{F}^{sca}_{\phi,j}(t;\boldsymbol{\mu}) := -\int_\Gamma \rho_0[\mathbf{v}^{inc}(\mathbf{x},t;\boldsymbol{\mu})\cdot\mathbf{n}_s(\mathbf{x})]N^f_j(\mathbf{x})d\mathbf{x}$ with $\mathbf{N}^s$ and N^f denote respectively the finite element basis of the structural and the fluid part. For the case of TNT (Trinitrotoluene) explosive material, we recall that a good approximation of the incident pressure p^{inc} and the incident velocity $\mathbf{v}^{inc}$ (whose the radial component v^{inc}_r is non-zero) can be expressed analytically as follows (see Section 2.2):

$$p^{inc}(r,t) = P_c\left[\frac{a_c}{r}\right]^{1+A}\mathcal{F}\left(\left[\frac{a_c}{r}\right]^B\frac{\tau}{T_c}\right)H(\tau) \tag{5.33}$$

$$v^{inc}_r(r,t) = \frac{p(r,t)}{\rho_0 c_0} + \frac{P_c T_c}{\rho_0 r}\left[\frac{a_c}{r}\right]^{1+A-B}(1+A-B)\mathcal{G}\left(\left[\frac{a_c}{r}\right]^B\frac{\tau}{T_c}\right)H(\tau) + \frac{p(r,t)}{\rho_0}\frac{\tau}{r}B \tag{5.34}$$

where the constant P_c, v_c, A and B are given by the relation (2.9) according to [106] and the relation (2.10) according to [40]. H is Heaviside function, $\tau = t-(r-R_l)/c_0$ and we denote by $R_l = 20a_c$ with a_c is the charge radius, $T_c = a_c/v_c$ and $r > R_l$ denotes the distance from the center of charge. The function $\mathcal{F}$ is defined by $\mathcal{F}(t) = 0.8251e^{-1.338t} + 0.1749e^{-0.1805t}$. The function $\mathcal{G}$ is defined by $\mathcal{G}(t) = 1.5856 - 0.6167e^{-1.338t} - 0.9690e^{-0.1805t}$. For a given value of mass M_{tnt} (which represents here the parameter of problem), the radius of charge a_c can be approximated by $a_c \approx (\frac{M_{tnt}}{4\pi\rho_{tnt}})^{1/3}$ where ρ_{tnt} is the mass density of TNT which is approximately given by $\rho_{tnt} \approx 1.52\cdot 10^3$ kg/m^3.

Here, we denote by d_{min} and d_{max} the distance of the center of charge to the closest (the stand-off point) and the farthest point of the structure Ω_s. Without loss of generality, we assume that the front of the shock wave arrived at the stand-off point at $t = 0$ so that the retarded time τ in Equation (5.33) and (5.34) is defined by $\tau = t-(r-d_{min})/c_0$. With T denotes the final time of interest, the first step of the methodology consist of applying the EIM on the function $p^{inc}(\mathbf{x};\mu)$ and $v^{inc}_r(\mathbf{x};\mu)$, where $\mathbf{x} := (r,t) \in [d_{min}, d_{max}]\times[0,T]$ and $\mu = M_{tnt} \in \mathcal{D}$, to obtain an approximation in form:

$$p^{inc}(r,t;\mu) \approx p^{inc}_{N_p^{EIM}}(r,t;\mu) := \sum_{i=1}^{N_p^{EIM}} \alpha^p_i(\mu)p^{inc}(r,t;\mu^p_i) \tag{5.35}$$

$$v^{inc}_r(r,t;\mu) \approx v^{inc}_{r,N_v^{EIM}}(r,t;\mu) := \sum_{i=1}^{N_v^{EIM}} \alpha^v_i(\mu)v^{inc}_r(r,t;\mu^v_i) \tag{5.36}$$

Then, injecting the approximation of p^{inc} and v_r^{inc} given by the relation (5.35)-(5.36) in the definition of $\mathbf{F}_s^{sca}$ and $\mathbf{F}_\phi^{sca}$ implies that the right-hand side vector of the finite element model formulated in $(\mathbf{u}_s, \phi^{sca})$ couple of Equation (5.32) can be approximated by:

$$\mathbf{F}_{u\phi}^{sca}(t;\mu) \approx \sum_{i=1}^{N_p^{EIM}} \alpha_i^p(\mu) \begin{bmatrix} \mathbf{F}_s^{sca}(t;\mu_i^p) \\ \mathbf{0} \end{bmatrix} + \sum_{i=1}^{N_v^{EIM}} \alpha_i^v(\mu) \begin{bmatrix} \mathbf{0} \\ \mathbf{F}_\phi^{sca}(t;\mu_i^v) \end{bmatrix} \tag{5.37}$$

As a result, by computing in the offline stage $\mathbf{X}_{u\phi}^p(t;\mu_i^p)$ the solution of the problem (2.23) with the right-hand side vector $\begin{bmatrix} \mathbf{F}_s^{sca}(t;\mu_i^p)^T & \mathbf{0}^T \end{bmatrix}^T$ for $i = 1, \cdots, N_p^{EIM}$ and $\mathbf{X}_{u\phi}^v(t;\mu_i^v)$ the solution of the problem (2.23) with the right-hand side vector $\begin{bmatrix} \mathbf{0}^T & \mathbf{F}_\phi^{sca}(t;\mu_i^v)^T \end{bmatrix}^T$ for $i = 1, \cdots, N_v^{EIM}$, we can obtain by linearity of the problem an approximation of the solution, for any new values of parameter $\mu = M_{tnt} \in \mathcal{D}$ at the online stage, with the following relation:

$$\mathbf{X}_{u\phi}^{sca}(t;\mu) \approx \sum_{i=1}^{N_p^{EIM}} \alpha_i^p(\mu) \mathbf{X}_{u\phi}^p(t;\mu_i^p) + \sum_{i=1}^{N_v^{EIM}} \alpha_i^v(\mu) \mathbf{X}_{u\phi}^v(t;\mu_i^v) \tag{5.38}$$

Remark 5.2.7 It should be noted that in the definition of $\mathbf{F}_s^{sca}$ the incident pressure $p^{inc}(\mathbf{x},t,\mu)$ is defined for $\mathbf{x} \in \Gamma$ by: $p^{inc}(\mathbf{x},t,\mu) = p^{inc}(r,t,\mu)$, where $r := ||\mathbf{x} - \mathbf{x}_{exp}||$ with $\mathbf{x}_{exp}$ denotes the position of the explosion. Hence, when the position of explosion $\mathbf{x}_{exp}$ is fixed, an accurate approximation of $p^{inc}(r,t,\mu)$ in form $p^{inc}(r,t,\mu) \approx \sum_{i=1}^M \alpha_i(\mu) p^{inc}(r,t;\mu_i)$ implies that we would also have an accurate approximation for $p^{inc}(\mathbf{x},t,\mu)$ in form $p^{inc}(\mathbf{x},t,\mu) \approx \sum_{i=1}^M \alpha_i(\mu) p^{inc}(\mathbf{x},t;\mu_i)$ so that the right-hand side $\mathbf{F}_s^{sca}$ can be approximated accurately by $\mathbf{F}_s^{sca}(t;\mu) \approx \sum_{i=1}^M \alpha_i(\mu) \mathbf{F}_s^{sca}(t;\mu_i)$. The same conclusion is also valid for the incident velocity v_r^{inc}. On the contrary, this conclusion is not valid for the case that the position of the explosion is the parameter of the problem, *i.e* $\boldsymbol{\mu} = \mathbf{x}_{exp}$. To explain this, we recall that for a fixed time t the kernel of the function $p^{inc}(\mathbf{x},t;\mu)$ can be expressed explicitly by $\mathrm{Ker}(p^{inc}(\cdot,t;\boldsymbol{\mu})) = \{\mathbf{x} \in \Gamma, \text{such that } ||\mathbf{x} - \boldsymbol{\mu}|| < c_0 t\}$ assuming that the incident pressure arrived at stand-off point at $t = 0$. Thus, for any $t < d_{max}/c_0$ we can remark that $\mathrm{Ker}(p^{inc}(\cdot,t;\boldsymbol{\mu}_i)) \neq \mathrm{Ker}(p^{inc}(\cdot,t;\boldsymbol{\mu}_j))$ for all $\boldsymbol{\mu}_i \neq \boldsymbol{\mu}_j$ which indicates that the function $p^{inc}(\mathbf{x},t;\boldsymbol{\mu})$ can not be approximated accurately by $\sum_{i=1}^M \alpha_i(\mu) p^{inc}(\mathbf{x},t;\boldsymbol{\mu}_i)$ when $\boldsymbol{\mu} \neq \boldsymbol{\mu}_i, \forall i = 1, \cdots, M$ and $t < d_{max}/c_0$.

As a remark, the proposed methodology above results in an non-intrusive procedure in the sense that we need to compute the solutions $\mathbf{X}_{u\phi}^p$ and $\mathbf{X}_{u\phi}^v$ which are not the solutions of our problem of interest. Next, we propose to exploit the idea presented in Section 5.2.3 (which is originally proposed in [33]) to obtain approximation of $\mathbf{X}_{u\phi}^{sca}$ in the following form:

$$\mathbf{X}_{u\phi}^{sca}(t;\mu) \approx \sum_{i=1}^{N_{pv}^{EIM}} \alpha_i^{pv}(\mu) \mathbf{X}_{u\phi}^{sca}(t;\mu_i^{pv}) \tag{5.39}$$

so that it requires only to compute the solution of our problem of interest for some values of parameters at the offline stage. The idea consists of approximating the coefficients vector $\boldsymbol{\alpha}(\mu) := \left(\alpha_1^p(\mu), \cdots, \alpha_{N_p^{EIM}}^p(\mu), \alpha_1^v(\mu), \cdots, \alpha_{N_v^{EIM}}^v(\mu)\right)^T$, whose components are defined in the

approximation (5.35)-(5.36), in form:

$$\boldsymbol{\alpha}(\mu) \approx \sum_{i=1}^{N_{pv}^{EIM}} \alpha_i^{pv}(\mu)\boldsymbol{\alpha}(\mu_i^{pv}) \tag{5.40}$$

To achieve that, it suffices to apply the Greedy EIM algorithm 16 with the parametrized function $g : (i,\mu) \in \{1,\cdots,N_p^{EIM}+N_v^{EIM}\} \times \mathcal{D} \to \mathbb{R}$ defined by $g(i,\mu) = \alpha_i^p(\mu)$ if $1 \leq i \leq N_p^{EIM}$ and $g(i,\mu) = \alpha_{i-N_p^{EIM}}^v(\mu)$ if $i > N_p^{EIM}$. Because the dimension of $\{g(.,\mu), \mu \in \mathcal{D}\}$ is at most equal to $N_p^{EIM}+N_v^{EIM}$, the Greedy EIM algorithm 16 will reach a machine precision after at most $N_p^{EIM}+N_v^{EIM}$ iterations. Using the approximation (5.40) in the relation (5.35)-(5.36) leads to:

$$\begin{pmatrix} p^{inc}_{N_p^{EIM}}(r,t;\mu) \\ v^{inc}_{r,N_v^{EIM}}(r,t;\mu) \end{pmatrix} = \begin{pmatrix} \sum_{j=1}^{N_p^{EIM}} \alpha_j^p(\mu) p^{inc}(r,t;\mu_j^p) \\ \sum_{j=1}^{N_v^{EIM}} \alpha_j^v(\mu) v_r^{inc}(r,t;\mu_j^v) \end{pmatrix} \tag{5.41}$$

$$\approx \begin{pmatrix} \sum_{j=1}^{N_p^{EIM}} \sum_{i=1}^{N_{pv}^{EIM}} \alpha_i^{pv}(\mu)\alpha_j(\mu_i^{pv}) p^{inc}(r,t;\mu_j^p) \\ \sum_{j=1}^{N_v^{EIM}} \sum_{i=1}^{N_{pv}^{EIM}} \alpha_i^{pv}(\mu)\alpha_j(\mu_i^{pv}) v_r^{inc}(r,t;\mu_j^v) \end{pmatrix} \tag{5.42}$$

$$\approx \sum_{i=1}^{N_{pv}^{EIM}} \alpha_i^{pv}(\mu) \begin{pmatrix} \sum_{j=1}^{N_p^{EIM}} \alpha_j(\mu_i^{pv}) p^{inc}(r,t;\mu_j^p) \\ \sum_{j=1}^{N_v^{EIM}} \alpha_j(\mu_i^{pv}) v_r^{inc}(r,t;\mu_j^v) \end{pmatrix} \tag{5.43}$$

$$\approx \begin{pmatrix} p^{inc,1}_{N_{pv}^{EIM}}(r,t;\mu) \\ v^{inc,1}_{r,N_{pv}^{EIM}}(r,t;\mu) \end{pmatrix} := \sum_{i=1}^{N_{pv}^{EIM}} \alpha_i^{pv}(\mu) \begin{pmatrix} p^{inc}_{N_p^{EIM}}(r,t;\mu_i^{pv}) \\ v^{inc}_{r,N_v^{EIM}}(r,t;\mu_i^{pv}) \end{pmatrix} \tag{5.44}$$

Since we have $p^{inc}(r,t;\mu) \approx p^{inc}_{N_p^{EIM}}(r,t;\mu)$ and $v_r^{inc}(r,t;\mu) \approx v^{inc}_{r,N_v^{EIM}}(r,t;\mu)$, we can then conclude that:

$$\begin{pmatrix} p^{inc}(r,t;\mu) \\ v_r^{inc}(r,t;\mu) \end{pmatrix} \approx \begin{pmatrix} p^{inc,2}_{N_{pv}^{EIM}}(r,t;\mu) \\ v^{inc,2}_{r,N_{pv}^{EIM}}(r,t;\mu) \end{pmatrix} := \sum_{i=1}^{N_{pv}^{EIM}} \alpha_i^{pv}(\mu) \begin{pmatrix} p^{inc}(r,t;\mu_i^{pv}) \\ v_r^{inc}(r,t;\mu_i^{pv}) \end{pmatrix} \tag{5.45}$$

Then, injecting this new approximation of p^{inc} and v_r^{inc} given by the relation (5.45) in the definition of $\mathbf{F}_s^{sca}$ and $\mathbf{F}_\phi^{sca}$ implies that the right-hand side of the finite element model formulated in $(\mathbf{u}_s, \phi^{sca})$ of Equation (5.32) can be approximated by:

$$\mathbf{F}_{u\phi}^{sca}(t;\mu) \approx \sum_{i=1}^{N_{pv}^{EIM}} \alpha_i^{pv}(\mu)\mathbf{F}_{u\phi}^{sca}(t;\mu_i^{pv}) \tag{5.46}$$

which, by linearity of the problem, allows us to conclude that the approximation of the solution of our problem for any values of the parameter in $\mathcal{D}$ can be obtained by the desired relation (5.39).

Remark 5.2.8 An alternative way to obtain an approximation in form (5.45) is to apply the Greedy EIM algorithm 16 with a parametrized function $g_{pv} : (\mathbf{x} := (i,r,t),\mu) \in \{1,2\} \times [d_{min}, d_{max}] \times [0,T] \times \mathcal{D} \to \mathbb{R}$ defined by $g_{pv}(\mathbf{x},\mu) = p^{inc}(r,t;\mu)$ if $i = 1$ and $g_{pv}(\mathbf{x},\mu) = v_r^{inc}(r,t;\mu)$ if $i = 2$, rather than applying it separately for p^{inc} and v_r^{inc}. However, we can remark from Equation (5.33)-(5.34) that p^{inc} and v_r^{inc} are not in same order of magnitude. As a result,

it can occur that all the magical points chosen by the Greedy EIM algorithm 16 correspond to only p^{inc} which would results in a relatively significant error for v_r^{inc}. To remedy this, we can use parametrized function $\tilde{g}_{pv} : (\mathbf{x} := (i, r, t), \mu) \in \{1, 2\} \times [d_{min}, d_{max}] \times [0, T] \times \mathcal{D} \to \mathbb{R}$ defined by $\tilde{g}_{pv}(\mathbf{x}, \mu) = p^{inc}(r, t; \mu)$ if $i = 1$ and $\tilde{g}_{pv}(\mathbf{x}, \mu) = \tilde{c}v_r^{inc}(r, t; \mu)$ if $i = 2$, where the constant $\tilde{c}$ to be determined in order to ensure that p^{inc} and $\tilde{c}v_r^{inc}$ have a same order of magnitude. Since the second and the last term in the expression of v_r^{inc} given by Equation (5.34) are relatively small compared to the first term, it is recommended to use $\tilde{c} = \rho_0 c_0$.

Numerical experiments

We propose now to illustrate numerically the accuracy of the proposed approximation. To do so, we consider the study case proposed in Section 4.6 of Chapter 4. In the considered study case, we have an elastic ring with a spring-mass system submitted to an underwater explosion's shock wave. A graphical representation of this study case is given by Figure 5.2. Here, we also consider that the elastic ring has a radius $R = 1$ m, a thickness $h = 0.01$ m and Poisson's ration $\nu = 0.28$. The excitation is induced by an acoustic shock wave generated by an underwater explosion of M_{tnt} kilograms of Trinitrotoluene (TNT), which is considered here as the only parameter of the problem, located at $(d, 0)$ with $d = 20$ m. The profile the considered shock wave are modelled by Equation (2.12) for the pressure and Equation (2.15) for the fluid particle's velocity using the value of constants P_c, v_c, A and B of Equation (2.10) provided by [40]. At $t = 0$, we assume that the shock wave arrives at the stand-off point $(0, R + h/2)$ of the structure. The density and the speed sound of the fluid are given by $\rho_0 = 1\ 000$ kg/m^3, $c_0 = 1\ 500$ m/s. The system of *spring-mass* is suspended at the point $(R - h/2, 0)$ which represents the closest point in the interior part of the ring to the explosion.

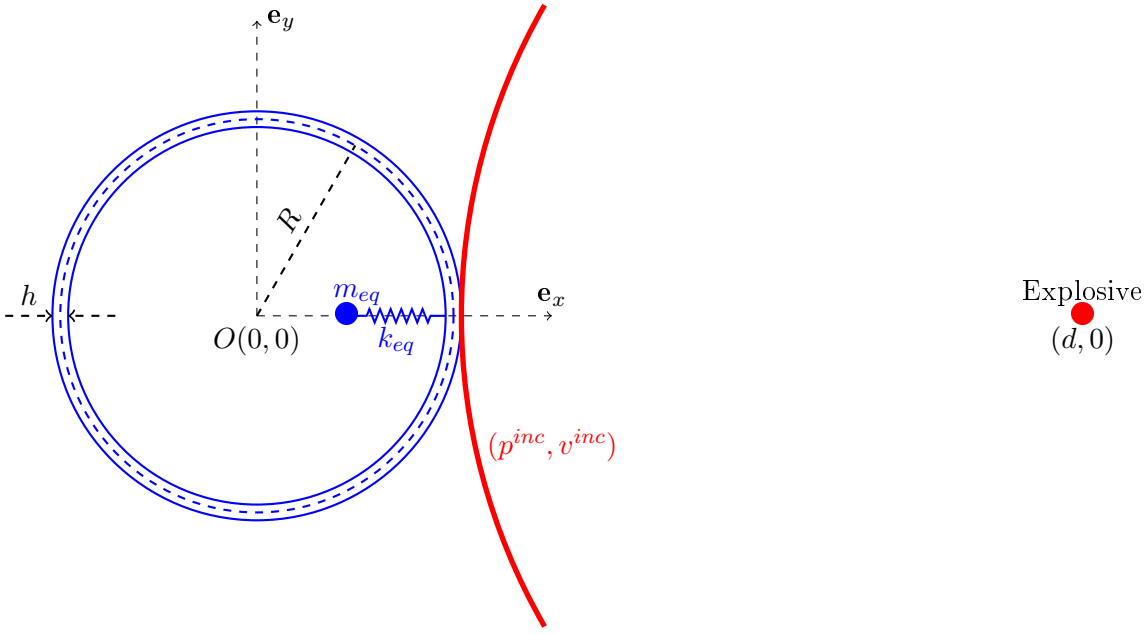

Figure 5.2: Graphical representation of the study case in context of the application of EIM for approximating the solutions of the interaction of structure and underwater explosion's shock wave where the mass of Trinitrotoluene (TNT) represents the only parameter in the problem

In our numerical experiments, we set $m_{eq} = 500$ and $f_{eq} = 250$ and the parameter space $\mathcal{D}_{M_{tnt}} = [100, 1000]$. In our study case, the values d_{min} and d_{max}, the distance of the center of charge to the closest (the stand-off point) and the farthest point of the structure, are given by $d_{min} = d - R - h/2$ and $d_{max} = d + R + h/2$. For time discretization, we set the time step by $\Delta t = 2 \cdot 10^{-5} s$, which means the the incident wave need $N_t = 200$ time step for travelling a distance of $6R$. The final time of interest is $T = 6R/c_0$. In this study, the output of interest refers to the acceleration of the point-mass in the spring-mass system.

To begin, we are interested in the convergence of the EIM for p^{inc} and v_r^{inc}. For that purpose, we devise the interval $[d_{min}, d_{max}]$ into 100 of equidistant points. The convergence of the Greedy EIM algorithm 16 applying on the function $p^{inc}(\mathbf{x}; \mu)$ and $v_r^{inc}(\mathbf{x}; \mu)$, where $\mathbf{x} := (r, t) \in [d_{min}, d_{max}] \times [0, T]$ with a training set $\mathcal{D}_{M_{tnt}}^{train}$ of 100 values generated randomly is reported in Figure 5.3.

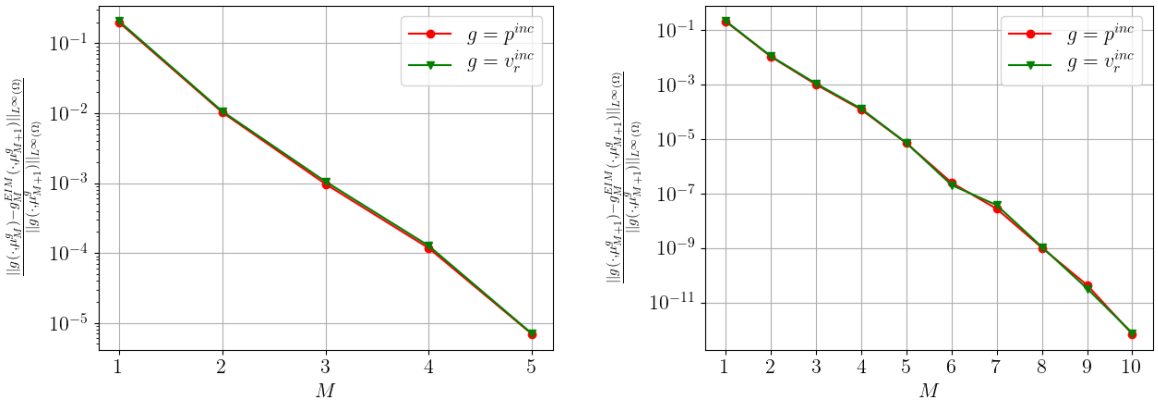

(a) Zoom on $M \in [1, 5]$ (b) For $M \in [1, 10]$

Figure 5.3: Evolution of error indicator in the greedy EIM algorithm 16 for p^{inc} and v_r^{inc} for the case where mass of TNT is considered as the parameter

Here, we define the error indicator as the relative error of the EIM approximation evaluated at the next value of parameter to be chosen in the step 5 of Greedy EIM algorithm 16. Figure 5.3 shows that the convergence of the error indicator are almost in the same rate for both v_r^{inc} and p^{inc}. This result can be explained by the fact in the expression of v_r^{inc}, the second and the third term of right-hand side of Equation (5.34) are relatively small compared to the first term which is collinear to p^{inc}. It should be pointed out that when increasing the distance d between the charge and the structure, these two terms tend to zeros which implies that $v_r^{inc} \approx p^{inc}/(\rho_0 c_0)$. As a result, for the case $d = 100$ m whose results is not given here, we have observed that the EIM algorithm chooses the same values of parameter and the same magical points for both v_r^{inc} and p^{inc}.

Next, let us put the focus on the convergence of the Greedy EIM algorithm 16 applying on the coefficients vector $\boldsymbol{\alpha}(\mu) := \left(\alpha_1^p(\mu), \cdots, \alpha_{N_p^{EIM}}^p(\mu), \alpha_1^v(\mu), \cdots, \alpha_{N_v^{EIM}}^v(\mu)\right)^T$, whose components are defined in the approximation (5.35)-(5.36). Since the convergence of the error indicator are almost in the same rate for both v_r^{inc} and p^{inc}, we only consider here the case $N_p^{EIM} = N_v^{EIM}$. The convergence of the Greedy EIM algorithm 16 applying on the coefficients vector $\boldsymbol{\alpha}(\mu)$ for different values of N_p^{EIM} are reported in Figure 5.4. As can be expected, we

observed in Figure 5.4 that the error indicator in the greedy EIM algorithm 16 reaches a value in order of machine precision after at most $N_p^{EIM} + N_v^{EIM}$ iterations.

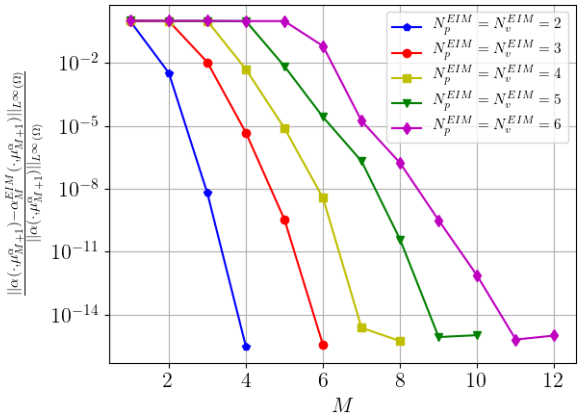

Figure 5.4: Evolution of error indicator in the greedy EIM algorithm 16 applying on the coefficient vector $\boldsymbol{\alpha}$

We now turn to the accuracy of the proposed approximations. For a given test sample $\mathcal{D}_{test}$, we are interested in the errors e_g defined by

$$e_g = \max_{\mu \in \mathcal{D}_{test}} \max_{t \in [0,T]} \frac{||g(\cdot,t,\mu) - g_M^{EIM}(\cdot,t,\mu)||_{L^\infty([d_{min},d_{max}])}}{||g(\cdot,t,\mu)||_{L^\infty([d_{min},d_{max}])}}, \text{ for } g \in \{p^{inc}, v_r^{inc}\} \tag{5.47}$$

where M denotes the number of terms in EIM approximation, in order to ensure an accurate approximation for every time step.

With a test sample $\mathcal{D}_{M_{tnt}}^{test}$ consisting of 50 values of parameter chosen randomly, the errors e_g for the approximation provides by employing the EIM separately for p^{inc} and v_r^{inc}, as given by the relation (5.35)-(5.36), are illustrated by Figure 5.5.

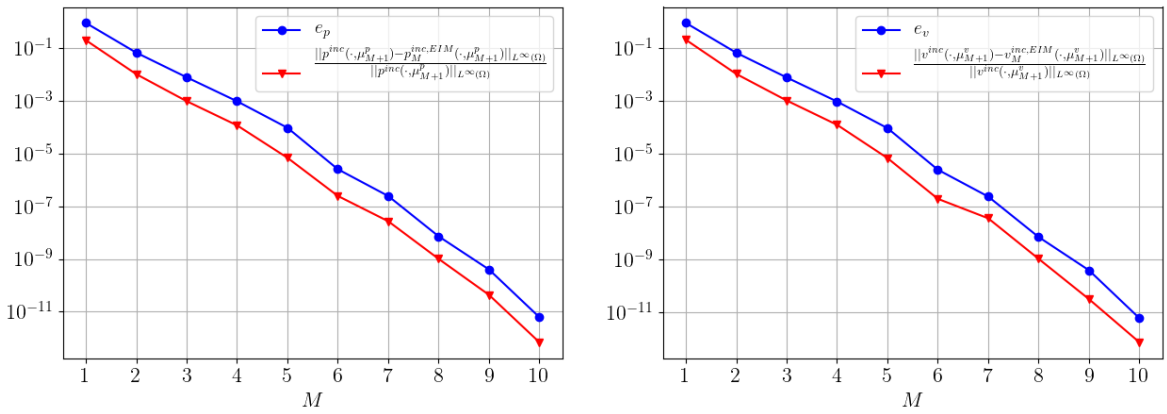

(a) Case of p^{inc} (b) Case of v_r^{inc}

Figure 5.5: Error of approximation of p^{inc} and v_r^{inc} by EIM approximation

Figure 5.5 shows that the error indicator (in red), which is based on the error in norm $||\cdot||_{L^\infty([d_{min},d_{max}]\times[0,T])}$ evaluated at the next value of parameter to be chosen by the step 5 of the Greedy EIM algorithm 16, provides a good estimate of the error e_g (in blue), defined in Equation (5.47), for both case of $g = p^{inc}$ and $g = v_r^{inc}$.

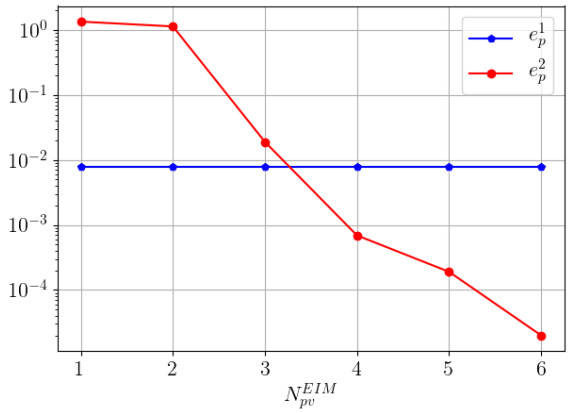

(a) Case of $g = p^{inc}$ with $N_p^{EIM} = N_v^{EIM} = 3$

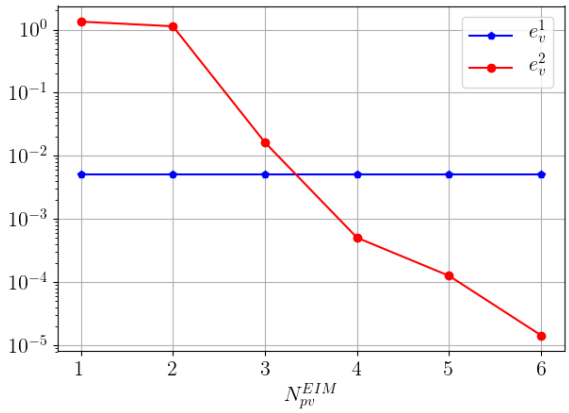

(b) Case of $g = v_r^{inc}$ with $N_p^{EIM} = N_v^{EIM} = 3$

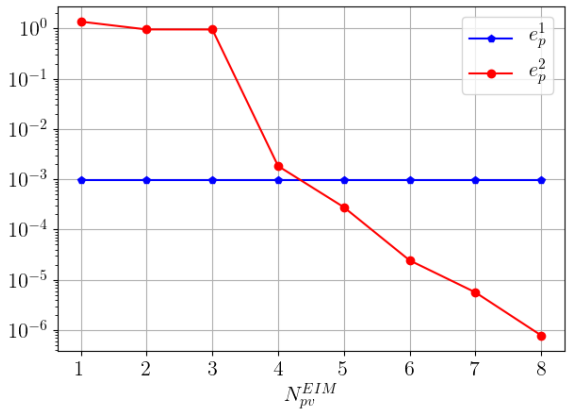

(c) Case of $g = p^{inc}$ with $N_p^{EIM} = N_v^{EIM} = 4$

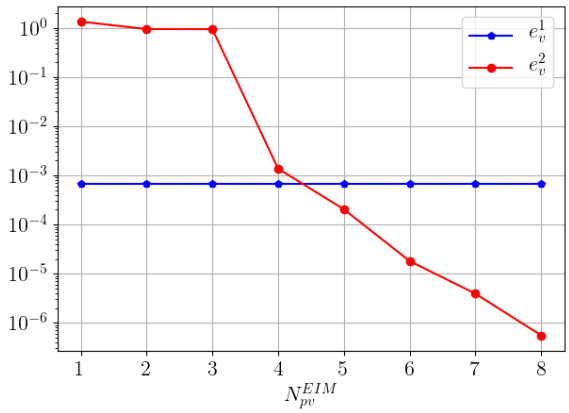

(d) Case of $g = v_r^{inc}$ with $N_p^{EIM} = N_v^{EIM} = 4$

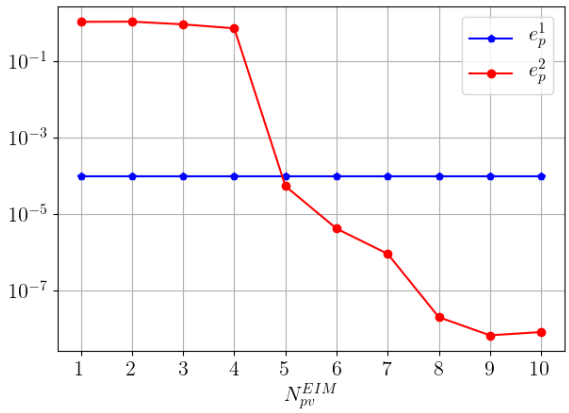

(e) Case of $g = p^{inc}$ with $N_p^{EIM} = N_v^{EIM} = 5$

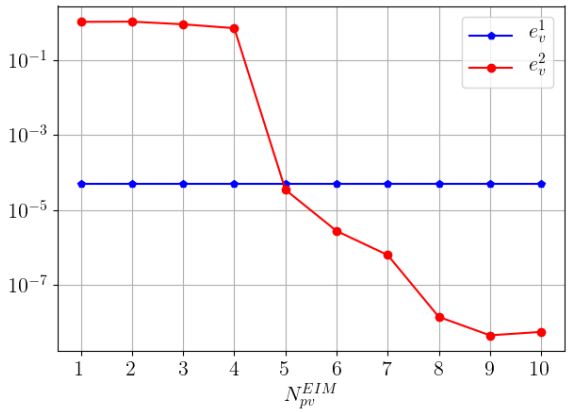

(f) Case of $g = v_r^{inc}$ with $N_p^{EIM} = N_v^{EIM} = 5$

Figure 5.6: Error of EIM approximations for $g = p^{inv}, v_r^{inv}$ in the classical case and in the case with a non-intrusive procedure

In what follows, we note for $g \in \{p^{inc}, v_r^{inc}\}$:

- e_g^1 as the error between g defined in Equation (5.33)-(5.34) and its approximation by the classical EIM as given in the relation (5.35)-(5.36)

- e_g^2 as the error between g defined in Equation (5.33)-(5.34) and its approximation, in the non-intrusive procedure, given by the relation (5.45)

The norm used to define the error e_g^1 and e_g^2 here is the same as e_g in Equation (5.47).

In Figure 5.6, we plot the evolution of errors e_g^1 and e_g^2 in function of N_{pv}^{EIM} in the same graph for different values of N_p^{EIM} and N_v^{EIM}. We observe that in order to achieve the same order of accuracy in the approximation (5.45) in the non-intrusive procedure as in the case where we apply EIM algorithm separately for p^{inc} and v_r^{inc}, it requires that the number of N_{pv}^{EIM} in approximation of the coefficients vector $\boldsymbol{\alpha}(\mu)$ in the relation (5.40) is equal to N_p^{EIM} and N_v^{EIM}. This can be due to the fact that the second and the third term in the definition of v_r^{inc} given by Equation (5.34) are relatively small compared to the first term, so that v_r^{inc} is almost collinear with p^{inc}. It should also be pointed out that when $N_{pv}^{EIM} > N_p^{EIM} = N_v^{EIM}$ the approximation (5.45) in non-intrusive procedure provided a better accuracy then the classical approximation by EIM separately of the relation (5.35)-(5.36).

It is worth to recall that the number of solutions of the problem of interest to be solved in offline stage in the proposed non-intrusive procedure is N_{pv}^{EIM}. For the case where we seek separately EIM approximation for p^{inc} and v_r^{inc}, it requires $N_p^{EIM} + N_v^{EIM}$ problems (in which each problem is of the same complexity as our problem of interest) to be solved at offline stage. As a result, we can expect that using the proposed non-intrusive procedure can reduce significantly the complexity required at the offline stage compared to the naive approach where we apply EIM algorithm separately for p^{inc} and v_r^{inc}.

In order to show the accuracy of the output of interest in the problem provided by EIM approximation (5.38) and (5.39), we define the error by:

$$\Delta_l^{EIM}(\boldsymbol{\mu}) := \frac{\left(\int_0^T \left|a_{m_{eq}}(t;\boldsymbol{\mu}) - a_{m_{eq}}^{EIM}(t;\boldsymbol{\mu})\right|^2 dt\right)^{1/2}}{\left(\int_0^T \left|a_{m_{eq}}(t;\boldsymbol{\mu})\right|^2 dt\right)^{1/2}} \tag{5.48}$$

where the superscript ^{EIM} refers to the values provided by the approximation (5.38) or (5.39) and $a_{m_{eq}}$ denotes the acceleration of the point mass in the *spring mass* system.

In our study, we use the same mesh as in the study case of Section 4.6 with the finite element model in $(\mathbf{u}_s, \phi^{sca})$. Newmark scheme (with $\beta = \frac{1}{4}(1-\alpha)^2$, $\gamma = 1/2 - \alpha$ where $\alpha = -0.1$) is used for time-discretization. The error on the output of interest in the case where we approximate p^{inc} and v_r^{inc} by EIM separately is reported in Figure 5.7.

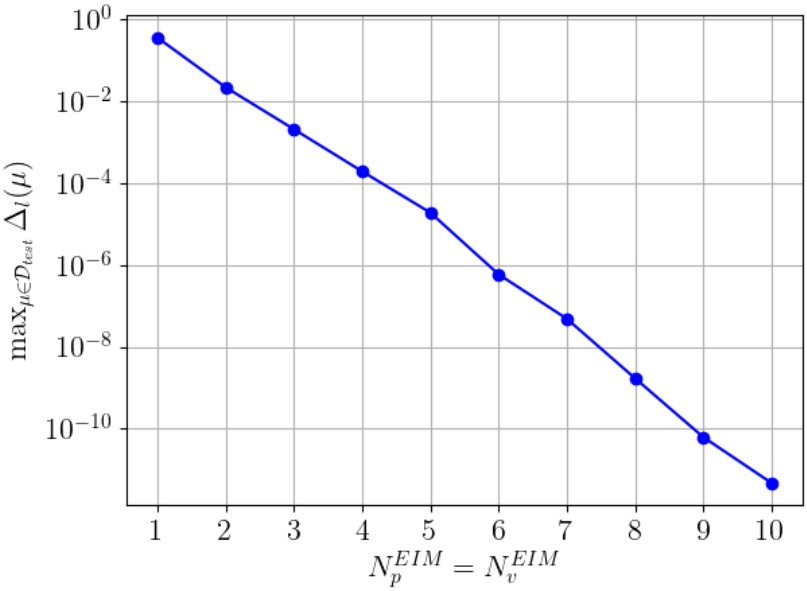

Figure 5.7: Evolution of error of the acceleration of m_{eq} using the approximation of right-hand side by greedy EIM algorithm 16 for the case where M_{tnt} represents the parameter

For the proposed non-intrusive procedure (5.39), the accuracy of the output of interest is reported by Figure 5.8. As for the error between p^{inc}, v_r^{inc} and its approximation by relation (5.45), we can also see in Figure 5.8 that in order to achieve the same order of accuracy for the approximation of the output of interest in the non-intrusive procedure as in the case where we apply EIM algorithm separately for p^{inc} and v_r^{inc}, it requires that the number of N_{pv}^{EIM} in approximation of the coefficients vector $\boldsymbol{\alpha}(\mu)$ by the relation (5.40) is equal to N_p^{EIM} and N_v^{EIM}.

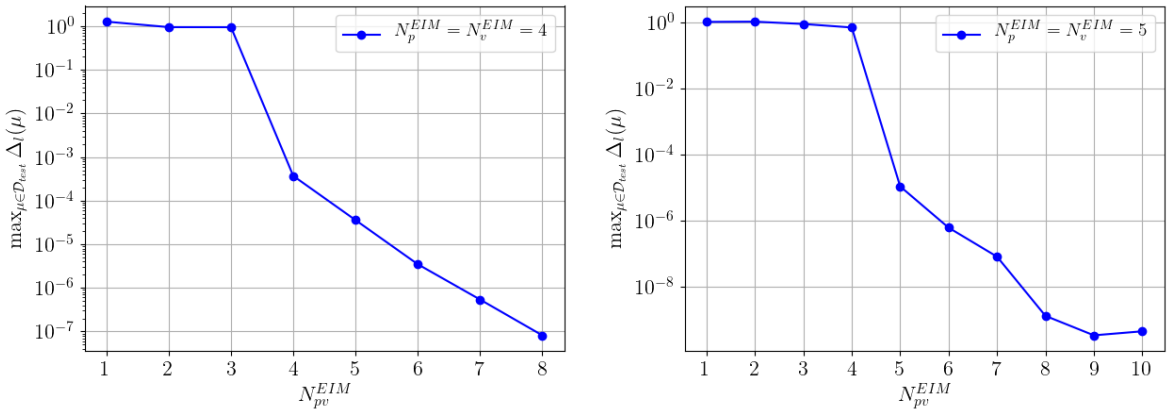

(a) Case of $N_p^{EIM} = N_v^{EIM} = 4$ (b) Case of $N_p^{EIM} = N_v^{EIM} = 5$

Figure 5.8: Evolution of error of the acceleration of m_{eq} using the approximation of the right-hand side vector by a non-intrusive procedure for the case where M_{tnt} represents the parameter

Finally, we present in Figure 5.9 the time evolution of the acceleration of the point mass in the *spring-mass* system given by the finite element model and its approximation by the proposed non-intrusive procedure with $N_{pv}^{EIM} = N_{p}^{EIM} = N_{v}^{EIM} = 4$ (in dashed lines) for some selected values of the parameters.

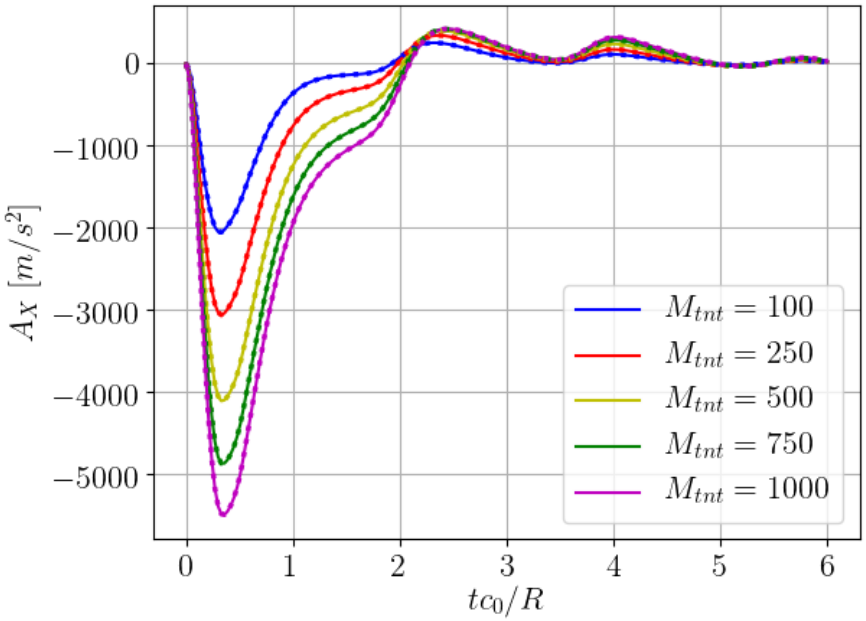

Figure 5.9: Time evolution of acceleration of m_{eq} in the *spring-mass* system for the different values of mass of TNT. The approximation provided by EIM via relation (5.39) is represented by dashed lines.

As a conclusion, both classical EIM and its variant for a non-intrusive procedure can be employed to approximate accurately the solution of an parametrized interaction of submerged structure and underwater explosion's shock wave problem in the case of mass of explosive material is the only parameter of the problem. Here, we would like to emphasize that we are under assumption that the left-hand side of the problem is independent of parameter.

For the case where the left-hand side of the problem also depends on the parameter, we will see Section 5.5 that we can turn to the reduced order modelling techniques in which the procedure proposed here allows us to obtain an approximation in form of affine dependent in parameter for the the right-hand side vector, which is one of the main ingredients for ensuring the performance of the reduced order model in online stage.

5.3 Parametrization of a varying shape domain (mesh) by means of a solid extension

One of the main challenges in the reduced order modelling for the case where the shape of the domain represents one of the parameters in the problem is the automatisation of the construction of the domain (or the mesh) while varying the value of parameter in an inexpensive

way. The mesh motion strategy which is often referred to as Solid Extension Mesh Moving Technique (SEMMT) [115, 117] is chosen in our work. For other alternatives, we refer to [111, 57]. In what follows, we give a short presentation of the so-called Solid Extension Mesh Moving Technique (SEMMT) in Section 5.3.1. The application of EIM for reducing the computational cost in the proposed technique is then presented in Section 5.3.2

5.3.1 Presentation of mesh motion strategy technique

Here, we denote by $\Omega_{ref} \subset \mathbb{R}^d$, $d = 2$ or 3, by the reference domain and $\mathcal{T}_h^{ref}$ a volumetric mesh of that reference domain. The main idea of the mesh motion strategy is to construct a parametrized mesh $\mathcal{T}_h(\boldsymbol{\mu})$ for a parametrized domain $\Omega(\boldsymbol{\mu})$ by moving the reference mesh $\mathcal{T}_h^{ref}$ with respect to a displacement field which is a solution of an elasticity problem on the reference domain, with a non-homogeneous Dirichlet boundary conditions to be defined in function of $\boldsymbol{\mu} \in \mathcal{D}$. By doing so, the strategy ensures that geometric embedding of $\mathcal{T}_h(\boldsymbol{\mu})$ (i.e., its nodes positions) is modified so that $\mathcal{T}_h(\boldsymbol{\mu})$ conforms to $\Omega(\boldsymbol{\mu})$ while keeping the mesh topology (i.e., its connectivity) of the reference mesh $\mathcal{T}_h^{ref}$.

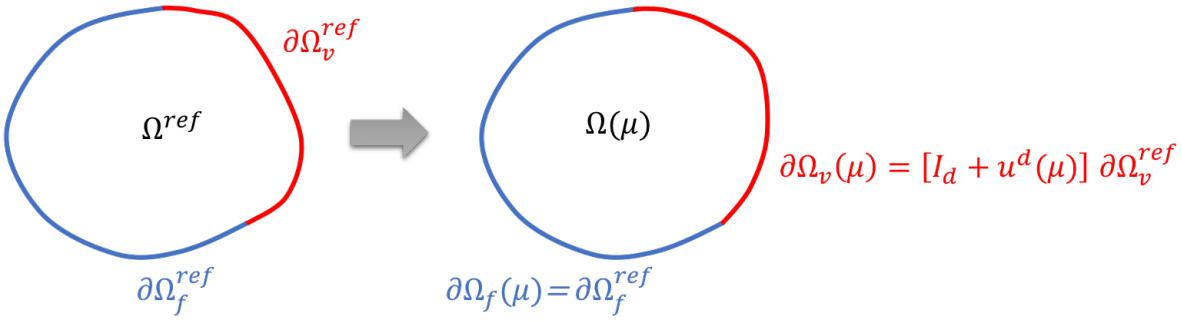

Figure 5.10: Geometrical representation of the reference domain and the parametrized domain

Without loss of generality, we assume that the boundary of the parametrized domain $\Omega(\boldsymbol{\mu})$ can be split into two parts: $\partial\Omega(\boldsymbol{\mu}) = \partial\Omega_f \cup \partial\Omega_v(\boldsymbol{\mu})$ where $\partial\Omega_f$ is the fixed boundary (it can be an empty set) and $\partial\Omega_v$ is the parameter dependent boundary. We suppose that the domain of reference Ω^{ref} can also be split into two parts: $\partial\Omega^{ref} = \partial\Omega_f^{ref} \cup \partial\Omega_v^{ref}$ where $\partial\Omega_f^{ref}$ coincides with $\partial\Omega_v^{ref}$ and there is a bijective application $\mathbf{T}^\mu = \mathbf{I}_d + \mathbf{u}^d(\boldsymbol{\mu})$ which transforms $\partial\Omega_v^{ref}$ into $\partial\Omega_v^\mu$ (see Figure 5.10). A displacement field $\mathbf{u} : \Omega^{ref} \to \mathbb{R}^d$ which allows us to transform the reference mesh $\mathcal{T}_h^{ref}$ into $\mathcal{T}_h(\boldsymbol{\mu}) = \{\mathbf{x} \in \mathbb{R}^d, \mathbf{x} = \mathbf{x}_{ref} + \mathbf{u}(\mathbf{x}_{ref}), \mathbf{x}_{ref} \in \mathcal{T}_h^{ref}\}$ a conform mesh of $\Omega(\boldsymbol{\mu})$, can be obtained as the solution of the following elasticity problem:

$$\begin{cases} -\text{div}\ \underline{\underline{\sigma}}(\mathbf{u}) = \mathbf{0} & \text{in } \Omega^{ref} \\ \mathbf{u} = \mathbf{0} & \text{on } \partial\Omega_f^{ref} \\ \mathbf{u} = \mathbf{u}^d(\boldsymbol{\mu}) & \text{on } \partial\Omega_v^{ref} \end{cases} \tag{5.49}$$

where $\underline{\underline{\sigma}}(\mathbf{u})$ is Cauchy stress tensor which is related to the displacement field $\mathbf{u}$ by: $\underline{\underline{\sigma}}(\mathbf{u}) = \lambda\ \text{div}(\mathbf{u})\underline{\underline{\mathbf{1}}} + 2\mu\underline{\underline{\epsilon}}(\mathbf{u})$ where $\underline{\underline{\mathbf{1}}}$ is identity tensor, $(\lambda, \mu) = (\frac{E\nu}{(1+\nu)(1-2\nu)}, \frac{E}{2(1+\nu)})$ are Lamé coefficients, with E the Young's modulus and ν the Poisson's ratio, $\underline{\underline{\epsilon}}(\mathbf{u}) := \left(\nabla\mathbf{u} + \nabla\mathbf{u}^T\right)/2$ denotes the linearised strain tensor and $\mathbf{u}^d(\boldsymbol{\mu}) \in H^{1/2}(\partial\Omega_v^{ref})^d$ to be defined.

For the sake of generality, let us consider the case where the parametrized domain $\Omega(\boldsymbol{\mu})$ is composed of two subdomains: $\Omega(\boldsymbol{\mu}) := \Omega_s(\boldsymbol{\mu}) \cup \Omega_f(\boldsymbol{\mu})$, for instance the case of a vibro-acoustic coupling where Ω_s and Ω_f denote respectively the structural and the fluid domain. We assume that the interface $\Gamma(\boldsymbol{\mu}) := \partial\Omega_s(\boldsymbol{\mu}) \cap \partial\Omega_f(\boldsymbol{\mu})$ can be split into two parts $\Gamma(\boldsymbol{\mu}) = \Gamma_f^{\mu} \cup \Gamma_v^{\mu}$ where Γ_v^{μ} is the parameter dependent boundary and Γ_f^{μ} is the fixed boundary (possibly empty) which coincides with the interface Γ_f^{ref} of the reference domain $\Omega^{ref} := \Omega_s^{ref} \cup \Omega_f^{ref}$ with $\Gamma^{ref} := \partial\Omega_s^{ref} \cap \partial\Omega_f^{ref} = \Gamma_f^{ref} \cup \Gamma_v^{ref}$. A displacement field which allows us to construct a mesh $\mathcal{T}_h^{\mu}$ of the parametrized domain $\Omega(\boldsymbol{\mu})$, by moving the position of nodes in the mesh of the reference domain $\mathcal{T}_h^{ref}$, can be obtained as the solution of the following elasticity problems, for $i \in \{s, f\}$:

$$\begin{cases} -\text{div}\ \underline{\underline{\sigma}}(\mathbf{u}_i) = \mathbf{0} & \text{in } \Omega_i^{ref} \\ \mathbf{u}_i = \mathbf{0} & \text{sur } \partial\Omega_i^{ref} \backslash \Gamma_v^{ref} \\ \mathbf{u}_i = \mathbf{u}^d(\boldsymbol{\mu}) & \text{sur } \Gamma_v^{ref} \end{cases} \tag{5.50}$$

where $\mathbf{u}_s$ and $\mathbf{u}_f$ denote respectively the displacement fields for Ω_s^{ref} and Ω_f^{ref}, $\mathbf{u}^d(\boldsymbol{\mu}) \in H^{1/2}(\Gamma_v^{ref})^d$ to be defined in order to ensure that the bijective application $\mathbf{T}^{\mu} = \mathbf{I}_d + \mathbf{u}^d(\boldsymbol{\mu})$ transforms Γ_v^{ref} into Γ_v^{μ}. Thanks to the third equation of the system (5.50), if the mesh of reference is conform, in the sense that the nodes of the domain Ω_s^{ref} and Ω_f^{ref} coincide at the interface Γ^{ref}, the mesh of the parametrized domain obtained by the proposed displacement field is also conform. The extension to the case where the parametrized domain is composed of $N \geq 2$ subdomains, the proposed strategy is straightforward.

Now, let us focus on how to construct the boundary displacement $\mathbf{u}^d(\boldsymbol{\mu})$. We restrict ourselves to the case where a parametrization of the boundary Γ_v^{ref} and Γ_v^{μ} are possible. We denote by $\boldsymbol{\gamma}_{ref} : \mathbf{t} \in [0,1]^{d-1} \to \mathbf{x}_{ref}(t) \in \Gamma_v^{ref}$ and $\boldsymbol{\gamma}_{\boldsymbol{\mu}} : \mathbf{t} \in [0,1]^{d-1} \to \mathbf{x}_{\boldsymbol{\mu}}(t) \in \Gamma_v^{\boldsymbol{\mu}}$ two bijective continuous applications representing a parametrization of Γ_v^{ref} and Γ_v^{μ}, respectively. The boundary displacement $\mathbf{u}^d(\boldsymbol{\mu})$ can be defined as follows:

$$\mathbf{u}^d(\boldsymbol{\mu})(t) = \mathbf{x}_{\boldsymbol{\mu}}(t) - \mathbf{x}_{ref}(t) \tag{5.51}$$

or equivalently:

$$\mathbf{u}^d(\boldsymbol{\mu})(\mathbf{x}_{ref}) = \boldsymbol{\gamma}_{\boldsymbol{\mu}}(\boldsymbol{\gamma}_{ref}^{-1}(\mathbf{x}_{ref})) - \mathbf{x}^{ref} \tag{5.52}$$

Remark 5.3.1 For $d = 2$, in the case where the boundary $\Gamma_v^{\boldsymbol{\mu}}$ can be described by the graph of a parametrized function $y_{\boldsymbol{\mu}} = f_{\boldsymbol{\mu}}(x_{\boldsymbol{\mu}}; \boldsymbol{\mu})$, where $x_{\boldsymbol{\mu}} \in [a(\boldsymbol{\mu}), b(\boldsymbol{\mu})] \subset \mathbb{R}$, we recall that a parametrization of the boundary Γ_v^{ref} can be defined as:

$$\boldsymbol{\gamma}_{\boldsymbol{\mu}} : t \in [0,1] \to \begin{pmatrix} x_{\boldsymbol{\mu}}(t) \\ y_{\boldsymbol{\mu}}(t) \end{pmatrix} = \begin{pmatrix} a(\boldsymbol{\mu}) + t\,[b(\boldsymbol{\mu}) - a(\boldsymbol{\mu})] \\ f_{\boldsymbol{\mu}}(x_{\boldsymbol{\mu}}(t); \boldsymbol{\mu}) \end{pmatrix} \in \Gamma_v^{\boldsymbol{\mu}} \tag{5.53}$$

If the reference boundary Γ_v^{ref} can also be described by the graph of a function $y_{ref} = f_{ref}(x_{ref})$, where $x \in [a, b] \subset \mathbb{R}$, and we parametrize the reference boundary Γ_v^{ref} as:

$$\boldsymbol{\gamma}_{\boldsymbol{\mu}} : t \in [0,1] \to \begin{pmatrix} x_{ref}(t) \\ y_{ref}(t) \end{pmatrix} = \begin{pmatrix} a + t(b-a) \\ f_{ref}(x_{ref}(t)) \end{pmatrix} \in \Gamma_v^{ref} \tag{5.54}$$

then, the boundary displacement $\mathbf{u}^d(\boldsymbol{\mu})$ can be defined as follows:

$$\mathbf{u}^d(\boldsymbol{\mu}) : \begin{pmatrix} x_{ref} \\ y_{ref} \end{pmatrix} \in \Gamma_v^{ref} \rightarrow \begin{pmatrix} x_{\boldsymbol{\mu}} \\ y_{\boldsymbol{\mu}} \end{pmatrix} = \begin{pmatrix} a(\boldsymbol{\mu}) + t(x_{ref}) \left[b(\boldsymbol{\mu}) - a(\boldsymbol{\mu}) \right] - x_{ref} \\ f_{\boldsymbol{\mu}}(x_{\boldsymbol{\mu}}(x_{ref}); \boldsymbol{\mu}) - y_{ref} \end{pmatrix} \in \Gamma_v^{\boldsymbol{\mu}} \tag{5.55}$$

where $t(x_{ref}) = \frac{x_{ref} - a}{b - a}$.

Remark 5.3.2 For $d = 3$, in the case where the boundary $\Gamma_v^{\boldsymbol{\mu}}$ can be described by the surface of a parametrized function $z_{\boldsymbol{\mu}} = f_{\boldsymbol{\mu}}(x_{\boldsymbol{\mu}}, y_{\boldsymbol{\mu}}; \boldsymbol{\mu})$, where $(x_{\boldsymbol{\mu}}, y_{\boldsymbol{\mu}}) \in [a(\boldsymbol{\mu}), b(\boldsymbol{\mu})] \times [c(\boldsymbol{\mu}), d(\boldsymbol{\mu})] \subset \mathbb{R}^2$, we recall that a parametrization of the boundary Γ_v^{ref} can be defined as:

$$\boldsymbol{\gamma}_{ref} : \mathfrak{t} = (t_1, t_2) \in [0,1]^2 \rightarrow \begin{pmatrix} x_{\boldsymbol{\mu}}(t) \\ y_{\boldsymbol{\mu}}(t) \\ z_{\boldsymbol{\mu}}(t) \end{pmatrix} = \begin{pmatrix} a(\boldsymbol{\mu}) + t_1 \left[b(\boldsymbol{\mu}) - a(\boldsymbol{\mu}) \right] \\ c(\boldsymbol{\mu}) + t_2 \left[d(\boldsymbol{\mu}) - c(\boldsymbol{\mu}) \right] \\ f_{\boldsymbol{\mu}}(x_{\boldsymbol{\mu}}(t_1), y_{\boldsymbol{\mu}}(t_2); \boldsymbol{\mu}) \end{pmatrix} \in \Gamma_v^{\boldsymbol{\mu}} \tag{5.56}$$

If the reference boundary Γ_v^{ref} can also be described by the surface of a function $z_{ref} = f_{ref}(x_{ref}, y_{ref})$, where $(x, y) \in [a, b] \times [c, d] \subset \mathbb{R}^2$, and we parametrize the reference boundary Γ_v^{ref} as:

$$\boldsymbol{\gamma}_{ref} : \mathfrak{t} = (t_1, t_2) \in [0,1]^2 \rightarrow \begin{pmatrix} x_{ref}(t) \\ y_{ref}(t) \\ z_{ref}(t) \end{pmatrix} = \begin{pmatrix} a + t_1(b - a) \\ c + t_2(d - c) \\ f_{ref}(x_{ref}(t_1), x_{ref}(t_2)) \end{pmatrix} \in \Gamma_v^{ref} \tag{5.57}$$

then, the boundary displacement $\mathbf{u}^d(\boldsymbol{\mu})$ can be defined as follows:

$$\mathbf{u}^d(\boldsymbol{\mu}) : \begin{pmatrix} x_{ref} \\ y_{ref} \\ z_{ref} \end{pmatrix} \in \Gamma_v^{ref} \rightarrow \begin{pmatrix} x_{\boldsymbol{\mu}} \\ y_{\boldsymbol{\mu}} \\ z_{\boldsymbol{\mu}} \end{pmatrix} = \begin{pmatrix} a(\boldsymbol{\mu}) + t_1(x_{ref}) \left[b(\boldsymbol{\mu}) - a(\boldsymbol{\mu}) \right] - x_{ref} \\ c(\boldsymbol{\mu}) + t_2(x_{ref}) \left[d(\boldsymbol{\mu}) - c(\boldsymbol{\mu}) \right] - y_{ref} \\ f_{\boldsymbol{\mu}}(x_{\boldsymbol{\mu}}(x_{ref}), y_{\boldsymbol{\mu}}(x_{ref}); \boldsymbol{\mu}) - z_{ref} \end{pmatrix} \in \Gamma_v^{\boldsymbol{\mu}} \tag{5.58}$$

where $t_1(x_{ref}) = \frac{x_{ref} - a}{b - a}$, $t_2(y_{ref}) = \frac{y_{ref} - c}{d - c}$.

Remark 5.3.3 In the most general cases where a parametrization of the boundary $\Gamma_v^{\boldsymbol{\mu}}$ is not possible and $\Gamma_v^{\boldsymbol{\mu}}$ can only be characterized implicitly by the set of points in $\mathbb{R}^d$ such that $f(\mathbf{x}; \boldsymbol{\mu}) = 0$, we refer to [35] for an alternative approach based on a penalization technique.

In order to illustrate the methodology of the proposed strategy, we provide in what follows two examples.

Example 1: Case of a parametrized 2D domain

As the first example, we consider a parametrized 2D domain $\Omega(\boldsymbol{\mu}) := \{(x, y) \in]0,1[\times]0, 1/2[, \frac{x^2}{a^2} + \frac{y^2}{b^2} > 1\}$ where $\boldsymbol{\mu} := (a, b) \in [0.2, 0.4]^2$ is the parameter. We define the reference domain as $\Omega^{ref} = \Omega(\boldsymbol{\mu}_{ref})$ where $\boldsymbol{\mu}_{ref} = (r, r)$, $r = 0.3$ (see Figure 5.11).

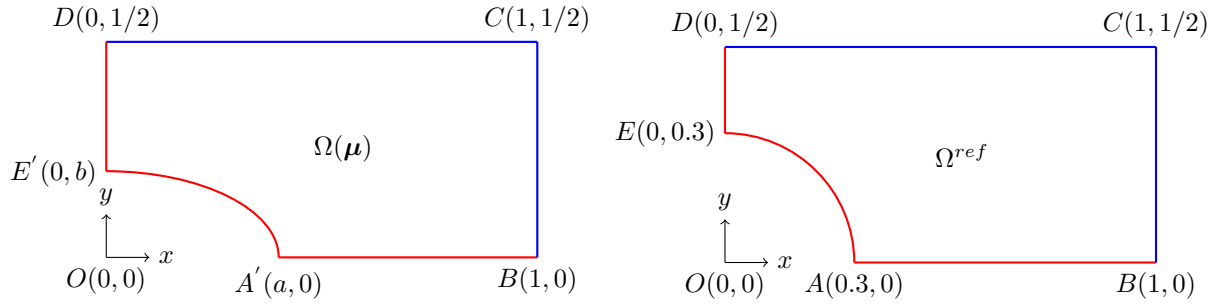

Figure 5.11: The geometry of the parametrized domain (left) and the geometry of the reference domain (right) for the first example

The parameter dependent boundary $\partial\Omega_v^{ref}$ and the fixed boundary $\partial\Omega_f^{ref}$ can be defined respectively by $\partial\Omega_v^{ref} = DE \cup EA \cup AB$ (in red in Figure 5.11) and $\partial\Omega_f^{ref} = BC \cup CD$ (in blue in Figure 5.11). A boundary displacement field $\mathbf{u}^d(\boldsymbol{\mu}) = \left[u_x^d(\boldsymbol{\mu}), u_y^d(\boldsymbol{\mu})\right]^T$ which allows us to transform $\partial\Omega_v^{ref}$ into $\partial\Omega_v^{\boldsymbol{\mu}} := DE^{'} \cup E^{'}A^{'} \cup A^{'}B$ can be defined by:

$$\begin{cases} u_x^d(x,y;\boldsymbol{\mu}) = 0 & \text{on } DE \\ u_y^d(x,y;\boldsymbol{\mu}) = b + \dfrac{y-r}{1/2-r}(1/2-b) - y & \text{on } DE \\ u_x^d(x,y;\boldsymbol{\mu}) = (\dfrac{a}{r} - 1)x & \text{on } EA \\ u_y^d(x,y;\boldsymbol{\mu}) = (\dfrac{b}{r} - 1)y & \text{on } EA \\ u_x^d(x,y;\boldsymbol{\mu}) = a + \dfrac{x-r}{1-r}(1-a) - x & \text{on } AB \\ u_y^d(x,y;\boldsymbol{\mu}) = 0 & \text{on } AB \end{cases} \tag{5.59}$$

In the linear elasticity problem (5.49) with homogeneous Dirichlet boundary condition on $\partial\Omega_f^{ref}$ and non-homogeneous Dirichlet boundary condition defined by Equation (5.59) on $\partial\Omega_v^{ref}$, we choose to set the Young modulus to $E = 2.1{\cdot}10^{11}$ Pa and the Poisson's ratio to $\nu = 0.3$. The mesh of the reference domain which consists of 1 553 linear triangular elements and 843 nodes and the deformed mesh through the displacement fields which is the solution of the proposed linear elasticity problem for some values of a and $b \in [0.2, 0.4]$ are illustrated in Figure 5.12.

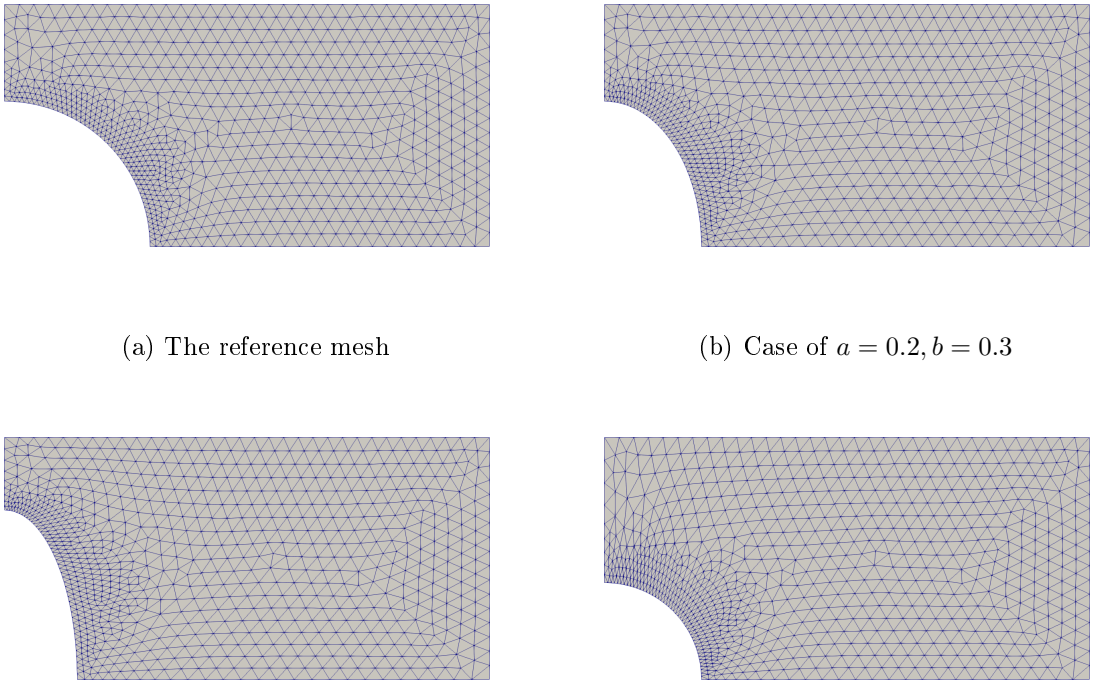

(a) The reference mesh

(b) Case of $a = 0.2, b = 0.3$

(c) Case of $a = 0.15, b = 0.35$

(d) Case of $a = 0.2, b = 0.2$

Figure 5.12: The reference mesh (top left) and the deformed mesh in the first example

Example 2: Case of the domain consist of two parametrized subdomains

For the second example, we choose to deal with the case where the parametrized domain is composed by two main subdomains and we seek to make the form of interface vary between the two domains. Here, we consider $\Omega(\boldsymbol{\mu}) := \Omega_s(\boldsymbol{\mu}) \cup \Omega_f(\boldsymbol{\mu})$ where $\Omega_s(\boldsymbol{\mu}) := \{(x, y) \in [-1/2, 1/2]^2, \frac{x^2}{a^2} + \frac{y^2}{b^2} > 1\}$, $\Omega_f(\boldsymbol{\mu}) := \{(x, y) \in [-1/2, 1/2]^2, \frac{x^2}{a^2} + \frac{y^2}{b^2} < 1\}$ and $\boldsymbol{\mu} = (a, b) \in [0.2, 0.3]^2$ denotes the parameter of the problem. The interface between $\Omega_s(\boldsymbol{\mu})$ and $\Omega_f(\boldsymbol{\mu})$ is characterized by $\Gamma(\boldsymbol{\mu}) := \partial\Omega_s(\boldsymbol{\mu}) \cap \partial\Omega_s(\boldsymbol{\mu}) = \{(x, y) \in [-1/2, 1/2]^2, \frac{x^2}{a^2} + \frac{y^2}{b^2} = 1\}$. We consider that the reference domain Ω^{ref} is the particular case of $\Omega(\boldsymbol{\mu})$ where $\boldsymbol{\mu}_{ref} = (r, r)$ with $r = 0.25$ (see Figure 5.13).

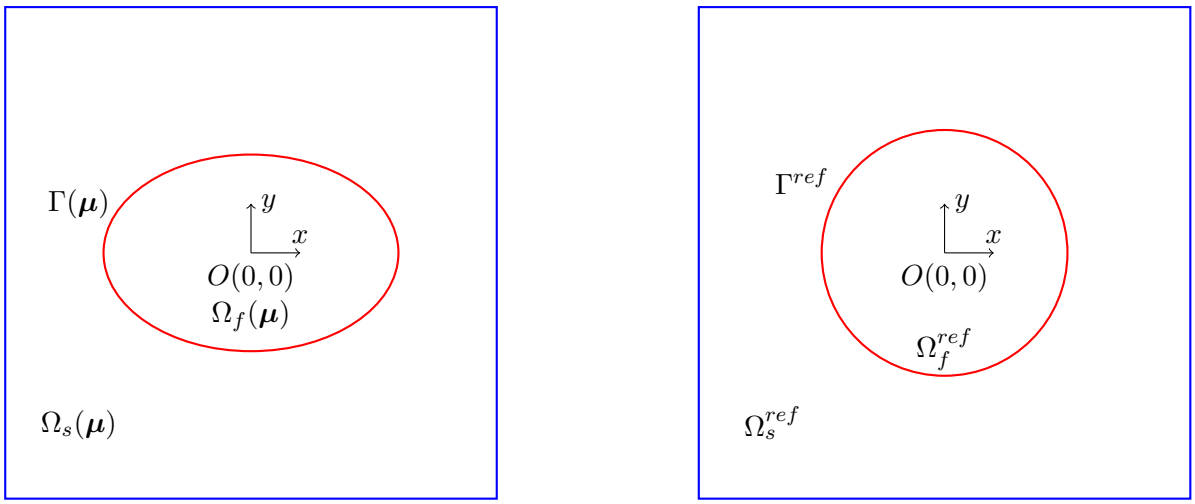

Figure 5.13: The geometry of the parametrized domain (left) and the geometry of the reference domain (right) for the second example

An interface displacement $\mathbf{u}^d(\boldsymbol{\mu}) = \left[u_x^d(\boldsymbol{\mu}), u_y^d(\boldsymbol{\mu})\right]^T$ which allows us to transform Γ^{ref} into $\Gamma(\boldsymbol{\mu})$ can be defined as:

$$\begin{cases} u_x^d(x, y; \boldsymbol{\mu}) = (\dfrac{a}{r} - 1)x \\ u_y^d(x, y; \boldsymbol{\mu}) = (\dfrac{b}{r} - 1)y \end{cases} \tag{5.60}$$

In the linear elasticity problems (5.50) with homogeneous Dirichlet boundary condition on $\partial\Omega_i^{ref} \backslash \Gamma^{ref}, i = \{s, f\}$ and non-homogeneous Dirichlet boundary condition defined by Equation (5.60) on Γ^{ref}, we choose to set the Young modulus to $E = 2.1 \cdot 10^{11}$ Pa and the Poisson's ratio to $\nu = 0.3$. The mesh of the reference domain consists of 4 194 quadratic triangular elements and 8 704 nodes for Ω_s^{ref}, of 1 592 quadratic triangular elements and 3 341 nodes for Ω_f^{ref} and of 312 nodes on the interface Γ^{ref}. The reference mesh and the deformed mesh through the displacement fields which is the solution of the proposed linear elasticity problems for some values of a and $b \in [0.2, 0.3]$ are reported by Figure 5.14 in which the interface $\Gamma(\boldsymbol{\mu})$ is marked in white curve.

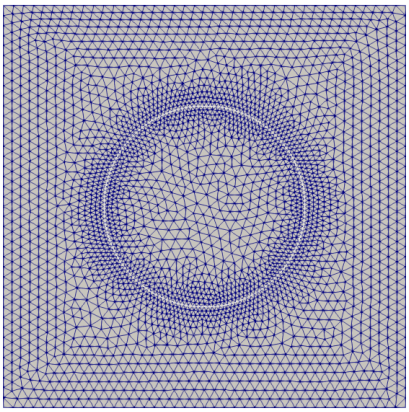

(a) The reference mesh

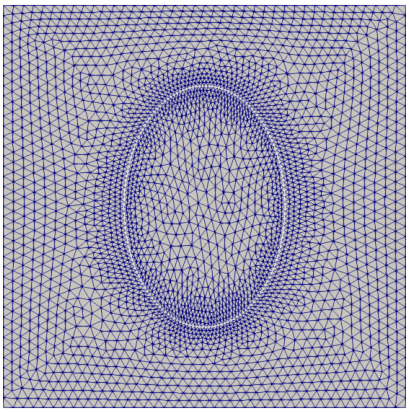

(b) Case of $a = 0.2, b = 0.3$

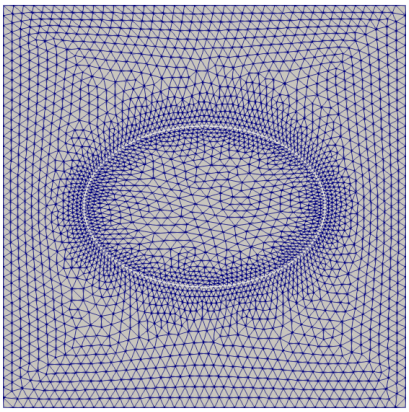

(c) Case of $a = 0.3, b = 0.2$

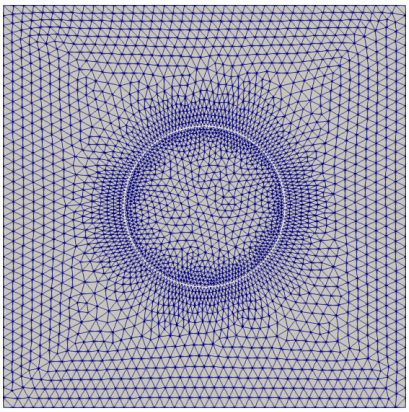

(d) Case of $a = 0.2, b = 0.2$

Figure 5.14: The reference mesh (top left) and the deformed mesh in the second example

5.3.2 Approximation of the solution of the parametrized elasticity problem by EIM

Now that we have presented a strategy of automatisation of the mesh construction for a parametrized domain, we seek now to exploit the EIM, presented in Section 5.2, to reduced its computational cost while varying the geometrical parameter value $\boldsymbol{\mu}^g \in \mathcal{D}^g$. To begin, let us recall briefly the resolution of the elasticity problem (5.49) with a non-homogeneous Dirichlet boundary condition by finite element method. We introduce a Hilbert space $\mathbf{V} := \{\mathbf{v} \in H^1(\Omega^{ref})^d, \mathbf{v} = \mathbf{0}$ on Γ_f^{ref} and $\mathbf{v} = \mathbf{u}^d(\boldsymbol{\mu})$ on $\Gamma_v^{ref}\}$. The corresponding weak formulation of the problem (5.49) reads:

$$\begin{cases} \text{Find } \mathbf{u} \in \mathbf{V} \text{ such that} \\ a(\mathbf{u}, \mathbf{v}) = 0, \forall \mathbf{v} \in H_0^1(\Omega^{ref})^d \end{cases} \tag{5.61}$$

where a is a bilinear form on $\in H^1(\Omega^{ref})^d$ defined by:

$$a(\mathbf{u}, \mathbf{v}) := \int_\Omega \left[2\mu \underline{\underline{\epsilon}}(\mathbf{u}) : \underline{\underline{\epsilon}}(\mathbf{v}) + \lambda \text{div}(\mathbf{u}) \text{div}(\mathbf{v})\right] d\mathbf{x} \tag{5.62}$$

To simplify our presentation, we consider in what follows the case where $d = 1$. We denote by $\{\varphi_1, \cdots \varphi_n\}$ the nodal basis of Lagrange finite element corresponding to the nodes $\{a_1, \cdots, a_n\}$. Without loss of generality, we assume that the nodes $\{a_1, \cdots, a_D\}$ located at the boundary $\partial\Omega^{ref}$. We can then introduce the finite element trial and test functions spaces as:

$$\begin{cases} \mathbf{V}_h = \text{span}\{\varphi_1, \cdots, \varphi_n\} \subset \mathbf{V} \\ \mathbf{V}_{h0} = \text{span}\{\varphi_{D+1}, \cdots, \varphi_n\} \subset H_0^1(\Omega^{ref}) \end{cases} \tag{5.63}$$

By seeking the approximation of u in $\mathbf{V}_h$, that is $u = \sum_{i=1}^n u_i \varphi_i$, the problem yields to the linear system:

$$\begin{bmatrix} \mathbf{I}_{DD} & \mathbf{0} \\ \mathbf{K}_{ID} & \mathbf{K}_{II} \end{bmatrix} \begin{bmatrix} \mathbf{U}_D(\boldsymbol{\mu}^g) \\ \mathbf{U}_I(\boldsymbol{\mu}) \end{bmatrix} = \begin{bmatrix} \mathbf{U}_D^d(\boldsymbol{\mu}^g) \\ \mathbf{0} \end{bmatrix} \tag{5.64}$$

where $\mathbf{U}_D := (u_1, \cdots, u_D) \in \mathbb{R}^D$, $\mathbf{U}_I := (u_{D+1}, \cdots, u_N) \in \mathbb{R}^{n-D}$, $\mathbf{U}_D^d(\boldsymbol{\mu}^g) \in \mathbb{R}^D$ is defined by $[\mathbf{U}_D^d(\boldsymbol{\mu}^g)]_i = u^d(\boldsymbol{\mu}^g)(a_i)$ for $i \in \{1, \cdots, D\}$, $\mathbf{K}_{II} \in \mathbb{R}^{(n-D)\times(n-D)}$ and $\mathbf{K}_{DI} \in \mathbb{R}^{(n-D)\times D}$ are defined by $(\mathbf{K}_{II})_{ij} = a(\varphi_{j+D}, \varphi_{i+D})$, for $i, j \in \{1, \cdots, n-D\}$ and $(\mathbf{K}_{ID})_{ij} = a(\varphi_j, \varphi_{i+D})$, $i \in \{1, \cdots, n-D\}$, $j \in \{1, \cdots, D\}$. The linear system (5.64) is equivalent to:

$$\begin{bmatrix} \mathbf{I}_{DD} & \mathbf{0} \\ \mathbf{0} & \mathbf{K}_{II} \end{bmatrix} \begin{bmatrix} \mathbf{U}_D(\boldsymbol{\mu}^g) \\ \mathbf{U}_I(\boldsymbol{\mu}^g) \end{bmatrix} = \begin{bmatrix} \mathbf{U}_D^d(\boldsymbol{\mu}^g) \\ -\mathbf{K}_{ID}\mathbf{U}_D^d(\boldsymbol{\mu}^g) \end{bmatrix} \tag{5.65}$$

We remark that the elasticity problem (5.49) depends on the parameters only through its right-hand side. Hence, by using the EIM to obtain an approximation of $\mathbf{U}_D^d(\boldsymbol{\mu}^g)$ as $\mathbf{U}_D^d(\boldsymbol{\mu}^g) \approx \sum_{i=1}^M \alpha_i(\boldsymbol{\mu}^g)\mathbf{U}_D^d(\boldsymbol{\mu}_i^{*,g})$, as presented in Section 5.2.4, we can obtain by linearity of the problem an approximation of $\mathbf{U}_I(\boldsymbol{\mu})$ for all $\boldsymbol{\mu} \in \mathcal{D}$ as:

$$\mathbf{U}_I(\boldsymbol{\mu}) \approx \mathbf{U}_I^{EIM}(\boldsymbol{\mu}^g) := \sum_{i=1}^M \alpha_i(\boldsymbol{\mu}^g)\mathbf{U}_I(\boldsymbol{\mu}_i^{*,g}) \tag{5.66}$$

Since the value of the displacement of the nodes located at Γ_v^{ref} is determined by $\mathbf{u}^d(\boldsymbol{\mu}^g)$ which can be expressed as an analytical function in the case where a parametrization of Γ_v^{ref} is possible, it ensures that these nodes locate exactly on $\Gamma_v^{\boldsymbol{\mu}^g}$ after the modification of the reference mesh via the displacement field $\mathbf{u}$. Note that using the approximation by Equation (5.66) for $\mathbf{U}_I(\boldsymbol{\mu}^g)$ impacts only on the positions of the nodes located in interior of $\mathcal{T}_h(\boldsymbol{\mu}^g)$. Thus, it could be expected that this approximation does not have a major impact on the quality of the mesh compared to the case where we use $\mathbf{U}_I(\boldsymbol{\mu}^g)$ rather than $\mathbf{U}_I^{EIM}(\boldsymbol{\mu}^g)$.

Finally, we remark that the approximation of $\mathbf{U}_I$ by $\mathbf{U}_I^{EIM}$ of Equation (5.66), for any new value of the parameter $\boldsymbol{\mu}^g \in \mathcal{D}$ at the online stage, can be obtained in $O(M(n-D))$ after having pre-computed at the offline stage $\mathbf{U}_I(\boldsymbol{\mu}^g)$ for $\boldsymbol{\mu}^g \in \{\boldsymbol{\mu}_i^{*,g}, 1 \leq i \leq M\}$.

Remark 5.3.4 Additional parameters, for instance via the Young modulus E as a function depending on the spatial variable $\mathbf{x} \in \Omega$ and the parameter $\boldsymbol{\mu}^g \in \mathcal{D}^g$, could be introduced in the problem (5.49) in order to ameliorate the quality of the mesh of the parametrized domain. This implies that the operator $\mathbf{K}_{II}$ at the left hand side of Equation (5.65) is $\boldsymbol{\mu}^g$-dependent. For this case, in order to obtain an approximation of $\mathbf{U}_I(\boldsymbol{\mu}^g)$ in an inexpensive way, we can turn to the reduced order modelling technique, see for instance [92, 43].

5.4 Reduced order modelling for non-affinely parametrized time-domain vibro-acoustic FE model

In the previous sections, we have presented how to exploit the EIM for finding an approximation of any non-affine dependence operator in a affine dependence form (with a purely algebraic and black box way) and for the mesh construction of a varying shape domain based on the Solid Extension Mesh Moving Technique (SEMMT) in a complexity linear in n_{elas}, where n_{elas} denotes the number of degrees of freedom in the corresponding linear elasticity problem. In this section, we aim to exploit these results to develop an efficient reduced order modelling technique framework for the case non-affinely parametrized with a variability of the geometrical domain.

In what follows, we consider that the parameter vector $\boldsymbol{\mu}$ is written as $\boldsymbol{\mu} = (\boldsymbol{\mu}^p, \boldsymbol{\mu}^g) \in \mathcal{D} = \mathcal{D}^p \times \mathcal{D}^g \subset \mathbb{R}^{n_p+n_g}$ where $\boldsymbol{\mu}^p$ represents vector of physical parameters and $\boldsymbol{\mu}^g$ represents vector of geometrical parameters. Before talking about the reduced order modelling, let us clarify the notion of the full model in the case where the parameter vector of the problem contains at least one geometrical parameters, i.e $n_g \geq 1$. Here, we denote by $\mathcal{T}_h^{ref}$ the reference mesh corresponding to the reference domain Ω^{ref}. For $\boldsymbol{\mu}^g \in \mathcal{D}^g$, we denote by $\mathbf{u}(\boldsymbol{\mu}^g)$ the displacement fields which transform the reference mesh $\mathcal{T}_h^{ref}$ into a conform mesh $\mathcal{T}_h(\boldsymbol{\mu}^g)$ of the parametrized domain $\Omega(\boldsymbol{\mu}^g)$. In our work, we recall that the displacement fields $\mathbf{u}(\boldsymbol{\mu}^g)$ is defined as the solution of an appropriate parametrized linear elasticity problem on $\mathcal{T}_h^{ref}$ (see Section 5.3.1). As a result, the notion of full model considered here refers to the following parametrized ordinary second order differential equation:

$$\mathbf{M}(\boldsymbol{\mu})\ddot{\mathbf{X}}(t;\boldsymbol{\mu}) + \mathbf{C}(\boldsymbol{\mu})\dot{\mathbf{X}}(t;\boldsymbol{\mu}) + \mathbf{K}(\boldsymbol{\mu})\mathbf{X}(t;\boldsymbol{\mu}) = \sum_{i=1}^{N_F} \theta_i(t)\mathbf{F}_i(\boldsymbol{\mu}) \tag{5.67}$$

where the matrices $\mathbf{M}, \mathbf{C}, \mathbf{K}$ and the vector $\mathbf{F}_i$ are constructed based on the parametrized mesh $\mathcal{T}_h(\boldsymbol{\mu}^g) = \{\mathbf{x} \in \mathbb{R}^d, \mathbf{x} = \mathbf{x}_{ref} + \mathbf{u}(\boldsymbol{\mu}^g)(\mathbf{x}_{ref}), \mathbf{x}_{ref} \in \mathcal{T}_h^{ref}\}$.

In the reduced order modelling technique framework proposed here, the offline stage can be split into three main steps. The presentations of each step are given in the following subsections.

5.4.1 Step 1: Reduction of the complexity in the construction of the parametrized mesh

In order to construct the finite element models (5.67) for any new values of geometrical parameter $\boldsymbol{\mu}^g$, it is necessary to compute $\mathbf{u}(\boldsymbol{\mu}^g)$ which is the solution of a linear elasticity problem on $\mathcal{T}_h^{ref}$, thus in a complexity of the resolution of a linear system $n_{elas} \times n_{elas}$, where n_{elas} depends on the dimension of the full order model (5.67) via the characteristic of the reference mesh $\mathcal{T}_h^{ref}$. The first step of our reduced order modelling framework is to exploit the EIM for constructing an approximation of the displacement field $\mathbf{u}(\boldsymbol{\mu}^g)$, which allows us to transform the reference domain to the parametrized domain, for any new value of $\boldsymbol{\mu}^g \in \mathcal{D}^g$ at online stage with a complexity linear in the number of degrees of freedoms in the elasticity problem (as presented in Section 5.3.2). In this stage, we start by finding an approximation in affine form of the boundary displacement $\mathbf{u}^d(\boldsymbol{\mu}^g)$ which transforms the boundary of $\partial\Omega^{ref}$ to $\partial\Omega(\boldsymbol{\mu}^g)$ by

the Greedy EIM algorithm 16, that is:

$$\mathbf{u}^d(\boldsymbol{\mu}^g) \approx \mathbf{u}^{d,EIM}(\boldsymbol{\mu}^g) := \sum_{i=1}^{N_{\mathbf{u}^d}^{EIM}} \alpha_i(\boldsymbol{\mu}^g)\mathbf{u}^d(\boldsymbol{\mu}_i^{*,g}) \tag{5.68}$$

Thanks to the fact that the left-hand side of the linear elasticity problem (5.64) is $\boldsymbol{\mu}^g$-independent, using the approximation of $\mathbf{u}^d(\boldsymbol{\mu}^g)$ by $\mathbf{u}^{d,EIM}(\boldsymbol{\mu}^g)$ defined in Equation (5.68) leads to:

$$\mathbf{u}(\boldsymbol{\mu}^g) \approx \mathbf{u}^{EIM}(\boldsymbol{\mu}^g) := \sum_{i=1}^{N_{\mathbf{u}^d}^{EIM}} \alpha_i(\boldsymbol{\mu}^g)\mathbf{u}(\boldsymbol{\mu}_i^{*,g}) \tag{5.69}$$

To summary, the first step of the reduced order modelling framework consists simply of replacing parametrized mesh $\mathcal{T}_h(\boldsymbol{\mu}^g) = \{\mathbf{x} \in \mathbb{R}^d, \mathbf{x} = \mathbf{x}_{ref} + \mathbf{u}(\boldsymbol{\mu}^g)(\mathbf{x}_{ref}), \mathbf{x}_{ref} \in \mathcal{T}_h^{ref}\}$ by its approximation $\mathcal{T}_h^{EIM}(\boldsymbol{\mu}^g) = \{\mathbf{x} \in \mathbb{R}^d, \mathbf{x} = \mathbf{x}_{ref} + \mathbf{u}^{EIM}(\boldsymbol{\mu}^g)(\mathbf{x}_{ref}), \mathbf{x}_{ref} \in \mathcal{T}_h^{ref}\}$.

Remark 5.4.1 Using the relation (5.69), the construction of mesh for any new geometry $\boldsymbol{\mu}^g \in \mathcal{D}^g$ requires then a complexity in $O(n_{elas}N_{\mathbf{u}^d}^{EIM})$, where n_{elas} is the number of degrees of freedom in the linear elasticity problem (5.64), provided that the displacement fields $\mathbf{u}$ are pre-computed and saved at the offline stage for the value of parameters $(\boldsymbol{\mu}_i^{*,g})_{1\leq i\leq N_{\mathbf{u}^d}^{EIM}}$ chosen by the Greedy EIM algorithm 16. Here, we emphasize that the complexity of the computation of $\mathbf{u}^{EIM}(\boldsymbol{\mu}^g)$ still depends on the number of degrees of freedom in the linear elasticity problem (5.49). However, we will see in Remark 5.4.3 of the next section that in the computation of the EIM's approximation of the operator and the right-hand side vector of the problem in the online stage, it requires only the value of the displacement field $\mathbf{u}^{EIM}(\boldsymbol{\mu}^g)$ for some nodes of the reference mesh, and not for all nodes of the mesh, thus it can be done in a complexity independent of n_{elas}.

Remark 5.4.2 For the case where the left-hand side of the linear elasticity problem (5.64) is $\boldsymbol{\mu}^g$-dependent, we can rely on the reduced order modelling technique to obtain an approximation of $\mathbf{u}(\boldsymbol{\mu}^g)$ in a complexity of $O(n_{elas}N_{elas})$ where N_{elas} denotes the dimension of the reduced order model of the elasticity problem (5.64), see for instance in [92, 43].

5.4.2 Step 2: Application of EIM to obtain an approximation in affine dependence in parameter for $\mathbf{M}, \mathbf{C}, \mathbf{K}$ and $\mathbf{F}$

The second step consists of applying the EIM with a purely black-box way to obtain an approximation in form of affine dependence in parameter for $\mathbf{M}, \mathbf{C}, \mathbf{K}$ and $\mathbf{F}$ as presented in Section 5.2.4. To do so, for $A \in \{M, C, K, F\}$, we compute $\mathbf{A}(\boldsymbol{\mu})$ for all values of the parameter $\boldsymbol{\mu} = (\boldsymbol{\mu}^p, \boldsymbol{\mu}^g)$ in a chosen training set $\mathcal{D}_{train,EIM}^A$ and run the Algorithm 19 for the case of matrix and the Algorithm 17 for the case of vector. At the end of this second step, we have transformed the full order model (5.67) into an approximative full order model:

$$\mathbf{M}^{EIM}(\boldsymbol{\mu})\ddot{\mathbf{X}}(t;\boldsymbol{\mu}) + \mathbf{C}^{EIM}(\boldsymbol{\mu})\dot{\mathbf{X}}(t;\boldsymbol{\mu}) + \mathbf{K}^{EIM}(\boldsymbol{\mu})\mathbf{X}(t;\boldsymbol{\mu}) = \sum_{i=1}^{N_F} \theta_i(t)\mathbf{F}_i^{EIM}(\boldsymbol{\mu}) \tag{5.70}$$

where the matrices $\mathbf{M}^{EIM}, \mathbf{C}^{EIM}, \mathbf{K}^{EIM}$ and the vector $\mathbf{F}_i^{EIM}, i = 1, \cdots, N_F$ are now affine dependence in parameter and are defined on the parametrized mesh $\mathcal{T}_h^{EIM}(\boldsymbol{\mu}^g) = \{\mathbf{x} \in \mathbb{R}^d, \mathbf{x} =$

$\mathbf{x}_{ref} + \mathbf{u}^{EIM}(\boldsymbol{\mu}^g)(\mathbf{x}_{ref}), \mathbf{x}_{ref} \in \mathcal{T}_h^{ref}\}$.

Remark 5.4.3 We recall that in the computation of the coefficient $(\theta_l^A(\boldsymbol{\mu}))_{1\leq l\leq N_A^{EIM}}$, for any new values of parameter $\boldsymbol{\mu} \in \mathcal{D}$, in the EIM's approximation (5.21) requires only the values of $\mathbf{A}$ at the magical indices chosen by EIM algorithm. Thanks to the property of the local support of the finite element basis functions, these values can be computed with a complexity independent of the dimension of the full model. It is sufficient to compute the elementary terms corresponding to $\mathbf{A}$ only for the reduced elements e^A which have a non-zeros contribution to the value of $\mathbf{A}$ at the magical indices (identified by Algorithm 18 for the case of vector and by Algorithm 20 for the case of matrix) and restrict the assembling procedure on this group of elements in the mesh. As a result, it is **very important** to note that it requires only to compute the new geometry of this group of elements e^A in the mesh and not the new geometry of the entire mesh. This allows us to compute the coefficient $(\theta_l^A(\boldsymbol{\mu}))_{1\leq l\leq N_A^{EIM}}$ with a complexity independent of the total number of node in the mesh. The complexity depends only on the number of nodes in the group of elements e^A.

Remark 5.4.4 In the context of the interaction of submerged structure and shock wave problem, the right-hand side vector $\mathbf{F}(t;\boldsymbol{\mu})$ depends on $\boldsymbol{\mu}^g$ only in the case where the fluid-structure interface Γ is $\boldsymbol{\mu}^g$-dependent. For the case where the mass of explosive material represents one of the parameter of the problem and that the interface Γ is independent of parameter, we recommend to use the non-intrusive approximation given by Equation (5.46) since the underlying linear form of $\mathbf{F}(t;\boldsymbol{\mu})$ is known explicitly. Furthermore, it can also be noted that applying EIM on a parametrized function p^{inc}, v_r^{inc} requires a computational cost, for both in offline and online stage, less than its variant in black box way for its corresponding parameter-dependent vector $\mathbf{F}(t;\boldsymbol{\mu})$ as proposed in Section 5.2.4.

Remark 5.4.5 On the contrary to the first step, the second step could induce an instability in the approximative full order model (5.70) for the case of time-domain vibro-acoustic problem. As a reminder, the demonstration of the stability property of the finite element models of time-domain vibro-acoustic problem given in Chapter 3 is under the hypothesis that the mass matrices $\mathbf{M}_s, \mathbf{M}_f$ are symmetric and positive definite, the stiffness matrices $\mathbf{K}_s, \mathbf{K}_f$ are symmetric and positives semi-definite and that the the damping matrices $\mathbf{C}_s, \mathbf{C}_f$ are positives semi-definite, see for instance Lemma 3.1.4 for $(\mathbf{u}_s, \phi)$ based formulation. In the EIM's approximation, it can only be ensured that the matrices $\mathbf{M}_s^{EIM}, \mathbf{M}_f^{EIM}, \mathbf{K}_s^{EIM}, \mathbf{K}_f^{EIM}$ are symmetric. The positive (semi-) definiteness property of $\mathbf{M}_s^{EIM}, \mathbf{M}_f^{EIM}, \mathbf{K}_s^{EIM}, \mathbf{K}_f^{EIM}, \mathbf{C}_s^{EIM}$ and $\mathbf{C}_f^{EIM}$ are not mathematically guaranteed. However, thanks to the Bauer-Fike theorem mentioned in Remark 5.2.2, we believe that the property of positive definite of the mass matrices $\mathbf{M}_s^{EIM}, \mathbf{M}_f^{EIM}$ could be recovered by increasing the number of terms in the EIM's approximation. For the positive semi-definiteness property, it could also be expected that this property can be recovered by increasing the number of terms in the EIM's approximation under condition that the kernel of the parametrized matrix $\mathbf{A}(\boldsymbol{\mu})$ under consideration is $\boldsymbol{\mu}$-independent, as mentioned in Remark 5.2.3. For the stiffness matrix of fluid part $\mathbf{K}_f$, this condition is achieved as its kernel represents the constant pressure mode which is clearly independent of $\boldsymbol{\mu}$. For the stiffness matrix of structure part $\mathbf{K}_s$, its kernel represents the rigid body modes and is of six dimensions in the case of 3D-configuration (of three dimensions in the case of 2D-configuration). It refers to three modes of translation and three modes of rotation. The

three translation modes are $\boldsymbol{\mu}$-independent. In the opposition, the three rotation modes can be $\boldsymbol{\mu}^g$-dependent via the position of nodes in the mesh depending on the chosen finite element types. For the case of the classical finite elements, such as tetrahedron with 6 or 10 nodes and hexahedron with 9, 20 or 27 nodes, where the nodes contain only the degree of freedom of translation, the three rotation modes are $\boldsymbol{\mu}^g$-dependent. For the case of the finite element of type shell element [21] or Discrete Kirchhoff Triangular (DKT) elements [20] where the nodes contain also the degrees of freedom of rotation, it has to be verified if the three rotation modes are $\boldsymbol{\mu}^g$-independent. It should also be remarked that in the case where there is a Dirichlet condition at a portion of boundary of structure part aiming to avoid these rotation modes, we also believe that the property of $\mathbf{K}_s$ could be preserved by increasing simply the number of terms in the EIM's approximation. To sum up, in the case where the geometry of structure domain is also considered as a parameter of the problem, we would like to alert that the instability of the approximative full order model (5.70) might not be avoided by simply increasing the number of terms in the EIM's approximation.

5.4.3 Step 3: Construction of Petrov-Galerkin reduced order model with the reduced basis based on POD-Greedy algorithm

Now that we have transformed the full order model (5.67) into an approximative full order model (5.70) in which all the operators and the right-hand size are affine parametric dependence, the next and the last step consist of constructing an appropriated parametrized Petrov-Galerkin reduced order model corresponding to the approximative full order model (5.70), with the same approach as presented in the previous chapter.

For a given trial and test reduced basis $\mathbf{V}, \mathbf{W} \in \mathbb{R}^{n\times N}$, we recall that the Petrov-Galerkin projection reduced order model of the approximative full model (5.70) writes:

$$\mathbf{M}_r^{EIM}(\boldsymbol{\mu})\ddot{\mathbf{X}}_r(t;\boldsymbol{\mu}) + \mathbf{C}_r^{EIM}(\boldsymbol{\mu})\dot{\mathbf{X}}_r(t;\boldsymbol{\mu}) + \mathbf{K}_r^{EIM}(\boldsymbol{\mu})\mathbf{X}_r(t;\boldsymbol{\mu}) = \sum_{i=1}^{N_F}\theta_i(t)\mathbf{F}_{i,r}^{EIM}(\boldsymbol{\mu}) \tag{5.71}$$

where the reduced matrices and vectors are defined by:

$$\begin{aligned} \mathbf{M}_r^{EIM}(\boldsymbol{\mu}) &= \mathbf{W}^T\mathbf{M}^{EIM}(\boldsymbol{\mu})\mathbf{V}, \quad \mathbf{C}_r^{EIM}(\boldsymbol{\mu}) = \mathbf{W}^T\mathbf{C}^{EIM}(\boldsymbol{\mu})\mathbf{V} \\ \mathbf{K}_r^{EIM}(\boldsymbol{\mu}) &= \mathbf{W}^T\mathbf{K}^{EIM}(\boldsymbol{\mu})\mathbf{V}, \quad \mathbf{F}_{i,r}^{EIM}(\boldsymbol{\mu}) = \mathbf{W}^T\mathbf{F}_{i,r}^{EIM}(\boldsymbol{\mu}), 1 \leq i \leq N_F \end{aligned} \tag{5.72}$$

We would like also to recall that approximation of the solution of the full order model (5.70) by the reduced order model (5.71) is defined by $\mathbf{X}(t;\boldsymbol{\mu}) = \mathbf{V}\mathbf{X}_r(t;\boldsymbol{\mu})$. For the case where the output of interest can be written as a linear (quadratic) form, its approximation by the reduced order model (5.71) is given by $S_l^{rom}(t;\boldsymbol{\mu}) = \mathbf{L}_r^T\mathbf{X}_r(t;\boldsymbol{\mu})$ ($S_q^{rom}(t;\boldsymbol{\mu}) = \mathbf{X}_r^T(t;\boldsymbol{\mu})\mathbf{Q}_r\mathbf{X}_r(t;\boldsymbol{\mu})$) , where the reduced vector $\mathbf{L}_r \in \mathbb{R}^N$ is defined by $\mathbf{L}_r^T = \mathbf{L}^T\mathbf{V}$ (the reduced matrix $\mathbf{Q}_r \in \mathbb{R}^{N\times N}$ is defined by $\mathbf{Q}_r = \mathbf{V}^T\mathbf{Q}\mathbf{V}$). For the construction of the reduced basis $\mathbf{V}$ in the context of parametrized time-domain vibro-acoustic problem, we recall that we have introduced in the previous chapter some modifications in the classical POD-Greedy in order to ensure the stability of the reduced order model. For the formulation in $(\mathbf{u}_s, \phi)$, the proposed POD-Greedy algorithm is outlined by Algorithm 13. For the formulation in $(\mathbf{u}_s, p)$ and $(\mathbf{u}_s, p, \varphi)$, the proposed POD-Greedy algorithm are outlined respectively by Algorithm 14 and 15.

5.4.4 Workflow

To sum up, we condense the results from the preceding sections into a structured workflow for constructing an efficient reduced order model of a non-affinely parametrized time-domain vibro-acoustic finite element models. A schematic of this workflow is depicted in Figure 5.15 in which we would like to emphasize that the three steps presented in the above sections are performed in offline stage.

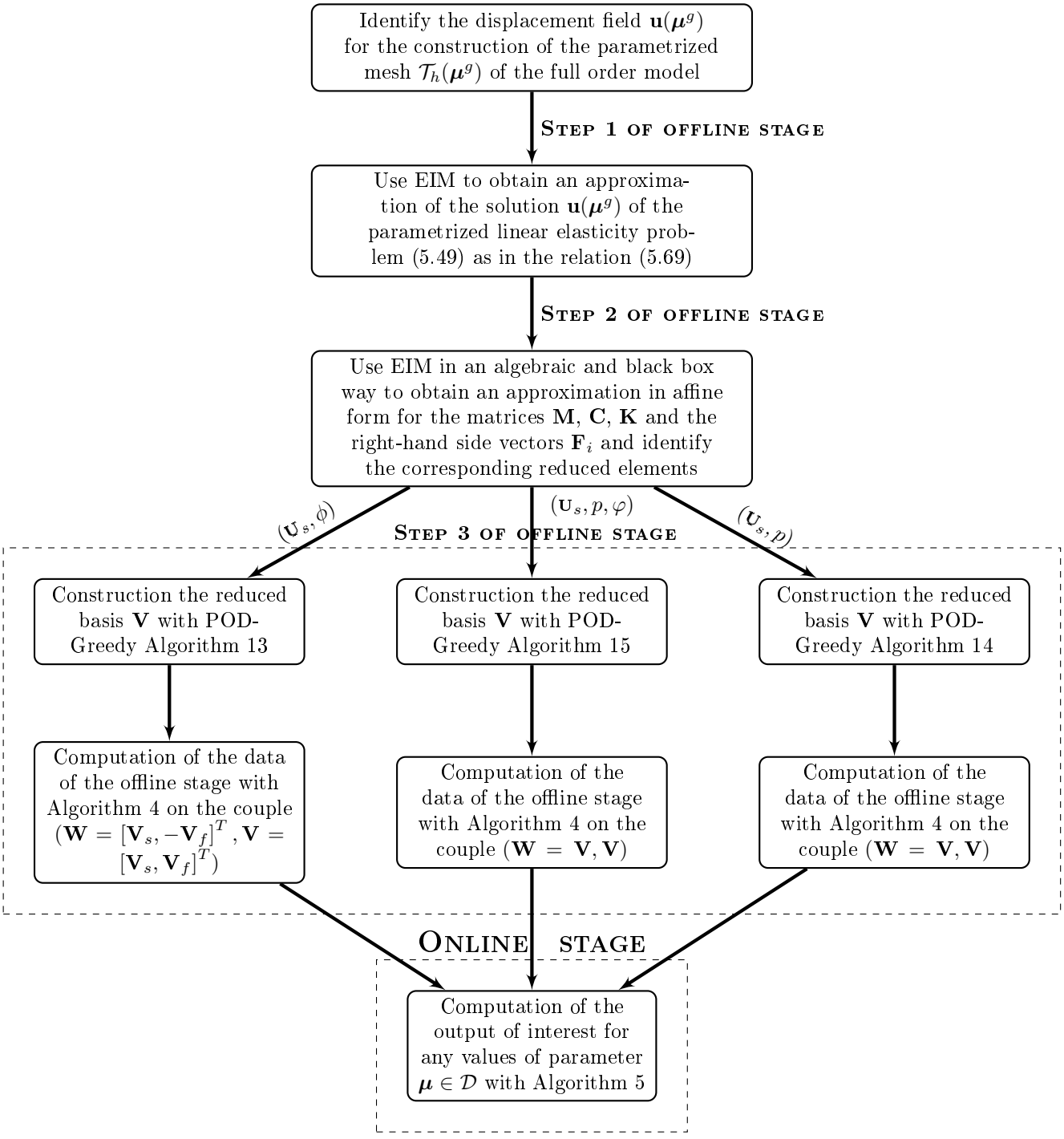

Figure 5.15: Workflow for the case of non-affine dependence in parameter

5.5 Numerical results

The aim of this section is to illustrate numerically the efficiency of our reduced order modelling framework in a simple study case, of interaction of submerged structure and shock wave problem, before applying it in the industrial cases. Here, we will consider only the case of the formulation in $(\mathbf{u}_s, \phi^{sca})$ (see Section 2.4.1). However, it should be noted that the methodology can also be applied in for the three other three formulations presented in Section 2.4.

Presentation of the study case

A graphical representation of the study case is presented in Figure 5.16. The structural part consists of an elastic ring of radius R and thickness h and an elastic structure in form of T on which a spring-mass system is suspended. The structure under consideration is subjected to an acoustic shock wave induced by an underwater explosion of M_{tnt} kilograms of Trinitrotoluene (TNT) detonated at $(d, 0)$. At $t = 0$, we assume that the shock wave arrives at the stand-off point $(R, 0)$.

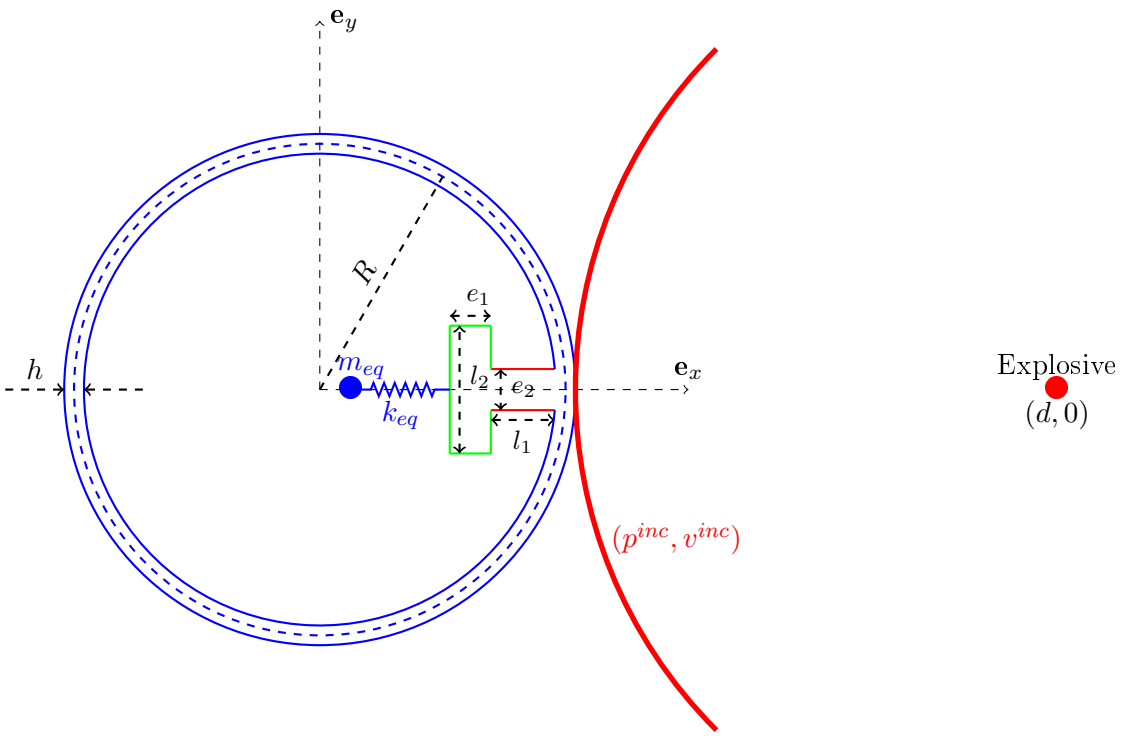

Figure 5.16: Graphical representation of the first study case

For numerical application, we use $R = 2$ m, $h = 0.5$ m, $e_1 = e_2 = 0.2$ m and $d = 50$ m. Both the elastic ring and the structure in T-form have Young's modulus $E = 200$ GPa, mass density $\rho_s = 7\,800$ kg/m^3 and Poisson's ratio $\nu = 0.28$. The density and the speed sound of the fluid are given by $\rho_0 = 1\,000$ kg/m^3, $c_0 = 1\,500$ m/s. For the characteristics of the shock wave which are modelled by Equation (2.12) for incident pressure and by Equation (2.15) for incident fluid particle's velocity, we use the value of constants P_c, v_c, A and B provided by Equation (2.10) according to [40].

The parameter vector in the problem is defined by $\boldsymbol{\mu} := (m_{eq}, f_{eq}, M_{tnt}, l_1, l_2)$ where m_{eq} and $f_{eq} := \frac{1}{2\pi}\sqrt{\frac{k_{eq}}{m_{eq}}}$ are respectively the mass and the frequency of the spring-mass system, M_{tnt} is the mass of Trinitrotoluene (TNT) in explosion and l_1, l_2 are the lengths of the structure in T-form. The parameter spaces is set by $\mathcal{D} := [10, 1000] \times [250, 1000] \times [100, 1000] \times [0.9\bar{l}_1, 1.1\bar{l}_1] \times [0.9\bar{l}_2, 1.1\bar{l}_2] \subset \mathbb{R}^5$ where $\bar{l}_1 = \bar{l}_2 = 0.8$ m are the nominal values of the lengths of the structure in T-form. Here, the vector of geometrical parameter $\boldsymbol{\mu}^g$ is defined by $\boldsymbol{\mu}^g := (l_1, l_2)$. The geometry of reference is chosen as the particular case where $\boldsymbol{\mu}^g = (\bar{l}_1, \bar{l}_2)$.

Full order model and output of interest

In order to approximate the Sommerfeld radiation condition, a truncated fluid domain in form of a circle of radius $R_{bgt} = 4$ m is employed. On the boundary of the truncated fluid domain, the BGT-1 boundary condition (1.35) is applied in order to approximate the outgoing sound wave by a cylindrical wave for which we use the value of impedance $Z_R = 2\rho_0 R_{bgt}$ and $Z_C = \rho_0 c_0$. In finite element modelling, we use **quadratic triangular elements** both for the structure and the fluid part. The reference mesh of structure part is illustrated in Figure 5.17. In the reference mesh, the largest element size in the fluid part and structure part are respectively 0.08 m and 0.04 m.

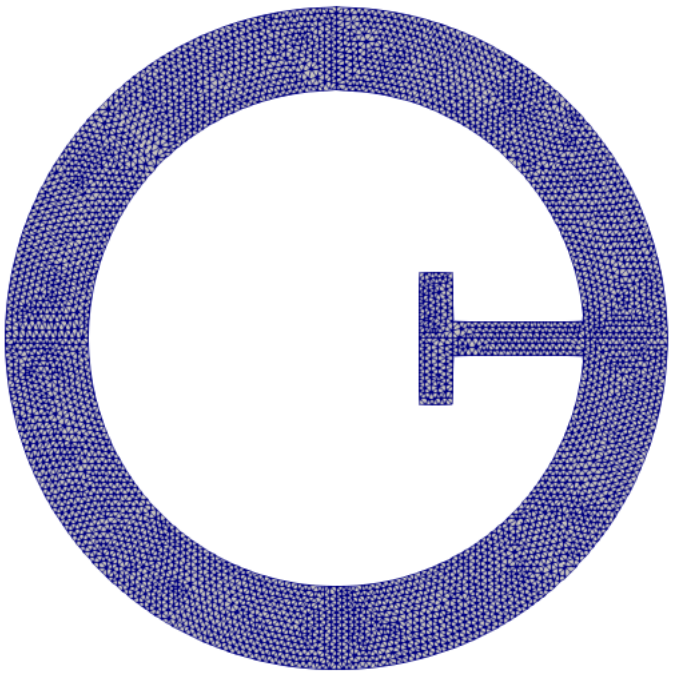

Figure 5.17: The structural part in the reference mesh.

Here, we denote by Γ_1, Γ_2 and Γ_3 the boundary of the structural part Ω_s which are respectively marked in blue, red and green in Figure 5.16. In order to transform the geometry (mesh) of reference to a new geometry (mesh), we solve the elasticity problem (5.49) which is

defined only on the structure part with the following boundary displacement:

$$\begin{cases} u_x^d(x,y;\boldsymbol{\mu}^g) = 0 & \text{on } \Gamma_1 \\ u_y^d(x,y;\boldsymbol{\mu}^g) = 0 & \text{on } \Gamma_1 \\ u_y^d(x,y;\boldsymbol{\mu}^g) = 0 & \text{on } \Gamma_2 \\ u_x^d(x,y;\boldsymbol{\mu}^g) = -(l_1 - \bar{l}_1) & \text{on } \Gamma_3 \\ u_y^d(x,y;\boldsymbol{\mu}^g) = \dfrac{l_2 - \bar{l}_2}{\bar{l}_2} y & \text{on } \Gamma_3 \end{cases} \tag{5.73}$$

In our study, we use the same values of Young's modulus and Poisson's ratio in the elasticity problem (5.49) as in the fluid-structure interaction problem. It should be noted that we impose in Equation (5.73) that the boundary displacement on Γ_1 is zero so that the fluid-structure interface $\Gamma \subset \Gamma_1$ is independent of $\boldsymbol{\mu}^g$. As a result, the position of nodes in fluid part do not change in function of $\boldsymbol{\mu}^g$. Thus, a coupling damping matrix $\mathbf{C}_{u\phi}^{ext}$ in finite element model (2.23) is $\boldsymbol{\mu}$-independent in this study case.

In the finite element model, we have 61 243 degrees of freedoms, 31 525 of which correspond to the structural part (one of which corresponds to the point mass in the spring-mass system) and 29 718 of which correspond to the acoustic fluid part. For time-discretization of finite element model, Newmark scheme (with $\beta = \frac{1}{4}(1-\alpha)^2$ and $\gamma = 1/2 - \alpha$ where $\alpha = -0.2$) is employed by using the time step $\Delta t = 4 \cdot 10^{-5}$ which means that the shock wave needs 100 times step in order to travel the distance of $3R$. The final time of interest is set by $T = 6R/c_0$ so that the total number of time steps is $N_t = 200$. In this study case, the acceleration $a_{m_{eq}}$ of the point mass in the spring-mass system represents the output of interest.

Errors introduced by the approximative full order model

In this study case, we note that the boundary displacement $\mathbf{u}^d$ exhibits a trivial affine decomposition such that it can be exactly recovered by EIM with two basis functions. As a result, the first step presented in Section 5.4.1 of our framework does not introduce any error. To access to the influence of the tolerance ϵ_{EIM} used for approximating the full order model, we are interested in the error defined by:

$$\Delta_l(\boldsymbol{\mu}) := \frac{\left(\int_0^T \left| a_{m_{eq}}^{fom}(t;\boldsymbol{\mu}) - a_{m_{eq}}^{fom,EIM}(t;\boldsymbol{\mu}) \right|^2 dt \right)^{1/2}}{\left(\int_0^T \left| a_{m_{eq}}(t;\boldsymbol{\mu}) \right|^2 dt \right)^{1/2}} \tag{5.74}$$

where the superscripts ^{fom} and ^{fom,EIM} refer respectively to the values provided by the original full model and the approximative full order model proposed in the second step of our framework.

For the left-hand side operators, we only run the algebraic version of EIM algorithm outlined in Algorithm 19 with the mass matrix $\mathbf{M}_{u\phi}$ and the stiffness matrix $\mathbf{K}_{u\phi}$ since the damping matrix $\mathbf{C}_{u\phi}^{ext}$ is $\boldsymbol{\mu}$-independent. With a training sample $\mathcal{D}_{train}^{EIM} \subset \mathcal{D}$ consisting of 100 values of parameters chosen randomly, the convergence of the error indicator (which is defined as the relative error evaluated at the value of parameter which maximizes the residual) for the both

matrices $\mathbf{M}_{u\phi}$ and $\mathbf{K}_{u\phi}$ are reported by Figure 5.18.

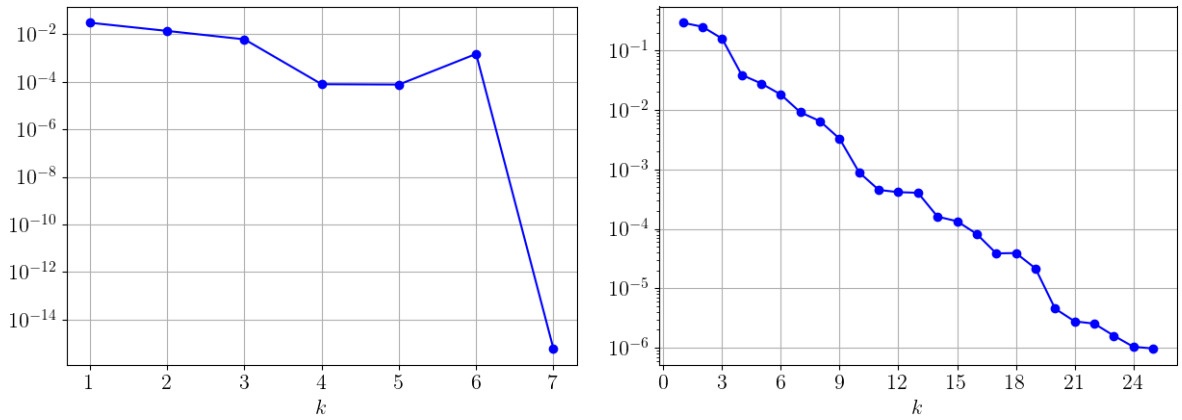

(a) Case of mass matrix $\mathbf{M}_{u\phi}$ (b) Case of stiffness matrix $\mathbf{K}_{u\phi}$

Figure 5.18: The evolution of error indicator in EIM algorithm 19 applied on $\mathbf{M}_{u\phi}$ and $\mathbf{K}_{u\phi}$

Based on the decay of the value of error indicator, the number of terms to be retained in EIM approximation in the case where $\epsilon_{EIM} = 10^{-6}$ is $N_M^{EIM} = 7$ for the mass matrix and $N_K^{EIM} = 25$ for the stiffness matrix. The corresponding reduced elements in the structure in T-form part are then displayed in Figure 5.19.

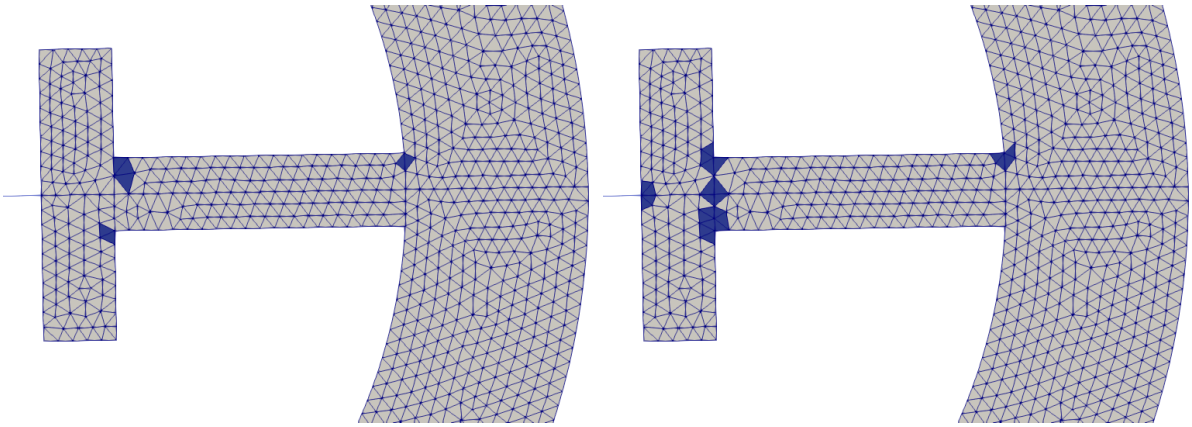

(a) Case of mass matrix $\mathbf{M}_{u\phi}$ (b) Case of stiffness matrix $\mathbf{K}_{u\phi}$

Figure 5.19: The corresponding reduced elements (marked in blue) in the structure in T-form part.

For the right-hand side, the parameter dependence is only via the mass of explosive. According to Remark 5.4.4, we will use the approximation in affine form of the relation (5.46) in which, from the numerical results presented in Section 5.2.5, we set $N_{pv}^{EIM} = N_p^{EIM} = N_v^{EIM}$ where N_p^{EIM} and N_v^{EIM} are determined by EIM Algorithm 16 applied on the incident pressure p^{inc} and incident fluid particle's velocity v_r^{inc} with respect to the given tolerance ϵ_{EIM}. With a training sample $\mathcal{D}_{M_{tnt}} \subset [100, 1000]$ consisting of 100 values chosen randomly, the decay of the error indicator, which is defined as the relative error evaluated at the value of parameter which maximizes the residual (*i.e* the next value of parameter to be chosen by EIM algorithm), are

displayed in Figure 5.20.

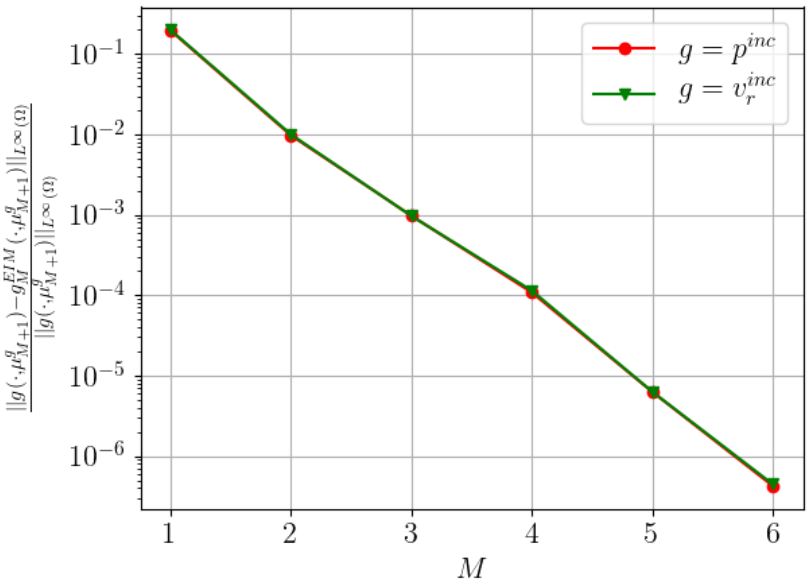

Figure 5.20: The convergence of error indicator in EIM algorithm 16 applying on p^{inc} and v_r^{inc}

Figure 5.20 indicates that it requires respectively $N_p^{EIM} = N_v^{EIM} = 5$ and $N_p^{EIM} = N_v^{EIM} = 6$ in order to respect to the stopping criterion $\epsilon_{EIM} = 10^{-4}$ and $\epsilon_{EIM} = 10^{-6}$.

From a test sample $\mathcal{D}_{test} \subset \mathcal{D}$ consisting of 50 values of parameters chosen randomly, the errors introduced in full order model approximation by the second step of our framework is summarized by Table 5.1.

ϵ_{EIM}	Number of terms in EIM			Errors		
	N_M^{EIM}	N_K^{EIM}	N_{pv}^{EIM}	$\max_{\boldsymbol{\mu}\in\mathcal{D}_{test}} \Delta_l(\boldsymbol{\mu})$	$\min_{\boldsymbol{\mu}\in\mathcal{D}_{test}} \Delta_l(\boldsymbol{\mu})$	$\text{moy}_{\boldsymbol{\mu}\in\mathcal{D}_{test}} \Delta_l(\boldsymbol{\mu})$
10^{-4}	7	16	5	$1.82 \cdot 10^{-1}$	$2.93 \cdot 10^{-4}$	$1.1 \cdot 10^{-2}$
10^{-6}	7	25	6	$4.66 \cdot 10^{-3}$	$5.42 \cdot 10^{-5}$	$5.84 \cdot 10^{-4}$

Table 5.1: The errors introduced by the approximative full order model.

Convergence of POD-Greedy algorithm and efficiency of the reduced order models

Next, we run the POD-Greedy algorithm 13 for both case of $\epsilon_{EIM} = 10^{-4}$ and $\epsilon_{EIM} = 10^{-6}$ with the value of ϵ_{POD} set by 10^{-4}. For both cases, we use the same training sample $\mathcal{D}_{train}^k$ which is chosen randomly at each iteration with $|\mathcal{D}_{train}^k| = 50$. The evolution of error indicator and the error of output of interest evaluated at $\boldsymbol{\mu}_{k+1}^* = \text{argmax}_{\boldsymbol{\mu}\in\mathcal{D}_{train}^k} \Delta_l(\boldsymbol{\mu})$ are displayed in Figure 5.21. The dimension of the corresponding reduced basis are reported by Figure 5.22.

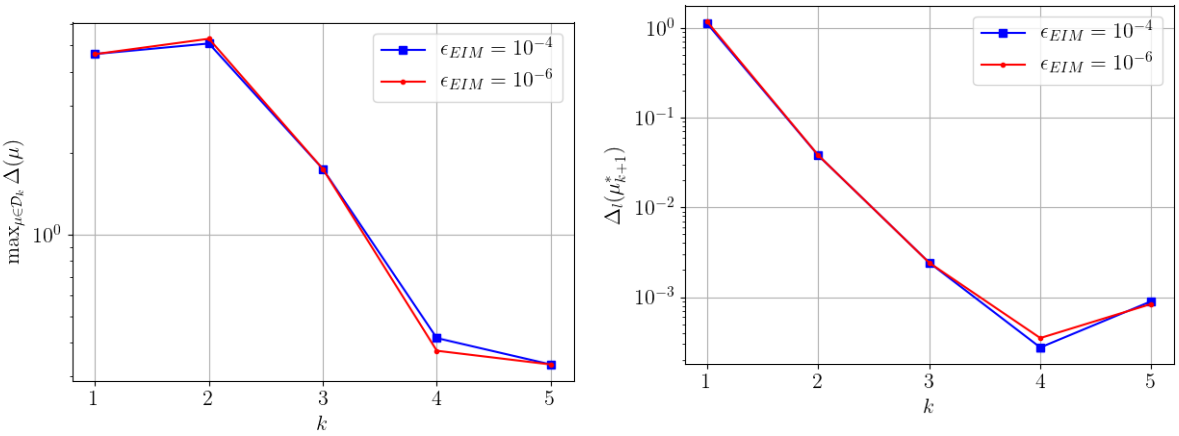

(a) Indicator error Δ

(b) Error of output of interest for $\boldsymbol{\mu}^*_{k+1} = \text{argmax}_{\boldsymbol{\mu} \in \mathcal{D}^k_{train}} \Delta_l(\boldsymbol{\mu})$

Figure 5.21: The convergence of POD-Greedy algorithm

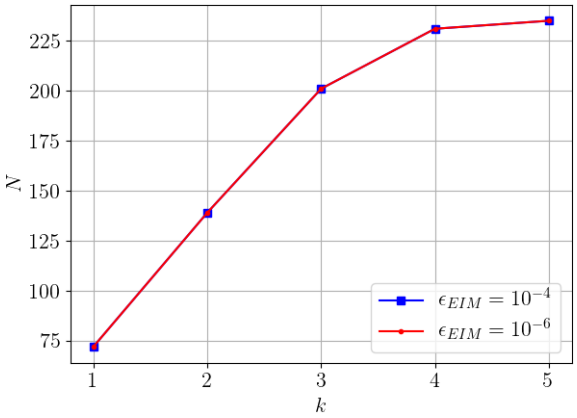

Figure 5.22: Size of the reduced basis

We observed that in both case, POD-Greedy algorithm chose the same value of parameter for enriching the basis and that we have the same evolution of the dimension of the reduced basis. This can be explained by the fact that we have a small error between the approximative full order model with $\epsilon_{EIM} = 10^{-4}$ and the case of $\epsilon_{EIM} = 10^{-6}$. As in the numerical results presented in the previous chapter, we remark again that the indicator error based on the norm of residual is very pessimist for predicting the error on the output of interest, which is represented by the acceleration of the point mass of *spring-mass* system.

We now turn to the accuracy of the obtained reduced order models. Here, we denote by $\Delta_l^{rom,fom}$ the error between the reduced order model and the full order model, by $\Delta_l^{rom,\ app\ fom}$ the error between the reduced order model and the approximative full model and by $\Delta_l^{fom,\ appfom}$ the error between the approximative full model and the original full order model. The evolution of errors $\Delta_l^{rom,fom}$, $\Delta_l^{rom,\ app\ fom}$ during the iterations of POD-Greedy Algorithm and the error $\Delta_l^{fom,\ app\ fom}$ are reported by Figure 5.23.

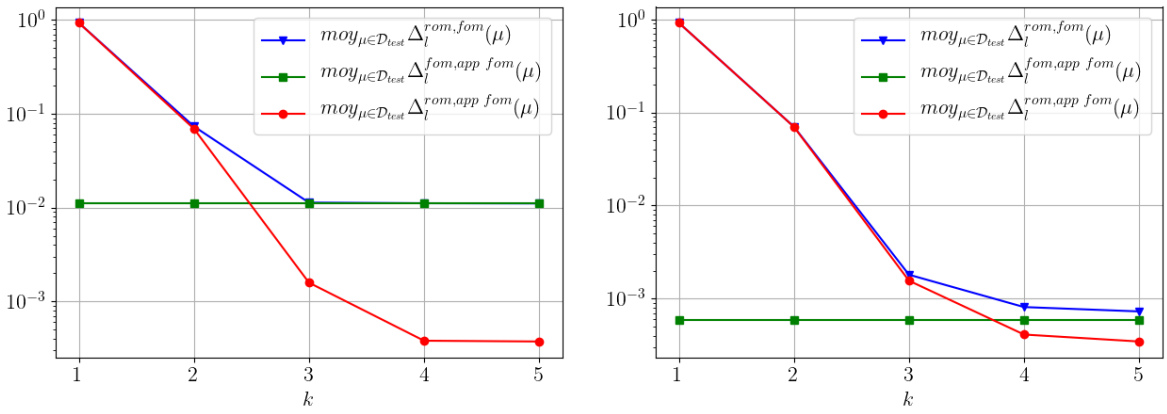

(a) Case of $\epsilon_{EIM} = 10^{-4}$ (b) Case of $\epsilon_{EIM} = 10^{-6}$

Figure 5.23: The evolution of accuracy of reduced order model.

Figure 5.23 shows that the error $\Delta_l^{rom,fom}$ is bounded after 3 iterations of POD-Greedy algorithm for the case of $\epsilon_{EIM} = 10^{-4}$ and after 4 iterations for the case $\epsilon_{EIM} = 10^{-6}$. This is due to the domination of the error $\Delta_l^{fom,\ app\ fom}$ introduced in the second step of the proposed framework which aims to recover the affine parametric dependence property.

In this numerical study, the development is not yet accomplished for the computation of new mesh by changing only the position of reduced elements which is necessary in order to ensure that the complexity of online stage depends only on the dimension of the reduced order model (see Remark 5.4.3). Even though, we would like to point out that the reduced order model obtained with 3 iterations of POD-Greedy algorithm in the case of $\epsilon_{EIM} = 10^{-4}$, which already provides an average error less than 2%, takes about 3 seconds. In comparison with the full order model which takes about 45 seconds, we have in this case a factor 15 as time-speed up.

5.6 Conclusions

In this chapter, we expose a reduced order modelling framework for a non-affinely parametrized time-domain vibro-acoustic finite element model. We start with a presentation of the Empirical Interpolation Method. Next, we derived its applications for approximating the right-hand side vector of an interaction between a submerged structure and a shock wave problem in an affine parametric dependence form for the case where the mass of explosive material is one of parameter of the problem. We also derive its application in purely algebraic and black box way for any non-affinely parametrized matrix/vector resulting from a finite element discretization. With a parametrization of a varying shape domain (mesh) using the Solid Extension Mesh Moving Technique (SEMMT) and the application of EIM for recovering approximately the property of affine dependence in parameter, the reduced order modelling framework proposed in Chapter 4 can then be extended to the case of non-affinely parametric dependence with/without the variability of geometry.

A simple numerical study case with five parameters, two of which are geometrical parameters, is presented in order to highlight the efficiency of the proposed framework. Since the development is not yet accomplished for the computation of new mesh by changing only the

position of reduced elements at online stage, numerical results presented here do not show a very high performance of the reduced order models. Thus, a short-term objective is to optimize the complexity in online stage and to apply the proposed framework into industrial cases.

Conclusions and perspectives

The main objective of this thesis is to propose and develop some reduced order modelling frameworks for parametrized time-domain vibro-acoustic finite element model into an industrial software, *code_ aster*, with the aim of applying the approach on an industrial problem: « the design of structures subjected to underwater explosion's primary shock wave ».

In the first part, we exposed the different formulations of vibro-acoustic finite elements models and we remark that the formulation based on structure displacement - fluid pressure - fluid displacement potential $(\mathbf{u}_s, p, \varphi)$, which is the only formulation already implemented in *code_ aster*, is not the best formulation to be employed in the context of our industrial problem of interest which is the problem of interaction of submerged structure and acoustic shock wave. As a result, we developed two new formulations, formulation in structure displacement - fluid pressure $(\mathbf{u}_s, p)$ and in structure displacement - fluid velocity potential $(\mathbf{u}_s, \phi)$, in *code_ aster*. The excitation induced by an acoustic shock wave is then developed and validated numerically with two study cases for each formulation.

In the second part, we start with an overview on the stabilization techniques for Petrov-Galerkin based model order reduction of the three formulations considered in the thesis. At first, we propose to use the reduced basis based on the corresponding frequency modes, whose frequencies are selected by a Greedy algorithm. According to the proposed stabilization techniques, some modifications are introduced in the classical Greedy algorithm. Numerical results confirm the stability of the obtained reduced order model. Concerning the accuracy, we observe that the proposed reduced basis results in an inaccurate reduced order model especially in the case where the excitation is of high frequency. Therefore, we turn to an alternative for the construction of an accurate reduced basis. The construction of the reduced basis with a POD-Greedy algorithm is considered in this work. With some modifications for ensuring the stability of the reduced order model and an inexpensive error indicator based on the norm of residual, we derive an efficient reduced order modelling framework for parametrized time-domain vibro-acoustic problem. The extension of the proposed framework into the case of non-affine dependence in parameter is also given by exploiting the well-known Empirical Interpolation Method (EIM) with a purely algebraic and black box way and the so-called Solid Extension Mesh Moving Technique (SEMMT) for parametrizing the varying shape domain (mesh). In the context of the interaction of submerged structure and acoustic shock wave problem, numerical results on both simple study cases and industrial cases show that the efficiency of the proposed model order reduction techniques is very promising.

With these promising results, the proposed reduced order modelling framework should be pursued in several directions:

- **Extension to the case of a vibro-acoustic problem with a free surface.** Only the case without a free surface in the fluid part are considered in this thesis. Taking into account the effect of free surface in the model is necessary in order to tackle a more complex and general case which can occurs for instance when the submarine is submerged at a shallow depth of the sea, and of course for the case of the ships.

- **Application in other contexts of vibro-acoustic problem.** In this thesis, we only put the interest on vibro-acoustic phenomena resulting from the interaction of submerged structure and acoustic shock wave problem. However, it should be mentioned that the developed reduced order modelling framework can readily be applied for any parametrized time-domain vibration and vibro-acoustic problem. It should also be interesting to point out if the error indicator based on the norm of residual and the error estimator in energy norm proposed in this thesis are still very pessimist in other contexts of vibro-acoustic problems, such as in dimensioning of structures for seismic problem in nuclear industry, acoustic discretion problem in naval and automotive industry, ...

- **Introduction of dual problems for linear output of interest.** For the case where the output of interest is a linear form, a dual problem can be introduced in order to double the convergence rate of the accuracy of the output of interest predicted by the reduced order model. For stationary problems, it has been widely investigated in [38, 123, 73, 91]. For time-domain vibro-acoustic problem, it should be exploited the idea proposed in [62] in a context of parametrized parabolic problem.

- **Extension to the case where the Dirichlet condition is treated by Lagrange multiplier.** In this thesis, we restrict ourselves to the case where the Dirichlet condition is treated by the elimination method. Thus, it can not yet be applied to a more general case, for instance when we aim to impose a part of structure to have a rigid behaviour. A possible approach for the case of Lagrange method is to follow the idea in [41] for non-linear transient heat conduction problem, in which it has been proposed to construct a reduced basis for physical ($i.e$ temperature) and Lagrange multiplier degrees of freedom separately.

- **Application of the reduced order models in optimization problem.** With a complexity relatively inexpensive compared to the full order model, it should also be interesting to apply on other problems such as in optimization problem (for instance, see [93] for the case of a stationary problem with quadratic functional cost and [49] for the case of the parabolic problem with a linear functional cost).

- **Extension to the case with non-linear structural.** A more challenging problem is to extend the approach to the case where the structure under consideration has a non-linear behaviour. To start, we advise to exploit some ideas from [26] which aims at tackling the parametrized non-linear elasticity in stationary regime.

Part III

Appendices

Appendix A

Numerical time-integration with Newmark method

In this appendix, we give a review on Newmark method [101] which is one of the most widely used numerical integration methods for the second Order Differential Equations (ODE). For example, the second-order ordinary differential equation obtained after a spatial discretization by the finite element method of a structural dynamic or a time-domain vibro-acoustic problem.

Here, we consider a general second-order ordinary differential equation:

$$\begin{cases} \mathbf{M}\ddot{\mathbf{X}}(t) + \mathbf{C}\dot{\mathbf{X}}(t) + \mathbf{K}\mathbf{X}(t) = \mathbf{F}(t) \\ \mathbf{X}(t=0) = \mathbf{X}_0 \\ \dot{\mathbf{X}}(t=0) = \dot{\mathbf{X}}_0 \end{cases} \tag{A.1}$$

where the matrices $\mathbf{M}, \mathbf{C}$ and $\mathbf{K}$ are in $\mathbb{R}^{n\times n}$ and the right-hand side $\mathbf{F}$ is a time dependent vector of $\mathbb{R}^n$ and we assume that the time interval of interest $[0, T]$ is partitioned into N_t equidistant time steps $\{t_n\}_{n=0}^{N_t}$, of size $\Delta t = T/N_t$. Let $\mathbf{X}_n$, $\dot{\mathbf{X}}_n$ and $\ddot{\mathbf{X}}_n$ be respectively the displacement, velocity and acceleration at the time step $t_n = n\Delta t$, the Newmark method [101] consists of using the following approximations for the velocity $\dot{\mathbf{X}}_{n+1}$ and the displacement $\mathbf{X}_{n+1}$:

$$\begin{aligned} \dot{\mathbf{X}}_{n+1} &= \dot{\mathbf{X}}_n + \Delta t \left[(1-\gamma)\ddot{\mathbf{X}}_n + \gamma\ddot{\mathbf{X}}_{n+1}\right] \\ \mathbf{X}_{n+1} &= \mathbf{X}_n + \Delta t\dot{\mathbf{X}}_n + (\Delta t)^2\left[(1/2-\beta)\ddot{\mathbf{X}}_n + \beta\ddot{\mathbf{X}}_{n+1}\right] \end{aligned} \tag{A.2}$$

where β, γ are the two parameters of the method, in the equilibrium equation written at t_{n+1}, that is:

$$\mathbf{M}\ddot{\mathbf{X}}_{n+1} + \mathbf{C}\dot{\mathbf{X}}_{n+1} + \mathbf{K}\mathbf{X}_{n+1} = \mathbf{F}(t_{n+1}) \tag{A.3}$$

In what follows, we note:

$$\begin{aligned} &a_0 = \frac{1}{\beta\Delta t^2}, a_1 = \frac{\gamma}{\beta\Delta t}, a_2 = \frac{1}{\beta\Delta t}, a_3 = \frac{1}{2\beta} - 1 \\ &a_4 = \frac{\gamma}{\beta} - 1, a_5 = \frac{\Delta t}{2}(\frac{\gamma}{\beta} - 2), a_6 = \Delta t(1-\gamma), a_7 = \gamma\Delta t \end{aligned} \tag{A.4}$$

The relation (A.2) is equivalent to:

$$\begin{aligned}\ddot{\mathbf{X}}_{n+1} &= a_0(\mathbf{X}_{n+1} - \mathbf{X}_n) - a_2\dot{\mathbf{X}}_n - a_3\ddot{\mathbf{X}}_n \\ \dot{\mathbf{X}}_{n+1} &= \dot{\mathbf{X}}_n + a_6\ddot{\mathbf{X}}_n + a_7\ddot{\mathbf{X}}_{n+1}\end{aligned} \tag{A.5}$$

Eliminating $\ddot{\mathbf{X}}_{n+1}$ and $\dot{\mathbf{X}}_{n+1}$ in Equation (A.3) by using the relation (A.5), leads to:

$$\tilde{\mathbf{K}}\mathbf{X}_{n+1} = \tilde{\mathbf{F}}(t_{n+1}) \tag{A.6}$$

where

$$\begin{aligned}\tilde{\mathbf{K}} &= \mathbf{K} + a_0\mathbf{M} + a_1\mathbf{C} \\ \tilde{\mathbf{F}}(t_{n+1}) &= \mathbf{F}(t_{n+1}) + \mathbf{C}\left\{a_1\mathbf{X}_n + a_4\dot{\mathbf{X}}_n + a_5\ddot{\mathbf{X}}_n\right\} + \mathbf{M}\left\{a_0\mathbf{X}_n + a_2\dot{\mathbf{X}}_n + a_3\ddot{\mathbf{X}}_n\right\}\end{aligned} \tag{A.7}$$

The equation (A.6) allows us to compute the displacement $\ddot{\mathbf{X}}_{n+1}$ from the value of $\mathbf{X}_n$, $\dot{\mathbf{X}}_n$ and $\ddot{\mathbf{X}}_n$. After that the value of the displacement $\ddot{\mathbf{X}}_{n+1}$ is computed, we can update the value of the acceleration $\ddot{\mathbf{X}}_{n+1}$ and the velocity $\dot{\mathbf{X}}_{n+1}$ by using the relation (A.5). The implementation of the Newmark method is summarized in Algorithm 21.

Algorithm 21 Numerical integration with Newmark method

Input: Size of time step Δt, Number of time step N_t, Parameters (γ, β), Initial conditions $\mathbf{X}_0, \dot{\mathbf{X}}_0$

Output: Values of $\mathbf{X}_n, \dot{\mathbf{X}}_n, \ddot{\mathbf{X}}_n$, for all $1 \leq n \leq N_t$

1: Compute the coefficients $(a_i)_{0\leq i\leq 7}$ in Equation (A.4)

2: Compute the initial acceleration $\ddot{\mathbf{X}}_0$ by:

$$\ddot{\mathbf{X}}_0 = \mathbf{M}^{-1}\left\{\mathbf{F}(0) - \mathbf{C}\dot{\mathbf{X}}_0 - \mathbf{K}\mathbf{X}_0\right\} \tag{A.8}$$

3: Compute and factorize the matrix $\tilde{\mathbf{K}} = \mathbf{K} + a_0\mathbf{M} + a_1\mathbf{C}$

4: **for** $n = 0, \cdots, N_t - 1$ **do**

5: Compute $\tilde{\mathbf{F}}(t_{n+1}) = \mathbf{F}(t_{n+1}) + \mathbf{C}\left\{a_1\mathbf{X}_n + a_4\dot{\mathbf{X}}_n + a_5\ddot{\mathbf{X}}_n\right\} + \mathbf{M}\left\{a_0\mathbf{X}_n + a_2\dot{\mathbf{X}}_n + a_3\ddot{\mathbf{X}}_n\right\}$

6: Compute the displacement $\mathbf{X}_{n+1}$ by solving the following linear system:

$$\tilde{\mathbf{K}}\mathbf{X}_{n+1} = \tilde{\mathbf{F}}(t_{n+1}) \tag{A.9}$$

7: Compute the acceleration $\ddot{\mathbf{X}}_{n+1}$ and the velocity $\dot{\mathbf{X}}_{n+1}$ by the following relations:

$$\begin{aligned}\ddot{\mathbf{X}}_{n+1} &= a_0(\mathbf{X}_{n+1} - \mathbf{X}_n) - a_2\dot{\mathbf{X}}_n - a_3\ddot{\mathbf{X}}_n \\ \dot{\mathbf{X}}_{n+1} &= \dot{\mathbf{X}}_n + a_6\ddot{\mathbf{X}}_n + a_7\ddot{\mathbf{X}}_{n+1}\end{aligned} \tag{A.10}$$

8: **end for**

Properties of the Newmark method

Now, we give an overview on some important properties of Newmark method. To start, let us recall the notion « *consistency* » of the numerical scheme. A numerical scheme is called *consistent* if it reduces to the original system of differential equations as the size of time step Δt tends to zeros. Equivalently speaking, let $\mathbf{\Pi}(\mathbf{X})$ be a system of differential equations and we denote the corresponding numerical scheme by $\mathbf{\Pi}_{\Delta t}(\mathbf{X})$, we say that the numerical scheme $\mathbf{\Pi}_{\Delta t}$ is consistent if the *truncation error*, defined by $\mathbf{\Pi}(\mathbf{X}) - \mathbf{\Pi}_{\Delta t}(\mathbf{X})$, tends to zeros when $\Delta t \to 0$ for any sufficiently smooth solution $\mathbf{X}$. Furthermore, we say that the numerical scheme is consistent *of order p* if the *truncation error* tends to zeros in $O(\Delta t^p)$. Another important notion of the numerical scheme is « *stability* » property. A numerical scheme is called *stable* if the error caused by a small perturbation in the numerical solution at time step t_n remains bounded for all t_{n+j}, $\forall j \geq 0$.

The analysis on *consistency and stability* properties of the Newmark family scheme is classically done with a system without damping by using spectral analysis, see for instance [58, 72]. The *consistency and stability* of Newmark scheme depend on the value of its two parameters (γ, β). For the case where $\gamma = 1/2$, the Newmark scheme is consistent of order 2. In the case where $\gamma \neq 1/2$, the consistency of the Newmark scheme is only of order 1. Assuming that the mass matrix $\mathbf{M}$ is symmetric and positive definite and that the stiffness matrix $\mathbf{K}$ is symmetric and semi-positive definite, the Newmark method is

- Unstable if $\gamma < 1/2$
- Unconditionally stable if $\gamma \geq 1/2$ and $2\beta - \gamma \geq 0$
- Conditionally stable if $\gamma \geq 1/2$ and $2\beta - \gamma < 0$. In this case, the stability is achieved if the size of time step Δt verifies the following inequality:

$$\Delta t \leq \min_{1 \leq i \leq n} \frac{1}{\lambda_i} \frac{2}{\sqrt{2\gamma - 4\beta}}$$

  where λ is the eigenvalue of the Generalized Eigenvalue problem: $\mathbf{KX} = \lambda \mathbf{MX}$.

One of the most used Newmark scheme is the case where $\gamma = 1/2$ and $\beta = 1/4$ since it provides an unconditionally stable scheme with a consistent of order 2 and without any numerical dissipation. However, in some cases, a small numerical dissipation is required in order to damp out the unwanted contribution of high-frequency modes, for instance in the case where the excitation is a discontinuous function in time as in the study case in Section 2.5 of Chapter 2. For the case where $\gamma < 1/2$, the Newmark scheme introduces a negative damping which results in instability. For the case where $\gamma > 1/2$, it can be shown that the numerical dissipation is proportional to $(\gamma - 1/2)\Delta t$. Hence, it is commonly practice to introduce a negative value parameter α for controlling the numerical dissipation via the relation $\gamma = 1/2 - \alpha$. To have an increasing numerical dissipation as a function of frequency, it is sufficient to chose $\beta \geq \frac{1}{4}(1 - \alpha)^2$, in which the case of equality leads to an optimum compromise between the precision and the numerical damping in high frequency modes.

Time complexity of the Newmark method for the case of a direct solver

With the assumption that we have partitioned the time interval of interest $[0, T]$ into a set of *equidistant* time steps $\{t_n\}_{n=1}^{N_t}$ of size Δt, the matrix $\tilde{\mathbf{K}}$ of the left hand-side of Equation (A.6), which allows us to compute the displacement $\mathbf{X}_{n+1}$ at the new time steps, does not change during the iteration. Hence, in practical use, when a direct solver is employed for the resolution of the linear system (A.6), the matrix $\tilde{\mathbf{K}}$ is factorized into a form: $\tilde{\mathbf{K}} = \mathbf{LU}$ where $\mathbf{L}$ and $\mathbf{U}$ are respectively lower and upper triangular matrices, before entering the loop of the step 4 of Algorithm 21. By doing so, the cost of the resolution of the linear system (A.6) at each iteration is in $O(n^2)$.

Therefore, the total complexity of Algorithm 21, when a direct solver is used, is in $O(\text{fac}_{LU}(\tilde{\mathbf{K}}) + n^2 N_t)$ where N_t is the number of time steps and $O(\text{fac}_{LU}(\tilde{\mathbf{K}}))$ denotes the complexity of the factorization $\mathbf{LU}$ of the matrix $\tilde{\mathbf{K}}$ which depends strongly on its sparse structure.

Appendix B

Semi-analytical solution of the study case of Section 2.5.1

In this appendix, we give a short presentation of the construction of a semi-analytical solution of the study case presented in Section 2.5.1. For the presentation in more detail, we refer to [82].

We assume here that the thickness h of the ring is very small compared to its radius R. Under this hypothesis, using Love-Kirchoff model (see for instance [113]) for describing the dynamical of structure derives the following equations:

$$\begin{cases} \rho_s h \ddot{U}_\theta - \dfrac{Eh}{(1-\nu^2)R^2}\left[(1+k^2)\dfrac{\partial^2 U_\theta}{\partial\theta^2} + \dfrac{\partial U_r}{\partial\theta} - k^2\dfrac{\partial^3 U_r}{\partial\theta^3}\right] = 0 \\ \rho_s h \ddot{U}_r + \dfrac{Eh}{(1-\nu^2)R^2}\left[U_r + k^2\dfrac{\partial^4 U_r}{\partial\theta^4} + \dfrac{\partial U_\theta}{\partial\theta} - k^2\dfrac{\partial^3 U_\theta}{\partial\theta^3}\right] = -p^{tot} \end{cases} \tag{B.1}$$

where U_r, U_θ are radial and ortho-radial displacements. The constant k^2 is equal to $h^2/(12R^2)$. Next, let us render structural and fluid variables dimensionless using the following table of of normalization.

Variable	Factor of normalization
Displacement	R
Times	R/c_0
Pressure	$\rho_0 c_0^2$
Velocity potential	Rc_0

Table B.1: Table of normalization

The equivalent of Equations (B.1) in term of dimensionless radial and of ortho-radial displacement reads as:

$$\begin{bmatrix} \ddot{U}_\theta \\ \ddot{U}_r \end{bmatrix} + \mathcal{C}^2 \begin{bmatrix} -(1+k^2)\frac{\partial^2}{\partial\theta^2} & -(\frac{\partial}{\partial\theta} - k^2\frac{\partial^3}{\partial\theta^3}) \\ \frac{\partial}{\partial\theta} - k^2\frac{\partial^3}{\partial\theta^3} & 1 + k^2\frac{\partial^4}{\partial\theta^4} \end{bmatrix} \begin{bmatrix} U_\theta \\ U_r \end{bmatrix} = \mathcal{K} \begin{bmatrix} 0 \\ -p^{tot} \end{bmatrix} \tag{B.2}$$

where the dimensionless constants $\mathcal{C}$, $\mathcal{K}$ are defined by:

$$\mathcal{C} = \frac{c_l}{c_0}, \mathcal{K} = \frac{\mathcal{M}}{\mathcal{E}} \tag{B.3}$$

with $\mathcal{M} = \rho_s/\rho_0, \mathcal{E} = h/R$ and $c_l = \sqrt{E/(\rho_s(1-\nu^2))}$. Since the functions U_r, U_θ are $2\pi-$ periodic in θ, they can be expressed in form of Fourier series as:

$$\begin{bmatrix} U_\theta(\theta,t) \\ U_r(\theta,t) \end{bmatrix} = \begin{bmatrix} U_\theta^0(t) \\ U_r^0(t) \end{bmatrix} + \sum_{n=1}^{\infty} \begin{bmatrix} U_\theta^{Sn}(t)\cos(n\theta) \\ U_r^{Sn}(t)\cos(n\theta) \end{bmatrix} + \sum_{n=1}^{\infty} \begin{bmatrix} U_\theta^{An}(t)\sin(n\theta) \\ U_r^{An}(t)\sin(n\theta) \end{bmatrix} \tag{B.4}$$

The total pressure at the interface fluid-structure is also a $2\pi-$ periodic in θ. Thus, it can be written as Fourier series:

$$p^{tot}|_{r=1} = p_{tot}^0(t) + \sum_{n=1}^{\infty} p_{tot}^{Sn}(t)\cos(n\theta) + \sum_{n=1}^{\infty} p_{tot}^{An}(t)\sin(n\theta) \tag{B.5}$$

Injecting the relations (B.4)-(B.5) in Equation (B.2) with some obvious manipulations leads to the following equations:

$$\ddot{U}_\theta^0(t) = 0 \tag{B.6}$$

$$\ddot{U}_r^0(t) + \mathcal{C}^2 = -\mathcal{K}p_{tot}^0 \tag{B.7}$$

$$\begin{bmatrix} \ddot{U}_\theta^{Sn}(t) \\ \ddot{U}_r^{Sn}(t) \end{bmatrix} + \mathcal{C}^2 \begin{bmatrix} (1+k^2)n^2 & (1+k^2n^2)n \\ (1+k^2n^2)n & (1+k^2n^4) \end{bmatrix} \begin{bmatrix} U_\theta^{Sn}(t) \\ U_r^{Sn}(t) \end{bmatrix} = \mathcal{K} \begin{bmatrix} 0 \\ -p_{tot}^{Sn} \end{bmatrix} \tag{B.8}$$

$$\begin{bmatrix} \ddot{U}_\theta^{An}(t) \\ \ddot{U}_r^{An}(t) \end{bmatrix} + \mathcal{C}^2 \begin{bmatrix} (1+k^2)n^2 & -(1+k^2n^2)n \\ -(1+k^2n^2)n & (1+k^2n^4) \end{bmatrix} \begin{bmatrix} U_\theta^{An}(t) \\ U_r^{An}(t) \end{bmatrix} = \mathcal{K} \begin{bmatrix} 0 \\ -p_{tot}^{An} \end{bmatrix} \tag{B.9}$$

where p_{tot}^0, p_{tot}^{Sn} and p_{tot}^{An} are Fourier coefficients of the total pressure at the interface fluid-structure.

In the fluid part, we chose to use the velocity potential ϕ to describe its state. By using Table B.1, the wave equation in term of dimensionless velocity potential ϕ written in Laplace domain and in cylindrical coordinate is given by:

$$\left[\frac{\partial^2}{\partial r^2} + \frac{1}{r}\frac{\partial}{\partial r} + \frac{1}{r^2}\frac{\partial^2}{\partial \theta^2} - s^2\right]\hat{\phi}(r,\theta,s) = 0 \tag{B.10}$$

where s denotes the Laplace variable and $\hat{\phi}$ denotes the Laplace transformed of ϕ. The analytical solution of Equation (B.10) can be expressed as (see [2]) :

$$\hat{\phi}(r,\theta,s) = \sum_{n=0}^{\infty} A_n(s)K_n(rs)\cos(n\theta) + \sum_{n=0}^{\infty} B_n(s)K_n(rs)\sin(n\theta) \tag{B.11}$$

where the function K_n is modified Bessel function order n of the second kind and the coefficients A_n, B_n are to be determined by using the boundary conditions. We recall that the total velocity

potential can be decomposed by three components: $\phi^{tot} = \phi^{inc} + \phi^{ref} + \phi^{rad}$, where the first term is the data of the problem. We recall that $\hat{\phi}^{ref}$ and $\hat{\phi}^{rad}$ also verify the wave equation (B.10). Therefore, they can be analytically expressed by Equation (B.11). The boundary conditions of $\hat{\phi}^{ref}$ and $\hat{\phi}^{rad}$ are respectively given by:

$$\frac{\partial \hat{\phi}^{ref}}{\partial r}|_{r=1} = -\mathbf{v}^{inc}|_{r=1} \cdot \mathbf{e}_r, \quad \frac{\partial \hat{\phi}^{rad}}{\partial r}|_{r=1} = s\hat{U}_r \tag{B.12}$$

where $\mathbf{v}^{inc}|_{r=1}$ denotes the incident velocity of fluid particles on the fluid-structure interface. We remark that the function $\mathbf{v}^{inc}|_{r=1} \cdot \mathbf{e}_r$ is 2π-periodic also in θ. Hence, $\mathbf{v}^{inc}|_{r=1} \cdot \mathbf{e}_r$ can be written as the following Fourier series:

$$\mathbf{v}^{inc}|_{r=1} \cdot \mathbf{e}_r = \hat{v}^0_{inc}(s) + \sum_{n=1}^{\infty} \hat{v}^{Sn}_{inc}(s)\cos(n\theta) + \sum_{n=1}^{\infty} \hat{v}^{An}_{inc}(s)\sin(n\theta) \tag{B.13}$$

where

$$\begin{aligned}
\hat{v}^0_{inc}(s) &= \frac{1}{2\pi}\int_0^{2\pi} \mathbf{v}^{inc}|_{r=1} \cdot \mathbf{e}_r d\theta \\
\hat{v}^{Sn}_{inc}(s) &= \frac{1}{2\pi}\int_0^{\pi} \mathbf{v}^{inc}|_{r=1} \cdot \mathbf{e}_r \cos(n\theta) d\theta \\
\hat{v}^{An}_{inc}(s) &= \frac{1}{2\pi}\int_0^{\pi} \mathbf{v}^{inc}|_{r=1} \cdot \mathbf{e}_r \sin(n\theta) d\theta
\end{aligned}$$

By combining Equation (B.13) with the first equation of (B.12), we can determine the value of the coefficients A_n and B_n in Equation (B.11) for the reflected velocity potential ϕ^{ref}. By combing the second equation of (B.4) written in Laplace domain with the second equation of (B.12), we can determine the value of the coefficients A_n and B_n in Equation (B.11) for the radiated velocity potential ϕ^{rad} provided that the value of U_r is known. The reflected and radiated velocity potential can be expressed explicitly by:

$$\begin{aligned}
\hat{\phi}^{ref}(r,\theta,s) &= \hat{\mathcal{Z}}_0(r,s)v^0_{inc}(s) + \sum_{n=1}^{\infty} \hat{\mathcal{Z}}_n(r,s)\left[\hat{v}^{Sn}_{inc}(s)\cos(n\theta) + \hat{v}^{An}_{inc}(s)\sin(n\theta)\right] \\
\hat{\phi}^{ray}(r,\theta,s) &= -\hat{\mathcal{Z}}_0(r,s)s\hat{U}^0_r(s) - \sum_{n=1}^{\infty} \hat{\mathcal{Z}}_n(r,s)\left[s\hat{U}^{Sn}_r(s)\cos(n\theta) + s\hat{U}^{An}_r(s)\sin(n\theta)\right]
\end{aligned} \tag{B.14}$$

where the complex functions $\hat{\mathcal{Z}}_n(r,s)$ are defined by:

$$\hat{\mathcal{Z}}_0(r,s) = -\frac{K_n(rs)}{sK'(s)} = \frac{K_n(rs)}{sK_{n+1} - nK_n(s)} \tag{B.15}$$

In Laplace domain, the relation between p and ϕ given by Equation (1.17), in term of dimensionless variables given by Table B.1, writes: $\hat{p} = -s\hat{\phi}$. This relation implies that the

expression of the dimensionless reflected and radiated pressure can be written as:

$$\begin{aligned}\hat{p}^{ref}(r,\theta,s) &= -\hat{\mathcal{Z}}_0(r,s)sv^0_{inc}(s) - \sum_{n=1}^{\infty}\hat{\mathcal{Z}}_n(r,s)\left[s\hat{v}^{Sn}_{inc}(s)\cos(n\theta) + s\hat{v}^{An}_{inc}(s)\sin(n\theta)\right]\\ \hat{p}^{ray}(r,\theta,s) &= \hat{\mathcal{Z}}_0(r,s)s^2\hat{U}^0_r(s) + \sum_{n=1}^{\infty}\hat{\mathcal{Z}}_n(r,s)\left[s^2\hat{U}^{Sn}_r(s)\cos(n\theta) + s^2\hat{U}^{An}_r(s)\sin(n\theta)\right]\end{aligned} \tag{B.16}$$

The reflected pressure can be then computed numerically using the first equation of (B.16) by truncating the Fourier series and using a numerical inverse Laplace transform algorithm. With the same approach, the radiated pressure can be computed using the second equation of (B.16) provided that $\hat{U}^{Sn}_r(s)$ and $\hat{U}^{An}_r(s)$ are known.

To compute the radial and ortho-radial displacement in Laplace domain, we need to evaluate the pressure at the fluid-structure interface. At interface where $r = 1$, we can write the incident pressure in Laplace domain in form of Fourier series as:

$$\hat{p}^{inc}(1,\theta,s) = \hat{p}^0_{inc}(s) + \sum_{n=1}^{\infty}\hat{p}^{Sn}_{inc}(s)\cos(n\theta) + \sum_{n=1}^{\infty}\hat{p}^{An}_{inc}(s)\sin(n\theta) \tag{B.17}$$

Combining Equation (B.16) and Equation (B.17), the total pressure at fluid-structure interface is given by:

$$\begin{aligned}\hat{p}_{tot}(1,\theta,s) &= \hat{p}^0_{inc}(s) - \hat{\mathcal{Z}}_0(r,s)sv^0_{inc}(s) + \hat{\mathcal{Z}}_0(r,s)s^2\hat{U}^0_r(s)\\ &+ \sum_{n=1}^{\infty}\left[\hat{p}^{Sn}_{inc}(s) - \hat{\mathcal{Z}}_n(1,s)s\hat{v}^{Sn}_{inc}(s) + \hat{\mathcal{Z}}_n(1,s)s^2\hat{U}^{Sn}_r(s)\right]\cos(n\theta)\\ &+ \sum_{n=1}^{\infty}\left[\hat{p}^{An}_{inc}(s) - \hat{\mathcal{Z}}_n(1,s)s\hat{v}^{An}_{inc}(s) + \hat{\mathcal{Z}}_n(1,s)s^2\hat{U}^{An}_r(s)\right]\sin(n\theta)\end{aligned} \tag{B.18}$$

Injecting the relation (B.18) in Equations (B.7)-(B.8) and (B.9) written in Laplace domain leads to the following linear systems:

$$\begin{aligned}\hat{M}_0(s)\hat{U}^0_r(s) &= -\mathcal{K}\left(\hat{p}^0_{inc}(s) - \hat{\mathcal{Z}}_0(1,s)s\hat{v}^0_{inc}(s)\right)\\ \hat{\boldsymbol{M}}^{\boldsymbol{S}}_{\boldsymbol{n}}(s)\begin{bmatrix}\hat{U}^{Sn}_\theta(s)\\ \hat{U}^{Sn}_r(s)\end{bmatrix} &= -\mathcal{K}\begin{bmatrix}0\\ \hat{p}^{Sn}_{inc} - \hat{\mathcal{Z}}_n(1,s)s\hat{v}^{Sn}_{inc}(s)\end{bmatrix}\\ \hat{\boldsymbol{M}}^{\boldsymbol{A}}_{\boldsymbol{n}}(s)\begin{bmatrix}\hat{U}^{An}_\theta(s)\\ \hat{U}^{An}_r(s)\end{bmatrix} &= -\mathcal{K}\begin{bmatrix}0\\ \hat{p}^{An}_{inc}(s) - \hat{\mathcal{Z}}_n(1,s)s\hat{v}^{An}_{inc}(s)\end{bmatrix}\end{aligned} \tag{B.19}$$

where

$$\begin{aligned}\hat{M}_0(s) &= s^2\left(1 + \hat{\mathcal{Z}}_0(1,s)\right) + \mathcal{C}^2\\ \hat{\boldsymbol{M}}^{\boldsymbol{S}}_{\boldsymbol{n}}(s) &= \begin{bmatrix}s^2 + \mathcal{C}^2(1+k^2)n^2 & \mathcal{C}^2(1+k^2)n^2\\ \mathcal{C}^2(1+k^2)n^2 & s^2\left(1 + \mathcal{K}\hat{\mathcal{Z}}_n(1,s)\right) + \mathcal{C}^2(1+k^2n^4)\end{bmatrix}\\ \hat{\boldsymbol{M}}^{\boldsymbol{A}}_{\boldsymbol{n}}(s) &= \begin{bmatrix}s^2 + \mathcal{C}^2(1+k^2)n^2 & -\mathcal{C}^2(1+k^2)n^2\\ -\mathcal{C}^2(1+k^2)n^2 & s^2\left(1 + \mathcal{K}\hat{\mathcal{Z}}_n(1,s)\right) + \mathcal{C}^2(1+k^2n^4)\end{bmatrix}\end{aligned} \tag{B.20}$$

With Equation (B.19), the coefficients $\hat{U}_\theta^{Sn}(s)$, $\hat{U}_\theta^{An}(s)$, $\hat{U}_r^{Sn}(s)$ and $\hat{U}_r^{An}(s)$ can be computed with a resolution of the linear systems 2×2. Therefore, we can obtain a semi-analytical solution of p^{rad}, U_θ and U_r by truncating their corresponding Fourier series in Laplace domain and by using a numerical inverse Laplace transform algorithm in order to turn back to time-domain.

For numerical applications, the semi-analytical solutions used in Section 2.5.1 are obtained by devising the interval $[0, 2\pi]$ into 800 of equidistant points in order to compute numerically the Fourier coefficients p_{inc}^{Sn}, p_{inc}^{An}, v_{inc}^{Sn} and v_{inc}^{An} using the Midpoint rule. All Fourier series representing the analytical solutions in Laplace domain are then truncated using the 200 number of modes, *i.e* $N_{mode} = 200$. To return to time-domain, we use the numerical algorithm of inversion Laplace transform proposed in [47].

Appendix C

Expression of residual norm in the case of affine parametric dependence

In this appendix, we give a short demonstration of the expression of the norm of the right-hand side and the residual, given by Equation (4.10), for the case of affine parametric dependence.

Let us begin by the first equation of (4.10). Since we consider that the right-hand side vector of the problem can be expressed as:

$$\mathbf{F}(\boldsymbol{\mu}) = \sum_{i=1}^{N_F} \theta_i^F(t;\boldsymbol{\mu})\mathbf{F}_i \tag{C.1}$$

we have:

$$\begin{aligned} ||\mathbf{F}(t;\boldsymbol{\mu})||^2 &= \langle \sum_{i=1}^{N_F} \theta_i^F(t;\boldsymbol{\mu})\mathbf{F}_i, \sum_{j=1}^{N_F} \theta_j^F(t;\boldsymbol{\mu})\mathbf{F}_j \rangle \\ &= \sum_{i=1}^{N_F}\sum_{j=1}^{N_F} \theta_i^F(t;\boldsymbol{\mu})\theta_j^F(t;\boldsymbol{\mu})\langle \mathbf{F}_i, \mathbf{F}_j \rangle \\ &= \boldsymbol{\Theta}_F^T(t;\boldsymbol{\mu})\mathbf{M}_{FF}\boldsymbol{\Theta}_F(t;\boldsymbol{\mu}) \end{aligned} \tag{C.2}$$

where the vector $\boldsymbol{\Theta}_F(t;\boldsymbol{\mu}) \in \mathbb{R}^{N_F}$ is defined by $\boldsymbol{\Theta}_F(t;\boldsymbol{\mu}) = \left[\theta_1^F(t;\boldsymbol{\mu}), \cdots, \theta_{N_F}^F(t;\boldsymbol{\mu})\right]^T \in \mathbb{R}^{N_F}$ and the matrix $\mathbf{M}_{FF} \in \mathbb{R}^{N_F \times N_F}$ is independent of $\boldsymbol{\mu}$ and is defined by $(\mathbf{M}_{FF})_{ij} = \langle \mathbf{F}_i, \mathbf{F}_j \rangle$.

We recall that the residual vector is defined by:

$$\mathbf{R}(t;\boldsymbol{\mu}) := \mathbf{F}(t;\boldsymbol{\mu}) - \mathbf{M}(\boldsymbol{\mu})\mathbf{V}\ddot{\mathbf{X}}_r(t;\boldsymbol{\mu}) - \mathbf{C}(\boldsymbol{\mu})\mathbf{V}\dot{\mathbf{X}}_r(t;\boldsymbol{\mu}) - \mathbf{K}(\boldsymbol{\mu})\mathbf{V}\mathbf{X}_r(t;\boldsymbol{\mu}) \tag{C.3}$$

Thus, we have:

$$
\begin{aligned}
||\mathbf{R}(t;\boldsymbol{\mu})||^2 = \langle &\mathbf{F}(t;\boldsymbol{\mu}) - \mathbf{M}(\boldsymbol{\mu})\mathbf{V}\ddot{\mathbf{X}}_r(t;\boldsymbol{\mu}) - \mathbf{C}(\boldsymbol{\mu})\mathbf{V}\dot{\mathbf{X}}_r(t;\boldsymbol{\mu}) + \mathbf{K}(\boldsymbol{\mu})\mathbf{V}\mathbf{X}_r(t;\boldsymbol{\mu}),\\
&\mathbf{F}(t;\boldsymbol{\mu}) - \mathbf{M}(\boldsymbol{\mu})\mathbf{V}\ddot{\mathbf{X}}_r(t;\boldsymbol{\mu}) - \mathbf{C}(\boldsymbol{\mu})\mathbf{V}\dot{\mathbf{X}}_r(t;\boldsymbol{\mu}) + \mathbf{K}(\boldsymbol{\mu})\mathbf{V}\mathbf{X}_r(t;\boldsymbol{\mu})\rangle\\
&= ||\mathbf{F}(t;\boldsymbol{\mu})||^2 + ||\mathbf{M}(\boldsymbol{\mu})\mathbf{V}\ddot{\mathbf{X}}_r(t;\boldsymbol{\mu})||^2 + ||\mathbf{C}(\boldsymbol{\mu})\mathbf{V}\dot{\mathbf{X}}_r(t;\boldsymbol{\mu})||^2 + ||\mathbf{K}(\boldsymbol{\mu})\mathbf{V}\mathbf{X}_r(t;\boldsymbol{\mu})||^2\\
&+ 2\Big(\langle \mathbf{M}(\boldsymbol{\mu})\mathbf{V}\ddot{\mathbf{X}}_r(t;\boldsymbol{\mu}), \mathbf{C}(\boldsymbol{\mu})\mathbf{V}\dot{\mathbf{X}}_r(t;\boldsymbol{\mu})\rangle + \langle \mathbf{M}(\boldsymbol{\mu})\mathbf{V}\ddot{\mathbf{X}}_r(t;\boldsymbol{\mu}), \mathbf{K}(\boldsymbol{\mu})\mathbf{V}\mathbf{X}_r(t;\boldsymbol{\mu})\rangle\\
&+\langle \mathbf{C}(\boldsymbol{\mu})\mathbf{V}\dot{\mathbf{X}}_r(t;\boldsymbol{\mu}), \mathbf{K}(\boldsymbol{\mu})\mathbf{V}\mathbf{X}_r(t;\boldsymbol{\mu})\rangle\Big)\\
&- 2\Big(\langle \mathbf{F}(t;\boldsymbol{\mu}), \mathbf{M}(\boldsymbol{\mu})\mathbf{V}\ddot{\mathbf{X}}_r(t;\boldsymbol{\mu})\rangle + \langle \mathbf{F}(t;\boldsymbol{\mu}), \mathbf{C}(\boldsymbol{\mu})\mathbf{V}\dot{\mathbf{X}}_r(t;\boldsymbol{\mu})\rangle\\
&+ \langle \mathbf{F}(t;\boldsymbol{\mu}), \mathbf{K}(\boldsymbol{\mu})\mathbf{V}\mathbf{X}_r(t;\boldsymbol{\mu})\rangle)
\end{aligned}
\tag{C.4}
$$

We remark that the first term of the right hand-side of the relation (C.4) is the square of the right-hand side norm. In the following, we use the notation: $\mathbf{X}_r^M(t;\boldsymbol{\mu}) := \ddot{\mathbf{X}}_r(t;\boldsymbol{\mu})$, $\mathbf{X}_r^C(t;\boldsymbol{\mu}) := \dot{\mathbf{X}}_r(t;\boldsymbol{\mu})$ and $\mathbf{X}_r^K(t;\boldsymbol{\mu}) := \mathbf{X}_r(t;\boldsymbol{\mu})$. For $i \in \{1,\cdots,N\}$, we denote by $x_{r,i}^A(t;\boldsymbol{\mu})$ the i^{th} component of the vector $\mathbf{X}_r^A(t;\boldsymbol{\mu})$ and by $\mathbf{v}_i \in \mathbb{R}^n$ the i^{th} column of the given basis $\mathbf{V} \in \mathbb{R}^{n\times N}$. For $A, B \in \{M, C, K\}$, we have:

$$
\begin{aligned}
\langle \mathbf{A}(\boldsymbol{\mu})\mathbf{V}\mathbf{X}_r^A(t;\boldsymbol{\mu}), \mathbf{B}(\boldsymbol{\mu})\mathbf{V}\mathbf{X}_r^B(t;\boldsymbol{\mu})\rangle &= \langle \mathbf{A}(\boldsymbol{\mu})\sum_{i=1}^N x_{r,i}^A(t;\boldsymbol{\mu})\mathbf{v}_i, \mathbf{B}(\boldsymbol{\mu})\sum_{j=1}^N x_{r,j}^B(t;\boldsymbol{\mu})\mathbf{v}_j\rangle\\
&= \sum_{i=1}^N\sum_{j=1}^N x_{r,i}^A(t;\boldsymbol{\mu})x_{r,j}^B(t;\boldsymbol{\mu})\langle \mathbf{A}(\boldsymbol{\mu})\mathbf{v}_i, \mathbf{B}(\boldsymbol{\mu})\mathbf{v}_j\rangle\\
&= \mathbf{X}_r^A(t;\boldsymbol{\mu})\mathbf{M}_{AB}(\boldsymbol{\mu})\mathbf{X}_r^B(t;\boldsymbol{\mu})
\end{aligned}
\tag{C.5}
$$

where the matrix $\mathbf{M}_{AB}(\boldsymbol{\mu}) \in \mathbb{R}^{N\times N}$ is $\boldsymbol{\mu}$-dependent and is defined by $(\mathbf{M}_{AB}(\boldsymbol{\mu}))_{ij} := \langle \mathbf{A}(\boldsymbol{\mu})\mathbf{v}_i, \mathbf{B}(\boldsymbol{\mu})\mathbf{v}_j\rangle$. Using the affine decomposition of $\mathbf{A}(\boldsymbol{\mu})$:

$$
\mathbf{A}(\boldsymbol{\mu}) = \sum_{i=1}^{N_A}\theta_i^A(\boldsymbol{\mu})\mathbf{A}_i \ , \forall \mathbf{A} = \{\mathbf{M}, \mathbf{C}, \mathbf{K}\}
\tag{C.6}
$$

leads to:

$$
\begin{aligned}
\langle \mathbf{A}(\boldsymbol{\mu})\mathbf{v}_i, \mathbf{B}(\boldsymbol{\mu})\mathbf{v}_j\rangle &= \langle \sum_{l=1}^{N_A}\theta_l^A(\boldsymbol{\mu})\mathbf{A}_l\mathbf{v}_i, \sum_{k=1}^{N_B}\theta_k^B(\boldsymbol{\mu})\mathbf{B}_k\mathbf{v}_j\rangle\\
&= \sum_{l=1}^{N_A}\sum_{k=1}^{N_B}\theta_l^A(\boldsymbol{\mu})\theta_k^B(\boldsymbol{\mu})\langle \mathbf{A}_l\mathbf{v}_i, \mathbf{B}_k\mathbf{v}_j\rangle
\end{aligned}
\tag{C.7}
$$

Thus, we have:

$$
\mathbf{M}_{AB}(\boldsymbol{\mu}) = \sum_{l=1}^{N_A}\sum_{k=1}^{N_B}\theta_l^A(\boldsymbol{\mu})\theta_k^B(\boldsymbol{\mu})\mathbf{M}_{A_lB_k}
\tag{C.8}
$$

where the matrices $\mathbf{M}_{A_lB_k} \in \mathbb{R}^{N\times N}$, for $l \in \{1,\cdots,N_A\}$ and $k \in \{1,\cdots,N_B\}$, are $\boldsymbol{\mu}$-independent and are defined by $(\mathbf{M}_{A_lB_k})_{ij} := \langle \mathbf{A}_l\mathbf{v}_i, \mathbf{B}_k\mathbf{v}_j\rangle$.

Now, let us put the focus in the last three terms of the right-hand side of Equation (C.4). Using the affine decomposition of Equation (C.1), we have, for $A \in \{M, C, K\}$:

$$\begin{aligned}
\langle \mathbf{F}(t;\boldsymbol{\mu}), \mathbf{A}(\boldsymbol{\mu})\mathbf{V}\mathbf{X}_r^A(t;\boldsymbol{\mu})\rangle &= \langle \sum_{i=1}^{N_F} \theta_i^F(t;\boldsymbol{\mu})\mathbf{F}_i, \mathbf{A}(\boldsymbol{\mu})\mathbf{V}\mathbf{X}_r^A(t;\boldsymbol{\mu})\rangle \\
&= \langle \sum_{i=1}^{N_F} \theta_i^F(t;\boldsymbol{\mu})\mathbf{F}_i, \mathbf{A}(\boldsymbol{\mu}) \sum_{j=1}^{N} x_{r,j}^A(t;\boldsymbol{\mu})\mathbf{v}_j\rangle \\
&= \sum_{i=1}^{N_F}\sum_{j=1}^{N} \theta_i^F(t;\boldsymbol{\mu}) x_{r,j}^A(t;\boldsymbol{\mu}) \langle \mathbf{F}_i, \mathbf{A}(\boldsymbol{\mu})\mathbf{v}_j\rangle \\
&= \boldsymbol{\Theta}_F^T(t;\boldsymbol{\mu})\mathbf{M}_{AF}(\boldsymbol{\mu})\mathbf{X}_r^A(t;\boldsymbol{\mu})
\end{aligned} \tag{C.9}$$

where the matrix $\mathbf{M}_{AF}(\boldsymbol{\mu}) \in \mathbb{R}^{N_F \times N}$ is $\boldsymbol{\mu}$-dependent and is defined by $(\mathbf{M}_{AF}(\boldsymbol{\mu}))_{ij} := \langle \mathbf{F}_i, \mathbf{A}(\boldsymbol{\mu})\mathbf{v}_j\rangle$. Using the affine decomposition assumption of Equation (C.6) leads to:

$$\begin{aligned}
\langle \mathbf{F}_i, \mathbf{A}(\boldsymbol{\mu})\mathbf{v}_j\rangle &= \langle \mathbf{F}_i, \sum_{l=1}^{N_A} \theta_l^A(\boldsymbol{\mu})\mathbf{A}_l\mathbf{v}_j\rangle \\
&= \sum_{l=1}^{N_A} \theta_l^A(\boldsymbol{\mu})\langle \mathbf{F}_i, \mathbf{A}_l\mathbf{v}_j\rangle
\end{aligned} \tag{C.10}$$

Thus, we have:

$$\mathbf{M}_{AF}(\boldsymbol{\mu}) = \sum_{l=1}^{N_A} \theta_l^A(\boldsymbol{\mu})\mathbf{M}_{A_lF} \tag{C.11}$$

where the matrices $\mathbf{M}_{A_lF} \in \mathbb{R}^{N_F \times N}$, for $l \in \{1, \cdots, N_A\}$, are $\boldsymbol{\mu}$-independent and are defined by $(\mathbf{M}_{A_lF})_{ij} := \langle \mathbf{F}_i, \mathbf{A}_l\mathbf{v}_j\rangle$.

To conclude, by injecting the relations (C.2)-(C.5) and (C.9) in Equation (C.4), we obtain the desired relation:

$$\begin{aligned}
||\mathbf{R}(t;\boldsymbol{\mu})||^2 &= \boldsymbol{\Theta}_F^T(t;\boldsymbol{\mu})\mathbf{M}_{FF}\boldsymbol{\Theta}_F(t;\boldsymbol{\mu}) \\
&+ \ddot{\mathbf{X}}_r^T(t;\boldsymbol{\mu})\mathbf{M}_{MM}(\boldsymbol{\mu})\ddot{\mathbf{X}}_r(t;\boldsymbol{\mu}) + \dot{\mathbf{X}}_r^T(t;\boldsymbol{\mu})\mathbf{M}_{CC}(\boldsymbol{\mu})\dot{\mathbf{X}}_r(t;\boldsymbol{\mu}) + \mathbf{X}_r^T(t;\boldsymbol{\mu})\mathbf{M}_{KK}(\boldsymbol{\mu})\mathbf{X}_r(t;\boldsymbol{\mu}) \\
&+ 2\left(\ddot{\mathbf{X}}_r^T(t;\boldsymbol{\mu})\mathbf{M}_{MC}(\boldsymbol{\mu})\dot{\mathbf{X}}_r(t;\boldsymbol{\mu}) + \ddot{\mathbf{X}}_r^T(t;\boldsymbol{\mu})\mathbf{M}_{MK}(\boldsymbol{\mu})\mathbf{X}_r(t;\boldsymbol{\mu}) + \dot{\mathbf{X}}_r^T(t)\mathbf{M}_{CK}(\boldsymbol{\mu})\mathbf{X}_r(t)\right) \\
&- 2\left(\boldsymbol{\Theta}_F^T(t;\boldsymbol{\mu})\mathbf{M}_{MF}(\boldsymbol{\mu})\ddot{\mathbf{X}}_r(t;\boldsymbol{\mu}) + \boldsymbol{\Theta}_F^T(t;\boldsymbol{\mu})\mathbf{M}_{CF}(\boldsymbol{\mu})\dot{\mathbf{X}}_r(t;\boldsymbol{\mu}) + \boldsymbol{\Theta}_F^T(t;\boldsymbol{\mu})\mathbf{M}_{KF}(\boldsymbol{\mu})\mathbf{X}_r(t;\boldsymbol{\mu})\right)
\end{aligned} \tag{C.12}$$

□

Appendix D

Implementation in *code_aster*

In this appendix, we give a short overview of our work of implementation in the industrial finite element open-source software, *code_aster*. We start with a presentation of our developments in the finite element models of vibro-acoustic coupling in the first section. The definition of the new operators developed for the reduced order modelling framework proposed in this thesis are then presented in Section D.2.

D.1 Implementation of the FE models of vibro-acoustic coupling in *code_aster*

The formulation in $(\mathbf{u}_s, p, \varphi)$ is actually the only formulation already implemented in the official version of *code_aster*. The development of the two new formulations: formulation in $(\mathbf{u}_s, p)$ and in $(\mathbf{u}_s, \phi)$, is done with a personal version and will be integrated in the official version latter. In our work, we chose to not modify the name of command but to modify of the underlying definition of the elementary matrices. As a result, we will have three branches in our development framework as depicted in Figure D.1.

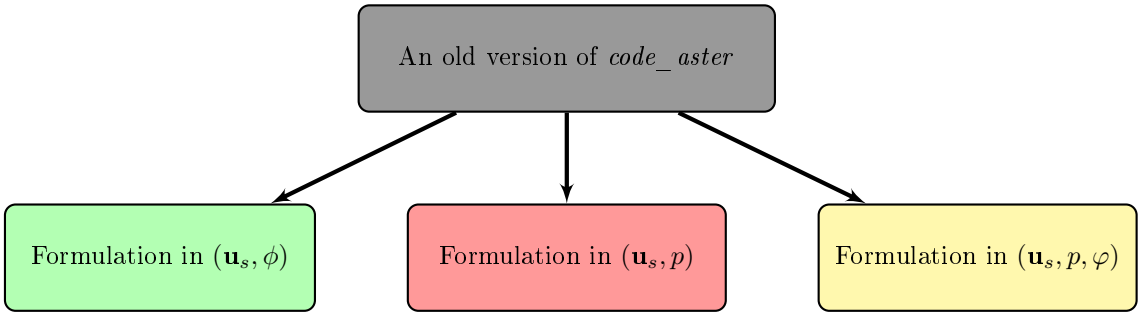

Figure D.1: The three branches in our development framework

In the context of vibro-acoustic coupling, the fluid-structure mesh can be divided into three parts: structural part, fluid part and fluid-structure interface. In our implementation, only the definition of elementary matrices in the fluid part and fluid-structure interface change in function of the formulation.

In *code_aster*, the computation of the element matrices is done by the operator CALC_MATR_ELEM. We summarize the definition of the elementary matrices of each formulation in Table D.1, D.2 and D.3 (in which the notation $\mathbf{A}^e$ refers to the elementary contribution corresponding to the matrix $\mathbf{A}$) for option MASS_MECA, option RIGI_MECA and AMOR_MECA which compute respectively the elementary mass, stiffness and damping matrices of the problem. We recall that the definition of $\mathbf{M}_s, \mathbf{M}_f, \mathbf{K}_s, \mathbf{K}_f$ and $\mathbf{K}_c$ are given in Section 1.2.1.

Option	Formulation in $(\mathbf{u}_s, \phi)$		
	Structural part	Fluid part	Interface fluid-structure
MASS_MECA	$\mathbf{M}_s^e \begin{bmatrix}\mathbf{U}_s^e\end{bmatrix}$	$\mathbf{M}_f^e \begin{bmatrix}\mathbf{P}^e\end{bmatrix}$	$\begin{bmatrix}\mathbf{0} & \mathbf{0}\\ -\rho_0\mathbf{K}_c^{e,T} & \mathbf{0}\end{bmatrix} \begin{bmatrix}\mathbf{U}_s^e\\ \mathbf{P}^e\end{bmatrix}$
RIGI_MECA	$\mathbf{K}_s^e \begin{bmatrix}\mathbf{U}_s^e\end{bmatrix}$	$\mathbf{K}_f^e \begin{bmatrix}\mathbf{P}^e\end{bmatrix}$	$\begin{bmatrix}\mathbf{0} & \mathbf{K}_c^e\\ \mathbf{0} & \mathbf{0}\end{bmatrix} \begin{bmatrix}\mathbf{U}_s^e\\ \mathbf{P}^e\end{bmatrix}$
AMOR_MECA	$\mathbf{0}$	$\mathbf{0}$	$\mathbf{0}$

Table D.1: Definition of elementary matrices in the formulation in $(\mathbf{u}_s, p)$

Option	Formulation in $(\mathbf{u}_s, \phi)$		
	Structural part	Fluid part	Interface fluid-structure
MASS_MECA	$\mathbf{M}_s^e \begin{bmatrix}\mathbf{U}_s^e\end{bmatrix}$	$-\rho_0\mathbf{M}_f^e \begin{bmatrix}\mathbf{\Phi}^e\end{bmatrix}$	$\mathbf{0}$
RIGI_MECA	$\mathbf{K}_s^e \begin{bmatrix}\mathbf{U}_s^e\end{bmatrix}$	$-\rho_0\mathbf{K}_f^e \begin{bmatrix}\mathbf{\Phi}^e\end{bmatrix}$	$\mathbf{0}$
AMOR_MECA	$\mathbf{0}$	$\mathbf{0}$	$\begin{bmatrix}\mathbf{0} & -\rho_0\mathbf{K}_c^T\\ -\rho_0\mathbf{K}_c^{e,T} & \mathbf{0}\end{bmatrix} \begin{bmatrix}\mathbf{U}_s^e\\ \mathbf{\Phi}^e\end{bmatrix}$

Table D.2: Definition of elementary matrices in the formulation in $(\mathbf{u}_s, \phi)$

Option	Formulation in $(\mathbf{u}_s, p, \varphi)$		
	Structural part	Fluid part	Interface fluid-structure
MASS_MECA	$\mathbf{M}_s^e \begin{bmatrix}\mathbf{U}_s^e\end{bmatrix}$	$\begin{bmatrix}\mathbf{0} & \mathbf{M}_f^e\\ \mathbf{M}_f^e & -\rho_0\mathbf{K}_f^e\end{bmatrix} \begin{bmatrix}\mathbf{P}^e\\ \boldsymbol{\varphi}^e\end{bmatrix}$	$\begin{bmatrix}\mathbf{0} & \mathbf{0} & -\rho_0\mathbf{K}_c^e\\ \mathbf{0} & \mathbf{0} & \mathbf{0}\\ -\rho_0\mathbf{K}_c^{e,T} & \mathbf{0} & \mathbf{0}\end{bmatrix} \begin{bmatrix}\mathbf{U}_s^e\\ \mathbf{P}^e\\ \boldsymbol{\varphi}^e\end{bmatrix}$
RIGI_MECA	$\mathbf{K}_s^e \begin{bmatrix}\mathbf{U}_s^e\end{bmatrix}$	$\begin{bmatrix}\frac{1}{\rho_0}\mathbf{M}_f^e & \mathbf{0}\\ \mathbf{0} & \mathbf{0}\end{bmatrix} \begin{bmatrix}\mathbf{P}^e\\ \boldsymbol{\varphi}^e\end{bmatrix}$	$\mathbf{0}$
AMOR_MECA	$\mathbf{0}$	$\mathbf{0}$	$\mathbf{0}$

Table D.3: Definition of elementary matrices in the formulation in $(\mathbf{u}_s, p, \varphi)$

Now that we have redefined all elementary matrices for the operator CALC_MATR_ELEM, we can assemble the matrices for the new formulations with operator ASSE_MATRICE with the same approach as the formulation in $(\mathbf{u}_s, p, \varphi)$ and use the obtained results to compute the response in time-domain or frequency-domain with operator DYNA_VIBRA, or for the modal analysis with operator CALC_MODE.

Next, let us discuss on the impact of the modelling of the Sommerfeld radiation's condition by the BGT-1 method [22]. The computation of the elementary terms of the impedance matrix is done with the operation CALC_MATR_ELEM via option IMPE_MECA.

In the formulation in $(\mathbf{u}_s, p)$, the elementary terms of the impedance matrix is defined by $\frac{\rho_0}{Z}\mathbf{Q}^e \left[\mathbf{P}^e\right]$ (see Equation (1.41) for the definition of the impedance matrix $\mathbf{Q}$). To take into account the BGT-1 boundary condition (1.35) in the model, we start by computing the elementary terms of the impedance matrix of the elements on the truncated boundary Γ_∞, for the values $Z = Z_c = \rho_0 c_0$ and $Z = Z_R = \rho_0 R$. We recall that ρ_0 denotes the density of the fluid, c_0 denotes the speed of sound in the fluid and R denotes the radius of the truncated fluid domain. An assembling procedure are then performed in order to construct the following matrices:

$$\mathbf{I}_{up}^C := \begin{bmatrix} \mathbf{0} & \mathbf{0} \\ \mathbf{0} & \frac{\rho_0}{Z_C}\mathbf{Q} \end{bmatrix}, \mathbf{I}_{up}^R := \begin{bmatrix} \mathbf{0} & \mathbf{0} \\ \mathbf{0} & \frac{\rho_0}{Z_R}\mathbf{Q} \end{bmatrix}, \tag{D.1}$$

The matrix $\mathbf{I}_{up}^C$ represents the damping matrix $\mathbf{C}_{up}^{ext}$ in Equation (1.40). To obtain the matrix $\mathbf{K}_{up}^{ext}$ in Equation (1.40), it is sufficient to make an addition of the matrix $\mathbf{K}_{up}$ of Equation (1.38), which can be obtained by assembling the elementary stiffness matrices computed by the operator CALC_MATR_ELEM, with the matrix $\mathbf{I}_{up}^R$.

The same procedure holds for the case of the formulation in $(\mathbf{u}_s, \phi)$ and in $(\mathbf{u}_s, p, \varphi)$. In the formulation in $(\mathbf{u}_s, \phi)$, the elementary impedance matrix is defined by $-\frac{\rho_0^2}{Z}\mathbf{Q}^e \left[\mathbf{\Phi}^e\right]$. The matrices to be computed with an assembling procedure are given by:

$$\mathbf{I}_{u\phi}^C := \begin{bmatrix} \mathbf{0} & \mathbf{0} \\ \mathbf{0} & -\frac{\rho_0^2}{Z_C}\mathbf{Q} \end{bmatrix}, \mathbf{I}_{u\phi}^R := \begin{bmatrix} \mathbf{0} & \mathbf{0} \\ \mathbf{0} & -\frac{\rho_0^2}{Z_R}\mathbf{Q} \end{bmatrix}, \tag{D.2}$$

To obtain the matrix $\mathbf{C}_{u\phi}^{ext}$ and $\mathbf{K}_{u\phi}^{ext}$ in Equation (1.46), we make an addition of the matrix $\mathbf{C}_{u\phi}$ and $\mathbf{K}_{u\phi}$ of Equation (1.44) with $\mathbf{I}_{u\phi}^C$ and $\mathbf{I}_{u\phi}^R$, respectively.

For the formulation in $(\mathbf{u}_s, p, \varphi)$ which is the only formulation already implemented in the official version of *code_aster*, the elementary impedance matrix is defined by $\begin{bmatrix} \mathbf{0} & \mathbf{0} \\ \mathbf{0} & -\frac{\rho_0^2}{Z}\mathbf{Q}^e \end{bmatrix} \begin{bmatrix} \mathbf{P}^e \\ \boldsymbol{\varphi}^e \end{bmatrix}$. The matrices to be computed with an assembling procedure are given by:

$$\mathbf{I}_{up\varphi}^C := \begin{bmatrix} \mathbf{0} & \mathbf{0} & \mathbf{0} \\ \mathbf{0} & \mathbf{0} & \mathbf{0} \\ \mathbf{0} & \mathbf{0} & -\frac{\rho_0^2}{Z_C}\mathbf{Q} \end{bmatrix}, \mathbf{I}_{up\varphi}^R := \begin{bmatrix} \mathbf{0} & \mathbf{0} & \mathbf{0} \\ \mathbf{0} & \mathbf{0} & \mathbf{0} \\ \mathbf{0} & \mathbf{0} & -\frac{\rho_0^2}{Z_R}\mathbf{Q} \end{bmatrix}, \tag{D.3}$$

The matrix $\mathbf{I}_{up\varphi}^C$ represents the matrix $\mathbf{I}_{up\varphi}^{ext}$ in Equation (1.51). To obtain the matrix $\mathbf{M}_{up\varphi}^{ext}$ in Equation (1.51), we make an addition of the matrix $\mathbf{M}_{up\varphi}$ of Equation (1.49) with $\mathbf{I}_{u\phi}^R$.

To obtain the damping matrix $\mathbf{C}_{up\varphi}^{ext}$ in Equation (1.53), we also developed in the branch of the formulation in $(\mathbf{u}_s, p, \varphi)$ an other option, namely IMPE_MECA_NEW, in the operator CALC_MATR_ELEM, for computing the elementary matrix:

$$\begin{bmatrix} \mathbf{0} & \mathbf{0} \\ \frac{\rho_0}{Z}\mathbf{Q}^e & \mathbf{0} \end{bmatrix} \begin{bmatrix} \mathbf{P}^e \\ \boldsymbol{\varphi}^e \end{bmatrix} \tag{D.4}$$

which allows us to obtain directly the non-symmetric matrix $\mathbf{C}_{up\varphi}^{ext}$, by setting $Z = Z_C = \rho_0 c_0$, after the assembling procedure.

D.2 Implementation of the reduced order modelling techniques in *code_aster*

Some new operators are developed in the context of the proposed reduced order modelling techniques. They can be distinguished in two main categories. The first category refers to all the operators whose the definition are different in each formulation, such as:

- DEFI_BASE_REDUITE: which computes the reduced basis. For this operator, we developed three main options: GLOUTON, POD and CONCATENATION. The option GLOUTON refers to the construction of the reduced basis based on the corresponding frequency domain. In this option, the Classical Greedy Algorithm 1 is implemented for the formulation in $(\mathbf{u}_s, \phi)$. The modified greedy algorithms 2 and 3 are implemented for the formulation in $(\mathbf{u}_s, p)$ and $(\mathbf{u}_s, p, \varphi)$, respectively. For the option «POD», the computation of the reduced basis with Algorithm 6 is implemented for the formulation in $(\mathbf{u}_s, \phi)$. In this option, we begin by computing the reduced basis for the fluid part $\mathbf{V}_f$ and the structure part $\mathbf{V}_s$ respectively by Algorithm 6 before transforming them into the output reduced basis in form $\begin{bmatrix} \mathbf{V}_s & \mathbf{0} \\ \mathbf{0} & \mathbf{V}_f \end{bmatrix}$ for the formulation in $(\mathbf{u}_s, p)$ and into the output reduced basis in form $\begin{bmatrix} \mathbf{V}_s & \mathbf{0} & \mathbf{0} \\ \mathbf{0} & \mathbf{V}_f & \mathbf{0} \\ \mathbf{0} & \mathbf{0} & \mathbf{V}_f \end{bmatrix}$ for the formulation in $(\mathbf{u}_s, p, \varphi)$. At the end, the same concatenation procedure of two basis with Algorithm 11 is implemented for the option «CONCATENATION» for each formulation.

- PROD_MATR_BASE and PROD_VECT_BASE: which compute the reduced matrix and the reduced vector, respectively. For the formulation in $(\mathbf{u}_s, p)$ and $(\mathbf{u}_s, p, \varphi)$, the reduced matrix or the reduced vector are always computed by mean of Galerkin projection. For the formulation in $(\mathbf{u}_s, \phi)$, we also allow the case of the Petrov-Galerkin projection as in Lemma 3.2.2, via a keyword STABILISE_IFS, in order to stabilize the time-domain reduced order model.

The second category refers to all the operators which are common for each formulation, such as:

- COMB_VECT_GENE and COMB_MATR_ASSE: which allow us make a linear combination of the reduced vectors and the reduced matrices, respectively.

- CALC_DONNEE_RESI: which computes the required data for an online-efficient evaluation of the error indicator based on the norm of residual. In this operator, we also developed an option to make a linear combination of the results previously computed by this operator.

- DYNA_TRAN_EMPI: which takes as input the reduced mass, stiffness, damping matrix and the reduced vector and solve the corresponding reduced order model. In this operator,

we also introduce an option to compute the value of error indicator based on the norm of the residual.

- CALC_RESU_MOR: which takes as input the data provided by DYNA_TRAN_EMPI and a reduced vector (case linear) or a reduced matrix (case quadratic) and computes the physical output of interest predicted by the reduced order model.
- CALC_EIM: which computes the magical indices and the values of the parameters chosen by the Greedy EIM algorithm 17 (for the case of vector) and the Greedy EIM algorithm 19 (for the case of matrix).
- DEFI_DOMAINE_REDUIT_EIM: which takes as input the data computed by CALC_EIM and creates, in the given mesh, a group of the reduced elements chosen by Algorithm 18 for the case of vector and Algorithm 20 for the case of matrix.
- CALC_COEF_EIM: which computes the coefficients $(\theta_l^A(\boldsymbol{\mu}))_{1\leq l\leq N_A^{EIM}}$ or $(\theta_l^F(\boldsymbol{\mu}))_{1\leq l\leq N_F^{EIM}}$ in the approximation by EIM as in Equation (5.21).

We have also introduced some developments in the operator CALC_MATR_ELEM. In this operator, we add a new keyword GROUP_MA which allows us to compute the elementary contribution only on the given group of elements, for instance the reduced elements in the context of EIM approximation with a purely algebraic and black box way as presented in Section 5.2.4.

Bibliography

[1] N. Abdelmalek. Round off error analysis for Gram-Schmidt method and solution of linear least squares problems. *BIT 11 (1971), 345-368.*

[2] M. Abramowitz, I. A. Stegun. Handbook of mathematical functions. *Dover (1970)*

[3] B. O. Almroth, P. Stern, and F. A. Brogan. Automatic choice of global shape functions in structural analysis. *AIAA Journal, 16:525-528, May 1978.*

[4] D. Amsallem, C. Farhat, An online method for interpolating linear parametric reduced-order models. *SIAM J Sci Comput. 2011;33(5):2169-98.*

[5] D. Amsallem, C. Farhat, Interpolation method for adapting reduced-order models and application to aeroelasticity. *AIAA J. 2008;46(7):1803-13.*

[6] D. Amsallem, J. Cortial, K. Carlberg, and C. Farhat, A method for interpolating onmanifolds structural dynamics reduced-order models, *Internat. J. Numer. Methods Engrg.,80 (2009), pp. 1241-1258.*

[7] D. Amsallem, C. Farhat, Stabilization of projection-based reduced-order models. and model reduction. *International Journal for Numerical Methods in Engineering 2012; 91:358-377.*

[8] D. Amsallem, B. Haasdonk, PEBL-ROM: Projection-error based local reduced-order models. *Advanced Modeling and Simulation in Engineering Sciences 2016; 3(1):6.*

[9] R. J. Astley, G. J. Macaulay, J. P. Coyette, L. Cremers, Three-dimensional wave-envelope elements of variable order for acoustic radiation and scattering. Part I. Formulation in the frequency domain, *J. Acoust. Soc. Am. 103 (1) (1998) 49-63.*

[10] R. J. Astley, J. P. Coyette, L. Cremers, Three-dimensional wave-envelope elements of variable order for acoustic radiation and scattering. Part II. Formulation in the time domain, *J. Acoust. Soc. Am. 103 (1) (1998) 64-72.*

[11] R. J. Astley, J. A. Hamilton, The stability of infinite element schemes for transient wave problems, *Comput. Methods Appl. Mech. Engrg. 195 (29-32) (2006) 3553-3571.*

[12] N. Aubry, P. Holmes, J. Lumley, and E. Stone, The dynamics of coherent structures in the wall region of a turbulent boundary layer, *J. Fluid Mech.192(1988), no. 115, 173355.*

[13] Z. Bai, Y. Su, Dimension Reduction of Large-Scale Second-Order Dynamical Systems via a Second-Order Arnoldi Method, *SIAM J. Sci. Comput., 26(5), 1692-1709.*

[14] Z. Bai, Krylov subspace techniques for reduced-order modeling of large-scale dynamical systems, *PhD thesis, Univ. of Illinois, Urbana-Champaign, (1997).*

[15] Z. Bai and Y. Su, Structure-Preserving Model Reduction Using a Krylov Subspace Projection Formulation , *Commun. Math. Sci. Volume 3, Number 2 (2005), 179-199.*

[16] T. Baker, Mesh movement and metamorphosis. *Engrg. Comput.18(3), 188–198 (2002)*

[17] M. Barrault, Y. Maday , N. C. Nguyen, and A. T. Patera. An empirical interpolation method: application to efficient reduced-basis discretization of partial differential equations. *Comptes Rendus Mathematique, 339(9):667-672 (2004)* .

[18] A. Barrett and G. Reddien. On the reduced basis method. *Z. Angew. Math. Mech., 75(7):543-549, 1995.*

[19] J. L. Batoz, G. Dhatt. Modeling of the structures by finite elements. *Volume 1, Hermes Edition (1990)*

[20] J. L. Batoz, G. Dhatt. Modélisation des structures par éléments finis. Volume 2 - poutres et plaques. *HERMES, PARIS, 1990*

[21] J. L. Batoz, G. Dhatt. Modélisation des structures par éléments finis. Volume 3, Coques. *HERMES, PARIS, 1992*

[22] A. Bayliss, M. Gunzburger, E. Turkel, Boundary Conditions for the Numerical Solution of Elliptic Equations in Exterior Regions, *SIAM J. Appl. Math., 42(2), 430-451.*

[23] J. P. Berenger, A perfectly matched layer for the absorption of electromagnetic waves, *J. Comput. Phys. 114 (2) (1994) 185-200.*

[24] P. Binev, A. Cohen, W. Dahmen, R. DeVore, G. Petrova, and P. Wojtaszczyk. Convergence rates for greedy algorithms in reduced basis methods. *SIAM J. Math. Anal., 43(3):1457-1472, 2011.*

[25] B. Bond, L. Daniel, Guaranteed stable projection-based model reduction for indefinite and unstable linear systems. *Proceedings of the 2008 IEEE/ACM International Conference on Computer-Aided Design, San Jose, California, USA, 2008; 728-735.*

[26] D. Bonomi, A. Manzoni and A. Quarteroni, A matrix discrete empirical interpolation method for the efficient model reduction of parametrized non-linear PDEs: application to non-linear elasticity problems. *in MATHICSE Technical Report, EPFL, 2016.*

[27] M. Bordiec, Réduction de modèles pour les problèmes vibro-acoustique transitoires, *Mémoire de Master 2, Université de Nantes, Naval Group Research (2017).*

[28] K. Brochard, Modélisation analytique de la réponse d'un cylindre immergé à une explosion sous-marine. *PhD Thesis, Ecole Centrale de Nantes, (2018).*

[29] D. S. Burnett, A three-dimensional acoustic infinite element based on a prolate spheroidal multipole expansion, *J. Comput. Phys. 114 (2) (1994) 185-200.*

[30] N. Cagniart, Y. Maday, and B. Stamm. Model order reduction for problems with large convection effects. *Preprint hal-01395571, HAL, 2016. Available from https://hal.archives-ouvertes.fr.*

[31] F. Casenave, Accurate a posteriori error evaluation in the reduced basis method. *C. R. Math. Acad. Sci. Paris 350 (2012) 539-542.*

[32] F. Casenave, A. Ern, and T. Lelièvre, Accurate and online-efficient evaluation of the a posteriori error bound in the reduced basis method,*ESAIM Math. Model. Numer. Anal.,48 (2014), pp. 207-229.*

[33] F. Casenave, A. Ern, T. Lelièvre, A nonintrusive reduced basis method applied to aeroacoustic simulations, *Advances in Computational Mathematics 41 (5) (2015) 961-986.*

[34] A. Castagnotto and A. Lohmann, A new framework for h2-optimal model reduction, *Mathematical and Computer Modelling of Dynamical Systems, pages 1-22, 2018.*

[35] Rachida Chakir, Charles Dapogny, Caroline Japhet, Yvon Maday, Jean-Baptiste Montavon, Olivier Pantz and Anthony Patera, Component Mapping Automation for Parametric Component Reduced Basis Techniques (RB-Component). `https://hal-univ-paris13.archives-ouvertes.fr/hal-01736669/document`

[36] Y. Chahlaoui, D. Lemonnier, A. Vandendorpe, P. Van Dooren, Second-order balanced truncation, *Linear Algebra and its Applications 415 (2006) 373-384.*

[37] S. Chaturantabut, D. Sorensen, Nonlinear model reduction via discrete empirical interpolation, *SIAM J. Sci. Comput.32 (5) (2010) 2737-2764.*

[38] Yanlai Chen, Jan S. Hesthaven, Yvon Maday, Jeromino Rodriguez, Certified reduced basis methods and output bounds for the harmonic Maxwell's equations, *SIAM J. Sci. Comput., 32(2), 970-996.*

[39] A. Cohen, R. DeVore, Kolmogorov widths under holomorphic mappings, *IMA Journal of Numerical Analysis, (2015).*

[40] R. H. Cole, Underwater Explosions. *NJ, USA : Princeton University Press (1948)*

[41] A. Cosimo, A. Cardona and S. Idelsohn. General treatment of essential boundary conditions in reduced order morels for non-linear problems. *Advanced Modeling and Simulation in Engineering Sciences 3 (1) (2016) 3:7*

[42] Frederick A. Costanzo, Underwater Explosion Phenomena and Shock Physics, *Proceedings of the IMAC-XXVIII, Florida USA, February 2010.*

[43] N. Dal Santo, A. Manzoni, Hyper-reduced order models for parametrized unsteady Navier-Stokes equations on domains with variable shape, *in MOX-Report No.07, 2019.*

[44] J. W. Daniel, W. B. Gragg, L. Kaufman and G. W. Stewart. Re-orthogonalization and Stable Algorithms for Updating the Gram-Schmidt QR Factorization. *Math. Comp. 30 (1976), 772-795.*

[45] Achiya Dax. A modified Gram-Schmidt algorithm with iterative orthogonalization and column pivoting. *Linear Algebra and its Applications 310 (2000) 25-42*

[46] J. Degroote, J. Vierendeels, and K. Willcox, Interpolation among reduced-order matri-ces to obtain parameterized models for design, optimization and probabilistic analysis, *Internat. J. Numer. Methods Fluids, 63 (2010), pp. 207-230*

[47] F. R. de Hoog, J. H. Knight, A. N. Stokes, An Improved Method for Numerical Inversion of Laplace Transforms. *SIAM J. Sci. and Stat. Comput., 3(3), 357-366.*

[48] M. Dihlmann, M. Drohmann, B. Haasdonk, Model reduction of parametrized evolution problems using the reduced basis method with adaptive time-partitioning. *Proceedings of ADMOS 2011, V International Conference on Adaptive Modeling and Simulation, 2011.*

[49] M. Dihlmann and B. Haasdonk. Certified PDE-constrained parameter optimization using reduced basis surrogate models for evolution problems problems. *Submitted to the Journal of Computational Optimization and Applications, 2013.*

[50] G. Duan. Analysis and Design of Descriptor Linear Systems.*Springer: New York, 2010.*

[51] A. Ern and J.-L. Guermond. Theory and Practice of Finite Elements. *vol. 159 of Applied Mathematical Series, Springer, New York, 2004*

[52] Electricité de France. Finite element *code_aster*, Analyses de Structures Thermo-Élastiques pour des Etudes et des Recherches. *Open source on www.code-aster.org, 1989-2020.*

[53] G. C. Everstine, A symmetric potential formulation for fluid-structure interaction, *Journal of Sound and Vibration (1981) 79(l), 157-16.*

[54] G. C. Everstine, Finite element formulations of structural acoustics problems, *Computers & Structure Vol. 65, No.3, pp. 307-321, 1997.*

[55] T. E. Farley, H. G. Snay, Unclassified data from classified source. In Explosions Effects and Properties : Part II Explosion Effect in Water. *Edited by M.M. Swisdak (1978).*

[56] Lambert Fick, Yvon Maday, Anthony T. Patera, Tommaso Taddei, A Reduced Basis Technique for Long-Time Unsteady Turbulent Flows, *Journal of Computational Physics, October 2017.*

[57] J. Gain and D. Bechmann. A survey of spatial deformation from a user-centered perspective. *ACM Trans. Graph., 27(4):107:1-107:21, 2008.*

[58] M. Géradin and D. Rixen. Théorie des vibrations - application à la dynamique des structures. *Masson, 1997.*

[59] L. Giraud, J. Langou and M. Rozloznik. On the round-off error analysis of the Gram-Schmidt algorithm with re-orthogonalization. *CERFACS Technical Report No. TR/-PA/02/33.*

[60] G. Golub, C. Van Loan, Matrix Computations, *Baltimore: Johns Hopkins University Press (4 edition).*

[61] M. Grepl, Y. Maday, N. Nguyen, and A.T. Patera. Efficient reduced-basis treatment ofnonaffine and nonlinear partial differential equations. *Esaim Math. Model. Numer. Anal.,41(3):575-605, (2007)*

[62] M. A. Grepl, A. T. Patera, A Posteriori error bounds for reduced-basis approximations of parametrized parabolic partial differential equations. *M2AN (Math. Model. Numer. Anal.) 39(1), 157-181 (2005)*

[63] S. Gugercin, C. Beattie, and A. C. Antoulas, H2 model reduction for large-scale linear dynamical systems, *Siam J. Matrix Anal. Appl., 30(2):609-638, 2008*

[64] B. Haasdonk and M. Ohlberger. Reduced basis method for finite volume approximations of parametrized linear evolution equations. *ESAIM: Mathematical Modelling and Numerical Analysis-Modélisation Mathématique et Analyse Numérique, 42(2):277-302, 2008.*

[65] B. Haasdonk. Convergence rates of the POD-greedy method. *Technical Report 23, SimTech Preprint 2011, University of Stuttgart, 2011.*

[66] B. Haasdonk, Reduced Basis Methods for Parametrized PDEs. A Tutorial Introduction for Stationary and Instationary Problems.

[67] I. Harari, R. Djellouli, Analytical study of the effect of wave number on the performance of local absorbing boundary conditions for acoustic scattering, *Applied Numerical Mathematics 50 (2004) 15-47.*

[68] B. Helenbrook, Mesh deformation using the biharmonic operator. *Int. J. Numer. Methods Engrg.56(7), 1007-1021 (2003)*

[69] C. Himpe, T. Leibner, and S. Rave,Hierarchical Approximate Proper Orthogonal Decomposition, *preprint,* `https://arxiv.org/abs/1607.05210v3`, *2017.*

[70] W. Hoffmann. Iterative Algorithms for Gram-Schmidt Orthogonalization. *Computing 41 (1989), 335-348.*

[71] H. Hotelling. Analysis of a complex of statistical variables into principal components. *The Journal of educational psychology, pages 498-520, 1933.*

[72] Thomas J. R. Hughes. The Finite element method : linear static and dynamic finite element analysis. *Prentice-Hall, 1987.*

[73] D. B. P. Huynh and A. T. Patera, Reduced basis approximation and a posteriori error estimation for stress intensity factors. *Int J Numer Methods Eng 72(10):1219-1259*

[74] P. S. Johansson, H. I. Andersson, and E. M. Rønquist. Reduced-basis modeling of turbulent plane channel flow. *Compu. Fluids, 35(2):189-207, 2006.*

[75] W. Johnson, A. Poyton, H. Singh, F. W. Travis, Experiments in the underwater explosion stretch forming of clamped circular blanks. *Int. J. Mech. Sci., 8, 237-270 (1966)*

[76] I. Kalashnikova, B. van Bloemen Waanders, S. Arunajatesan, M. Barone, Stabilization of projection-based reduced order models for linear time-invariant systems via optimization-based eigenvalue reassignment. *Computer Methods in Applied Mechanics and Engineering 2014; 272:251-270.*

[77] K. Karhunen. Zur spektral theorie stochastischer prozesse. *Suomalainen tiedeakatemia, 1946.*

[78] J. B. Keller, D. Givoli, Exact non-reflecting boundary conditions, *J. Comput. Phys. 82 (1) (1989) 172-192.*

[79] A. Kolmogoroff, über die beste Annäherung von Funktionen einer gegebenen Funktionenklasse, *Anals of Math.37(1963), 107-110.*

[80] K. Kunisch and S. Volkwein, Galerkin proper orthogonal decomposition methods for parabolic problems. *Numer. Math.90(2001) 117-148.*

[81] P. Kurschner, Balanced truncation model order reduction in limited time intervals for large systems. *Advances in Computational Mathematics (2018) 1-24*

[82] C. Leblond, Modélisation de phénomènes fortement instationnaires en milieux couplés. Application au dimensionnement de structures immergées aux explosions sous-marines. *Thèse de doctorat de l'université de Nantes, (2007).*

[83] C. Leblond, J.-F. Sigrist, A reduced basis approach for the parametric low frequency response of submerged viscoelastic structures, *Finite Elements in Analysis and Design 119 (2016) 15-29.*

[84] C. Leblond, M. Abbas, J. Vernet-Castex, S. Prigent, J.-F. Sigrist, Application de la méthode de Base Réduite pour la réponse vibroacoustique de structures immergées avec paramètres incertains, *Conférence: CSMA 2017 - 13eme Colloque National en Calul des Structures.*

[85] C. Leblond, M. Chevreuil, C. Allery, C. Beghein, A Goal-oriented model reduction technique for parametric fluid-structure problems. *Conference: ECCM - ECFD 2018, Glasgow, UK*

[86] P. Le Tallec, Modélisation et calcul des milieux continus, *Edition de l'Ecole Polytechnique (2009).*

[87] M. Loève. Fonctions aléatoires de second ordre. *CR Acad. Sci. Paris, 220:380, 1945*

[88] Y. Maday, B. Stamm, Locally adaptive greedy approximations for anisotropic parameter reduced basis spaces. *SIAM J. Sci. Comput., 35 (2013), pp. A2417-A2441.*

[89] H. Maitournam, Matériaux et structures anélastiques, *Edition de l'Ecole Polytechnique (2017).*

[90] A. Manzoni, A. Quarteroni, and G. Rozza. Shape optimization of cardiovascular geometries byreduced basis methods and free-form deformation techniques. *Int. J. Numer. Methods Fluids,70(5):646-670, (2012).*

[91] A. Manzoni. An efficient computational framework for reduced basis approximation and a posteriori error estimation of parametrized Navier-Stokes flows. *ESAIM Math. Modelling Numer. Anal., 48(4):1199-1226, 2014.*

[92] A. Manzoni and F. Negri, Automatic reduction of PDEs defined on domains with variable shape, *in MATHICSE Technical Report, EPFL, 2016.*

[93] A. Manzoni and S. Pagani, A certified reduced basis method for PDE-constrained parametric optimization problems by an adjoint-based approach. *in MATHICSE Technical Report, EPFL, 2015.*

[94] M. Medvinsky, S. Tsynkov, E. Turkel, Direct implementation of high order BGT artificial boundary conditions, *Journal of Computational Physics Volume 376, 1 January 2019, Pages 98-128.*

[95] J. M. Melenk , On n-widths for elliptic problems, *Journal of mathematical analysis and applications ,247, 1, pp 272-289, 2000*

[96] B. Moore , Principal component analysis in linear systems: controllability, observability, and model reduction. *IEEE Transactions on Automatic Control 1981; 26:17-32.*

[97] H. J.-P. Morand, R. Ohayon, Fluid Structure Interaction: Applied Numerical Methods, *Wiley, 1995.*

[98] R. Mosquera R, A. Hamdouni, A. El Hamidi, C. Allery, POD basis interpolation via Inverse distance weighting on Grassmann manifolds. *Discr Contin Dyn Syst Series S. 2018;12(6):1743-59.*

[99] R. Mosquera R, A. Hamdouni, A. El Hamidi, A. Falaize, Generalization of the Neville-Aitken interpolation algorithm on Grassmann manifolds: applications to reduced order model. 2019. `https://arxiv.org/pdf/1907.02831.pdf.`

[100] F. Negri, A. Manzoni, and D. Amsallem. Efficient model reduction of parametrized systems by matrix discrete empirical interpolation. *J. Comp. Phys., 303:431-454, 2015.*

[101] Nathan M. Newmark, A method of computational for structural dynamics. *Journal of Engineering Mechanics Division ASCE, 85 :67-94, 1959.*

[102] A. K. Noor and J. M. Peters. Reduced basis technique for nonlinear analysis of structures. *AIAA Journal, 45(172):487-496, April 1980*

[103] S. Pagani, A. Manzoni, A. Quarteroni, Numerical approximation of parametrized problems in cardiac electrophysiology by a local reduced basis method. *Computer Methods in Applied Mechanics and Engineering. 2018;340:530-558.*

[104] B. N. Parlett. The Symmetric Eigenvalue Problem. *Englewood Cliffs, N.J., Prentice-Hall, pp. 105-109, 1980.*

[105] K. Pearson. On lines and planes of closest fit to systems of points in space. *The London, Edinburgh, and Dublin Philosophical Magazine and Journal of Science, 2(11):559-572, 1901.*

[106] R. S. Price, Similitude Equations for Explosives Fired Underwater. *Technical Report NSWC TR 80-299. NSWC. (1979)*

[107] A. Quarteroni, G. Rozza, and A. Manzoni. Certified reduced basis approximation for parametrized partial differential equations and applications. *Journal of Mathematics in Industry,1(1):1-49,2011*

[108] R. Rajendran, K. Narasimhan, Deformation and fracture behaviour of plate specimens subjected to underwater explosion. *a review. Int. J. Impact Eng., 32, 1945-1963 (2006).*

[109] Q. Rakotomalala, L. Khoun, C. Leblond and J.-F. Sigrist, An advanced semi-analytical model for the study of naval shock problems. *submitted to Journal of Sound and Vibration, 2020.*

[110] Werner C. Rheinboldt. On the theory and error estimation of the reduced basis method for multi-parameter problems. *Nonlinear Anal., 21(11):849-858, 1993*

[111] J. A. Samareh. A survey of shape parametrization techniques. *Technical Report NASA/CP-1999-209136, NASA, 1999.*

[112] R.-J. Scavuzzo, G.-D. Hill and P.-W. Saxe, The spectrum-dip effect of deck mounted systems. *Shock & Vibration 17, 55-69, 2010.*

[113] J. F. Sigrist, Fluid Structure Interaction: An Introduction to Finite Element Coupling, *Wiley, 2015.*

[114] H. G. Snay, Hydrodynamics of underwater explosion. In Symposium of naval hydrodynamics. *National Academy of Science, Washington D.C., (pp. 325-352) (1956).*

[115] K. Stein, T. Tezduyar, R. Benney, Mesh moving techniques for fluid-structure interactions with large displacements. *J. Appl. Mech.70(1), 58-63 (2003)*

[116] E. Swift, J. C. Decius, Measurement of bubble pulse phenomena. III. Radius and period studies. *In Underwater Explosion Research, Vol. II, Office of Naval Research, Washington D.C. Eds. G.K. Hartmann and E.G. Hill. (1947)*

[117] K. Stein, T. Tezduyar, R. Benney, Automatic mesh update with the solid-extension mesh moving technique. *Comput. Meth. Appl. Mech. Engrg.193(21), 2019-2032 (2004)*

[118] M. M. Swisdak, Explosion Effects and Properties : II - Explosion Effects in Water. *Naval Surface Warfare Center Report NSWC/WOL TR 76-116. (1978)*

[119] L. Silveira, M. Kamon, I. Elfadel, J. White, A coordinate-transformed Arnoldi algorithm for generating guaranteed stable reduced-order models of RLC circuits. *Proceedings of the 1996 IEEE/ACM International Conference on Computer-aided Design (CAD), San Jose, California, 1996; 228-294.*

[120] T. Tonn, Reduced-Basis Method (rbm) for Non-Affine Elliptic Parametrized PDEs (Motivated by Optimization in Hydromechnanics), *Ph.D. thesis, Ulm University, Germany, 2012.*

[121] A. van de Walle, F. Naets, E. Deckers, W. Desmet, Stability-preserving model-order reduction for time-domain simulation of vibro-acoustic FE models, *Internat. J. Numer. Methods Engrg. 109 (6) (2017) 889-912.*

[122] S. van Ophem, O. Atak, E. Deckers, W. Desmet, *Stable model order reduction for time-domain exterior vibro-acoustic finite element simulations*, CMAME 325 (2017), 240-264.

[123] K. Veroy, Reduced Basis Methods Applied to Problems in Elasticity : Analysis and Applications. *PhD thesis, Massachusetts Institute of Technology, 2003.*

[124] S. Veys, Un Framework de calcul pour la méthode des bases réduites : applications à des problèmes non-linéaire multi-physiques, *Thèse de doctorat de l'université de Grenoble, 2014.*

[125] Z. Wang, I. Akhtar, J. Borggaard, and T. Iliescu, Proper orthogonal decomposition closure models for turbulent flows: A numerical comparison. *Comput. Meth. Appl. Mech. Engrg.237-240(2012), 10-26.*

[126] S. Wyatt, Issues in Interpolatory Model Reduction: Inexact Solves,Second-order Systems and DAEs, *PhD thesis, Univ. Virginia, (2012).*

[127] O. C. Zienkiewicz, R. L. Taylor and J. Z. Zhu. The Finite Element Method: Its Basis and Fundamentals. *Elsevier Science:Oxford, 2005.*

Titre : Réduction de modèles pour les problèmes vibro-acoustique transitoires paramétriques - Application aux problèmes de pré-dimensionnement de structures immergées aux ondes de choc d'explosion.

Résumé : Dans cette thèse, nous développons une technique de réduction de modèles pour les problèmes vibro-acoustiques transitoires paramétriques dans un code de calcul par éléments finis industriel, *code_aster*, dans le but de traiter des problèmes de complexité industrielle. En particulier, l'approche est illustrée ici pour le problème du dimensionnement des structures immergées assujetties à une explosion sous-marine. Trois formulations du couplage vibro-acoustique sont considérées dans ce travail : formulation en déplacement structure - pression fluide (u_s, p), formulation en déplacement structure - potentiel de vitesse fluide (u_s, ϕ) et formulation en déplacement structure - potentiel de déplacement fluide - pression fluide (u_s, p, φ). Pour commencer, nous implémentons dans *code_aster* deux nouvelles formulations, les formulations en (u_s, p), et en (u_s, ϕ) ainsi que les chargements provenant d'une onde de choc. Ensuite, différentes techniques de stabilisation de modèles d'ordre réduit basé sur la projection de Petrov-Galerkin sont proposées. Selon les techniques de stabilisation proposées, nous ajoutons quelques modifications dans l'algorithme glouton et POD-Glouton classiques dans la construction de la base réduite. Nous traitons aussi le cas où la dépendance en paramètre n'est pas affine. Dans ce cas, nous proposons d'utiliser la Méthode d'Interpolation Empirique (EIM) de manière purement algébrique et en boite noire pour retrouver une approximation sous la forme affine en paramètre. Ce point est nécessaire dans la construction d'un procédure hors-ligne/enligne efficace pour assurer la performance des modèles d'ordre réduits dans la phase en ligne. Le cas où la géométrie de la structure est considérée comme un paramètre du problème est aussi abordé dans cette thèse. Dans ce cas, nous choisissons la méthode basée sur le déplacement d'un maillage au sens d'un solide déformable (SEMMT) pour paramétrer la variabilité de la forme de la structure. Quelques études numériques et les applications industrielles sont aussi présentées pour illustrer l'efficacité des techniques de réduction de modèles proposées.

Mots clés : Méthode des éléments finis, Couplage vibro-acoustique, Interaction de la structure immergée et l'onde de choc acoustique, Explosion sous-marine, Réduction de modèles, Méthode d'Interpolation Empirique (EIM), Technique de déplacement du maillage au sens d'un solide déformable (SEMMT), Algorithme POD-Glouton.

Title: Reduced order modelling for parametrized time-domain vibro-acoustic problems - Application to the design of structures subjected to underwater explosions.

Abstract: In this thesis, we developed a reduced order modelling framework for parametrized time-domain vibro-acoustic finite element model into an open-source industrial software, *code_aster*, with the aim of tackling large scale industrial problems. In particular, it is illustrated here for the design of submerged structures subjected to underwater explosion. Three formulations of vibro-acoustic coupling are considered in this work: formulation in structure displacement - fluid pressure - fluid displacement potential (u_s, p, φ), in structure displacement - fluid pressure (u_s, p), and in structure displacement - fluid velocity potential (u_s, ϕ). First, we implement with in *code_aster* two new formulations, in (u_s, p) and in (u_s, ϕ), and the excitation induced by the primary acoustic shock wave. Next, different stabilization techniques for Petrov-Galerkin projection based model order reduction are proposed for each formulation. According to the stabilization techniques in hand, we propose to make some modifications in the classical Greedy and POD-Greedy algorithm for the construction of the reduced basis. We deal both in the case of affine and non-affine parametrized problems. In the case of non-affine parametrized problem, we propose to exploit the Empirical Interpolation Method (EIM) in a purely algebraic and black box way for recovering an approximation with an affine parameter dependence. This is one of the main ingredients for the construction of an efficient offline/online decomposition procedure to ensure the performance of the reduced order models at the online stage. We also consider the case where the geometry of the structure domain represents the parameter of the problem, for which we chose to employ the Solid Extension Mesh Moving Technique (SEMMT) for parametrizing the varying shape domain (mesh). Some numerical studies and some industrial applications are also performed in order to illustrate the efficiency of the proposed reduced order modelling framework.

Keywords: Finite element method, Vibro-acoustic coupling, Interaction of submerged structure and acoustic shock wave, Underwater explosion, Model order reduction, Empirical Interpolation Method (EIM), Solid Extension Mesh Moving Technique (SEMMT), POD-Greedy Algorithm.